TSSM

Technical Summary

Supplementary Material

Coordinating Lead Authors:
Thomas F. Stocker (Switzerland), Qin Dahe (China), Gian-Kasper Plattner (Switzerland)

Lead Authors:
Lisa V. Alexander (Australia), Simon K. Allen (Switzerland/New Zealand), Nathaniel L. Bindoff (Australia), François-Marie Bréon (France), John A. Church (Australia), Ulrich Cubasch (Germany), Seita Emori (Japan), Piers Forster (UK), Pierre Friedlingstein (UK/Belgium), Nathan Gillett (Canada), Jonathan M. Gregory (UK), Dennis L. Hartmann (USA), Eystein Jansen (Norway), Ben Kirtman (USA), Reto Knutti (Switzerland), Krishna Kumar Kanikicharla (India), Peter Lemke (Germany), Jochem Marotzke (Germany), Valérie Masson-Delmotte (France), Gerald A. Meehl (USA), Igor I. Mokhov (Russian Federation), Shilong Piao (China), Venkatachalam Ramaswamy (USA), David Randall (USA), Monika Rhein (Germany), Maisa Rojas (Chile), Christopher Sabine (USA), Drew Shindell (USA), Lynne D. Talley (USA), David G. Vaughan (UK), Shang-Ping Xie (USA)

Contributing Authors:
Myles R. Allen (UK), Olivier Boucher (France), Don Chambers (USA), Jens Hesselbjerg Christensen (Denmark), Philippe Ciais (France), Peter U. Clark (USA), Matthew Collins (UK), Josefino C. Comiso (USA), Viviane Vasconcellos de Menezes (Australia/Brazil), Richard A. Feely (USA), Thierry Fichefet (Belgium), Gregory Flato (Canada), Jesús Fidel González Rouco (Spain), Ed Hawkins (UK), Paul J. Hezel (Belgium/USA), Gregory C. Johnson (USA), Simon A. Josey (UK), Georg Kaser (Austria/Italy), Albert M.G. Klein Tank (Netherlands), Janina Körper (Germany), Gunnar Myhre (Norway), Timothy Osborn (UK), Scott B. Power (Australia), Stephen R. Rintoul (Australia), Joeri Rogelj (Switzerland/Belgium), Matilde Rusticucci (Argentina), Michael Schulz (Germany), Jan Sedláček (Switzerland), Peter A. Stott (UK), Rowan Sutton (UK), Peter W. Thorne (USA/Norway/UK), Donald Wuebbles (USA)

Review Editors:
Sylvie Joussaume (France), Joyce Penner (USA), Fredolin Tangang (Malaysia)

This supplementary material should be cited as:
Stocker, T.F., D. Qin, G.-K. Plattner, L.V. Alexander, S.K. Allen, N.L. Bindoff, F.-M. Bréon, J.A. Church, U. Cubasch, S. Emori, P. Forster, P. Friedlingstein, N. Gillett, J.M. Gregory, D.L. Hartmann, E. Jansen, B. Kirtman, R. Knutti, K. Krishna Kumar, P. Lemke, J. Marotzke, V. Masson-Delmotte, G.A. Meehl, I.I. Mokhov, S. Piao, V. Ramaswamy, D. Randall, M. Rhein, M. Rojas, C. Sabine, D. Shindell, L.D. Talley, D.G. Vaughan and S.-P. Xie, 2013: Technical Summary Supplementary Material. In: *Climate Change 2013: The Physical Science Basis. Contribution of Working Group I to the Fifth Assessment Report of the Intergovernmental Panel on Climate Change* [Stocker, T.F., D. Qin, G.-K. Plattner, M. Tignor, S.K. Allen, J. Boschung, A. Nauels, Y. Xia, V. Bex and P.M. Midgley (eds.)]. Available from www.climatechange2013.org and www.ipcc.ch.

Table of Contents

TS.SM.1 Notes and Technical Details on Observed Global Surface Temperature Figures in the Summary for Policymakers – Figure SPM.1

Data and programming code (IDL) used to create Summary for Policymakers and Technical Summary figures originating from Sections 2.4 and 2.5 of Chapter 2 can be obtained from the IPCC WGI AR5 website www.climatechange2013.org.

TS.SM.1.1 Annual and Decadal Global Surface Temperature Anomalies – Figure SPM.1a

Global Mean Surface Temperature (GMST) anomalies as provided by the dataset producers are given normalized relative to a 1961–1990 climatology from the latest version (as at 15 March 2013) of three combined Land-Surface Air Temperature (LSAT) and Sea Surface Temperature (SST) datasets. These combined datasets and the corresponding colours used in Figure SPM.1a are:

HadCRUT4 (version 4.1.1.0) – black
NASA GISS – blue
NCDC MLOST (version 3.5.2) – orange.

An overview of methodological diversity between these three temperature datasets is provided in Table 2.SM.6 of the Supplementary Material to Chapter 2, and full comprehensive details on the construction process for these datasets are provided in the references cited in this table. For time-series of LSAT only, and SST only, the reader is referred to Figure TS.1.

For the decadal anomalies, 90% confidence intervals are shown for the HadCRUT4 dataset (based on Morice et al., 2012).

TS.SM.1.2 Maps of Observed Changes in Surface Temperature – Figure SPM.1b

Maps of observed changes in surface temperature are based on trends calculated from the 3 datasets listed above for the period 1901–2012. See the Supplementary Material of Chapter 2 for a detailed description of the methodology used for trend and uncertainty calculations (Section 2.SM.3.3). Trends have been calculated only for those grid boxes with greater than 70% complete records and more than 20% data availability in the first and last 10% of the time period. White areas indicate incomplete or missing data. Black plus signs (+) indicate grid boxes where trends are significant at the 2-tailed 10% significance level (i.e., a trend of zero lies outside the 90% confidence interval).

The Technical Summary provides maps for all 3 datasets (Figure TS.2), while the Summary for Policymakers provides a map based on NCDC MLOST only (Figure SPM.1b).

TS.SM.2 Notes and Technical Details on Observed Change in Precipitation Over Land Figures in the Summary for Policymakers – Figure SPM.2

Data and programming code (IDL) used to create Summary for Policymakers and Technical Summary figures originating from Sections 2.4 and 2.5 of Chapter 2 can be obtained from the IPCC WGI AR5 website www.climatechange2013.org.

TS.SM.2.1 Map of Observed Changes in Precipitation Over Land – Figure SPM.2

Maps of observed changes in annual precipitation over land show trends calculated from 3 datasets:

CRU TS 3.10.01 (updated from Mitchell and Jones, 2005)
GHCN V2 (updated through 2011; Vose et al., 1992)
GPCC V6 (Becker et al., 2013)

Trends in annual precipitation are expressed per decade, and are calculated for the time periods 1901–2010 and 1951–2010. See the Supplementary Material of Chapter 2 for a detailed description of the methodology used for trend and uncertainty calculations (Section 2.SM.3.3). Trends have been calculated only for those grid boxes with greater than 70% complete records and more than 20% data availability in first and last 10% of the time period. White areas indicate incomplete or missing data. Black plus signs (+) indicate grid boxes where trends are significant at the 2-tailed 10% significance level (i.e., a trend of zero lies outside the 90% confidence interval).

The Technical Summary provides maps for all 3 datasets (TS TFE.1, Figure 2), while the Summary for Policymakers provides a map based on GPCC only (Figure SPM.2).

TS.SM.3 Notes and Technical Details on Observed Indicators of a Changing Global Climate Figures for the Summary for Policymakers – Figure SPM.3

This material documents the provenance of the data and plotting procedures that were used to create Figure SPM.3 in the IPCC WGI Fifth Assessment Report. This figure is closely derived from Figure TS.1 and FAQ 2.1, Figure 2 (see Chapter 2 Supplementary Material Section 2.SM.5), but includes fewer observed indicators. In addition, Figure SPM.3 includes an estimate of uncertainty for those datasets where this is available and has been assessed, illustrated with shading. Figure SPM.3 includes datasets and parameters assessed in Chapters 3 (ocean heat content, sea level), and 4 (snow cover, sea ice).

TS.SM.3.1 Northern Hemisphere Spring Snow Cover – Figure SPM.3a

TS.SM.3.1.1 Datasets

Green: Northern Hemisphere annual March-April average snow-cover extent based on an updated series from Brown and Robinson (2011), 1922–2012.

Shaded uncertainty estimate indicated by the 95% confidence interval.

TS.SM.3.1.2 Plotting Techniques

Annual values are plotted.

TS.SM.3.2 Arctic Summer Sea Ice Extent – Figure SPM.3b

All datasets provide Arctic annual July-August-September average sea ice extent.

Green: Updated from Walsh and Chapman (2001). Annual values are from 1900–1978.

Blue: Hadley Centre Sea Ice and Sea Surface Temperature dataset (HadISST1.2) (Rayner et al., 2003). Annual values are from 1900–1939 and 1953–2012. Values are excluded for the period 1940–1952 because the available data showed no change. It was a period when *in situ* data were very sparse and the gaps were filled in for completeness with climatology. For this assessment, this was not considered sufficiently robust and therefore the data during the period were excluded from the time series.

Red: Bootstrap algorithm (SBA) applied to data from the Scanning Multichannel Microwave Radiometer (SMMR) (updated from Comiso and Nishio, 2008). Annual values are from 1979–2012.

Black: NASA Team algorithm (NT1) applied to data from the Special Sensor Microwave/Imager (SSM/I) (Cavalieri et al., 1984) – updated in Cavalieri and Parkinson (2012) and Parkinson and Cavalieri (2012). Annual values are from 1979–2011.

Yellow: Bootstrap algorithm (ABA) applied to data from the Advanced Microwave Scanning Radiometer - Earth Observing System (AMSR-E) (updated from Comiso and Nishio, 2008). Annual values are from 2002–2011.

Orange: Revised NASA Team algorithm (NT2) applied to data from the Advanced Microwave Scanning Radiometer - Earth Observing System (AMSR-E) (updated from Markus and Cavalieri, 2000). Annual values are from 2002–2011.

Uncertainty estimates for each data point in the plots have been calculated based on the interannual variability of the ice extents. The systematic errors are not considered because they are generally unknown and are expected to be approximately constant from one year to another and would not change the results of trend analyses significantly. The interannual variability of the extent and actual area of the sea ice cover during the satellite era (since 1979) can be quantified accurately because of global coverage at good temporal resolution and the high contrast in the signature of ice free and ice covered oceans. The uncertainty (shaded range) that is shown is 1 standard deviation of the more than 30 years of satellite data, assuming a Gaussian distribution. The standard deviation is calculated after the data have been linearly detrended.

For the pre-satellite data (pre 1979), the true interannual variability is not known because available data are sparse and limited to only a few locations. Based on the expected quality of the Walsh and Chapman (2001) data and because of the lack of a better procedure, we use 1.75 standard deviations for the period 1880 to 1952 when data were sparse and 1.5 standard deviation for the period 1953 to 1978 when significantly more data were available. For the HadISST1.2 data set, which includes both pre- and post-satellite data (Rayner et al., 2003), we use 1 standard deviation for the entire period since 1900, calculated after the data has been linearly detrended.

TS.SM.3.2.2 Plotting Techniques

Annual values are plotted.

TS.SM.3.3 Global Average Upper Ocean Heat Content – Figure SPM.3c

TS.SM.3.3.1 Datasets

All datasets provide global annual upper-ocean (0 to 700 m depth) heat content anomalies.

Blue: Updated from Palmer et al. (2007). Annual values are from 1950–2011.

Green: Updated from Domingues et al. (2008). Annual values, smoothed with a 3-year running mean, are from 1950–2011.

Yellow: Updated from Ishii and Kimoto (2009). Annual values are from 1950–2011.

Orange: Updated from Smith and Murphy (2007). Annual values are from 1950–2010.

Black: Updated from Levitus et al. (2012). Annual values are from 1955–2011.

Uncertainty estimates are as reported in the cited publications. These are one standard error of the mean, except for Levitus et al. (2012) which provide one standard deviation. No uncertainty estimate is available for Smith and Murphy (2007).

TS.SM.3.3.2 Plotting Techniques

The published ocean heat content anomaly datasets are relative to different climatological reference periods. Therefore, the datasets have been aligned in Figure SPM.3c for the period 2006–2010, five years that are well measured by Argo, and then plotted relative to the resulting mean of all curves for 1970, a time when the increasing availability of annual data from XBTs causes the uncertainty estimates to reduce considerably. Specifically the alignment procedure for Figure SPM.3c involved the following steps:

Obtain all five upper ocean heat content anomaly time series.
1. Recognize that all the time-series values are annual values, centered on the middle of calendar years.
2. Find the average value of each time series for the years 2006–2010.
3. Subtract the average 2006–2010 value for each time series from that specific time-series.
4. Find the value of each time series for the year 1970.
5. Average these five values from the year 1970.
6. Subtract this 1970 average value from all of the time-series.

TS.SM.3.4 Global Average Sea Level – Figure SPM.3d

TS.SM.3.4.1 Datasets

Black: Church and White (2011) tide gauge reconstruction. Annual values are from 1900–2009.

Yellow: Jevrejeva et al. (2008) tide gauge reconstruction. Annual values are from 1900–2002.

Green: Ray and Douglas (2011) tide gauge reconstruction. Annual values are from 1900–2007.

Red: Nerem et al. (2010) satellite altimetry. A 1-year moving average boxcar filter has been applied to give annual values from 1993–2009.

Shaded uncertainty estimates are one standard error as reported in the cited publications. The one standard error on the 1-year averaged altimetry data (Nerem et al., 2010) is estimated at ±1 mm, and thus considerably smaller than for all other datasets.

TS.SM.3.4.2 Plotting Techniques

The published Global Mean Sea Level (GMSL) datasets use arbitrary and different reference periods where they start from zero. Furthermore, the altimetry data begins only in 1993. Therefore, the datasets have been aligned in Figure SPM.3d to a common reference period of time using the following steps:

1. The longest running record (Church and White, 2011) is taken as the reference to which all other datasets are aligned.
2. GMSL from Church and White (2011) is calculated relative to the average for the period 1900–1905, and the resulting value for the year 1993 (127 mm) is identified.
3. All other records are then adjusted to give the same value of 127 mm in 1993 (i.e., for each dataset the offset required to give 127 mm in 1993 is applied to all annual values in that dataset).

TS.SM.4 Notes and Technical Details on Observed Changes in the Global Carbon Cycle Figures in the Summary for Policymakers – Figure SPM.4

TS.SM.4.1 Atmospheric Concentrations of Carbon Dioxide – Figure SPM.4a

The top panel of Figure TS.5, and panel (a) of Figure SPM.4 show time series of atmospheric concentrations of carbon dioxide (CO_2). CO_2 concentrations are expressed as a mole fraction in dry air, micromol/mol, abbreviated as ppm. Time series are shown for the Mauna Loa Observatory (red in Figure SPM.4a), and South Pole (black in Figure SPM.4a). Data were accessed from the following sources (active at the time of publication):

1. Mauna Loa Observatory
   ftp://ftp.cmdl.noaa.gov/ccg/co2/trends/co2_mm_mlo.txt.

Monthly averages are plotted from March 1958 to August 2012. For further details on the measurements see Keeling et al. (1976a) and Thoning et al. (1989).

2. South Pole
   http://scrippsco2.ucsd.edu/data/flask_co2_and_isotopic/monthly_co2/monthly_spo.csv

Monthly averages are plotted from June 1957 to February 2012. For further details on the measurements see Keeling et al. (1976b; 2001).

TS.SM.4.2 Ocean Surface Carbon Dioxide and *In Situ* pH – Figure SPM.4b

The top panel of Figure TS.5, and panel (b) of Figure SPM.4 show time series of observed partial pressure of dissolved CO_2 (pCO_2 given in µatm) at the ocean surface, together with time series of ocean surface *in situ* pH (total scale). All ocean time series are plotted as 12-month running means (6 months before to 6 months after the sample date) for each 6-month period centered on 1 January and 2 July of each year. Data for both pCO_2 and *in situ* pH were measured at the following stations and obtained from the following sources (active at the time of publication):

1. Hawaii Ocean Time-Series program (HOT) from the station ALOHA (updated from, Dore et al., 2009)
   http://hahana.soest.hawaii.edu/hot/products/HOT_surface_CO2.txt

Shown as light green and light blue time series in Figure SPM.4b, for *in situ* pH and pCO_2 respectably. Data were plotted for the period 1988–2011.

Further technical details regarding the data are available from the readme file: http://hahana.soest.hawaii.edu/hot/products/HOT_surface_CO2_readme.pdf.

2. Bermuda Atlantic Time-Series Study (BATS): http://bats.bios.edu/bats_form_bottle.html

Shown as green and blue time series in Figure SPM.4b, for *in situ* pH and pCO_2, respectively, but not shown in Figure TS.5. Data were plotted for the period 1991 – 2011.

Measured dissolved inorganic carbon (DIC) and total alkalinity (TA) at *in situ* temperature were used to calculate pH on the total scale as well as pCO_2 in µatm.

Further technical details are described in Bates (2007).

3. European Station for Time series in the Ocean (ESTOC; see González-Dávila and Santana-Casiano, 2009): http://cdiac.ornl.gov/ftp/oceans/ESTOC_data

Shown as dark green and dark blue time series in Figure SPM.4b, for *in situ* pH and pCO_2, respectively, but not shown in Figure TS.5. Data were plotted for the period 1996–2009.

Further technical details regarding the data are available from González-Dávila (2010).

Note that the data for Figure SPM.4 (and Figure TS.5) provided at the external sources cited above may be subject to revision based on recalibration, and other quality control procedures conducted over time by the data providers.

TS.SM.5 Notes and Technical Details on Radiative Forcing Estimates Figure in the Summary for Policy Makers – Figure SPM.5

This material documents the underlying traceability for values that were used to create Figure SPM.5 in the IPCC WG1 Fifth Assessment Report. This figure is closely related to Figures TS.6 and TS.7 and Chapter 8, Figures 8.14 to 8.18. The reader is therefore referred to the Supplementary Material of Chapter 8 for detailed information on methods and sources used to estimate forcing values.

Figure SPM.5 (and Figure TS.7) plots Radiative Forcing (RF) estimates in 2011 relative to 1750 and aggregated uncertainties for the main drivers of climate change. This figure is different from similar figures shown in previous IPCC report SPMs (though an analogous figure was shown in Chapter 2 of AR4) as it evaluates the RF based on the emissions rather than the concentration changes. An emitted compound changes the atmospheric concentration of the same substance but may also impact that of other atmospheric constituents through chemistry processes.

Values are global average RF, partitioned according to the emitted compounds or processes that result in a combination of drivers. In calculations of RF for well-mixed greenhouse gases and aerosols in this report, physical variables, except for the ocean and sea ice, are allowed to respond to perturbations with rapid adjustments. The resulting forcing is called Effective Radiative Forcing (ERF) in the underlying report. For all drivers other than well-mixed greenhouse gases and aerosols, rapid adjustments are less well characterized and assumed to be small, and thus the traditional RF is used.

The ‘level of confidence’ given in Figure SPM.5 is based on Table 8.5.

For the main emitted compounds of CO_2, CH_4, Halocarbons, N_2O, CO, NMVOC and NO_x, the underlying values, their sources, and uncertainties can be found in the Chapter 8 Supplementary Material, Tables 8.SM.6 and 8.SM.7.

The value of –0.27 W m^{-2} for aerosols and precursors shown in Figure SPM.5 results from –0.35 W m^{-2} from RFari (Table 8.6) with the addition of 0.04 W m^{-2} from BC-on-snow and the subtraction of the small nitrate contribution from NO_x of –0.04 W m^{-2} (Table 8.SM.6).

The value of –0.55 W m^{-2} for cloud adjustments due to aerosols given in Figure SPM.5 results from the combination of ERFaci –0.45 [–1.2 to 0.0] W m^{-2} and rapid adjustment of ari –0.1 [–0.3 to +0.1] W m^{-2} as reported in Figure TS.7. Detailed information can be found in Chapter 8 and the Chapter 8 Supplementary Material, Table 8.SM.6.

The values for albedo changes due to land use and changes in solar irradiance come from Table 8.6 of Chapter 8.

Total anthropogenic RF relative to 1750 is based on values given in Table 8.6 (for 2011) and Figure 8.18 (values for 1950 and 1980 given in the caption).

TS.SM.6 Notes and Technical Details on Comparison of Observed and Simulated Climate Change Figures for the Summary for Policymakers – Figure SPM.6

Figure SPM.6 and the related Figure TS.12 are reduced versions of Figure 10.21 in Chapter 10. The reader is therefore referred to the detailed description of the main components of Figure 10.21 for datasets and methods used (see the Chapter 10 Supplementary Material, Section 10.SM.1). Here, mainly the differences of Figure SPM.6 and TS.12 from Figure 10.21 are listed.

Figures SPM.6 and TS.12 show time series of decadal average, plotted on a common axis and at the centre of each decade. The decadal averages are taken from the annual time series that Figure 10.21 is based on. Figure TS.12 features the multi-model mean as dark blue and dark red line, while Figure SPM.6 only features the 5–95% confidence interval. Note that the precipitation plot from Figure 10.21 are not included in the Technical Summary and SPM versions of this figure.

TS.SM.6.1 Continental Temperatures

The same model simulations and observational data sets are used as for Figure 10.21. Continental land areas are based on the IPCC Special Report on Managing the Risks of Extreme Events and Disasters to Advance Climate Change Adaptation (SREX) defined regions (IPCC, 2012) shown pictorially in the bottom right most panel of Figure 10.7. Temperature anomalies in Figure SPM.6 are with respect to 1880–1919 (except for Antarctica where anomalies are relative to 1950–2010).

TS.SM.6.2 Ocean Heat Content

The same model simulations and observational data sets are used as for Figure 10.21.

TS.SM.6.3 Sea Ice

The same model simulations and observational data sets are used as for Figure 10.21.

TS.SM.6.4 Data Quality

For land and ocean surface temperatures panels, solid lines indicate where data spatial coverage of areas being examined is above 50% coverage and dashed lines where coverage is below 50%. For example, data coverage of Antarctica never goes above 50% of the land area of the continent. For ocean heat content and sea-ice panels, the solid line is where the coverage of data is good and higher in quality, and the dashed line is where the data coverage is only adequate, based respectively on the spatial coverage and instrument type and on the presence of satellite measurements.

TS.SM.7 Notes and Technical Details on CMIP5 Simulated Time Series Figures in the Summary for Policymakers – Figure SPM.7

This material documents the provenance of the data and plotting procedures that were used to create Figure SPM.7, based on Climate Model Intercomparison Project Phase 5 (CMIP5) model results as of March, 2013. This figure is closely derived from Figures 12.5 and TS.15 (global average surface temperature), 12.28 and TS.17 (sea ice), 6.28 and TS.20a (ocean surface pH), but includes fewer model scenarios. The reader is referred to the Technical Summary and the Chapters 12 and 6 where all RCP scenarios are given for the respective quantity.

TS.SM.7.1 Global Average Surface Temperature Change (Figure SPM.7a) and Global Ocean Surface pH (Figure SPM.7c)

Step 1 – Analyzed simulations
The simulations considered are annual or monthly mean fields from different model simulations carried out as part of the CMIP5 project (when applicable the variable name as given in the CMIP5 archive is indicated in square brackets). The time series between 1850 and 2005 originate from the historical simulations. The two time series of the future projections are from RCP2.6 and RCP8.5. The box plots showing the change at the end of the century additionally use RCP4.5 end RCP6.0. Table TS.SM.1 lists the models and ensemble simulations used for panels (a) and panel (c). Only one ensemble simulation per model is used. All models are weighted equally except for sea ice (panel (b)) where a subset of models is considered.

Step 2a – Interpolation
For panel (a), the monthly temperature fields [tas] are re-gridded to a 2.5° × 2.5° grid using bilinear interpolation. No special treatment is used at the land-sea border.

For panel (c), the monthly temperature [tos] and salinity [sos] fields are first averaged to yield annual means. Then, annual-mean temperature, salinity, dissolved inorganic carbon [dissic] and alkalinity [talk] fields are re-gridded to a 1° × 1° using bilinear interpolation. For the model MIROC-ESM-CHEM the upper-most layers of the 3-dimensional fields of monthly sea water potential temperature [thetao] and monthly sea water salinity [so] are used.

Step 2b – Derivation of pH
For each model, surface pH was computed from simulated DIC, alkalinity, temperature, and salinity. Before computation each simulated input field was corrected for its decadal mean bias relative to modern observations, using the approach of Orr et al. (2005) and Orr (2011). That is, pH was computed after first removing from each model field, the average difference between the model mean during 1989–1998

Table TS.SM.1 | Models and ensembles used for panels (a) and (c).

Model	Ensemble Member	Historical	RCP2.6	RCP4.5	RCP6.0	RCP8.5
ACCESS1.0	r1i1p1	(a)		(a)		(a)
ACCESS1.3	r1i1p1	(a)		(a)		(a)
BCC-CSM1.1	r1i1p1	(a)	(a)	(a)	(a)	(a)
BCC-CSM1.1(m)	r1i1p1	(a)	(a)	(a)	(a)	
BNU-ESM	r1i1p1	(a)	(a)	(a)		(a)
CanESM2	r1i1p1	(a) (c)	(a) (c)	(a) (c)		(a) (c)
CCSM4	r1i1p1	(a)	(a)	(a)	(a)	(a)
CESM1(BGC)	r1i1p1	(a)		(a)		(a)
CESM1(CAM5)	r1i1p1	(a)	(a)	(a)	(a)	(a)
CMCC-CM	r1i1p1	(a)		(a)		(a)
CMCC-CMS	r1i1p1	(a)		(a)		(a)
CNRM-CM5	r1i1p1	(a)		(a)		(a)
CSIRO-Mk3.6.0	r1i1p1	(a)	(a)	(a)	(a)	(a)
EC-EARTH	r8i1p1	(a)	(a)	(a)		(a)

(continued on next page)

Table TS.SM.1 (continued)

Model	Ensemble Member	Historical	RCP2.6	RCP4.5	RCP6.0	RCP8.5
FGOALS-g2	r1i1p1	(a)	(a)	(a)		(a)
FIO-ESM	r1i1p1	(a)	(a)	(a)	(a)	(a)
GFDL-CM3	r1i1p1	(a)	(a)	(a)	(a)	(a)
GFDL-ESM2G	r1i1p1	(a) (c)	(a) (c)	(a) (c)	(a) (c)	(a) (c)
GFDL-ESM2M	r1i1p1	(a) (c)	(a) (c)	(a) (c)	(a) (c)	(a) (c)
GISS-E2-H	r1i1p1	(a)	(a)	(a)	(a)	(a)
GISS-E2-H	r1i1p2	(a)	(a)	(a)	(a)	(a)
GISS-E2-H	r1i1p3	(a)	(a)	(a)	(a)	(a)
GISS-E2-H-CC	r1i1p1	(a)		(a)		
GISS-E2-R	r1i1p1	(a)	(a)	(a)	(a)	(a)
GISS-E2-R	r1i1p2	(a)	(a)	(a)	(a)	(a)
GISS-E2-R	r1i1p3	(a)	(a)	(a)	(a)	(a)
GISS-E2-R-CC	r1i1p1	(a)		(a)		
HadGEM2-AO	r1i1p1	(a)	(a)	(a)	(a)	(a)
HadGEM2-CC	r1i1p1	(a) (c)		(a) (c)		(a)
HadGEM2-ES	r2i1p1	(a)	(a)	(a)	(a)	(a)
INM-CM4	r1i1p1	(a)		(a)		(a)
IPSL-CM5A-LR	r1i1p1	(a) (c)	(a) (c)	(a) (c)	(a) (c)	(a) (c)
IPSL-CM5A-MR	r1i1p1	(a) (c)	(a) (c)	(a) (c)	(a)	(a) (c)
IPSL-CM5B-LR	r1i1p1	(a) (c)		(a)		(a) (c)
MIROC5	r1i1p1	(a)	(a)	(a)	(a)	(a)
MIROC-ESM	r1i1p1	(a) (c)	(a) (c)	(a) (c)	(a)	(a) (c)
MIROC-ESM-CHEM	r1i1p1	(a) (c)	(a) (c)	(a) (c)	(a) (c)	(a) (c)
MPI-ESM-LR	r1i1p1	(a) (c)	(a) (c)	(a) (c)		(a) (c)
MPI-ESM-MR	r1i1p1	(a) (c)	(a) (c)	(a) (c)		(a) (c)
MRI-CGCM3	r1i1p1	(a)	(a)	(a)	(a)	(a)
NorESM1-M	r1i1p1	(a)	(a)	(a)	(a)	(a)
NorESM1-ME	r1i1p1	(a) (c)	(a)	(a) (c)	(a)	(a)

and the observational reference. For observed fields, the GLODAP gridded data product (Key et al., 2004) for DIC and alkalinity along with the 2009 World Ocean Atlas climatology for temperature, salinity, and concentrations of phosphate and silica (Locarnini et al., 2010; Antonov et al., 2010; Garcia et al., 2010) were used. Changes to the concentrations of phosphate and silica were assumed to be zero, because not all models provided those variables. pH was computed using routines based on the standard OCMIP carbonate chemistry adapted for earlier studies (Orr, 2011) to compute all carbonate system variables and use recommended constants from the Guide to Best Practices for Ocean CO_2 Measurements (Dickson et al., 2007).

Step 3 – Global and annual mean

The monthly (temperature) or annual (pH) surface fields are averaged (weighted by the cosine of the latitude) to obtain the global mean values. The monthly global mean temperature values are averaged to annual means.

Step 4 – Reference period

The average from 1986 to 2005 of the annual means for each model is computed and is subtracted from the respective model time series to obtain the corresponding temperature anomalies.

Step 5 – Mean and standard deviation

The mean and standard deviation over all the models is calculated. For the time period after 2006 all the possible models that are listed in Table TS.SM.1 are used. If a model provided several RCPs based on the same historical simulation, that historical simulation is counted only once.

Step 6 – Uncertainty estimates

First, for each model the average from 2081 to 2100 is computed from the above mentioned time series. Then, in a second step, the multi-model average and standard deviation over all model averages are calculated. The *likely* ranges on the right of the figure show the mean plus/minus 1.64 times the standard deviation across the model averages. The shading on the time series indicates the mean value plus/minus 1.64 times the standard deviation across the models for each year.

Step 7 – Graphical display

To close the multi-model mean time series at the year 2005 when the historical simulation ends and the RCP begins, the value at year 2005 is assigned to belong to both the historical time series and also to the corresponding RCP.

TS.SM.7.2 Northern Hemisphere September Sea Ice Extent – Figure SPM.7b

Step 1 – Analyzed simulations

Table TS.SM.2 provides the model and RIP ensemble member included from each RCP to create the multi-model mean time series of the NH September sea ice extent [sic] shown in Figure SPM.7b. In most cases, the first ensemble member (r1i1p1) was used. A selection algorithm produces a subset of models that most closely match observations, and is detailed below. The corresponding historical ensemble member is catenated with the respective RCP scenario ensemble member to create a continuous time series from 1850–2100.

Step 2 – Time series of NH September sea ice extent

Using the sea ice concentration field, a mask of the sea ice concentration >15% for each month of data for the Northern Hemisphere was created. For each month, the sea ice extent is the sum of the area of the ocean [areacello] times the ocean fraction [sftof] times the mask of sic >15% at each grid point. The time series are computed on the original model grids, which is usually the ocean grid. In some cases,

Table TS.SM.2 | Models and ensemble members used.

Model	Ensemble Member	RCP2.6	Historical/RCP4.5	RCP6.0	RCP8.5
ACCESS1.0	r1i1p1		x		x
ACCESS1.3	r1i1p1		x		x
BCC-CSM1.1	r1i1p1	x	x	x	x
BCC-CSM1.1(m)	r1i1p1	x	x	x	x
BNU-ESM	r1i1p1	x	x		x
CanESM2	r1i1p1	x	x		x
CCSM4	r1i1p1	x	x	x	x
CESM1(BGC)	r1i1p1		x		x
CESM1(CAM5)	r1i1p1	x	x	x	x
CESM1(WACCM)	r2i1p1	x	x		x
CMCC-CM	r1i1p1		x		x
CMCC-CMS	r1i1p1		x		x
CNRM-CM5	r1i1p1	x	x		x
CSIRO-Mk3.6.0	r1i1p1	x	x	x	x
EC-EARTH	r1i1p1		x		x
	r8i1p1	x			
FGOALS-g2	r1i1p1	x	x		x
FIO-ESM	r1i1p1	x	x	x	x
GFDL-CM3	r1i1p1	x	x	x	x
GFDL-ESM2G	r1i1p1	x	x	x	x
GFDL-ESM2M	r1i1p1	x	x	x	x
GISS-E2-H	r1i1p1	x	x	x	x
GISS-E2-H-CC	r1i1p1		x		
GISS-E2-R	r1i1p1	x	x	x	x
GISS-E2-R-CC	r1i1p1		x		
HadGEM2-AO	r1i1p1	x	x	x	x
HadGEM2-CC	r1i1p1		x		x
HadGEM2-ES	r2i1p1	x	x	x	x
INM-CM4	r1i1p1		x		x
IPSL-CM5A-LR	r1i1p1	x	x	x	x
IPSL-CM5A-MR	r1i1p1	x	x	x	x
IPSL-CM5B-LR	r1i1p1		x		x
MIROC5	r1i1p1	x	x	x	x
MIROC-ESM	r1i1p1	x	x	x	x
MIROC-ESM-CHEM	r1i1p1	x	x	x	x
MPI-ESM-LR	r1i1p1	x	x		x
MPI-ESM-MR	r1i1p1	x	x		x
MRI-CGCM3	r1i1p1	x	x	x	x
NorESM1-M	r1i1p1	x	x	x	x
NorESM1-ME	r1i1p1	x	x	x	x

sea ice concentration is on the atmospheric grid. In cases where the grid area was not available for regular grids, a regular lat-lon grid was constructed based on the grid dimensions following

areacello=((dlat*2π/360)*R_earth) .* ((dlon*2 π/360).*(R_earth*cos(LAT))),

with R_earth being the radius of Earth (6,371,000 m), dlat and dlon being the differentials in lat/lon in each dimension, and LAT being the latitude in radians.

If the ocean fraction was unavailable, it was assumed that the ocean fraction was 1 where the sea ice concentration was greater than 0%.

Step 3 – Create multi-model mean time series

The multi-model mean time series of sea ice extent is computed across all model members in Table TS.SM.2. A five-year running mean is applied to this time series. This is plotted as the dotted line in the figure. Some time series start later than 1850 or end earlier than 2100, and these are treated as missing values for those years.

Step 4 – Select models that most closely match observations

The selection process is done in a series of steps which compare the models to observed/reanalyzed data. This selection process is based on the underlying assessment of Chapter 12 and referenced therein. The method proposed by Massonnet et al. (2012) is applied here to the full set of models that provided sea ice output fields to the CMIP5 database. For the model selection, all available ensemble members are used for all of the models that provide simulations for Historical and RCP4.5. These ensemble members are listed in Table TS.SM.3.

Four diagnostics from the models are compared to the same quantities in observations or reanalyses. The diagnostics are: (a) September Arctic sea ice extent (1986–2005), (b) Annual mean Arctic sea ice volume (1986–2005), (c) Amplitude of the seasonal cycle of Arctic sea ice extent (1986–2005), and (d) Trend in September Arctic sea ice extent (1979–2012). Computation of each diagnostic is described and then the method for comparison is described below.

Step 4a – Computation of diagnostic quantities

(a) Sea ice extent is computed for each model ensemble member as outlined above to get the total area where sea ice concentration is >15%. For each ensemble member, an average September sea ice extent is then computed for the years 1986–2005. Observations for sea ice extent use the monthly mean sea ice extents from Comiso and Nishio (2008, updated 2012). The observations were computed in the same way as in the models (i.e., these are the monthly mean extents computed from the observed monthly mean sea ice concentration).

(b) Sea ice volume is computed as the sum of the sea ice thickness field [sit] times the ocean area [areacello] times the ocean fraction [sftof], since the sea ice thickness is given as thickness averaged over the entire ocean grid cell. Caveats for the grids are the same as discussed in Step 2 above. The time series of monthly sea ice volume for each ensemble member is then annually averaged for the period 1986–2005. The bias-adjusted PIOMAS (Pan-Arctic Ice-Ocean Modelling and Assimilation System) reanalysis data (Schweiger et al., 2011) is used to provide estimates for sea ice volume for comparison to the models.

(c) The amplitude of the seasonal cycle of Arctic sea ice extent is computed for each model from a climatology of monthly sea ice extent for 1986–2005. The amplitude is the difference between the maximum (March) and minimum (September) sea ice extent for each model ensemble member. Amplitude of seasonal cycle for observations are computed in the same way from Comiso and Nishio (2008, updated 2012).

(d) The linear trend in September sea ice extent is computed for the period 1979–2012. Again observations are taken from Comiso and Nishio (2008, updated 2012).

Step 4b – Estimation of natural variability for model ensembles

For models with multiple ensemble members, a standard deviation is computed for each of the diagnostics for each ensemble member. Then the mean of all the standard deviations is computed, and using this value, a ±2 standard deviation interval is constructed around the ensemble mean or single realization of each diagnostic for each model.

Step 4c – Model selection - Comparison of modeled diagnostics to observed/reanalyzed diagnostic

For each of the observed/reanalyzed diagnostics, a ±–20% interval is constructed around the mean value for the given period. A model is retained in the selection if, for each diagnostic, either the ±2 standard deviation around the model ensemble mean diagnostic overlaps the ±20% interval around the observed/reanalysed value of the diagnostic OR at least one ensemble member from that model gives a value for the diagnostic that falls within ±20% of the observed/reanalysed data. A model is selected only if all four diagnostic values meet this criterion.

Results of the selection

The model diagnostics are calculated using RCP4.5 which has the largest number of models. Five models are selected by this process: ACCESS1.0, ACCESS1.3, GFDL-CM3, IPSL-CM5A-MR, MPI-ESM-MR, and all five models have simulations for both RCP8.5 and RCP4.5. For RCP2.6 only three of this subset have simulations (GFDL-CM3, IPSL-CM5A-MR, MPI-ESM-MR), and for RCP6.0, only two models have simulations (GFDL-CM3, IPSL-CM5A-MR).

Step 5 – Time series of sea ice extent for the selected models

The multi-model mean time series of September sea ice extent is calculated for the selected models. The solid line shows the multi-model mean smoothed with a five-year running mean, and the shading represents the minimum and maximum range of the selected model time series, also smoothed by the same five year running mean.

The shaded bars on the right are the multi-model mean and the mean of the maximum and minimum range for the selected models for the period 2081–2100.

Table TS.SM.3 | Models and ensembles used for model selection, RCP4.5.

Model	Ensemble Member RCP4.5
ACCESS1.0	r1i1p1
ACCESS1.3	r1i1p1
BCC-CSM1.1	r1i1p1
BCC-CSM1.1(m)	r1i1p1
BNU-ESM	r1i1p1
CanESM2	r1i1p1 r2i1p1 r3i1p1 r4i1p1 r5i1p1
CCSM4	r1i1p1 r2i1p1 r3i1p1 r4i1p1 r5i1p1 r6i1p1
CESM1(BGC)	r1i1p1
CESM1(CAM5)	r1i1p1 r2i1p1 r3i1p1
CESM1(WACCM)	r2i1p1
CMCC-CM	r1i1p1
CMCC-CMS	r1i1p1
CNRM-CM5	r1i1p1
CSIRO-Mk3.6.0	r1i1p1 r2i1p1 r3i1p1 r4i1p1 r5i1p1 r6i1p1 r7i1p1 r8i1p1 r9i1p1 10i1p1
EC-EARTH	r1i1p1 r2i1p1 r3i1p1 r6i1p1 r7i1p1 r8i1p1 r9i1p1 10i1p1 11i1p1 12i1p1 13i1p1 14i1p1
FGOALS-g2	r1i1p1
FIO-ESM	r1i1p1 r2i1p1 r3i1p1
GFDL-CM3	r1i1p1 r3i1p1 r5i1p1
GFDL-ESM2G	r1i1p1
GFDL-ESM2M	r1i1p1
GISS-E2-H	r1i1p1 r2i1p1 r3i1p1 r4i1p1 r5i1p1
GISS-E2-H-CC	r1i1p1
GISS-E2-R	r1i1p1 r2i1p1 r3i1p1 r4i1p1 r5i1p1 r6i1p1
GISS-E2-R-CC	r1i1p1
HadGEM2-AO	r1i1p1
HadGEM2-CC	r1i1p1
HadGEM2-ES	r2i1p1 r3i1p1 r4i1p1
INM-CM4	r1i1p1
IPSL-CM5A-LR	r1i1p1 r2i1p1 r3i1p1 r4i1p1
IPSL-CM5A-MR	r1i1p1
IPSL-CM5B-LR	r1i1p1
MIROC5	r1i1p1 r2i1p1 r3i1p1
MIROC-ESM	r1i1p1
MIROC-ESM-CHEM	r1i1p1
MPI-ESM-LR	r1i1p1 r2i1p1 r3i1p1
MPI-ESM-MR	r1i1p1 r2i1p1 r3i1p1
MRI-CGCM3	r1i1p1
NorESM1-M	r1i1p1
NorESM1-ME	r1i1p1

TS.SM.8 Notes and Technical Details on Maps Showing CMIP5 Results in the Summary for Policymakers – Figure SPM.8

This material documents the provenance of the data and plotting procedures that were used to create Figure SPM.8, based on CMIP5 model results as of March, 2013. This figure is closely derived from Figures 12.11 and TS.15 (global average surface temperature), TS.16 (precipitation), 12.29 and TS.17 (sea ice), 6.28 and TS.20b (ocean surface pH), but includes fewer model scenarios. The reader is referred to the Technical Summary or the Chapters 12 and 6 where all RCP scenarios are given for the respective quantity.

TS.SM.8.1 Change in Average Surface Temperature (Figure SPM.8a) and Change in Average Precipitation (Figure SPM.8b)

Step 1 – Analyzed simulations

The simulations considered are monthly mean fields of surface temperature [tas] and precipitation [pr] from different model simulations carried out as part of the CMIP5 project (when applicable the variable name as given in the CMIP5 archive is indicated in square brackets). Table TS.SM.4 lists the models and ensemble members used for these panels. Only one ensemble member per model is used.

Step 2 – Interpolation

In a first step the monthly fields are re-gridded to a 2.5° × 2.5° grid using bilinear interpolation. No special treatment is used at the land-sea border.

Step 3 – Annual average and period

The monthly mean values are averaged to annual means. Then in a second step the time mean is computed over the 20-year period of interest.

Table TS.SM.4 | Models and ensemble members used.

Model	Ensemble Member	RCP2.6	Historical/RCP4.5	RCP6.0	RCP8.5
ACCESS1.0	r1i1p1		x		x
ACCESS1.3	r1i1p1		x		x
BCC-CSM1.1	r1i1p1	x	x	x	x
BCC-CSM1.1(m)	r1i1p1	x	x	x	
BNU-ESM	r1i1p1	x	x		x
CanESM2	r1i1p1	x	x		x
CCSM4	r1i1p1	x	x	x	x
CESM1(BGC)	r1i1p1		x		x
CESM1(CAM5)	r1i1p1	x	x	x	x
CMCC-CM	r1i1p1		x		x
CMCC-CMS	r1i1p1		x		x
CNRM-CM5	r1i1p1		x		x
CSIRO-Mk3.6.0	r1i1p1	x	x	x	x
EC-EARTH	r8i1p1	x	x		x
FGOALS-g2	r1i1p1	x	x		x
FIO-ESM	r1i1p1	x	x	x	x
GFDL-CM3	r1i1p1	x	x	x	x
GFDL-ESM2G	r1i1p1	x	x	x	x
GFDL-ESM2M	r1i1p1		x	x	x
GISS-E2-H	r1i1p1	x	x	x	x
GISS-E2-H	r1i1p2	x	x	x	x
GISS-E2-H	r1i1p3	x	x	x	x
GISS-E2-H-CC	r1i1p1		x		
GISS-E2-R	r1i1p1	x	x	x	x
GISS-E2-R	r1i1p2	x	x	x	x
GISS-E2-R	r1i1p3	x	x	x	x
GISS-E2-R-CC	r1i1p1		x		
HadGEM2-AO	r1i1p1	x	x	x	x
HadGEM2-CC	r1i1p1		x		x
HadGEM2-ES	r2i1p1	x	x	x	x
INM-CM4	r1i1p1		x		x
IPSL-CM5A-LR	r1i1p1	x	x	x	x
IPSL-CM5A-MR	r1i1p1	x	x	x	x
IPSL-CM5B-LR	r1i1p1		x		x
MIROC5	r1i1p1	x	x	x	x
MIROC-ESM	r1i1p1	x	x	x	x
MIROC-ESM-CHEM	r1i1p1	x	x	x	x
MPI-ESM-LR	r1i1p1	x	x		x
MPI-ESM-MR	r1i1p1	x	x		x
MRI-CGCM3	r1i1p1	x	x	x	x
NorESM1-M	r1i1p1	x	x	x	x
NorESM1-ME	r1i1p1	x	x	x	x

Step 4 – Time average and anomalies
The average from 1986 to 2005 of the annual means for each model is computed as the reference value and the annual mean from 2081 to 2100 are computed as the future period for the two RCPs. For each model the reference value is then subtracted from the future period value.

Step 5 – Calculation of the significance

Step 5a – Natural variability
To compute the natural variability all the models that provide more than 500 years of pre-industrial control simulation [piControl] are used. A list of these models is given in Table TS.SM.5. For each model the first 100 years are discarded to minimize problems with model initialization. Re-gridding and calculation of annual means is done as described in steps 2 and 3. The control runs are divided into 20-year non-overlapping periods. If the available data are not a multiple of 20-year the remaining years after the last 20-year period are not used in the calculation.

Averages over the 20-year periods are computed for every grid point. A quadratic trend is subtracted from this time series of 20-year averaged periods to remove potential model drift at each grid point. Finally for each model the standard deviation is computed over the different 20-year periods and for each grid point.

Table TS.SM.5 | Models and ensemble members from the piControl experiments used for the calculation of the natural variability.

Model	Ensemble Member
ACCESS1.0	r1i1p1
ACCESS1.3	r1i1p1
BCC-CSM1.1	r1i1p1
BNU-ESM	r1i1p1
CanESM2	r1i1p1
CCSM4	r1i1p1
CESM1(BGC)	r1i1p1
CMCC-CMS	r1i1p1
CNRM-CM5	r1i1p1
CSIRO-Mk3-6-0	r1i1p1
FGOALS-g2	r1i1p1
FIO-ESM	r1i1p1
GFDL-CM3	r1i1p1
GFDL-ESM2G	r1i1p1
GFDL-ESM2M	r1i1p1
GISS-E2-H	r1i1p2
GISS-E2-H	r1i1p3
GISS-E2-R	r1i1p2
GISS-E2-R	r1i1p3
INM-CM4	r1i1p1
IPSL-CM5A-LR	r1i1p1
MIROC5	r1i1p1
MIROC-ESM	r1i1p1
MPI-ESM-LR	r1i1p1
MPI-ESM-MR	r1i1p1
MPI-ESM-P	r1i1p1
MRI-CGCM3	r1i1p1
NorESM1-M	r1i1p1

To obtain the final value of the natural variability the median of the standard deviations of the different models is multiplied with the square root of 2 (the natural variability characterizes the typical difference between two 20-year periods, rather than the difference of one period from the long-term mean, the former being larger than the latter by the square root of two).

Step 5b – Testing for significance
For each model the projected change is taken relative to its reference period and then the multi-model average at every grid point is computed. In a second step, at each grid point the number of models with positive and negative change are counted.

If more than 90% of the models agree on the sign of the change and the multi-model mean change is larger than 2 times the natural variability (as defined above) this grid point is said to be significant and robust across models.

Step 5c – Check for non-significance
Again, for each model the projected change is taken relative to the reference period and then the multi-model average at every grid point is computed.

If the multi-model mean change at one grid point is less than the natural variability (as defined above) the value is said to be non-significant.

Step 6 – Graphical display
For each model the projected change is taken relative to the reference period and then the multi-model average at every grid point is computed. The locations that are significant and robust (as described in step 5b) are marked by small black dots and the locations that are non-significant (as described in step 5c) are marked by hatching.

For panel b, all calculations are performed as absolute changes. To show the relative changes, the multi-model mean precipitation change is divided by the multi-model mean of the reference period.

TS.SM.8.2 Northern Hemisphere September Sea Ice Extent (Figure SPM.8c)

Step 1 – Analyzed simulations and subset of models
The simulations analyzed here are the same as those listed for Figure SPM.7b. The subset of models are the same that are selected for Figure SPM.7b outlined in the following Step 4. Only one ensemble member from each model is used to create these figures.

Step 2 – Computation of mean sea ice concentration
For each model ensemble member, the mean sea ice concentration [sic] is calculated for the two periods, 1986–2005 and 2081–2100, on the native model grid (see also recipe for Figure SPM.7b).

Step 3 – Regrid sea ice concentration to common grid
SOSIE (http://sosie.sourceforge.net/) is used to regrid the mean sea ice concentration to a common 1° × 1° grid, applying the bilinear

interpolation scheme (SOSIE: cmethod = 'bilin'). Further, the regridded sea ice concentrations are 'drowned' across the land-sea boundary to eliminate low-biased interpolated values in the area of land-sea transition (SOSIE: ldrown = T). With this approach, interpolation artifacts can occur throughout the Canadian Archipelago, since each model represents this area quite differently. Comparison of individual models on their native grid allows to identify and mask such areas. Note that, for these reasons the interpolated sea ice concentrations shall not be used for quantitative interpretation, but only for visualization purposes. For visualization the MATLAB land-ocean mask is overlaid.

Step 4 – Calculate multi-model mean sea ice concentration

For each RCP, RCP2.6 and RCP8.5, and each period, 1986–2005 and 2081–2100, the mean sea ice concentration is calculated in each grid cell on the common grid. The same is done for the subset of models for each period. For RCP2.6 this subset is GFDL-CM3, IPSL-CM5A-MR, MPI-ESM-MR. For RCP8.5 this subset is ACCESS1.0, ACCESS1.3, GFDL-CM3, IPSL-CM5A-MR, MPI-ESM-MR.

Step 5 – Contour the multi-model mean sea ice concentration of 15%

The multi-model mean sea ice concentration is contoured at 15% according to the following:

1986–2005: multi-model mean all models: white line
1986–2005: subset models: light blue line
2081–2100: multi-model mean all models: white filled patch
2081–2100: subset models: light blue filled patch

Note for RCP8.5 there is no sea ice concentration >15% for the subset of models.

The decision was taken to contour the 15% contour of mean sea ice concentration to make this figure consistent with Figure 12.29, which shows a contour plot of the multi-model mean sea ice concentrations. It is also possible to make binary fields of sea ice concentration >15%, take the mean of those binary fields (for both 20 year averages and then in multi-model averages), and contour the 50% contour of the mean binary field as the mean sea ice extent. This option was not chosen here.

TS.SM.8.3 Change in Ocean Surface pH (Figure SPM.8d)

Step 1 – Analyzed simulations

The simulations considered are annual or monthly mean fields from different model simulations carried out as part of the CMIP5 project (when applicable the variable name as given in the CMIP5 archive is indicated in square brackets). Table TS.SM.6 lists the models and ensemble members used for these panels. Only one ensemble member per model is used.

Step 2a – Interpolation

In a first step, the monthly temperature [tos] and salinity [sos] fields are first averaged to yield annual means. For the model MIROC-ESM-CHEM the upper-most layer of the 3-dimensional fields of monthly sea water potential temperature [thetao] and monthly sea water salinity [so] are used. Then, annual-mean temperature, salinity, dissolved inorganic carbon [dissic] and alkalinity [talk] fields are re-gridded to a 1° × 1° using bilinear interpolation.

Step 2b – Derivation of pH

For each model, surface pH was computed from simulated DIC, alkalinity, temperature, and salinity. Before computation each simulated input field was corrected for its decadal mean bias relative to modern observations, using the approach used in Orr et al. (2005) and Orr (2011). That is, pH was computed after first removing from each model field, the average difference between the model mean during 1989–1998 and the observational reference. For observed fields, we used the GLODAP gridded data product (Key et al., 2004) for DIC and alkalinity along with the 2009 World Ocean Atlas climatology for temperature, salinity, and concentrations of phosphate and silica (Locarnini et al., 2010; Antonov et al., 2010; Garcia et al., 2010). Changes to the concentrations of phosphate and silica were assumed to be zero, because all models did not provide those variables. pH was computed using routines based on the standard OCMIP carbonate chemistry adapted for earlier studies (Orr, 2011) to compute all carbonate system variables and use recommended constants from the Guide to Best Practices for Ocean CO_2 Measurements (Dickson et al., 2007).

Step 3 – Average of 20-year period

The time mean is computed over the 20-year period of interest.

Table TS.SM.6 | Models and ensemble members used.

Model	Ensemble Member	Historical	RCP2.6	RCP4.5	RCP6.0	RCP8.5
CanESM2	r1i1p1	d	d	d		d
GFDL-ESM2G	r1i1p1	d	d	d	d	d
GFDL-ESM2M	r1i1p1	d	d	d	d	d
HadGEM2-CC	r1i1p1	d		d		d
IPSL-CM5A-LR	r1i1p1	d	d	d	d	d
IPSL-CM5A-MR	r1i1p1	d	d	d		d
IPSL-CM5B-LR	r1i1p1	d		d		d
MIROC-ESM	r1i1p1	d	d	d	d	d
MIROC-ESM-CHEM	r1i1p1	d	d	d	d	d
MPI-ESM-LR	r1i1p1	d	d	d		d
MPI-ESM-MR	r1i1p1	d	d	d		d
NorESM1-ME	r1i1p1	d		d		

Step 4 – Time average and anomalies
The average from 1986 to 2005 of the annual means for each model is computed as the reference value and the annual mean from 2081 to 2100 is computed as the future period for the two RCPs. For each model the reference value is then subtracted.

Step 5 – Graphical display
For each model the projected change is taken relative to the reference period and the multi-model mean at every grid point is computed.

TS.SM.9 Notes and Technical Details on the Sea Level Projection Figure for the Summary for Policymakers – Figure SPM.9

A full and comprehensive description of the methods used in the projections of global mean sea level for the 21st century is provided in the Supplementary Material to Chapter 13 (see Section 13.SM.1). Further plotting details used to produce Figure SPM.9, and the related Figure TS.22 are provided here.

TS.SM.9.1 Projected Global Mean Sea Level Rise

Projections are given from process-based models of global mean sea level rise relative to 1986–2005 for the four emissions scenarios RCP2.6, RCP4.5, RCP6.0 and RCP8.5.

The *likely* range for each RCP timeseries is delimited by the data in files rcpXX_sumlower and rcpXX_sumupper, while the median timeseries is the data in file rcpXX_summid, where 'XX' stands for the respective RCP scenario. These data files are available from the WGI AR5 website www.climatechange2013.org. The coloured vertical bars with horizontal lines for the four RCP scenarios indicate the *likely* ranges and medians for these scenarios as given in Table 13.5 of Chapter 13.

Note that in Figure SPM.9, projected time series are shown only for RCP2.6 and RCP8.5. Figure TS.22 include time series for all four RCP scenarios.

Projected contributions to sea level rise in 2081–2100 relative to 1986–2005 for the four RCP scenarios are provided in Figure TS.21.

TS.SM.10 Notes and Technical Details on the Summary for Policymakers Figure Plotting Global Mean Temperature Increase as a Function of Cumulative Total Global CO_2 Emissions – Figure SPM.10

Figure SPM.10 contains data from CO_2 only simulations and the RCP simulations. This figure is closely derived from TS TFE.8, Figure 1. CO_2 only simulations are represented by grey-shaded patches and thin black lines, RCP data by coloured lines and patches. CMIP5 results are taken from the archive as of March 15, 2013. Note that the thick black line represents the historical time period of the RCP runs.

TS.SM.10.1 Part A – CO_2 Only Runs

The thin black line represents the multi-model mean of the decadal averaged global-mean temperature response of the models listed in Table TS.SM.7 to a global 1% CO_2 only forcing increase as performed as part of CMIP5, as a function of the decadal averaged global-mean diagnosed carbon emissions.

The dark grey patch represents the 90% range surrounding the decadal averaged model response of the CMIP5 models listed in Table TS.SM.7 and is calculated as follows: Diagnosed carbon emissions and temperature response data of the above-defined CMIP5 models (computed as in Gillett et al., 2013) is scaled, respectively, by dividing by the standard deviation over all available decadal-averaged data points for a specific scenario. The 90% range is computed in polar coordinates. The radius stretches along the x-axis (cumulative emissions) and the angle is the one between the slope from (0, 0) to a respective scaled point (cumulative emissions, temperature anomaly) and the x-axis. For each scaled point the radius and angle are computed. A number of n (n = 20) segments are defined by regularly spaced steps along the maximum radius of all available decadal-averaged data points of a specific scenario (scaled as described earlier). From all points that fall within the boundaries of each respective radius segment, the 5th and 95th percentiles in terms of available angles is computed. These percentiles are then assigned to the radius corresponding to the middle of the current radius segment. Each of these mid-segment radii and its corresponding pair of angles are then transformed back to Cartesian coordinates. Finally, the 90% range is drawn by connecting all 5th and 95th percentile points of a specific scenario in a hull.

Table TS.SM.7 | Models that were included in the shown results of the CO2 only 1% increase CMIP5 runs (dark grey patch and thin black line).

Model	Ensemble Member
GFDL-ESM2G	r1i1p1
INM-CM4	r1i1p1
GFDL-ESM2M	r1i1p1
IPSL-CM5B-LR	r1i1p1
BCC-CSM1.1	r1i1p1
MPI-ESM-MR	r1i1p1
IPSL-CM5A-MR	r1i1p1
IPSL-CM5A-LR	r1i1p1
MPI-ESM-LR	r1i1p1
NorESM1-ME	r1i1p1
CESM1(BGC)	r1i1p1
HadGEM2-ES	r1i1p1
MIROC-ESM	r1i1p1
CanESM2	r1i1p1
BNU-ESM	r1i1p1

TS.SM.10.2 Part B – RCP Runs

Data of the RCP runs (coloured lines and patches) is prepared with the same methodology as the data for the CO_2 only runs as described in the previous section. Note that markers show decadal time steps, and that the labels in Figure SPM.10 (and TS TFE.8, Figure 1) denote the cumulative global carbon emissions from 1870 until (but not including) that year (i.e., label 2050 is placed next to the marker of the 2040–2049 decade). The 90% range is computed for n (n = 12) regularly spaced steps along the maximum radius available for each RCP (scaled as described earlier). Available Earth System Models (ESM) for the respective RCP are listed in Table TS.SM.8, available Earth System Models of Intermediate Complexity (EMIC) in Table TS.SM.9.

Following operations are carried out onto the data:

- Decadal means of global-mean temperature change are computed relative to the 1861–1880 base period.
- Emissions from the ESMs for the different scenarios are computed as in Jones et al. (2013).
- Land-use change emission estimated for each RCP are added to all EMICs, and to the ESMs that diagnose fossil-fuel emission only (see Table TS.SM.8). Land-use change emissions are obtained from http://www.pik-potsdam.de/~mmalte/rcps/ for each RCP, respectively. Note that the data for Figure SPM.10 provided at the external sources cited above may be subject to changes in the future by the owners. Furthermore, no guarantee is provided that the web-links cited above remain active.
- Decadal-mean cumulative emissions are computed from cumulative carbon emissions relative to 1870.
- Each RCP range is drawn as long as data is available for all models or until temperatures have peaked. The encompassing range shown in Figure SPM.10 (and TS TFE.8, Figure 1) is constructed by connecting the outer last points of each single RCP range and is filled as long as data are available for all models for RCP8.5. Beyond this point, the range is illustratively extended by further progressing along the radius while keeping the angles fixed at those available at the last point with data from all models for RCP8.5. The fading out of the range is illustrative.

Table TS.SM.8 | Overview of RCP model runs available in the CMIP5 archive, as used in Figure SPM.10 (and TS TFE.8, Figure 1).

Model	Ensemble Member	RCP2.6	RCP4.5	RCP6.0	RCP8.5
BCC-CSM1.1	r1i1p1	x*	x*	x*	x*
CanESM2	r1i1p1	x	x		x
CESM1(BGC)	r1i1p1		x		x
GFDL-ESM2G	r1i1p1	x	x	x	x
GFDL-ESM2M	r1i1p1	x	x	x	x
HadGEM2-CC	r1i1p1		x		x
HadGEM2-ES	r2i1p1	x	x	x	x
INM-CM4	r1i1p1		x*		x*
IPSL-CM5A-LR	r1i1p1	x	x	x	x
IPSL-CM5A-MR	r1i1p1	x	x		x
IPSL-CM5B-LR	r1i1p1		x		x
MIROC-ESM	r1i1p1	x	x	x	x
MIROC-ESM-CHEM	r1i1p1	x	x	x	x
MPI-ESM-LR	r1i1p1	x	x		x
NorESM1-ME	r1i1p1	x	x	x	x

Notes:
* runs do not include explicit land-use change modelling. Models diagnose fossil-fuel and land-use change emissions jointly and therefore do not require adding land-use change emissions.

Table TS.SM.9 | Overview of EMIC RCP model runs from (Eby et al. 2013; Zickfeld et al. 2013), as used in Figure SPM.10 (and TS TFE.8, Figure 1). EMICs output is available from http://www.climate.uvic.ca/EMICAR5.

Model	RCP2.6	RCP4.5	RCP6.0	RCP8.5
Bern3D	x	x	x	x
DCESS	x	x	x	x
GENIE	x	x	x	x
IGSM	x	x	x	x
UVic	x	x	x	x

References

Antonov, J. I., et al., 2010: *World Ocean Atlas 2009*, *Volume 2: Salinity* [Levitus, S. (Ed.)]. NOAA Atlas NESDIS 69, 184 pp.

Bates , N .R ., 2007: Interannual variability of the oceanic CO_2 sink in the subtropical gyre of the North Atlantic Ocean over the last two decades. *J. Geophys. Res. Oceans*, **112**, C09013.

Becker, A., et al., 2013: A description of the global land-surface precipitation data products of the Global Precipitation Climatology Centre with sample applications including centennial (trend) analysis from 1901–present. *Earth Sys. Sci. Data*, **5**, 71–99.

Brown, R. D., and D. A. Robinson, 2011: Northern Hemisphere spring snow cover variability and change over 1922–2010 including an assessment of uncertainty. *Cryosphere*, **5**, 219–229.

Cavalieri, D. J., and C. L. Parkinson, 2012: Arctic sea ice variability and trends, 1979-2010. *Cryosphere*, **6**, 957–979.

Cavalieri, D. J., P. Gloersen, and W. J. Campbell, 1984: Determination of sea ice parameters with the Nimbus-7 SMMR. *J. Geophys. Res. Atmos.*, **89**, 5355–5369.

Church, J. A., and N. J. White, 2011: Sea-Level Rise from the Late 19th to the Early 21st Century. *Surv. Geophys.*, **32**, 585–602.

Comiso, J. C., and F. Nishio, 2008: Trends in the sea ice cover using enhanced and compatible AMSR-E, SSM/I, and SMMR data. *J. Geophys. Res. Oceans*, **113**, C02S07.

Dickson, A.G., C. L. Sabine, and J. R. Christian, J.R., (eds.), 2007: *Guide to best practices for ocean CO_2 measurements*. PICES Special Publication 3, 191 pp.

Domingues, C. M., J. A. Church, N. J. White, P. J. Gleckler, S. E. Wijffels, P. M. Barker, and J. R. Dunn, 2008: Improved estimates of upper-ocean warming and multi-decadal sea-level rise. *Nature*, **453**, 1090–1094.

Dore, J. E., R. Lukas, D. W. Sadler, M. J. Church, and D. M. Karl, 2009: Physical and biogeochemical modulation of ocean acidification in the central North Pacific. *Proc. Natl. Acad. Sci. U.S.A.*, **106**, 12235–12240.

Eby, M., et al., 2013: Historical and idealized climate model experiments: an intercomparison of Earth system models of intermediate complexity. *Clim. Past*, **9**, 1111–1140.

Garcia, H. E., R. A. Locarnini, T. P. Boyer, J. I. Antonov, O. K. Baranova, M. M. Zweng, and D. R. Johnson, 2010: *World Ocean Atlas 2009*, *Volume 3: Dissolved Oxygen, Apparent Oxygen Utilization, and Oxygen Saturation* [Levitus, S. (Ed.)]. NOAA Atlas NESDIS 70, 344 pp.

Gillett, N. P., V. K. Arora, D. Matthews, and M. R. Allen, 2013: Constraining the Ratio of Global Warming to Cumulative CO_2 Emissions Using CMIP5 Simulations. *J. Clim.*, **26**, 6844–6858.

González-Dávila, M., and J. M. Santana-Casiano, 2009: Sea Surface and Atmospheric fCO_2 data measured during the ESTOC Time Series cruises from 1995–2009. Oak Ridge National Laboratory, US Department of Energy, Oak Ridge, Tennessee. http://cdiac.ornl.gov/ftp/oceans/ESTOC_data/.

González-Dávila, M., J. M. Santana-Casiano, J. M. Rueda, and O. Llinás, 2010: Water column distribution of the carbonate system variables in the ESTOC site from 1995 to 2004. *Biogeosciences*, **7**, 3067–3081.

IPCC, 2012: *Managing the Risks of Extreme Events and Disasters to Advance Climate Change Adaptation. A Special Report of Working Groups I and II of the Intergovernmental Panel on Climate Change* [Field, C.B., et al., (eds.)]. Cambridge University Press, Cambridge, UK, and New York, NY, USA, 582 pp.

Ishii, M., and M. Kimoto, 2009: Reevaluation of historical ocean heat content variations with time-varying XBT and MBT depth bias corrections. *J. Oceanogr.*, **65**, 287–299.

Jevrejeva, S., J. C. Moore, A. Grinsted, and P. L. Woodworth, 2008: Recent global sea level acceleration started over 200 years ago? *Geophys. Res. Lett.*, **35**, L08715.

Jones, C., et al., 2013: Twenty-First Century Compatible CO_2 Emissions and Airborne Fraction Simulated by CMIP5 Earth System Models under Four Representative Concentration Pathways. *J. Clim.*, **26**, 4398–4413.

Keeling, C., R. Bacastow, A. Bainbridge, C. Ekdahl, P. Guenther, L. Waterman, and J. Chin, 1976a: Atmospheric Carbon-Dioxide Variations at Mauna-Loa Observatory, Hawaii. *Tellus*, **28**, 538–551.

Keeling, C. D., J. A. Adams, and C. A. Ekdahl, 1976b: Atmospheric Carbon-Dioxide Variations at South Pole. *Tellus*, **28**, 553–564.

Keeling, C. D., S. C. Piper, R. B. Bacastow, M. Wahlen, T. P. Whorf, M. Heimann, and H. A. Meijer, 2001: Exchanges of atmospheric CO_2 and $^{13}CO_2$ with the terrestrial biosphere and oceans from 1978 to 2000. I. Global aspects, SIO Reference Series, No. 01–06. Scripps Institution of Oceanography, San Diego, 88 pp.

Key, R. M., et al., 2004: A global ocean carbon climatology: Results from Global Data Analysis Project (GLODAP). *Glob. Biogeoch. Cycles*, **18**, GB4031.

Le Quéré, C., et al., 2013: The global carbon budget 1959–2011. *Earth Syst. Sci. Data*, **5**, 165–185.

Levitus, S., et al., 2012: World ocean heat content and thermosteric sea level change (0-2000 m), 1955–2010. *Geophys. Res. Lett.,* **39,** L10603.

Locarnini, R. A., et al., 2010: *World Ocean Atlas 2009*, *Volume 1: Temperature* [Levitus, S. (Ed.)]. NOAA Atlas NESDIS 68, 184 pp.

Markus, T., and D. J. Cavalieri, 2000: An enhancement of the NASA Team sea ice algorithm. *IEEE Trans. Geosci. Remote Sens.*, **38**, 1387–1398.

Massonnet, F., T. Fichefet, H. Goosse, C. M. Bitz, G. Philippon-Berthier, M. M. Holland, and P.-Y. Barriat, 2012: Constraining projections of summer Arctic sea ice. *Cryosphere*, **6**, 1383–1394.

Mitchell, T. D., and P. D. Jones, 2005: An improved method of constructing a database of monthly climate observations and associated high-resolution grids. *Int. J. Climatol.*, **25**, 693–712.

Morice, C. P., J. J. Kennedy, N. A. Rayner, and P. D. Jones, 2012: Quantifying uncertainties in global and regional temperature change using an ensemble of observational estimates: The HadCRUT4 data set. *J. Geophys. Res. Atmos.*, **117**, 22.

Nerem, R. S., D. P. Chambers, C. Choe, and G. T. Mitchum, 2010: Estimating Mean Sea Level Change from the TOPEX and Jason Altimeter Missions. *Mar. Geod.*, **33**, 435–446.

Orr, J.C. et al., 2005: Anthropogenic ocean acidification over the twenty-first century and its impact on calcifying organisms. *Nature*, **437**, 681-686.

Orr, J. C., 2011: Recent and future changes in ocean carbonate chemistry. In: *Ocean Acidification* [Gattuso, S.-P., and L. Hansson (eds.)]. Oxford University Press, Oxford, United Kingdom and New York, NY, USA, 352 pp.

Palmer, M. D., K. Haines, S. F. B. Tett, and T. J. Ansell, 2007: Isolating the signal of ocean global warming. *Geophys. Res. Lett.*, **34**, L23610.

Parkinson, C. L., and D. J. Cavalieri, 2012: Antarctic Sea Ice Variability and Trends, 1979-2010. *Cryosphere*, **6**, 871–880.

Ray, R. D., and B. C. Douglas, 2011: Experiments in reconstructing twentieth-century sea levels. *Prog. Oceanogr.*, **91**, 496–515.

Rayner, N. A., et al., 2003: Global analyses of sea surface temperature, sea ice, and night marine air temperature since the late nineteenth century. *J. Geophys. Res. Atmos.*, **108**, 4407.

Schweiger, A., R. Lindsay, J. L. Zhang, M. Steele, H. Stern, R. Kwok, 2011: Uncertainty in modeled Arctic sea ice volume. *J. Geophys. Res. Oceans*, **116**, C00D06.

Smith, D. M., and J. M. Murphy, 2007: An objective ocean temperature and salinity analysis using covariances from a global climate model. *J. Geophys. Res. Oceans*, **112**, C02022.

Thoning, K. W., P. P. Tans, and W. D. Komhyr, 1989: Atmospheric carbon dioxide at Mauna Loa Observatory 2. Analysis of the NOAA GMCC data, 1974-1985. *J. Geophys. Res.*, **94**, 8549–8565.

Vose, R. S., Oak Ridge National Laboratory. Environmental Sciences Division., U.S. Global Change Research Program, United States. Dept. of Energy. Office of Health and Environmental Research., Carbon Dioxide Information Analysis Center (U.S.), and Martin Marietta Energy Systems Inc., 1992: *The global historical climatology network: long-term monthly temperature, precipitation, sea level pressure, and station pressure data.* Carbon Dioxide Information Analysis Center. Available to the public from N.T.I.S., 1 v.

Walsh, J. E., and W. L. Chapman, 2001: 20th-century sea-ice variations from observational data. *Ann. Glaciol.*, **33**, 444–448.

Zickfeld, K., et al., 2013: Long-Term Climate Change Commitment and Reversibility: An EMIC Intercomparison. *J. Clim.*, **26**, 5782–5809.

Please note that all external web-links cited in this document were active at the time of publication, but no guarantee is provided that these links remain active.

2SM

Observations: Atmosphere and Surface

Supplementary Material

Coordinating Lead Authors:
Dennis L. Hartmann (USA), Albert M.G. Klein Tank (Netherlands), Matilde Rusticucci (Argentina)

Lead Authors:
Lisa V. Alexander (Australia), Stefan Brönnimann (Switzerland), Yassine Abdul-Rahman Charabi (Oman), Frank J. Dentener (EU/Netherlands), Edward J. Dlugokencky (USA), David R. Easterling (USA), Alexey Kaplan (USA), Brian J. Soden (USA), Peter W. Thorne (USA/Norway/UK), Martin Wild (Switzerland), Panmao Zhai (China)

Contributing Authors:
Robert Adler (USA), Richard Allan (UK), Robert Allan (UK), Donald Blake (USA), Owen Cooper (USA), Aiguo Dai (USA), Robert Davis (USA), Sean Davis (USA), Markus Donat (Australia), Vitali Fioletov (Canada), Erich Fischer (Switzerland), Leopold Haimberger (Austria), Ben Ho (USA), John Kennedy (UK), Elizabeth Kent (UK), Stefan Kinne (Germany), James Kossin (USA), Norman Loeb (USA), Carl Mears (USA), Christopher Merchant (UK), Steve Montzka (USA), Colin Morice (UK), Cathrine Lund Myhre (Norway), Joel Norris (USA), David Parker (UK), Bill Randel (USA), Andreas Richter (Germany), Matthew Rigby (UK), Ben Santer (USA), Dian Seidel (USA), Tom Smith (USA), David Stephenson (UK), Ryan Teuling (Netherlands), Junhong Wang (USA), Xiaolan Wang (Canada), Ray Weiss (USA), Kate Willett (UK), Simon Wood (UK)

Review Editors:
Jim Hurrell (USA), Jose Marengo (Brazil), Fredolin Tangang (Malaysia), Pedro Viterbo (Portugal)

This chapter supplementary material should be cited as:
Hartmann, D.L., A.M.G. Klein Tank, M. Rusticucci, L. Alexander, S. Brönnimann, Y. Charabi, F. Dentener, E. Dlugokencky, D. Easterling, A. Kaplan, B. Soden, P. Thorne, M. Wild and P.M. Zhai, 2013: Observations: Atmosphere and Surface Supplementary Material. In: *Climate Change 2013: The Physical Science Basis. Contribution of Working Group I to the Fifth Assessment Report of the Intergovernmental Panel on Climate Change* [Stocker, T.F., D. Qin, G.-K. Plattner, M. Tignor, S.K. Allen, J. Boschung, A. Nauels, Y. Xia, V. Bex and P.M. Midgley (eds.)]. Available from www.climatechange2013.org and www.ipcc.ch.

Table of Contents

2.SM.1 Introduction

The Chapter 2 Supplementary Material includes data or methods for which there was not space in the printed document, but that are regarded as being valuable documentation for the main report or for subsequent scientific studies.

2.SM.2 Changes in Atmospheric Composition

2.SM.2.1 Long-Lived Greenhouse Gases

Table 2.SM.1 contains the full list of species compiled for Chapter 8 to use for radiative forcing calculations. Following are discussions of additional species not discussed in Section 2.2.1 of the main text.

2.SM.2.1.1 Hydrofluorocarbons

New measurements of several hydrofluorocarbons (HFCs) have been reported since AR4: HFC-365mfc (Stemmler et al., 2007), HFC-245fa (Vollmer et al., 2006), HFC-227ea (Laube et al., 2010) and HFC-236fa (Vollmer et al., 2011). Observation-based estimates of emissions show a mix of poor to good agreement with bottom-up inventories (Vollmer et al., 2011). Atmospheric abundances of these four minor HFCs were <2 ppt in 2011, but their atmospheric burdens are increasing rapidly, with relative increases >8% yr^{-1}.

2.SM.2.1.2 Perfluorocarbons

Atmospheric measurements of high molecular weight perfluorocarbons (PFCs) have also been reported, including fully fluorine-substituted alkanes (C_3 to C_8) (Saito et al., 2010; Ivy et al., 2012); and octafluorocyclobutane (c-C_4F_8) (Saito et al., 2010; Oram et al., 2012). All are currently <2 ppt, except when pollution events are observed at the air sampling sites.

2.SM.2.1.3 Nitrogen Trifluoride and Sulfuryl Fluoride

Since AR4, atmospheric observations of two new species were reported: NF_3 and SO_2F_2. Prather and Hsu (2008) reported the potential importance of NF_3 for radiative forcing. It is a substitute for PFCs as a plasma source in the semiconductor industry, has a lifetime of 500 years, and a GWP100 = 16,100 (GWPs are described in Chapter 8). Arnold et al. (2013) determined 0.59 ppt for its global annual mean mole fraction in 2008, growing from almost zero in 1978. In 2011, NF_3 was at 0.86 ppt, increasing by 0.49 ppt since 2005. Initial bottom-up inventories underestimated its emissions; based on the atmospheric observations, NF_3 emissions were 1.18 ± 0.21 Gg in 2011. SO_2F_2 replaces CH_3Br as a fumigant. Its GWP100 ≈ 4740, is comparable to CFC-11. A new estimate of its lifetime, 36 ± 11 year (Muhle et al., 2009), is significantly longer than previous estimates. Its global annual mean mole fraction in 2011 was 1.71 ppt and it increased by 0.36 ppt from 2005 to 2011.

2.SM.2.1.4 Halons

Atmospheric abundances of halons, except for halon-1301, have been decreasing. All have relatively small atmospheric abundances, ≤5 ppt, and are unlikely to accumulate to levels that can significantly affect radiative forcing either directly or indirectly through destruction of stratospheric ozone, if current emission projections are followed (WMO, 2011).

2.SM.2.2 Near-Term Climate Forcers

Figure 2.SM.1 shows ozone trends based on yearly average ozone values at the surface or within the lower troposphere beginning at different starting points since 1970. Most of the surface sites are in rural locations so that they are representative of regional air quality; however, many of the Asian sites are urban. Trend values are from the peer-reviewed literature listed in Table 2.SM.2.

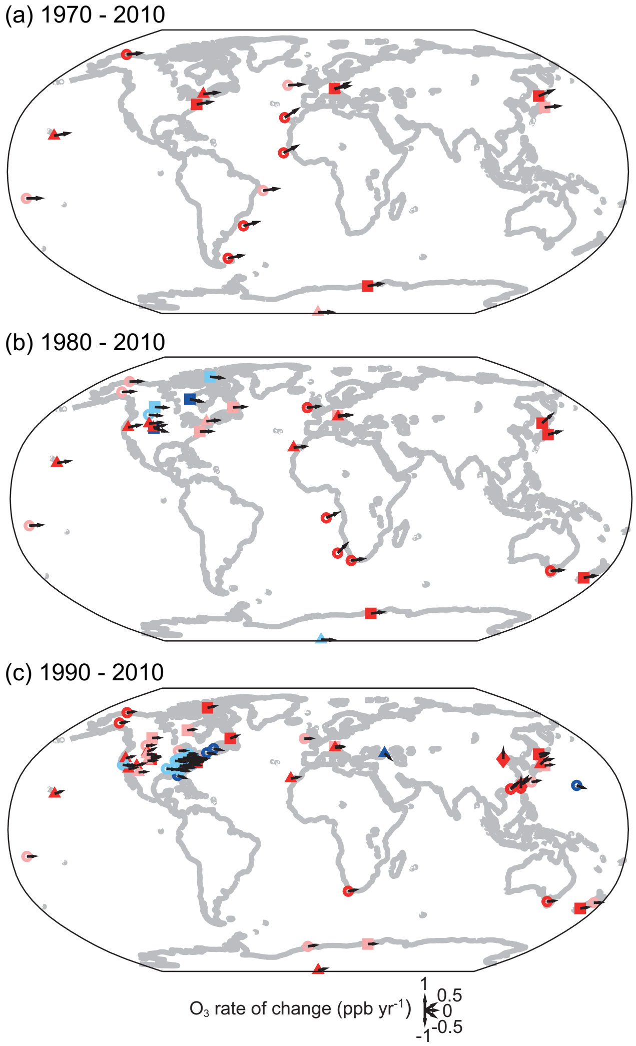

Figure 2.SM.1 | Ozone trends based on yearly average ozone values at the surface or within the lower troposphere (a) beginning between 1970 and 1979 and ending between 2000 and 2010. (b) Beginning between 1980 and 1989 and ending between 2000 and 2010 and (c) beginning between 1990 and 1999 and ending between 2000 and 2010. Measurements were made at the surface below 1 km (circles), at the surface above 1 km (triangles), in the lower troposphere by ozonesondes (squares) and in the lower troposphere by aircraft (diamonds). Vectors indicate the ozone rate of change as shown in the legend. Colors indicate ozone trends that are statistically significant and positive (red), statistically non-significant and positive (pink), statistically nonsignificant and negative (light blue) and statistically significant and negative (blue). Trend values are from the peer-reviewed literature listed in Table 2.SM.2.

Table 2.SM.1 | Global annual mean mole fractions for long-lived greenhouse gases (LLGHGs) for use in calculating radiative forcing in Chapter 8, indication if significant natural source exists, references to the data used to calculate global means and summary of standard scales used.

Species	2011 Global Annual Mean (ppt)[a]	Relative Difference[b]	Data Source[c]	Natural Source	References	Scale
CO_2 (ppm)	390.46	Negligible	NOAA SIO		Keeling et al. (1976); Zhao and Tans (2006)	N07; 08A
CH_4 (ppb)	1803.15	Negligible		Yes	Dlugokencky et al. (2005); Rigby et al. (2008)	TU; N04
N_2O (ppb)	324.15	0.1%		Yes	Prinn et al. (1990); Hall et al. (2007)	S98; N06A
C_2F_6	4.16		AGAGE		Muhle et al. (2010)	S07
C_3F_8	0.55		AGAGE		Muhle et al. (2010)	S07
CCl_4	85.7	–1.7%			Simmonds et al. (1998); Thompson (2004)[e]	S05; N08
CF_4	79.0		AGAGE	Yes	Muhle et al. (2010)	S05
CFC-11	237.7	–0.7%			Cunnold et al. (1997); Thompson (2004)[e]	S05; N92
CFC-113	74.3	–0.1%			Fraser et al. (1996); Thompson (2004)[e]; Miller et al. (2008)	S05; N03
CFC-115	8.37		AGAGE		Miller et al. (2008)	S05; N08
CFC-12	528.4	0.4%			Cunnold et al. (1997); Thompson (2004)[e]	S05; N08
CH_2Cl_2	25.9	–18.7%			Thompson (2004)[e]	UB98
CH_3Br	7.11	1.7%		Yes	Thompson (2004)[e]	S05; N03
CH_3CCl_3	6.31	–0.1%			Thompson (2004)[e]; Prinn et al. (2005); Montzka et al. (2011)	S05; N03
CH_3Cl	534.1	–1.6%		Yes	Thompson (2004); Miller et al. (2008)[e]	S98; N03
$CHCl_3$	7.41		AGAGE[d]	Yes	Prinn et al. (2000); Miller et al. (2008)	S05; N03
H-1211	4.07	2.2%			Thompson (2004)[e]; Miller et al. (2008)	S05; N06
H-1301	3.23	2.8%			Thompson (2004)[e]; Miller et al. (2008)	S05; N06
H-2402	0.45		NOAA		Butler et al. (1998)	N92
HCFC-141b	21.4	0.3%			O'Doherty et al. (2004); Thompson (2004); Miller et al. (2008); Montzka et al. (2009)	S05; N94
HCFC-142b	21.1	1.9%			O'Doherty et al. (2004); Thompson (2004); Miller et al. (2008); Montzka et al. (2009)	S05; N94
HCFC-22	213.0	0.4%			O'Doherty et al. (2004); Montzka et al. (1993); Miller et al. (2008)	S05; N06
HFC-125	9.58		AGAGE[d]		O'Doherty et al. (2009)	UB98; N08
HFC-134a	62.5	–0.3%			Montzka et al. (1996); O'Doherty et al. (2004); Miller et al. (2008)	S05; N00
HFC-143a	12.0		AGAGE[d]		Miller et al. (2008)	S07; N08
HFC-152a	6.42		AGAGE		Greally et al. (2007); Miller et al. (2008)	S05
HFC-227ea	0.65		AGAGE[d]		Laube et al. (2010); Vollmer et al. (2011)	E05; N11
HFC-23	24.0		AGAGE[d]		Miller et al. (2010)	S07; N08
HFC-236fa	0.08		AGAGE		Vollmer et al. (2011)	E09
HFC-245fa	1.24		AGAGE		Vollmer et al. (2006)	E05
HFC-32	4.92		AGAGE[d]		Miller et al. (2008)	S07; N08
HFC-365mfc	0.58		AGAGE[d]		Vollmer et al. (2011); Stemmler et al. (2007)	E03; N11
SF_6	7.28	–0.6%			Rigby et al. (2010); Hall et al. (2011)	S05; N06
SO_2F_2	1.71		AGAGE		Muhle et al. (2009)	S07
NF_3	0.86		AGAGE		Weiss et al. (2008); Arnold et al. (2013)	S12

Notes:

AGAGE = Advanced Global Atmospheric Gases Experiment; NOAA = National Oceanic and Atmospheric Administration, Earth System Research Laboratory, Global Monitoring Division; SIO = Scripps Institution of Oceanography, University of California, San Diego. CFC-11 = CCl_3F; CFC-113 = $CClF_2CCl_2F$; CFC-12 = CCl_2F_2; HCFC-22 = $CHClF_2$; HCFC-141b = CH_3CCl_2F; HCFC-142b = CH_3CClF_2; HFC-125 = CHF_2CF_3; HFC-134a = CH_2FCF_3; HFC-143a = CH_3CF_3; HFC-152a = CH_3CHF_2; HFC-23 = CHF_3, CFC-115 = $CClF_2CF_3$, H-1211 = $CBrClF_2$, H-1301 = $CBrF_3$, H-2402 = $CBrF_2CBrF_2$, HFC-227ea = CF_3CHFCF_3, HFC-236fa = $CF_3CH_2CF_3$, HFC-245fa = $CHF_2CH_2CF_3$, HFC-32 = CH_2F_2, HFC-365mfc = $CH_3CF_2CH_2CF_3$.

[a] Global surface annual mean dry-air mole fraction.

[b] Relative difference between AGAGE and NOAA 2011 global annual mean values (AGAGE – NOAA)/average).

[c] Source of data. Blank space indicated NOAA + AGAGE.

[d] Value listed from AGAGE data only, but NOAA maintains a scale and has unpublished data.

[e] Updated information about NOAA standard scales available at: http://www.esrl.noaa.gov/gmd/ccl/summary_table.html. Scale: Standard gas scales used to calibrate instrument response. AGAGE/SIO: TU = Tohoku University CH_4 scale; SXX = Scripps Institution of Oceanography (SIO) trace gas scale developed in year 1998 (e.g., S98 = SIO-98); Sp = SIO-provisional; UB98 = Bristol University scale developed in 1998; E03 = Empa-2003; E09 = Empa-2009-p (provisional); 08A = Scripps Institution of Oceanography 08A CO_2 standard scale. NOAA: N08 = NOAA scale developed in year 2008.

Table 2.SM.2 | Ozone trends reported in the literature, using data sets with at least 10 years of measurements. To understand ozone trends in air masses that are representative of regional or baseline conditions, measurements are from rural sites. However, in East Asia data are so limited that trends are also assessed in urban areas. Unless otherwise noted, trends are reported in ppb yr^{-1} with 95% confidence limits. Trends that are statistically significant at the 95% confidence level are shown in bold font. Trends are based on annual data unless seasons are specified. *Units are not listed for trend values reported in units of ppb yr^{-1}, but units are reported for trend values reported in percent per year.

Measurement Region	Site or Seasonal Information	Trend, ppb yr^{-1} (or percent per year)*	Period	Reference	Remarks
Europe					
Alpine high elevation surface sites, 3.0–3.6 km above sea level	A composite of Zugspitze, Jungfraujoch and Sonnblick	**0.87 ± 0.13** **0.33 ± 0.10** **–0.16 ± 0.14**	1978–1989 1990–1999 2000–2009	Logan et al. 2012)	Unfiltered data, although data from January to May, 1982 at Zugspitze were dropped. Quadratic fit to seasonal time series for 1978–2009.
Alpine high elevation surface site, 3.0 km above sea level	Zugspitze	**0.39 ± 0.06** **0.14 ± 0.06** 0.05 ± 0.08	1978–2010 1981–2010 1991–2010	Oltmans et al. (2013)	Annual trend is determined from monthly means using an autoregressive model that incorporates explanatory variables and a cubic polynomial fit.
Surface, rural central Europe	Hohenpeissenberg	**0.26 ± 0.07**	1971–2010	Parrish et al. (2012)	Filtered to remove very local contamination. The trend reported here is based on yearly averages and linear regression following the methods of Parrish et al. (2012).
Surface, west coast of Ireland	Mace Head	**0.31 ± 0.10**	1989–2010	Parrish et al. (2012)	See entry above. In addition the data were filtered to represent baseline transport conditions.
Surface, west coast of Ireland	Mace Head	**0.09 ± 0.08** 0.01 ± 0.10	1988–2010 1991–2010	Oltmans et al. (2013)	Daytime unfiltered data. Annual trend calculated from monthly means using an autoregressive model that incorporates explanatory variables and a cubic polynomial fit.
Surface, rural northern German coast	Arkona-Zingst	**0.32 ± 0.05**	1957–2010	Parrish et al. (2012)	Trend reported here is based on unfiltered yearly averages and linear regression following methods of Parrish et al. (2012).
Surface, alpine valley	Arosa	**0.40 ± 0.09**	1950–2000	Parrish et al. (2012)	See entry above. No measurements were made from the late 1950s through 1988.
Surface, rural elevated site in southeast Europe	Kislovodsk High Mountain Station	**–0.65 ± 0.01**	1991–2006	Tarasova et al. (2009)	Unfiltered data. Linear regression of all available hourly data.
Northern Europe mid-troposphere, 500 hPa	Composite of ozonesondes from Ny Alesund and Sodankyla	**0.25 ± 0.21**	1990–2006	Hess and Zbinden (2013)	Unfiltered data. Linear regression of 12-month running mean of monthly ozone deviations. This 17-year trend was calculated by P. Hess using the same method as for the 1990–2000 and 2000–2006 trends reported in the paper.
Central Europe lower free troposphere, 2.6–3.8 km above sea level	MOZAIC MOZAIC Hohenpeissenberg Payerne	0.15 ± 0.15 **–0.21 ± 0.20** **–0.20 ± 0.16** **–0.25 ± 0.17**	1995–2008 1998–2008 1998–2008 1998–2008	Logan et al. (2012)	Unfiltered data; see entry below. Trends at alpine sites for 1998–2008 show similar rates.
Central Europe mid- free troposphere, 5–6.1 km above sea level	MOZAIC MOZAIC Hohenpeissenberg Payerne	**0.33 ± 0.21** –0.08 ± 0.30 –0.1 ± 0.17 **–0.43 ± 0.19**	1995–2008 1998–2008 1998–2008 1998–2008	Logan et al. (2012)	Unfiltered data. Linear regression, with annual trend calculated from four seasonal trends; trends and annual cycle fit to monthly means. MOZAIC is a composite of aircraft flights to five European airports. Others are sonde stations.
North America					
Northeastern USA, rural mountaintop	Whiteface Mountain Summit, New York	**0.09 ± 0.06** 0.07 ± 0.08 **–0.22 ± 0.12**	1973–2010 1981–2010 1991–2010	Oltmans et al. (2013)	Annual trend is determined from monthly means using an autoregressive model that incorporates explanatory variables and a cubic polynomial fit.
Eastern USA, rural surface sites	Winter, 36 sites Spring, 40 sites Summer, 41 sites	0.12 (**44%, 0%**) –0.03 (**5%, 8%**) –0.45 (**0%, 66%**)	1990–2010	Cooper et al. (2012)	Mid-day data only. Linear regression of seasonal medians at a site. The reported trend is the average of the individual trends in the region. Values in parentheses indicate the percent of sites with statistically significant positive or negative trends, respectively.
Western USA, rural surface sites	Winter, 11 sites Spring, 12 sites Summer, 12 sites	0.12 (**36%, 0%**) 0.19 (**50%, 0%**) 0.10 (**17%, 8%**)	1990–2010	Cooper et al. (2012)	See entry above.
USA west coast, marine boundary layer	Composite of several sites	**0.27 ± 0.13**	1988–2010	Parrish et al. (2012)	Trend reported here is based on yearly averages and linear regression following methods of Parrish et al. (2012). Data were filtered to represent baseline transport conditions.
High latitudes, surface	Denali, central Alaska	0.04 ± 0.08 **0.15 ± 0.10**	1987–2010 1991–2010	Parrish et al. (2012)	Annual trend is determined from monthly means using an autoregressive model that incorporates explanatory variables and a cubic polynomial fit.
Arctic, surface	Barrow, Alaska	**0.09 ± 0.06** 0.03 ± 0.06 **0.13 ± 0.10**	1973–2010 1981–2010 1991–2010	Oltmans et al. (2013)	See entry above.
Eastern USA, free troposphere, 500 hPa	Annual composite of Wallops Island ozonesondes and MOZAIC aircraft profiles.	**0.41 ± 0.32**	1994–2006	Hess and Zbinden (2013)	Unfiltered data. Linear regression of annually averaged values for years when both ozonesonde and MOZAIC profiles were available. This 13-year trend was calculated by P. Hess using the same method as for the 1994–2000 and 2000–2006 trends reported in the paper.

Table 2.SM.2 (continued)

Measurement Region	Site or Seasonal Information	Trend, ppb yr^{-1} (or percent per year)*	Period	Reference	Remarks
Mid-Atlantic USA, coastal Virginia, surface–850 hPa	Wallops Island ozonesondes	**0.16 ± 0.12** 0.02 ± 0.16 **0.27 ± 0.22**	1971–2010 1981–2010 1991–2010	Oltmans et al. (2013)	Annual trend is determined from monthly means using an autoregressive model that incorporates explanatory variables and a cubic polynomial fit.
850–700 hPa	Wallops Island ozonesondes	0.08 ± 0.10 0.01 ± 0.12 **0.33 ± 0.14**	1971–2010 1981–2010 1991–2010	Oltmans et al. (2013)	See entry above.
700–500 hPa	Wallops Island ozonesondes	0.09 ± 0.10 0.01 ± 0.14 **0.27 ± 0.14**	1971–2010 1981–2010 1991–2010	Oltmans et al. (2013)	See entry above.
500–300 hPa	Wallops Island ozonesondes	–0.00 ± 0.18 0.20 ± 0.20 0.09 ± 0.32	1971–2010 1981–2010 1991–2010	Oltmans et al. (2013)	See entry above.
Western USA, surface–700 hPa	Boulder ozonesondes	**–0.24 ± 0.14** **0.19 ± 0.16**	1981–2010 1991–2010	Oltmans et al. (2013)	See entry above.
700–500 hPa	Boulder ozonesondes	**–0.36 ± 0.10** 0.06 ± 0.12	1981–2010 1991–2010	Oltmans et al. (2013)	See entry above.
500–300 hPa	Boulder ozonesondes	**–0.38 ± 0.18** 0.12 ± 0.26	1981–2010 1991–2010	Oltmans et al. (2013)	See entry above.
Eastern Canada, surface–850 hPa	Goose Bay ozonesondes	0.04 ± 0.10 **0.32 ± 0.12**	1981–2010 1991–2010	Oltmans et al. 2013)	See entry above.
850–700 hPa	Goose Bay ozonesondes	0.05 ± 0.12 **0.40 ± 0.16**	1981–2010 1991–2010	Oltmans et al. (2013)	See entry above.
700–500 hPa	Goose Bay ozonesondes	0.10 ± 0.12 **0.51 ± 0.16**	1981–2010 1991–2010	Oltmans et al. (2013)	See entry above.
500–300 hPa	Goose Bay ozonesondes	0.14 ± 0.28 **0.68 ± 0.32**	1981–2010 1991–2010	Oltmans et al. (2013)	See entry above.
Central Canada, surface–850 hPa	Churchill ozonesondes	**–0.18 ± 0.08** 0.09 ± 0.12	1981–2010 1991–2010	Oltmans et al. (2013)	See entry above.
850–700 hPa	Churchill ozonesondes	**–0.12 ± 0.10** 0.10 ± 0.16	1981–2010 1991–2010	Oltmans et al. (2013)	See entry above.
700–500 hPa	Churchill ozonesondes	–0.06 ± 0.10 **0.31 ± 0.16**	1981–2010 1991–2010	Oltmans et al. (2013)	See entry above.
500–300 hPa	Churchill ozonesondes	–0.05 ± 0.30 **0.55 ± 0.40**	1981–2010 1991–2010	Oltmans et al. (2013)	See entry above.
Western Canada, surface–850 hPa	Edmonton ozonesondes	–0.05 ± 0.10 0.02 ± 0.16	1981–2010 1991–2010	Oltmans et al. (2013)	See entry above.
850–700 hPa	Edmonton ozonesondes	**0.13 ± 0.10** **0.31 ± 0.12**	1981–2010 1991–2010	Oltmans et al. (2013)	See entry above.
700–500 hPa	Edmonton ozonesondes	**0.13 ± 0.10** **0.45 ± 0.12**	1981–2010 1991–2010	Oltmans et al. (2013)	See entry above.
500–300 hPa	Edmonton ozonesondes	**0.21 ± 0.20** **0.69 ± 0.26**	1981–2010 1991–2010	Oltmans et al. (2013)	See entry above.
Arctic Canada, surface–850 hPa	Resolute ozonesondes	–0.09 ± 0.12 **0.21 ± 0.16**	1981–2010 1991–2010	Oltmans et al. (2013)	See entry above.
850–700 hPa	Resolute ozonesondes	0.03 ± 0.12 **0.39 ± 0.18**	1981–2010 1991–2010	Oltmans et al. (2013)	See entry above.
700–500 hPa	Resolute ozonesondes	–0.00 ± 0.14 **0.40 ± 0.18**	1981–2010 1991–2010	Oltmans et al. (2013)	See entry above.
500–300 hPa	Resolute ozonesondes	0.00 ± 0.42 **1.17 ± 0.64**	1981–2010 1991–2010	Oltmans et al. (2013)	See entry above.
Western North America free troposphere (3–8 km)	Spring	**0.52 ± 0.20** **0.41 ± 0.27**	1984–2011 1995–2011	Cooper et al. (2012)	Unfiltered data. Linear regression based on median values of all available measurements (lidar, ozonesonde and aircraft) in the 3–8 km range during April to May.
Asia					
Mountaintop site in western Japan	Mt. Happo, 1.85 km above sea level	**0.65 ± 0.32**	1991–2011	Parrish et al. 2012)	Trend reported here is based on unfiltered yearly averages and linear regression following methods of Parrish et al., 2012.
Surface, rural eastern Japan	Ryori	0.22 ± 0.90	1991–2010	Oltmans et al. 2013)	Annual trend is determined from monthly means using an autoregressive model that incorporates explanatory variables and a cubic polynomial fit.

(continued on next page)

Table 2.SM.2 (continued)

Measurement Region	Site or Seasonal Information	Trend, ppb yr^{-1} (or percent per year)*	Period	Reference	Remarks
Japanese marine boundary layer	Composite of 3 sites in western Japan	0.31 ± 0.34	1998–2011	Parrish et al. 2012)	Trend reported here is based on unfiltered yearly averages & linear regression following methods of Parrish et al., 2012.
Beijing, China, boundary layer	Annual Summer afternoons	**~1** **~3**	1997–2004	Ding et al. 2008)	The rate of change was derived from a comparison of mean MOZAIC aircraft profiles during the periods 1995–1999 and 2000–2005.
Northern Taiwan, China, elevated surface site	YangMing	**0.54 ± 0.21**	1994–2007	Lin et al. 2010)	Unfiltered data. Linear regression of annual means, using data from all times of day.
Taiwan, China Surface	Composite of 3 coastal sites near urban emissions.	**0.52 ± 0.10**	1994–2007	Lin et al. 2010)	Unfiltered data. Linear regression of annual means, using data from all times of day.
Taiwan, China surface	Composite of 12 urban sites in the north of the country.	**0.75 ± 0.07**	1994–2007	Lin et al. 2010)	Unfiltered data. Linear regression of annual means, using data from all times of day.
Taiwan, China, surface	Composite of 4 sites in southern Taiwan, near urban emissions.	~1.5	1997–2006	Li et al. 2010)	Unfiltered data. Linear regression using monthly means. The reported trend was inferred from the regression line in Figure 2. Significance at the 95% confidence limit was not specified.
Hong Kong, surface	Hok Tsui coastal site on southern tip of Hong Kong Island	**0.58**	1994–2007	Wang et al. 2009b)	Unfiltered data. Linear regression of monthly means, using all months and all times of day. This site is often upwind of the Hong Kong urban area.
Northern Japan, surface–850 hPa	Sapporo ozonesondes	**0.35 ± 0.10** **0.63 ± 0.12** **0.15 ± 0.14**	1971–2010 1981–2010 1991–2010	Oltmans et al. 2013)	Annual trend is determined from monthly means using an autoregressive model that incorporates explanatory variables and a cubic polynomial fit.
850–700 hPa	Sapporo ozonesondes	**0.23 ± 0.10** **0.48 ± 0.12** –0.02 ± 0.12	1971–2010 1981–2010 1991–2010	Oltmans et al. 2013)	See entry above
700–500 hPa	Sapporo ozonesondes	**0.23 ± 0.10** **0.38 ± 0.12** 0.07 ± 0.14	1971–2010 1981–2010 1991–2010	Oltmans et al. 2013)	See entry above
500–300 hPa	Sapporo ozonesondes	0.16 ± 0.20 0.10 ± 0.20 –0.03 ± 0.28	1971–2010 1981–2010 1991–2010	Oltmans et al. 2013)	See entry above
Central Japan, surface–850 hPa	Tsukuba ozonesondes	0.08 ± 0.14 **0.23 ± 0.22** 0.09 ± 0.30	1971–2010 1981–2010 1991–2010	Oltmans et al. 2013)	See entry above
850–700 hPa	Tsukuba ozonesondes	**0.16 ± 0.12** **0.21 ± 0.16** 0.09 ± 0.24	1971–2010 1981–2010 1991–2010	Oltmans et al. 2013)	See entry above
700–500 hPa	Tsukuba ozonesondes	**0.16 ± 0.10** **0.23 ± 0.14** **0.21 ± 0.20**	1971–2010 1981–2010 1991–2010	Oltmans et al. 2013)	See entry above
500–300 hPa	Tsukuba ozonesondes	**0.34 ± 0.20** **0.41 ± 0.26** 0.92 ± 1.12	1971–2010 1981–2010 1991–2010	Oltmans et al. 2013)	See entry above
Southern Japan, surface–850 hPa	Naha ozonesondes	0.17 ± 0.20	1991–2010	Oltmans et al. 2013)	See entry above
850–700 hPa	Naha ozonesondes	0.09 ± 0.20	1991–2010	Oltmans et al. 2013)	See entry above
700–500 hPa	Naha ozonesondes	**0.21 ± 0.20**	1991–2010	Oltmans et al. 2013)	See entry above
500–300 hPa	Naha ozonesondes	0.22 ± 0.22	1991–2010	Oltmans et al. 2013)	See entry above
South Asia, tropospheric column ozone as measured by satellites	A broad region including much of India, southeast Asia and Indonesia	**0.3–0.7 % yr^{-1}**	1979–2005	Beig and Singh, 2007)	The decadal trend was calculated using a multifunctional regression model. Here the trend is converted to percent yr^{-1}.
North Pacific Ocean tropics and subtropics					
Minamitorishima, Japan	Remote Japanese island 4000 km east of southern China	**–0.29 ± 0.14**	1994–2010	Oltmans et al. 2013)	Annual trend is determined from monthly means using an autoregressive model that incorporates explanatory variables and a cubic polynomial fit.
Mauna Loa, Hawaii	3.4 km above sea level	**0.16 ± 0.08** **0.14 ± 0.08** **0.31 ± 0.14**	1974–2010 1981–2010 1991–2010	Oltmans et al. 2013)	See entry above. Only night time data were used to ensure downslope flow conditions.

(continued on next page)

Table 2.SM.2 (continued)

Measurement Region	Site or Seasonal Information	Trend, ppb yr^{-1} (or percent per year)*	Period	Reference	Remarks
Hawaii, USA surface–850 hPa	Hilo ozonesondes	**–0.38 ± 0.16** **0.25 ± 0.18**	1982–2010 1991–2010	Oltmans et al. 2013)	See entry above
850–700 hPa	Hilo ozonesondes	0.04 ± 0.16 0.15 ± 0.22	1982–2010 1991–2010	Oltmans et al. 2013)	See entry above
700–500 hPa	Hilo ozonesondes	0.11 ± 0.16 0.14 ± 0.24	1982–2010 1991–2010	Oltmans et al. 2013)	See entry above
500–300 hPa	Hilo ozonesondes	0.09 ± 0.16 0.05 ± 0.26	1982–2010 1991–2010	Oltmans et al. 2013)	See entry above
Northern Hemisphere Atlantic Ocean					
Marine boundary layer, eastern North Atlantic Ocean	40°N–60°N 20°N–40°N 0°–20°N	0.05 **0.51** **0.42**	1977–2002	Lelieveld et al. 2004)	Unfiltered measurements from ships traversing the indicated regions. The 95% confidence limits were not reported, although statistical significance was.
Marine boundary layer, western North Atlantic Ocean	Bermuda	**0.31 ± 0.25** (winter) 0.27 ± 0.29 (spring) **0.30 ± 0.16** (summer) 0.05 ± 0.33 (autumn)	1989–2010	Parrish et al. 2012)	Unfiltered data. Linear regression of seasonal averages. There is a data gap of 5 years in the middle of the record.
Canary Islands, subtropical marine location west of North Africa	Izana, Tenerife, 2800 m above sea level.	**0.14 ± 0.10**	1991–2010	Oltmans et al. 2013)	Annual trend is determined from monthly means using an autoregressive model that incorporates explanatory variables and a cubic polynomial fit. Only night time data were used to ensure downslope flow conditions.
Northern Hemisphere upper troposphere		Seasons with a significant increase in ozone			
Western USA Northeast USA N. Atlantic Ocean Europe Middle East Northern India South China Northern Japan Southern Japan		None **Winter, spring** **Winter** **Spring** **Spring, summer** **Spring, summer** **Summer** **Summer, autumn** **All seasons**	Ozone change between 1975–1979 and 1994–2001	Schnadt Poberaj et al. 2009)	Ozone changes were calculated for various regions of the northern hemisphere upper troposphere that were sampled by the NASA GASP aircraft program in the 1970s and by the European MOZAIC program in the 1990s. No region had a statistically significant decrease in ozone, in any season.
Southern Hemisphere					
Tropical South Pacific Ocean, marine boundary layer	Samoa	0.01 ± 0.04 **0.05 ± 0.04** 0.02 ± 0.68	1976–2010 1981–2010 1991–2010	Oltmans et al. 2013)	Annual trend is determined from monthly means using an autoregressive model that incorporates explanatory variables and a cubic polynomial fit.
Marine boundary layer, western South Atlantic Ocean	40°S–60°S 20°S–40°S 0°S–20°S	**0.17** **0.24** 0.12	1977–2002	Lelieveld et al. 2004)	Unfiltered measurements from ships traversing the indicated regions. The 95% confidence limits were not reported, although statistical significance was.
Marine boundary layer, eastern South Atlantic Ocean	20°S–40°S 0°–20°S	**0.68** **0.37**	1977–2002	Lelieveld et al. 2004)	See entry above
Mid-latitude marine boundary layer	Cape Point, South Africa	**0.13 ± 0.02** **0.17 ± 0.04**	1983–2010 1991–2010	Oltmans et al. 2013)	Annual trend is determined from monthly means using an autoregressive model that incorporates explanatory variables and a cubic polynomial fit.
Mid-latitude marine boundary layer	Cape Grim, Tasmania, Australia	**0.06 ± 0.02** **0.09 ± 0.04**	1982–2010 1991–2010	Oltmans et al. 2013)	See entry above
Mid-latitude rural coastal site	Baring Head, New Zealand	0.01 ± 0.06	1991–2010	Oltmans et al. 2013)	See entry above
Antarctica, Ekström ice shelf, 10 km from the ocean	Neumayer	0.13 ± 0.16	1995–2005	Helmig et al. 2007)	Unfiltered data. Linear regression based on annual median values.
Antarctica, 2.8 km above sea level	South Pole	0.01 ± 0.04 –0.01 ± 0.41 **0.20 ± 0.04**	1975–2010 1981–2010 1991–2010	Oltmans et al. 2013)	Annual trend is determined from monthly means using an autoregressive model that incorporates explanatory variables and a cubic polynomial fit.
Tropical Indian Ocean, La Reunion Island ozonesonde profiles	2–4 km a.s.l 4–10 km a.s.l. 10–16 km a.s.l.	0.01 ± 0.69 % yr^{-1} 0.44 ± 0.58 % yr^{-1} **1.23 ± 0.58 % yr^{-1}**	1992–2008	Clain et al. 2009)	Unfiltered ozonesonde measurements. Linear regression of all available year-round measurements.
Subtropical South Africa, Irene ozonesonde profiles	2–4 km a.s.l 4–10 km a.s.l. 10–16 km a.s.l.	**1.44 ± 0.40 % yr^{-1}** **0.40 ± 0.33 % yr^{-1}** 0.19 ± 0.35 % yr^{-1}	1990–2008	Clain et al. 2009)	Unfiltered ozonesonde measurements. Linear regression of all available year-round measurements. No data for 1994–1997.
Southern New Zealand surface–850 hPa	Lauder, ozonesondes	**0.15 ± 0.06** **0.12 ± 0.08**	1986–2010 1991–2010	Oltmans et al. 2013)	Annual trend is determined from monthly means using an autoregressive model that incorporates explanatory variables and a cubic polynomial fit.

(continued on next page)

Table 2.SM.2 (continued)

Measurement Region	Site or Seasonal Information	Trend, ppb yr^{-1} (or percent per year)*	Period	Reference	Remarks
850–700 hPa	Lauder, ozonesondes	**0.14 ± 0.06** **0.10 ± 0.06**	1986–2010 1991–2010	Oltmans et al. 2013)	See entry above
700–500 hPa	Lauder, ozonesondes	**0.16 ± 0.08** **0.20 ± 0.08**	1986–2010 1991–2010	Oltmans et al. 2013)	See entry above
500–300 hPa	Lauder, ozonesondes	0.06 ± 0.12 0.12 ± 0.14	1986–2010 1991–2010	Oltmans et al. 2013)	See entry above
Coastal Antarctica, surface–850 hPa	Syowa, ozonesondes	**0.15 ± 0.06** **0.10 ± 0.06** 0.02 ± 0.08	1971–2010 1981–2010 1991–2010	Oltmans et al. 2013)	See entry above
850–700 hPa	Syowa, ozonesondes	0.06 ± 0.06 0.03 ± 0.06 0.06 ± 0.06	1971–2010 1981–2010 1991–2010	Oltmans et al. 2013)	See entry above
700–500 hPa	Syowa, ozonesondes	**0.05 ± 0.04** 0.01 ± 0.06 **0.12 ± 0.08**	1971–2010 1981–2010 1991–2010	Oltmans et al. 2013)	See entry above
500–300 hPa	Syowa, ozonesondes	–0.10 ± 0.10 –0.07 ± 0.14 0.18 ± 0.16	1971–2010 1981–2010 1991–2010	Oltmans et al. 2013)	See entry above
Central Antarctica, 700–500 hPa	South Pole, ozonesondes	**0.05 ± 0.04** **0.08 ± 0.06**	1986–2010 1991–2010	Oltmans et al. 2013)	See entry above
500–300 hPa	South Pole, ozonesondes	0.12 ± 0.14 0.09 ± 0.18	1986–2010 1991–2010	Oltmans et al. 2013)	See entry above

2.SM.2.3 Aerosols

Comprehensive, long-term and high-quality observations of aerosols were initiated mainly after 2000, and are currently available only at a few locations and regions. The monitoring and observations of aerosols are still to a large degree uncoordinated on the continental and global scale, despite the crucial importance of aerosols as short-lived climate forcers. A few long-term background measurements of aerosol properties are performed within the framework of WMO GAW (World Meteorological Organisation Global Atmosphere Watch program); however, the data coverage is low. An overview and critical evaluation of worldwide, quality assured, aerosol trend measurements does not exist at present. For studies of aerosol–climate interactions, it is crucial that the sites are representative for regional/rural conditions, with low influence of local pollution and that the measurements are harmonised among sites and networks, and provided as homogeneous time series.

Regional air pollution networks in Europe and North America are the most reliable source of information on long-term surface aerosol trends in these parts of the world. In Europe, the European Monitoring and Evaluation Programme (EMEP) network provides regionally representative measurements of aerosol composition since the 1980s; these measurements are described in annual reports, and they are available via www.emep.int. Torseth et al. (2012) provide an overview of results from two or three decades of EMEP measurements, as discussed in Section 2.2.3.

In North America, the U.S. Clean Air Status and Trends Network (CASTNET) and the Canadian Air and Precipitation Monitoring Network (CAPMoN) provide regionally representative long-term measurements of major ions in aerosols, including sulphate (Hidy and Pennell, 2010); these networks do not report $PM_{2.5}$. The U.S. Interagency Monitoring of Protected Visual Environments (IMPROVE) Network has measured $PM_{2.5}$ and PM_{10} (particulate matter with aerodynamic diameters <2.5 and <10 µm, respectively) mass, total aerosol composition and visibility at about 60 regional stations since 1989 (Hand et al., 2011). Canadian CAPMoN network results are summarized in Canada (2012).

In Asia, the Acid Deposition Network East Asia (EANET, 2011) has measured particulate matter and deposition since 2001, but thus far no trend studies have been published. In China, CAWNET (China Atmosphere Watch Network) and CARSNET (Calibration campaign of the China Aerosol Remote Sensing NETwork) recently began systematic aerosol observations (Zhang et al., 2012); however, only a few years of data are available. An analysis of population weighted $PM_{2.5}$ measurements reported in Brauer et al. (2012) showed that China has the worlds highest average $PM_{2.5}$ (55 µg m^{-3}), more than twice the global average, indicating a strong influence of pollutant emissions. An analysis (Qu et al., 2010) of reconstructed urban PM_{10} time series (2000–2006) from reported air pollution indices in 86 Chinese cities suggests that median aerosol concentrations declined from 108 to 95 µg m^{-3} in 16 northern cities and increased slightly from 52 to 60 µg m^{-3} in 12 southern cities. Quan et al. (2011) report strong declines in visibility commencing in the 1970s in the eastern provinces of China, and continuing through the 2000s. They link these reduced visibility levels to emission changes and high PM levels. See the discussion of visibility measurements in Section 2.2.3.1 and in Wang et al. (2009a, 2012).

In some other Asian regions long-term measurements from individual research groups or small networks are becoming available, but it is often difficult to assess the significance of these measurements for larger regions.

In India, the Central Pollution Control Board (CPCB), Government of India, is executing a nation-wide programme of ambient air quality monitoring known as the National Air Quality Monitoring Programme (NAMP). The network consists of 342 monitoring stations covering 127 cities/towns in 26 States and 4 Union Territories. The State of Environment Report (Ministery of Environment and Forest, 2009) reported annual average levels of respirable particulate matter (approximately PM_{10}) in residential areas of major cities ranging from 120 to 160 µg m^{-3} (Delhi), 80 to 120 µg m^{-3} (Mumbai), 30 to 90 µg m^{-3} (Chennai), and 120 to 140 µg m^{-3} (Kolkata); in these cities' trends are mostly stable or increasing for 2000–2007. No details on the robustness of trends are given, and the validity of these trends for rural regions is not reported.

Surface-based remote sensing of aerosols, as discussed in Section 2.2.3.1, is based mainly on results from the global AERONET network (Holben et al., 1998). However, coverage of AERONET over several regions is poor. Since AR4, several other regional networks were established such as ARFINET covering India(Krishna Moorthy et al., 2013); AEROCAN over Canada (http://www.aerocanonline.com/), and SKYNET over Japan (Kim et al., 2004); these data are not included in this analysis.

2.SM.2.3.1 North American Sulphate Trends

In Section 2.2.3.2 overall declines of SO_4^{2-} from the IMPROVE (Hand et al., 2011) network are on the order of 2 to 4% yr^{-1}, but slightly larger (about 6% yr^{-1}) along the east coast of the USA. SO_4^{2-} declines in winter were somewhat larger than in other seasons. These trends are consistent with average trends reported by CASTNET (2010) of –0.045 µg S m^{-3} yr^{-1} for the period 1990–2008 in the eastern US, and a decrease of CASTNET aerosol sulphate concentrations by –21% in the East and Northeast, –22% in the Midwest, and –20% in the South between the two periods 1990–1994 and 2000–2004 (Sickles and Shadwick, 2007a). Indirect evidence for declining sulphate particulate concentrations is found in an analysis of SO_4^{2-} wet deposition by 20 to 30% over a time period of 15 years (Sickles and Shadwick, 2007b), corresponding to a trend of about –1.4 to –2.1% yr^{-1}. In Canada, aerosol sulphate concentrations declined by 30 to 45% between 1991–1993 and 2004–2006 at non-urban CAPMoN sites in the eastern half of the country. These declines are consistent with the trends of inorganic aerosol components reported by Quinn et al. (2009) at Barrow, Alaska, ranging between –2.3% yr^{-1} for SO_4^{2-} to –6.4% for NH_4. Hidy and Pennell (2010) show remarkable agreement of $PM_{2.5}$ and SO_4^{2-} declines in Canada, pointing to common emission sources of $PM_{2.5}$ and SO_4^{2-}.

2.SM.2.3.2 Black (Light Absorbing) and Elemental Carbon Trends

The terms black carbon (BC), also referred to as light absorbing carbon (LAC), and elemental carbon (EC) refer to the analysis method: optical methods (aerosol light absorption) or filter measurements using thermal methods, respectively. For a detailed discussion on methods, see Bond et al. (2013). The measurements are associated with large uncertainties; intercomparisons show differences of a factor of 2 to 3 for optical methods, and a factor of 4 for thermal methods (Vignati et al., 2010) which also renders quantitative comparison of LAC time series uncertain. In addition, although there is a general lack of BC/EC measurements, long-term time series are even scarcer.

In Europe, long-term EC and organic carbon (OC) data have been available at two stations (in Norway and Italy) starting in 2001 (Yttri et al., 2011). Torseth et al. (2012) report slight decreases over these 9 years, but with no assessment of statistical significance. In North America, the combined IMPROVE and CSN network (Hand et al., 2011) is measuring elemental and organic carbon. However, trend analysis of long-term data are reported only (Hand et al., 2011) for total carbon (TC = black carbon + organic carbon), as an upgrade in sampling techniques around 2005 led to a different measured ratio of EC and OC. These TC measurements indicate highly significant (95% confidence) downward trends of total carbon between 2.5 and 7.5% yr^{-1} along the east and west coasts of the USA, and smaller and less significant ($p < 0.15$) trends in other USA regions from 1989 to 2008. Sharma et al. (2006) published long-term measurements of equivalent BC at Alert, Canada and Barrow, Alaska, USA. Decreases were 54% at Alert and 27% at Barrow for 1989–2003; part of the trend difference was associated with changes in circulation patterns, that is, the phase of North Atlantic Oscillation (NAO).

In China, constant EC concentrations until the late 1970s have been derived from sediments at Chaohu and Lake Taihu in Eastern China (Han et al., 2011), followed by a sharp increase afterwards, corresponding to the rapid industrialization of China in the last three decades. An analysis of broadband radiometer data from 1957 to 2007 (Wang and Shi, 2010) showed a slight decrease in absorption of aerosol after 1990, likely due to LAC, while there was no significant change in the scattering fraction of aerosol.

In India, downward trends in BC of 250 ng m^{-3} yr^{-1} (from 4000 to 2000 ng m^{-3}) in the period 2001–2009 were observed at the southern station of Trivandrum, with the largest changes occurring in 2007–2009 (Krishna Moorthy et al., 2009). At the northern Kanpur station increases of Aerosol Optical Depth (AOD) during the post-monsoon period and winter were observed for 2001–2010, attributed to anthropogenic emission changes, with declining trends during the pre-monsoon and monsoon seasons, attributed to changes in natural emissions (Kaskaoutis et al., 2012).

2.SM.2.4 Carbon Monoxide Surface Measurements

Analysis of carbon monoxide (CO) data from the NOAA ESRL GMD global cooperative air sampling network (data path: ftp://ftp.cmdl.noaa.gov/ccg/co/flask/) indicates a small decrease in globally averaged CO from 2006 to 2010. These findings are corroborated by analysis of 1994–2012 AGAGE baseline CO measurements at Mace Head, Ireland (updated from Prinn et al. (2000), http://agage.eas.gatech.edu/data.htm) which showed large variability until 2005, and smaller variability together with stable or slightly decreasing CO from 2006–2012. The observations are consistent with estimates of a slight decline in global anthropogenic CO emissions over the same time, although East Asian emissions may have increased (Granier et al., 2011).

2.SM.3 Quantifying Changes in the Mean: Trend Models and Estimation in Box 2.2

The Supplementary Material provides a detailed description of the method used to estimate linear trends in Chapter 2 and compares the results of this relatively simple method with those of a wide variety of other methods for fitting lines to data and estimating their uncertainty. It is demonstrated that the differences among the methods are rather small compared to the uncertainty estimates of each method. Details of the smoothing method used to produce the result shown in Box 2.2, Figure 1, are also provided.

2.SM.3.1 Methods of Estimating Linear Trends and Uncertainties

Several different methods of calculating linear trends and their uncertainties are illustrated here by application to the annual mean time series of globally averaged Earth surface temperatures from the HadCRUT4 data set (see Section 2.4.3 for details). The methods used are described briefly below. The conclusion of this analysis is that, for time series like the one used here, the trend line slope and its uncertainty limits are very similar for most of the methods that take into account dependency in the data sets in the form of the first-order autoregressive model AR(1). These results are similar to those obtained by the Restricted Maximum Likelihood (REML) method used in AR4. The similarity of the AR4 method results to those of the methods investigated here was determined by applying these methods to AR4 data sets and obtaining similar results for linear trends and their uncertainties (not shown).

2.SM.3.2 Comparison of Trend Slope Calculation Methods

We would like to fit a straight line to a given time series of observations $\{y_i\}$ that correspond to an independent variable (instants of time) $\{x_i\}$:

$$y_i = a + bx_i + e_i\,, i = 1, \cdots, N$$

where a and b are constant parameters to be determined, while $\{e_i\}$ represents residual variability in observations (with regard to the straight line $y = a + bx$). Without any additional assumptions, one can find the least squares solution for the trend line, that is, $\hat{a}$ and $\hat{b}$ that minimizes the overall squared error $\sum_1^N e_i^2$ in the equation above:

$$\hat{b} = \frac{\sum_{i=1}^N (x_i - m_x)(y_i - m_y)}{\sum_{i=1}^N (x_i - m_x)^2}, \quad \hat{a} = m_y - \hat{b}m_x \qquad \text{(2.SM.1)}$$

where m_x and m_y are sample means of x and y, respectively:

$$m_x = \frac{1}{N}\sum_{i=1}^N x_i\,, \quad m_y = \frac{1}{N}\sum_{i=1}^N y_i \qquad \text{(2.SM.2)}$$

Data residuals (or errors in the linear fit) are

$$\hat{e}_i = y_i - (\hat{a} + \hat{b}x_i)\,, i = 1, \cdots, N \qquad \text{(2.SM.3)}$$

To estimate uncertainty in $\hat{a}$ and $\hat{b}$, it is useful to view $\{e_i\}$ as a realization of some random process $\{\varepsilon_i\}$. Then the estimates of $\hat{a}$ and $\hat{b}$ can be interpreted as random variables and inferences can be made about their uncertainties, that is, deviations from their "true" values. Assumptions made about $\{\varepsilon_i\}$ affect, in general, the estimates of $\hat{a}$ and $\hat{b}$, and, usually to a larger extent, the uncertainties (confidence intervals) for these estimates.

1. Ordinary least squares (OLS) is the best known case of this kind of analysis. It assumes that all ε_i are independent identically distributed (i.i.d.) random variables with normal distribution $N\ (0, \sigma_e^2)$. While σ_e is usually considered unknown, in this case its unbiased estimate can be obtained from data residuals (2.SM.3) as

$$\hat{\sigma}_e^2 = \frac{1}{N-2}\sum_{i=1}^N \hat{e}_i^2\,. \qquad \text{(2.SM.4)}$$

Note that $N - 2$ appears in the denominator instead of N because two degrees of freedom out of the original N were spent on fitting two parameters a and b.

The trend slope $\hat{b}$ estimated by equation (2.SM.1) will also be normally distributed: $N\ (0, \sigma_b^2)$, and its standard deviation σ_b can be estimated using the σ_e estimate:

$$\hat{\sigma}_b = \hat{\sigma}_e / S_x\,, \quad S_x^2 = \sum_{i=1}^N (x_i - m_x)^2. \qquad \text{(2.SM.5)}$$

Under the assumptions made about ε_i, the random variable defined as

$$U = \frac{\hat{b} - b}{\hat{\sigma}_b}$$

has a known probability distribution, a Student's t with $N - 2$ degrees of freedom. To form a confidence interval for $\hat{b}$ such that it contains the true value of b with probability p, define

$$q = t_{\frac{1+p}{2}}(N-2) \qquad \text{(2.SM.6)}$$

that is, the $\frac{1+\mathrm{p}}{2}$-quantile of Student's $t(N - 2)$ distribution. Random-variables with this distribution lie in the interval $(-q, q)$ with probability p. From this statement applied to U, it is inferred that the interval $(\hat{b} - q\hat{\sigma}_b, \hat{b} + q\hat{\sigma}_b)$ contains b with probability p, or, as it is usually stated,

$$\hat{b} = \hat{b} \pm q\,\hat{\sigma}_b \qquad \text{(2.SM.7)}$$

where $\hat{b}$, $\hat{\sigma}_b$, and q are given by formulas (2.SM.1) to (2.SM.6).

2. OLS with reduced number of degrees of freedom by Santer et al. (2008), hereafter **S2008**. The standard OLS assumption about independence of the residual deviations of data from the straight line is often unrealistic. A better approximation to reality is a model for serially correlated error, a.k.a. first-order autoregressive model AR(1):

$$\hat{\varepsilon}_{i+1} = \rho\varepsilon_i + \delta_i\,, i = 1, \cdots, N-1 \qquad \text{(2.SM.8)}$$

where δ_i, not ε_i, are now thought of as independent random variables. For a certain class of statistical estimation problems, this kind of data interdependence acts as if the sample size was reduced to N_r:

$$N_r = N\frac{1-\rho}{1+\rho} \qquad \text{(2.SM.9)}$$

For example, if calculations by formulas (2.SM.1) to (2.SM.5) are carried through for a large sample with data dependency due to the AR(1) model (2.SM.8), replacing $N-2$ by N_r-2 in the denominator of (4) results in a correct estimate of the trend error's standard deviation σ_b by formula (2.SM.5). Based on these theoretical considerations, Santer et al. (2008) employed a heuristic procedure that carries this calculation ahead using the value of ρ estimated from the sample of the OLS data residuals $\{\hat{e}_i\}$. Estimated $\hat{\rho}$ is the correlation coefficient between two $N-1$-long subsamples lagged by one time step:

$$\hat{\rho} = \frac{S_{12}}{\sqrt{S_{11}S_{22}}}, \quad S_{12} = \sum_{i=1}^{N-1}\left(\hat{e}_i - m_1\right)\left(\hat{e}_{i+1} - m_2\right) \tag{2.SM.10}$$

$$S_{11} = \sum_{i=1}^{N-1}\left(\hat{e}_i - m_1\right)^2, \quad S_{22} = \sum_{i=2}^{N}\left(\hat{e}_i - m_2\right)^2 \tag{2.SM.11}$$

$$m_1 = \frac{1}{N-1}\sum_{i=1}^{N-1}\hat{e}_i, \qquad m_2 = \frac{1}{N-1}\sum_{i=2}^{N}\hat{e}_{i+1} \tag{2.SM.12}$$

(It is assumed that the timeseries are avalable on a uniform time grid without any gaps).

Furthermore, S2008 used N_r-2 in place of $N-2$ as a degree-of-freedom parameter for Student's t in (2.SM.6). Even though in case of AR(1) error the sampling distribution of U is not that of Student's t, S2008 have calculated confidence intervals for b using formulas (2.SM.1) to (2.SM.7), with (2.SM.4) and (2.SM.6) modified by the replacement of $N-2$ by N_r-2, with N_r computed by (2.SM.9) using ρ estimated according to (2.SM.10) to (2.SM.12). Their extensive numerical experiments suggested that this heuristic strategy results in reliable, conservative uncertainty estimates for the trend slope.

3. Generalized Least Squares (GLS). Rewrite the same problem as discussed above in matrix notation. Let $\mathbf{X} = [\mathbf{X}^0\ \mathbf{X}^1]$ be an $N \times 2$ matrix, and $\mathbf{Y}$ and $\mathbf{E}$ N-dimensional column-vectors such that

$$\mathbf{X}^0 = [1\cdots1]^T,\ \mathbf{X}^1 = [x_1\cdots x_N]^T,\ \mathbf{Y} = [y_i\cdots y_N]^T,\ \mathbf{E} = [e_1\cdots e_N]^T$$

Let also $\mathbf{c}^T = [a\ b]$. Then the linear trend estimation problem becomes

$$\mathbf{Y} = \mathbf{Xc} + \mathbf{E}$$

Let $\mathbf{E}$ be a random vector from the multivariate normal distribution N (0, $\mathbf{V}$), where $\mathbf{V}$ is a covariance matrix. The optimal estimator of $\mathbf{c}$ is

$$\hat{\mathbf{c}} = (\mathbf{X}^T\,\mathbf{V}^{-1}\,\mathbf{X})^{-1}\,\mathbf{X}^T\,\mathbf{V}^{-1}\,\mathbf{Y}$$

and the covariance matrix for $\hat{\mathbf{c}}$ is

$$\mathbf{P} = (\mathbf{X}^T\,\mathbf{V}^{-1}\,\mathbf{X})^{-1}$$

For the practical implementation of this method, $\mathbf{V}$ is unknown. Here we assume that $\mathbf{V}$ is a covariance matrix of an AR(1) process: $\mathbf{V} = (v_{ij})$, $v_{ij} = \sigma_e^2\,\rho^{|i-j|}$ where σ_e^2 and ρ are estimated as variance and lag-1 autocorrelation coefficient respectively from data residuals of the initial OLS fit, as described in equations (2.SM.4) and (2.SM.10) to (2.SM.12).

4. Prewhitening. First OLS is performed, and $\hat{\rho}$ is estimated as in (2.SM.10) above. Then the time series is prewhitened as

$$y_i' = \frac{y_{i+1} - \hat{\rho}\,y_i}{1-\hat{\rho}}, \qquad i = 1,\cdots,N-1 \tag{2.SM.13}$$

The OLS is applied to timeseries $\{y_i'\}$ and corresponding times $\{x_i,\ i = 1, \cdots, N-1\}$. The prewhitening scheme (2.SM.13) does not change the value of the "true" trend coefficient b.

5. Sen–Theil trend estimator, or median slope method: Nonparametric estimate of the linear trend based on Kendall's τ, from Sen (1968). Relaxes the usual requirement of normal distribution of $\{\varepsilon_i\}$, but does assume i.i.d $\{\varepsilon_i\}$. No reduction of effective sample size is done.

6. Wang and Swail (2001) iterative method (WS2001). A method of trend calculation iterating between computing Sen–Theil trend slope for time series prewhitened as in equation (2.SM.13), computing data residuals of the original time series with regards to the line with this new slope, estimating $\hat{\rho}$ from these residuals (as in Equations (2.SM.10) to (2.SM.12)), prewhitening the original time series using this $\hat{\rho}$ value, etc. Zhang and Zwiers (2004) compared this method with other approaches, including Maximum Likelihood for linear trends with AR(1) error, and found it to perform best, especially for short time series.

Table 2.SM.3 | Trends (degrees Celsius per decade) and 90% confidence intervals for HadCRUT4 global mean annual time series for periods 1901–2011, 1901–1950 and 1951–2011 calculated by methods described in the Supplementary Material. Effective sample size N_r and lagged by one time step correlation coefficient for residuals $\hat{\rho}$ are given for methods that compute them. Note differences in the width of confidence intervals between methods that assume independence of data deviations from the straight line (OLS and Sen–Theil methods) and those that allow AR(1) dependence in the data (all other methods). Two of these methods use non-parametric trend estimation (Sen–Theil and WS2001).

Method	1901–2011			1901–1950			1951–2011		
	Trend	N_r	$\hat{\rho}$	Trend	N_r	$\hat{\rho}$	Trend	N_r	$\hat{\rho}$
OLS	0.075 ± 0.006			0.107 ± 0.016			0.107 ± 0.015		
S2008	0.075 ± 0.013	28	0.599	0.107 ± 0.026	21	0.407	0.107 ± 0.028	21	0.494
GLS	0.073 ± 0.012		0.599	0.100 ± 0.023		0.407	0.104 ± 0.025		0.494
Prewhitening	0.077 ± 0.013		0.594	0.113 ± 0.022		0.362	0.111 ± 0.026		0.488
Sen–Theil	0.075 (–0.006, +0.007)			0.113 (–0.019, +0.019)			0.109 (–0.017, +0.019)		
WS2001	0.079 (–0.014, +0.012)		0.596	0.114 (–0.026, +0.023)		0.352	0.110 (–0.028, +0.029)		0.487

2.SM.3.3 Method for Calculating Linear Trends and Their Uncertainties for General Use Within Chapter 2

The method applied in this chapter is a slight modification of the S2008 method. The sample size is not reduced ($N_r = N$), if the estimated $\hat{\rho}$ is negative. The method was also modified for use with time series where some data is missing. The formula (2.SM.9) for the effective sample size is still used. This formula was designed to give precise results for trend error when used for long time series of fully available data. In the presence of missing data (and shorter time series) this formula underestimates N_r further and thus results in wider (more conservative) confidence intervals (compared to the cases without missing data). The final procedure is as follows.

The time series of observations $\{y_i\}$ corresponds to instants of time $\{x_i, i = 1, \cdots, N\}$ that form a uniform grid. In some cases, observations y_i are missing. Formally, two sets of indices I_a and I_m are introduced that correspond to available and missing observations, respectively. Obviously, the union of the two sets includes all the possible data locations and the two sets do not intersect,

$$\{1, \cdots, N\} = I_a \cup I_m, I_a \cap I_m = \varnothing$$

The size of I_a is N_a.

First, OLS is performed for available observations:

$$\hat{b} = \frac{\sum_{i\in I_a}(x_i - m_x)(y_i - m_y)}{\sum_{i\in I_a}(x_i - m_x)^2}, \quad \hat{a} = m_y - \hat{b}m_x$$

where m_x and m_y are sample means of x and y over I_a, respectively:

$$m_x = \frac{1}{N_a}\sum_{i\in I_a} x_i, \quad m_y = \frac{1}{N_a}\sum_{i\in I_a} y_i$$

Data residuals (or trend line misfits) are

$$\hat{e}_i = y_i - (\hat{a} + \hat{b}x_i), i \in I_a$$

Lag-one correlation coefficient of $\{\hat{e}_i\}$ can be estimated over the subset of indices $I_c = \{ i : i \in I_a \; \& \; (i + 1) \in I_a\}$. Let N_c be the size of I_c. Then

$$\hat{\rho} = \frac{S_{12}}{\sqrt{S_{11}S_{22}}}, \quad S_{12} = \sum_{i\in I_c}(\hat{e}_i - m_1)(\hat{e}_{i+1} - m_2)$$

$$S_{11} = \sum_{i\in I_c}(\hat{e}_i - m_1)^2, \quad S_{22} = \sum_{i\in I_c}(\hat{e}_{i+1} - m_2)^2$$

$$m_1 = \frac{1}{N_c}\sum_{i\in I_c}\hat{e}_i, \quad m_2 = \frac{1}{N_c}\sum_{i\in I_c}\hat{e}_{i+1}$$

A provision is made for not raising the effective sample size if estimated $\hat{\rho}$ is negative:

$$\hat{\rho}_+ = \max(\hat{\rho}, 0)$$

The resulting $\hat{\rho}_+$ is used to obtain the effective sample size of the set of available observations:

$$N_r = N_a \frac{1 - \hat{\rho}_+}{1 + \hat{\rho}_+}$$

which is then used to estimate the variance of data deviations from the trend line:

$$\hat{\sigma}_e^2 = \frac{1}{N_r - 2}\sum_{i\in I_a}\hat{e}_i^2.$$

Therefore the variance of trend slope estimator is obtained:

$$\hat{\sigma}_b = \hat{\sigma}_e / S_x, \quad S_x^2 = \sum_{i\in I_a}(x_i - m_x)^2.$$

To construct a confidence interval for probability level p, let

$$q = t_{\frac{1+p}{2}}(N_r - 2)$$

be the $\frac{1+p}{2}$-quantile of Student's $t(N_r - 2)$ distribution. Finally

$$b = \hat{b} \pm q\,\hat{\sigma}_b$$

where $\hat{b}$, $\hat{\sigma}_b$, and q are given by formulas above.

2.SM.3.4 Smoothing Spline Method

An alternative approach is to estimate local trends using non-parametric trend models obtained by penalized smoothing of time series (e.g., Wahba, 1990; Wood, 2006; Section 6.7.2). The value in any year is considered to be the sum of a non-parametric smooth trend and a low-order autoregressive noise term. The trend is represented locally by cubic spline polynomials (Scinocca et al., 2010) and the smoothing parameter is estimated using REML allowing for serial correlation in the residuals.

2.SM.4 Changes in Temperature

2.SM.4.1 Change in Surface *In Situ* Observations Over Time

Observations are available for much of the global land surface starting in the mid-1800s or early 1900s. Availability is reduced in the most recent years owing in large part to international data exchange delays for monthly data summaries, although these have improved from many countries since AR4. Synoptic reports (used in reanalyses), and daily reports (used to analyse extremes) are also exchanged, and there has been no such decrease in their exchange. Non-digitized temperature records continue to be found in various country archives and are being digitized (Allan et al., 2011; Brunet and Jones, 2011). Efforts to create a single comprehensive raw digital data holding with provenance tracking and version control have advanced (Thorne et al., 2011; Lawrimore et al., 2013). Most historical sea surface temperature (SST) observations arise from ships, with buoy measurements and satellite data becoming a significant contribution in the 1980s. Digital archives such as the International Comprehensive Ocean-Atmosphere Data Set (ICOADS, currently version 2.5, Woodruff et al., 2011) are constantly augmented as paper archives are imaged and digitized (Brohan et al., 2009). Despite substantial efforts in data assembly, the total number of available SST observations and the percentage of the Earth's surface area that they cover remain very low for years before 1850 and drop drastically during the two World Wars. The sampling of land and marine records through time which form the basis for the *in situ* land-surface air temperature (LSAT) and SST records detailed in the chapter are summarized in Figure 2.SM.2.

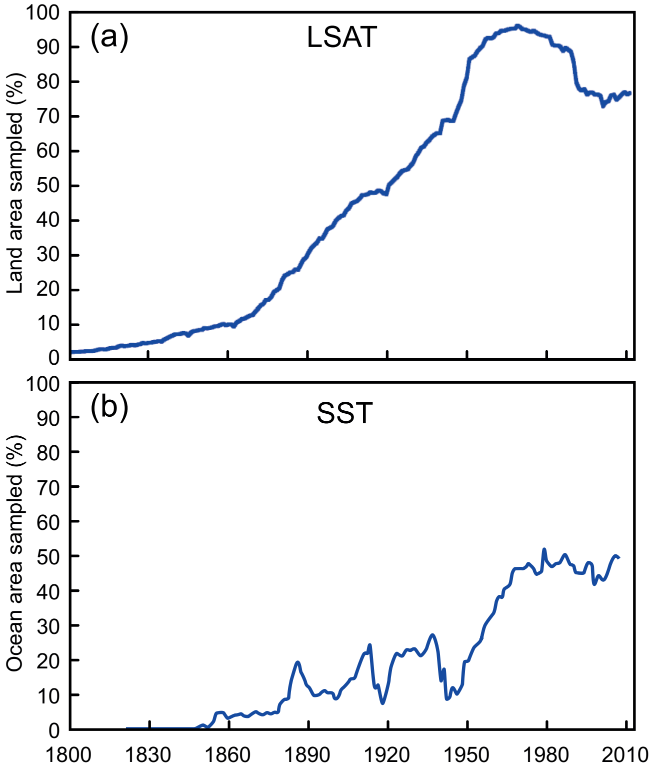

Figure 2.SM.2 | Change in percentage of possible sampled area for land records (top panel) and marine records (lower panel). Land data come from GHCNv3.2.0 and marine data from the ICOADS *in situ* record.

2.SM.4.2 Land Surface Air Temperature Data Set Innovations

Improvements have been made to the historical global data sets of land-based station observations used in AR4. Basic descriptions of the methods for the current versions of all data sets are given in Table 2.SM.4. All use monthly average temperature series from stations around the globe. Global Historical Climatology Network (GHCN) V3 improvements (Lawrimore et al., 2011) included elimination of "duplicate" time series for many stations, updating more station data with the most recent data, the application of enhanced quality assurance procedures (Durre et al., 2010) and a new pairwise homogenization approach for individual station time series (Menne and Williams, 2009). Two version increments to this V3 product to fix coding issues have since accrued that have served to slightly increase the centennial time-scale trends. Goddard Institute of Space Studies (GISS) continues to provide an estimate based primarily on GHCN but with different station inclusion criteria, additional night-light-based urban adjustments and a distinct gridding and infilling method (Hansen et al., 2010). CRUTEM4 (Jones et al., 2012) incorporates additional series above and beyond those in CRUTEM3 and also newly homogenized versions of the records for a number of stations and countries. It continues the model of incorporating the best available estimates for each station arising from research papers or individual national meteorological services with access to the best metadata on the assumption that such efforts have had most attention paid to them. In contrast, all other products considered in AR5 undertake a globally consistent homogenization processing of a given set of input data, although those data may well have been processed and adjusted at source. A new data product from a group based predominantly at Berkeley (Rohde et al., 2013) uses a kriging technique, commonly used in geostatistics, to create a global mean timeseries accounting for time-varying station biases by treating each apparently homogeneous segment as a unique record. This is substantially methodologically distinct from earlier efforts and so helps us to better explore structural uncertainty (Box 2.1) in LSAT estimates.

2.SM.4.3 Sea Surface Temperature Data Improvements and Data Set Innovations

2.SM.4.3.1 In Situ Sea Surface Temperature Data Records

Because of the irregular nature of sampling in space and time, when a large portion of observations are made from moving platforms (ships and drifting buoys), it is customary to use statistical summaries of "binned" observations (most commonly, by grid boxes) rather than individual observed values (Table 2.SM.5). Means or medians of all SST

Table 2.SM.4 | Summary of methods used by producers of global land-surface air temperature (LSAT) products. Basic methodological details are included to give a flavour of the methodological diversity. Further details can be found in the papers describing the data set construction processes cited in the text.

Dataset	Start of Record	Number of Stations	Quality Control and Homogeneity Adjustments	Infilling	Averaging Procedure
CRUTEM4 (Jones et al., 2012)	1856	5696 (4891 used in gridding)	Source specific QC and homogeneity applied generally to source data prior to collation	None	Average of the two hemispheric averages (derived by area weighted average of grid boxes) weighted 2/3 Northern Hemisphere and 1/3 Southern Hemisphere
GHCNv3 (Lawrimore et al., 2011)	1880	7280	Outlier and neighbour QC and pairwise comparison based adjustments	Limited infilling by eigenvectors (for global mean calculations only; Smith et al., 2008)	Average of grid boxes area weighted
GISS (Hansen et al., 2010)	1880	c.6300	Night lights based adjustments for urban influences	Averages to 40 large scale bins	Average of the bins with areal weighting.
Berkeley (Rohde et al., 2013)	1753	39028	Individual outliers are implicitly down-weighted. Neighbour-based test to identify breaks and each apparently homogeneous segment treated separately.	No gridding, but kriging produces field estimate based on the station constraint at each timestep.	Kriged field estimate limited to maximum 1500 km distance from any station

values in a given bin that pass quality control procedures are generally used. Standard deviations and numbers of observations in individual bins are useful for estimating uncertainties. These procedures usually serve as an initial step for producing more sophisticated gridded SST products which involve bias correction and, for "analyzed" products, interpolation and smoothing. Since AR4, many marine observations have been digitized (Brohan et al., 2009; Allan et al., 2011; Wilkinson et al., 2011), substantially improving the coverage of the latest ICOADS Release 2.5 (Woodruff et al., 2011) and of the newer data sets based on it (e.g., HadSST3, HadNMAT2).

Since AR4, major innovations have primarily been around understanding of post-1940 biases. Since 1940, ships making measurements of SST have used a variety of methods (Kent et al., 2010), each with characteristic biases (Kennedy et al., 2011a). These offsets have varied over time (Kent and Kaplan, 2006; Kent and Taylor, 2006), and for the period 2002–2007 ship SSTs are overall biased warm by 0.12°C to 0.18°C on average compared to the buoy data (Reynolds et al., 2010; Kennedy et al., 2011b, 2012). Since the 1980s, drifting and moored buoys have been producing an increasingly large fraction of global SST observations and these have tended to be colder than ship-based measurements.

Although more variable than SSTs, marine air temperatures (MATs) are assumed to be physically constrained to track SST variability because of the continuous air–sea heat exchange, at least on large spatial and temporal scales (monthly to annual, ocean basin to hemispheric). However, longer-term variations noted in some locations and periods, for example, Christy et al. (2001) and Smith and Reynolds (2002), necessitate a degree of caution. Regardless, MAT data provide a useful additional record of marine region temperature changes. Adjustments have been applied to account for the change in observing height and for the use of non-standard practices during World War II (Rayner et al., 2003) and the 19th century (Bottomley et al., 1990). Because of biases due to solar heating, only Nighttime Marine Air Temperature (NMAT) data sets have been widely used in climate analyses so far. The progress on the analytical correction of solar heating biases in recent daytime MAT data (Berry et al., 2004) allowed their use in a recent analysis (Berry and Kent, 2009). Table 2.SM.5 gives a brief description of well-known historical SST and NMAT products, organized by their type.

2.SM.4.3.2 Comparing Different Types of Data and Their Errors

Comparisons are complicated because different measurement technologies target somewhat different physical characteristics of the surface ocean. Infrared (IR) and microwave (MW) radiometers sense water temperature of the top 10 to 20 μm and 1 to 2 mm respectively, whereas *in situ* SST measurements are made in the depth range between 10 cm and several meters; these are often called "bulk" SST, with an implicit assumption that the ocean surface layer is well-mixed. This assumption is valid only for nighttime conditions or when surface winds are strong. Otherwise, the surface layer is stratified and its temperature exhibits diurnal variability (Kawai and Wada, 2007; Kennedy et al., 2007), such that measured temperature values vary with the depth and time of day of observation (Donlon et al., 2007). Aside from the diurnal variability, an independent phenomenon of a thermal skin layer takes place in the top 1 mm or so of the ocean surface and results in a strong temperature gradient across this layer (usually, cooling towards the surface) which is especially enhanced in the top 100 μm. Although all *in situ* and satellite measurements might be affected by diurnal variability, only IR satellite data are subject to the thermal skin effect. IR radiometers are said to measure "skin" temperature. Temperature at the bottom of the thermal skin layer is called "subskin temperature." MW radiometer measurements are close to this variable. To estimate error variance or to verify uncertainty estimates for SST observations by comparison of different kinds of SST data, data values have ideally to be adjusted for time and depth differences by modelling the skin effect and diurnal variability; in lieu of a model, geophysical errors are reduced by constraining the comparison to the nighttime data only which minimizes the diurnal variability effects.

Table 2.SM.5 | Data Sets of SST and NMAT Observations Used in Section 2.4.2. These data sets belong to the following categories: a database of individual *in situ* observations, gridded data sets of climate anomalies (with bucket and potentially additional bias corrections applied) and globally complete interpolated data sets based on the latter products.

Data Set	Period	Space–Time Grid Resolution	Bucket/ Bias Corrections Applied
Historical Database of In Situ Observations			
International Comprehensive Ocean – Atmosphere Data Set (ICOADS), Release 2.5 (Woodruff et al., 2011)	1662–present; 1800–present, 1960–present	Individual reports; 2° × 2° monthly summaries; 1° × 1° monthly summaries	None
Gridded Data Sets of Observed Climate Anomalies			
U.K.M.O. Hadley Centre SST, v.2 (HadSST2) (Rayner et al., 2006)	1850 – present	5° × 5° monthly	Bucket correction for pre-1941 period
U.K.M.O. Hadley Centre SST, v.3 (HadSST3) (Kennedy et al., 2011a; Kennedy et al., 2011b)	1850 – present	5° × 5° monthly	Bias correction for the entire period based on percentages of different types of observations
U.K.M.O. Hadley Centre NMAT, v.2 (HadNMAT2) (Kent et al., 2013)	1886–2010	5° × 5° monthly	Adjustments for changes in observation heights and for non-standard observing practices
Globally Complete Objective Analyses (Interpolated Products) of Historical SST Records			
U.K.M.O. Hadley Centre Interpolated SST, v.1 (HadISST) (Rayner et al., 2003)	1870 – present	1° × 1° monthly	Bucket corrections for pre-1941 period
JMA Centennial *in situ* Observation Based Estimates of SST (COBE SST) (Ishii et al., 2005)	1891 – present	1° × 1° monthly	Bucket corrections for pre-1941 period
NOAA Extended Reconstruction of SST, v. 3b (ERSSTv3b) (Smith et al., 2005, 2008)	1854 – present	2° × 2° monthly	Bucket corrections for pre-1941 period

Comparisons between *in situ* measurements and different satellite instruments have been used to assess the uncertainties in the individual measurement techniques. Random error magnitudes on Along Track Scanning Radiometer (ATSR) measurements have been estimated (O'Carroll et al., 2008; Embury et al., 2012; Kennedy et al., 2012) to lie between 0.1°C and 0.2°C. The uncertainties associated with random errors for Advanced Along Track Scanninr Radiometer (AATSR) measurements are therefore much lower than for ships (about 1°C to 1.5°C: Kent and Challenor (2006); Kent et al. (1999); Kent and Berry (2005) Reynolds et al. (2002); Kennedy et al. (2012)) or drifting buoys (0.15°C to 0.65°C: Kennedy et al. (2012); Reynolds et al. (2002); Emery et al. (2001); O'Carroll et al. (2008)).

Characterizing relative mean biases between different systems informs the procedures for homogenizing and combining different kinds of measurements. Embury et al. (2012) found average biases of less than 0.1°C between reprocessed AATSR retrievals and drifting buoy observations and of about 0.1°C between ATSR2 retrievals and buoys. Using an earlier AATSR data set, Kennedy et al. (2012) found that ship measurements were warmer relative to matched satellite SSTs than drifting buoys, suggesting ship measurements were biased relative to drifting buoy measurements by 0.18°C. They hypothesized that HadSST2 contained an increasing cool bias because of a decrease in the relative proportion of warm-biased ship observations. They applied a time-varying adjustment to the HadSST2 global means in the form of 0.18°C times the fraction of drifting buoys compared to the 1991–1995 period. This correction improved the consistency between trends in global average anomalies from the *in situ* and ATSR data sets. However, Kennedy et al. (2011b) found a smaller relative bias between ships and drifting buoys and found that changes in the biases associated with ship measurements might have been as large, or larger than, this effect.

2.SM.4.3.3 Differences in Long-Term Average Temperature Anomalies Used in Other Chapters

Figure 2.SM.3 shows the differences between selected periods that are utilized in other chapters of the report analysed in a consistent manner for those three data sets considered in Section 2.4.3. Uncertainty estimates have been calculated for HadCRUT4 using the HadCRUT4 uncertainty model (Morice et al., 2012). To allow estimates of coverage uncertainty to be made for these differences between long-term averages, HadCM3 control run fields (which are much longer) were used in place of the National centers for Environmental Prediction (NCEP) reanalysis as the globally complete reference data. It was verified that this does not greatly alter the uncertainty estimates when a subset of HadCM3 control of the same length as NCEP is used so it should not be a first-order effect.

Temperature difference between the periods of 1946-2012 and 1880-1945:
HadCRUT4: 0.38°C ± 0.04°C (90% confidence interval)
GISTEMP: 0.40°C
MLOST: 0.39°C

Temperature difference between the periods of 1986-2005 and 1850-1900:
HadCRUT4: 0.61°C ± 0.06°C (90% confidence interval)
GISTEMP: N/A
MLOST: N/A

Temperature difference between the periods of 2003-2012 and 1850-1900:
HadCRUT4: 0.78°C ± 0.06°C (90% confidence interval)
GISTEMP: N/A
MLOST: N/A

Temperature difference between the periods of 1986-2005 and 1886-1905:
HadCRUT4: 0.66°C ± 0.06°C (90% confidence interval)
GISTEMP: 0.66°C
MLOST: 0.66°C

Temperature difference between the periods of 1986-2005 and 1961-1990:
HadCRUT4: 0.30°C ± 0.03°C (90% confidence interval)
GISTEMP: 0.31°C
MLOST: 0.30°C

Temperature difference between the periods of 1986-2005 and 1980-1999:
HadCRUT4: 0.11°C ± 0.02°C (90% confidence interval)
GISTEMP: 0.11°C
MLOST: 0.11°C

2.SM.4.4 Technical Developments in Combined Land and SST Products

Table 2.SM.6 summarizes current methodological approaches. For HadCRUT4 both the land and the ocean data sources have been updated and the product now consists of 100 equi-probable solutions (Morice et al., 2012). The post-1990s period is now more consistent with the remaining products—it exhibits a greater rate of warming than the previous version over this period. NOAA's Merged Land-Ocean Surface Temperature (MLOST) analysis product has incorporated GHCNv3 and ERSST3b and reinstated high-latitude land data but is otherwise methodologically unchanged from the version considered in AR4 (Vose et al., 2012). Since AR4, NASA GISS have undertaken updates and a published sensitivity analysis focussed primarily around their urban heat island adjustments approach (Section 2.4.1.3) and choice of product and method for merging pre-satellite era and satellite era SSTs (Hansen et al., 2010). For SST several alternative data sets or combinations of data sets were considered and these choices had an impact of the order 0.04°C for the net change over the period of record. An improved concatenation of pre-satellite era and satellite era SST products removed a small apparent cooling bias in recent times. As of December 2012 GISS changed the operational SST version they used to ERSST3b. Following the release of their code the GISS method has been independently replicated in a completely different programming language (Barnes and Jones, 2011) which builds a degree of confidence in the veracity of the processing.

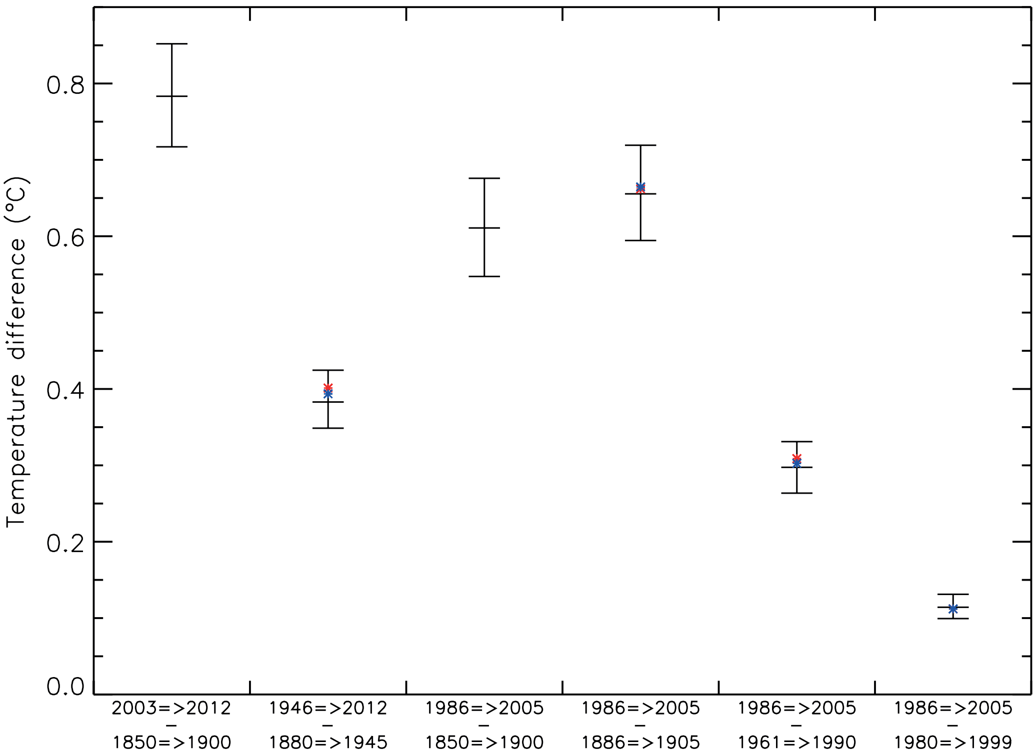

Figure 2.SM.3 | Differences in multi-year average temperatures as calculated from HadCRUT4, GISS and NCDC MLOST for six pairs of periods. The median and 5 to 95% confidence interval for differences calculated from HadCRUT4 are shown in black. Period differences for GISS are shown in red. Period differences for NCDC MLOST are shown in blue.

Table 2.SM.6 | Methodological details for the current global merged gridded surface temperature products. Only gross methodological details are included to give a flavour of the methodological diversity; further details can be found in the papers describing the data set construction processes.

Dataset	Start Date	Land Data Set	Marine Data Set	Merging of Land and Marine	Infilling	Averaging Technique
HadCRUT4 (100 versions) (Morice et al., 2012)	1850	CRUTEM4 (100 versions)	HadSST3 (100 versions)	Weighted average based on the percentage coverage	None, spatial coverage incompleteness accounted for in error model	Sum of area weighted grid box averages for Northern and Southern Hemisphere / 2
MLOST (Vose et al., 2012)	1880	GHCNv3	ERSST3b	Weighted average based on the percentage coverage	Low-frequency component filtered. Anomaly spatial covariance patterns for high-frequency component. Land and ocean interpolated separately.	Area weighted average of available gridbox values
NASA GISS (Hansen et al., 2010)	1880	GHCNv3, USHCNv2 plus Antarctic SCAR data	ERSST3b	Priority given to land data	Radius of influence up to 1200 km for land data	After gridding, non-missing values are averaged over the zones 90°S–23.6S, 23.6°S–0°, 0°–23.6°N, 23.6°N–90°N; and the four means are averaged with 3:2:2:3 weighting to represent their area.

2.SM.4.5 Technical Advances in Radiosonde Records

There now exist five estimates of radiosonde temperature evolution, which are based on a very broad range of methodological approaches to station selection, identification of artificial timeseries breaks and adjustments (Table 2.SM.7). HadAT and RATPAC were discussed in AR4 and no further technical innovations have accrued for the operational versions of these products. Development of an automated version of HadAT and discussion of efforts to characterize the resulting parametric uncertainty are summarized in the main text. A group at the University of Vienna have produced RAOBCORE and RICH (Haimberger, 2007) using ERA reanalysis products (Box 2.3) as a basis for identifying breaks. Given the relative sparseness of the observing network this may have advantageous properties in many regions compared to more traditional intra-station or neighbour-based approaches. Breakpoints are identified through reanalysis background departures using a statistical breakpoint test for both these products. Uncertainties in adjustments arising from the use of reanalyses fields to estimate the adjustments for RAOBCORE have been addressed by several variants and sensitivity studies (Haimberger, 2004, 2007; Haimberger et al., 2008).

Table 2.SM.7 | Summary of methodologies used to create the radiosonde products considered in this report. Except IUK (1960), all time series begin in 1958. Only gross methodological details are included to give a flavour of the methodological diversity; further details can be found in the papers describing the data set construction processes. Between these data set approaches a very broad range of processing choices have been considered.

Dataset	Temporal Resolution	Number of Stations	Homogeneity Test	Adjustment Method
HadAT2 (Thorne et al., 2005)	Seasonal / monthly	676	KS-test on difference series from neighbour averages together with metadata, manually interpreted	Target minus neighbour difference series based.
RATPAC (Free et al., 2005)	monthly	87	Multiple indicators and metadata assessed manually by three investigators until 1996, first difference method with *t*-test and metadata after 1995	Manually based adjustments prior to 1996, first difference derived breaks after 1995.
IUK (Sherwood et al., 2008)	Individual launch	527	Derived hierarchically looking (1) for breaks in 00Z-12Z series, (2) breaks in the series with twice daily measures, and (3) once daily ascents. Breakpoint detection was undertaken at the monthly time scale with no recourse to metadata	Relaxation to an iterative solution minimum given breaks and set of spatial and temporal basis functions.
RICH-obs (64 member ensemble) (Haimberger et al., 2012)	Individual launch	2881	SNHT test on the difference between the observed data and ERA reanalysis product background expectation field modified by metadata information.	Difference between station and a number of apparently homogeneous neighbours
RICH-tau (64 member ensemble) (Haimberger et al., 2012)	Individual launch	2881	As above	Difference between station innovation (candidate station and reanalysis background expectation field) and innovation estimates for apparently homogeneous neighbors.
RAOBCORE (Haimberger et al., 2012)	Individual launch	2881	As above	Difference between candidate station and reanalysis background expectation field

The RICH products use the same breakpoint locations but have only an indirect dependency on the reanalyses as the adjustments are neighbour based. Two varieties of RICH have been developed (Haimberger et al., 2012). The first uses pairwise neighbour difference series to estimate the required adjustment. The second uses differences in station innovations relative to the reanalyses fields. Both variants have been run in ensemble mode and the resulting uncertainty estimates are discussed in the main text. Sherwood and colleagues developed an iterative universal kriging approach for radiosonde data (Sherwood, 2007) and applied this to a global network (Sherwood et al., 2008) to create IUK (iterative universal kriging). The algorithm requires a set of break locations and the raw data and then fits an optimal estimate of the homogenized series based upon a number of basis functions including leading modes of variability. Breakpoint locations were defined by tests on the station series and without recourse to metadata.

2.SM.4.6 Advances in Microwave Sounding Unit Satellite Records

Gross methodological details of the microwave sounding unit (MSU) products are summarized in Table 2.SM.8. The University of Alabama in Huntsville (UAH) data set removed an apparent seasonal cycle artefact in the latter part of their record related to the introduction of Advanced Microwave Sounding Unit (AMSU) in version 5.3 and changed the climatological baseline to 1981–2010 to produce version 5.4. Both changes had negligible impact on trend estimates.

Version 3.2 of the RSS product (Mears and Wentz, 2009a, 2009b) for the first time incorporated a subset of AMSU instruments. It was concluded that an instantaneous correction is required to merge MSU and AMSU as they sense slightly different layers and that there will also be a systematic long-term impact unless real-world trends are vertically invariant (Mears et al., 2011). Using HadAT data this impact was estimated to be no more than 5% of the trend. Two more significant changes were accounting for latitudinal error structure dependencies, and a more physical handling of instrument body temperature effect issues in response to (Grody et al., 2004). In early 2011 version 3.3 was released which incorporated all the AMSU instruments and led to a de-emphasising of the last MSU instrument which still remained operational after 15 years, a trend reduction over the post-1998 period, and a reduction in apparent noise.

The new NOAA STAR analysis used a fundamentally distinct approach for the critical inter-satellite warm target calibration step (Zou et al., 2006). Satellites orbit in a pole-to-pole configuration with typically two satellites in operation at any time. Over most of the globe they never intersect. The exception is the polar regions where they quasi-regularly (typically once every 24 to 48 hours but this is orbital geometry dependent) sample in close proximity in space (<111 km) and time (<100 s). The STAR technique uses these Simultaneous Nadir Overpass (SNO) measures to characterize inter-satellite biases and the impact of instrument body temperature effects before accounting for diurnal drift. SNO estimates remain two point comparisons between uncertain measures over a geographically limited domain, so cannot guarantee absolute accuracy. For humidity satellite measures the geographic domain has been shown to be an issue (John et al., 2012), but it is at present unclear whether this extends to temperature measurements. Initially they produced Mid-Troposphere (MT) near-nadir measures since 1987 over the oceans (Zou et al., 2006); then included more view angles and additional channels including LS and multichannel recombinations (Zou et al., 2009); then extended back to 1979 and included land and residual instrument body temperature effects building upon the UAH methodology and diurnal corrections based upon RSS (Zou and Wang, 2010). In the latest version 2.0, STAR incorporated the AMSU observations inter-calibrated by the SNO method to extend to the present (Zou and Wang, 2011).

Table 2.SM.8 | Summary of methodologies used to create the MSU products considered in this report. All time series begin in 1978–1979. Only gross methodological details are included to give a flavour of the methodological diversity, further details can be found in the papers describing the data set construction processes.

Dataset	Inter-Satellite Calibration	Diurnal Drift Adjustments	Calibration Target Temperature Effect	MSU/AMSU Weighting Function Offsets
UAH (Christy et al., 2003)	Backbone method – adjusting all other satellites to a subset of long-lived satellites	Cross-scan differences used to infer adjustments. Measurements are adjusted to refer to the measurement time at the beginning of each satellite's mission.	Calibration target coefficients are determined as solution to system of daily equations to explain the difference between co-orbiting satellites	No accounting for differences beyond inter-satellite calibration.
RSS (Mears and Wentz, 2009a, 2009b)	Stepwise pairwise adjustments of all satellites based on difference in means. Adjustments are a function of latitude and constant in time.	Climate model output used to infer diurnal cycle. All measurements adjusted to refer to local midnight.	Values of the target temperature factors and scene temperature factors are obtained from a regression using all satellites of the same type together.	Stepwise adjustment to account for the change in weighting functions.
STAR (Zou and Wang, 2011)	Simultaneous nadir overpass measures	RSS adjustments are multiplied by a constant factor to minimize inter-satellite differences.	Largely captured in the SNO satellite intercomparison but residual artefacts are removed using the UAH method.	Channel frequency shifts on each satellite estimated and adjusted for.

2.SM.4.7 Stratospheric Sounding Unit Data Background

The Stratospheric Sounding Unit (SSU) instruments provide the only long-term near-global temperature data above the lower stratosphere, extending from the upper troposphere to the lower mesosphere (Randel et al., 2009; Seidel, 2011), with the series terminating in 2006. In theory, five channels of AMSU should be able to continue this series (Kobayashi et al., 2009) but despite incipient efforts at an AMSU-only record (Mo, 2009) and plans to merge AMSU and SSU, the current long-term series ends in 2006. The raw record has three unique additional issues to those encountered in MSU data set construction. The satellite carries a cell of CO_2 which tends to leak pressure through water egress on the ground and degassing post-launch, causing a spurious increase in observed temperatures. Compounding this the CO_2 content within the cells varies among SSU instruments (Kobayashi et al., 2009). At the higher altitudes sensed, large diurnal and semi-diurnal tides (due to absorption of solar radiation) require substantial corrections (Brownscombe et al., 1985). Finally, long-term temperature trends derived from SSU need adjustment for increasing atmospheric CO_2 (Shine et al., 2008) as this affects radiation transmission in this band.

2.SM.4.8 Global Positioning System–Radio Occultation Data Background

Global Positioning System (GPS) radio occultation (RO) fundamental observations are time delay of the occulted signal's phase traversing the atmosphere. It is based on GPS radio signals that are bent and retarded by the atmospheric refractivity field, related mainly to pressure and temperature, during their propagation to a GPS receiver on a Low Earth Orbit (LEO) satellite. An occultation event occurs whenever a GPS satellite sets (or rises from) behind the horizon and its signals are occulted by the Earth's limb. The fundamental measurement is the signal phase which is based on precise timing with atomic clocks. Potential clock errors of GPS or LEO satellites are removed by differencing methods using an additional GPS satellite as reference and by relating the measurement to even more stable oscillators on the ground. Thus, GPS RO is anchored to the international time standard and currently the only self-calibrated raw satellite measurement with SI traceability, in principle (Leroy et al., 2006; Arndt et al., 2010). Subsequent analysis converts the time delay to temperature and other parameters, which inevitably adds some degree of uncertainty to the temperature data, which is not the directly measured quantity but rather inferred with the inference being dependent on the precision of available data for other dependent parameters and how the data are processed. GPS RO measurements have several attributes that make them suited for climate studies: (1) they exhibit no satellite-to-satellite bias (Hajj et al., 2004; Ho et al., 2009a), (2) they are of very high precision (Anthes et al., 2008; Foelsche et al., 2009; Ho et al., 2009a), (3) they are not affected by clouds and precipitation, and (4) they are insensitive to retrieval error when used to estimate interannual trends in the climate system (Ho et al., 2009b). GPS–RO observations can be used to derive atmospheric temperature profiles in the upper troposphere and lower stratosphere (UT/LS) (Hajj et al., 2004; Kuo et al., 2004; Ho et al., 2009a).

2.SM.5 FAQ 2.1, Figure 2

This material documents the provenance of the data that was input to FAQ 2.1, Figure 2 in the IPCC WG1 Fifth Assessment Report. The code will also be archived at the website along with a static version of the data files when the final report is published. Two have been truncated (one marine air temperature and one sea surface temperature) for explicitly source documented and acknowledged significant issues. The FAQ includes datasets and parameters discussed in the remaining observational chapters. The data in each panel replicates that data utilized in the underlying chapters.

Land surface air temperature anomalies relative to 1961–1990:
Dark Grey: Berkeley (Rohde et al., 2013)
Green: NCDC (Lawrimore et al., 2011)
Blue: GISS (Hansen et al., 2010)
Red: CRUTEM4 (Jones et al., 2012)

Global lower tropospheric MSU-equivalent temperature anomalies relative to 1981–2010 from satellites and radiosondes.
Black : HadAT2 (Thorne et al., 2005)
Orange : RAOBCORE (Haimberger et al., 2012)
Dark Grey: RICH-obs (Haimberger et al., 2012)
Yellow: RICH-tau (Haimberger et al., 2012)
Green: RATPAC (Free et al., 2005)
Blue: RSS (Mears and Wentz, 2009a)
Red: UAH (Christy et al., 2003)

Sea-surface temperature anomalies relative to 1961–1990:
Dark Grey: ERSSTv3b (Smith et al., 2008)
Black: COBE (Ishii et al., 2005)
Green: HadISST (Rayner et al., 2006)
Red: ICOADS (Worley et al., 2005)
Yellow: HadSST3 (Kennedy et al., 2011b)

Ocean heat content anomalies (0–700 m). All data sets normalized relative to 2006–2010 and then rebased to be zero average across all data sets at 1971 as per Chapter 3, Figure 3.2.
Blue: Palmer et al. (2007)
Green: Domingues et al. (2008)
Yellow: Ishii and Kimoto (2009)
Orange: Smith and Murphy (2007)
Black: Levitus et al. (2012)

Marine air temperature anomalies relative to 1961–1990
Red: HadNMAT2 (Kent et al., 2013)
Blue: (Ishii et al., 2005). Series shown only after 1900 due to known but uncorrected biases in earlier data

Land surface specific humidity anomalies relative to 1981–2000
Green: HadCRUH (Willett et al., 2008)
Blue: (Dai, 2006)
Red: ERA Interim Reanalyses (Dee et al., 2011)
Black: HadISDH (Willett et al., 2013)

Sea level anomalies relative to 1961–1990:
Black: Church and White (2011)
Yellow: Jevrejeva et al. (2008)
Green: Ray and Douglas (2011)
Red: Nerem et al. (2010)
Orange: Ablain et al. (2009)
Blue: Leuliette and Scharroo (2010)

Northern Hemisphere March–April snow cover anomalies relative to 1967–1990
Blue: Brown (2000)
Red: Robinson and Frei (2000)
Note: Figures 4.19 and SPM-2a (green line) show a combined record of the above two data sets which includes an estimate of uncertainty (updated from Brown and Robinson, 2011).

Summer (July–August–September) average Arctic sea ice extent (absolute values)
Green: Walsh and Chapman (2001)
Blue: HadISST1.2 (Rayner et al., 2003)
Red: SMMR - SBA (Comiso and Nishio, 2008)
Black: SSM/I - NT1 (Cavalieri et al., 1984) – updated in Cavalieri and Parkinson (2012) and Parkinson and Cavalieri (2012)
Yellow: AMSR2 – ABA (Comiso and Nishio, 2008)
Orange: AMSR2 – NT2 (Markus and Cavalieri, 2000)

Glacier mass balance relative to 1961–1970.
Dark grey: Cogley area weighted as updated from (Cogley, 2009). Area weighted extrapolation from directly and geodetically measured glacire mass balances. Updated to the complete Randoph Glacier Inventory [RGI] (Arendt et al., 2012)
Green: Leclercq et al. (2011)
Blue: Marzeion et al. (2012)

2.SM.6 Changes in the Hydrological Cycle

2.SM.6.1 Precipitation Trends

Figure 2.SM.4 shows the spatial variability of long-term trends (1901–2010) and more recent trends (1951–2010) over land in annual precipitation using the climate research unit (CRU), GHCN, and GPCC data sets. Rather than absolute trends (in mm per year per decade, as in Figure 2.29) trends are calculated relative to local climatology. The spatial patterns of these trends (which can be directly compared to the trends in model precipitation reported in later chapters) are broadly similar.

2.SM.6.2 Radiosonde Humidity Data

Since AR4 there have been three distinct efforts to homogenize the tropospheric humidity records from operational radiosonde measurements (Durre et al., 2009; McCarthy et al., 2009; Dai et al., 2011) (Table 2.SM.9).

2.SM.7 Changes in Extreme Events

Although trends in extremes indices for temperature agree within uncertainty ranges (Table 2.11), note that there are differences in the way that each data set has been constructed. These include (1) using different input station networks: HadGHCND and GHCNDEX use almost identical input data, that is, from the Global Historical Climatology Network-Daily (GHCN-Daily) data set (Durre et al., 2010; Menne et al., 2012) but different averaging methods, while HadEX2 primarily

Table 2.SM.9 | Methodologically distinct aspects of the three approaches to homogenizing tropospheric humidity records from radiosondes.

Data Set	Region Considered	Time Resolution and Reporting Levels	Neighbours	First Guess[a]	Automated	Variables Homogenized
Durre et al. (2009)	NH	Monthly, mandatory and significant levels to 500 hPa	Pairwise homogenization	No	Yes	Column integrated water vapour
McCarthy et al. (2009)	NH	Monthly, mandatory levels to 300 hPa	All neighbour average, iterative	Yes	Yes	Temperature, specific humidity, relative humidity
Dai et al. (2011)	Globe	Observation resolution, mandatory levels to 100 hPa	None	Yes	Yes	Dew-point depression

Notes:

[a] First guess refers to whether a manually imputed first guess for known metadata types was incorporated prior to formal homogenization efforts.

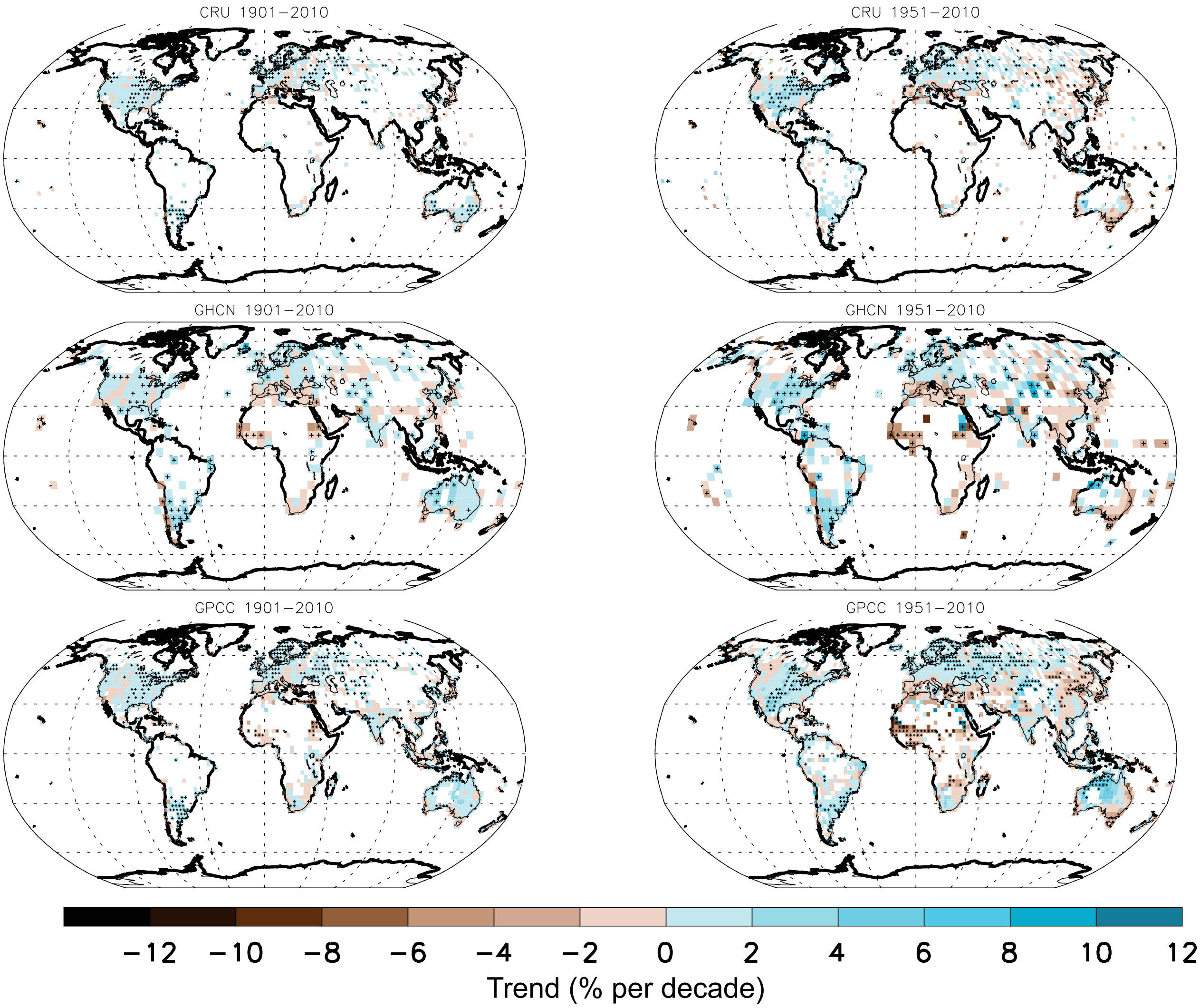

Figure 2.SM.4 | Trends in precipitation over land from the CRU, GHCN and Global Precipitation Climatology Centre (GPCC) data sets for 1901–2010 (left hand panels) and 1951–2010 (right-hand panels) as in Figure 2.29, but now in percent per decade relative to local climatology rather than in mm yr^{-1} per decade.

uses data from individual researchers or Meteororogical Services, and (2) in one case the indices are calculated from a daily gridded temperature data set (HadGHCND) while in the other two cases indices are first calculated at the station level and then gridded. This order of operation could be important to the physical interpretation of the result (Zhang et al., 2011) and its use in model evaluation for example (Chapter 9). Comparison of these three data sets presents a measure of the structural uncertainty that exists when estimating trends in global temperature extremes (Box 2.1) while still in all cases indicating a robust warming trend over the latter part of the 20th century.

A description of each data set is as follows.

2.SM.7.1 HadEX2

Unlike GHCNDEX (see later) most of the data for HadEX2 (Donat et al., 2013b) come from individual researchers or regional data sets. While HadEX2 updates a previous data set, HadEX (Alexander et al., 2006), it is not just an extension of that data set but rather represents the latest acquisition of station data. The level of quality control, however, varies from country to country. A subset of GHCN-Daily is used for the USA but whereby only selected National Weather Service Cooperative and First-Order weather observing sites with reasonably long records are used (Peterson et al., 2008) and where station time series were determined (e.g., by the statistical analysis described in Menne and Williams (2005)) to be free of significant discontinuities after 1950 caused by, e.g., changes in station location, changes in time of observation. The indices are usually pre-calculated at source before being combined into the data set using standard software (Zhang et al., 2011). In most cases the data have been carefully assessed for quality and homogeneity by researchers in the country of origin, for example, Canada (Mekis and Vincent, 2011; Vincent et al., 2012), Australia (Trewin, 2012), and where data from regional workshops were used extensive post-processing and analysis was performed (e.g., Aguilar et al., 2009; Caesar et al., 2011) to ensure data quality and homogeneity. The number of stations used in the gridding varies depending on the index being calculated (see Box 2.4, Table 1 for the types of indices calculated). For temperature indices this ranges from about 6500 to 7400 stations and for precipitation is about 11,500 stations. Data are produced on a 3.75° × 2.5° longitude/latitude grid and are available from 1901 to 2010.

2.SM.7.2 GHCNDEX

The GHCN-Daily data set (Durre et al., 2010; Menne et al., 2012) on which GHCNDEX is based currently contains about 29,000 stations with daily maximum and minimum temperature and more than 80,000 stations with daily precipitation (Donat et al., 2013a). These data have been obtained from numerous data sources that have been integrated and undergone extensive quality assurance reviews (Durre et al., 2010). Although the database is updated regularly over Europe, North America and Australia as well as at several hundred synoptic stations across numerous countries, many records from Asia, Africa and South America do not contain data from the most recent years. While many records are short or incomplete, many others, especially in North America, Europe and Australia, date back well into the 19th century. At present, however, there are no bias adjustments available for GHCN-Daily to account for historical changes in instrumentation, observing practice, station location or site conditions. Only stations with at least 40 years of valid data after 1950 are used to create GHCNDEX, as this helps to minimize the effect of varying station density. Subsequently this step reduces the number of stations used for gridding by a factor of six or seven. For example, there are approximately 4700 temperature stations for gridding the warmest maximum temperature (TXx) and about 11,500 precipitation stations for gridding the maximum one-day precipitation total (Rx1day) (see Box 2.4, Table 1 for index definitions). However, because of the criteria limiting station length, the spatial distribution of stations is confined mostly to regions outside of Africa, South America and India. Data are produced on a 2.5° × 2.5° longitude/latitude grid and are available for years from 1951 to the present.

2.SM.7.3 HadGHCND

Also uses GHCN-Daily as input (see earlier) but the order of operation is different, that is, in this case gridding of daily maximum and minimum temperatures is done first and then indices are calculated. Only temperature based indices are available. Data are produced on a 3.75° × 2.5° longitude/latitude grid and are available for years from 1951 to the present.

2.SM.8 Box 2.5: Patterns and Indices of Climate Variability

Box 2.5, Table 1 lists some prominent modes of large-scale climate variability and indices used for defining them. Further characterization including comments for each index is provided in Table 2.SM.10.

Table 2.SM.10 | Established indices of climate variability with global or regional influence. Columns are: (1) name of a climate phenomenon, (2) name of the index, (3) index definition, (4) primary references, (5) comments, including when available, characterization of the index or its spatial pattern as a dominant variability mode.

Climate Phenomenon		Index Name	Index Definition	Primary References	Characterization / Comments
El Niño – Southern Oscillation (ENSO)	Traditional indices of ENSO-related Tropical Pacific climate variability	NIÑO3	SST anomaly averaged over [5°S–5°N, 150°W–90°W]	Rasmusson and Wallace (1983), Cane (1986)	Traditional SST-based ENSO index, "devised by the Climate Analysis Center of NOAA [*now: Climate Prediction Center*] because a warming in this region strongly influences the global atmosphere" (Cane et al., 1986).
		NIÑO1	Same as above but for [10°S–5°S, 90°W–80°W]		Introduced along with NIÑO3 by NOAA's Climate Analysis Center (now: Climate Prediction Center) about 1983–1984 to describe other details of ENSO-related tropical Pacific SST variability.
		NIÑO2	Same as above but for [5°S–0°, 90°W–80°W]		
		NIÑO1+2	Same as above but for [10°S–0°, 90°W–80°W]		
		NIÑO4	Same as above but for [5°S–5°N, 160°E–150°W]		
		NIÑO3.4	Same as above but for [5°S–5°N, 170°W–120°W]	Trenberth (1997)	Used by W MO, NOAA to define El Niño/La Niña events. Detrended form is close to the first PC of linearly detrended global field of monthly SST anomalies (Deser et al., 2010)
		Troup Southern Oscillation Index (SOI)	Standardized for each calendar month SLP difference: Tahiti minus Darwin, × 10	Troup (1965)	Used by Australian Bureau of Meteorology
		SOI	Standardized difference of standardized SLP anomalies: Tahiti minus Darwin	Trenberth (1984)	Maximizes signal-to-noise ratio of linear combinations of Darwin/Tahiti records
		Darwin SOI	Standardized Darwin SLP anomaly	Trenberth and Hoar (1996)	Introduced to avoid use of the Tahiti record, considered suspicious before 1935.
		Equatorial SOI (EQSOI)	Standardized difference of standardized SLP anomalies over equatorial [5°S–5°N] Pacific Ocean: [130°W–80°W] minus [90°E–140°E]	Bell and Halpert (1998)	
	Indices of ENSO events evolution and for identifying different types of events	Trans-Niño Index (TNI)	Standardized NINO1+2 minus standardized NINO4	Trenberth and Stepaniak (2001)	Nearly uncorrelated with NINO3.4
		El Niño Modoki Index (EMI)	SSTA: [165°E–140°W, 10°S–10°N] minus ½[110°W–70°W, 15°S–5°N] minus ½[125°E–145°E, 10°S–20°N]	Ashok et al. (2007)	Defines "typical El Niño Modoki events" as those with the seasonal EMI value (JJAS or DJF means) no less than 0.7σ, where σ is the seasonal EMI standard.
		Indices of Eastern Pacific (EP) and Central Pacific (CP) types of ENSO events	EP Index: leading PC of the tropical Pacific SSTA with subtracted predictions from a linear regression on NINO4; CP index: same as EP but with NINO1+2 used in place of NINO4.	Kao and Yu (2009)	
		E and C Indices	45° orthogonal rotation of the two leading PCs of the equatorial Pacific SSTA. Approximate formulas: C = 1.7*NIÑO4 -0.1*NIÑO1+2, E = NIÑO1+2 – 0.5*NIÑO4	Takahashi et al. (2011)	Constructed to be mutually uncorrelated; many other SST-based ENSO indices are well approximated by linear combinations of E and C.
Pacific Decadal and Interdecadal Variability Intedecadal Pacific Oscillation (IPO) North Pacific Index (NPI)		Pacific Decadal Oscillation (PDO)	First PC of monthly N. Pacific SST anomaly field [20°N–70°N] with subtracted global mean; sign is selected to anti-correlate with NPI	Mantua et al. (1997); Zhang et al. (1997)	
		Projection of a global SST anomaly field onto the IPO pattern, which is found as one of the leading EOFs of a low-pass filtered global SST field; sign is selected to correlate with PDO	Folland et al. (1999); Power et al. (1999) ; **Parker et al.** (2007)	IPO pattern was the third EOF for the 1911–1995 period and half power at 13.3 years; second EOF for 1891–2005 data and 11 years half power.	
		SLP [30°N–65°N; 160°E–140°W]	Trenberth and Hurrell (1994)		

(continued on next page)

Table 2.SM.10 (continued)

Climate Phenomenon		Index Name	Index Definition	Primary References	Characterization / Comments
NAO		Lisbon/ Ponta Delgada-Stykkisholmur/ Reykjavik North Atlantic Oscillation (NAO) Index	Lisbon/Ponta Delgada minus Stykkisholmur/ Reykjavik standardized SLP anomalies	Hurrell (1995)	Appears as a primary NH teleconnection pattern both in SLP and 500 hPa geopotential heigh (Z500) anomalies (Wallace and Gutzler, 1981); one of rotated PCs of NH Z700 (Barnston and Livezey, 1987). SLP anomalies can be monthly, seasonal or annual averages, resulting in the NAO index of corresponding temporal resolution (Hurrell, 1995). In Jones et al. (1997) definition, temporal averaging is applied to monthly NAO index values. NAO index is typically interpreted for boreal winter season (e.g., DJFM or NDJFM means).
		Gibraltar – South-west Iceland NAO Index	Gibraltar minus south-west Iceland / Reykjavik standardized monthly surface pressure anomalies	Jones et al. (1997)	
		PC-based NAO Index	Leading PC of SLP anomalies over the Atlantic sector [20°N–80°N, 90°W–40°E]; sign is selected to correlate with station-based NAO indices.	Hurrell (1995)	
		Summer NAO (SNAO)	Leading PC of daily SLP anomalies for July and August over the North Atlantic region [25°N–70°N, 70°W–50°E]; sign is selected to correlate with station-based (winter) NAO indices.	Folland et al. (2009)	Calculations with daily, 10-day, or July–August mean SLP data result in the same spatial pattern "characterized by a more northerly location and smaller spatial scale than its winter counterpart."
		Model-oriented NAO index	Difference between DJF SLP averages [90°W–60°E, 20°N–55°N] minus [90°W–60°E, 55°N–90°N].	Stephenson et al. (2006)	NAO index which is less sensitive to climate models' shifts of locations of maximum variability.
Annular modes	Northern Annular Mode (NAM), a.k.a. Arctic Oscillation (AO)	PC-based NAM (AO) index	First PC of the monthly mean SLP anomalies poleward of 20°N; sign is selected to correlate with NAO indices.	Thompson and Wallace (1998, 2000)	Closely related to the NAO.
	Southern Annular Mode (SAM) a.k.a. Antarctic Oscillation (AAO),	PC-based SAM index	First PC of 850 hPa or 700 hPa height anomalies south of 20°S; sign is selected to correlate with grid-based AAO and SAM indices	Thompson and Wallace (2000)	
		Grid-based SAM index: 40°S–65°S difference	Difference between normalized zonal mean SLP at 40°S and 65°S, using gridded SLP fields	Gong and Wang (1999)	
		Grid-based SAM index: 40°S–70°S difference	Same as above but uses latitudes 40°S and 70°S	Nan and Li (2003)	
		Station-based SAM index: 40°S–65°S	Difference in normalized zonal mean SLP at 40°S and 65°S, using station data	Marshall (2003)	
Pacific/North America (PNA) atmospheric teleconnection		PNA index based on centers of action	¼[Z(20°N, 160°W) – Z(45°N, 165°W) + Z(55°N, 115°W) – Z(30°N, 85°W)], Z is the location's standardized 500 hPa geopotential height anomaly	Wallace and Gutzler (1981)	A primary NH teleconnection (Wallace and Gutzler, 1981) in SLP and in 500 hPa geopotential height anomalies (Z500); second leading rotated PC of the NH Z700 (Barnston and Livezey, 1987). CPC now uses this procedure for Z500 and provides monthly updates for the results.
		PNA from rotated PC (RPC) calculation	Amplitude of the PNA pattern in the decomposition of the 500 hPa geopotential (Z500) anomaly field into the set of leading rotated EOFs obtained from the RPCA analysis of the NH Z500 monthly anomalies; sign is selected for positive correlation with the centers of action PNA index	Barnston and Livezey (1987).	
Pacific/South America (PSA) atmospheric teleconnection		PSA1 and PSA2 mode indices (PC-based)	Second and third PCs respectively of SH 500 hPa seasonal geopotential height anomaly	Mo and Paegle (2001)	Calculation was done with NCEP-NCAR reanalysis for January 1949 to March 2000. First three PCs were explaining 20%, 13% and 11% of the total variance, respectively. There are many published variations on this procedure, involving temporal filtering, using austral winter data only, PC rotation, different variables (e.g., 200 hPa streamfunction). PSA1 is positive during El Niño events (sign-selecting convention).
		PSA index based on centers of action from the 1972-1982 El Niño events composite	[–Z(35°S, 150°W) + Z(60°S, 120°W) – Z(45°S, 60°W)], Z is the location's JJA 500 hPa geopotential height anomaly	Karoly (1989)	Approximates PSA1 of the previous definition.
		PSA index based on centers of action and La Niña response sign	–[-Z(45°S, 170°W) + Z(67.5°S, 120°W) – Z(50°S, 45°W)]/3, Z is the location's 500 hPa geopotential height anomaly	Yuan and Li (2008)	Approximates (–1)*PSA1 of the PC-based definition above.

(continued on next page)

Table 2.SM.10 (continued)

Atlantic Ocean Multidecadal Variability		Atlantic Multidecadal Oscillation (AMO) index	10-year running mean of de-trended Atlantic mean SST anomalies [0°–70°N]	Enfield et al. (2001)	Called "virtually identical" to the smoothed leading rotated N. Atlantic PC.
		Revised AMO index	As above, but subtracts global anomaly mean (60°S–60°N) instead of de-trending	Trenberth and Shea (2006)	
Tropical Atlantic Ocean variability	Atlantic Ocean Niño Mode (AONM)	ATL3	SST anomalies averaged over [3°S–3°N, 20°W–0°]	Zebiak (1993)	Identified as the two leading PCs of detrended tropical Atlantic monthly SSTA (20°S–20°N): 38% and 25% variance respectively for HadISST1, 1900–2008 (Deser et al. 2010a).
		PC-based AONM	First PC of the detrended tropical Atlantic monthly SSTA (20°S–20°N); sign is selected to correlate with ATL3	Deser et al. (2010)	
	Tropical Atlantic Meridional Mode (AMM)	PC-based AMM Index	Second PC of the detrended tropical Atlantic monthly SSTA (20°S–20°N)		
Tropical Indian Ocean variability	Indian Ocean Basin Mode (IOBM)	Basin mean index (BMI)	SST anomalies averaged over [40°–110°E, 20°S–20°N]	Yang et al. (2007)	
		IOBM, PC-based Index	The first PC of the IO detrended SST anomalies (40°E–110° E, 20°S–20°N); sign is selected by correlation with IOB basin mean index	Deser et al. (2010)	Identified as the two leading PCs of detrended tropical Indian Ocean monthly SSTA (20°S–20°N): 39% and 12% of the variance, respectively, for HadISST1, 1900–2008 (Deser et al. 2010a).
	Indian Ocean Dipole Mode (IODM)	PC-based IODM index	The second PC of the IO detrended SST anomalies (40°E–110° E, 20°S–20°N); sign is selected to correlate with DMI		
		Dipole Mode Index (DMI)	SST anomalies difference: [50°E–70°E, 10°S–10°N)] – [90°E–110°E, 10°S–0°]	Saji et al. (1999)	

References

Ablain, M., A. Cazenave, G. Valladeau, and S. Guinehut, 2009: A new assessment of the error budget of global mean sea level rate estimated by satellite altimetry over 1993–2008. *Ocean Sci.*, **5**, 193–201.

Aguilar, E., et al., 2009: Changes in temperature and precipitation extremes in western central Africa, Guinea Conakry, and Zimbabwe, 1955–2006. *J. Geophys. Res. Atmos.*, **114,** D02115.

Alexander, L. V., et al., 2006: Global observed changes in daily climate extremes of temperature and precipitation. *J. Geophys. Res. Atmos.*, **111,** D05109.

Allan, R., P. Brohan, G. P. Compo, R. Stone, J. Luterbacher, and S. Bronnimann, 2011: The International Atmospheric Circulation Reconstructions over the Earth (ACRE) initiative. *Bull. Am. Meteorol. Soc.*, **92**, 1421-1425.

Anthes, R. A., et al., 2008: The COSMOC/FORMOSAT-3 - Mission early results. *Bull. Am. Meteorol. Soc.*, **89**, 313–+.

Arendt, A., et al., 2012: Randolph Glacier Inventory [v2.0]: A Dataset of Global Glacier Outlines. Global Land Ice Measurements from Space. Digital media. http://nsidc.org/data/docs/noaa/g01130_glacier_inventory

Arndt, D. S., M. O. Baringer, and M. R. Johnson, 2010: State of the Climate in 2009. *Bull. Am. Meteorol. Soc.*, **91**, S1–S224.

Ashok, K., S. K. Behera, S. A. Rao, H. Y. Weng, and T. Yamagata, 2007: El Niño Modoki and its possible teleconnection. *J. Geophys. Res. Oceans*, **112,** C11007.

Barnes, N., and D. Jones, 2011: Clear climate code: Rewriting legacy science software for clarity. *IEEE Software*, **28**, 36–42.

Barnston, A. G., and R. E. Livezey, 1987: Classification, seasonality and persistence of low-frequency atmospheric circulation patterns. *Mon. Weather Rev.*, **115**, 1083–1126.

Beig, G., and V. Singh, 2007: Trends in tropical tropospheric column ozone from satellite data and MOZART model. *Geophys. Res. Lett.*, **34**, L17801.

Bell, G. D., and M. S. Halpert, 1998: Climate assessment for 1997. *Bull. Am. Meteorol. Soc.*, **79**, S1–S50.

Berry, D. I., and E. C. Kent, 2009: A new air-sea interaction gridded dataset from ICOADS with uncertainty estimates. *Bull. Am. Meteor. Soc.*, **90**, 645-656.

Berry, D. I., E. C. Kent, and P. K. Taylor, 2004: An analytical model of heating errors in marine air temperatures from ships. *J. Atmos. Ocean. Technol.*, **21**, 1198–1215.

Bond, T. C., et al., 2013: Bounding the role of black carbon in the climate system: A scientific assessment. *J. Geophys. Res. Atmos.*, 118, 5380–5552.

Bottomley, M., C. K. Folland, J. Hsiung, R. E. Newell, and D. E. Parker, 1990: Global ocean surface temperature atlas "GOSTA". Meteorological Office, Bracknell, UK and Department of Earth, Atmospheric and Planetary Sciences, Massachusetts Institute of Technology, Cambridge, MA, USA, 20 pp.

Brauer, M., et al., 2012: Exposure assessment for estimation of the global burden of disease attributable to outdoor air pollution. *Environ. Sci. Technol.*, **46**, 652–660.

Brohan, P., R. Allan, J. E. Freeman, A. M. Waple, D. Wheeler, C. Wilkinson, and S. Woodruff, 2009: Marine observations of old weather. *Bull. Am. Meteorol. Soc.*, **90**, 219-230.

Brown, R. D., 2000: Northern Hemisphere snow cover variability and change, 1915–97. *J. Clim.*, **13**, 2339–2355.

Brown, R. D., and D. A. Robinson, 2011: Northern Hemisphere spring snow cover variability and change over 1922–2010 including an assessment of uncertainty. *Cryosphere*, **5**, 219–229.

Brownscombe, J. L., J. Nash, G. Vaughan, and C. F. Rogers, 1985: Solar tides in the middle atmosphere. 1. Description of satellite-observations and comparison with theoretical calculations at equinox. *Q. J. R. Meteorol. Soc.*, **111**, 677–689.

Brunet, M., and P. Jones, 2011: Data rescue initiatives: Bringing historical climate data into the 21st century. *Clim. Res.*, **47**, 29–40.

Butler, J., S. Montzka, A. Clarke, J. Lobert, and J. Elkins, 1998: Growth and distribution of halons in the atmosphere. *J. Geophys. Res. Atmos.*, **103**, 1503–1511.

Caesar, J., et al., 2011: Changes in temperature and precipitation extremes over the Indo-Pacific region from 1971 to 2005. *Int. J. Climatol.*, **31**, 791–801.

Canada, 2012: Canadian Smog Science Assessment—Highlights and Key Messages. Environment Canada and Health Canada, 64 pp.

Cane, M. A., 1986: El-Niño. *Annu. Rev. Earth Planet. Sci.*, **14**, 43–70.

Cane, M. A., S. E. Zebiak, and S. C. Dolan, 1986: Experimental forecasts of El Niño. *Nature*, **321**, 827–832.

CASTNET, 2010: Clean Air Status and Trends Network (CASTNET) 2008 Annual Report. US Environmental Protection Agency, Washington, DC, 80 pp.

Cavalieri, D. J., and C. L. Parkinson, 2012: Arctic sea ice variability and trends, 1979–2010. *Cryosphere*, **6**, 957–979.

Cavalieri, D. J., P. Gloersen, and W. J. Campbell, 1984: Determination of sea ice parameters with the Nimbus-7 SMMR. *J. Geophys. Res. Atmos.*, **89**, 5355–5369.

Christy, J. R., R. W. Spencer, W. B. Norris, W. D. Braswell, and D. E. Parker, 2003: Error estimates of version 5.0 of MSU-AMSU bulk atmospheric temperatures. *J. Atmos. Ocean. Technol.*, **20**, 613–629.

Christy, J. R., D. E. Parker, S. J. Brown, I. Macadam, M. Stendel, and W. B. Norris, 2001: Differential trends in tropical sea surface and atmospheric temperatures since 1979. *Geophys. Res. Lett.*, **28**, 183–186.

Church, J. A., and N. J. White, 2011: Sea-level rise from the late 19th to the early 21st century. *Surv. Geophys.*, **32**, 585–602.

Clain, G., et al., 2009: Tropospheric ozone climatology at two Southern Hemisphere tropical/subtropical sites (Reunion Island and Irene, South Africa) from ozonesondes, LIDAR, and in situ aircraft measurements. *Atmos. Chem. Phys.*, **9**, 1723–1734.

Cogley, J. G., 2009: Geodetic and direct mass-balance measurements: comparison and joint analysis. *Ann. Glaciol.*, **50**, 96–100.

Comiso, J. C., and F. Nishio, 2008: Trends in the sea ice cover using enhanced and compatible AMSR-E, SSM/I, and SMMR data. *J. Geophys. Res. Oceans*, **113,** C02S07.

Cooper, O. R., R. S. Gao, D. Tarasick, T. Leblanc, and C. Sweeney, 2012: Long-term ozone trends at rural ozone monitoring sites across the United States, 1990–2010. *J. Geophys. Res.*, **117,** D22307.

Cunnold, D., et al., 1997: GAGE/AGAGE measurements indicating reductions in global emissions of CCl3F and CCl2F2 in 1992–1994. *J. Geophys. Res. Atmos.*, **102**, 1259–1269.

Dai, A., 2006: Recent climatology, variability, and trends in global surface humidity. *J. Clim.*, **19**, 3589–3606.

Dai, A. G., J. H. Wang, P. W. Thorne, D. E. Parker, L. Haimberger, and X. L. L. Wang, 2011: A new approach to homogenize daily radiosonde humidity data. *J. Clim.*, **24**, 965–991.

Dee, D. P., et al., 2011: The ERA-Interim reanalysis: Configuration and performance of the data assimilation system. *Q. J. R. Meteorol. Soc.*, **137**, 553–597.

Deser, C., M. A. Alexander, S. P. Xie, and A. S. Phillips, 2010: Sea surface temperature variability: Patterns and mechanisms. *Annu. Rev. Mar. Sci.*, **2**, 115–143.

Ding, A. J., T. Wang, V. Thouret, J. P. Cammas, and P. Nedelec, 2008: Tropospheric ozone climatology over Beijing: analysis of aircraft data from the MOZAIC program. *Atmos. Chem. Phys.*, **8**, 1–13.

Dlugokencky, E., et al., 2005: Conversion of NOAA atmospheric dry air CH4 mole fractions to a gravimetrically prepared standard scale. *J. Geophys. Res. Atmos.*, **110,** D18306.

Domingues, C. M., J. A. Church, N. J. White, P. J. Gleckler, S. E. Wijffels, P. M. Barker, and J. R. Dunn, 2008: Improved estimates of upper-ocean warming and multi-decadal sea-level rise. *Nature*, **453**, 1090–1093.

Donat, M. G., L. V. Alexander, H. Yang, I. Durre, R. Vose, and J. Caesar, 2013a: Global land-based datasets for monitoring climatic extremes. *Bull. Am. Meteor. Soc.*, **94**, 997-1006.

Donat, M. G., et al., 2013b: Updated analyses of temperature and precipitation extreme indices since the beginning of the twentieth century: The HadEX2 dataset. *J. Geophys. Res. Atmos.*, **118**, 2098-2118.

Donlon, C., et al., 2007: The global ocean data assimilation experiment high-resolution sea surface temperature pilot project. *Bull. Am. Meteorol. Soc.*, **88**, 1197–1213.

Durre, I., C. N. Williams, X. G. Yin, and R. S. Vose, 2009: Radiosonde-based trends in precipitable water over the Northern Hemisphere: An update. *J. Geophys. Res. Atmos.*, **114,** D05112.

Durre, I., M. J. Menne, B. E. Gleason, T. G. Houston, and R. S. Vose, 2010: Comprehensive automated quality assurance of daily surface observations. *J. Appl. Meteorol. Climatol.*, **49**, 1615–1633.

EANET, 2011: EANET Data report on the acid deposition in the East Asian Region 2009. Acid Deposition Monitoring Network in East Asia,

Embury, O., C. J. Merchant, and G. K. Corlett, 2012: A reprocessing for Climate of Sea Surface Temperature from the Along-Track Scanning Radiometers: Preliminary validation, accounting for skin and diurnal variability. *Remote Sens. Environ.*, **116**, 62-78 .

Emery, W. J., D. J. Baldwin, P. Schlussel, and R. W. Reynolds, 2001: Accuracy of *in situ* sea surface temperatures used to calibrate infrared satellite measurements. *J. Geophys. Res. Oceans*, **106**, 2387–2405.

Enfield, D. B., A. M. Mestas-Nunez, and P. J. Trimble, 2001: The Atlantic multidecadal oscillation and its relation to rainfall and river flows in the continental US. *Geophys. Res. Lett.*, **28**, 2077–2080.

Foelsche, U., B. Pirscher, M. Borsche, G. Kirchengast, and J. Wickert, 2009: Assessing the climate monitoring utility of radio occultation data: From CHAMP to FORMOSAT-3/COSMIC. *Terres. Atmos. Ocean. Sci.*, **20**, 155–170.

Folland, C. K., D. E. Parker, A. Colman, and W. R., 1999: Large scale modes of ocean surface temperature since the late nineteenth century. In: *Beyond El Nino: Decadal and Interdecadal Climate Variability* [A. Navarra (ed.)]. Springer-Verlag, New York, NY, USA, and Heidelberg, Germany, pp. 73–102.

Folland, C. K., J. Knight, H. W. Linderholm, D. Fereday, S. Ineson, and J. W. Hurrell, 2009: The summer North Atlantic Oscillation: Past, present, and future. *J. Clim.*, **22**, 1082–1103.

Fraser, P., et al., 1996: Lifetime and emission estimates of 1,1,2–trichlorotrifluorethane (CFC-113) from daily global background observations June 1982 June 1994. *J. Geophys. Res. Atmos.*, **101**, 12585–12599.

Free, M., D. J. Seidel, J. K. Angell, J. Lanzante, I. Durre, and T. C. Peterson, 2005: Radiosonde Atmospheric Temperature Products for Assessing Climate (RATPAC): A new data set of large-area anomaly time series. *J. Geophys. Res. Atmos.*, **110,** D22101.

Gong, D. Y., and S. W. Wang, 1999: Definition of Antarctic Oscillation Index. *Geophys. Res. Lett.*, **26**, 459–462.

Granier, C., et al., 2011: Evolution of anthropogenic and biomass burning emissions of air pollutants at global and regional scales during the 1980–2010 period. *Clim. Change*, **109**, 163–190.

Greally, B., et al., 2007: Observations of 1,1-difluoroethane (HFC-152a) at AGAGE and SOGE monitoring stations in 1994–2004 and derived global and regional emission estimates. *J. Geophys. Res. Atmos.*, **112,** D06308.

Grody, N. C., K. Y. Vinnikov, M. D. Goldberg, J. T. Sullivan, and J. D. Tarpley, 2004: Calibration of multisatellite observations for climatic studies: Microwave Sounding Unit (MSU). *J. Geophys. Res. Atmos.*, **109,** D24104.

Haimberger, L., 2004: Checking the temporal homogeneity of radiosonde data in the Alpine region using ERA-40 analysis feedback data. *Meteorol. Z.*, **13**, 123–129.

Haimberger, L., 2007: Homogenization of radiosonde temperature time series using innovation statistics. *J. Clim.*, **20**, 1377–1403.

Haimberger, L., C. Tavolato, and S. Sperka, 2008: Toward elimination of the warm bias in historic radiosonde temperature records - Some new results from a comprehensive intercomparison of upper-air data. *J. Clim.*, **21**, 4587–4606.

Haimberger, L., C. Tavolato, and S. Sperka, 2012: Homogenization of the global radiosonde temperature dataset through combined comparison with reanalysis background series and neighboring stations. *J. Clim.*, **25**, 8108-8131.

Hajj, G. A., et al., 2004: CHAMP and SAC-C atmospheric occultation results and intercomparisons. *J. Geophys. Res. Atmos.*, **109,** D06109.

Hall, B., G. Dutton, and J. Elkins, 2007: The NOAA nitrous oxide standard scale for atmospheric observations. *J. Geophys. Res. Atmos.*, **112,** D09305.

Hall, B., et al., 2011: Improving measurements of SF6 for the study of atmospheric transport and emissions. *Atmos. Meas. Tech.*, **4**, 2441–2451.

Han, Y. M., et al., 2011: Comparison of elemental carbon in lake sediments measured by three different methods and 150-year pollution history in eastern China. *Environ. Sci. Technol.*, **45**, 5287–5293.

Hand, J. L., et al., 2011: IMPROVE, spatial and seasonal patterns and temporal variability of haze and its constituents in the United States, Report V, ISSN 0737-5352-87, CIRA, Fort Collins, Colorado.

Hansen, J., R. Ruedy, M. Sato, and K. Lo, 2010: Global surface temperature change. *Rev. Geophys.*, **48,** RG4004.

Helmig, D., et al., 2007: A review of surface ozone in the polar regions. *Atmos. Environ.*, **41,** 5138–5161.

Hess, P. G., and R. Zbinden, 2013: Stratospheric impact on tropospheric ozone variability and trends: 1990–2009. *Atmos. Chem. Phys.*, **13**, 649–674.

Hidy, G. M., and G. T. Pennell, 2010: Multipollutant air quality management: 2010 critical review. *J. Air Waste Manage. Assoc.*, **60**, 645–674.

Ho, S. P., M. Goldberg, Y. H. Kuo, C. Z. Zou, and W. Schreiner, 2009a: Calibration of temperature in the Lower Stratosphere from microwave measurements using COSMIC radio occultation data: Preliminary results. *Terres. Atmos. Ocean. Sci.*, **20**, 87–100.

Ho, S. P., et al., 2009b: Estimating the uncertainty of using GPS radio occultation data for climate monitoring: Intercomparison of CHAMP refractivity climate records from 2002 to 2006 from different data centers. *J. Geophys. Res. Atmos.*, **114,** D23107.

Holben, B. N., et al., 1998: AERONET—A federated instrument network and data archive for aerosol characterization. *Remote Sens. Environ.*, **66**, 1–16.

Hurrell, J. W., 1995: Decadal trends in the North Atlantic Oscillation: Regional temperatures and precipitation. *Science*, **269**, 676–679.

Ishii, M., and M. Kimoto, 2009: Reevaluation of historical ocean heat content variations with time-varying XBT and MBT depth bias corrections. *J. Oceanogr.*, **65**, 287–299.

Ishii, M., A. Shouji, S. Sugimoto, and T. Matsumoto, 2005: Objective analyses of sea-surface temperature and marine meteorological variables for the 20th century using icoads and the Kobe collection. *Int. J. Climatol.*, **25**, 865–879.

Ivy, D., et al., 2012: Atmospheric histories and growth trends of C4F10, C5F12, C6F14, C7F16 and C8F18. *Atmos. Chem. Phys.*, **12**, 4313–4325.

Jevrejeva, S., J. C. Moore, A. Grinsted, and P. L. Woodworth, 2008: Recent global sea level acceleration started over 200 years ago? *Geophys. Res. Lett.*, **35,** L08715.

John, V. O., G. Holl, S. A. Buehler, B. Candy, R. W. Saunders, and D. E. Parker, 2012: Understanding intersatellite biases of microwave humidity sounders using global simultaneous nadir overpasses. *J. Geophys. Res. Atmos.*, **117**, D02305.

Jones, P. D., T. Jonsson, and D. Wheeler, 1997: Extension to the North Atlantic Oscillation using early instrumental pressure observations from Gibraltar and south-west Iceland. *Int. J. Climatol.*, **17**, 1433–1450.

Jones, P. D., D. H. Lister, T. J. Osborn, C. Harpham, M. Salmon, and C. P. Morice, 2012: Hemispheric and large-scale land-surface air temperature variations: An extensive revision and an update to 2010. *J. Geophys. Res. Atmos.*, **117**, 29.

Kao, H. Y., and J. Y. Yu, 2009: Contrasting Eastern-Pacific and Central-Pacific Types of ENSO. *J. Clim.*, **22**, 615–632.

Karoly, D., 1989: Southern-Hemisphere circulation features associated with El Niño—Southern Oscillation events. *J. Clim.*, **2**, 1239–1252.

Kaskaoutis, D. G., S. R. P, R. Gautam, M. Sharma, P. G. Kosmopoulos, and S. N. Tripathi, 2012: Variability and trends of aerosol properties over Kanpur, northern India using AERONET data (2001–10). *Environ. Res. Lett.*, **7**, 024003.

Kawai, Y., and A. Wada, 2007: Diurnal sea surface temperature variation and its impact on the atmosphere and ocean: A review. *J. Oceanogr.*, **63**, 721–744.

Keeling, C., R. Bacastow, A. Bainbridge, C. Ekdahl, P. Guenther, L. Waterman, and J. Chin, 1976: Atmospheric carbon-dioxide variations at Mauna-Loa Observatory, Hawaii. *Tellus*, **28**, 538–551.

Kennedy, J. J., P. Brohan, and S. F. B. Tett, 2007: A global climatology of the diurnal variations in sea-surface temperature and implications for MSU temperature trends. *Geophys. Res. Lett.*, **34,** L05712.

Kennedy, J. J., N. A. Rayner, and R. O. Smith, 2012: Using AATSR data to assess the quality of in situ sea surface temperature observations for climate studies. *Remote Sens. Environ.*, **116**, 79–92.

Kennedy, J. J., N. A. Rayner, R. O. Smith, D. E. Parker, and M. Saunby, 2011a: Reassessing biases and other uncertainties in sea surface temperature observations measured in situ since 1850: 2. Biases and homogenization. *J. Geophys. Res. Atmos.*, **116**, 22.

Kennedy, J. J., N. A. Rayner, R. O. Smith, D. E. Parker, and M. Saunby, 2011a: Reassessing biases and other uncertainties in sea surface temperature observations measured in situ since 1850: 2. Biases and homogenization. *J. Geophys. Res. Atmos.*, **116**, D14104.

Kent, E. C., and D. I. Berry, 2005: Quantifying random measurement errors in voluntary observing ships' meteorological observations. *Int. J. Climatol.*, **25**, 843–856.

Kent, E. C., and P. G. Challenor, 2006: Toward estimating climatic trends in SST. Part II: Random errors. *J. Atmos. Ocean. Technol.*, **23**, 476–486.

Kent, E. C., and A. Kaplan, 2006: Toward estimating climatic trends in SST. Part III: Systematic biases. *J. Atmos. Ocean. Technol.*, **23**, 487–500.

Kent, E. C., and P. K. Taylor, 2006: Toward estimating climatic trends in SST. Part I: Methods of measurement. *J. Atmos. Ocean. Technol.*, **23**, 464–475.

Kent, E. C., P. G. Challenor, and P. K. Taylor, 1999: A statistical determination of the random observational errors present in voluntary observing ships meteorological reports. *J. Atmos. Ocean. Technol.*, **16**, 905–914.

Kent, E. C., J. J. Kennedy, D. I. Berry, and R. O. Smith, 2010: Effects of instrumentation changes on sea surface temperature measured in situ. *Clim. Change*, **1**, 718–728.

Kent, E. C., N. A. Rayner, D. I. Berry, M. Saunby, B. I. Moat, J. J. Kennedy, and D. E. Parker, 2013: Global analysis of night marine air temperature and its uncertainty since 1880, the HadNMAT2 Dataset, *J. Geophys. Res.*, **118**, 1281-1298.

Kim, D.-H., B.-J. Sohn, T. Nakajima, T. Takamura, T. Takemura, B.-C. Choi, and S.-C. Yoon, 2004: Aerosol optical properties over east Asia determined from ground-based sky radiation measurements. *J. Geophys. Res.*, **109**, D02209.

Kobayashi, S., M. Matricardi, D. Dee, and S. Uppala, 2009: Toward a consistent reanalysis of the upper stratosphere based on radiance measurements from SSU and AMSU-A. *Q. J. R. Meteorol. Soc.*, **135**, 2086–2099.

Krishna Moorthy, K., S. Suresh Babu, M. R. Manoj, and S. K. Satheesh, 2013: Buildup of aerosols over the Indian Region. *Geophys. Res. Lett.*, doi:10.1002/grl.50165, in press.

Krishna Moorthy, K., S. S. Babu, S. K. Satheesh, S. Lal, M. M. Sarin, and S. Ramachandran, 2009: Climate implications of atmospheric aerosols and trace gases: Indian Scenario, Climate Sense. World Meteorological Organisation, Geneva, Switzerland, pp. 157–160.

Kuo, Y. H., T. K. Wee, S. Sokolovskiy, C. Rocken, W. Schreiner, D. Hunt, and R. A. Anthes, 2004: Inversion and error estimation of GPS radio occultation data. *J. Meteorol. Soc. Jpn.*, **82**, 507–531.

Laube, J., et al., 2010: Accelerating growth of HFC-227ea (1,1,1,2,3,3,3-heptafluoropropane) in the atmosphere. *Atmos. Chem. Phys.*, **10**, 5903–5910.

Lawrimore, J., J. Rennie, and P. Thorne, 2013: Responding to the need for better global temperature Ddata. *EOS Trans. Am. Geophys. Union*, **94**, 61–62.

Lawrimore, J. H., M. J. Menne, B. E. Gleason, C. N. Williams, D. B. Wuertz, R. S. Vose, and J. Rennie, 2011: An overview of the Global Historical Climatology Network monthly mean temperature data set, version 3. *J. Geophys. Res. Atmos.*, **116**, D19121.

Leclercq, P. W., J. Oerlemans, and J. G. Cogley, 2011: Estimating the glacier contribution to sea-level rise for the period 1800–2005. *Surv. Geophys.*, **32**, 519–535.

Lelieveld, J., J. van Aardenne, H. Fischer, M. de Reus, J. Williams, and P. Winkler, 2004: Increasing ozone over the Atlantic Ocean. *Science*, **304**, 1483–1487.

Leroy, S. S., J. G. Anderson, and J. A. Dykema, 2006: Testing climate models using GPS radio occultation: A sensitivity analysis. *J. Geophys. Res. Atmos*, **111**, D17105.

Leuliette, E. W., and R. Scharroo, 2010: Integrating Jason-2 into a multiple-altimeter climate data record. *Mar. Geodesy*, **33**, 504–517.

Levitus, S., et al., 2012: World ocean heat content and thermosteric sea level change (0–2000 m), 1955–2010. *Geophys. Res. Lett.*, **39**, L10603.

Li, H. C., K. S. Chen, C. H. Huang, and H. K. Wang, 2010: Meteorologically adjusted long-term trend of ground-level ozone concentrations in Kaohsiung County, southern Taiwan. *Atmos. Environ.*, **44**, 3605–3608.

Lin, Y. K., T. H. Lin, and C. S.C., 2010: The changes in different ozone metrics and their implications following precursor reductions over northern Taiwan from 1994 to 2007. *Environ. Monit. Assess.*, **169**, 143–157.

Logan, J. A., et al., 2012: Changes in Ozone over Europe since 1990: analysis of ozone measurements from sondes, regular Aircraft (MOZAIC), and alpine surface sites. *J. Geophys. Res.*, **117**, D09301.

Mantua, N. J., S. R. Hare, Y. Zhang, J. M. Wallace, and R. C. Francis, 1997: A Pacific interdecadal climate oscillation with impacts on salmon production. *Bull. Am. Meteorol. Soc.*, **78**, 1069–1079.

Markus, T., and D. J. Cavalieri, 2000: An enhancement of the NASA Team sea ice algorithm. *Ieee Trans. Geosci. Remote Sens*, **38**, 1387–1398.

Marshall, G. J., 2003: Trends in the southern annular mode from observations and reanalyses. *J. Clim.*, **16**, 4134–4143.

Marzeion, B., A. H. Jarosch, and M. Hofer, 2012: Past and future sea-level change from the surface mass balance of glaciers. *Cryosphere*, **6**, 1295–1322.

McCarthy, M. P., P. W. Thorne, and H. A. Titchner, 2009: An analysis of tropospheric humidity trends from radiosondes. *J. Clim.*, **22**, 5820–5838.

Mears, C. A., and F. J. Wentz, 2009a: Construction of the Remote Sensing Systems V3.2 Atmospheric temperature records from the MSU and AMSU Microwave Sounders. *J. Atmos. Ocean. Technol.*, **26**, 1040–1056.

Mears, C. A., and F. J. Wentz, 2009b: Construction of the RSS V3.2 Lower-Tropospheric temperature dataset from the MSU and AMSU Microwave Sounders. *J. Atmos. Ocean. Technol.*, **26**, 1493–1509.

Mears, C. A., F. J. Wentz, P. Thorne, and D. Bernie, 2011: Assessing uncertainty in estimates of atmospheric temperature changes from MSU and AMSU using a Monte-Carlo estimation technique. *J. Geophys. Res. Atmos.*, **116**.

Mekis, É., and L. A. Vincent, 2011: An overview of the second generation adjusted daily precipitation dataset for trend analysis in Canada. *Atmos. Ocean*, **49**, 163–177.

Menne, M. J., and C. N. Williams, 2005: Detection of undocumented changepoints using multiple test statistics and composite reference series. *J. Clim.*, **18**, 4271–4286.

Menne, M. J., and C. N. Williams, 2009: Homogenization of temperature series via pairwise comparisons. *J. Clim.*, **22**, 1700–1717.

Menne, M. J., I. Durre, B. G. Gleason, T. G. Houston, and R. S. Vose, 2012: An overview of the Global Historical Climatology Network-Daily database. *J. Atmos. Ocean. Technol.*, **29**, 897–910.

Miller, B., R. Weiss, P. Salameh, T. Tanhua, B. Greally, J. Muhle, and P. Simmonds, 2008: Medusa: A sample preconcentration and GC/MS detector system for in situ measurements of atmospheric trace halocarbons, hydrocarbons, and sulfur compounds. *Anal. Chem.*, **80**, 1536-1545 .

Miller, B., et al., 2010: HFC-23 (CHF3) emission trend response to HCFC-22 (CHClF2) production and recent HFC-23 emission abatement measures. *Atmos. Chem. Phys.*, **10**, 7875-7890.

Ministery of Environment and Forest, G. o. I., 2009: State of Environmnet Report, India–2009. Ministery of Environment and Forest, 194 pp.

Mo, K., and J. Paegle, 2001: The Pacific-South American modes and their downstream effects. *Int. J. Climatol.*, **21**, 1211–1229.

Mo, T., 2009: A study of the NOAA-15 AMSU-A brightness temperatures from 1998 through 2007. *J. Geophys. Res. Atmos.*, **114**.

Montzka, S., B. Hall, and J. Elkins, 2009: Accelerated increases observed for hydrochlorofluorocarbons since 2004 in the global atmosphere. *Geophys. Res. Lett.*, **36**, L03804.

Montzka, S., R. Myers, J. Butler, J. Elkins, and S. Cummings, 1993: Global tropospheric distribution and calibration scale of HCFC-22. *Geophys. Res. Lett.*, **20**, 703–706.

Montzka, S., M. Krol, E. Dlugokencky, B. Hall, P. Jockel, and J. Lelieveld, 2011: Small interannual variability of global atmospheric hydroxyl. *Science*, **331**, 67-69.

Montzka, S., R. Myers, J. Butler, J. Elkins, L. Lock, A. Clarke, and A. Goldstein, 1996: Observations of HFC-134a in the remote troposphere. *Geophys. Res. Lett.*, **23**, 169–172.

Morice, C. P., J. J. Kennedy, N. A. Rayner, and P. D. Jones, 2012: Quantifying uncertainties in global and regional temperature change using an ensemble of observational estimates: The HadCRUT4 data set. *J. Geophys. Res. Atmos.*, **117**, 22.

Muhle, J., et al., 2009: Sulfuryl fluoride in the global atmosphere. *J. Geophys. Res. Atmos.*, **114**, D05306.

Muhle, J., et al., 2010: Perfluorocarbons in the global atmosphere: Tetrafluoromethane, hexafluoroethane, and octafluoropropane. *Atmos. Chem. Phys.*, **10**, 5145-5164.

Nan, S., and J. P. Li, 2003: The relationship between the summer precipitation in the Yangtze River Valley and the boreal spring Southern Hemisphere annular mode. *Geophys. Res. Lett.*, **30,** 2266.

Nerem, R. S., D. P. Chambers, C. Choe, and G. T. Mitchum, 2010: Estimating mean sea level change from the TOPEX and Jason Altimeter Missions. *Mar. Geodesy*, **33**, 435–446.

O'Carroll, A. G., J. R. Eyre, and R. W. Saunders, 2008: Three-way error analysis between AATSR, AMSR-E, and in situ sea surface temperature observations. *J. Atmos. Ocean. Technol.*, **25**, 1197–1207.

O'Doherty, S., et al., 2004: Rapid growth of hydrofluorocarbon 134a and hydrochlorofluorocarbons 141b, 142b, and 22 from Advanced Global Atmospheric Gases Experiment (AGAGE) observations at Cape Grim, Tasmania, and Mace Head, Ireland. *J. Geophys. Res. Atmos.*, **109,** D06310.

O'Doherty, S., et al., 2009: Global and regional emissions of HFC-125 (CHF2CF3) from in situ and air archive atmospheric observations at AGAGE and SOGE observatories. *J. Geophys. Res. Atmos.*, **114**, D23304.

Oltmans, S. J., et al., 2013: Recent tropospheric ozone changes—A pattern dominated by slow or no growth. *Atmos. Environ.*, **67**, 331–351.

Oram, D., et al., 2012: Long-term tropospheric trend of octafluorocyclobutane (c-C4F8 or PFC-318). *Atmos. Chem. Phys.*, **12**, 261–269.

Palmer, M. D., K. Haines, S. F. B. Tett, and T. J. Ansell, 2007: Isolating the signal of ocean global warming. *Geophys. Res. Lett.*, **34**, 6.

Parker, D., C. Folland, A. Scaife, J. Knight, A. Colman, P. Baines, and B. Dong, 2007: Decadal to multidecadal variability and the climate change background. *J. Geophys. Res. Atmos.*, **112.** D18115.

Parkinson, C. L., and D. J. Cavalieri, 2012: Antarctic Sea ice variability and trends, 1979–2010. *Cryosphere*, **6**, 871–880.

Parrish, D. D., et al., 2012: Long-term changes in lower tropospheric baseline ozone concentrations at northern mid-latitudes. *Atmos. Chem. Phys.*, **12**, 11485–11504.

Peterson, T. C., X. B. Zhang, M. Brunet-India, and J. L. Vazquez-Aguirre, 2008: Changes in North American extremes derived from daily weather data. *J. Geophys. Res. Atmos.*, **113,** D07113.

Power, S., T. Casey, C. Folland, A. Colman, and V. Mehta, 1999: Inter-decadal modulation of the impact of ENSO on Australia. *Clim. Dyn.*, **15**, 319–324.

Prather, M., and J. Hsu, 2008: NF3, the greenhouse gas missing from Kyoto. *Geophys. Res. Lett.*, 35, L12810.

Prinn, R., et al., 1990: Atmospheric emissions and trends of nitrous oxide deduced from 10 years of ALE-GAGE Data. *J. Geophys. Res.*, **95**, 18, 369–18, 385.

Prinn, R., et al., 2000: A history of chemically and radiatively important gases in air deduced from ALE/GAGE/AGAGE. *J. Geophys. Res. Atmos.*, **105**, 17751–17792.

Prinn, R., et al., 2005: Evidence for variability of atmospheric hydroxyl radicals over the past quarter century. *Geophys. Res. Lett.*, L07809.

Qu, W. J., R. Arimoto, X. Y. Zhang, C. H. Zhao, Y. Q. Wang, L. F. Sheng, and G. Fu, 2010: Spatial distribution and interannual variation of surface PM10 concentrations over eighty-six Chinese cities. *Atmos. Chem. Phys.*, **10**, 5641–5662.

Quan, J., Q. Zhang, H. He, J. Liu, M. Huang, and H. Jin, 2011: Analysis of the formation of fog and haze in North China Plain (NCP). *Atmos. Chem. Phys.*, **11**, 8205–8214.

Quinn, P. K., T. S. Bates, K. Schulz, and G. E. Shaw, 2009: Decadal trends in aerosol chemical composition at Barrow, Alaska: 1976–2008. *Atmos. Chem. Phys.*, **9**, 8883–8888.

Randel, W. J., et al., 2009: An update of observed stratospheric temperature trends. *J. Geophys. Res. Atmos.*, **114,** D02107.

Rasmusson, E. M., and J. M. Wallace, 1983: Meteorological aspects of the El Niño-Southern Oscillation. *Science*, **222**, 1195–1202.

Ray, R. D., and B. C. Douglas, 2011: Experiments in reconstructing twentieth-century sea levels. *Prog. Oceanogr.*, **91**, 496–515.

Rayner, N. A., et al., 2003: Global analyses of sea surface temperature, sea ice, and night marine air temperature since the late nineteenth century. *J. Geophys. Res. Atmos.*, **108**, 37.

Rayner, N. A., et al., 2006: Improved analyses of changes and uncertainties in sea surface temperature measured in situ sice the mid-nineteenth century: The HadSST2 dataset. *J. Clim.*, **19**, 446–469.

Reynolds, R. W., C. L. Gentemann, and G. K. Corlett, 2010: Evaluation of AATSR and TMI Satellite SST Data. *J. Clim.*, **23**, 152–165.

Reynolds, R. W., N. A. Rayner, T. M. Smith, D. C. Stokes, W. Wang, and A. M. S. Ams, 2002: *An Improved In Situ and Satellite SST Analysis, J. Climate*, **15**, 1609-1625.

Rigby, M., et al., 2008: Renewed growth of atmospheric methane. *Geophys. Res. Lett.*, **35**, L22805.

Rigby, M., et al., 2010: History of atmospheric SF6 from 1973 to 2008. *Atmos. Chem. Phys.*, **10**, 10305-10320.

Robinson, D. A., and A. Frei, 2000: Seasonal variability of Northern Hemisphere snow extent using visible satellite data. *Prof. Geogr.*, **52**, 307–315.

Rohde, R., et al., 2013: Berkeley earth temperature averaging process. *Geoinform. Geostat. An Overview*, **1:2**, doi:10.4172/2327-4581.1000103.

Saito, T., Y. Yokouchi, A. Stohl, S. Taguchi, and H. Mukai, 2010: Large emissions of perfluorocarbons in East Asia deduced from continuous atmospheric measurements. *Environ. Sci. Technol.*, **44**, 4089–4095.

Saji, N. H., B. N. Goswami, P. N. Vinayachandran, and T. Yamagata, 1999: A dipole mode in the tropical Indian Ocean. *Nature*, **401**, 360–363.

Santer, B., et al., 2008: Consistency of modelled and observed temperature trends in the tropical troposphere. *Int. J. Climatol.*, **28**, 1703–1722.

Schnadt Poberaj, C., J. Staehelin, D. Brunner, V. Thouret, H. De Backer, and R. Stübi, 2009: Long-term changes in UT/LS ozone between the late 1970s and the 1990s deduced from the GASP and MOZAIC aircraft programs and from ozonesondes. *Atmos. Chem. Phys.*, **9**, 5343–5369.

Scinocca, J. F., D. B. Stephenson, T. C. Bailey, and J. Austin, 2010: Estimates of past and future ozone trends from multimodel simulations using a flexible smoothing spline methodology. *J. Geophys. Res. Atmos.*, **115**.

Seidel, D. J., Gillett, N. P., Lanzante, J. R., Shine, K. P., Thorne, P. W., 2011: Stratospheric temperature trends: Our evolving understanding.

SEN, P., 1968: Estimates of regression coefficient based on Kendalls tau. *J. Am. Stat. Assoc.*, **63**, 1379-1389.

Sharma, S., E. Andrews, L. A. Barrie, J. A. Ogren, and D. Lavoué, 2006: Variations and sources of the equivalent black carbon in the high Arctic revealed by long-term observations at Alert and Barrow: 1989–2003. *J. Geophys. Res.*, **111**, D14208.

Sherwood, S. C., 2007: Simultaneous detection of climate change and observing biases in a network with incomplete sampling. *J. Clim.*, **20**, 4047–4062.

Sherwood, S. C., C. L. Meyer, R. J. Allen, and H. A. Titchner, 2008: Robust tropospheric warming revealed by iteratively homogenized radiosonde data. *J. Clim.*, **21**, 5336–5350.

Shine, K. P., J. J. Barnett, and W. J. Randel, 2008: Temperature trends derived from Stratospheric Sounding Unit radiances: The effect of increasing CO_2 on the weighting function. *Geophys. Res. Lett.*, **35,** L02710.

Sickles, J. E., II, and D. S. Shadwick, 2007a: Changes in air quality and atmospheric deposition in the eastern United States: 1990–2004. *J. Geophys. Res.*, **112**, D17301.

Sickles, J. E., II, and D. S. Shadwick, 2007b: Seasonal and regional air quality and atmospheric deposition in the eastern United States. *J. Geophys. Res.*, **112**, D17302.

Simmonds, P., et al., 1998: Global trends and emission estimates of CCl4 from in situ background observations from July 1978 to June 1996. *J. Geophys. Res. Atmos.*, **103**, 31331–31331.

Smith, D. M., and J. M. Murphy, 2007: An objective ocean temperature and salinity analysis using covariances from a global climate model. *J. Geophys. Res. Oceans*, **112**, C02022.

Smith, T. M., and R. W. Reynolds, 2002: Bias corrections for historical sea surface temperatures based on marine air temperatures. *J. Clim.*, **15**, 73–87.

Smith, T. M., T. C. Peterson, J. H. Lawrimore, and R. W. Reynolds, 2005: New surface temperature analyses for climate monitoring. *Geophys. Res. Lett.*, **32,** L14712.

Smith, T. M., R. W. Reynolds, T. C. Peterson, and J. Lawrimore, 2008: Improvements to NOAA's historical merged land-ocean surface temperature analysis (1880–2006). *J. Clim.*, **21**, 2283–2296.

Stemmler, K., et al., 2007: European emissions of HFC-365mfc, a chlorine-free substitute for the foam blowing agents HCFC-141b and CFC-11. *Environ. Sci. Technol.*, **41**, 1145–1151.

Stephenson, D. B., V. Pavan, M. Collins, M. M. Junge, R. Quadrelli, and C. M. G. Participating, 2006: North Atlantic Oscillation response to transient greenhouse gas forcing and the impact on European winter climate: A CMIP2 multi-model assessment. *Clim. Dynam.*, **27**, 401-420.

Takahashi, K., A. Montecinos, K. Goubanova, and B. Dewitte, 2011: ENSO regimes: Reinterpreting the canonical and Modoki El Niño. *Geophys. Res. Lett.*, **38,** L10704.

Tarasova, O. A., I. A. Senik, M. G. Sosonkin, J. Cui, J. Staehelin, and A. S. H. Prevot, 2009: Surface ozone at the Caucasian site Kislovodsk High Mountain Station and the Swiss Alpine site Jungfraujoch: data analysis and trends (1990–2006). *Atmos. Chem. Phys.*, **9**, 4157–4175.

Thompson, D. W. J., and J. M. Wallace, 1998: The Arctic Oscillation signature in the wintertime geopotential height and temperature fields. *Geophys. Res. Lett.*, **25**, 1297–1300.

Thompson, D. W. J., and J. M. Wallace, 2000: Annular modes in the extratropical circulation. Part I: Month-to-month variability. *J. Clim.*, **13**, 1000–1016.

Thompson, T. A., et al., 2004: Halocarbons and other atmospheric trace species. *Climate Monitoring and Diagnostics Laboratory Summary Report*. NOAA CMDL, Boulder, Colorado, pp.115–135.

Thorne, P. W., D. E. Parker, S. F. B. Tett, P. D. Jones, M. McCarthy, H. Coleman, and P. Brohan, 2005: Revisiting radiosonde upper air temperatures from 1958 to 2002. *J. Geophys. Res. Atmos.*, **110**, 17.

Thorne, P. W., et al., 2011: Guiding the creation of a comprehensive surface temperature resource for 21st century climate science. *Bull. Am. Meteorol. Soc.*, **92**, 40-47.

Torseth, K., et al., 2012: Introduction to the European Monitoring and Evaluation Programme (EMEP) and observed atmospheric composition change during 1972–2009. *Atmos. Chem. Phys. Discuss.*, **12**, 1733–1820.

Trenberth, K. E., 1984: Signal versus noise in the Southern Oscillation. *Mon. Weather Rev.*, **112**, 326–332.

Trenberth, K. E., 1997: The definition of El Niño. *Bull. Am. Meteorol. Soc.*, **78**, 2771–2777.

Trenberth, K. E., and J. W. Hurrell, 1994: Decadal atmosphere-ocean variations in the Pacific. *Clim. Dyn.*, **9**, 303–319.

Trenberth, K. E., and T. J. Hoar, 1996: The 1990–1995 El Niño Southern Oscillation event: Longest on record. *Geophys. Res. Lett.*, **23**, 57–60.

Trenberth, K. E., and D. P. Stepaniak, 2001: Indices of El Niño evolution. *J. Clim.*, **14**, 1697–1701.

Trenberth, K. E., and D. J. Shea, 2006: Atlantic hurricanes and natural variability in 2005. *Geophys. Res. Lett.*, **33,** L12704.

Trewin, B., 2012: A daily homogenized temperature data set for Australia. *Int. J. Climatol.*, 33, 1510-1529.

Troup, A. J., 1965: Southern Oscillation. *Q. J. R. Meteorol. Soc.*, **91**, 490–.

Vignati, E., M. Karl, M. Krol, J. Wilson, P. Stier, and F. Cavalli, 2010: Sources of uncertainties in modelling black carbon at the global scale. *Atmos. Chem. Phys.*, **10**, 2595–2611.

Vincent, L. A., X. L. L. Wang, E. J. Milewska, H. Wan, F. Yang, and V. Swail, 2012: A second generation of homogenized Canadian monthly surface air temperature for climate trend analysis. *J. Geophys. Res. Atmos.*, **117,** D18110.

Vollmer, M., S. Reimann, D. Folini, L. Porter, and L. Steele, 2006: First appearance and rapid growth of anthropogenic HFC-245fa (CHF2CH2CF3) in the atmosphere. *Geophys. Res. Lett.*, **33,** L20806.

Vollmer, M., et al., 2011: Atmospheric histories and global emissions of the anthropogenic hydrofluorocarbons HFC-365mfc, HFC-245fa, HFC-227ea, and HFC-236fa. *J. Geophys. Res. Atmos.*, **116,** D08304.

Vose, R. S., et al., 2012b: NOAA's Merged Land-Ocean Surface Temperature Analysis. *Bull. Am. Meteor. Soc.*, **93**, 1677–1685.

Wahba, G., 1990: *Spline Models for Observational Data*. Society for Industrial and Applied Mathematics, Philadelphia, PA, 169pp.

Wallace, J. M., and D. S. Gutzler, 1981: Teleconnections in the geopotential height field during the Northern Hemisphere winter. *Mon. Weather Rev.*, **109**, 784–812.

Walsh, J. E., and W. L. Chapman, 2001: 20th-century sea-ice variations from observational data. *Ann. Glaciol.,* **33**, 444–448.

Wang, B., and G. Shi, 2010: Long term trends of atmospheric absorbing and scattering optical depths over China region estimated from the routine observation data of surface solar irradiances. *J. Geophys. Res. Atmos.*, **115**, D00K28

Wang, K., R. E. Dickinson, and S. Liang, 2009a: Clear sky visibility has decreased over land globally from 1973 to 2007. *Science*, **323**, 1468–1470.

Wang, K. C., R. E. Dickinson, L. Su, and K. E. Trenberth, 2012: Contrasting trends of mass and optical properties of aerosols over the Northern Hemisphere from 1992 to 2011. *Atmos. Chem. Phys.*, **12**, 9387–9398.

Wang, T., et al., 2009b: Increasing surface ozone concentrations in the background atmosphere of Southern China, 1994–2007. *Atmos. Chem. Phys.*, **9**, 6217–6227.

Wang, X. L. L., and V. R. Swail, 2001: Changes of extreme wave heights in Northern Hemisphere oceans and related atmospheric circulation regimes. *J. Clim.*, **14**, 2204–2221.

Weiss, R., J. Muhle, P. Salameh, and C. Harth, 2008: Nitrogen trifluoride in the global atmosphere. *Geophys. Res. Lett.*, **35**, L20821.

Wilkinson, C., et al., 2011: Recovery of logbooks and international marine data: the RECLAIM project. *Int. J. Climatol.*, **31**, 968–979.

Willett, K. M., P. D. Jones, N. P. Gillett, and P. W. Thorne, 2008: Recent changes in surface humidity: Development of the HadCRUH dataset. *J. Clim.*, **21**, 5364–5383.

Willett, K. M., et al., 2013: HadISDH: An updateable land surface specific humidity product for climate monitoring. *Clim. Past*, **9**, 657–677.

WMO, 2011: Scientific assessment of ozone depletion: 2010, Global Ozone Research and Monitoring Project–Report No. 52. World Meteorological Organization, Geneva, Switzerland.

Wood, S. N., 2006: *Generalized Additive Models: An Introduction with R*. CRC/Chapman & Hall, Boca Raton, FL, USA.

Woodruff, S. D., et al., 2011: ICOADS Release 2.5: Extensions and Enhancements to the Surface Marine Meteorological Archive. *Int. J. Climatol.*, **31**, 951–967.

Worley, S. J., S. D. Woodruff, R. W. Reynolds, S. J. Lubker, and N. Lott, 2005: ICOADS release 2.1 data and products. *Int. J. Climatol.*, **25**, 823–842.

Yang, J., Q. Liu, S.-P. Xie, Z. Liu, and L. Wu, 2007: Impact of the Indian Ocean SST basin mode on the Asian summer monsoon. *Geophys. Res. Lett.*, **34,** L02708.

Yttri, K. E., et al., 2011: Transboundary particulate matter in Europe, Status Report 2011. *Co-operative Programme for Monitoring and Evaluation of the Long Range Transmission of Air Pollutants (Joint CCC, MSC-W, CEIP and CIAM report 2011)*. NILU - Chemical Coordinating Centre - CCC, http://www.nilu.no/projects/ccc/reports/.

Yuan, X., and C. Li, 2008: Climate modes in southern high latitudes and their impacts on Antarctic sea ice. *J. Geophys. Res. Oceans*, **113,** C06S91.

Zebiak, S. E., 1993: Air-sea interaction in the equatorial Atlantic region. *J. Clim.*, **6**, 1567–1568.

Zhang, X., and F. Zwiers, 2004: Comment on "Applicability of prewhitening to eliminate the influence of serial correlation on the Mann-Kendall test" by Sheng Yue and Chun Yuan Wang. *Water Resourc. Res.*, **40,** W03805.

Zhang, X., et al., 2011: Indices for monitoring changes in extremes based on daily temperature and precipitation data. *Wiley Interdis. Rev. Clim. Change*, **2**, 851-870.

Zhang, X. Y., Y. Q. Wang, T. Niu, X. C. Zhang, S. L. Gong, Y. M. Zhang, and J. Y. Sun, 2012: Atmospheric aerosol compositions in China: Spatial/temporal variability, chemical signature, regional haze distribution and comparisons with global aerosols. *Atmos. Chem. Phys.*, **12**, 779–799.

Zhang, Y., J. M. Wallace, and D. S. Battisti, 1997: ENSO-like interdecadal variability: 1900–93. *J. Clim.*, **10**, 1004-1020.

Zhao, C., and P. Tans, 2006: Estimating uncertainty of the WMO mole fraction scale for carbon dioxide in air. *J. Geophys. Res. Atmos.*, **111,** D08S09.

Zou, C. Z., and W. H. Wang, 2010: Stability of the MSU-derived atmospheric temperature trend. *J. Atmos. Ocean. Technol.*, **27**, 1960–1971.

Zou, C.-Z., and W. Wang, 2011: Intersatellite calibration of AMSU-A observations for weather and climate applications. *J. Geophys. Res. Atmos.*, D23113.

Zou, C. Z., M. Gao, and M. D. Goldberg, 2009: Error structure and atmospheric temperature trends in observations from the Microwave Sounding Unit. *J. Clim.*, **22**, 1661–1681.

Zou, C. Z., M. D. Goldberg, Z. H. Cheng, N. C. Grody, J. T. Sullivan, C. Y. Cao, and D. Tarpley, 2006: Recalibration of microwave sounding unit for climate studies using simultaneous nadir overpasses. *J. Geophys. Res. Atmos.*, **111,** D19114.

4SM

Observations: Cryosphere

Supplementary Material

Coordinating Lead Authors:

David G. Vaughan (UK), Josefino C. Comiso (USA)

Lead Authors:

Ian Allison (Australia), Jorge Carrasco (Chile), Georg Kaser (Austria/Italy), Ronald Kwok (USA), Philip Mote (USA), Tavi Murray (UK), Frank Paul (Switzerland/Germany), Jiawen Ren (China), Eric Rignot (USA), Olga Solomina (Russian Federation), Konrad Steffen (USA/Switzerland), Tingjun Zhang (USA/China)

Contributing Authors:

Anthony A. Arendt (USA), David B. Bahr (USA), Michiel van den Broeke (Netherlands), Ross Brown (Canada), J. Graham Cogley (Canada), Alex S. Gardner (USA), Sebastian Gerland (Norway), Stephan Gruber (Switzerland), Christian Haas (Canada), Jon Ove Hagen (Norway), Regine Hock (USA), David Holland (USA), Matthias Huss (Switzerland), Thorsten Markus (USA), Ben Marzeion (Austria), Rob Massom (Australia), Geir Moholdt (USA), Pier Paul Overduin (Germany), Antony Payne (UK), W. Tad Pfeffer (USA), Terry Prowse (Canada), Valentina Radić (Canada), David Robinson (USA), Martin Sharp (Canada), Nikolay Shiklomanov (USA), Sharon Smith (Canada), Sharon Stammerjohn (USA), Isabella Velicogna (USA), Peter Wadhams (UK), Anthony Worby (Australia), Lin Zhao (China)

Review Editors:

Jonathan Bamber (UK), Philippe Huybrechts (Belgium), Peter Lemke (Germany)

This chapter supplementary material should be cited as:

Vaughan, D.G., J.C. Comiso, I. Allison, J. Carrasco, G. Kaser, R. Kwok, P. Mote, T. Murray, F. Paul, J. Ren, E. Rignot, O. Solomina, K. Steffen and T. Zhang, 2013: Observations: Cryosphere Supplementary Material. In: *Climate Change 2013: The Physical Science Basis. Contribution of Working Group I to the Fifth Assessment Report of the Intergovernmental Panel on Climate Change* [Stocker, T.F., D. Qin, G.-K. Plattner, M. Tignor, S.K. Allen, J. Boschung, A. Nauels, Y. Xia, V. Bex and P.M. Midgley (eds.)]. Available from www.climatechange2013.org and www.ipcc.ch.

Table of Contents

4.SM.1 Supplementary Material for the Sea Ice Section

Most of the published studies on the large-scale variability and trends of the global sea ice cover that have been published in recent years were based primarily on results from analysis of passive microwave satellite data (Parkinson et al., 1999; e.g., Zwally et al., 2002; Stroeve et al., 2007; Comiso and Nishio, 2008; Stammerjohn et al., 2008; Cavalieri and Parkinson, 2012; Parkinson and Cavalieri, 2012)

The first satellite-borne imaging passive microwave sensor was the Nimbus-5/Electrically Scanning Microwave Radiometer (ESMR), which provided quantitative measurements of the extent and variability of the sea ice cover in both hemispheres from 1973 to 1976 (Zwally et al., 1983; Parkinson et al., 1987). However, with only one channel and a system that scanned a wide field of view (between –50 and +50 degrees off-nadir, causing changes in incidence angle and footprint size), gaps in the record from a few days to a few months and an unknown bias, these data have not been included in time series variability and trend analysis in Chapter 4.

The data that are most frequently used are those from the multichannel, conically scanning (i.e., constant incident angle) and dual polarized microwave radiometers that provide more accurate and more consistent ice concentration and hence ice extent and ice area (see Glossary for definitions) products. This series started with the Nimbus-7 Scanning Multichannel Microwave Radiometer (SMMR) which was launched in October 1978 and provided, for the first time, measurements that allowed unambiguous determination of sea ice concentration (Gloersen et al., 1993).

Several algorithms for deriving sea ice concentration using different techniques and utilizing different sets of channels have been developed (Svendsen et al., 1983; Cavalieri et al., 1984; Swift et al., 1985; Comiso, 1986; Steffen et al., 1992). The most commonly used techniques for sea ice studies are the Nimbus-7 National Aeronautics and Space Administration (NASA) Team algorithm (NT1, Cavalieri et al., 1984) and the Bootstrap algorithm (Comiso, 1986). SMMR was eventually succeeded by a series of Special Sensor Microwave/Imager (SSM/I) sensors and the two systems now provide a continuous set of data from November 1978 to the present. Subsequently, a more capable and improved sensor, Advanced Microwave Scanning Radiometer - Earth Observing System (AMSR-E), was launched on board the NASA/Aqua satellite and this has provided higher resolution and improved sea ice data from May 2002 to October 2011. The algorithms currently used for this sensor are the AMSR-E Bootstrap Algorithm (ABA) and the NASA Team Algorithm, Version 2 (NT2) as discussed in Markus and Cavalieri (2000). With some enhancements ABA was also adapted and used to reprocess SMMR and SSM/I data, and called SSM/I (or SMMR) Bootstrap Algorithm (SBA) as discussed in Comiso and Nishio (2008).

Using the SBA, AMSR-E data were used as the baseline and basis for improving the SMMR and SSM/I ice data sets used in Chapter 4. NT2 addressed some of the problems associated with NT1, such as erroneously low ice concentrations within the pack caused by unpredictable polarization ratios. Comparisons of NT2 and Bootstrap data have shown good agreement (Comiso and Parkinson, 2008; Parkinson and Comiso, 2008) in analyzed trends and variability. NT2 data, however, could not be used for the entire historical data because it requires the use of 89 GHz data, which is not available in SMMR and in the early part of the SSM/I time series. The time series that has been used as an alternative to the NT2 time series has thus been the NT1 time series which provides values different from NT2. In the meantime, the Hadley Centre, in collaboration with National Oceanic and Atmospheric Administration (NOAA), constructed another sea ice record referred to as HadISST_Ice. The data set has been assembled together with sea surface temperature (SST) at a relatively coarser resolution (1° latitude by 1° longitude) and for a longer time series. The data set as described in Rayner et al., (2003) made use of atlases, *in situ* data and ice centre data (as in, Walsh and Chapman, 2001) for the pre-satellite era. Starting in 1979, satellite data including those from NT1 have been used. The use of satellite data in the Hadley data set, however, apparently has had some problems of consistency because, apparently spurious, sudden increases in ice concentration from one year to another have been identified (e.g., Screen, 2011), making the data set difficult to use for variability and trend analysis. Also, as Screen (2011) pointed out, there are large differences in ice extent and ice area distributions derived from NT1 data compared with those derived from NT2 data.

The results presented in Section 4.2 make use of mainly SBA data for consistency with those presented in AR4. To assess the robustness of the conclusions of Section 4.2 to changes in the data sets used, a comparative analysis of results from SBA, NT1 and Hadley (i.e., HadISST1_Ice) data is presented.

Time series plots of monthly anomalies in ice extent as derived from SBA, NT1 and Hadley for the period November 1978 to December 2011 are presented in Figure 4.SM.1. Although data up to December 2012 are presented in Chapter 4, data available for HadISST1_Ice and NT1 for this comparison goes up to December 2011 only. The NT1 data set used is an update version of that presented in Cavalieri and Parkinson (2012) and Parkinson and Cavalieri (2012). The plots in Figure 4.SM.1a and 4.SM.1b for SBA and NT1, respectively show very similar patterns, but the Hadley plot (Figure 4.SM.1c) shows deviations from the other two, especially from 1984 to 1986 and from 2007 to 2012, where the amplitudes of the interannual variation are significantly higher. Using linear regression, the derived trends are estimated to be –3.73% per decade for SBA, –4.22% per decade for NT1 and –2.0% per decade for Hadley. The trends from SBA and NT1 differ slightly but provide similar trend information but that from Hadley is about half the other two, with a much more modest decline. The difference in the trend values for the Hadley data is likely due to the anomalous deviation of the data from the other two data sets as indicated in the preceding text. The corresponding estimates for the trends in sea ice area data are –4.35%, –4.71% and –2.8% per decade, respectively, all relatively higher than those for ice extent but again providing similar trend results for SBA and NT1 but a significantly lesser rate of decline for Hadley.

In the Antarctic, the trends are more modest and in the opposite direction as depicted in Figure 4.SM.2. Again, the patterns of the interannual variability are very similar for all three, with the Hadley data being the most different, exhibiting higher short-term fluctuations and a more positive trend. Trend results are +1.44%, +1.34% and +2.48% per decade for SBA, NT1 and Hadley, respectively. Again, the results from SBA and NT1 are slightly different but provide similar trend information while Hadley provides a considerably higher trend. The corresponding trends in ice area are +2.07%, +1.57% and +3.07% per decade, for SBA, NT1 and Hadley, respectively. The discrepancy in the trends for ice area between the SBA and NT1 results is in part due to lower concentration averages for NT1 compared with SBA data as indicated in the preceding text. However, they provide similar conclusions about the changes in the ice cover. The Hadley trend is again substantially higher than those of the other two.

For a more detailed comparison, September monthly sea ice extents for SBA, NT1 and Hadley for all years from 1979 to 2011 are plotted together in Figure 4.SM.3a. For completeness, ABA and NT2 ice extents using AMSR-E data are also shown for the period 2002–2011. The values from all three primary data sources are very similar, with the SBA showing the highest values and Hadley normally lowest. Values from AMSR-E data using ABA and NT2 are relatively lower because of higher resolution as discussed in Comiso and Nishio (2008), but otherwise there is good consistency. There are greater discrepancies among the three data sources when sea ice areas are plotted (Figure 4.SM.3b), with NT1 and Hadley showing good agreement up to 1997 and significant disagreement after that. The higher ice area values for SBA are associated with higher ice concentration values derived from the data than the other two, as discussed previously. The values for ABA and NT2 from AMSR-E (which have been used as the baseline) are in good agreement and also agree well with the SBA values. Large difference between NT1 and NT2 values are evident, as has been observed by Screen (2011). Nevertheless, the trends in extent for SBA and NT1 are –10.2% and –10.5% per decade, respectively, basically providing the same conclusion, while the trend in extent for the Hadley data is –8.0% per decade. The trends for ice area are also similar enough at –11.3% (SBA) and –12.5% per decade (NT1) while the trend for Hadley data is –10.2% per decade.

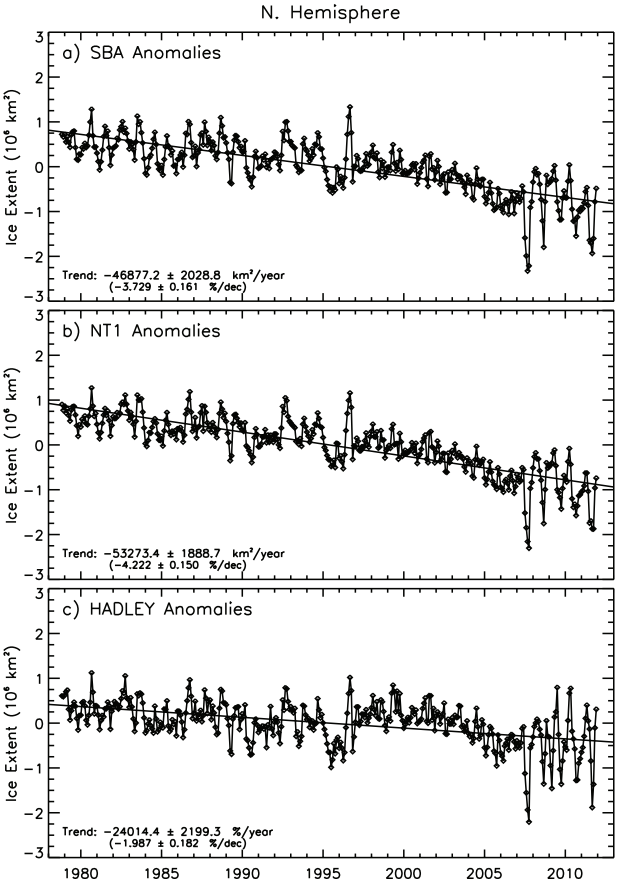

Figure 4.SM.1 | Monthly anomalies of ice extent from November 1978 to December 2011 using (a) SBA, (b) NT1 and (c) Hadley data in the Northern Hemisphere. Trends are shown with uncertainty calculated at 1 standard deviation (1σ).

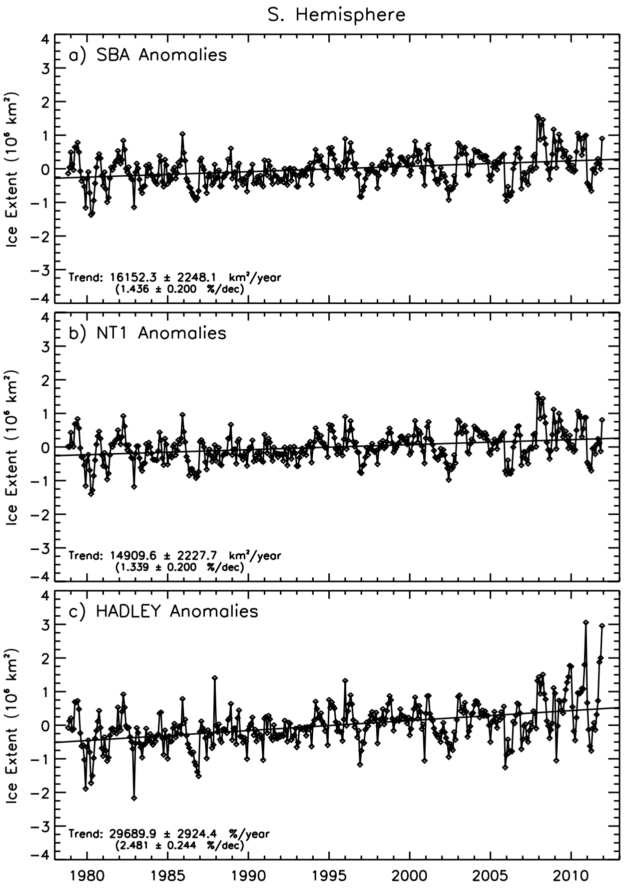

Figure 4.SM.2 | Monthly anomalies of ice extent from November 1978 to December 2011 using (a) SBA, (b) NT1 and (c) Hadley data in the Southern Hemisphere. Trends are shown with uncertainty calculated at 1 standard deviation (1σ).

Another data set that is available and has been used for sea ice studies is that from the Arctic Radiation and Turbulence Interaction Study (ARTIST) provided by the University of Bremen. The data make use of only the 89-GHz channels (horizontal and vertical polarized data) to generate relatively high resolution data from AMSR-E (5 to 6 km). High resolution is needed in many mesoscale studies. However, the 89-GHz radiation is very sensitive to weather and changes in the snow cover conditions, and the data should be used with care because they may be partly contaminated by incorrect values, especially under adverse weather conditions. Also, the ARTIST time series data from Aqua/AMSR-E is, as yet, too short for meaningful sea ice variability and trend studies.

Of the three satellite data sets that are currently available for sea ice variability and trend analysis, SBA and NT1 provides basically the same

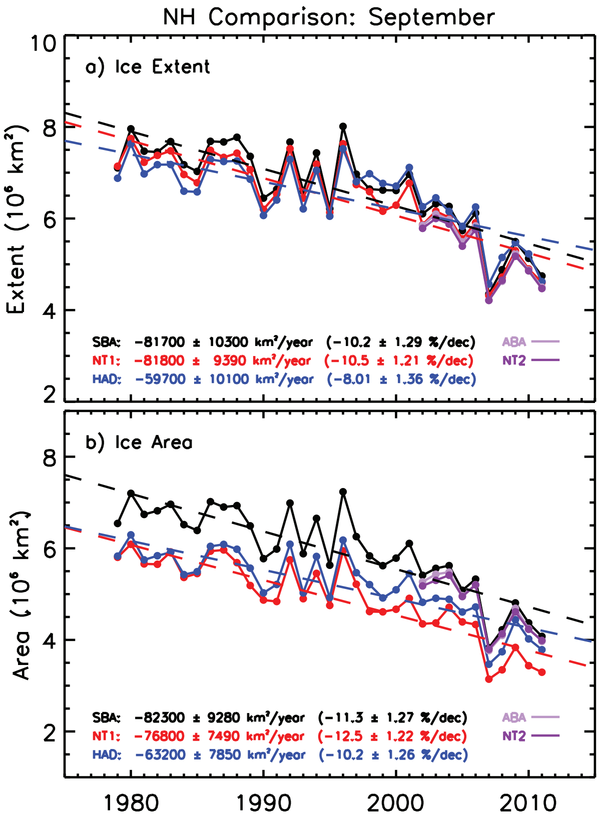

Figure 4.SM.3 | Monthly estimates of (a) sea ice extent and (b) sea ice area for the month of September from 1979 to 2011 for the Northern Hemisphere. Trends are shown with uncertainty calculated at 1 standard deviation (1σ).

patterns of interannual variability and approximately similar trends. The distributions are similar enough to provide basically the same information and conclusions about the trend of the changing sea ice cover. The patterns of variability provided by the Hadley data set are generally similar to those of SBA and NT1 but there are years when the data are suspect, as has been identified by Screen (2011). This is the primary reason for the discrepancies in the trends of the Hadley data compared with those of the SBA and NT1 data.

4.SM.2 Details of Studies of Glacier Area Change

Table 4.SM.1 provides an overview of studies reporting glacier area changes over entire mountain ranges or larger regions. Where available, area change rates are also given for sub-periods that have been extracted from the respective publications, partly using a linear extrapolation of given change rates to determine values for a common year in all sub-regions. In some studies, the glacier count is not given.

Table 4.SM.1 | Overview of studies presenting glacier area changes. **Bold** values in the column 'Change rate' indicate values shown in Figure 4.10. Values in *italics* refer to the entire period with 'Area covered' giving the value for the last year. Change rates are given for some regions to three decimals to avoid overlap of lines in Figure 4.10. For three regions (5, 9, and 12) studies on area changes were not found.

RGI Region	Country / Region	Sub-region / Mountain Range	Start Year	End Year	Number of Years	Glacier Count	Area Covered (km^2)	Relative Change (%)	Change Rate ($\% a^{-1}$)	Reference
1	USA, AK	Chugach Mountains	1952	2007	55	347	1285.7	–23	**–0.42**	Le Bris et al. (2011)
2	USA	North Cascades	1958	1998	40	321	117.3	–7.0	**–0.18**	Granshaw and Fountain (2006)
2	Canada	Rocky Mountains	1985	2001	16	523	1056.7	–7.6	–0.48	Tennant et al. (2012)
			2001	2006	5	523	976.5	–9.9	–1.98	
			1985	*2006*	*21*	*523*	*880.0*	*–16.7*	*–0.80*	
2	USA	Wind River Range	1966	2006	40	n/a	45.9	–37.7	**–0.94**	Thompson et al. (2011)
2	Canada	Yukon	1959	2007	48	n/a	11622	–21.9	**–0.456**	Barrand and Sharp (2010)
2	Canada	Rocky Mountains[a]	1985	2005	20	14329	30063	–11.1	**–0.555**	Bolch et al. (2010)
2	Canada	Clemenceau Icefield	1985	2001	16	123	313	–13.4	**–0.84**	Jiskoot et al. (2009)
		Chaba Group	1985	2001	16	53	97	–28.9	**–1.81**	
2	Canada	Rocky Mountains	1952	2001	49	59	40	–15	**–0.31**	Debeer and Sharp (2007)
		Columbia Mountains	1952	2001	49	403	397	–5.0	**–0.10**	
		Coast Mountains	1964	2002	38	1053	2397	–5.0	**–0.13**	
3	Canada	Queen Elizabeth Island	1960	2000	40	1274	107071	–2.7	**–0.07**	Sharp et al. (2013)
3	Canada	North Ellesmere	1960	2000	40	473	27556	–3.4	–0.09	Sharp et al. (2013)
		Agassiz	1960	2000	40	296	21645	–1.3	–0.03	
		Axel/Meighen / Melville	1960	2000	40	165	12231	–1.7	–0.04	
		Prince of Wales	1960	2000	40	39	19558	–0.9	–0.02	
		South Ellesmere	1960	2000	40	187	10696	–5.9	–0.15	
		Devon Island	1960	2000	40	114	15344	–4.0	–0.10	
4	Canada	Bylot Island	1959	2001	42	n/a	5036	–5.0	**–0.119**	Dowdeswell et al. (2007)
4	Canada	Barnes Ice Cap	1958	2000	42	n/a	5995	–2.0	**–0.048**	Sharp et al. (2013)
		Penny Ice Cap	1959	2000	41	n/a	6604	–1.9	**–0.046**	
		Terra Nivea	1958	2000	42	n/a	197	–14.0	**–0.33**	
		Grinnel Ice Cap	1958	2000	42	n/a	135	–10.9	**–0.26**	
4	Canada	Baffin Island	1975	2000	25	264	2187	–12.5	**–0.16**	Paul and Svoboda (2009)
5	Greenland	n/a								
6	Iceland	Four ice caps	1998	2011	13	4	1004.5	–7.6	**–0.58**	Johannesson et al. (2013)
7	Svalbard	Glaciers $>1 km^2$	1990	2008	18	n/a	5204.7	–4.6	**–0.26**	König et al. (2013)
8	Norway	Jostedalbreen	1966	2006	40	297	725.1	–9	**–0.225**	Paul et al. (2011)
8	Norway	Jotunheimen	1965	2003	38	164	229.5	–12.4	**–0.33**	Andreassen et al. (2008)
8	Norway	Svartisen	1968	1999	31	300	518.0	–1.1	**–0.04**	Paul and Andreassen (2009)
9	Russian Arctic	n/a								
10	Russian Federation	Ural	1956	2000	44	30	9.17	–22.3	**–0.51**	Shahgedanova et al. (2012)
10	Russian Federation	Kodar Mountains	1995	2001	6	34	11.72	–18.7	–3.11	Stokes et al. (2013)
			2001	2010	9	34	9.53	–26.4	–2.94	
			1995	*2010*	*15*	*34*	*7.01*	*–40.2*	*–2.68*	
10	Russian Federation	Altai Chuya Ridges	1952	2004	52	126	284	–19.7	**–0.38**	Shahgedanova et al. (2010)
10	Russian Federation	Altai	1952	2008	56	1030	805	–10.2	**–0.182**	Narozhniy and Zemtsov (2011)
11	Austria	Alps	1969	1998	29	925	567	–17.1	**–0.59**	Lambrecht and Kuhn (2007)
11	Austria	Ötztaler Alps	1997	2006	9	81	116	–8.2	**–0.9**	Abermann et al. (2009)
11	Switzerland	Alps	1973	1999	26	938	1171.2	–16.1	**–0.62**	Paul et al. (2004)
			1985	1998	13	471	372.2	–18.0	**–1.38**	
11	Spain	Pyrenees	1982	1994	12	10	6.08	–20.9	–1.97	Gonzales Trueba et al. (2008)
			1994	2001	7	10	4.81	–39.7	–5.6	
			1982	*2001*	*19*	*10*	*6.08*	*–52.3*	*–2.75*	

(continued on next page)

Table 4.SM.1 (continued)

RGI Region	Country / Region	Sub-region / Mountain Range	Start Year	End Year	Number of Years	Glacier Count	Area Covered (km²)	Relative Change (%)	Change Rate (% a⁻¹)	Reference
11	Italy	Aosta Valley	1975	1999	24	174	163.9	–16.7	–0.7	Diolaiuti et al. (2012)
			1999	2005	6	174	136.6	–12.4	–2.07	
			1975	*2005*	*30*	*174*	*119.6*	*–27.0*	***–0.9***	
11	Italy	South Tyrol	1983	1997	14	205	136.6	–19.7	–1.41	Knoll and Kerschner (2009)
			1997	2006	9	302	109.7	–11.9	–1.32	
			1983	2006	23	205	136.6	–31.6	**–1.37**	
11	Italy	Lombardy	1992	1999	7	249	117.4	–10.8	–1.54	Citterio et al. (2007)
12	Caucasus	n/a								
13	Mongolia	Altai Mountains	1989	2009	20	n/a	213	–4.2	**–0.21**	Krumwiede et al. (2013)
13	China	Muztag Ata and Konggur Mountains (East Pamir)	1962	1990	28	n/a	838.2	–3.4	–0.12	Shangguan et al. (2006)
			1990	1999	9	n/a	809.9	–4.6	–0.52	
			1962	*1999*	*37*		*772.2*	*–7.9*	***–0.214***	
13	China (Tarim Basin)	Quarqan	1977	2001	24	399	752.6	–3.4	**–0.14**	Shangguan et al. (2009)
		Keliya	1970	1999	29	731	1306.5	–3.1	**–0.11**	
		Hotan	1968	2000	32	2487	5131.8	–0.7	**–0.02**	
		Yarkant	1974	2001	27	1421	3170.6	–6.1	**–0.23**	
		Pamir	1964	2001	37	880	2085.4	–7.9	**–0.21**	
		Tienshan	1964	2000	36	1249	4039.2	–1.3	**–0.04**	
		Kaidu	1964	2000	36	498	405.8	–7.1	**–0.20**	
13	China (Tibet)	Gongga Mountains	1966	1989	23	74	257.7	–5.8	–0.25	Pan et al. (2012b)
			1989	2009	20	75	242.8	–5.9	–0.29	
			1966	*2009*	*43*	*76*	*228.5*	*–11.3*	***–0.26***	
13	Kyrgistan	Pskem	1968	2000	32	525	219.8	–19.47	–0.61	Narama et al. (2010)
			2000	2007	7	525	177.0	–6.69	**–0.96**	
		Ili-Kungoy	1971	1999	28	735	672.2	–12.18	–0.44	
			1999	2007	8	735	590.3	–4.12	**–0.52**	
		At-Bashi	1968	2000	32	192	113.6	–12.06	–0.38	
			2000	2007	7	192	99.9	–4.20	**–0.60**	
		SE-Fergana	1968	2000	32	306	190.1	–9.21	–0.29	
			2000	2007	7	306	172.6	–0.52	**–0.07**	
13	China	Qilian Mountains[a]	1956	2003	47	910	397.4	–21.7	**–0.462**	Wang et al. (2011)
13	China	Karlik Shan	1971	1992	21	n/a	126	–2.63	–0.13	Wang et al. (2009)
			1992	2001	9	n/a	122.7	–2.67	–0.27	
			1971	*2001*	*30*	*n/a*	*119.4*	*5.2*	***–0.17***	
13	China	Lenglongling[a]	1972	2007	35	179	86.2	–28.3	**–0.81**	Pan et al. (2012a)
13	Kyrgistan	Akshiirak	1977	2003	26	178	406.8	–8.6	**–0.33**	Aizen et al. (2007)
		Ala Archa	1981	2003	22	48	40.62	–10.6	**–0.48**	
14	Himalaya	Ten basins mean[a]	1962	2004	42	1868	6332	–15.8	**–0.38**	Kulkarni et al. (2011)
14	India	Kang Yatze	1969	1991	23	121	96.4	–13.0	–0.56	Schmidt and Nusser (2012)
			1991	2010	18	121	83.9	–1.5	–0.09	
			1969	*2010*	*41*	*121*	*96.4*	*–14.4*	***–0.35***	
14	India	Gharwal Himalaya[a]	1968	2006	38	82	600	–4.6	**–0.121**	Bhambri et al. (2011)
15	Nepal	Khumbu Himal	1976	2006	30	n/a	3211.9	–15.6	**–0.52**	Nie et al. (2010)
15	Nepal	Khumbu Himal	1962	2005	43	n/a	92.3	–5.3	**–0.123**	Bolch et al. (2008)
15	Nepal	Sagarmatha National Park	1962	2001	39	29	403.9	–4.9	**–0.126**	Salerno et al. (2008)

(continued on next page)

Table 4.SM.1 (continued)

RGI Region	Country / Region	Sub-region / Mountain Range	Start Year	End Year	Number of Years	Glacier Count	Area Covered (km^2)	Relative Change (%)	Change Rate ($\% a^{-1}$)	Reference
16	Peru	Cordillera Coropuna	1955	2003	48	711	123	–54	**–1.125**	Silverio and Jaquet (2012)Peru
16	Peru	Cordillera Blanca	1970	1990	20	n/a	190	–12.8	–0.64	Baraer et al. (2012)
			1990	2009	19		165	–17.4	–0.92	
			1970	*2009*	*39*		*136.3*	*–28.0*	***–0.72***	
16	Peru	Cordillera Vilcanota	1985	1996	11	n/a	444	–22.5	–2.05	Salzmann et al. (2013)
			1996	2006	10		344	–13.7	–1.37	
			1985	*2006*	21		*297*	*–33.2*	***–1.58***	
16	Peru	Quelcaya Ice Cap	1985	2000	15	n/a	55.7	–17.6	–1.17	Salzmann et al. (2013)
			2000	2009	9		45.9	–3.1	–0.34	
			1985	*2009*	*24*		*42.8*	*–23.1*	***–0.96***	
16	Indonesia	Puncack Jaya	1942	1972	30	10	9.9	–30.3	–1.01	Klein and Kincaid (2006)
			1972	2002	30	5	6.9	–66.2	–2.23	
			1942	*2002*	*60*		2.15	–78.3	***–1.30***	
16	Columbia	Six mountain ranges[a]	1959	1987	28	n/a	106.8	–21.9	–0.78	Ceballos et al. (2006)
			1987	2002	15		83.5	–33.5	–2.23	
			1959	*2002*	*43*		*45.6*	*–48.1*	***–1.18***	
16	Peru	Cordillera Blanca	1970	2003	33	445	665.1	–22.4	**–0.68**	Racoviteanu et al. (2008)
16	Tansania	Kilimandscharo[a]	1962	2011	49	n/a	7.32	–76.0	**–1.55**	Cullen et al. (2013)
17	Chile	Gran Campo Nevado	1942	2002	60	81	252.6	–14.4	**–0.24**	Schneider et al. (2007)
17	Chile / Argentina	San Lorenzo Mountains	1985	2000	15	213	239.0	–9.9	–0.66	Falaschi et al. (2013)
			2000	2008	8	213	215.4	–9.7	–1.21	
			1985	*2008*	*23*	*213*	*206.9*	*–13.4*	***–0.58***	
17	Chile / Argentina	Patagonia	1986	2001	15	183	23743	–2.2	–0.14	Davies and Glasser (2012)
			2001	2011	10	165	23229	–2.2	–0.22	
			1986	*2011*	*25*	*183*	*22717*	*–4.3*	***–0.17***	
17	Chile	Northern Patagonia Icefield	1979	2001	22	>70[b]	4093	–3.4	**–0.15**	Rivera et al. (2007)
17	Chile	Aconcagua Basin	1955	2003	48		151	–19.9	**–0.41**	Bown et al. (2008)
18	New Zealand	Southern Alps	1978	2002	24	n/a	513	–16.6	**–0.69**	Gjermundsen et al. (2011)
19	Antarctica	Kerguelen Island[a]	1963	2001	38	n/a	703	–21	**–0.55**	Berthier et al. (2009)
19	Antarctica	King George Island	1956	1995	39	n/a	1250	–7.0	**–0.179**	Rückamp et al. (2011)
			2000	2008	8	n/a		–1.6	**–0.20**	

Notes:

(a) More detailed analyses (e.g., sub-regions, other periods) are available in the respective papers.

(b) Glaciers <0.5 km^2 were not counted separately.

References

Abermann, J., A. Lambrecht, A. Fischer, and M. Kuhn, 2009: Quantifying changes and trends in glacier area and volume in the Austrian Otztal Alps (1969–1997–2006). *Cryosphere*, **3**, 205–215.

Aizen, V. B., V. A. Kuzmichenok, A. B. Surazakov, and E. M. Aizen, 2007: Glacier changes in the Tien Shan as determined from topographic and remotely sensed data. *Global Planet. Change*, **56**, 328–340.

Andreassen, L. M., F. Paul, A. Kaab, and J. E. Hausberg, 2008: Landsat-derived glacier inventory for Jotunheimen, Norway, and deduced glacier changes since the 1930s. *Cryosphere*, **2**, 131–145.

Baraer, M., et al., 2012: Glacier recession and water resources in Peru's Cordillera Blanca. *J. Glaciol.*, **58**, 134–150.

Barrand, N. E., and M. J. Sharp, 2010: Sustained rapid shrinkage of Yukon glaciers since the 1957–1958 International Geophysical Year. *Geophys. Res. Lett.*, **37**, L07501.

Berthier, E., R. Le Bris, L. Mabileau, L. Testut, and F. Remy, 2009: Ice wastage on the Kerguelen Islands (49 degrees S, 69 degrees E) between 1963 and 2006. *J. Geophys. Res. Earth Surf.*, **114**, 11.

Bhambri, R., T. Bolch, R. K. Chaujar, and S. C. Kulshreshtha, 2011: Glacier changes in the Garhwal Himalaya, India, from 1968 to 2006 based on remote sensing. *J. Glaciol.*, **57**, 543-556.

Bolch, T., B. Menounos, and R. Wheate, 2010: Landsat-based inventory of glaciers in western Canada, 1985–2005. *Remote Sens. Environ.*, **114**, 127–137.

Bolch, T., M. Buchroithner, T. Pieczonka, and A. Kunert, 2008: Planimetric and volumetric glacier changes in the Khumbu Himal, Nepal, since 1962 using Corona, Landsat TM and ASTER data. *J. Glaciol.*, **54**, 592–600.

Bown, F., A. Rivera, and C. Acuna, 2008: Recent glacier variations at the Aconcagua basin, central Chilean Andes. *Ann. Glaciol.,* **48**, 43–48.

Cavalieri, D. J., and C. L. Parkinson, 2012: Arctic sea ice variability and trends, 1979–2010. *Cryosphere*, **6**, 957–979.

Cavalieri, D. J., P. Gloersen, and W. J. Campbell, 1984: Determination of sea ice parameters with the Nimbus-7 SMMR. *J. Geophys. Res. Atmos.*, **89**, 5355–5369.

Ceballos, J. L., C. Euscategui, J. Ramirez, M. Canon, C. Huggel, W. Haeberli, and H. Machguth, 2006: Fast shrinkage of tropical glaciers in Colombia. *Ann. Glaciol.,* **43***,* 194–201.

Citterio, M., G. Diolaiuti, C. Smiraglia, C. D'Agata, T. Carnielli, G. Stella, and G. B. Siletto, 2007: The fluctuations of Italian glaciers during the last century: A contribution to knowledge about Alpine glacier changes. *Geograf. Annal. A*, **89A**, 167–184.

Comiso, J. C., 1986: Characteristics of winter sea ice from satellite multispectreal microwave observations *J. Geophys. Res. Oceans*, **91**, 975–994.

Comiso, J. C., and F. Nishio, 2008: Trends in the sea ice cover using enhanced and compatible AMSR-E, SSM/I, and SMMR data. *J. Geophys. Res. Oceans*, **113**, C02S07.

Comiso, J. C., and C. L. Parkinson, 2008: Arctic sea ice parameters from AMSR-E using two techniques, and comparisons with sea ice from SSM/I. *J. Geophys. Res.*, **113**, C02S05.

Cullen, N. J., P. Sirguey, T. Moelg, G. Kaser, M. Winkler, and S. J. Fitzsimons, 2013: A century of ice retreat on Kilimanjaro: The mapping reloaded. *Cryosphere*, **7**, 419–431.

Davies, B. J., and N. F. Glasser, 2012: Accelerating shrinkage of Patagonian glaciers from the "Little Ice Age" (c. AD 1870) to 2011. *J. Glaciol.*, **58**, 1063–1084.

Debeer, C. M., and M. J. Sharp, 2007: Recent changes in glacier area and volume within the southern Canadian Cordillera. *Ann. Glaciol.,* **46**, 215–221.

Diolaiuti, G. A., D. Bocchiola, M. Vagliasindi, C. D'Agata, and C. Smiraglia, 2012: The 1975–2005 glacier changes in Aosta Valley (Italy) and the relations with climate evolution. *Prog. Phys. Geogr.*, **36**, 764–785.

Dowdeswell, E. K., J. A. Dowdeswell, and F. Cawkwell, 2007: On the glaciers of Bylot Island, Nunavut, Arctic Canada. *Arct. Antarct. Alp. Res.*, **39**, 402-411.

Falaschi, D., C. Bravo, M. Masiokas, R. Villalba, and A. Rivera, 2013: First glacier inventory and recent changes in glacier area in the Monte San Lorenzo Region (47°S), Southern Patagonian Andes, South America. *Arct. Antarct. Alp. Res.*, **45**, 19–28.

Gjermundsen, E. F., R. Mathieu, A. Kääb, T. Chinn, B. Fitzharris, and J. O. Hagen, 2011: Assessment of multispectral glacier mapping methods and derivation of glacier area changes, 1978–2002, in the central Southern Alps, New Zealand, from ASTER satellite data, field survey and existing inventory data. *J. Glaciol.*, **57**, 667–683.

Gloersen, P., W. J. Campbell, D. J. Cavalieri, J. C. Comiso, C. L. Parkinson, and H. J. Zwally, 1993: Satellite passive microwave observations and analysis of Arctic and Antarctic sea-ice. *Ann. Glaciol.*, **17**, 149–154.

Gonzales Trueba, J. J., R. Martin Moreno, E. Martinez de Pison, and E. Serrano, 2008: Little Ice Age' glaciation and current glaciers in the Iberian Peninsula. *Holocene*, **18**, 551–568.

Granshaw, F. D., and A. G. Fountain, 2006: Glacier change (1958–1998) in the North Cascades National Park Complex, Washington, USA. *J. Glaciol.*, **52**, 251–256.

Jiskoot, H., C. J. Curran, D. L. Tessler, and L. R. Shenton, 2009: Changes in Clemenceau Icefield and Chaba Group glaciers, Canada, related to hypsometry, tributary detachment, length-slope and area-aspect relations. *Ann. Glaciol.*, **50**, 133–143.

Johannesson, T., et al., 2013: Ice-volume changes, bias estimation of mass-balance measurements and changes in subglacial lakes derived by lidar mapping of the surface of Icelandic glaciers. *Ann. Glaciol.*, **54**, 63–74.

Klein, A. G., and J. L. Kincaid, 2006: Retreat of glaciers on Puncak Jaya, Irian Jaya, determined from 2000 and 2002 IKONOS satellite images. *J. Glaciol.*, **52**, 65–79.

Knoll, C., and H. Kerschner, 2009: A glacier inventory for South Tyrol, Italy, based on airborne laser-scanner data. *Ann. Glaciol.*, **50**, 46–52.

König, M., C. Nuth, J. Kohler, G. Moholdt, and R. Pettersson, 2013: A digital glacier database for Svalbard. In: *Global Land Ice Measurements form Space* [J. S. Kargel, G. J. Leonard, M. P. Bishop, A. Kääb and B. Raup (eds.)]. Springer Praxis, New York, NY, USA, 229-239.

Krumwiede, B. S., U. Kamp, G. J. Leonard, A. Dashtseren, and M. Walther, 2013: Recent glacier changes in the Mongolian Altai Mountains: Case studies from Munkh Khairkhan and Tavan Bogd. In: *Global Land Ice Measurements from Space* [J. S. Kargel, G. J. Leonard, M. P. Bishop, A. Kääb and B. Raup (eds.)]. Springer-Praxis, New York, NY, USA, 481-507.

Kulkarni, A. V., B. P. Rathore, S. K. Singh, and I. M. Bahuguna, 2011: Understanding changes in the Himalayan cryosphere using remote sensing techniques. *Int. J. Remote Sens.*, **32**, 601–615.

Lambrecht, A., and M. Kuhn, 2007: Glacier changes in the Austrian Alps during the last three decades, derived from the new Austrian glacier inventory. *Ann. Glaciol.,* **46**, 177–184.

Le Bris, R., F. Paul, H. Frey, and T. Bolch, 2011: A new satellite-derived glacier inventory for western Alaska. *Ann. Glaciol.*, **52**, 135-143.

Markus, T., and D. J. Cavalieri, 2000: An enhancement of the NASA Team sea ice algorithm. *IEEE Trans. Geosci. Remote Sens.*, **38**, 1387–1398.

Narama, C., A. Kaab, M. Duishonakunov, and K. Abdrakhmatov, 2010: Spatial variability of recent glacier area changes in the Tien Shan Mountains, Central Asia, using Corona (similar to 1970), Landsat (similar to 2000), and ALOS (similar to 2007) satellite data. *Global Planet. Change*, **71**, 42–54.

Narozhniy, Y., and V. Zemtsov, 2011: Current state of the Altai Glaciers (Russia) and trends over the period of instrumental observations 1952–2008. *Ambio*, **40**, 575-588.

Nie, Y., Y. L. Zhang, L. S. Liu, and J. P. Zhang, 2010: Glacial change in the vicinity of Mt. Qomolangma (Everest), central high Himalayas since 1976. *J. Geograph. Sci.*, **20**, 667–686.

Pan, B., B. Cao, J. Wang, G. Zhang, C. Zhang, Z. Hu, and B. Huang, 2012a: Glacier variations in response to climate change from 1972 to 2007 in the western Lenglongling mountains, northeastern Tibetan Plateau. *J. Glaciol.*, **58**, 879–888.

Pan, B. T., G. L. Zhang, J. Wang, B. Cao, H. P. Geng, C. Zhang, and Y. P. Ji, 2012b: Glacier changes from 1966–2009 in the Gongga Mountains, on the south-eastern margin of the Qinghai-Tibetan Plateau and their climatic forcing. *Cryosphere*, **6**, 1087–1101.

Parkinson, C. L., and J. C. Comiso, 2008: Antarctic sea ice parameters from AMSR-E data using two techniques and comparisons with sea ice from SSM/I. *J. Geophys. Res. Oceans*, **113**, C02S06.

Parkinson, C. L., and D. J. Cavalieri, 2012: Antarctic Sea Ice Variability and Trends, 1979–2010. *Cryosphere*, **6**, 871–880.

Parkinson, C. L., D. J. Cavalieri, P. Gloersen, H. J. Zwally, and J. C. Comiso, 1999: Arctic sea ice extents, areas, and trends, 1978–1996. *J. Geophys. Res. Oceans*, **104**, 20837–20856.

Parkinson, C. L., J. C. Comiso, H. J. Zwally, D. J. Cavalieri, P. Gloersen, and W. Campbell, 1987: Analysis of northern hemisphere sea ice from satellite passive microwave data. *Ann. Glaciol.*, **9**, 1–8.

Paul, F., and L. M. Andreassen, 2009: A new glacier inventory for the Svartisen region, Norway, from Landsat ETM plus data: challenges and change assessment. *J. Glaciol.*, **55**, 607–618.

Paul, F., and F. Svoboda, 2009: A new glacier inventory on southern Baffin Island, Canada, from ASTER data: II. Data analysis, glacier change and applications. *Ann. Glaciol.*, **50**, 22–31.

Paul, F., L. M. Andreassen, and S. H. Winsvold, 2011: A new glacier inventory for the Jostedalsbreen region, Norway, from Landsat TM scenes of 2006 and changes since 1966. *Ann. Glaciol.*, **52**, 153-162.

Paul, F., A. Kaab, M. Maisch, T. Kellenberger, and W. Haeberli, 2004: Rapid disintegration of Alpine glaciers observed with satellite data. *Geophys. Res. Lett.*, **31**, 4.

Racoviteanu, A. E., Y. Arnaud, M. W. Williams, and J. Ordonez, 2008: Decadal changes in glacier parameters in the Cordillera Blanca, Peru, derived from remote sensing. *J. Glaciol.*, **54**, 499–510.

Rayner, N. A., et al., 2003: Global analyses of SST, sea ice and night marine air temperature since the late nineteenth century. *J. Geophys. Res.*, **108**, 4407.

Rivera, A., T. Benham, G. Casassa, J. Bamber, and J. A. Dowdeswell, 2007: Ice elevation and areal changes of glaciers from the Northern Patagonia Icefield, Chile. *Global Planet. Change*, **59**, 126–137.

Rückamp, M., M. Braun, S. Suckro, and N. Blindow, 2011: Observed glacial changes on the King George Island ice cap, Antarctica, in the last decade. *Global Planet. Change*, **79**, 99–109.

Salerno, F., E. Buraschi, G. Bruccoleri, G. Tartari, and C. Smiraglia, 2008: Glacier surface-area changes in Sagarmatha national park, Nepal, in the second half of the 20th century, by comparison of historical maps. *J. Glaciol.*, **54**, 738–752.

Salzmann, N., C. Huggel, M. Rohrer, W. Silverio, B. G. Mark, P. Burns, and C. Portocarrero, 2013: Glacier changes and climate trends derived from multiple sources in the data scarce Cordillera Vilcanota region, southern Peruvian Andes. *Cryosphere*, **7**, 103–118.

Schmidt, S., and M. Nusser, 2012: Changes of High Altitude Glaciers from 1969 to 2010 in the Trans-Himalayan Kang Yatze Massif, Ladakh, Northwest India. *Arct. Antarct. Alp. Res.*, **44**, 107–121.

Schneider, C., M. Schnirch, C. Acuna, G. Casassa, and R. Kilian, 2007: Glacier inventory of the Gran Campo Nevado Ice Cap in the Southern Andes and glacier changes observed during recent decades. *Global Planet. Change*, **59**, 87–100.

Screen, J. A., 2011: Sudden increase in Antarctic sea ice: Fact or artifact? *Geophys. Res. Lett.*, **38**, L13702.

Shahgedanova, M., G. Nosenko, T. Khromova, and A. Muraveyev, 2010: Glacier shrinkage and climatic change in the Russian Altai from the mid-20th century: An assessment using remote sensing and PRECIS regional climate model. *J. Geophys. Res. Atmos.*, **115**, 12.

Shahgedanova, M., G. Nosenko, I. Bushueva, and M. Ivanov, 2012: Changes in area and geodetic mass balance of small glaciers, Polar Urals, Russia, 1950–2008. *J. Glaciol.*, **58**, 953–964.

Shangguan, D., S. Liu, Y. Ding, L. Ding, J. Xu, and L. Jing, 2009: Glacier changes during the last forty years in the Tarim Interior River basin, northwest China. *Prog. Nat. Sci.*, **19**, 727–732.

Shangguan, D., et al., 2006: Monitoring the glacier changes in the Muztag Ata and Konggur mountains, east Pamirs, based on Chinese Glacier Inventory and recent satellite imagery. *Ann. Glaciol.*, **43**, 79–85.

Sharp, M., et al., 2013: Remote Sensing of Recent Glacier Changes in the Canadian Arctic. In: *Global Land Ice Measurements from Space* [J. S. Kargel, G. J. Leonard, M. P. Bishop, A. Kääb and B. Raup (eds.)]. Springer-Praxis, New York, NY, USA, in press.

Silverio, W., and J.-M. Jaquet, 2012: Multi-temporal and multi-source cartography of the glacial cover of Nevado Coropuna (Arequipa, Peru) between 1955 and 2003. *Int. J. Remote Sens.*, **33**.

Stammerjohn, S. E., D. G. Martinson, R. C. Smith, X. Yuan, and D. Rind, 2008: Trends in Antarctic annual sea ice retreat and advance and their relation to El Niño-Southern Oscillation and Southern Annular Mode variability. *J. Geophys. Res. Oceans*, **113**, C03S90.

Steffen, K., D. J. Cavalieri, J. C. Comiso, K. St Germain, P. Gloersen, J. Key, and I. Rubinstein, 1992: The estimation of geophysical parameters using Passive Microwave Algorithms. In: *Microwave Remote Sensing of Sea Ice* [F. D. Carsey (ed.)]. American Geophysical Union, Washington, DC, pp. 201–231.

Stokes, C. R., M. Shahgedanova, I. S. Evans, and V. V. Popovnin, 2013: Accelerated loss of alpine glaciers in the Kodar Mountains, south-eastern Siberia. *Global Planet. Change*, **101**, 82–96.

Stroeve, J., M. M. Holland, W. Meier, T. Scambos, and M. Serreze, 2007: Arctic sea ice decline: Faster than forecast. *Geophys. Res. Lett.*, **34**, L09501.

Svendsen, E., et al., 1983: Norvegian Remote-Sensing Experiment—Evaluation of the NIMBUS-7 Scanning Multichannel Microwave Radiometer for Sea Ice Research. *J. Geophys. Res. Oceans Atmos.*, **88**, 2781–2791.

Swift, C. T., L. S. Fedor, and R. O. Ramseier, 1985: An algorithm to measure sea ice concentration with microwave radiometers. *J. Geophys. Res. Oceans*, **90**, 1087–1099.

Tennant, C., B. Menounos, R. Wheate, and J. J. Clague, 2012: Area change of glaciers in the Canadian Rocky Mountains, 1919 to 2006. *Cryosphere*, **6**, 1541–1552.

Thompson, D., G. Tootle, G. Kerr, R. Sivanpillai, and L. Pochop, 2011: Glacier variability in the Wind River Range, Wyoming. *J. Hydrol. Engng.*, **16**, 798-805.

Walsh, J. E., and W. L. Chapman, 2001: 20th-century sea-ice variations from observational data. *Ann. Glaciol.,* **33**, 444–448.

Wang, P., Z. Li, and W. Gao, 2011: Rapid Shrinking of Glaciers in the Middle Qilian Mountain Region of Northwest China during the Last similar to 50 Years. *J. Earth Sci.*, **22**, 539–548.

Wang, Y. T., S. G. Hou, and Y. P. Liu, 2009: Glacier changes in the Karlik Shan, eastern Tien Shan, during 1971/72–2001/02. *Ann. Glaciol.*, **50**, 39–45.

Zwally, H. J., C. L. Parkinson, and J. C. Comiso, 1983: Variability of Antarctic sea ice and changes in carbon dioxide. *Science*, **220**, 1005–1012.

Zwally, H. J., J. C. Comiso, C. L. Parkinson, D. J. Cavalieri, and P. Gloersen, 2002: Variability of Antarctic sea ice 1979–1998. *J. Geophys. Res.*, **107**, 1029–1047.

6SM

Carbon and Other Biogeochemical Cycles
Supplementary Material

Coordinating Lead Authors:
Philippe Ciais (France), Christopher Sabine (USA)

Lead Authors:
Govindasamy Bala (India), Laurent Bopp (France), Victor Brovkin (Germany/Russian Federation), Josep Canadell (Australia), Abha Chhabra (India), Ruth DeFries (USA), James Galloway (USA), Martin Heimann (Germany), Christopher Jones (UK), Corinne Le Quéré (UK), Ranga B. Myneni (USA), Shilong Piao (China), Peter Thornton (USA)

Contributing Authors:
Anders Ahlström (Sweden), Alessandro Anav (UK/Italy), Oliver Andrews (UK), David Archer (USA), Vivek Arora (Canada), Gordon Bonan (USA), Alberto Vieira Borges (Belgium/Portugal), Philippe Bousquet (France), Lex Bouwman (Netherlands), Lori M. Bruhwiler (USA), Kenneth Caldeira (USA), Long Cao (China), Jérôme Chappellaz (France), Frédéric Chevallier (France), Cory Cleveland (USA), Peter Cox (UK), Frank J. Dentener (EU/Netherlands), Scott C. Doney (USA), Jan Willem Erisman (Netherlands), Eugenie S. Euskirchen (USA), Pierre Friedlingstein (UK/Belgium), Nicolas Gruber (Switzerland), Kevin Gurney (USA), Elisabeth A. Holland (Fiji/USA), Brett Hopwood (USA), Richard A. Houghton (USA), Joanna I. House (UK), Sander Houweling (Netherlands), Stephen Hunter (UK), George Hurtt (USA), Andrew D. Jacobson (USA), Atul Jain (USA), Fortunat Joos (Switzerland), Johann Jungclaus (Germany), Jed O. Kaplan (Switzerland/Belgium/USA), Etsushi Kato (Japan), Ralph Keeling (USA), Samar Khatiwala (USA), Stefanie Kirschke (France/Germany), Kees Klein Goldewijk (Netherlands), Silvia Kloster (Germany), Charles Koven (USA), Carolien Kroeze (Netherlands), Jean-François Lamarque (USA/Belgium), Keith Lassey (New Zealand), Rachel M. Law (Australia), Andrew Lenton (Australia), Mark R. Lomas (UK), Yiqi Luo (USA), Takashi Maki (Japan), Gregg Marland (USA), H. Damon Matthews (Canada), Emilio Mayorga (USA), Joe R. Melton (Canada), Nicolas Metzl (France), Guy Munhoven (Belgium/Luxembourg), Yosuke Niwa (Japan), Richard J. Norby (USA), Fiona O'Connor (UK/Ireland), James Orr (France), Geun-Ha Park (USA), Prabir Patra (Japan/India), Anna Peregon (France/Russian Federation), Wouter Peters (Netherlands), Philippe Peylin (France), Stephen Piper (USA), Julia Pongratz (Germany), Ben Poulter (France/USA), Peter A. Raymond (USA), Peter Rayner (Australia), Andy Ridgwell (UK), Bruno Ringeval (Netherlands/France), Christian Rödenbeck (Germany), Marielle Saunois (France), Andreas Schmittner (USA/Germany), Edward Schuur (USA), Stephen Sitch (UK), Renato Spahni (Switzerland), Benjamin Stocker (Switzerland), Taro Takahashi (USA), Rona L. Thompson (Norway/New Zealand), Jerry Tjiputra (Norway/Indonesia), Guido van der Werf (Netherlands), Detlef van Vuuren (Netherlands), Apostolos Voulgarakis (UK/Greece), Rita Wania (Austria), Sönke Zaehle (Germany), Ning Zeng (USA)

Review Editors:
Christoph Heinze (Norway), Pieter Tans (USA), Timo Vesala (Finland)

This chapter supplementary material should be cited as:
Ciais, P., C. Sabine, G. Bala, L. Bopp, V. Brovkin, J. Canadell, A. Chhabra, R. DeFries, J. Galloway, M. Heimann, C. Jones, C. Le Quéré, R.B. Myneni, S. Piao and P. Thornton, 2013: Carbon and Other Biogeochemical Cycles Supplementary Material. In: *Climate Change 2013: The Physical Science Basis. Contribution of Working Group I to the Fifth Assessment Report of the Intergovernmental Panel on Climate Change* [Stocker, T.F., D. Qin, G.-K. Plattner, M. Tignor, S.K. Allen, J. Boschung, A. Nauels, Y. Xia, V. Bex and P.M. Midgley (eds.)]. Available from www.climatechange2013.org and www.ipcc.ch.

Table of Contents

6.SM.1 Supplementary Material to Section 6.4.6.1: Projections for Formation of Reactive Nitrogen by Human Activity

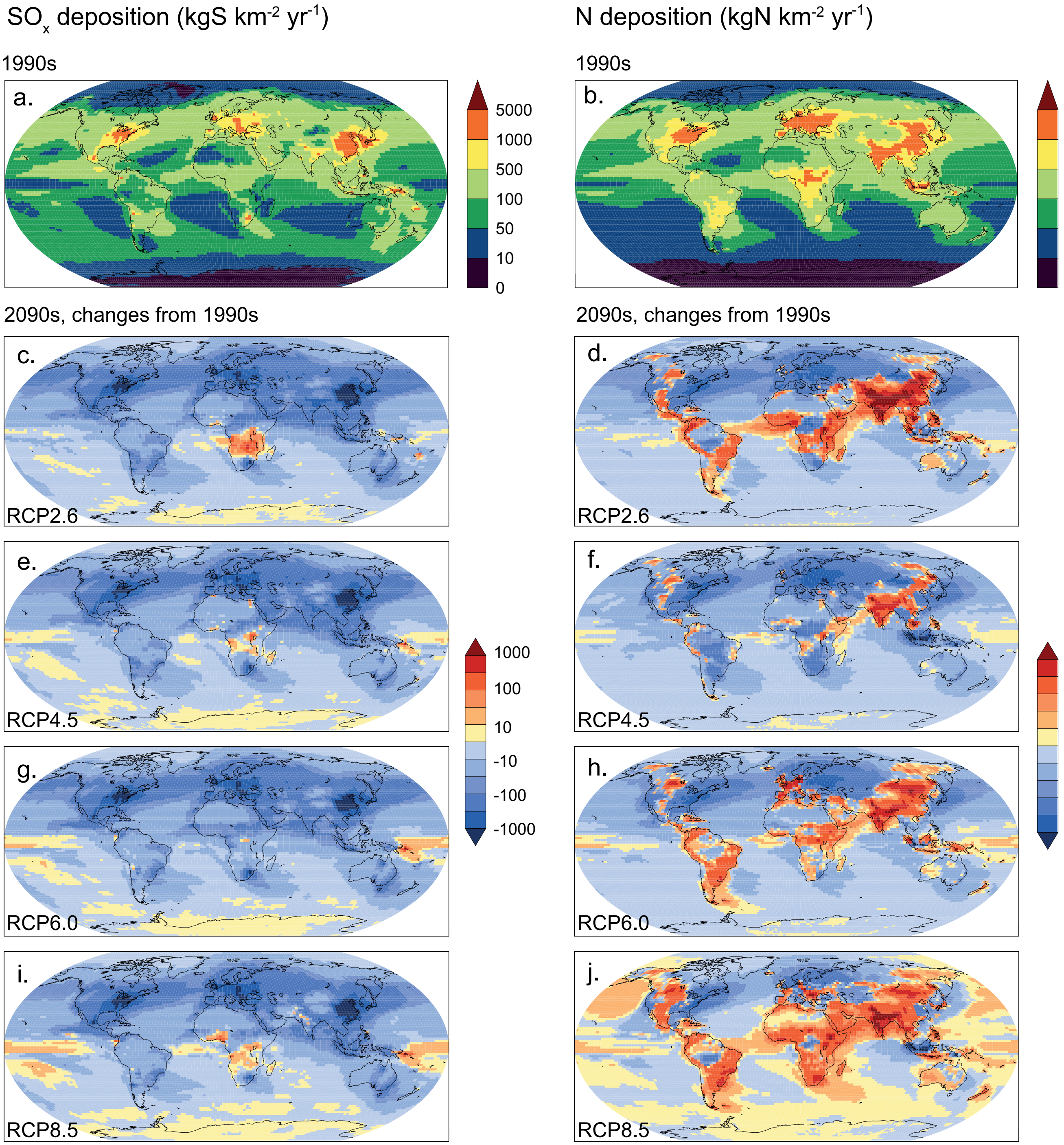

Figure 6.SM.1 | Spatial variability of nitrogen and SO$_x$ deposition in 1990s with projections to the 2090s (shown as difference relative to the 1990s), using the 2.6, 4.5, 6.0 and 8.5 Representative Concentration Pathway (RCP) scenarios, kg N km^{-2} yr^{-1}, adapted from Lamarque et al. (2011). Note that no information on the statistical significance of the shown differences is available. This is of particular relevance for areas with small changes.

The change in dissolved inorganic nitrogen (DIN) discharge under the Global Orchestration (GO) scenario of the Millennium Ecosystem Assessment (MEA) (the scenario with the most extreme pressures) was assessed by taking the change between the base year 2000, and the projection year, in this case 2050 (Figure 6.34b). Manure is the most important contributor as a result of assumed high per capita meat consumption, although there are considerable regional variations (Seitzinger et al., 2010). At the other extreme is the projected change in the riverine flux between 2000 and 2050 for the Adapting Mosaic scenario, the most ambitious in terms of nutrient managements of the MEA scenarios. These two scenarios provide a range of projections for future DIN riverine fluxes by the year 2050.

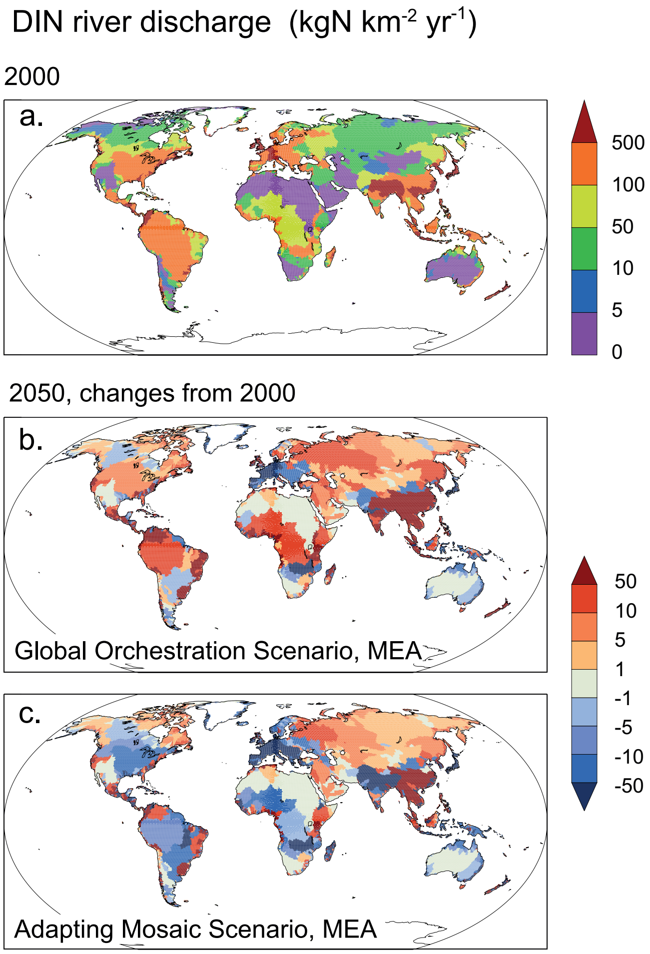

Figure 6.SM.2 | (a) Dissolved inorganic nitrogen (DIN) river discharge to coastal zone (mouth of rivers) in 2000, based on Global Nutrient Export from WaterSheds (NEWS) 2 model; change in DIN discharge from 2000 to 2050, based on the (b) Global Orchestration and (c) Adapting Mosaic scenarios from the Millennium Ecosystem Assessment (MEA) (Mayorga et al., 2010; Seitzinger et al., 2010). Units are kg N km^{-2} yr^{-1} of watershed area, as an average for each watershed. Global DIN export to the coastal zone in 2050 under the Global Orchestration and Adapting Mosaic scenarios changes by +5.5 and –0.4 TgN yr^{-1}, respectively, relative to the export of 18.9 TgN yr^{-1} in 2000 (Seitzinger et al., 2010).

References

Lamarque, J. F., et al., 2011: Global and regional evolution of short–lived radiatively–active gases and aerosols in the Representative Concentration Pathways. *Clim. Change*, **109**, 191–212.

Mayorga, E., et al., 2010: Global nutrient export from WaterSheds 2 (NEWS 2): Model development and implementation. *Environ. Model. Software*, **25**, 837–853.

Seitzinger, S. P., et al., 2010: Global river nutrient export: A scenario analysis of past and future trends. *Global Biogeochem. Cycles*, **24**, GB0A08.

7SM

Clouds and Aerosols
Supplementary Material

Coordinating Lead Authors:

Olivier Boucher (France), David Randall (USA)

Lead Authors:

Paulo Artaxo (Brazil), Christopher Bretherton (USA), Graham Feingold (USA), Piers Forster (UK), Veli-Matti Kerminen (Finland), Yutaka Kondo (Japan), Hong Liao (China), Ulrike Lohmann (Switzerland), Philip Rasch (USA), S.K. Satheesh (India), Steven Sherwood (Australia), Bjorn Stevens (Germany), Xiao-Ye Zhang (China)

Contributing Authors:

Govindasamy Bala (India), Nicolas Bellouin (UK), Angela Benedetti (UK), Sandrine Bony (France), Ken Caldeira (USA), Anthony Del Genio (USA), Maria Cristina Facchini (Italy), Mark Flanner (USA), Steven Ghan (USA), Claire Granier (France), Corinna Hoose (Germany), Andy Jones (UK), Makoto Koike (Japan), Ben Kravitz (USA), Benjamin Laken (Spain), Matthew Lebsock (USA), Natalie Mahowald (USA), Gunnar Myhre (Norway), Colin O'Dowd (Ireland), Alan Robock (USA), Bjørn Samset (Norway), Hauke Schmidt (Germany), Michael Schulz (Norway), Graeme Stephens (USA), Philip Stier (UK), Trude Storelvmo (USA), Dave Winker (USA), Matthew Wyant (USA)

Review Editors:

Sandro Fuzzi (Italy), Joyce Penner (USA), Venkatachalam Ramaswamy (USA), Claudia Stubenrauch (France)

This chapter supplementary material should be cited as:

Boucher, O., D. Randall, P. Artaxo, C. Bretherton, G. Feingold, P. Forster, V.-M. Kerminen, Y. Kondo, H. Liao, U. Lohmann, P. Rasch, S.K. Satheesh, S. Sherwood, B. Stevens and X.Y. Zhang, 2013: Clouds and Aerosols Supplementary Material. In: *Climate Change 2013: The Physical Science Basis. Contribution of Working Group I to the Fifth Assessment Report of the Intergovernmental Panel on Climate Change* [Stocker, T.F., D. Qin, G.-K. Plattner, M. Tignor, S.K. Allen, J. Boschung, A. Nauels, Y. Xia, V. Bex and P.M. Midgley (eds.)]. Available from www.climatechange2013.org and www.ipcc.ch.

Table of Contents

7.SM.1 Supplementary Material to Section 7.2.7.1

Forster et al. (2007) estimated the 2005 radiative forcing (RF) from contrails as +0.01 (–0.007 to +0.02) W m^{-2}, but neglected any increase due to traffic increase for previous estimates and considered 2000 estimates to be representative of 2005. Lee et al. (2009) scaled these estimates upward 18% to account for revised fuel use estimates, propulsive efficiency and flight routes for year 2005.

Estimates of the RF due to contrails published since AR4 are compiled in Table 7.SM.1. These have been scaled by scheduled air traffic distance (in millions of kilometres) as provided by http://www.airlines.org/Pages/Annual-Results-World-Airlines.aspx (see Table 7.SM.2) to produce RF estimates for the year 2011. This simple linear scaling assumes non-scheduled air traffic distance increases at the same rate as scheduled traffic as well as a constant likelihood of persistent contrail formation per kilometre flown despite the changing geographical distributions of flights. The trend in propulsive efficiency (which would increase the trend in contrail formation) and any saturation effect (which would decrease the trend in contrail formation) are neglected. It should be noted that the intervals provided by the individual studies in Table 7.SM.1 generally correspond to minimum–maximum values from sensitivity studies rather than statistical uncertainty ranges. The lower and upper bounds for the Spangenberg et al. (2013) study correspond to the most conservative and most sensitive contrail masks of Duda et al. (2013), respectively.

The average of RF estimates for the year 2011 since AR4 amounts to +0.012 W m^{-2}, which is rounded to +0.01 W m^{-2} to provide a central estimate for this assessment. The 90% uncertainty range is estimated empirically from the published sensitivity studies as 0.005 to 0.03 W m^{-2}. The lower bound is also justified by a sensitivity study to ice particle shape which rules out negative values for observed contrail optical depths (Markowicz and Witek, 2011a). The upper bound also accounts for the potential effect of sub-visible contrails, noting that only one published estimate extends significantly beyond 0.03 W m^{-2}. A *medium confidence* is attached to this estimate. An additional RF of +0.003 W m^{-2} is due to emissions of water vapour in the stratosphere by aviation as estimated by Lee et al. (2009).

Forster et al. (2007) quoted Sausen et al. (2005) to update the 2000 forcing for aviation-induced cirrus (including linear contrails) to +0.03 (+0.01 to +0.08) W m^{-2} but did not consider this to be a best estimate because of large uncertainties. In particular, observationally based estimates of aviation-induced cirrus forcing estimates may unintentionally include cirrus changes not directly caused by aviation.

Only a few estimates of the RF due to aviation-induced cirrus have been published since AR4 (Table 7.SM.3) and all focused on contrail cirrus. Schumann and Graf (2013) constrained their model with observations of the diurnal cycle of contrails and cirrus in a region with high air traffic relative to a region with little air traffic, and estimated a RF of +0.05 (0.04 to +0.08) W m^{-2} for contrails and contrail-induced cirrus in 2006, but their model has a large shortwave contribution, suggesting that larger estimates are possible (Myhre et al., 2009). An alternative approach was taken by Burkhardt and Kärcher (2011), who estimated a global forcing of +0.03 W m^{-2} from contrails and contrail cirrus within a climate model for the year 2002 (Burkhardt and Kärcher, 2009). Their RF for contrails and contrail-cirrus (+0.0375 W m^{-2}) is corrected here for the radiative impact due to the decrease in natural cirrus (–0.007 W m^{-2}). Based on these two studies we assess the combined contrail and contrail-induced cirrus ERF for the year 2011 to be +0.05 W m^{-2} neglecting the possibility that rapid adjustments

Table 7.SM.1 | Estimates of the contrail radiative forcing (RF) and their scaling to year 2011 (W m^{-2}). The uncertainty of the estimate by Markowicz and Witek (2011b) is calculated by combining the uncertainties due to crystal shape and contrail optical depth.

Reference	RF Due to Contrails	Reference Year	RF Due to Contrails Scaled to Year 2011
Forster et al. (2007) - AR4	+0.01 (–0.007 to +0.02)	2000 (2005)	+0.015 (–0.01 to +0.03)
Rädel and Shine (2008)	+0.006	2002	+0.009
Rap et al. (2010b) - offline	+0.012	2002	+0.018
Rap et al. (2010b) - online	+0.008 (+0.004 to 0.012)	2002	+0.012 (+0.006 to +0.018)
Kärcher et al. (2010)	+0.008 to +0.020	2000	+0.012 to +0.030
Burkhardt and Kärcher (2011)	+0.0043 (young contrails)	2002	+0.007
Frömming et al. (2011)	+0.0059 (+0.0049 to +0.0211)	2000	+0.009 (+0.007 to +0.032)
Markowicz and Witek (2011b)	+0.011 (+0.006 to +0.016)	2002	+0.017 (+0.010 to +0.024)
Voigt et al.(2011)	+0.0159 (+0.0111 to +0.0477)	2005	+0.020 (+0.014 to +0.060)
Yi et al. (2012)	+0.0113 (+0.0098 to +0.0165)	2006	+0.014 (+0.012 to +0.020)
Spengenberg et al. (2013)	+0.0057 (+0.0028 to +0.0171)	2006	+0.007 (+0.003 to +0.021)
This Assessment			**+0.01 (+0.005 to +0.03)**

Table 7.SM.2 | Scheduled air traffic distance (in millions of kilometres) as provided by http://www.airlines.org/Pages/Annual-Results-World-Airlines.aspx.

1992	2000	2001	2002	2003	2004	2005	2006	2007	2008	2009	2010	2011
15,690	25,517	25,612	25,418	26,264	29,163	30,862	32,099	34,109	35,368	34,039	36,833	38,530

Table 7.SM.3 | Estimates of the radiative forcing (RF)/effective radiative forcing (ERF) due to contrails and contrail cirrus and their scaling to year 2011 (W m^{-2}).

Reference	RF Due to Contrails and Contrail Cirrus	Reference Year	RF/ERF Due to Contrails and Contrail Cirrus Scaled to Year 2011
Stordal et al. (2005) / Sausen et al. (2005) - AR4	+0.03 (+0.01 to +0.08)	2000	+0.045 (+0.015 to +0.12)
Burkhardt and Kärcher (2011)	+0.03	2002	+0.045
Schumann and Graf (2013)	+0.05 (+0.04 to +0.08)[a]	2006	+0.060 (+0.040 to +0.119)[b]
This Assessment			**+0.05 (+0.02 to +0.15)**

Notes:

[a] The range is an expert judgment for a 1-σ interval.

[b] The range corresponds to a 90% uncertainty range.

may reduce this estimate (Ponater et al., 2005; Rap et al., 2010a). We further assess the 90% uncertainty range to be +0.02 to +0.15 W m^{-2} to take into account the large uncertainties associated with spreading rate, optical depth, ice particle shape and radiative transfer. A *low confidence* is attached to this estimate.

7.SM.2 Supplementary Material to Section 7.5.2.1

Figure 7.SM.1 shows the annual zonal mean radiative forcing due to aerosol–radiation interactions (RFari, in W m^{-2}) due to all anthropogenic aerosols from the different AeroCom II models that were combined in Figure 7.17.

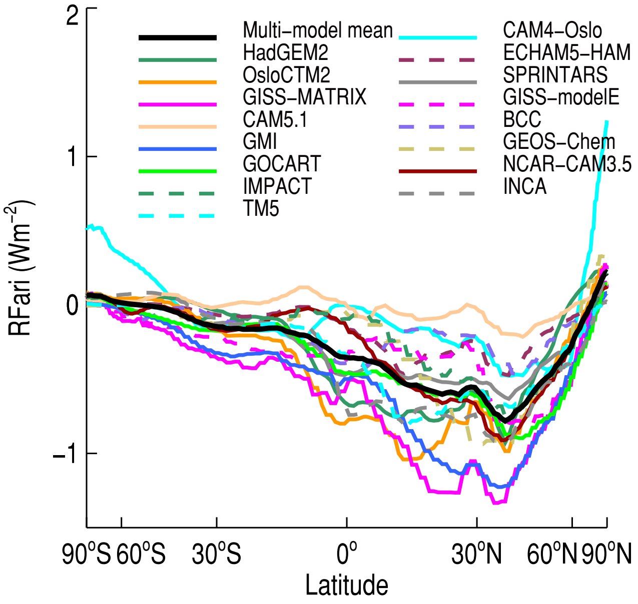

Figure 7.SM.1 | Annual zonal mean radiative forcing due to aerosol–radiation interactions (RFari, in W m^{-2}) due to all anthropogenic aerosols from the different AeroCom II models (Myhre et al., 2013). No adjustment for missing species in certain models has been applied. The forcings are for the 1850–2000 period. See also Figure 7.17.

References

Burkhardt, U., and B. Kärcher, 2009: Process-based simulation of contrail cirrus in a global climate model. *J. Geophys. Res.*, **114**, D16201.

Burkhardt, U., and B. Kärcher, 2011: Global radiative forcing from contrail cirrus. *Nature Clim. Change*, **1**, 54-58.

Duda, D. P., P. Minnis, K. Khlopenkov, T. L. Chee, and R. Boeke, 2013: Estimation of 2006 Northern Hemisphere contrail coverage using MODIS data. *Geophys. Res. Lett.*, **40**, 612-617.

Forster, P., et al., 2007: Changes in atmospheric constituents and in radiative forcing. In: *Climate Change 2007: The Physical Science Basis. Contribution of Working Group I to the Fourth Assessment Report of the Intergovernmental Panel on Climate Change* [Solomon, S., D. Qin, M. Manning, Z. Chen, M. Marquis, K. B. Averyt, M. Tignor and H. L. Miller (eds.)], pp. 129-234, Cambridge University Press, Cambridge, United Kingdom and New York, NY, USA.

Frömming, C., M. Ponater, U. Burkhardt, A. Stenke, S. Pechtl, and R. Sausen, 2011: Sensitivity of contrail coverage and contrail radiative forcing to selected key parameters. *Atmos. Environ.*, **45**, 1483-1490.

Kärcher, B., U. Burkhardt, M. Ponater, and C. Frömming, 2010: Importance of representing optical depth variability for estimates of global line-shaped contrail radiative forcing. *Proc. Natl. Acad. Sci. U.S.A.*, **107**, 19181–19184.

Lee, D., et al., 2009: Aviation and global climate change in the 21st century. *Atmos. Environ.*, **43**, 3520-3537.

Markowicz, K. M., and M. L. Witek, 2011a: Simulations of contrail optical properties and radiative forcing for various crystal shapes. *J. Appl. Meteorol. Climatol.*, **50**, 1740-1755.

Markowicz, K. M., and M. Witek, 2011b: Sensitivity study of global contrail radiative forcing due to particle shape. *J. Geophys. Res.*, **116**, D23203.

Myhre, G., et al., 2009: Intercomparison of radiative forcing calculations of stratospheric water vapour and contrails. *Meteorol. Z.*, **18**, 585-596.

Myhre, G., et al., 2013: Radiative forcing of the direct aerosol effect from AeroCom Phase II simulations. *Atmos. Chem. Phys.*, **13**, 1853-1877.

Ponater, M., S. Marquart, R. Sausen, and U. Schumann, 2005: On contrail climate sensitivity. *Geophys. Res. Lett.*, **32**, L10706.

Rädel, G., and K. P. Shine, 2008: Radiative forcing by persistent contrails and its dependence on cruise altitudes. *J. Geophys. Res.*, **113**, D07105.

Rap, A., P. M. Forster, J. M. Haywood, A. Jones, and O. Boucher, 2010a: Estimating the climate impact of linear contrails using the UK Met Office climate model. *Geophys. Res. Lett.*, **37**, L20703.

Rap, A., P. M. Forster, A. Jones, O. Boucher, J. M. Haywood, N. Bellouin, and R. R. De Leon, 2010b: Parameterization of contrails in the UK Met Office Climate Model. *J. Geophys. Res.*, **115**, D10205.

Sausen, R., et al., 2005: Aviation radiative forcing in 2000: An update on IPCC (1999). *Meteorol. Z.*, **14**, 555-561.

Schumann, U., and K. Graf, 2013: Aviation-induced cirrus and radiation changes at diurnal timescales. *J. Geophys. Res.*, **118**, 2404-2421.

Spangenberg, D. A., P. Minnis, S. T. Bedka, R. Palikonda, D. P. Duda, and F. G. Rose, 2013: Contrail radiative forcing over the Northern Hemisphere from 2006 Aqua MODIS data. *Geophys. Res. Lett.*, **40**, 595-600.

Stordal, F., G. Myhre, E. J. G. Stordal, W. B. Rossow, D. S. Lee, D. W. Arlander, and T. Svenby, 2005: Is there a trend in cirrus cloud cover due to aircraft traffic? *Atmos. Chem. Phys.*, **5**, 2155–2162.

Voigt, C., et al., 2011: Extinction and optical depth of contrails. *Geophys. Res. Lett.*, **38**, L11806.

Yi, B., P. Yang, K.-N. Liou, P. Minnis, and J. E. Penner, 2012: Simulation of the global contrail radiative forcing: A sensitivity analysis. *Geophys. Res. Lett.*, **39**, L00F03.

8SM

Anthropogenic and Natural Radiative Forcing

Supplementary Material

Coordinating Lead Authors:
Gunnar Myhre (Norway), Drew Shindell (USA)

Lead Authors:
François-Marie Bréon (France), William Collins (UK), Jan Fuglestvedt (Norway), Jianping Huang (China), Dorothy Koch (USA), Jean-François Lamarque (USA), David Lee (UK), Blanca Mendoza (Mexico), Teruyuki Nakajima (Japan), Alan Robock (USA), Graeme Stephens (USA), Toshihiko Takemura (Japan), Hua Zhang (China)

Contributing Authors:
Borgar Aamaas (Norway), Olivier Boucher (France), Stig B. Dalsøren (Norway), John S. Daniel (USA), Piers Forster (UK), Claire Granier (France), Joanna Haigh (UK), Øivind Hodnebrog (Norway), Jed O. Kaplan (Switzerland/Belgium/USA), George Marston (UK), Claus J. Nielsen (Norway), Brian C. O'Neill (USA), Glen P. Peters (Norway), Julia Pongratz (Germany), Michael Prather (USA), Venkatachalam Ramaswamy (USA), Raphael Roth (Switzerland), Leon Rotstayn (Australia), Steven J. Smith (USA), David Stevenson (UK), Jean-Paul Vernier (USA), Oliver Wild (UK), Paul Young (UK)

Review Editors:
Daniel Jacob (USA), A.R. Ravishankara (USA), Keith Shine (UK)

This chapter supplementary material should be cited as:
Myhre, G., D. Shindell, F.-M. Bréon, W. Collins, J. Fuglestvedt, J. Huang, D. Koch, J.-F. Lamarque, D. Lee, B. Mendoza, T. Nakajima, A. Robock, G. Stephens, T. Takemura and H. Zhang, 2013: Anthropogenic and Natural Radiative Forcing Supplementary Material. In: *Climate Change 2013: The Physical Science Basis. Contribution of Working Group I to the Fifth Assessment Report of the Intergovernmental Panel on Climate Change* [Stocker, T.F., D. Qin, G.-K. Plattner, M. Tignor, S.K. Allen, J. Boschung, A. Nauels, Y. Xia, V. Bex and P.M. Midgley (eds.)]. Available from www.climatechange2013.org and www.ipcc.ch.

Table of Contents

8.SM.1 Figures on Regional Emissions to Support Section 8.2.2

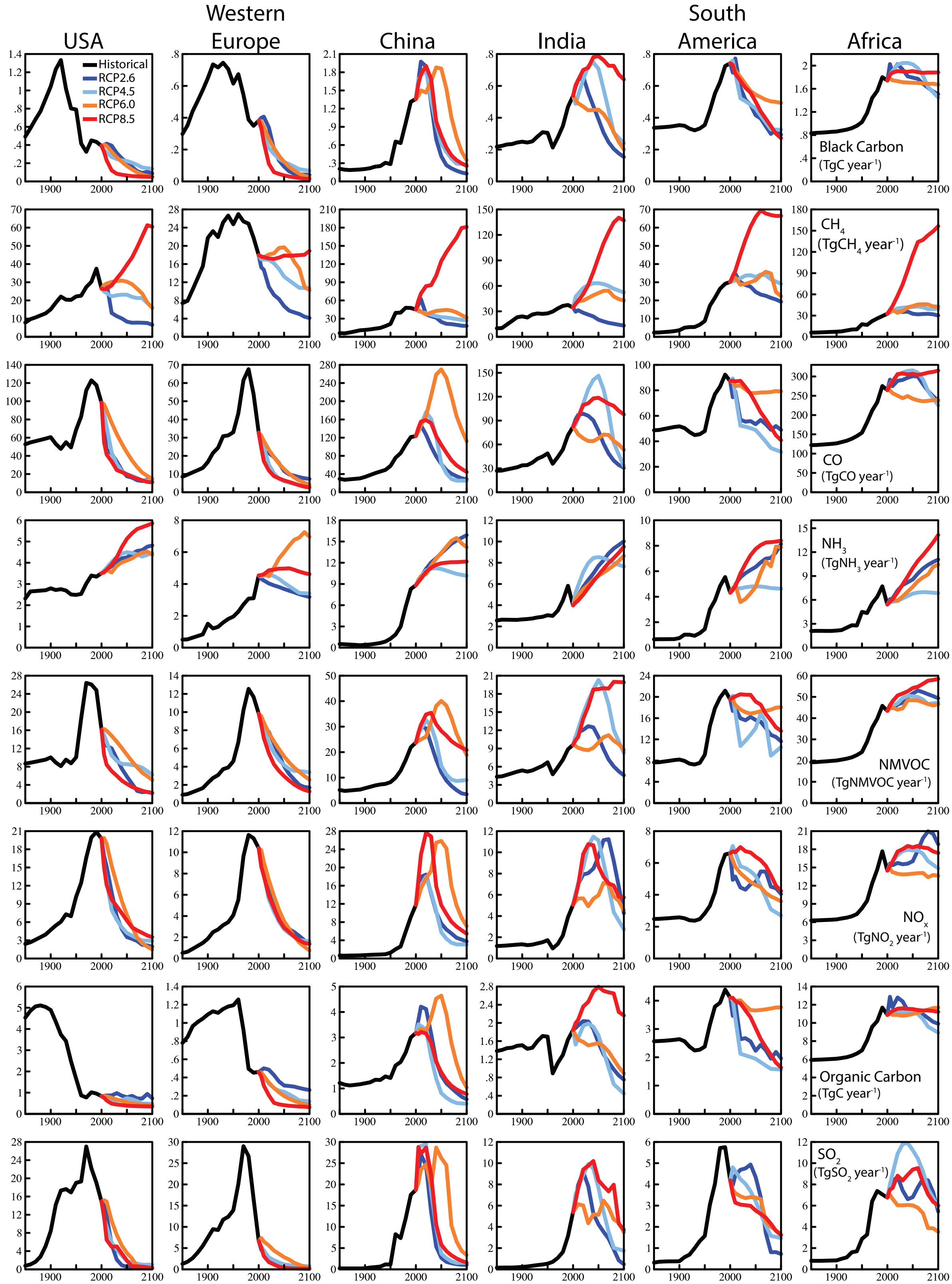

Figure 8.SM.1 | Time evolution of regional anthropogenic and biomass burning emissions 1850–2100 used in Coupled Model Intercomparison Project Phase 5 (CMIP5)/Atmospheric Chemistry and Climate Model Intercomparison Project (ACCMIP) following each Representative Concentration Pathway (RCP). Historical (1850–2000) values are from (Lamarque et al., 2010). RCP values are from (van Vuuren et al., 2011).

Methane

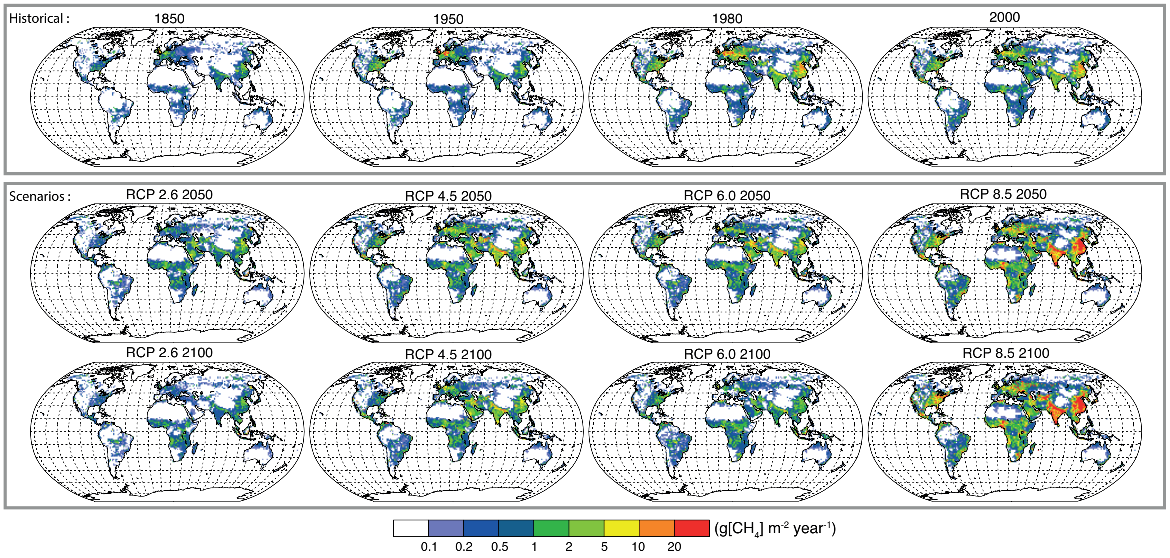

Carbone Monoxide

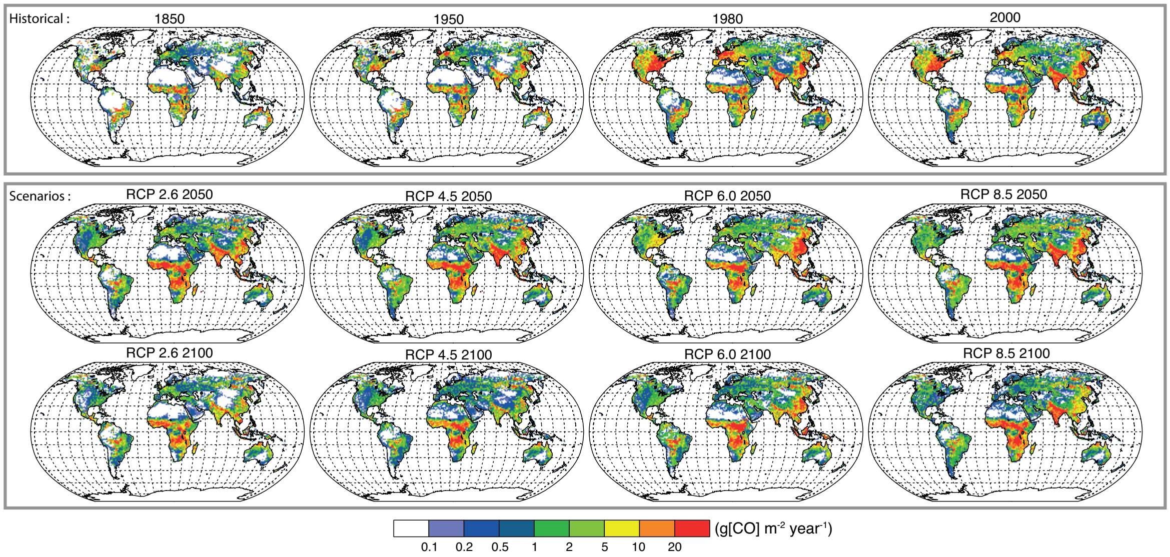

NMVOC

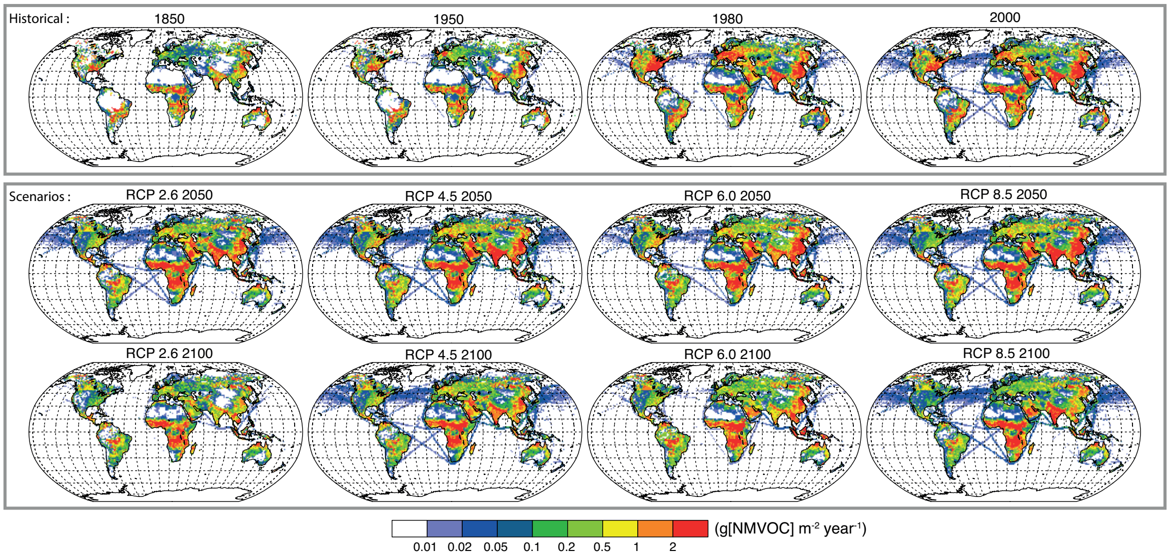

Figure 8.SM.2 | Time evolution of anthropogenic and biomass burning emissions 1850–2100 used in CMIP5/ACCMIP following each RCP. Historical (1850–2000) values are from Lamarque et al. (2010). RCP values are from van Vuuren et al. (2011).

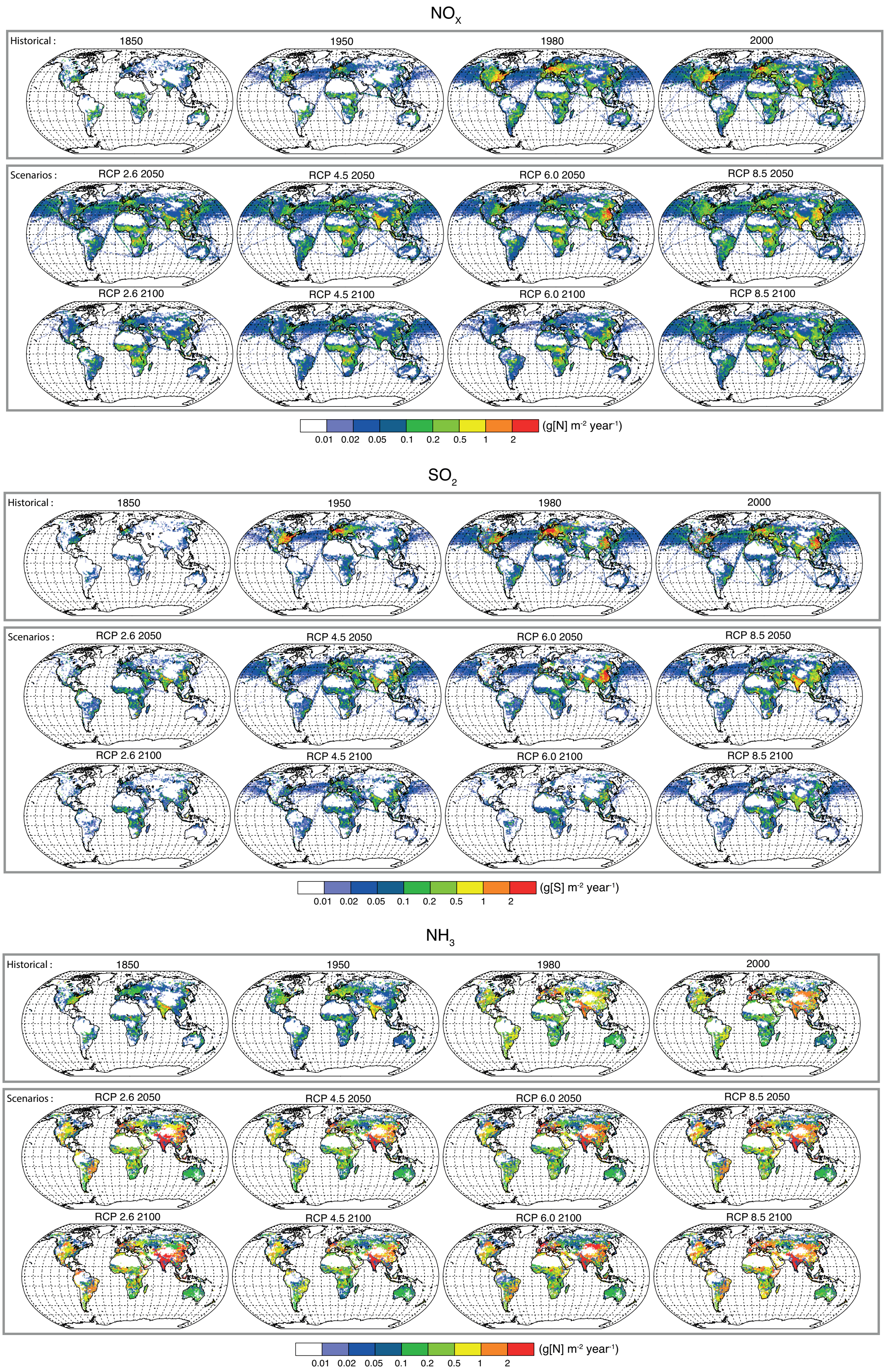

Figure 8.SM.2 | (continued)

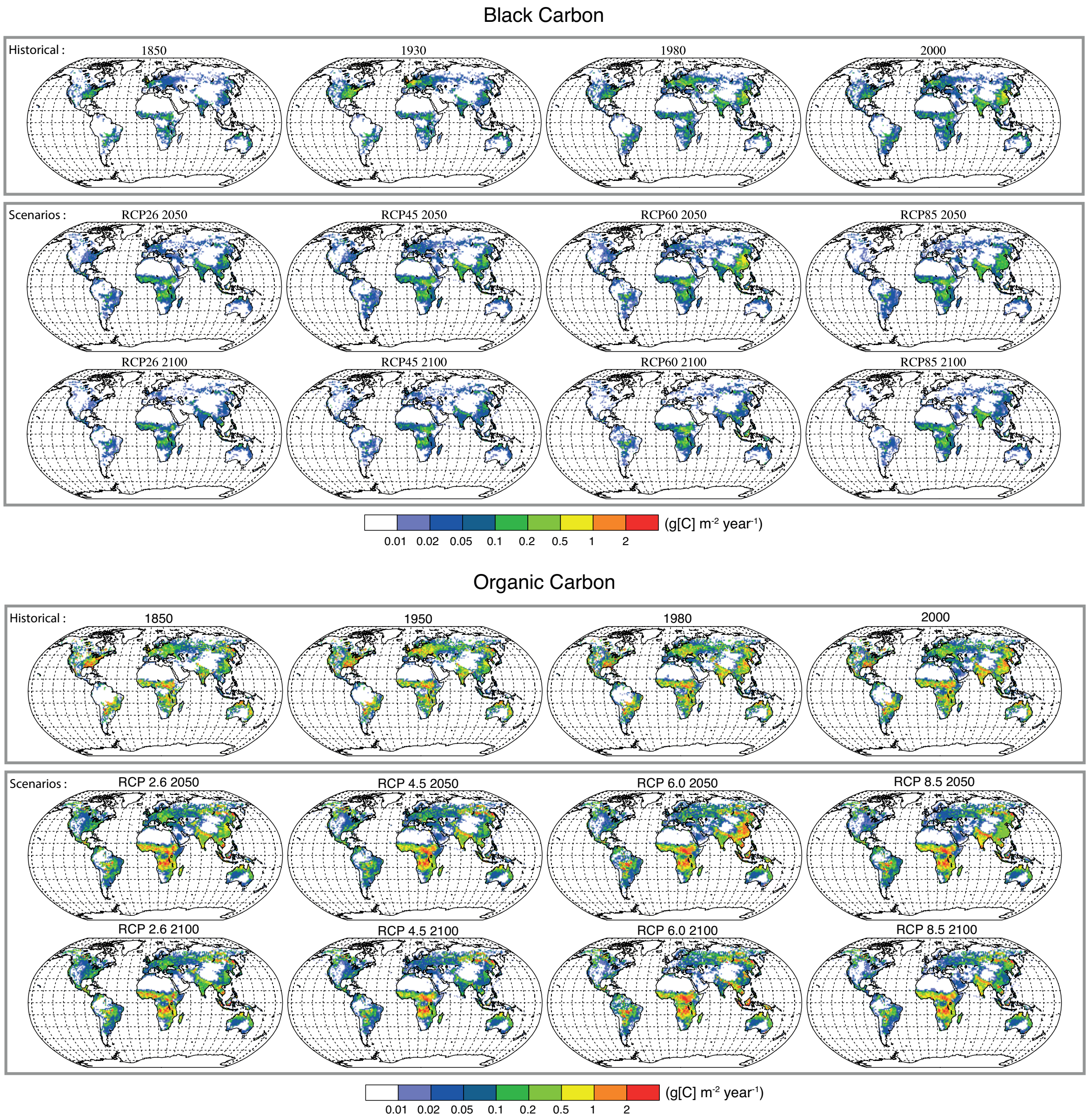

Figure 8.SM.2 | (continued)

8.SM.2 Description of Hydroxyl Radical Feedback and Perturbation Lifetime for Methane to Support Section 8.2.3

The methane lifetime with respect to tropospheric hydroxyl radical (OH) is estimated at 11.2 ± 1.3 years, while the lifetime of methane (CH_4) with respect to additional sinks is estimated at 120 ± 24 years (bacterial uptake in soils), 150 ± 50 years (stratospheric loss) and 200 ± 100 years (chlorine loss), respectively. This leads to a total CH_4 lifetime estimate of 9.25 ± 0.6 years, calculated by computing the total lifetime using the full range of each separate lifetime listed above. Note that adding the inverse values of the best estimates of the lifetimes gives 9.15 years, but the value based on full ranges is chosen here. Combining this information with the OH-lifetime sensitivity (s) for CH_4, s_OH (0.31 ± 0.04) by scaling s_OH with the ratio between total lifetime and OH-lifetime (9.25/11.2) leads to an overall estimate of s of 0.25 ± 0.03 and therefore gives a feedback factor $f = 1/(1 - s) = 1.34 \pm 0.06$ (for 1-σ range). The error estimate on f is estimated from the error estimate on s using error(f) = error(s) * df/ds.

The perturbation lifetime is therefore calculated by combining the range of values for the CH_4 lifetime with the range of values for the feedback factor, leading to a perturbation lifetime of 12.4 ± 1.4 years (for one sigma range) which is adopted for the metric calculations. Note that this value is slightly larger than the value obtained using the mean estimates from all parameters (12.3 years).

8.SM.3 Well-Mixed Greenhouse Gas Radiative Forcing Formulae and Uncertainties to Support Table 8.3

The formulae used to calculate the radiative forcings (RFs) from carbon dioxide (CO_2), CH_4 and nitrous oxide (N_2O) are taken from Myhre et al. (1998) Table 3 as in Third Assessment Report (TAR) and Fourth Assessment Report (AR4). They are listed here for convenience.

In calculating the uncertainties in the WMGHG RF we assume a ±10% (5 to 95% confidence interval) uncertainty in the radiative transfer modeling that is correlated across all species. We assume the uncertainties in the measurements of the 1750 and 2011 abundance levels of the gases are uncorrelated.

Table 8.SM.1 | Supplementary for Table 8.3: RF formulae for CO_2, CH_4 and N_2O.

Gas	RF (in W m^{-2})	Constant α
CO_2	$\Delta F = \alpha \ln\left(C/C_0\right)$	5.35
CH_4	$\Delta F = \alpha\left(\sqrt{M}-\sqrt{M_0}\right)-\left(f\left(M,N_0\right)-f\left(M_0,N_0\right)\right)$	0.036
N_2O	$\Delta F = \alpha\left(\sqrt{N}-\sqrt{N_0}\right)-\left(f\left(M_0,N\right)-f\left(M_0,N_0\right)\right)$	0.12

Notes:

$f(M, N) = 0.47 \ln [1+2.01\times10^{-5} (MN)0.75 + 5.31\times10^{-15} M (MN)^{1.52}]$

C is CO_2 in ppm.

M is CH_4 in ppb.

N is N_2O in ppb.

The subscript 0 denotes the unperturbed molar fraction for the species being evaluated. However, note that for the CH_4 forcing N_0 should refer to present-day N_2O, and for the N_2O forcing M_0 should refer to present-day CH_4.

Table 8.SM.2 | Supplementary for Table 8.3: Uncertainties in WMGHG RF.

	CO_2	CH_4	N_2O	Halogens	Total WMGHG
Uncertainty in 1750 level	2 ppm	25 ppb	7 ppb	0	
Uncertainty in 2011 level	0.16 ppm	2.5 ppb	0.1 ppb	0	
dRF 1750 level (W m^{-2})	0.039	0.01	0.023	0	0.047
dRF 2011 level (W m^{-2})	0.003	0.00	0.000	0	0.003
dRF radiative transfer modeling (W m^{-2})	0.182	0.05	0.017	0.036	0.283
Total uncertainty (W m^{-2})	0.186	0.05	0.029	0.036	0.287

8.SM.4 Total Solar Irradiance Reconstructions from 1750 to 2012 to Support Section 8.4.1

Table 8.SM.3 | Total Solar Irradiance (TSI, W m^{-2}) reconstruction since 1750 based on Ball et al. (2012) and Krivova et al.(2010) (annual resolution series). The series are standardized to the Physikalisch-Meteorologisches Observatorium Davos (PMOD) measurements of solar cycle 23 (1996–2008) (PMOD is already standardized to Total Irradiance Monitor (TIM)).

Year	TSI (W m^{-2})	Year	TSI (W m^{-2})	Year	TSI (W m^{-2})
1740	1360.71	1841	1361.05	1942	1361.22
1741	1360.73	1842	1360.96	1943	1360.96
1742	1360.79	1843	1360.90	1944	1360.93
1743	1360.59	1844	1360.83	1945	1361.14
1744	1360.52	1845	1360.81	1946	1361.18
1745	1360.49	1846	1360.83	1947	1361.68
1746	1360.49	1847	1360.55	1948	1362.07
1747	1360.47	1848	1360.87	1949	1361.90
1748	1360.70	1849	1361.32	1950	1361.80
1749	1360.98	1850	1361.18	1951	1361.27
1750	1361.00	1851	1361.12	1952	1361.33
1751	1360.90	1852	1361.15	1953	1361.18
1752	1360.79	1853	1361.08	1954	1361.02
1753	1360.76	1854	1360.93	1955	1361.12
1754	1360.69	1855	1360.80	1956	1361.47

(continued on next page)

Table 8.SM.3 (continued)

Year	TSI (W m^{-2})	Year	TSI (W m^{-2})	Year	TSI (W m^{-2})
1755	1360.61	1856	1360.73	1957	1361.95
1756	1360.60	1857	1360.73	1958	1362.43
1757	1360.65	1858	1360.86	1959	1362.17
1758	1360.64	1859	1360.95	1960	1362.11
1759	1360.26	1860	1361.22	1961	1361.81
1760	1360.19	1861	1361.26	1962	1361.37
1761	1360.89	1862	1361.10	1963	1361.28
1762	1360.95	1863	1361.04	1964	1361.14
1763	1360.87	1864	1360.88	1965	1361.06
1764	1360.84	1865	1360.87	1966	1361.09
1765	1360.61	1866	1360.85	1967	1361.40
1766	1360.65	1867	1360.73	1968	1361.63
1767	1360.74	1868	1360.72	1969	1361.57
1768	1361.12	1869	1360.96	1970	1361.68
1769	1361.37	1870	1360.80	1971	1361.60
1770	1361.59	1871	1361.19	1972	1361.56
1771	1361.41	1872	1361.09	1973	1361.32
1772	1361.38	1873	1361.11	1974	1361.17
1773	1361.12	1874	1361.00	1975	1361.05
1774	1360.99	1875	1360.89	1976	1360.98
1775	1360.72	1876	1360.79	1977	1361.29
1776	1360.67	1877	1360.76	1978	1361.95
1777	1360.74	1878	1360.70	1979	1362.23
1778	1361.12	1879	1360.68	1980	1362.10
1779	1360.75	1880	1360.71	1981	1362.08
1780	1360.50	1881	1360.95	1982	1361.69
1781	1360.58	1882	1360.86	1983	1361.67
1782	1360.80	1883	1360.78	1984	1361.12
1783	1360.52	1884	1361.13	1985	1361.09
1784	1360.57	1885	1361.02	1986	1361.09
1785	1360.66	1886	1360.90	1987	1361.11
1786	1360.84	1887	1360.76	1988	1361.70
1787	1361.00	1888	1360.73	1989	1362.11
1788	1361.25	1889	1360.70	1990	1361.86
1789	1360.76	1890	1360.70	1991	1361.93
1790	1360.58	1891	1360.86	1992	1362.00
1791	1360.59	1892	1361.03	1993	1361.46
1792	1360.63	1893	1361.26	1994	1361.20
1793	1360.53	1894	1361.53	1995	1361.15
1794	1360.53	1895	1361.38	1996	1361.02
1795	1360.80	1896	1361.17	1997	1361.12
1796	1360.76	1897	1360.98	1998	1361.46
1797	1360.69	1898	1360.91	1999	1361.76
1798	1360.68	1899	1360.88	2000	1361.93

(continued on next page)

Table 8.SM.3 (continued)

Year	TSI (W m^{-2})	Year	TSI (W m^{-2})	Year	TSI (W m^{-2})
1799	1360.66	1900	1360.80	2001	1361.84
1800	1360.60	1901	1360.69	2002	1361.79
1801	1360.85	1902	1360.65	2003	1361.31
1802	1360.93	1903	1360.74	2004	1361.09
1803	1360.76	1904	1361.08	2005	1360.92
1804	1360.71	1905	1360.89	2006	1360.88
1805	1360.67	1906	1361.21	2007	1360.88
1806	1360.74	1907	1361.00	2008	1360.82
1807	1360.58	1908	1361.15	2009	1360.81
1808	1360.53	1909	1360.99	2010	1361.01
1809	1360.53	1910	1360.96	2011	1361.22
1810	1360.49	1911	1360.77	2012	1361.42
1811	1360.48	1912	1360.67		
1812	1360.48	1913	1360.70		
1813	1360.50	1914	1360.76		
1814	1360.53	1915	1361.10		
1815	1360.55	1916	1361.50		
1816	1360.62	1917	1361.63		
1817	1360.65	1918	1361.89		
1818	1360.61	1919	1361.53		
1819	1360.60	1920	1361.29		
1820	1360.57	1921	1361.09		
1821	1360.53	1922	1360.90		
1822	1360.52	1923	1360.82		
1823	1360.50	1924	1360.79		
1824	1360.57	1925	1360.89		
1825	1360.62	1926	1361.15		
1826	1360.68	1927	1361.47		
1827	1360.87	1928	1361.24		
1828	1360.95	1929	1361.21		
1829	1360.96	1930	1361.35		
1830	1361.01	1931	1361.07		
1831	1361.01	1932	1360.89		
1832	1360.86	1933	1360.79		
1833	1360.75	1934	1360.80		
1834	1360.72	1935	1360.95		
1835	1360.76	1936	1361.50		
1836	1361.13	1937	1361.65		
1837	1361.40	1938	1361.59		
1838	1361.38	1939	1361.69		
1839	1361.21	1940	1361.51		
1840	1361.20	1941	1361.42		

8.SM.5 Table with Estimates of Radiative Forcing due to Solar Changes over the Industrial Era to Support Section 8.4.1

Table 8.SM.4 | Comparison of RF estimates between 1745 and 2008 minima.

Reference	Assumptions	RF (W m^{-2})	Comments
Wang et al. (2005)	Use a flux transport model to simulate the evolution of total and open magnetic flux without a secularly varying background	0.019 (7-year rm) 0.013 (annual)	
Wang et al. (2005)	Same as above but with a secularly varying background	0.071 (7-year rm) 0.065 (annual)	Used to estimate RF in AR4
Steinhilber et al. (2009)	Use the solar modulation potential obtained from cosmogenic isotopes	-0.02 (5-years resolutions)	
Krivova et al. (2010) Ball et al. (2012)	Use the evolution of the solar surface magnetic field, relying on time constants representing the decay and conversion of different surfaces magnetic field structures	0.048 (7-year rm) 0.045 (annual)	

Notes:

rm = running means. For the reconstructions based on solar surface magnetic structures, with annual resolution, the year of the minimum is 1745. However, for the Steinhilber et al. (2009) reconstruction, based on cosmogenic isotopes, the minimum is in 1765, because the resolution of the series is 5 years.

8.SM.6 Further Information on Total Solar Irradiance, Uncertainties and Change Since the Maunder Minimum to Support Section 8.4.1

The absolute measurements of TSI are extremely difficult with an absolute accuracy better than 0.1%. All TSI instruments since 1979 have been calibrated, relatively or absolutely. In order to maintain a reasonable accuracy in the annual to multi-decadal timeframe it is essential to have at least three independent sensors operating in space simultaneously. The fundamental difficulties of the absolute measurements are described in Butler et al. (2008). Fox et al. (2011) quantified how the uncertainty in satellite TSI measurements could be improved by an order of magnitude by adding primary SI traceability on board. For instance, to reduce from 3.60% for Moderate Resolution Imaging Spectrometer (MODIS)/Visible Infrared Imaging Radiometer Suite (VIIRS) to 0.30% for Traceable Radiometry Underpinning Terrestrial- and Helio-Studies (TRUTHS). This would reduce by 67 to 75% the time required to achieve trend accuracy.

The Spectral Irradiance Monitor (SIM) on board of the Solar Radiation and Climate Experiment (SORCE) measurements (Harder et al., 2009) suggest that over solar cycle (SC) 23 declining phase, the 200 to 400 nm ultraviolet (UV) flux decreased by two to six times more than expected from prior observations and model calculations and in phase with the TSI trend, whereas surprisingly the visible presents an opposite trend. However, SIM's solar spectral irradiance measurements from April 2004 to December 2008 and inferences of their climatic implications are incompatible with the historical solar UV irradiance database, coincident solar proxy data, current understanding of the sources of solar irradiance changes and empirical climate change attribution results, but are consistent with known effects of instrument sensitivity drifts. Thus what seems to be needed is improved characterization of the SIM/SORCE observations and extreme caution in studies of climate and atmospheric change (Haigh et al., 2010) until additional validation and uncertainty estimates are available (DeLand and Cebula, 2012; Lean and Deland, 2012).

8.SM.6.1 Uncertainties

1. PMOD RF and uncertainty between 1986 and 2008:
According to PMOD, 2009 is the year of the TSI minimum, but according to TIM it is 2008. We take the year 2008 as the year of the minimum.

The PMOD TSI mean for September 2008 was 1365.26 ± 0.16 W m^{-2}, whereas in the 1986 minimum it was 1365.57 ± 0.01 W m^{-2} (Frohlich, 2009).

Difference between 2008 and 1986 minima:
$1365.26 \pm 0.16 - 1365.57 \pm 0.01$

Applying the error propagation formula:
$(a \pm x) - (b \pm y) = (a - b) \pm [x^2 + y^2)]^{1/2}$

That for our case is:
$(1365.26 - 1365.57) \pm [(0.16)^2 + (0.01)^2]^{1/2} = -0.31 \pm 0.16$

The RF is:
$[-0.31 \pm 0.16] * 0.175 * 0.78 = -0.042 \pm 0.022 \sim \mathit{-0.04 \pm 0.02}$ W m^{-2}

8.SM.6.2 Standardization

We use the following expression to standardize the time series:
$[S_i - <S>] + <S^*>$

Where S_i is the annual TSI of the series that will be standardized.

$<S>$ is the TSI average of the whole time span of series that will be standardized.

$<S^*>$ is the TSI average of the series we are using as the standard. In our case the TIM TSI between 2003 and 2012 or the PMOD TSI for SC 23 (1996–2008).

For the RF estimates the years with minimum solar activity based on modern or historical observations are used as provided in the referenced literature. These years may in some cases be slightly different from the years with minimum annual mean TSI (see Table 8.SM.3), but these differences have a negligible impact on the RF estimates provided in Section 8.4.1.

8.SM.6.3 Total Solar Irradiance Variations Since the Maunder Minimum

For the Maunder minimum (MM)-to-present AR4 gives a RF positive range of 0.1 to 0.28 W m^{-2}, equivalent to 0.08 to 0.22 W m^{-2} used here. The estimates based on irradiance changes in Sun-like stars were included in this range but are not included in the Fifth Assessment Report (AR5) range because they are now considered incorrect: Baliunas and Jastrow (1990) found a bimodal separation between non-cycling MM-like state stars with the lowest Ca II brightness, and the higher emission Ca II cycling stars. More recent surveys have not reproduced their results and suggest that the selection of the original set was flawed (Wright (2004); also, stars in a MM-like state do not always exhibit Ca II emission brightness below that of solar minimum (Hall and Lockwood (2004).

The reconstructions in Schmidt et al. (2011) indicate a MM-to-present RF range of 0.08 to 0.18 W m^{-2}, which is within the AR4 range although narrower. Gray et al. (2010) point out that choosing the solar activity minima years of 1700 (Maunder) or 1800 (Dalton) would substantially increase the solar RF with respect to 1750-to-present while leaving the anthropogenic forcings essentially unchanged, and that these solar minima forcings would represent better the solar RF of the pre-industrial era.

Other recent estimates give various MM-to-present RF values: The analysis of Shapiro et al. (2011) falls outside the range 0.08 to 0.18 W m^{-2} reported above: 0.78 W m^{-2}. These authors used the semi-empirical photosphere model A (supergranule cell interior) of Fontenla et al. (1999). But Judge et al. (2012) indicate that by using such model Shapiro et al. (2011) overestimated the quiet-Sun irradiance variations by a factor of about two, then the RF would be 0.36 W m^{-2} , which is still outside the range of Schmidt et al. (2011). Studies of magnetic field indicators suggest that changes over the 19th and 20th centuries were more modest than those assumed in the Shapiro et al. (2011) reconstruction (Svalgaard and Cliver, 2010; Lockwood and Owens, 2011). Also, analysis by Feulner (2011) indicates that temperature simulations driven by such a large solar forcing are inconsistent with reconstructed and observed historical temperatures, although when a forcing in line with the range presented here is used they are consistent. Hence we do not include this larger forcing within our assessed range. Schrijver et al. (2011) and Foukal et al. (2011) find a RF which is consistent with the RF range given above (0.08 to 0.18 W m^{-2}).

Almost all the TSI reconstructions since pre-industrial times are based on the Sunspot Group Number (SGN; Hoyt and Schatten (1998). The SGN is preferred by researchers respect to the International Sunspot Number (Clette et al., 2007) because SGN starts at 1610 and it is the longest time series based on direct solar observations. As these two sunspot number versions are quite different in the historical period, using one or the other results in different trends since the MM (Hathaway et al., 2002) and therefore different RF estimates. Moreover, Svalgaard et al. (2012) have published some preliminary corrections to SGN that could imply a reduction in the RF since the MM.

8.SM.7 Method Description to Support Figure 8.16

In Figure 8.16, probability distributions are shown for the main climate drivers as well as for the total anthropogenic forcing. This paragraph describes how it was built.

For each of the major forcing agents, a best estimate and a 90% uncertainty range [P05; P95] was provided. The *best estimate* is the median of the probability distribution. The values are available in Table 8.6 and repeated below. For some forcing agents, the best estimate and the uncertainty range are provided for RF, and not for effective radiative forcing (ERF). In such a case, we assume that $ERF_{Best}=RF_{Best}$ and we assumed a quadratic 17% increase of the uncertainty range σ, that is:

$$\sigma_{ERF}^2 = \sigma_{RF}^2 + \left(0.17\, RF_{Best}\right)^2 \qquad (8.SM.1)$$

Most forcing agents considered here (WMGHG, ozone, stratospheric H_2O, land use change) have symmetrical uncertainty ranges (i.e., Best = (P05 + P95)/2). For these forcing agents, the probability distribution is assumed to be Gaussian, with a standard deviation as

$$\sigma = \frac{P95 - P05}{2f} \qquad (8.SM.2)$$

where $f \approx 1.645$ is the factor to convert one standard deviation to the 5-95% probability range.

The other forcing agents (black carbon on snow, contrails, aerosols) have non-symmetrical uncertainty ranges. For black carbon and snow, we assume a log-normal distribution as

$$P(x) = \frac{1}{x\,\sigma\sqrt{2\pi}} \exp\left(-\frac{\ln^2\left(x/x_0\right)}{2\sigma^2}\right) \qquad (8.SM.3)$$

with x_0 as the best estimate and σ adjusted to fit P05 and P50 (σ_{BC} = 0.5 ; $\sigma_{Contrails}$ = 0.65).

For the aerosols, which have a non-symmetrical uncertainty range, we build a probability distribution as

$$P(x) = \frac{1}{\sqrt{2\pi}} \frac{2}{\sigma_+ + \sigma_-} \exp\left(-\frac{\left(x - x_0\right)^2}{2\sigma^2}\right)$$
$$x \le x_0 \quad \sigma = \sigma_-$$
$$x \ge x_0 \quad \sigma = \sigma_+ \qquad (8.SM.4)$$

x_0, σ_- and σ_+ are adjusted to fit the best estimates and 90% uncertainty ranges:

$$x_0 \approx \frac{\frac{4}{5}\sqrt{\frac{2}{\pi}}\left(P05+P95\right)-\left(2\alpha+f\right)Best}{\frac{8}{5}\sqrt{\frac{2}{\pi}}-\left(2\alpha+f\right)}$$

$$\sigma_+ = \frac{\left(\alpha+f\right)\left(P95-x_0\right)+\alpha\left(x_0-P05\right)}{\left(\alpha+f\right)^2-\alpha^2}$$

and

$$\sigma_- = \frac{\left(\alpha+f\right)\left(x_0-P05\right)+\alpha\left(P95-x_0\right)}{\left(\alpha+f\right)^2-\alpha^2}$$

with

$$\alpha = 0.05\sqrt{\frac{\pi}{2}}\exp\left(\frac{f^2}{2}\right) \approx 0.2425 \qquad (8.SM.5)$$

The total anthropogenic ERF distribution was then derived through a Monte Carlo approach (10^6 independent shots), summing the random estimates of all components. This approach assumes that all forcing agent uncertainties are independent. The results are provided in Table 8.SM.5.

Table 8.SM.5 | Best estimate values and 5 and 95% ranges for RF and ERF. Yellow are the input values, green the extrapolated values (from RF to ERF) and red is the result of the Monte Carlo addition.

	RF			ERF		
Forcing agent	**Best**	**P05**	**P95**	**Best**	**P05**	**P95**
Well-mixed greenhouse gases				2.83	2.26	3.40
Ozone	0.350	0.15	0.55	0.350	0.141	0.559
Stratospheric H_2O	0.070	0.02	0.12	0.070	0.019	0.121
Surface albedo	–0.15	–0.25	–0.05	–0.150	–0.253	–0.047
Black carbon on snow	0.04	0.02	0.08	0.040	0.019	0.090
Contrails				0.05	0.02	0.15
Aerosols				–0.90	–1.90	–0.10
Total				2.29	1.13	3.33

8.SM.8 Table with Values and Uncertainties to Support Figure 8.17

Table 8.SM.6 | Radiative forcing (RF, in W m^{-2}) by emitted components as shown in Figure 8.17. The RF values are made consistent with Table 8.6. For emissions of CO_2, CH_4, CO, NMVOCs and NO_x the values for the influence on CO_2, CH_4 and ozone are based on Stevenson et al. (2013) and Shindell et al. (2009). The seven models altogether performing the calculations for these compounds (six models in Stevenson et al., (2013); and one model in Shindell et al., (2009) have been treated with equal weight. For CO, CH_4 and NMVOC only fossil fuel emissions have been taken into account. The split between NO_x and NH_3 of 40/60 on the RF of nitrate is from Shindell et al. (2009). The BC and OC from biomass burning is set to +0.2 and –0.2, respectively and thus a net RF of biomass burning of 0.0, in line with Table 8.4. BC ari is RF of BC from aerosol–radiation interaction, formerly denoted as direct aerosol effect. Unlike in AR4 (Table 2.13) the N_2O influence on RF of ozone has been set to zero, due to insufficient quantification of this and particularly the vertical profile of the ozone change. ERFaci is effective radiative forcing of aerosol–cloud interaction.

	CO_2	CH_4	N_2O	CFCs/ HCFCs	HFCs/ PFCs/ SF_6	BC ari	BC snow & ice	OC	Ozone	H_2O(Str)	Nitrate	Sul-phate	ERFaci	Total
Components emitted														
CO_2	1.68													**1.680**
CH_4	0.018	0.641							0.241	0.07				**0.970**
N_2O			0.17						0					**0.170**
CFCs/HCFCs/ halons				0.33					–0.15					**0.180**
HFCs/PFCs/SF_6					0.03									**0.030**
CO	0.087	0.072							0.075					**0.234**
NMVOC	0.033	0.025							0.042					**0.100**
NO_x		–0.254							0.143		–0.04			**–0.151**
NH_3											–0.07	0.01		**–0.060**
BC						0.60	0.04							**0.640**
OC								–0.29						**–0.290**
SO_2												–0.41		**–0.410**
Aerosols													–0.45	**–0.450**
SUM	**1.82**	**0.48**	**0.17**	**0.33**	**0.03**	**0.60**	**0.04**	**–0.29**	**0.35**	**0.07**	**–0.11**	**–0.40**	**–0.45**	

Table 8.SM.7 | Percentage uncertainty in values provided in Table 8.SM.6.

	Uncertainty (%)	Source
Components emitted		
CO_2	10	10% uncertainty in the total RF of CO_2 and combined with assumed 50% uncertainty for other contributions
CH_4	17	14% uncertainty in CH_4 contribution from Section 8.3.3, 55% uncertainty for contribution to ozone, 71% for stratospheric water vapour and 50% assumed for contribution to CO_2
N_2O	17	
CFCs/HCFCs/halons	85	10% uncertainty for direct effect and 100% for change in stratospheric ozone (see Section 8.3.3)
HFCs/PFCs/SF_6	10	
CO	24	30% uncertainty in CH_4 contribution Section 8.3.3, 37% for ozone contribution (Section 8.3.3) assumed 50% for contribution to CO_2
NMVOC	41	100% uncertainty in CH_4 contribution Section 8.3.3, 70% for ozone contribution and assumed 50% for contribution to CO_2
NO_x	(–124 to +116)	58% uncertainty in CH_4 contribution Section 8.3.3, 64% for ozone contribution and the range for nitrate as provided in Table 8.4
NH_3	(–172 to +73)	Same uncertainty as nitrate in Table 8.4
BC	(–61 to +70)	See Table 8.4 and Table 8.6 for BC from fossil fuel and biofuel and BC on snow and ice, respectively. BC from biomass burning is given as +0.2 (0.03 to 0.4); see Section 7.5.1.2
OC	(–63 to +72)	See Table 8.4 for OC from fossil fuel and biofuel. OC from biomass burning is given as –0.2 (–0.4 to –0.03); see Section 7.5.1.2
SO_2	50	See Table 8.4
ERFaci	(–167 to +100)	ERFaci –0.45 (–1.2 to 0.0); see Table 8.6

8.SM.9 Description of Forcing Time Series to Support Figure 8.18

Table 8.SM.8 | Supplementary for Figure 8.18: Time evolution forcing.

Forcing Agent	Data Sources for Time Evolution
WMGHG	WMGHG concentration as in Annex II. RF calculated based on formulas described in Section 8.3.2. Radiative efficiencies for halocarbons are given in Table 8.A.1.
Tropospheric ozone	Values for 1850, 1930, 1980 and 2000 from Atmospheric Chemistry and Climate Model Intercomparison Project (ACCMIP; Stevenson et al., 2013) and combined with higher temporal resolution from Oslo Chemical Transport Model 2 (Oslo CTM2; Skeie et al., 2011a).
Stratospheric ozone	The stratospheric ozone RF follows the functional shape of the Effective Equivalent Stratospheric Chlorine assuming a 3 years age of air (Daniel et al., 2010).
Stratospheric water vapour	RF is 15% of the CH_4 RF.
Total aerosol ERF	Values for 1850, 1930, 1980 and 2000 from ACCMIP (Shindell et al., 2013) combined with higher temporal results from Spectral Radiation-Transport Model for Aerosol Species (SPRINTARS) and Oslo CTM2 for the Industrial Era and Commonwealth Scientific and Industrial Research Organisation (CSIRO) and Geophysical Fluid Dynamics Laboratory (GFDL) models in addition for the 2000–2010 period. All four models included in Shindell et al. (2013). Note that Oslo CTM2 and CSIRO do not include rapid adjustment for the aerosol–cloud interaction.
Aerosol–radiation interaction	Values for 1850, 1930, 1980 and 2000 from ACCMIP (Shindell et al., 2013) combined with higher temporal results from Goddard Institute for Space Studies (GISS) and Oslo CTM2 models.
Surface albedo (land use change)	Based on an assessment of the time series from Skeie et al. (2011a), Hansen et al. (2011), Pongratz et al. (2009) and Schmidt et al. (2012). Time series scaled to fit the best estimate for 2011.
Surface albedo (BC on snow)	Values for 1850, 1930, 1980 and 2000 from ACCMIP (Lee et al., 2013) combined with higher temporal results from Oslo CTM2 (Skeie et al., 2011b).
Contrails	The best estimate for contrails (RF) or combined contrails and contrail induced cirrus (ERF) is scaled to aircraft kilometres flown in table downloaded from the following website: http://www.airlines.org/Pages/Annual-Results-World-Airlines.aspx.
Solar	TSI reconstructions (Krivova et al., 2010; Ball et al., 2012) standardized to Physikalisch-Meteorologisches Observatorium Davos (PMOD) and Total Irradiance Monitor (TIM) data is divided by 4 and multiplied by the Earth co-albedo (1 – 0.3) and multiplied with 0.78 to account for absorption in the stratosphere (see Section 8.4.1). TSI provided in the Supplementary Material Table 8.SM.3.
Volcanic aerosols	Mean of (Gao et al., 2008; Crowley and Unterman, 2013) between 1750 and 1850 and (Sato et al., 1993; updated version of April, 2013) from 1850 to present. RF is calculated as RF = AOD * (–25.0) W m^{-2}.

8.SM.10 Uncertainties in Trends in Forcing to Support Figure 8.19

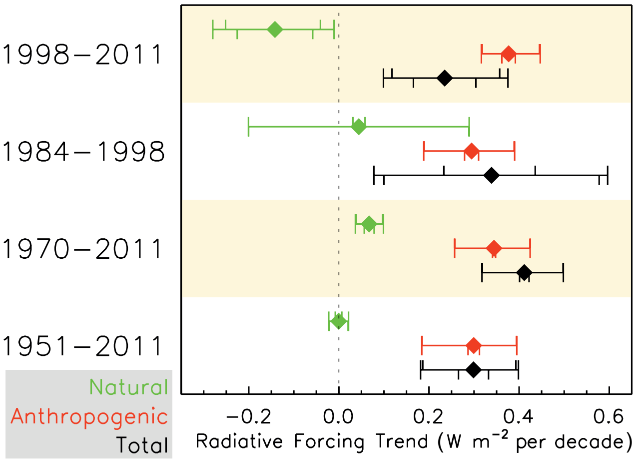

Figure 8.SM.3 | Linear trend in anthropogenic, natural and total forcing for the indicated years. The uncertainty ranges (90% confidence range) are combined from uncertainties in the forcing values (from Table 8.6) (upward vertical lines) and the uncertainties in selection of time period (downward vertical lines). Monte Carlo simulations were performed to derive uncertainties in the forcing based on ranges given in Table 8.6 and linear trends in forcing. The sensitivity to time periods has been derived from changing the time periods by ±2 years.

8.SM.11 Definition and Methods to Calculate Metric Values to Support Section 8.7.1

8.SM.11.1 Equations for the Global Warming Potential

The Absolute Global Warming Potential (AGWP) is the time-integrated radiative forcing due to a 1 kg *pulse* emission of gas *i* (usually in W m^{-2} yr kg^{-1}). The Global Warming Potential (GWP) for gas *i* is obtained by dividing the $AGWP_i$ by the AGWP of a reference gas, normally CO_2:

$$GWP_i(H) = \frac{AGWP_i(H)}{AGWP_{CO_2}(H)} = \frac{\int_0^H RF_i(t)\,dt}{\int_0^H RF_{CO_2}(t)\,dt} \qquad (8.SM.6)$$

where H is the time horizon; RF_i is the radiative forcing due to a *pulse* emission of a gas *i* given by

$$RF_i = A_i R_i \qquad (8.SM.7)$$

where A_i is the RF_i per unit mass increase in atmospheric abundance of species *i* (radiative efficiency (RE)), and R_i is the fraction of species *i* remaining in the atmosphere after the pulse emissions. The GWP are currently not defined using the Effective Radiative Forcing (ERF, Section 8.1.1.2), but this could be considered as a potential improvement of the concept.

For most species, R_i is based on a simple exponential decay,

$$R_i\left(t\right)=\exp\left(-\frac{t}{\tau_i}\right) \tag{8.SM.8}$$

where τ_i is the perturbation lifetime and thus, for these species,

$$AGWP_i\left(H\right)=\int_0^H RF_i\left(t\right)dt = A_i\tau\left(1-\exp\left(-\frac{H}{\tau}\right)\right) \tag{8.SM.9}$$

The atmospheric decay of a pulse consists of many different time scales (Prather, 1994). Nevertheless, for gases with atmospheric lifetimes larger than the mixing times of the major reservoirs (>3 years), the decay can be approximated as it is here with a single *e*-fold time equal to the perturbation lifetime. In this case the total integrated impacts are exact (Prather, 2007). For very short-lived gases (<1 year), the single *e*-fold also provides the correct integral, but the impacts occur over a longer time frame than expected from the perturbation lifetime.

For CO_2, R_i is more complicated because its atmospheric response time (or lifetime of a perturbation) cannot be represented by a simple exponential decay (Joos et al., 2013). The decay of a perturbation of atmospheric CO_2 following a pulse emission at time t is usually approximated by a sum of exponentials (Forster et al., 2007; Joos et al., 2013):

$$R_{CO_2}\left(t\right)=a_0+\sum_{i=1}^{N}a_i\exp\left(-\frac{t}{\tau_i}\right) \tag{8.SM.10}$$

The $AGWP_{CO2}$ is then (Shine et al., 2005):

$$AGWP_{CO_2}\left(H\right)=A_{CO_2}\left\{a_0H+\sum_{i=1}^{I}a_i\tau_i\left(1-\exp\left(-\frac{H}{\tau_i}\right)\right)\right\} \tag{8.SM.11}$$

8.SM.11.2 Equations for the Global Temperature Change Potential

The Absolute Global Temperature change Potential (AGTP) can be represented as (Boucher and Reddy, 2008; Fuglestvedt et al., 2010):

$$AGTP_i\left(H\right)=\int_0^H RF_i\left(t\right)R_T\left(H-t\right)dt \tag{8.SM.12}$$

where R_T is the climate response to a unit forcing and can be represented as a sum of exponentials,

$$R_T\left(t\right)=\sum_{j=1}^{M}\frac{c_j}{d_j}\exp\left(-\frac{t}{d_j}\right) \tag{8.SM.13}$$

where the parameters c_j are the components of the climate sensitivity and d_j are response times. The first term in the summation can crudely be associated with the response of the ocean mixed layer to a forcing and the higher order terms the response of the deep ocean (Li and Jarvis, 2009). The equilibrium climate sensitivity is given by the equilibrium response to a sustained unit forcing, $\lambda = \Sigma\, c_j$.

The simplest form of R_T is a single response term (M = 1) (Shine et al., 2005; Olivié et al., 2012). A better representation of the climate response, however, is two or three terms (M = 2, 3) (Boucher and Reddy, 2008; Li and Jarvis, 2009; Olivié et al., 2012). We use R_T from Boucher and Reddy (2008) which assumes two exponential terms and is based on the Hadley Centre Coupled Model version 3 (HadCM3) model (Table 8.SM.9). The climate sensitivity is 1.06 K (W m^{-2})$^{-1}$, equivalent to a 3.9 K equilibrium response to 2 × CO_2.

Using the equations above, the AGTP with a time horizon H for the non-CO_2 greenhouse gases:

$$AGTP_i\left(H\right)=A_i\sum_{j=1}^{2}\frac{\tau c_j}{\tau-d_j}\left(\exp\left(-\frac{H}{\tau}\right)-\exp\left(-\frac{H}{d_j}\right)\right) \tag{8.SM.14}$$

and the AGTP for CO_2 is

$$AGTP_{CO_2}(\mathrm{H})=A_{CO_2}\sum_{j=1}^{2}\left\{a_0c_j\left(1-\exp\left(-\frac{H}{d_j}\right)\right)+\sum_{i=1}^{3}\frac{a_i\tau_ic_j}{\tau_i-d_j}\left(\exp\left(-\frac{H}{\tau_i}\right)-\exp\left(-\frac{H}{d_j}\right)\right)\right\} \tag{8.SM.15}$$

Table 8.SM.9 | Parameter values for the response to a pulse of radiative forcing used in the AGTP calculations

	1st Term	2nd Term
c_j (K(W m^{-2})$^{-1}$)	0.631	0.429
d_j (years)	8.4	409.5

8.SM.11.3 Updates of Metric Values

The metric values need updating as a result of new scientific knowledge, but also because of changes in lifetimes and REs caused by changing atmospheric background conditions (Reisinger et al., 2011). For the reference gas CO_2, changes in $AGWP_{CO2}$ and $AGTP_{CO2}$ will affect the GWP and GTP of all other gases. With increasing CO_2 levels in the atmosphere the marginal RF is reduced, while at the same time the ocean uptake is reduced and airborne fraction increased (Caldeira and Kasting, 1993). These changes are in opposite directions, but do not totally cancel, and hence lead to changes in $AGWP_{CO2}$ (Figure 8.30) and $AGTP_{CO2}$.

To convert the RE values given per ppbv values to per kg (Shine et al., 2005), they must be multiplied by $(M_A/M_i)(10^9/T_M)$ where M_A is the mean molecular weight of air (28.97 kg kmol^{-1}), M_i is the molecular weight of species i and T_M is the total mass of the atmosphere, 5.1352 × 10^{18} kg (Trenberth and Smith, 2005).

8.SM.11.3.1 Metric Values for Carbon Dioxide

The radiative forcing for CO_2 can be approximated using the expression based on radiative transfer models (Myhre et al., 1998):

$$RF = \alpha \log\left(\frac{C_0 + \Delta C}{C_0}\right) \qquad (8.SM.16)$$

where $\alpha = 5.35$ W m^{-2}, C_0 is the reference concentration and ΔC is the change from the reference. The radiative efficiency is the change in RF for a change in the atmospheric abundance,

$$RE = \frac{\Delta RF}{\Delta C} = \alpha \left(\log\left(\frac{C_0 + \Delta C}{C_0}\right) \Big/ \Delta C \right) \qquad (8.SM.17)$$

or if $\Delta C \rightarrow 0$ then the derivative can be used:

$$RE = \left.\frac{dRF}{d\Delta C}\right|_{\Delta C = 0} = \frac{\alpha}{C_0} \qquad (8.SM.18)$$

At current CO_2 levels (391 ppm) and for $\Delta C = 1$ ppm, the radiative efficiency (RE) of CO_2 is 1.37 * 10^{-05} W m^{-2} ppb^{-1}. The difference between using $\Delta C = 1$ ppm and the derivate is 0.13%. For CO_2, using a molecular weight of 44.01 kg kmol^{-1}, the A becomes 1.7517 * 10^{-15} W m^{-2} kg^{-1}.

The impulse response function (IRF) has been updated from AR4. Table 8.SM.10 shows the parameters of the IRF used in AR5 based on Joos et al. (2013) and Figure 8.SM.4 shows the IRFs from the four previous IPCC assessment reports together with the new IRF used in AR5. Table 8.SM.11 gives calculated values for integrated IRF and AGWPs for CO_2.

Table 8.SM.10 | Parameter values for the sum of exponentials (Equation 8.SM.10) describing the fraction of CO_2 remaining in the atmosphere after a pulse emission of CO_2 (Joos et al., (2013).

	1st Term	2nd Term	3rd Term	4th Term
Coefficient (unitless)	0.2173	0.2240	0.2824	0.2763
Time Scale (τ_i, years)	-	394.4	36.54	4.304

Table 8.SM.11 | Mean and uncertainty range for the time-integrated IRF and AGWP from Joos et al. (2013). The AGWP for AR5 uses the integrated IRF based on Equation 8.SM.10 and Table 8.SM.9 and a radiative efficiency for a 1 ppm change at 391 ppm.

	20-Year	100-Year
Time-integrated IRF (year)		
Mean	14.2	52.4
5–95% range	12.2–16.3	39.5–65.2
AGWP (10^{-15} W m^{-2} yr kg^{-1})		
Mean	25.2	92.5
5 to 95% range	20.7–29.6	67.9–117
AR5 AGWP (10^{-15} W m^{-2} yr kg^{-1})	24.9	91.7

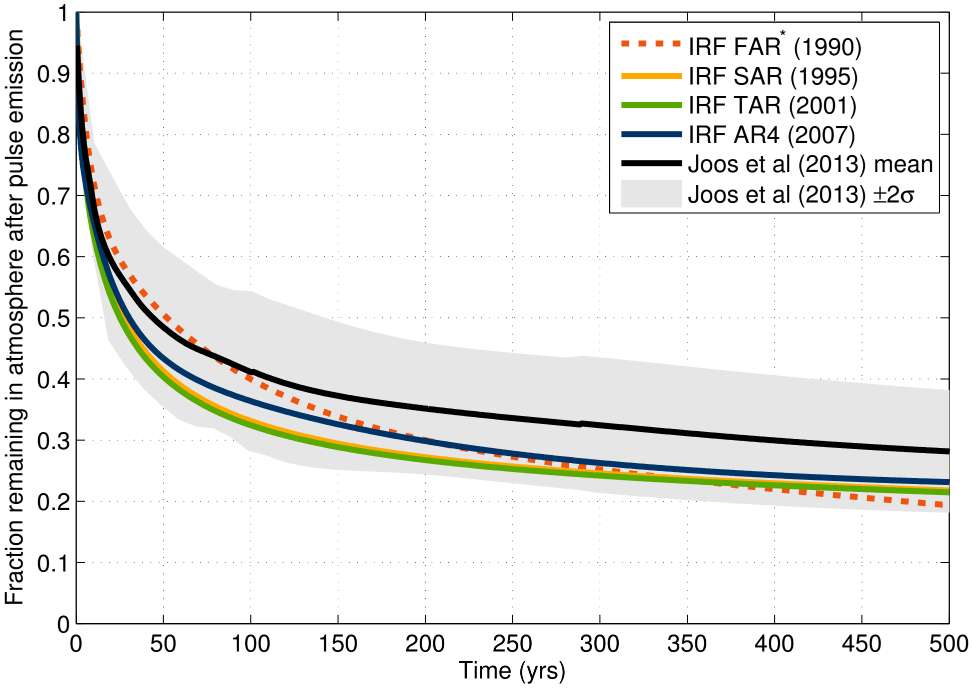

Figure 8.SM.4 | The impulse response functions (IRFs) from the five IPCC Assessment Reports. The First Assessment Report (FAR) IRF (dotted) is based on an unbalanced carbon-cycle model (ocean only) and thus is not directly comparable to the others. The Second Assessment Report (SAR) IRF is based the CO_2 response of the Bern model (Bern-SAR), an early generation reduced-form carbon cycle model (Joos et al., 1996), and uses a 10 GtC pulse emission into a constant background without temperature feedbacks (Enting et al., 1994). The IRF was not updated for the Third Assessment Report (TAR), but a different parameterisation was used in World Meterological Organisation (WMO)/United Nations Environment Programme (UNEP) Scientific Assessment of Ozone Depletion: 1998 (WMO, 1999) The Fourth Assessment Report (AR4) IRF is based on the Bern 2.5CC Earth System Model of Intermediate Complexity (EMIC) (Plattner et al., 2008). A pulse size of 40 GtC is used and includes temperature feedbacks. The Fifth Assessment Report (AR5) IRF is based on a model intercomparison and uses a pulse size of 100 GtC and includes temperature feedbacks (Joos et al., 2013). Apart from FAR, the changing IRF in each assessment report represents increasing background concentrations and improved models.

8.SM.11.3.2 Metric Values for Methane

The RE of CH_4 is scaled to include effects on ozone and stratospheric H_2O, so that the AGWP becomes

$$AGWP_{CH_4}(H) = (1+f_1+f_2) A_{CH_4} \int_0^H e^{-t/\tau} dt =$$

$$(1+f_1+f_2) A_{CH_4} \tau \left(1-e^{-H/\tau}\right) \qquad (8.SM.19)$$

where f_1 is due to effects on ozone and f_2 is due to stratospheric H_2O. The AGTP is modified in a similar way.

These indirect effects were included in AR4 by increasing the direct RF from CH_4 by 25% (due to tropospheric ozone) and 15% (due to stratospheric H_2O). New studies provide updated values and include more effects. By accounting for aerosol responses, Shindell et al. (2009) found that the GWP for CH_4 increased by about 40% while Collins et al. (2010) found that the GTP for CH_4 increased by 5 to 30% when the effect of ozone on CO_2 was included. Boucher et al. (2009) included the effect of CO_2 from oxidation of CH_4 from fossil sources and calculated a GWP_{100} higher than given in AR4 (27 to 28 versus 25). They found that CO_2 oxidation had a larger effect on GTP values and this effect was larger than the direct CH_4 effect for time horizons beyond 100 years.

In AR5 we use updated estimates for the indirect effects of CH_4 on ozone based on recent studies (Shindell et al., 2005; Shindell et al., 2009; Collins et al., 2013; Holmes et al., 2013; Stevenson et al., 2013). Based on these studies we assess the indirect effect on ozone (tropospheric and stratospheric) to $f_1 = 0.5$ (0.2 to 0.8) of the direct effect. The indirect RF from CH_4 via changes in stratospheric H_2O is retained as $f_2 = 0.15$ of the direct effect. Thus, we increase the direct effect of CH_4 by $f_1 + f_2 = 0.65$ to account for RF from both O_3 and stratospheric H_2O. We also present metric values for CH_4 of fossil origin (based on Boucher et al., (2009); Table 1). If these metric values are used the carbon emitted as CH_4 must not be included in the CO_2 emissions (which are often based on total carbon content).

8.SM.11.3.3 Metric Values for Nitrous Oxide

The indirect effect of increased N_2O abundance on CH_4 changes via stratospheric ozone, UV fluxes and OH levels is included in GWPs and GTPs. The reduction in CH_4 (–36 molecules per +100 molecules N_2O) offsets some of the climate impact from N_2O emissions. The AGWP becomes

$$AGWP_{N_2O}(H) = A_{N_2O}\left(1-0.36(1+f_1+f_2)\frac{RE_{CH_4}}{RE_{N_2O}}\right)\tau\left(1-e^{-H/\tau}\right) \qquad (8.SM.20)$$

where f_1 and f_2 are the indirect effects for CH_4. The AGTP is modified in a similar way.

8.SM.11.4 Time Horizons

In previous IPCC assessments, GWP values were given for 20-, 100- and 500-year time horizons, while here we only use 20 and 100 years. Instead of using GWP values for 500 years we show the response to emissions of some extremely long-lived gases such as PFCs; see Figure 8.SM.5. Once these gases are emitted they stay in the atmosphere and contribute to warming on very long time scales (99% of an emission of PFC-14 is still in the atmosphere after 500 years). For comparison

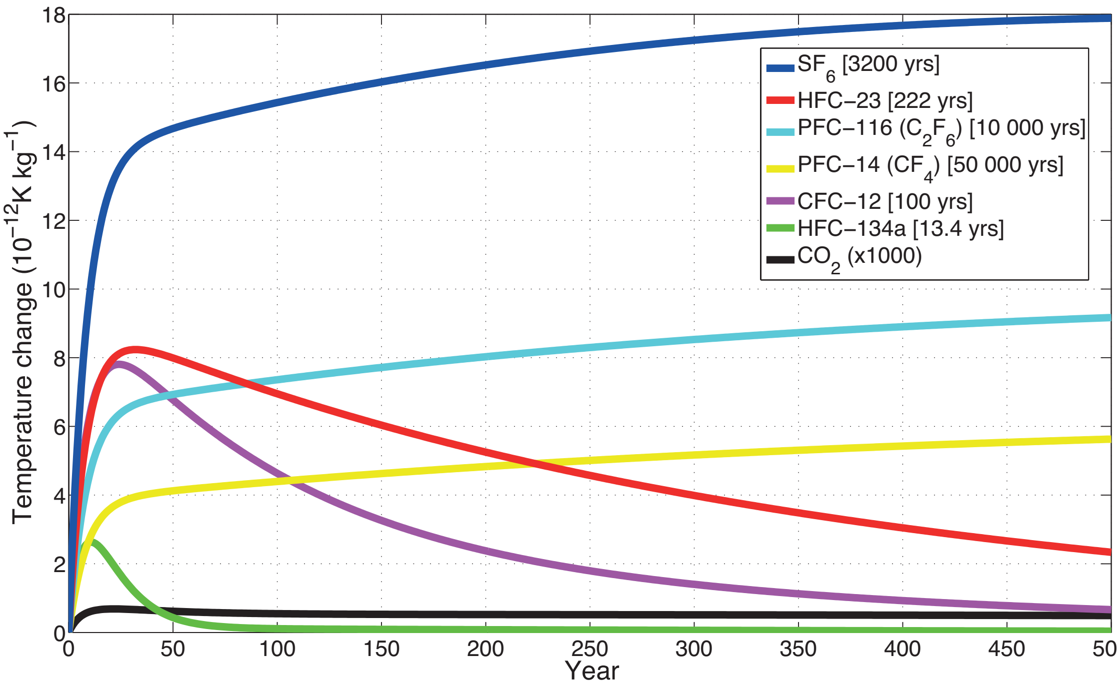

Figure 8.SM.5 | Temperature response due to 1-kg pulse emissions of greenhouse gases with a range of lifetimes (given in parentheses). Calculated with a temperature impulse response function taken from Boucher and Reddy (2008) which has a climate sensitivity of 1.06 K (W m^{-2})$^{-1}$, equivalent to a 3.9 K equilibrium response to 2 × CO_2 (unit for carbon dioxide is kg CO_2).

we also include gases with lifetimes of the order of centuries down to a decade. A 1 kg pulse of SF_6 has a temperature effect after 500 years that is of the order of 35,000 larger than that of CO_2. The corresponding numbers for CF_4 and C_2F_6 are 11,000 and 18,000, respectively. There are large uncertainties related to temperature responses (as well as the CO_2 response) on time-scales of centuries, but these results nevertheless indicate the persistence and long-lived warming effects of these gases.

One reason for not using a time horizon of 500 years is the increasing uncertainty in radiative efficiency, carbon uptake and ambiguity in the interpretation of GWP_{500}, especially for gases with short adjustment times relative to the time scale of the CO_2 perturbation. As explained in Section 8.7.1.2, the GWP gives the ratio of two integrals: one of a pulse of a non-CO_2 gas that decays to zero and that of the CO_2 response for which 20 to 40% of a pulse remains in the atmosphere for centuries. Figure 8.SM.5 also shows that the temperature response to a pulse of the relatively short-lived HFC-134a is close to zero for several centuries before the 500-year time horizon, while the GWP_{500} is 371. This example highlights how the integrated nature of GWP means that the GWP value at a particular time may give misleading information about the climate impacts at that time, as the time scale used in the GWP becomes very different from the residence time of the emitted compound.

8.SM.12 Uncertainty Calculations for Global Warming Potential to Support Section 8.7.1

In the absence of detailed uncertainty assessment, a first estimate of uncertainty for a given function, *f*, and input parameters, x_i, can be based on a first-order Taylor expansion of the variance in *f* leading to the well-known adding in quadrature approximation (Morgan and Henrion, 1990),

$$\Delta f = \sqrt{\sum_i (\Delta f_i)^2} = \sqrt{\sum_i \left(\frac{\partial f}{\partial x_i} \Delta x_i \right)^2} \qquad (8.SM.21)$$

where Δf represents the uncertainty of each term, defined as the sensitivity to a marginal change multiplied by the error in the term. This approximation assumes that the uncertainties are small, $\Delta x_i \ll x_i$, the uncertainties are normally distributed, *f* is smooth for the range of input values and, most importantly, the uncertainties are independent.

If *f* is a product of two terms ($f = xy$), then it can be shown that

$$\left(\frac{\Delta f}{f} \right)^2 = \left(\frac{\Delta x}{x} \right)^2 + \left(\frac{\Delta y}{y} \right)^2 \qquad (8.SM.22)$$

We estimate the uncertainty in $AGWP_{CO2}$ using the uncertainty in A_{CO2} and I_{CO2},

$$AGWP_{CO_2}(H) = A_{CO_2} I_{CO_2}(H)$$

where

$$I_{CO_2}(H) = \int_0^H IRF_{CO_2}(t)\,dt \qquad (8.SM.23)$$

In the case of the AGWP for non-CO_2 species, the expression becomes

$$\Delta AGWP = \sqrt{\left(\frac{\partial AGWP}{\partial A} \right)^2 \Delta A^2 + \left(\frac{\partial AGWP}{\partial \tau} \right)^2 \Delta \tau^2}$$

for

$$f = AGWP(A, \tau) \qquad (8.SM.24)$$

where the expressions for the AGWP are from Equations 8.SM.9, 8.SM.19 and 8.SM.20. The uncertainty in the AGWP for CO_2 is based on Equation 8.SM.23.

Table 8.SM.12 shows the uncertainty data and source used in the analysis. Many of the input parameters are given for a 1-σ range and we scale the uncertainty by 1.645 to convert to 90% confidence for consistency with rest of AR5. In some cases this represents a strong and uncertain assumption since the high-end uncertainties are not necessarily well defined. The estimated uncertainties should be seen as a rough first order evaluation to get an impression of the order of magnitude and the main contributions to total uncertainty.

Table 8.SM.13 shows the uncertainty for the AGWP of CO_2, CH_4, N_2O, CFC-11, CFC-12 and HFC-134a, Table 8.SM.14 shows the corresponding uncertainty for the GWPs, and Figure 8.SM.6 shows the contribution of each term Δf_i in Equation 8.SM.21 to the uncertainty. The uncertainty in AGWP is generally dominated by the perturbation lifetime, though this varies depending on the lifetime relative to the time horizon. The uncertainty in the $AGWP_{CH4}$ has an important contribution from the indirect effects, particularly the forcing from ozone changes. Except for CH_4, the uncertainty in the GWPs is dominated by the uncertainty in $AGWP_{CO2}$.

Table 8.SM.12 | Uncertainty data, assumptions and sources used for the analysis. Note that uncertainties are assumed to be normally distributed and further analysis is required to determine the correct distribution.

Term	Expected Value (x)	Uncertainty (±Δx, 5 to 95%)	Notes
A_{CO2}	Table 8.A.1	10%, Section 8.3.1	
I_{CO2}	Joos et al. (2013)	Joos et al. (2013)	
A_{CH4}	Table 8.A.1	10%, Section 8.3.1	Value before adjusting for ozone and stratospheric H_2O
τ_{CH4}	Section 8.2.3.3	18.57%, Section 8.2.3.3	One standard deviation uncertainty of 1.4/12.4 scaled by 1.645 to convert to 90% confidence
f_1	0.5 Ozone, see Equation 8.SM.19	60%	Uncertainty is 0.2–0.8
f_2	0.15, see Equation 8.SM.19	71.43%, Table 8.6	Uncertainty is 0.02–0.12
A_{N2O}	Table 8.A.1	10%, Section 8.3.1	
τ_{N2O}	Table 8.A.1	12.99%, Prather et al. (2012), Section 8.2.3.4	One standard deviation uncertainty of 7.9% scaled by 1.645 to convert to 90% confidence
$A_{CFC\text{-}11}$	Table 8.A.1	10%, Section 8.3.1	
$\tau_{CFC\text{-}11}$	Table 8.A.1	22.55%, Rigby et al. (2013)	One standard deviation uncertainty of 13.71% scaled by 1.645 to convert to 90% confidence
$A_{CFC\text{-}12}$	Table 8.A.1	10%, Section 8.3.1	
$\tau_{CFC\text{-}12}$	Table 8.A.1	28.76%, Rigby et al. (2013)	One standard deviation uncertainty of 17.49% scaled by 1.645 to convert to 90% confidence
$A_{HFC\text{-}134a}$	Table 8.A.1	10%, Section 8.3.1	
$\tau_{HFC\text{-}134a}$	Table 8.A.1	17.9%, Prather et al. (2012)	One standard deviation uncertainty of 10.9% scaled by 1.645 to convert to 90% confidence

Table 8.SM.13 | The estimated uncertainty in the AGWP for CO_2, CH_4, CFC-11, CFC-12, and HFC-134a showing the results of the full uncertainty analysis ('Full') and the effects of adding the uncertainty of different terms one at a time in the order (from left to right) of the next largest contributions. All values (±Δx) are percentages of the expected value, x, for a 90% confidence interval.

Time Horizon (years)	$\Delta AGWP_{CO2}$			$\Delta AGWP_{CH4}$				$\Delta AGWP_{N2O}$			
	$+I_{CO2}$	$+A_{CO2}$	Full	$+f_i$	$+\tau_{CH4}$	$+A_{CH4}$	Full	$+A_{N2O}$	$+\tau_{CH4}$	$+CH_4$	Full
20	14	18	18	19	22	24	24	11	11	11	11
100	25	26	26	19	27	29	29	11	12	12	12
500	28	30	30	19	27	29	29	11	26	16	16

Time Horizon (years)	$\Delta AGWP_{CFC\text{-}11}$			$\Delta AGWP_{CFC\text{-}12}$			$\Delta AGWP_{HFC\text{-}134a}$		
	$+\tau_{CFC\text{-}11}$	$+A_{CFC\text{-}11}$	Full	$+\tau_{CFC\text{-}12}$	$+A_{CFC\text{-}12}$	Full	$+\tau_{HFC\text{-}134a}$	$+A_{HFC\text{-}134a}$	Full
20	5	11	11	3	10	10	10	14	14
100	16	19	19	12	16	16	18	20	20
500	23	25	25	28	30	30	18	21	21

Table 8.SM.14 | The estimated uncertainty in the GWP for CH_4, N_2O, CFC-11, CFC-12, and HFC-134a showing the results of the full uncertainty analysis ('Full') and the effects of adding the uncertainty of different terms one at a time in the order (from left to right) of the next largest contributions. All values (±Δx) are percentages of the expected value, x, for a 90% confidence interval. $+CO_2$ represents the uncertainty in $AGWP_{CO2}$.

Time Horizon (years)	ΔGWP_{CH4}					ΔGWP_{N2O}				
	$+CO_2$	$+f_i$	$+\tau_{CH4}$	$+A_{CH4}$	Full	$+CO_2$	$+A_{N2O}$	$+\tau_{CH4}$	$+CH_4$	Full
20	18	26	28	30	30	18	21	21	21	21
100	26	33	38	39	39	26	29	29	29	29
500	30	35	40	41	41	30	32	34	34	34

Time Horizon (years)	$\Delta GWP_{CFC\text{-}11}$				$\Delta GWP_{CFC\text{-}12}$				$\Delta GWP_{HFC\text{-}134a}$			
	$+CO_2$	$+\tau_{CFC\text{-}11}$	$+A_{CFC\text{-}11}$	Full	$+CO_2$	$+\tau_{CFC\text{-}12}$	$+A_{CFC\text{-}12}$	Full	$+CO_2$	$+\tau_{HFC\text{-}134a}$	$+A_{HFC\text{-}134a}$	Full
20	18	18	21	21	18	18	20	20	18	20	23	23
100	26	31	33	33	26	29	31	31	26	32	33	33
500	30	37	39	39	30	41	42	42	30	35	36	36

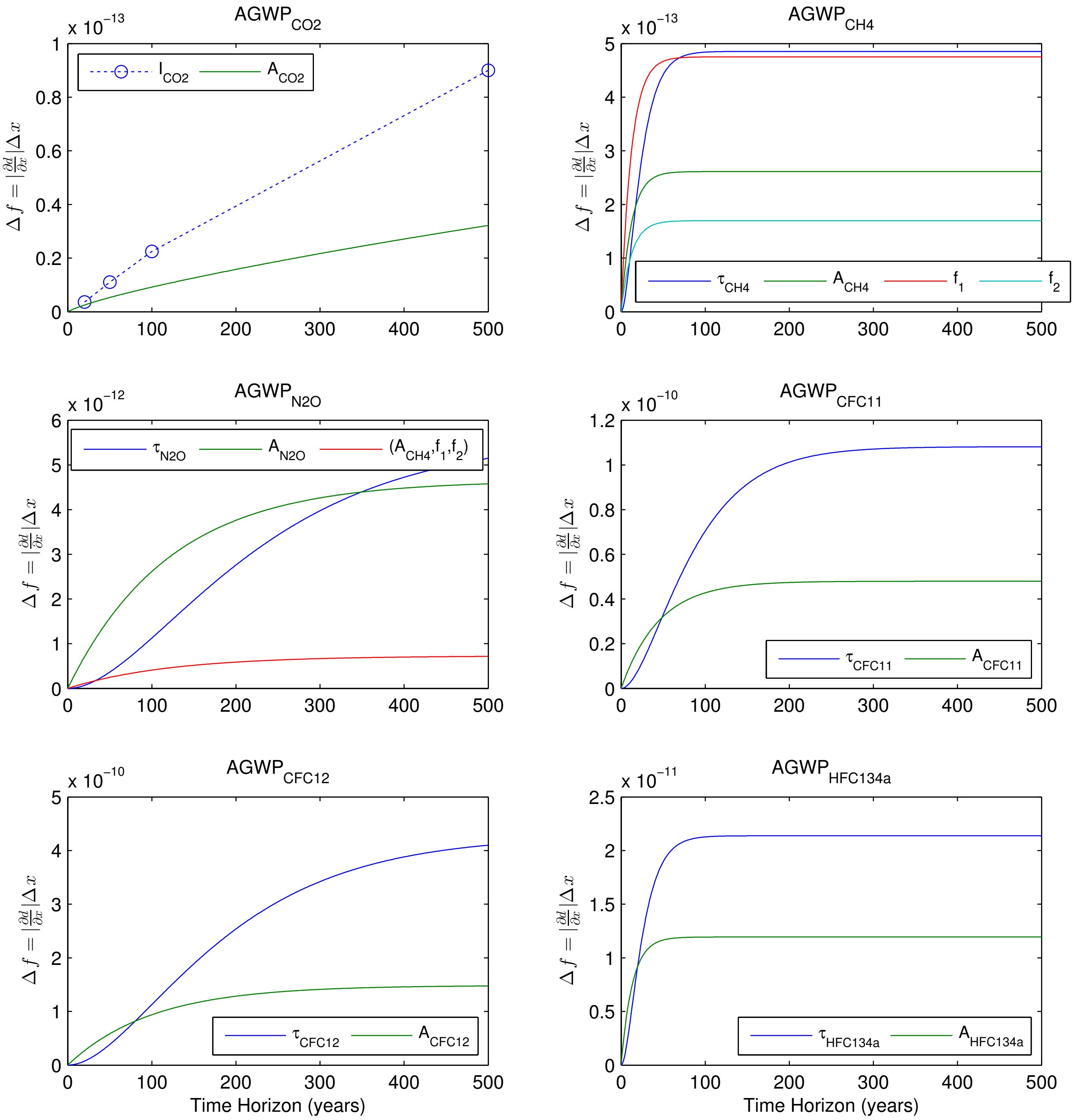

Figure 8.SM.6 | The contribution of each term to the uncertainty in the AGWP, ΔAGWP is obtained by adding each term in quadrature according to Equation 8.SM.21. I_{CO2} has data available only for four data points. For AGWP$_{N2O}$ the contribution from the radiative efficiency and indirect effect of CH_4 are combined in quadrature. In uncertainty analysis, the contributions are added in quadrature (Equation 8.SM.21), which will amplify the differences.

8.SM.13 Calculations of Metric Values for Halocarbons to Support Section 8.7.2

The method used to calculate the radiative efficiencies (REs) and GWPs in Table 8.A.1 is discussed briefly here. More details are available at the following website: http://cicero.uio.no/halocarbonmetrics/.

8.SM.13.1 Lifetimes

The lifetime of each compound is taken from WMO (2011) when available. For some compounds, when WMO lifetimes are not available, lifetimes are taken from the published literature (sources of lifetime estimates are given here: http://cicero.uio.no/halocarbonmetrics/). For a few compounds, lifetimes could not be found in the literature and only the RE (and not the GWP) could be calculated. The REs of these compounds, assuming a homogeneous mixing in the atmosphere, are given in Table 8.SM.15.

8.SM.13.2 Absorption Cross Sections

The absorption cross sections used for the RE and GWP calculations come from a variety of sources, including the High-Resolution Transmission (HITRAN)-2008 (Rothman et al., 2009) and Gestion et Etude des Informations Spectroscopiques Atmosphériques (GEISA)-2011 (Jacquinet-Husson et al., 2011) databases, authors of published papers, and supplementary material to published papers. A table that lists the absorption cross-sections used to calculate the RE for each compound can be found at the following website: http://cicero.uio.no/halocarbonmetrics/. Experimental absorption cross-sections have been used for the majority of compounds, but for a few compounds theoretical spectra were used because of unavailability of experimental spectra.

8.SM.13.3 Instantaneous Radiative Efficiency

The simple method from Pinnock et al. (1995) has been adopted here for the calculation of RE, except that a revised version of the Pinnock et al. curve has been used. This ensures a common method for deriving RE from absorption cross sections, and hence greater internal consistency, in contrast to the many different methods/assumptions used for calculation of RE used in the literature. The new curve, at 1 cm^{-1} spectral resolution (rather than the original 10 cm^{-1} resolution used in Pinnock et al., (1995) is based on calculations with the Oslo Line-by-Line (LBL) model (Myhre et al., 2006), and is shown in Figure 8.SM.7.

Table 8.SM.15 | Calculated radiative efficiencies (REs) for compounds where lifetime estimates are unknown. Note that homogeneous mixing in the atmosphere is assumed; hence the REs presented here are probably upper estimates.

Common Name or Chemical Name	Chemical Formula	Radiative Efficiency (W m^{-2} ppb^{-1})
1,1,1,3,3,3-Hexafluoro-2-(trifluoromethyl)-2-propanol	$(CF_3)_3COH$	0.38
HG’-10	$CH_3OCF_2OCH_3$	0.26
HG’-20	$CH_3O(CF_2O)_2CH_3$	0.72
HG’-30	$CH_3O(CF_2O)_3CH_3$	1.14
HFE-338mec3	$CF_3CFHCF_2OCF_2H$	0.51
Fluoromethyl carbonofluoridate	$FCOOCFH_2$	0.19
Difluoromethyl carbonofluoridate	$FCOOCF_2H$	0.33
Trifluoromethyl carbonofluoridate	$FCOOCF_3$	0.32
Perfluoroethyl carbonofluoridate	$FCOOCF_2CF_3$	0.48
2,2,2-Trifluoroethyl carbonofluoridate	$FCOOCH_2CF_3$	0.33
Perfluoropropyl carbonofluoridate	$FCOOCF_2CF_2CF_3$	0.53
Trifluoromethyl 2,2,2-trifluoroacetate	CF_3COOCF_3	0.49
Perfluoroethyl 2,2,2-trifluoroacetate	$CF_3COOCF_2CF_3$	0.62
1,1,1,3,3,3-Hexafluoropropan-2-yl 2,2,2-trifluoroacetate	$CF_3COOCH(CF_3)_2$	0.49
Vinyl 2,2,2-trifluoroacetate	$CF_3COOCH{=}CH_2$	0.39
Allyl 2,2,2-trifluoroacetate	$CF_3COOCH_2CHCH_2$	0.35
Phenyl 2,2,2-trifluoroacetate	CF_3COOPh	0.39
Methyl 2-fluoroacetate	$H_2CFCOOCH_3$	0.08
Difluoromethyl 2,2-difluoroacetate	$HCF_2COOCHF_2$	0.44
4,4,4-Trifluorobutanal	$CF_3(CH_2)_2CHO$	0.16

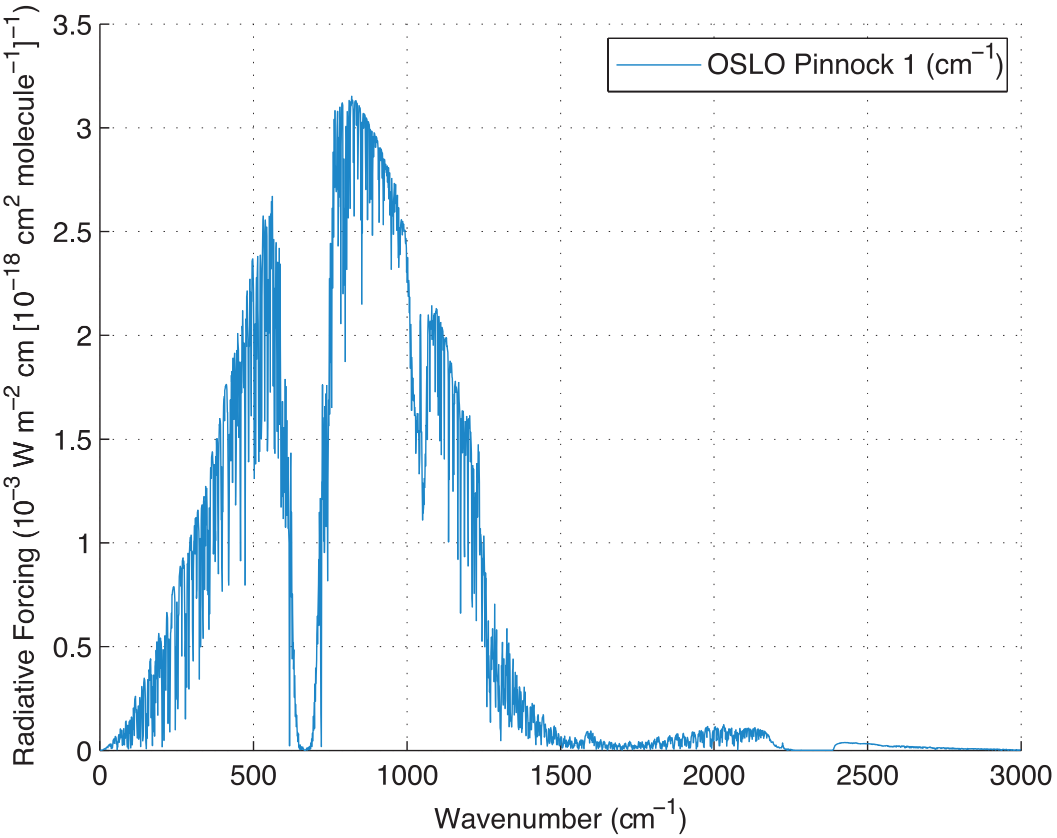

Figure 8.SM.7 | Radiative forcing efficiency (for a 0 to 1 ppbv increase in mixing ratio) per unit cross section calculated with the Oslo Line-by-Line (LBL) model.

8.SM.13.4 Stratospheric Temperature Adjustment

The revised Pinnock et al. curve shown in Figure 8.SM.7 applies for instantaneous radiative forcing efficiency. To take into account stratospheric temperature adjustment, a factor has been applied based on results from previous studies. For most compounds, the instantaneous REs have been increased by 10% (Pinnock et al., 1995; Myhre and Stordal, 1997; Jain et al., 2000; Naik et al., 2000; Forster et al., 2005) to account for stratospheric temperature adjustment. For a few selected compounds, explicit model calculations have been carried out using the Oslo LBL model (Myhre et al., 2006). These calculations show increases of 9.1%, 10.5%, and 10.5% for CFC-11, CFC-12 and CF_4, respectively, when taking into account the stratospheric temperature adjustment, while there is a reduction of 5.0% for HFC-41. The assumed increase of 10% for the remaining compounds is considered a good approximation, based on our calculations and the literature (e.g., Pinnock et al., 1995; Myhre and Stordal, 1997).

8.SM.13.5 Lifetime Correction

Fractional correction factors to the RE, to take into account the non-uniform mixing in the atmosphere, have previously been presented in Freckleton et al. (1998) and Sihra et al. (2001). Here, the method of Sihra et al. (2001) has been extended by including the results of Sellevag et al. (2004), and by carrying out new calculations using essentially the same models (Oslo CTM2, Søvde et al., 2008); and Oslo Broadband model, (Myhre and Stordal, 1997) and a similar setup as in Sellevag et al. (2004). One fractional correction curve has been calculated for the compounds dominated by loss through photolysis in the stratosphere, and one curve for compounds that are lost mainly by reaction with OH. The first curve was calculated by applying an exponential curve fit which gives the formula $f(\tau) = 1 - 0.1826\ \tau^{-0.3339}$, where f is the fractional correction and τ is the lifetime in years. The empirical fit for the latter curve was constrained to form an *S*-shaped curve with the formula $f(\tau) = (a\tau)^b / (1 + c\tau^d)$, and the constants have values $a = 2.962$, $b = 0.9312$, $c = 2.994$ and $d = 0.9302$. The resulting two curves are shown in Figure 8.SM.8 and have been applied when calculating REs and GWPs for compounds where the lifetime is known. For shorter-lived compounds (less than about 2 to 3 years), the fractional correction depends on where the compound is emitted and so no unique curve can be defined. Here it has been assumed that the geographical distribution is similar to the approach in Sellevag et al. (2004). These fractional corrections have been made to the RE after the instantaneous RE has been modified for stratospheric temperature adjustment as described in the paragraph above.

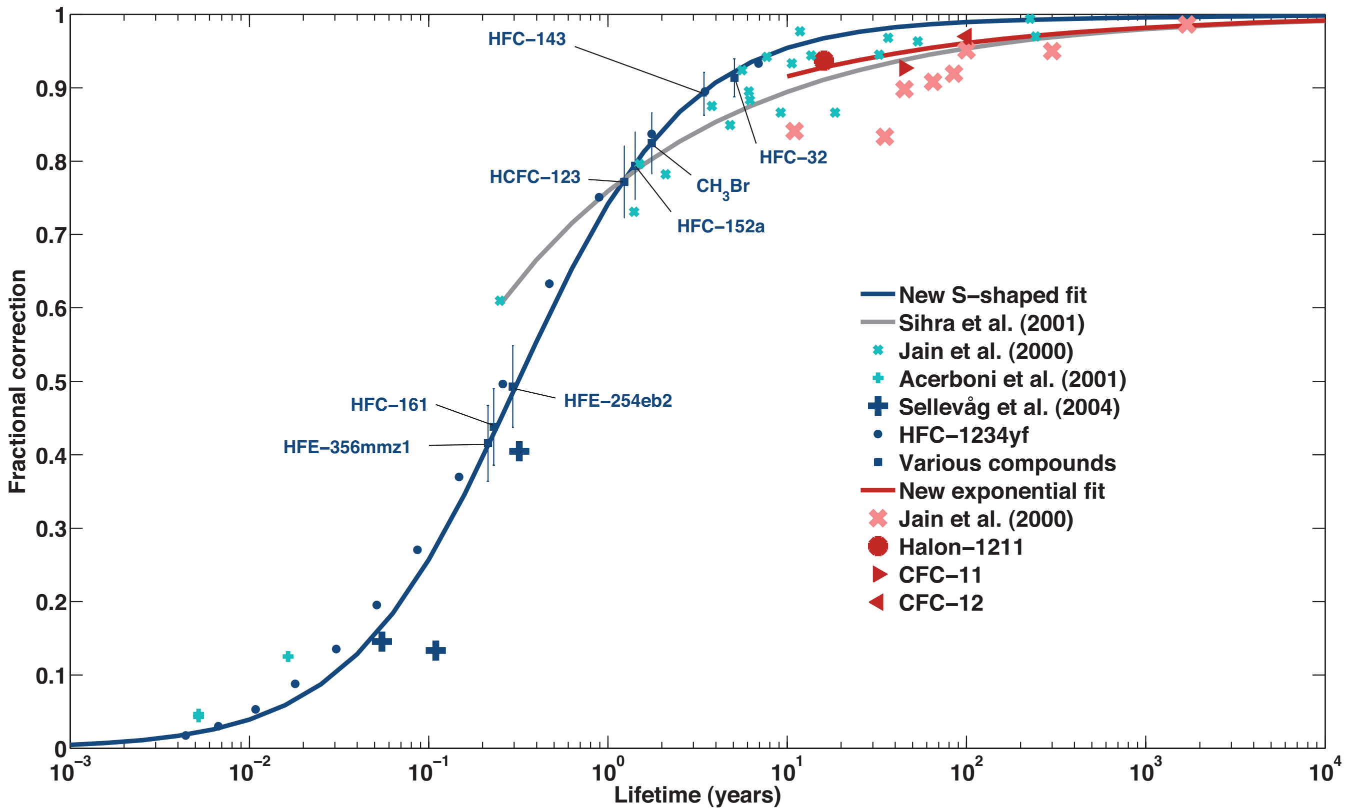

Figure 8.SM.8 | Factor needed to correct radiative efficiency (RE) to account for non-uniform vertical and horizontal distribution versus atmospheric lifetime. The red symbols are for compounds whose main loss mechanism is stratospheric photolysis while the blue symbols are for compounds that are lost in the troposphere mainly by reaction with OH. Dark blue symbols have been used in the calculation of the *S*-shaped fit and dark red symbols have been used in the calculation of the exponential fit. Light blue and light red symbols are shown for comparison. The curve from Sihra et al. (2001) represents an empirical least squares fit to the fractional correction factors from Jain et al. (2000). For compounds where several different absorption bands have been used in the RF calculations, both the mean and the standard deviation of the fractional corrections are shown.

8.SM.14 Metric Values for Other Near-Term Climate Forcers to Support Section 8.7.2

Derwent et al. (2001) report a GWP$_{100}$ of 5.8 for the effects of H$_2$ emissions on CH$_4$ and ozone. For global emissions of SO$_2$ Fuglestvedt et al. (2010) calculated GWPs of –140 and –40 for 20 and 100 years, respectively. The GTPs are –41 and –6.9 for the same time horizons (for both metrics the values are given on an SO$_2$ basis and account only for the aerosol radiation interaction of sulphate). For SO$_2$ Shindell et al. (2009) calculated –22 ± 20 (aerosol–radiation interaction only) and –76 ± 69 (aerosol–radiation interaction and aerosol–cloud interactions) for GWP$_{100}$, and –78 ± 70 and –268 ± 241 for GWP$_{20}$. For NH$_3$ Shindell et al. (2009) calculated –19 ± 22 (aerosol-radiation interaction only) and –15 ± 18 (aerosol–radiation interaction and aerosol–cloud interactions) for GWP$_{100}$, and –65 ± 76 and –53 ± 62 for GWP$_{20}$. Due to competition for ammonium between nitrate and sulphate, the net aerosol forcing from either SO$_2$ or NH$_3$ emissions is the residual of larger responses of opposite signs, which leads to the high uncertainty in their numbers. (These values are based on IRF for CO$_2$ from AR4.) The GWP$_{100}$ and GTP$_{100}$ values can be scaled by 0.94 and 0.92, respectively, to account for updated values for the reference gas CO$_2$.

8.SM.15 Metric Values for Halocarbons Including Climate–Carbon Feedback for Carbon Dioxide to Support Section 8.7.2

Table 8.SM.16 | GWP and GTP with climate–carbon feedbacks included for halocarbons. The additional effect (delta) and the total effect are given. (Climate–carbon feedbacks in response to the reference gas CO_2 are always included).

Acronym, Common Name or Chemical Name	AGWP 20-year (W m^{-2} yr kg^{-1})	GWP 20-year	AGWP 100-year (W m^{-2} yr kg^{-1})	GWP 100-year	AGTP 20-year (K kg^{-1})	GTP 20-year	AGTP 50-year (K kg^{-1})	GTP 50-year	AGTP 100-year (K kg^{-1})	GTP 100-year
CFC-11										
Delta	3.04E-12	122	6.32E-11	689	1.29E-13	189	4.32E-13	701	6.32E-13	1156
Total	1.75E-10	7020	4.91E-10	5352	4.84E-12	7078	3.45E-12	5589	1.91E-12	3491
CFC-12										
Delta	4.53E-12	182	1.20E-10	1308	1.94E-13	283	7.45E-13	1208	1.34E-12	2459
Total	2.74E-10	10,976	1.06E-09	11,547	7.90E-12	11,549	7.50E-12	12,160	5.96E-12	10,907
CFC-13										
Delta	4.40E-12	177	1.43E-10	1558	1.89E-13	277	8.09E-13	1312	1.76E-12	3221
Total	2.75E-10	11,040	1.42E-09	15,451	8.18E-12	11,960	9.58E-12	15,530	1.05E-11	19,144
CFC-113										
Delta	2.75E-12	110	6.99E-11	762	1.17E-13	171	4.41E-13	716	7.69E-13	1407
Total	1.65E-10	6600	6.04E-10	6586	4.72E-12	6902	4.29E-12	6963	3.22E-12	5880
CFC-114										
Delta	3.18E-12	127	9.38E-11	1023	1.36E-13	199	5.55E-13	900	1.11E-12	2026
Total	1.96E-10	7839	8.82E-10	9615	5.74E-12	8385	6.12E-12	9922	5.79E-12	10,579
CFC-115										
Delta	2.37E-12	95	7.81E-11	851	1.02E-13	149	4.39E-13	712	9.69E-13	1772
Total	1.49E-10	5954	7.81E-10	8516	4.42E-12	6463	5.25E-12	8517	5.88E-12	10,749
HCFC-21										
Delta	4.72E-13	19	2.91E-12	32	1.71E-14	25	2.16E-14	35	2.03E-14	37
Total	1.40E-11	562	1.65E-11	179	1.49E-13	217	3.75E-14	61	3.14E-14	57
HCFC-22										
Delta	2.88E-12	115	3.13E-11	342	1.18E-13	172	2.46E-13	399	2.44E-13	446
Total	1.35E-10	5395	1.93E-10	2106	2.99E-12	4368	7.59E-13	1230	3.87E-13	708
HCFC-122										
Delta	1.99E-13	8	1.17E-12	13	7.06E-15	10	8.66E-15	14	8.13E-15	15
Total	5.63E-12	226	6.60E-12	72	5.51E-14	81	1.49E-14	24	1.26E-14	23
HCFC-122a										
Delta	7.28E-13	29	5.00E-12	54	2.75E-14	40	3.78E-14	61	3.54E-14	65
Total	2.43E-11	975	2.87E-11	312	3.19E-13	466	6.77E-14	110	5.50E-14	101
HCFC-123										
Delta	2.61E-13	10	1.57E-12	17	9.35E-15	14	1.16E-14	19	1.09E-14	20
Total	7.54E-12	302	8.85E-12	96	7.64E-14	112	2.01E-14	33	1.69E-14	31
HCFC-123a										
Delta	9.98E-13	40	7.12E-12	78	3.82E-14	56	5.42E-14	88	5.08E-14	93
Total	3.47E-11	1390	4.10E-11	447	4.89E-13	715	9.86E-14	160	7.89E-14	144

(continued on next page)

Table 8.SM.16 (continued)

Acronym, Common Name or Chemical Name	AGWP 20-year (W m^{-2} yr kg^{-1})	**GWP 20-year**	AGWP 100-year (W m^{-2} yr kg^{-1})	**GWP 100-year**	AGTP 20-year (K kg^{-1})	**GTP 20-year**	AGTP 50-year (K kg^{-1})	**GTP 50-year**	AGTP 100-year (K kg^{-1})	GTP 100-year
HCFC-124										
Delta	1.24E-12	**50**	9.96E-12	**109**	4.87E-14	**71**	7.70E-14	**125**	7.24E-14	**132**
Total	4.79E-11	**1920**	5.82E-11	**635**	8.12E-13	**1187**	1.52E-13	**246**	1.13E-13	**206**
HCFC-132c										
Delta	8.93E-13	**36**	6.50E-12	**71**	3.43E-14	**50**	4.96E-14	**80**	4.65E-14	**85**
Total	3.16E-11	**1268**	3.75E-11	**409**	4.61E-13	**674**	9.10E-14	**148**	7.23E-14	**132**
HCFC-141b										
Delta	1.48E-12	**59**	1.43E-11	**156**	5.99E-14	**88**	1.12E-13	**182**	1.08E-13	**197**
Total	6.51E-11	**2608**	8.60E-11	**938**	1.33E-12	**1941**	2.80E-13	**453**	1.69E-13	**309**
HCFC-142b										
Delta	2.53E-12	**101**	3.33E-11	**363**	1.05E-13	**153**	2.56E-13	**415**	2.75E-13	**502**
Total	1.28E-10	**5125**	2.15E-10	**2345**	3.11E-12	**4546**	1.10E-12	**1787**	4.69E-13	**858**
HCFC-225ca										
Delta	4.02E-13	**16**	2.51E-12	**27**	1.47E-14	**21**	1.87E-14	**30**	1.75E-14	**32**
Total	1.21E-11	**485**	1.42E-11	**155**	1.31E-13	**192**	3.25E-14	**53**	2.72E-14	**50**
HCFC-225cb										
Delta	1.23E-12	**49**	9.92E-12	**108**	4.85E-14	**71**	7.67E-14	**124**	7.22E-14	**132**
Total	4.77E-11	**1913**	5.80E-11	**633**	8.09E-13	**1183**	1.51E-13	**245**	1.12E-13	**205**
(E)-1-Chloro-3,3,3-trifluoroprop-1-ene										
Delta	5.31E-15	**<1**	2.97E-14	**<1**	1.82E-16	**<1**	2.17E-16	**<1**	2.04E-16	<1
Total	1.42E-13	**6**	1.66E-13	**2**	1.28E-15	**2**	3.71E-16	**1**	3.16E-16	1
HFC-23										
Delta	4.45E-12	**178**	1.34E-10	**1459**	1.91E-13	**279**	7.85E-13	**1272**	1.59E-12	**2913**
Total	2.75E-10	**11,005**	1.27E-09	**13,856**	8.07E-12	**11,802**	8.78E-12	**14,232**	8.54E-12	**15,622**
HFC-32										
Delta	1.67E-12	**67**	1.29E-11	**141**	6.52E-14	**95**	9.91E-14	**161**	9.31E-14	**170**
Total	6.24E-11	**2502**	7.50E-11	**817**	9.97E-13	**1457**	1.88E-13	**305**	1.45E-13	**265**
HFC-41										
Delta	3.43E-13	**14**	2.27E-12	**25**	1.28E-14	**19**	1.70E-14	**28**	1.60E-14	**29**
Total	1.10E-11	**441**	1.29E-11	**141**	1.34E-13	**195**	3.01E-14	**49**	2.48E-14	**45**
HFC-125										
Delta	2.83E-12	**113**	4.79E-11	**522**	1.19E-13	**174**	3.49E-13	**566**	4.37E-13	**798**
Total	1.55E-10	**6207**	3.39E-10	**3691**	4.08E-12	**5971**	2.19E-12	**3543**	9.66E-13	**1766**
HFC-134										
Delta	2.06E-12	**82**	2.03E-11	**221**	8.31E-14	**122**	1.59E-13	**258**	1.54E-13	**282**
Total	9.14E-11	**3663**	1.23E-10	**1337**	1.90E-12	**2778**	4.13E-13	**670**	2.41E-13	**441**
HFC-134a										
Delta	1.97E-12	**79**	2.27E-11	**248**	8.07E-14	**118**	1.78E-13	**288**	1.80E-13	**329**
Total	9.45E-11	**3789**	1.42E-10	**1549**	2.17E-12	**3171**	6.11E-13	**991**	2.90E-13	**530**

(continued on next page)

Table 8.SM.16 (continued)

Acronym, Common Name or Chemical Name	AGWP 20-year (W m^{-2} yr kg^{-1})	**GWP 20-year**	AGWP 100-year (W m^{-2} yr kg^{-1})	**GWP 100-year**	AGTP 20-year (K kg^{-1})	**GTP 20-year**	AGTP 50-year (K kg^{-1})	**GTP 50-year**	AGTP 100-year (K kg^{-1})	GTP 100-year
HFC-143										
Delta	9.18E-13	**37**	6.35E-12	**69**	3.48E-14	**51**	4.81E-14	**78**	4.51E-14	**82**
Total	3.09E-11	**1239**	3.64E-11	**397**	4.10E-13	**600**	8.63E-14	**140**	7.00E-14	**128**
HFC-143a										
Delta	3.05E-12	**122**	6.45E-11	**703**	1.29E-13	**189**	4.38E-13	**710**	6.50E-13	**1189**
Total	1.76E-10	**7064**	5.05E-10	**5508**	4.89E-12	**7146**	3.56E-12	**5771**	2.02E-12	**3693**
HFC-152										
Delta	5.73E-14	**2**	3.27E-13	**4**	.1.99E-15	**3**	2.40E-15	**4**	2.25E-15	**4**
Total	1.56E-12	**63**	1.83E-12	**20**	1.45E-14	**21**	4.10E-15	**7**	3.49E-15	**6**
HFC-152a										
Delta	4.46E-13	**18**	2.71E-12	**30**	1.61E-14	**23**	2.01E-14	**33**	1.89E-14	35
Total	1.31E-11	**524**	1.53E-11	**167**	1.35E-13	**198**	3.49E-14	**57**	2.93E-14	54
HFC-161										
Delta	1.29E-14	**1**	7.26E-14	**1**	4.44E-16	**1**	5.30E-16	**1**	4.99E-16	**1**
Total	3.46E-13	**14**	4.06E-13	**4**	3.14E-15	**5**	9.06E-16	**1**	7.72E-16	**1**
HFC-227ca										
Delta	2.36E-12	**95**	3.99E-11	**435**	9.91E-14	**145**	2.91E-13	**472**	3.64E-13	**665**
Total	1.29E-10	**5175**	2.82E-10	**3077**	3.41E-12	**4978**	1.82E-12	**2954**	8.05E-13	**1472**
HFC-227ea										
Delta	2.40E-12	**96**	4.69E-11	**512**	1.01E-13	**148**	3.27E-13	**531**	4.56E-13	**835**
Total	1.36E-10	**5454**	3.54E-10	**3860**	3.72E-12	**5431**	2.45E-12	**3967**	1.25E-12	**2294**
HFC-236cb										
Delta	1.85E-12	**74**	2.12E-11	**231**	7.59E-14	**111**	1.66E-13	**269**	1.67E-13	**305**
Total	8.86E-11	**3550**	1.32E-10	**1438**	2.02E-12	**2953**	5.58E-13	**904**	2.68E-13	**490**
HFC-236ea										
Delta	2.28E-12	**92**	2.39E-11	**261**	9.30E-14	**136**	1.88E-13	**305**	1.84E-13	**337**
Total	1.05E-10	**4203**	1.46E-10	**1596**	2.27E-12	**3322**	5.41E-13	**878**	2.91E-13	**532**
HFC-236fa										
Delta	2.84E-12	**114**	8.64E-11	**942**	1.22E-13	**178**	5.05E-13	**818**	1.03E-12	**1890**
Total	1.76E-10	**7054**	8.25E-10	**8998**	5.18E-12	**7575**	5.69E-12	**9220**	5.61E-12	**10,267**
HFC-245ca										
Delta	1.62E-12	**65**	1.35E-11	**147**	6.39E-14	**93**	1.04E-13	**169**	9.85E-14	**180**
Total	6.42E-11	**2575**	7.91E-11	**863**	1.14E-12	**1663**	2.13E-13	**345**	1.53E-13	**281**
HFC-245cb										
Delta	2.94E-12	**118**	6.20E-11	**676**	1.24E-13	**182**	4.21E-13	**683**	6.25E-13	**1144**
Total	1.70E-10	**6795**	4.86E-10	**5298**	4.70E-12	**6875**	3.42E-12	**5552**	1.94E-12	**3553**
HFC-245ea										
Delta	6.73E-13	**27**	4.57E-12	**50**	2.54E-14	**37**	3.45E-14	**56**	3.23E-14	**59**
Total	2.22E-11	**890**	2.61E-11	**285**	2.84E-13	**415**	6.14E-14	**100**	5.02E-14	**92**

(continued on next page)

Table 8.SM.16 (continued)

Acronym, Common Name or Chemical Name	AGWP 20-year (W m^{-2} yr kg^{-1})	**GWP 20-year**	AGWP 100-year (W m^{-2} yr kg^{-1})	**GWP 100-year**	AGTP 20-year (K kg^{-1})	**GTP 20-year**	AGTP 50-year (K kg^{-1})	**GTP 50-year**	AGTP 100-year (K kg^{-1})	GTP 100-year
HFC-245eb										
Delta	8.37E-13	**34**	5.64E-12	**61**	3.15E-14	**46**	4.25E-14	**69**	3.99E-14	73
Total	2.74E-11	**1099**	3.23E-11	**352**	3.46E-13	**506**	7.56E-14	**123**	6.19E-14	113
HFC-245fa										
Delta	1.79E-12	**72**	1.59E-11	**174**	7.14E-14	**104**	1.24E-13	**202**	1.18E-13	**216**
Total	7.46E-11	**2992**	9.47E-11	**1032**	1.42E-12	**2079**	2.76E-13	**447**	1.84E-13	**337**
HFC-263fb										
Delta	2.50E-13	**10**	1.49E-12	**16**	8.93E-15	**13**	1.10E-14	**18**	1.04E-14	**19**
Total	7.18E-12	**288**	8.42E-12	**92**	7.20E-14	**105**	1.91E-14	**31**	1.61E-14	**29**
HFC-272ca										
Delta	4.31E-13	**17**	2.82E-12	**31**	1.60E-14	**23**	2.11E-14	**34**	1.98E-14	**36**
Total	1.36E-11	**547**	1.60E-11	**175**	1.62E-13	**236**	3.72E-14	**60**	3.07E-14	**56**
HFC-329p										
Delta	2.09E-12	**84**	3.55E-11	**387**	8.79E-14	**128**	2.59E-13	**420**	3.24E-13	**593**
Total	1.15E-10	**4594**	2.52E-10	**2742**	3.03E-12	**4423**	1.63E-12	**2638**	7.21E-13	**1318**
HFC-365mfc										
Delta	1.57E-12	**63**	1.48E-11	**161**	6.33E-14	**93**	1.16E-13	**188**	1.11E-13	**203**
Total	6.79E-11	**2724**	8.86E-11	**966**	1.36E-12	**1986**	2.77E-13	**450**	1.73E-13	**317**
HFC-43-10mee										
Delta	2.20E-12	**88**	2.80E-11	**305**	9.09E-14	**133**	2.16E-13	**351**	2.28E-13	**417**
Total	1.10E-10	**4403**	1.79E-10	**1952**	2.63E-12	**3851**	8.78E-13	**1424**	3.82E-13	**698**
HFC-1132a										
Delta	1.51E-16	**<1**	8.44E-16	**<1**	5.18E-18	**<1**	6.16E-18	**<1**	5.79E-18	**<1**
Total	4.04E-15	**<1**	4.73E-15	**<1**	3.61E-17	**<1**	1.05E-17	**<1**	8.98E-18	**<1**
HFC-1141										
Delta	6.04E-17	**<1**	3.38E-16	**<1**	2.07E-18	**<1**	2.47E-18	**<1**	2.32E-18	**<1**
Total	1.62E-15	**<1**	1.90E-15	**<1**	1.44E-17	**<1**	4.21E-18	**<1**	3.60E-18	**<1**
(Z)-HFC-1225ye										
Delta	8.31E-16	**<1**	4.65E-15	**<1**	2.85E-17	**<1**	3.39E-17	**<1**	3.19E-17	**<1**
Total	2.22E-14	**1**	2.60E-14	**<1**	1.99E-16	**<1**	5.80E-17	**<1**	4.95E-17	**<1**
(E)-HFC-1225ye										
Delta	2.81E-16	**<1**	1.57E-15	**<1**	9.64E-18	**<1**	1.15E-17	**<1**	1.08E-17	<1
Total	7.52E-15	**<1**	8.81E-15	**<1**	6.72E-17	**<1**	1.96E-17	**<1**	1.67E-17	<1
(Z)-HFC-1234ze										
Delta	1.01E-15	**<1**	5.68E-15	**<1**	3.48E-17	**<1**	4.14E-17	**<1**	3.90E-17	**<1**
Total	2.71E-14	**1**	3.18E-14	**<1**	2.43E-16	**<1**	7.08E-17	**<1**	6.04E-17	**<1**
HFC-1234yf										
Delta	1.25E-15	**<1**	7.02E-15	**<1**	4.31E-17	**<1**	5.12E-17	**<1**	4.82E-17	**<1**
Total	3.35E-14	**1**	3.93E-14	**<1**	3.00E-16	**<1**	8.75E-17	**<1**	7.47E-17	**<1**

(continued on next page)

Table 8.SM.16 (continued)

Acronym, Common Name or Chemical Name	AGWP 20-year (W m^{-2} yr kg^{-1})	GWP 20-year	AGWP 100-year (W m^{-2} yr kg^{-1})	GWP 100-year	AGTP 20-year (K kg^{-1})	GTP 20-year	AGTP 50-year (K kg^{-1})	GTP 50-year	AGTP 100-year (K kg^{-1})	GTP 100-year
(E)-HFC-1234ze										
Delta	3.40E-15	<1	1.90E-14	<1	1.17E-16	<1	1.39E-16	<1	1.30E-16	<1
Total	9.07E-14	4	1.06E-13	1	8.14E-16	1	2.37E-16	<1	2.02E-16	<1
(Z)-HFC-1336										
Delta	5.98E-15	<1	3.35E-14	<1	2.06E-16	<1	2.45E-16	<1	2.30E-16	<1
Total	1.60E-13	6	1.87E-13	2	1.44E-15	2	4.18E-16	1	3.56E-16	1
HFC-1243zf										
Delta	5.31E-16	<1	2.97E-15	<1	1.82E-17	<1	2.17E-17	<1	2.04E-17	<1
Total	1.42E-14	1	1.66E-14	<1	1.27E-16	<1	3.70E-17	<1	3.16E-17	<1
HFC-1345zfc										
Delta	4.49E-16	<1	2.51E-15	<1	1.54E-17	<1	1.83E-17	<1	1.72E-17	<1
Total	1.20E-14	<1	1.41E-14	<1	1.07E-16	<1	3.13E-17	<1	2.67E-17	<1
3,3,4,4,5,5,6,6,6-Nonafluorohex-1-ene										
Delta	4.84E-16	<1	2.71E-15	<1	1.66E-17	<1	1.98E-17	<1	1.86E-17	<1
Total	1.29E-14	1	1.52E-14	<1	1.16E-16	<1	3.38E-17	<1	2.88E-17	<1
3,3,4,4,5,5,6,6,7,7,8,8,8-Tridecafluorooct-1-ene										
Delta	3.84E-16	<1	2.15E-15	<1	1.32E-17	<1	1.57E-17	<1	1.47E-17	<1
Total	1.03E-14	<1	1.20E-14	<1	9.19E-17	<1	2.68E-17	<1	2.29E-17	<1
3,3,4,4,5,5,6,6,7,7,8,8,9,9,10,10,10-Heptadecafluorodec-1-ene										
Delta	3.31E-16	<1	1.85E-15	<1	1.14E-17	<1	1.35E-17	<1	1.27E-17	<1
Total	8.86E-15	<1	1.04E-14	<1	7.92E-17	<1	2.31E-17	<1	1.97E-17	<1
Methyl chloroform										
Delta	4.02E-13	16	3.05E-12	33	1.56E-14	23	2.34E-14	38	2.20E-14	40
Total	1.48E-11	594	1.77E-11	193	2.32E-13	339	4.42E-14	72	3.42E-14	63
Carbon tetrachloride										
Delta	1.64E-12	66	2.66E-11	290	6.86E-14	100	1.96E-13	318	2.39E-13	436
Total	8.86E-11	3550	1.85E-10	2019	2.31E-12	3378	1.16E-12	1887	5.01E-13	915
Methyl chloride										
Delta	4.09E-14	2	2.42E-13	3	1.45E-15	2	1.78E-15	3	1.67E-15	3
Total	1.16E-12	46	1.36E-12	15	1.14E-14	17	3.07E-15	5	2.59E-15	5
Methylene chloride										
Delta	3.12E-14	1	1.78E-13	2	1.08E-15	2	1.30E-15	2	1.22E-15	2
Total	8.49E-13	34	9.95E-13	11	7.86E-15	11	2.23E-15	4	1.90E-15	3
Chloroform										
Delta	5.73E-14	2	3.27E-13	4	1.99E-15	3	2.40E-15	4	2.25E-15	4
Total	1.56E-12	63	1.83E-12	20	1.45E-14	21	4.10E-15	7	3.49E-15	6
1,2-Dichloroethane										
Delta	3.18E-15	<1	1.79E-14	<1	1.10E-16	<1	1.31E-16	<1	1.23E-16	<1
Total	8.56E-14	3	1.00E-13	1	7.77E-16	1	2.24E-16	<1	1.91E-16	<1

(continued on next page)

Table 8.SM.16 (continued)

Acronym, Common Name or Chemical Name	AGWP 20-year (W m^{-2} yr kg^{-1})	GWP 20-year	AGWP 100-year (W m^{-2} yr kg^{-1})	GWP 100-year	AGTP 20-year (K kg^{-1})	GTP 20-year	AGTP 50-year (K kg^{-1})	GTP 50-year	AGTP 100-year (K kg^{-1})	GTP 100-year
Methyl bromide										
Delta	8.01E-15	**<1**	4.68E-14	**1**	2.82E-16	**<1**	3.44E-16	**1**	3.23E-16	**1**
Total	2.24E-13	**9**	2.63E-13	**3**	2.16E-15	**3**	5.91E-16	**1**	5.01E-16	**1**
Methylene bromide										
Delta	3.56E-15	**<1**	2.02E-14	**<1**	1.23E-16	**<1**	1.48E-16	**<1**	1.39E-16	**<1**
Total	9.66E-14	**4**	1.13E-13	**1**	8.90E-16	**1**	2.54E-16	**<1**	2.16E-16	**<1**
Halon-1201										
Delta	9.29E-13	**37**	7.16E-12	**78**	3.62E-14	**53**	5.50E-14	**89**	5.17E-14	**95**
Total	3.47E-11	**1390**	4.16E-11	**454**	5.54E-13	**809**	1.05E-13	**170**	8.04E-14	**147**
Halon-1202										
Delta	6.76E-13	**27**	4.50E-12	**49**	2.53E-14	**37**	3.38E-14	**55**	3.17E-14	**58**
Total	2.18E-11	**875**	2.57E-11	**280**	2.69E-13	**393**	5.99E-14	**97**	4.92E-14	**90**
Halon-1211										
Delta	2.34E-12	**94**	2.97E-11	**324**	9.67E-14	**141**	2.30E-13	**373**	2.42E-13	442
Total	1.17E-10	**4684**	1.90E-10	**2070**	2.80E-12	**4091**	9.28E-13	**1504**	4.04E-13	739
Halon-1301										
Delta	3.35E-12	**134**	7.91E-11	**862**	1.43E-13	**208**	5.15E-13	**835**	8.40E-13	**1536**
Total	1.98E-10	**7935**	6.56E-10	**7154**	5.61E-12	**8194**	4.68E-12	**7581**	3.12E-12	**5703**
Halon-2301										
Delta	4.89E-13	**20**	3.36E-12	**37**	1.85E-14	**27**	2.54E-14	**41**	2.38E-14	**44**
Total	1.63E-11	**655**	1.93E-11	**210**	2.14E-13	**313**	4.55E-14	**74**	3.70E-14	**68**
Halon-2311/Halothane										
Delta	1.38E-13	**6**	8.15E-13	**9**	4.90E-15	**7**	6.01E-15	**10**	5.64E-15	**10**
Total	3.91E-12	**157**	4.59E-12	**50**	3.84E-14	**56**	1.04E-14	**17**	8.75E-15	**16**
Halon-2401										
Delta	5.38E-13	**22**	3.58E-12	**39**	2.01E-14	**29**	2.69E-14	**44**	2.52E-14	**46**
Total	1.74E-11	**696**	2.04E-11	**223**	2.14E-13	**312**	4.77E-14	**77**	3.92E-14	**72**
Halon-2402										
Delta	1.68E-12	**68**	2.40E-11	**262**	7.01E-14	**102**	1.82E-13	**296**	2.04E-13	**373**
Total	8.76E-11	**3511**	1.59E-10	**1734**	2.19E-12	**3207**	8.90E-13	**1443**	3.70E-13	**676**
Nitrogen trifluoride										
Delta	5.19E-12	**208**	1.66E-10	**1815**	2.23E-13	**326**	9.48E-13	**1537**	2.04E-12	**3733**
Total	3.24E-10	**12,987,000**	1.64E-09	**17,885**	9.61E-12	**14,049**	1.11E-11	**18,041**	1.20E-11	**21,852**
Sulphur hexafluoride										
Delta	7.06E-12	**283**	2.37E-10	**2580**	3.03E-13	**444**	1.32E-12	**2139**	2.96E-12	**5416**
Total	4.44E-10	**17,783**	2.39E-09	**26,087**	1.32E-11	**19,348**	1.60E-11	**25,934**	1.84E-11	**33,631**
(Trifluoromethyl)sulphur pentafluoride										
Delta	5.46E-12	**219**	1.78E-10	**1946**	2.35E-13	**343**	1.01E-12	**1633**	2.21E-12	**4039**
Total	3.42E-10	**13,698**	1.78E-09	**19,396**	1.02E-11	**14,855**	1.20E-11	**19,443**	1.33E-11	**24,271**

(continued on next page)

Table 8.SM.16 (continued)

Acronym, Common Name or Chemical Name	AGWP 20-year (W m^{-2} yr kg^{-1})	**GWP 20-year**	AGWP 100-year (W m^{-2} yr kg^{-1})	**GWP 100-year**	AGTP 20-year (K kg^{-1})	**GTP 20-year**	AGTP 50-year (K kg^{-1})	**GTP 50-year**	AGTP 100-year (K kg^{-1})	**GTP 100-year**
Sulphuryl fluoride										
Delta	3.08E-12	**124**	5.84E-11	**637**	1.30E-13	**190**	4.12E-13	**668**	5.60E-13	**1024**
Total	1.74E-10	**6965**	4.34E-10	**4732**	4.71E-12	**6885**	2.96E-12	**4805**	1.46E-12	**2671**
PFC-14										
Delta	1.96E-12	**79**	6.64E-11	**724**	8.44E-14	**123**	3.69E-13	**598**	8.34E-13	1524
Total	1.24E-10	**4954**	6.74E-10	**7349**	3.69E-12	**5396**	4.49E-12	**7286**	5.23E-12	9563
PFC-116										
Delta	3.31E-12	**133**	1.12E-10	**1216**	1.42E-13	**208**	6.20E-13	**1006**	1.40E-12	**2560**
Total	2.08E-10	**8344**	1.13E-09	**12,340**	6.21E-12	**9085**	7.55E-12	**12,243**	8.76E-12	**16,016**
PFC-c216										
Delta	2.76E-12	**111**	9.26E-11	**1010**	1.19E-13	**174**	5.16E-13	**837**	1.16E-12	**2119**
Total	1.74E-10	**6964**	9.36E-10	**10,208**	5.18E-12	**7576**	6.26E-12	**10,149**	7.19E-12	**13,151**
PFC-218										
Delta	2.68E-12	**107**	8.97E-11	**978**	1.15E-13	**168**	5.00E-13	**812**	1.12E-12	**2051**
Total	1.68E-10	**6752**	9.06E-10	**9878**	5.02E-12	**7344**	6.06E-12	**9826**	6.95E-12	**12,705**
PFC-318										
Delta	2.87E-12	**115**	9.61E-11	**1048**	1.23E-13	**180**	5.36E-13	**869**	1.20E-12	**2199**
Total	1.80E-10	**7221**	9.71E-10	**10,592**	5.37E-12	**7856**	6.49E-12	**10,530**	7.47E-12	**13,655**
PFC-31-10										
Delta	2.77E-12	**111**	9.27E-11	**1011**	1.19E-13	**174**	5.17E-13	**839**	1.16E-12	**2121**
Total	1.74E-10	**6981**	9.37E-10	**10,213**	5.19E-12	**7594**	6.27E-12	**10,160**	7.18E-12	**13,137**
Perfluorocyclopentene										
Delta	6.63E-15	**<1**	3.72E-14	**<1**	2.28E-16	**<1**	2.71E-16	**<1**	2.55E-16	**<1**
Total	1.77E-13	**7**	2.08E-13	**2**	1.60E-15	**2**	4.63E-16	**1**	3.95E-16	**1**
PFC-41-12										
Delta	2.56E-12	**103**	8.59E-11	**937**	1.10E-13	**161**	4.79E-13	**776**	1.08E-12	**1968**
Total	1.61E-10	**6448**	8.70E-10	**9484**	4.80E-12	**7017**	5.81E-12	**9422**	6.70E-12	**12,253**
PFC-51-14										
Delta	2.38E-12	**95**	7.97E-11	**869**	1.02E-13	**149**	4.44E-13	**720**	9.97E-13	**1823**
Total	1.49E-10	**5988**	8.05E-10	**8780**	4.46E-12	**6514**	5.38E-12	**8730**	6.19E-12	**11,316**
PFC-61-16										
Delta	2.35E-12	**94**	7.88E-11	**859**	1.01E-13	**148**	4.39E-13	**712**	9.86E-13	**1802**
Total	1.48E-10	**5922**	7.96E-10	**8681**	4.41E-12	**6443**	5.32E-12	**8631**	6.12E-12	**11,183**
PFC-71-18										
Delta	2.29E-12	**92**	7.67E-11	**837**	9.84E-14	**144**	4.28E-13	**694**	9.60E-13	1756
Total	1.44E-10	**5769**	7.76E-10	**8456**	4.29E-12	**6276**	5.19E-12	**8408**	5.96E-12	10,894
PFC-91-18										
Delta	2.18E-12	**87**	7.26E-11	**791**	9.35E-14	**137**	4.05E-13	**658**	9.06E-13	**1657**
Total	1.37E-10	**5476**	7.32E-10	**7977**	4.07E-12	**5954**	4.90E-12	**7943**	5.59E-12	**10,222**

(continued on next page)

Table 8.SM.16 (continued)

Acronym, Common Name or Chemical Name	AGWP 20-year (W m^{-2} yr kg^{-1})	**GWP 20-year**	AGWP 100-year (W m^{-2} yr kg^{-1})	**GWP 100-year**	AGTP 20-year (K kg^{-1})	**GTP 20-year**	AGTP 50-year (K kg^{-1})	**GTP 50-year**	AGTP 100-year (K kg^{-1})	**GTP 100-year**
Perfluorodecalin(cis)										
Delta	2.19E-12	**88**	7.31E-11	**797**	9.42E-14	**138**	4.08E-13	**662**	9.13E-13	**1669**
Total	1.38E-10	**5515**	7.37E-10	**8033**	4.10E-12	**5997**	4.93E-12	**8000**	5.63E-12	**10,295**
Perfluorodecalin(trans)										
Delta	1.90E-12	**76**	6.35E-11	**692**	8.18E-14	**120**	3.55E-13	**575**	7.93E-13	**1450**
Total	1.20E-10	**4792**	6.40E-10	**6980**	3.56E-12	**5211**	4.29E-12	**6951**	4.89E-12	**8946**
PFC-1114										
Delta	1.03E-17	**<1**	5.78E-17	**<1**	3.55E-19	**<1**	4.22E-19	**<1**	3.96E-19	**<1**
Total	2.77E-16	**<1**	3.24E-16	**<1**	2.47E-18	**<1**	7.21E-19	**<1**	6.15E-19	**<1**
PFC-1216										
Delta	2.49E-16	**<1**	1.40E-15	**<1**	8.56E-18	**<1**	1.02E-17	**<1**	9.57E-18	**<1**
Total	6.67E-15	**<1**	7.82E-15	**<1**	5.97E-17	**<1**	1.74E-17	**<1**	1.48E-17	**<1**
Perfluorobuta-1,3-diene										
Delta	1.27E-17	**<1**	7.11E-17	**<1**	4.36E-19	**<1**	5.19E-19	**<1**	4.88E-19	**<1**
Total	3.40E-16	**<1**	3.99E-16	**<1**	3.04E-18	**<1**	8.86E-19	**<1**	7.57E-19	**<1**
Perfluorobut-1-ene										
Delta	3.25E-16	**<1**	1.82E-15	**<1**	1.11E-17	**<1**	1.33E-17	**<1**	1.25E-17	**<1**
Total	8.69E-15	**<1**	1.02E-14	**<1**	7.77E-17	**<1**	2.26E-17	**<1**	1.93E-17	**<1**
Perfluorobut-2-ene										
Delta	6.28E-15	**<1**	3.52E-14	**<1**	2.16E-16	**<1**	2.57E-16	**<1**	2.42E-16	**<1**
Total	1.68E-13	**7**	1.97E-13	**2**	1.51E-15	**2**	4.39E-16	**1**	3.74E-16	**1**
HFE-125										
Delta	5.18E-12	**208**	1.42E-10	**1549**	2.21E-13	**324**	8.68E-13	**1408**	1.62E-12	**2961**
Total	3.15E-10	**12,617**	1.28E-09	**13,951**	9.13E-12	**13,349**	9.01E-12	**14,615**	7.59E-12	**13,871**
HFE-134 (HG-00)										
Delta	5.51E-12	**221**	8.69E-11	**947**	2.31E-13	**337**	6.46E-13	**1047**	7.69E-13	1406
Total	2.96E-10	**11,857**	5.97E-10	**6512**	7.65E-12	**11,183**	3.67E-12	**5945**	1.55E-12	2837
HFE-143a										
Delta	1.33E-12	**53**	1.00E-11	**109**	5.16E-14	**75**	7.67E-14	**124**	7.19E-14	**132**
Total	4.86E-11	**1947**	5.80E-11	**632**	7.47E-13	**1091**	1.43E-13	**232**	1.12E-13	**205**
HFE-227ea										
Delta	3.88E-12	**156**	8.49E-11	**926**	1.65E-13	**241**	5.70E-13	**924**	8.70E-13	**1590**
Total	2.26E-10	**9058**	6.77E-10	**7377**	6.31E-12	**9224**	4.79E-12	**7773**	2.85E-12	**5217**
HCFE-235ca2 (enflurane)										
Delta	1.54E-12	**62**	1.12E-11	**122**	5.92E-14	**87**	8.55E-14	**139**	8.01E-14	**147**
Total	5.45E-11	**2185**	6.47E-11	**705**	7.95E-13	**1162**	1.57E-13	**254**	1.25E-13	**228**
HCFE-235da2 (isoflurane)										
Delta	1.37E-12	**55**	9.51E-12	**104**	5.21E-14	**76**	7.20E-14	**117**	6.75E-14	**123**
Total	4.63E-11	**1854**	5.45E-11	**595**	6.14E-13	**898**	1.29E-13	**209**	1.05E-13	**192**

(continued on next page)

Table 8.SM.16 (continued)

Acronym, Common Name or Chemical Name	AGWP 20-year (W m^{-2} yr kg^{-1})	**GWP 20-year**	AGWP 100-year (W m^{-2} yr kg^{-1})	**GWP 100-year**	AGTP 20-year (K kg^{-1})	**GTP 20-year**	AGTP 50-year (K kg^{-1})	**GTP 50-year**	AGTP 100-year (K kg^{-1})	GTP 100-year
HFE-236ca										
Delta	4.72E-12	**189**	6.86E-11	**748**	1.97E-13	**287**	5.19E-13	**842**	5.87E-13	**1074**
Total	2.47E-10	**9901**	4.58E-10	**4990**	6.23E-12	**9105**	2.62E-12	**4241**	1.09E-12	**1985**
HFE-236ea2 (desflurane)										
Delta	3.10E-12	**124**	3.22E-11	**351**	1.26E-13	**184**	2.53E-13	**410**	2.48E-13	**453**
Total	1.42E-10	**5678**	1.97E-10	**2143**	3.05E-12	**4463**	7.17E-13	**1163**	3.90E-13	**713**
HFE-236fa										
Delta	2.07E-12	**83**	1.82E-11	**199**	8.24E-14	**120**	1.42E-13	**230**	1.35E-13	**247**
Total	8.56E-11	**3431**	1.08E-10	**1177**	1.61E-12	**2358**	3.10E-13	**503**	2.10E-13	**384**
HFE-245cb2										
Delta	1.65E-12	**66**	1.25E-11	**136**	6.41E-14	**94**	9.58E-14	**155**	8.99E-14	**164**
Total	6.06E-11	**2430**	7.25E-11	**790**	9.41E-13	**1376**	1.80E-13	**292**	1.40E-13	**256**
HFE-245fa1										
Delta	1.86E-12	**74**	1.55E-11	**169**	7.34E-14	**107**	1.21E-13	**196**	1.14E-13	**208**
Total	7.41E-11	**2970**	9.15E-11	**997**	1.32E-12	**1932**	2.48E-13	**402**	1.77E-13	**324**
HFE-245fa2										
Delta	1.97E-12	**79**	1.54E-11	**168**	7.69E-14	**112**	1.19E-13	**193**	1.12E-13	204
Total	7.45E-11	**2987**	8.99E-11	**981**	1.22E-12	**1786**	2.29E-13	**372**	1.74E-13	318
2,2,3,3,3-Pentafluoropropan-1-ol										
Delta	6.60E-14	**3**	3.75E-13	**4**	2.29E-15	**3**	2.75E-15	**4**	2.58E-15	**5**
Total	1.79E-12	**72**	2.10E-12	**23**	1.65E-14	**24**	4.70E-15	**8**	4.00E-15	**7**
HFE-254cb1										
Delta	9.07E-13	**36**	5.88E-12	**64**	3.36E-14	**49**	4.41E-14	**71**	4.13E-14	**76**
Total	2.85E-11	**1141**	3.35E-11	**365**	3.33E-13	**487**	7.74E-14	**126**	6.41E-14	**117**
HFE-263fb2										
Delta	4.72E-15	**<1**	2.65E-14	**<1**	1.62E-16	**<1**	1.93E-16	**<1**	1.82E-16	**<1**
Total	1.26E-13	**5**	1.48E-13	**2**	1.13E-15	**2**	3.30E-16	**1**	2.81E-16	**1**
HFE-263m1										
Delta	1.03E-13	**4**	5.87E-13	**6**	3.57E-15	**5**	4.30E-15	**7**	4.04E-15	**7**
Total	2.80E-12	**112**	3.29E-12	**36**	2.61E-14	**38**	7.37E-15	**12**	6.26E-15	**11**
3,3,3-Trifluoropropan-1-ol										
Delta	1.39E-15	**<1**	7.77E-15	**<1**	4.77E-17	**<1**	5.67E-17	**<1**	5.33E-17	**<1**
Total	3.71E-14	**1**	4.35E-14	**<1**	3.32E-16	**<1**	9.69E-17	**<1**	8.27E-17	**<1**
HFE-329mcc2										
Delta	3.22E-12	**129**	4.88E-11	**532**	1.35E-13	**197**	3.66E-13	**593**	4.24E-13	**776**
Total	1.71E-10	**6847**	3.30E-10	**3598**	4.36E-12	**6379**	1.96E-12	**3175**	8.17E-13	**1494**
HFE-338mmz1										
Delta	2.87E-12	**115**	4.22E-11	**460**	1.20E-13	**175**	3.19E-13	**517**	3.63E-13	**663**
Total	1.51E-10	**6053**	2.83E-10	**3081**	3.82E-12	**5584**	1.63E-12	**2644**	6.77E-13	**1238**

(continued on next page)

Table 8.SM.16 (continued)

Acronym, Common Name or Chemical Name	AGWP 20-year (W m^{-2} yr kg^{-1})	**GWP 20-year**	AGWP 100-year (W m^{-2} yr kg^{-1})	**GWP 100-year**	AGTP 20-year (K kg^{-1})	**GTP 20-year**	AGTP 50-year (K kg^{-1})	**GTP 50-year**	AGTP 100-year (K kg^{-1})	GTP 100-year
HFE-338mcf2										
Delta	1.96E-12	**79**	1.73E-11	**189**	7.82E-14	**114**	1.35E-13	**219**	1.28E-13	**234**
Total	8.13E-11	**3258**	1.03E-10	**1118**	1.53E-12	**2239**	2.95E-13	**478**	2.00E-13	**365**
Sevoflurane (HFE-347mmz1)										
Delta	6.66E-13	**27**	4.24E-12	**46**	2.45E-14	**36**	3.17E-14	**51**	2.97E-14	**54**
Total	2.05E-11	**821**	2.41E-11	**262**	2.31E-13	**337**	5.54E-14	**90**	4.61E-14	**84**
HFE-347mcc3 (HFE-7000)										
Delta	1.33E-12	**53**	1.01E-11	**110**	5.17E-14	**76**	7.77E-14	**126**	7.29E-14	133
Total	4.91E-11	**1968**	5.88E-11	**641**	7.69E-13	**1125**	1.46E-13	**237**	1.13E-13	207
HFE-347mcf2										
Delta	1.91E-12	**77**	1.60E-11	**175**	7.57E-14	**111**	1.24E-13	**202**	1.18E-13	**215**
Total	7.64E-11	**3063**	9.43E-11	**1028**	1.36E-12	**1993**	2.55E-13	**414**	1.83E-13	**335**
HFE-347pcf2										
Delta	2.08E-12	**83**	1.68E-11	**183**	8.17E-14	**119**	1.30E-13	**211**	1.22E-13	**224**
Total	8.07E-11	**3236**	9.83E-11	**1072**	1.38E-12	**2015**	2.57E-13	**417**	1.90E-13	**348**
HFE-347mmy1										
Delta	1.00E-12	**40**	7.02E-12	**77**	3.82E-14	**56**	5.33E-14	**86**	4.99E-14	**91**
Total	3.42E-11	**1370**	4.04E-11	**440**	4.65E-13	**680**	9.61E-14	**156**	7.76E-14	**142**
HFE-356mec3										
Delta	1.06E-12	**42**	7.47E-12	**81**	4.04E-14	**59**	5.67E-14	**92**	5.32E-14	**97**
Total	3.64E-11	**1457**	4.29E-11	**468**	5.01E-13	**732**	1.03E-13	**166**	8.26E-14	**151**
HFE-356mff2										
Delta	5.90E-14	**2**	3.34E-13	**4**	2.04E-15	**3**	2.45E-15	**4**	2.30E-15	**4**
Total	1.60E-12	**64**	1.87E-12	**20**	1.46E-14	**21**	4.18E-15	**7**	3.56E-15	**7**
HFE-356pcf2										
Delta	1.72E-12	**69**	1.36E-11	**149**	6.72E-14	**98**	1.05E-13	**171**	9.89E-14	**181**
Total	6.57E-11	**2633**	7.96E-11	**867**	1.10E-12	**1601**	2.05E-13	**332**	1.54E-13	**281**
HFE-356pcf3										
Delta	1.25E-12	**50**	8.64E-12	**94**	4.74E-14	**69**	6.54E-14	**106**	6.13E-14	**112**
Total	4.20E-11	**1685**	4.96E-11	**540**	5.58E-13	**816**	1.17E-13	**190**	9.52E-14	**174**
HFE-356pcc3										
Delta	1.13E-12	**45**	7.97E-12	**87**	4.31E-14	**63**	6.05E-14	**98**	5.67E-14	**104**
Total	3.88E-11	**1555**	4.58E-11	**500**	5.34E-13	**781**	1.09E-13	**177**	8.81E-14	**161**
HFE-356mmz1										
Delta	4.79E-14	**2**	2.71E-13	**3**	1.66E-15	**2**	1.98E-15	**3**	1.86E-15	**3**
Total	1.29E-12	**52**	1.52E-12	**17**	1.18E-14	**17**	3.39E-15	**5**	2.89E-15	**5**
HFE-365mcf3										
Delta	3.31E-15	**<1**	1.85E-14	**<1**	1.14E-16	**<1**	1.35E-16	**<1**	1.27E-16	<1
Total	8.84E-14	**4**	1.04E-13	**1**	7.93E-16	**1**	2.31E-16	**<1**	1.97E-16	<1

(continued on next page)

Table 8.SM.16 (continued)

Acronym, Common Name or Chemical Name	AGWP 20-year (W m^{-2} yr kg^{-1})	**GWP 20-year**	AGWP 100-year (W m^{-2} yr kg^{-1})	**GWP 100-year**	AGTP 20-year (K kg^{-1})	**GTP 20-year**	AGTP 50-year (K kg^{-1})	**GTP 50-year**	AGTP 100-year (K kg^{-1})	GTP 100-year
HFE-365mcf2										
Delta	2.01E-13	**8**	1.16E-12	**13**	7.05E-15	**10**	8.53E-15	**14**	8.01E-15	**15**
Total	5.56E-12	**223**	6.52E-12	**71**	5.24E-14	**77**	1.46E-14	**24**	1.24E-14	**23**
HFE-374pc2										
Delta	1.57E-12	**63**	1.20E-11	**130**	6.11E-14	**89**	9.18E-14	**149**	8.62E-14	**158**
Total	5.80E-11	**2326**	6.95E-11	**758**	9.09E-13	**1329**	1.73E-13	**281**	1.34E-13	**245**
4,4,4-Trifluorobutan-1-ol										
Delta	6.72E-17	**<1**	3.76E-16	**<1**	2.31E-18	**<1**	2.74E-18	**<1**	2.58E-18	**<1**
Total	1.80E-15	**<1**	2.11E-15	**<1**	1.61E-17	**<1**	4.68E-18	**<1**	4.00E-18	**<1**
2,2,3,3,4,4,5,5-Octafluorocyclopentanol										
Delta	4.52E-14	**2**	2.56E-13	**3**	1.57E-15	**2**	1.88E-15	**3**	1.76E-15	**3**
Total	1.22E-12	**49**	1.44E-12	**16**	1.12E-14	**16**	3.21E-15	**5**	2.73E-15	**5**
HFE-43-10pccc124 (H-Galden 1040x, HG-11)										
Delta	4.23E-12	**170**	4.92E-11	**536**	1.74E-13	**254**	3.84E-13	**623**	3.90E-13	**713**
Total	2.04E-10	**8176**	3.07E-10	**3353**	4.69E-12	**6854**	1.33E-12	**2156**	6.28E-13	**1149**
HFE-449s1 (HFE-7100)										
Delta	1.08E-12	**43**	8.05E-12	**88**	4.17E-14	**61**	6.17E-14	**100**	5.79E-14	**106**
Total	3.91E-11	**1568**	4.66E-11	**509**	5.95E-13	**870**	1.15E-13	**186**	8.99E-14	**164**
n-HFE-7100										
Delta	1.24E-12	**50**	9.29E-12	**101**	4.82E-14	**70**	7.12E-14	**115**	6.68E-14	**122**
Total	4.52E-11	**1810**	5.38E-11	**587**	6.87E-13	**1004**	1.33E-13	**215**	1.04E-13	**190**
i-HFE-7100										
Delta	1.04E-12	**42**	7.79E-12	**85**	4.04E-14	**59**	5.96E-14	**97**	5.60E-14	**102**
Total	3.78E-11	**1517**	4.51E-11	**492**	5.76E-13	**842**	1.11E-13	**180**	8.70E-14	**159**
HFE-569sf2 (HFE-7200)										
Delta	1.93E-13	**8**	1.13E-12	**12**	6.81E-15	**10**	8.31E-15	**13**	7.80E-15	**14**
Total	5.40E-12	**217**	6.34E-12	**69**	5.20E-14	**76**	1.43E-14	**23**	1.21E-14	**22**
n-HFE-7200										
Delta	2.20E-13	**9**	1.28E-12	**14**	7.74E-15	**11**	9.44E-15	**15**	8.86E-15	16
Total	6.14E-12	**246**	7.21E-12	**79**	5.91E-14	**86**	1.62E-14	**26**	1.37E-14	25
i-HFE-7200										
Delta	1.51E-13	**6**	8.80E-13	**10**	5.31E-15	**8**	6.47E-15	**10**	6.08E-15	**11**
Total	4.21E-12	**169**	4.94E-12	**54**	4.05E-14	**59**	1.11E-14	**18**	9.42E-15	**17**
HFE-236ca12 (HG-10)										
Delta	5.21E-12	**209**	8.31E-11	**907**	2.18E-13	**319**	6.16E-13	**999**	7.39E-13	**1352**
Total	2.81E-10	**11,248**	5.74E-10	**6260**	7.28E-12	**10,646**	3.56E-12	**5769**	1.51E-12	**2769**
HFE-338pcc13 (HG-01)										
Delta	4.50E-12	**181**	5.11E-11	**557**	1.85E-13	**270**	4.00E-13	**648**	4.02E-13	**736**
Total	2.15E-10	**8607**	3.18E-10	**3466**	4.88E-12	**7129**	1.33E-12	**2153**	6.44E-13	**1178**

(continued on next page)

Table 8.SM.16 (continued)

Acronym, Common Name or Chemical Name	AGWP 20-year (W m^{-2} yr kg^{-1})	GWP 20-year	AGWP 100-year (W m^{-2} yr kg^{-1})	GWP 100-year	AGTP 20-year (K kg^{-1})	GTP 20-year	AGTP 50-year (K kg^{-1})	GTP 50-year	AGTP 100-year (K kg^{-1})	GTP 100-year
1,1,1,3,3,3-Hexafluoropropan-2-ol										
Delta	5.73E-13	23	3.57E-12	39	2.09E-14	31	2.66E-14	43	2.50E-14	46
Total	1.72E-11	691	2.02E-11	221	1.87E-13	274	4.64E-14	75	3.87E-14	71
HG-02										
Delta	4.22E-12	169	4.79E-11	523	1.73E-13	253	3.75E-13	608	3.77E-13	690
Total	2.01E-10	8072	2.98E-10	3250	4.57E-12	6686	1.25E-12	2019	6.04E-13	1105
HG-03										
Delta	4.42E-12	177	5.01E-11	547	1.81E-13	265	3.92E-13	636	3.95E-13	722
Total	2.11E-10	8443	3.12E-10	3400	4.78E-12	6993	1.30E-12	2112	6.32E-13	1155
HG-20										
Delta	5.16E-12	207	8.24E-11	898	2.16E-13	316	6.10E-13	990	7.32E-13	1339
Total	2.78E-10	11,143	5.69E-10	6201	7.21E-12	10,546	3.52E-12	5715	1.50E-12	2743
HG-21										
Delta	5.84E-12	234	6.79E-11	740	2.40E-13	351	5.30E-13	860	5.38E-13	984
Total	2.82E-10	11,285	4.24E-10	4628	6.47E-12	9461	1.84E-12	2976	8.67E-13	1586
HG-30										
Delta	7.14E-12	286	1.14E-10	1242	2.99E-13	437	8.44E-13	1369	1.01E-12	1852
Total	3.84E-10	15,408	7.86E-10	8575	9.98E-12	14,583	4.87E-12	7903	2.07E-12	3793
1-Ethoxy-1,1,2,2,3,3,3-heptafluoropropane										
Delta	2.07E-13	8	1.20E-12	13	7.28E-15	11	8.86E-15	14	8.32E-15	15
Total	5.77E-12	231	6.77E-12	74	5.52E-14	81	1.52E-14	25	1.29E-14	24
Fluoroxene										
Delta	1.93E-16	<1	1.08E-15	<1	6.62E-18	<1	7.88E-18	<1	7.41E-18	<1
Total	5.16E-15	<1	6.05E-15	<1	4.61E-17	<1	1.35E-17	<1	1.15E-17	<1
1,1,2,2-Tetrafluoro-1-(fluoromethoxy)ethane										
Delta	2.01E-12	80	1.64E-11	179	7.91E-14	116	1.27E-13	206	1.20E-13	219
Total	7.88E-11	3157	9.64E-11	1051	1.37E-12	1996	2.55E-13	413	1.87E-13	341
2-Ethoxy-3,3,4,4,5-pentafluorotetrahydro-2,5-bis[1,2,2,2-tetrafluoro-1-(trifluoromethyl)ethyl]-furan										
Delta	1.86E-13	7	1.10E-12	12	6.61E-15	10	8.12E-15	13	7.62E-15	14
Total	5.28E-12	212	6.19E-12	68	5.19E-14	76	1.40E-14	23	1.18E-14	22
Fluoro(methoxy)methane										
Delta	4.44E-14	2	2.51E-13	3	1.53E-15	2	1.83E-15	3	1.72E-15	3
Total	1.20E-12	48	1.40E-12	15	1.09E-14	16	3.13E-15	5	2.67E-15	5
Difluoro(methoxy)methane										
Delta	4.79E-13	19	2.85E-12	31	1.70E-14	25	2.10E-14	34	1.97E-14	36
Total	1.37E-11	547	1.60E-11	175	1.36E-13	198	3.62E-14	59	3.06E-14	56
Fluoro(fluoromethoxy)methane										
Delta	4.40E-13	18	2.59E-12	28	1.56E-14	23	1.91E-14	31	1.79E-14	33
Total	1.24E-11	497	1.45E-11	159	1.21E-13	176	3.28E-14	53	2.77E-14	51

(continued on next page)

Table 8.SM.16 (continued)

Acronym, Common Name or Chemical Name	AGWP 20-year (W m^{-2} yr kg^{-1})	GWP 20-year	AGWP 100-year (W m^{-2} yr kg^{-1})	GWP 100-year	AGTP 20-year (K kg^{-1})	GTP 20-year	AGTP 50-year (K kg^{-1})	GTP 50-year	AGTP 100-year (K kg^{-1})	GTP 100-year
Difluoro(fluoromethoxy)methane										
Delta	1.75E-12	70	1.20E-11	131	6.63E-14	97	9.05E-14	147	8.48E-14	155
Total	5.82E-11	2335	6.86E-11	748	7.55E-13	1103	1.62E-13	262	1.32E-13	241
Trifluoro(fluoromethoxy)methane										
Delta	1.97E-12	79	1.44E-11	157	7.58E-14	111	1.10E-13	179	1.03E-13	189
Total	7.02E-11	2812	8.33E-11	909	1.03E-12	1512	2.03E-13	329	1.61E-13	294
HG′-01										
Delta	6.94E-13	28	4.36E-12	48	2.54E-14	37	3.25E-14	53	3.05E-14	56
Total	2.10E-11	843	2.47E-11	269	2.31E-13	338	5.66E-14	92	4.72E-14	86
HG′-02										
Delta	7.38E-13	30	4.64E-12	51	2.70E-14	39	3.46E-14	56	3.24E-14	59
Total	2.24E-11	897	2.63E-11	287	2.46E-13	360	6.03E-14	98	5.03E-14	92
HG′-03										
Delta	6.91E-13	28	4.34E-12	47	2.53E-14	37	3.23E-14	52	3.03E-14	55
Total	2.09E-11	840	2.46E-11	268	2.30E-13	336	5.64E-14	91	4.70E-14	86
HFE-329me3										
Delta	3.20E-12	128	6.34E-11	691	1.35E-13	198	4.40E-13	714	6.20E-13	1133
Total	1.82E-10	7299	4.81E-10	5241	4.98E-12	7286	3.33E-12	5406	1.73E-12	3173
3,3,4,4, 5,5,6,6,7,7,7-Undecafluoroheptan-1-ol										
Delta	1.52E-15	<1	8.51E-15	<1	5.22E-17	<1	6.21E-17	<1	5.84E-17	<1
Total	4.06E-14	2	4.76E-14	1	3.64E-16	1	1.06E-16	<1	9.04E-17	<1
3,3,4,4,5,5,6,6,7,7,8,8,9,9, 9-Pentadecafluorononan-1-ol										
Delta	1.17E-15	<1	6.53E-15	<1	4.01E-17	<1	4.77E-17	<1	4.48E-17	<1
Total	3.12E-14	1	3.65E-14	<1	2.80E-16	<1	8.14E-17	<1	6.95E-17	<1
3,3,4,4,5,5,6,6,7,7,8,8,9,9,10,10,11,11,11-Nonadecafluoroundecan-1-ol										
Delta	6.69E-16	<1	3.75E-15	<1	2.30E-17	<1	2.73E-17	<1	2.57E-17	<1
Total	1.79E-14	1	2.10E-14	<1	1.60E-16	<1	4.67E-17	<1	3.98E-17	<1
2-Chloro-1,1,2-trifluoro-1-methoxyethane										
Delta	3.99E-13	16	2.41E-12	26	1.43E-14	21	1.79E-14	29	1.68E-14	31
Total	1.16E-11	465	1.36E-11	149	1.19E-13	174	3.09E-14	50	2.60E-14	48
PFPMIE (perfluoropolymethylisopropyl ether)										
Delta	3.04E-12	122	9.93E-11	1083	1.30E-13	191	5.60E-13	908	1.23E-12	2247
Total	1.90E-10	7619	9.89E-10	10,789	5.65E-12	8263	6.67E-12	10,815	7.38E-12	13,501
HFE-216										
Delta	7.45E-16	<1	4.17E-15	<1	2.56E-17	<1	3.04E-17	<1	2.86E-17	<1
Total	1.99E-14	1	2.34E-14	<1	1.78E-16	<1	5.20E-17	<1	4.44E-17	<1
Trifluoromethyl formate										
Delta	1.65E-12	66	1.14E-11	124	6.24E-14	91	8.62E-14	140	8.08E-14	148
Total	5.54E-11	2220	6.53E-11	712	7.36E-13	1075	1.55E-13	251	1.25E-13	229

(continued on next page)

Table 8.SM.16 (continued)

Acronym, Common Name or Chemical Name	AGWP 20-year (W m^{-2} yr kg^{-1})	GWP 20-year	AGWP 100-year (W m^{-2} yr kg^{-1})	GWP 100-year	AGTP 20-year (K kg^{-1})	GTP 20-year	AGTP 50-year (K kg^{-1})	GTP 50-year	AGTP 100-year (K kg^{-1})	GTP 100-year
Perfluoroethyl formate										
Delta	1.62E-12	65	1.12E-11	122	6.16E-14	90	8.50E-14	138	7.97E-14	146
Total	5.46E-11	2190	6.44E-11	703	7.26E-13	1061	1.53E-13	247	1.24E-13	226
Perfluoropropyl formate										
Delta	1.13E-12	45	7.34E-12	80	4.18E-14	61	5.51E-14	89	5.16E-14	94
Total	3.56E-11	1427	4.18E-11	456	4.22E-13	616	9.70E-14	157	8.01E-14	147
Perfluorobutyl formate										
Delta	1.14E-12	46	7.62E-12	83	4.27E-14	62	5.74E-14	93	5.38E-14	98
Total	3.70E-11	1485	4.36E-11	475	4.62E-13	675	1.02E-13	165	8.36E-14	153
2,2,2-Trifluoroethyl formate										
Delta	1.16E-13	5	6.66E-13	7	4.06E-15	6	4.88E-15	8	4.59E-15	8
Total	3.18E-12	128	3.73E-12	41	2.96E-14	43	8.36E-15	14	7.11E-15	13
3,3,3-Trifluoropropyl formate										
Delta	6.12E-14	2	3.47E-13	4	2.12E-15	3	2.54E-15	4	2.39E-15	4
Total	1.66E-12	66	1.94E-12	21	1.52E-14	22	4.34E-15	7	3.70E-15	7
1,2,2,2-Tetrafluoroethyl formate										
Delta	1.35E-12	54	9.12E-12	99	5.07E-14	74	6.89E-14	112	6.45E-14	118
Total	4.44E-11	1778	5.22E-11	569	5.67E-13	829	1.23E-13	199	1.00E-13	183
1,1,1,3,3,3-Hexafluoropropan-2-yl formate										
Delta	9.53E-13	38	6.46E-12	70	3.59E-14	52	4.88E-14	79	4.57E-14	84
Total	3.14E-11	1259	3.70E-11	403	4.02E-13	587	8.69E-14	141	7.10E-14	130
Perfluorobutyl acetate										
Delta	5.90E-15	<1	3.31E-14	<1	2.03E-16	<1	2.41E-16	<1	2.27E-16	<1
Total	1.58E-13	6	1.85E-13	2	1.42E-15	2	4.12E-16	1	3.52E-16	1
Perfluoropropyl acetate										
Delta	6.17E-15	<1	3.46E-14	<1	2.12E-16	<1	2.52E-16	<1	2.37E-16	<1
Total	1.65E-13	7	1.93E-13	2	1.48E-15	2	4.31E-16	1	3.67E-16	1
Perfluoroethyl acetate										
Delta	7.34E-15	<1	4.11E-14	<1	2.52E-16	<1	3.00E-16	<1	2.82E-16	1
Total	1.96E-13	8	2.30E-13	3	1.76E-15	3	5.12E-16	1	4.37E-16	1
Trifluoromethyl acetate										
Delta	7.39E-15	<1	4.14E-14	<1	2.54E-16	<1	3.02E-16	<1	2.84E-16	1
Total	1.97E-13	8	2.32E-13	3	1.77E-15	3	5.16E-16	1	4.40E-16	1
Methyl carbonofluoridate										
Delta	3.02E-13	12	1.88E-12	20	1.10E-14	16	1.40E-14	23	1.31E-14	24
Total	9.05E-12	363	1.06E-11	116	9.70E-14	142	2.43E-14	39	2.03E-14	37
1,1-Difluoroethyl carbonofluoridate										
Delta	9.41E-14	4	5.35E-13	6	3.26E-15	5	3.92E-15	6	3.68E-15	7
Total	2.55E-12	102	2.99E-12	33	2.35E-14	34	6.70E-15	11	5.70E-15	10

(continued on next page)

Table 8.SM.16 (continued)

Acronym, Common Name or Chemical Name	AGWP 20-year (W m^{-2} yr kg^{-1})	**GWP 20-year**	AGWP 100-year (W m^{-2} yr kg^{-1})	**GWP 100-year**	AGTP 20-year (K kg^{-1})	**GTP 20-year**	AGTP 50-year (K kg^{-1})	**GTP 50-year**	AGTP 100-year (K kg^{-1})	GTP 100-year
1,1-Difluoroethyl 2,2,2-trifluoroacetate										
Delta	1.08E-13	**4**	6.15E-13	**7**	3.75E-15	**5**	4.50E-15	**7**	4.23E-15	**8**
Total	2.94E-12	**118**	3.44E-12	**38**	2.70E-14	**40**	7.70E-15	**12**	6.55E-15	**12**
Ethyl 2,2,2-trifluoroacetate										
Delta	4.88E-15	**<1**	2.74E-14	**<1**	1.68E-16	**<1**	2.00E-16	**<1**	1.88E-16	**<1**
Total	1.31E-13	**5**	1.53E-13	**2**	1.17E-15	**2**	3.41E-16	**1**	2.91E-16	1
2,2,2-Trifluoroethyl 2,2,2-trifluoroacetate										
Delta	2.43E-14	**1**	1.37E-13	**1**	8.37E-16	**1**	9.98E-16	**2**	9.38E-16	**2**
Total	6.52E-13	**26**	7.64E-13	**8**	5.90E-15	**9**	1.70E-15	**3**	1.45E-15	**3**
Methyl 2,2,2-trifluoroacetate										
Delta	1.80E-13	**7**	1.04E-12	**11**	6.32E-15	**9**	7.65E-15	**12**	7.18E-15	**13**
Total	4.98E-12	**200**	5.84E-12	**64**	4.71E-14	**69**	1.31E-14	**21**	1.11E-14	**20**
Methyl 2,2-difluoroacetate										
Delta	1.16E-14	**0**	6.54E-14	**1**	4.01E-16	**1**	4.77E-16	**1**	4.49E-16	**1**
Total	3.12E-13	**12**	3.66E-13	**4**	2.81E-15	**4**	8.15E-16	**1**	6.95E-16	**1**
Difluoromethyl 2,2,2-trifluoroacetate										
Delta	9.52E-14	**4**	5.40E-13	**6**	3.30E-15	**5**	3.95E-15	**6**	3.71E-15	**7**
Total	2.58E-12	**103**	3.02E-12	**33**	2.37E-14	**35**	6.76E-15	**11**	5.75E-15	**11**
2,2,3,3,4,4,4-Heptafluorobutan-1-ol										
Delta	1.17E-13	**5**	6.72E-13	**7**	4.08E-15	**6**	4.93E-15	**8**	4.63E-15	**8**
Total	3.21E-12	**129**	3.77E-12	**41**	3.02E-14	**44**	8.45E-15	**14**	7.18E-15	13
1,1,2-Trifluoro-2-(trifluoromethoxy)-ethane										
Delta	2.27E-12	**91**	2.26E-11	**246**	9.20E-14	**134**	1.77E-13	**287**	1.72E-13	**314**
Total	1.01E-10	**4063**	1.37E-10	**1489**	2.12E-12	**3096**	4.65E-13	**754**	2.69E-13	**492**
1-Ethoxy-1,1,2,3,3,3-hexafluoropropane										
Delta	8.16E-14	**3**	4.66E-13	**5**	2.84E-15	**4**	3.41E-15	**6**	3.20E-15	**6**
Total	2.22E-12	**89**	2.61E-12	**28**	2.06E-14	**30**	5.84E-15	**9**	4.96E-15	**9**
1,1,1,2,2,3,3-Heptafluoro-3-(1,2,2,2-tetrafluoroethoxy)-propane										
Delta	3.40E-12	**136**	8.11E-11	**884**	1.45E-13	**212**	5.26E-13	**853**	8.65E-13	**1582**
Total	2.01E-10	**8075**	6.76E-10	**7371**	5.71E-12	**8353**	4.82E-12	**7812**	3.26E-12	**5960**
2,2,3,3-Tetrafluoro-1-propanol										
Delta	4.58E-14	**2**	2.59E-13	**3**	1.59E-15	**2**	1.90E-15	**3**	1.78E-15	**3**
Total	1.24E-12	**50**	1.45E-12	**16**	1.13E-14	**17**	3.24E-15	**5**	2.76E-15	**5**
2,2,3,4,4,4-Hexafluoro-1-butanol										
Delta	6.00E-14	**2**	3.40E-13	**4**	2.07E-15	**3**	2.48E-15	**4**	2.33E-15	**4**
Total	1.62E-12	**65**	1.90E-12	**21**	1.48E-14	**22**	4.25E-15	**7**	3.62E-15	7
2,2,3,3,4,4,4-Heptafluoro-1-butanol										
Delta	5.72E-14	**2**	3.25E-13	**4**	1.98E-15	**3**	2.38E-15	**4**	2.23E-15	**4**
Total	1.55E-12	**62**	1.82E-12	**20**	1.43E-14	**21**	4.07E-15	**7**	3.46E-15	**6**

(continued on next page)

Table 8.SM.16 (continued)

Acronym, Common Name or Chemical Name	AGWP 20-year (W m^{-2} yr kg^{-1})	**GWP 20-year**	AGWP 100-year (W m^{-2} yr kg^{-1})	**GWP 100-year**	AGTP 20-year (K kg^{-1})	**GTP 20-year**	AGTP 50-year (K kg^{-1})	**GTP 50-year**	AGTP 100-year (K kg^{-1})	GTP 100-year
1,1,2,2-Tetrafluoro-3-methoxy-propane										
Delta	1.87E-15	**<1**	1.05E-14	**<1**	6.43E-17	**<1**	7.65E-17	**<1**	7.19E-17	**<1**
Total	5.00E-14	**2**	5.86E-14	**1**	4.48E-16	**1**	1.31E-16	**<1**	1.11E-16	**<1**
Perfluoro-2-methyl-3-pentanone										
Delta	3.55E-16	**<1**	1.99E-15	**<1**	1.22E-17	**<1**	1.45E-17	**<1**	1.36E-17	**<1**
Total	9.49E-15	**<1**	1.11E-14	**<1**	8.49E-17	**<1**	2.48E-17	**<1**	2.11E-17	**<1**
3,3,3-Trifluoro-propanal										
Delta	3.83E-17	**<1**	2.14E-16	**<1**	1.31E-18	**<1**	1.56E-18	**<1**	1.47E-18	**<1**
Total	1.02E-15	**<1**	1.20E-15	**<1**	9.15E-18	**<1**	2.67E-18	**<1**	2.28E-18	**<1**
2-Fluoroethanol										
Delta	3.14E-15	**<1**	1.76E-14	**<1**	1.08E-16	**<1**	1.28E-16	**<1**	1.21E-16	**<1**
Total	8.39E-14	**3**	9.83E-14	**1**	7.53E-16	**1**	2.19E-16	**<1**	1.87E-16	<1
2,2-Difluoroethanol										
Delta	1.08E-14	**<1**	6.05E-14	**1**	3.71E-16	**1**	4.42E-16	**1**	4.15E-16	**1**
Total	2.88E-13	**12**	3.38E-13	**4**	2.60E-15	**4**	7.54E-16	**1**	6.43E-16	**1**
2,2,2-Trifluoroethanol										
Delta	7.01E-14	3	3.98E-13	4	2.43E-15	4	2.91E-15	5	2.74E-15	**5**
Total	1.90E-12	**76**	2.23E-12	**24**	1.75E-14	**26**	4.98E-15	**8**	4.24E-15	**8**
1,1′-Oxybis[2-(difluoromethoxy)-1,1,2,2-tetrafluoroethane										
Delta	4.65E-12	**186**	7.57E-11	**825**	1.95E-13	**285**	5.58E-13	**905**	6.78E-13	**1240**
Total	2.52E-10	**10,096**	5.27E-10	**5741**	6.57E-12	**9609**	3.31E-12	**5367**	1.42E-12	**2603**
1,1,3,3,4,4,6,6,7,7,9,9,10,10,12,12-hexadecafluoro-2,5,8,11-Tetraoxadodecane										
Delta	4.25E-12	**170**	6.91E-11	**754**	1.78E-13	**260**	5.10E-13	**827**	6.20E-13	**1133**
Total	2.30E-10	**9223**	4.81E-10	**5245**	6.00E-12	**8778**	3.02E-12	**4903**	1.30E-12	**2378**
1,1,3,3,4,4,6,6,7,7,9,9,10,10,12,12,13,13,15,15-Eicosafluoro-2,5,8,11,14-Pentaoxapentadecane										
Delta	3.43E-12	**138**	5.59E-11	**609**	1.44E-13	**211**	4.12E-13	**668**	5.01E-13	**916**
Total	1.86E-10	**7456**	3.89E-10	**4240**	4.85E-12	**7095**	2.44E-12	**3963**	1.05E-12	**1923**

8.SM.16 Metric Values to Support Figure 8.32 and Figure 8.33

Table 8.SM.17 | Metric values used for Figures 8.32 and 8.33.

Species	GWP_{10}	GWP_{20}	GWP_{50}	GWP_{100}	GTP_{10}	GTP_{20}	GTP_{50}	GTP_{100}
CO_2	1	1	1	1	1	1	1	1
CH_4	104.2	83.9	48.4	28.5	99.9	67.5	14.1	4.3
N_2O	246.6	263.7	275.6	264.8	253.5	276.9	281.8	234.2
BC	4349.2	2421.1	1139.3	658.6	2398.2	702.8	110.0	90.7
OC	–438.5	–244.1	–114.9	–66.4	–241.8	–70.9	–11.1	–9.1
SO_2	–253.5	–141.1	–66.4	–38.4	–139.6	–40.9	–6.4	–5.3
NOx	134.2	16.7	–15.6	–10.8	2.8	–86.3	–27.4	–2.8
CO	8.6	5.9	3.2	1.9	6.8	3.7	0.7	0.3

8.SM.17 Metric Values for Sectors to Support Section 8.7.2

Table 8.SM.18 | GWPs and GTPs for NO_X, BC, OC and SO_2 from various sectors (metrics for SO_2 are given on SO_2 basis, while for NO_X they are given on a nitrogen basis). For the reference gas CO_2, RE and IRF from AR4 are used in the calculations. The GWP_{100} and GTP_{100} values can be scaled by 0.94 and 0.92, respectively, to account for updated values for the reference gas CO_2. For 20 years the changes are negligible. ari is aerosol–radiation interaction.

Sector and emission region (if sub-global)	GWP		GTP	
	H = 20	H = 100	H = 20	H = 100
Aviation				
NO_X[a]	92 to 338	–21 to 67	–396 to –121	–5.8 to 7.9
NO_X[b]	120 to 470	–2.1 to 71	–590 to –200	–9.5 to 7.6
NO_X[h]	415	75	–239	8.6
Shipping				
NO_X[b]	–76 to –31	–36 to –25	–190 to –130	–6.1 to –4.2
NO_X[c]	–107	–73	–135	
SO_2[b]	–150 to –37	–43 to –11	–44 to –11	–6.1 to –1.5
SO_2, Arctic[e]	–47	–13		
OC, Arctic[e]	–151	–43		
BC ari, Arctic[e]	2037	579		
BC on snow, Arctic[e]	764	217		
Energy Related				
BC ari + albedo[g]	2,800 ± 1,800	790 ± 530		
OC Energy related[g]	–110 (–40,–210)	–30 (–12, –60)		
Industry/Power BC, Asia[f]	3,260	910		
Household BC, Asia[f]	2,680	750		
Transport BC, Asia[f]	2,640	740		
Transport BC, North America[f]	3,900	1,090		
Household OC, Asia[f]	–260	–72		
Transport OC, Asia[f]	–180	–50		
Industry/Power SO_2, Asia[f]	–106 (ari)	–30 (ari)		
Industry/Power SO_2, North America[f]	–215 (ari)	–60 (ari)		
Coal-fired power, NO_X[d]	20			
Coal-fired power, SO_2[d]	–189 (ari)	–53 (ari)		
Petroleum Production				
BC ari, Arctic	2,369	673		
BC on snow, Arctic[e]	4,104	1,166		
SO_2, Arctic[e]	–64	–18		
OC, Arctic[e]	–152	–43		
Open Biomass				
BC ari + albedo[g]	3,100 ± 1,300	880 ± 370		
OC[g]	–180 (–70, –360)	–53 (–20, –100)		

Notes:

[a] Myhre et al. (2011)

[b] Fuglestvedt et al. (2010)

[c] Collins et al. (2010)

[d] Shindell and Faluvegi (2010)

[e] Ødemark et al. (2012)

[f] Shindell et al. (2008)

[g] Bond et al. (2011)

[h] Köhler et al. (2013)

8.SM.18 Further Information on Temperature Impact from Various Sectors to Support Section 8.7.2

Table 8.SM.19 | Information about emissions and metric values used in calculations of temperature impacts of sectors.

Species	Global Emissions (Gg)	AGTP Values Based on	GTP_{20}	GTP_{100}
CO_2	3.69E+07	Joos et al. (2013) and AR5	1	1
CH_4	3.64E+05	Updated by AR5	67	4.3
N_2O	1.07E+04	Updated by AR5	277	234
HCFC-141b	7.68E-01	Updated by AR5	1853	111
HCF-142b	6.18E+00	Updated by AR5	4393	356
HFC-23	1.75E+01	Updated by AR5	11524	12709
HFC-32	2.36E+00	Updated by AR5	1362	94
HFC-125	3.00E+01	Updated by AR5	5797	967
HFC-134a	1.63E+02	Updated by AR5	3053	201
HFC-143a	3.25E+01	Updated by AR5	6957	2505
HFC-152a	2.79E+01	Updated by AR5	174	19
HFC-227ea	7.18E+00	Updated by AR5	5283	1500
HFC-236fa	1.59E-01	Updated by AR5	7397	8377
HFC-245fa	4.11E+00	Updated by AR5	1974	121
HFC-365mfc	1.73E+00	Updated by AR5	1893	114
HFC-43-10mee	2.69E-01	Updated by AR5	3718	281
SF_6	6.50E+00	Updated by AR5	18904	28215
NF_3	1.75E-01	Updated by AR5	13723	18119
PFC-14	1.12E+01	Updated by AR5	5272	8038
PFC-116	2.43E+00	Updated by AR5	8877	13456
PFC-218	4.13E-01	Updated by AR5	7176	10654
PFC-318	2.49E-02	Updated by AR5	7676	11456
PFC-3-1-10	1.96E-02	Updated by AR5	7419	11016
PFC-4-1-12	9.58E-06	Updated by AR5	6856	10284
PFC-5-1-14	3.78E-01	Updated by AR5	6365	9493
BC	5.31E+03	Bond et al. (2013) aerosol radiation interaction and albedo effect included in metric values	703	91
OC	1.36E+04	Fuglestvedt et al. (2010)	–71	–9.1
SO_2	1.27E+05 (in SO_2)	Fuglestvedt et al. (2010)	–41	–5.3
Contrails and CIC		Updated by AR5	0.75	0.10
Aircraft NO_x		Stevenson et al. (2004), as given by Fuglestvedt et al. (2010)	–204	6.7
Shipping NO_x		Fuglestvedt et al. (2008), as given by Fuglestvedt et al. (2010)	–162	–4.0
Surface NO_x	3.72E+04 (includes shipping and air, in N)	The global run in Wild et al. (2001), as given by Fuglestvedt et al. (2010)	–86	–2.8
CO	8.93E+05	Derwent et al. (2001), as given by Fuglestvedt et al. (2010)	3.7	0.27
VOC	1.60E+05	Collins et al. (2002) , as given Fuglestvedt et al. (2010)	7.4	0.61
NH_3	4.93E+04	Shindell et al. (2009)	–23	–3.0
ACI		(–0.45)/(–0.4)*SO_2, updated by AR5	–46	–5.9

AGTPs for the aerosols OC and SO_2 are from Fuglestvedt et al. (2010). For BC, the metric parameterization is based on Bond et al. (2013); the RF of the aerosol radiation interaction (0.71 W m^{-2}) and snow and ice albedo effects (0.1 + 0.03 W m^{-2}).

The parameters for the ozone precursors NO_x is from the global run in Wild et al. (2001), CO from Derwent et al. (2001) and VOC from Collins et al. (2002), as given by Fuglestvedt et al. (2010). For NO_x emissions from shipping and aircraft, the parameters are from Fuglestvedt et al. (2008) and Wild et al. (2001), respectively, as given by Fuglestvedt et al. (2010).

The parameters for the indirect effect of contrails and contrail induced cirrus (CIC) are updated for AR5. The lifetime is set to 5 hours, as in Fuglestvedt et al. (2010), while the REs are based on a radiative forcing of 10 m W m^{-2} and 50 m W m^{-2} for contrails and the sum of contrails and CIC, respectively. The calculations are based emissions from aviation of about 776 Tg(CO_2), which comes from EDGAR 2008 (http://edgar.jrc.ec.europa.eu/overview.php?v=42).

The aerosol–cloud interaction has been calculated with a scaling relative to the direct effect of sulphate. The scaling is –0.45 / –0.4 = 1.125 and is used across almost all sectors (i.e., no separate scaling used for aerosol–cloud interaction for shipping). We do not account for any aerosol–cloud interaction from the aviation sector, as we include the impact of contrails and CIC.

We have tested the effect of various aerosol–cloud interaction values and attributions to components (e.g., attributing aerosol–cloud interaction equally to OC and sulphate, setting the aerosol–cloud interaction at the maximum or minimum of its 90% confidence interval, choosing a larger BC forcing, etc.). The ranking of sectors for global emissions differs little between the different parameterizations and mostly for the shortest time horizons.

The calculations presented here do not include the climate–carbon feedback for non-CO_2 emissions, which can substantially increase those values (Collins et al., 2013). Emissions: Emission Database for Global Atmospheric Research (EDGAR) 2008 (http://edgar.jrc.ec.europa.eu/overview.php?v=42). VOC emissions are converted to carbon mass units based on IPCC (2006). BC and OC emissions for year 2005 are taken from Shindell et al. (2012). Emission data requires frequently updates when new information become available (e.g., Lam et al., (2012). BC and OC emission from biomass burning are taken from Lamarque et al. (2010).

Figure 8.34 is based on the calculations and data described above. Figure 8.SM.9 shows the net temperature responses as function of time for one year pulse emissions. Figure 8.SM.10 shows the net temperature responses as function of time assuming constant emissions from the various sectors.

Figures 8.32 and 8.33 are based on the emission data given above for CO_2, CH_4, N_2O, BC, OC, SO_2, NO_x and CO. The following metric values used are given in Table 8.SM.18.

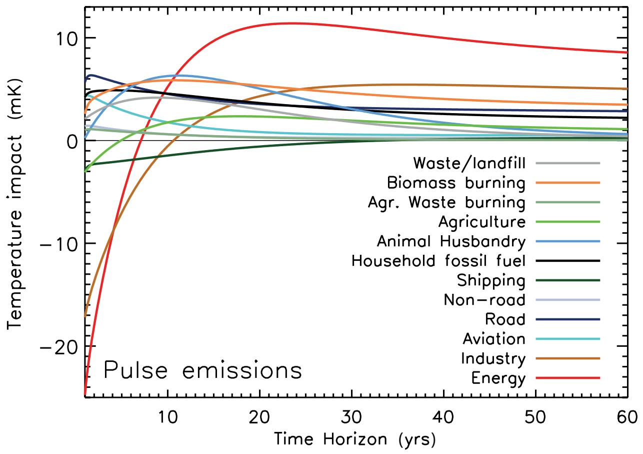

Figure 8.SM.9 | Temperature responses from the various sectors as function of time for 1-year pulse emissions.

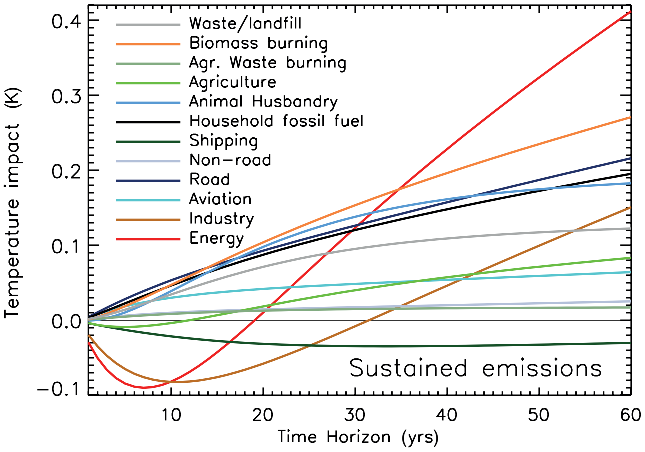

Figure 8.SM.10 | Temperature responses from the various sectors as function of time, assuming constant emissions.

References

Baliunas, S., and R. Jastrow, 1990: Evidence for long-term brightness changes of solar-type stars. *Nature*, **348**, 520–523.

Ball, W., Y. Unruh, N. Krivova, S. Solanki, T. Wenzler, D. Mortlock, and A. Jaffe, 2012: Reconstruction of total solar irradiance 1974–2009. *Astron. Astrophys.*, **541**, A27.

Bond, T., C. Zarzycki, M. Flanner, and D. Koch, 2011: Quantifying immediate radiative forcing by black carbon and organic matter with the Specific Forcing Pulse. *Atmos. Chem. Phys.*, **11**, 1505–1525.

Bond, T. C., et al., 2013: Bounding the role of black carbon in the climate system: A scientific assessment. *J. Geophys. Res. Atmos.*, **118**, 5380–5552.

Boucher, O., and M. Reddy, 2008: Climate trade-off between black carbon and carbon dioxide emissions. *Energ. Policy*, **36**, 193–200.

Boucher, O., P. Friedlingstein, B. Collins, and K. P. Shine, 2009: The indirect global warming potential and global temperature change potential due to methane oxidation. *Environ. Res. Lett.*, **4**, 044007.

Butler, J., B. Johnson, J. Rice, E. Shirley, and R. Barnes, 2008: Sources of differences in on-Orbital total solar irradiance measurements and description of a proposed laboratory intercomparison. *J. Res. Natl. Inst. Stand. Technol.*, **113**, 187–203.

Caldeira, K., and J. Kasting, 1993: Insensitivity of global warming potentials to carbon-dioxide emission scenarios. *Nature*, **366**, 251–253.

Clette, F., D. Berghmans, P. Vanlommel, R. Van der Linden, A. Koeckelenbergh, and L. Wauters, 2007: From the Wolf number to the International Sunspot Index: 25 years of SIDC. *Adv. Space Res.*, **40**, 919–928.

Collins, W., R. Derwent, C. Johnson, and D. Stevenson, 2002: The oxidation of organic compounds in the troposphere and their global warming potentials. *Clim. Change*, **52**, 453–479.

Collins, W. J., S. Sitch, and O. Boucher, 2010: How vegetation impacts affect climate metrics for ozone precursors. *J. Geophys. Res. Atmos.*, **115**, D23308.

Collins, W. J., M. M. Fry, H. Yu, J. S. Fuglestvedt, D. T. Shindell, and J. J. West, 2013: Global and regional temperature-change potentials for near-term climate forcers. *Atmos. Chem. Phys.*, **13**, 2471–2485.

Crowley, T. J., and M. B. Unterman, 2013: Technical details concerning development of a 1200-yr proxy index for global volcanism. *Earth Syst. Sci. Data*, **5**, 187–197.

Daniel, J., E. Fleming, R. Portmann, G. Velders, C. Jackman, and A. Ravishankara, 2010: Options to accelerate ozone recovery: Ozone and climate benefits. *Atmos. Chem. Phys.*, **10**, 7697–7707.

DeLand, M., and R. Cebula, 2012: Solar UV variations during the decline of Cycle 23. *J. Atmos. Sol. Terres. Phys.*, **77**, 225–234.

Derwent, R., W. Collins, C. Johnson, and D. Stevenson, 2001: Transient behaviour of tropospheric ozone precursors in a global 3-D CTM and their indirect greenhouse effects. *Clim. Change*, **49**, 463–487.

Enting, I. G., T. M. L. Wigley, and M. Heimann, 1994: *Future Emissions and Concentrations of Carbon Dioxide: Key Ocean/Atmosphere/Land Analyses.* CSIRO Division of Atmospheric Research Technical Paper no. 31.

Feulner, G., 2011: Are the most recent estimates for Maunder Minimum solar irradiance in agreement with temperature reconstructions? *Geophys. Res. Lett.*, **38**, L16706.

Fontenla, J., O. White, P. Fox, E. Avrett, and R. Kurucz, 1999: Calculation of solar irradiances. I. Synthesis of the solar spectrum. *Astrophys. J.*, **518**, 480–499.

Forster, P., et al., 2005: Resolution of the uncertainties in the radiative forcing of HFC-134a. *J. Quant. Spectrosc. Radiat. Transfer*, **93**, 447–460.

Forster, P., et al., 2007: Changes in atmospheric constituents and in radiative forcing. In: *Climate Change 2007: The Physical Science Basis. Contribution of Working Group I to the Fourth Assessment Report of the Intergovernmental Panel on Climate Change* [Solomon, S., D. Qin, M. Manning, Z. Chen, M. Marquis, K. B. Averyt, M. Tignor and H. L. Miller (eds.)] Cambridge University Press, Cambridge, United Kingdom and New York, NY, USA, 129–234.

Foukal, P., A. Ortiz, and R. Schnerr, 2011: Dimming of the 17th century sun. *Astrophys. J. Letters*, **733**, L38.

Fox, N., et al., 2011: Accurate radiometry from space: an essential tool for climate studies. *Philos. Trans. R. Soc. A*, **369**, 4028–4063.

Freckleton, R., E. Highwood, K. Shine, O. Wild, K. Law, and M. Sanderson, 1998: Greenhouse gas radiative forcing: Effects of averaging and inhomogeneities in trace gas distribution. *Q. J. R. Meteorol. Soc.*, **124**, 2099–2127.

Frohlich, C., 2009: Evidence of a long-term trend in total solar irradiance. *Astron. Astrophys.*, **501**, L27–U508.

Fuglestvedt, J., T. Berntsen, G. Myhre, K. Rypdal, and R. Skeie, 2008: Climate forcing from the transport sectors. *Proc. Natl. Acad. Sci. U.S.A.*, **105**, 454–458.

Fuglestvedt, J. S., et al., 2010: Transport impacts on atmosphere and climate: Metrics. *Atmos. Environ.*, **44**, 4648–4677.

Gao, C., A. Robock, and C. Ammann, 2008: Volcanic forcing of climate over the past 1500 years: An improved ice core-based index for climate models. *J. Geophys. Res. Atmos.*, **113**, D23111.

Gray, L., et al., 2010: Solar influences on climate. *Rev. Geophys.*, **48**, RG4001.

Haigh, J., A. Winning, R. Toumi, and J. Harder, 2010: An influence of solar spectral variations on radiative forcing of climate. *Nature*, **467**, 696–699.

Hall, J., and G. Lockwood, 2004: The chromospheric activity and variability of cycling and flat activity solar-analog stars. *Astrophys. J.*, **614**, 942–946.

Hansen, J., M. Sato, P. Kharecha, and K. von Schuckmann, 2011: Earth's energy imbalance and implications. *Atmos. Chem. Phys.*, **11**, 13421–13449.

Harder, J., J. Fontenla, P. Pilewskie, E. Richard, and T. Woods, 2009: Trends in solar spectral irradiance variability in the visible and infrared. *Geophys. Res. Lett.*, **36**, L07801.

Hathaway, D., R. Wilson, and E. Reichmann, 2002: Group sunspot numbers: Sunspot cycle characteristics. *Sol. Phys.*, **211**, 357–370.

Holmes, C. D., M. J. Prather, O. A. Søvde, and G. Myhre, 2013: Future methane, hydroxyl, and their uncertainties: Key climate and emission parameters for future predictions. *Atmos. Chem. Phys.*, **13**, 285–302.

Hoyt, D., and K. Schatten, 1998: Group Sunspot Numbers: A new solar activity reconstruction. *Sol. Phys.*, **179**, 189–219.

IPCC, 2006: *2006 IPCC Guidelines for National Greenhouse Gas Inventories*. Prepared by the National Greenhouse Gas Inventories Programme.

Jacquinet-Husson, N., et al., 2011: The 2009 edition of the GEISA spectroscopic database. *J. Quant. Spectrosc. Radiat. Transfer*, **112**, 2395–2445.

Jain, A. K., B. P. Briegleb, K. Minschwaner, and D. J. Wuebbles, 2000: Radiative forcings and global warming potentials of 39 greenhouse gases. *J. Geophys. Res. Atmos.*, **105**, 20773–20790.

Joos, F., M. Bruno, R. Fink, U. Siegenthaler, T. Stocker, and C. LeQuere, 1996: An efficient and accurate representation of complex oceanic and biospheric models of anthropogenic carbon uptake. *Tellus B*, **48**, 397–417.

Joos, F., et al., 2013: Carbon dioxide and climate impulse response functions for the computation of greenhouse gas metrics: A multi-model analysis. *Atmos. Chem. Phys.*, **13**, 2793–2825.

Judge, P., G. Lockwood, R. Radick, G. Henry, A. Shapiro, W. Schmutz, and C. Lindsey, 2012: Confronting a solar irradiance reconstruction with solar and stellar data (Research Note). *Astron. Astrophys.*, **544**, A88.

Koehler, M. O., G. Raedel, K. P. Shine, H. L. Rogers, and J. A. Pyle, 2013: Latitudinal variation of the effect of aviation NOx emissions on atmospheric ozone and methane and related climate metrics. *Atmos. Environ.*, **64**, 1–9.

Krivova, N., L. Vieira, and S. Solanki, 2010: Reconstruction of solar spectral irradiance since the Maunder minimum. *J. Geophys. Res. Space Phys.*, **115**, A12112.

Lam, N. L., et al., 2012: Household light makes global heat: High black carbon emissions from kerosene wick lamps. *Environ. Sci. Technol.*, **46**, 13531–13538.

Lamarque, J., et al., 2010: Historical (1850–2000) gridded anthropogenic and biomass burning emissions of reactive gases and aerosols: Methodology and application. *Atmos. Chem. Phys.*, **10**, 7017–7039.

Lean, J., and M. Deland, 2012: How does the sun's spectrum vary? *J. Clim.*, **25**, 2555–2560.

Lee, Y. H., et al., 2013: Evaluation of preindustrial to present-day black carbon and its albedo forcing from Atmospheric Chemistry and Climate Model Intercomparison Project (ACCMIP). *Atmos. Chem. Phys.*, **13**, 2607–2634.

Li, S., and A. Jarvis, 2009: Long run surface temperature dynamics of an A-OGCM: The HadCM3 4xCO_2 forcing experiment revisited. *Clim. Dyn.*, **33**, 817–825.

Lockwood, M., and M. Owens, 2011: Centennial changes in the heliospheric magnetic field and open solar flux: The consensus view from geomagnetic data and cosmogenic isotopes and its implications. *J. Geophys. Res. Space Phys.*, **116**, A04109.

Morgan, M. G., and M. Henrion, 1990: *A Guide to Dealing with Uncertainty in Quantitative Risk and Policy Analysis.* Cambridge University Press, Cambridge, United Kingdom, and New York, NY, USA.

Myhre, G., and F. Stordal, 1997: Role of spatial and temporal variations in the computation of radiative forcing and GWP. *J. Geophys. Res. Atmos.*, **102**, 11181–11200.

Myhre, G., E. J. Highwood, K. P. Shine, and F. Stordal, 1998: New estimates of radiative forcing due to well mixed greenhouse gases. *Geophys. Res. Lett.*, **25**, 2715–2718.

Myhre, G., F. Stordal, I. Gausemel, C. J. Nielsen, and E. Mahieu, 2006: Line-by-line calculations of thermal infrared radiation representative for global condition: CFC-12 as an example. *J. Quant. Spectrosc. Radiat. Transfer*, **97**, 317–331.

Myhre, G., et al., 2011: Radiative forcing due to changes in ozone and methane caused by the transport sector. *Atmos. Environ.*, **45**, 387–394.

Naik, V., A. K. Jain, K. O. Patten, and D. J. Wuebbles, 2000: Consistent sets of atmospheric lifetimes and radiative forcings on climate for CFC replacements: HCFCs and HFCs. *J. Geophys. Res. Atmos.*, **105**, 6903–6914.

Ødemark, K., S. B. Dalsoren, B. H. Samset, T. K. Berntsen, J. S. Fuglestvedt, and G. Myhre, 2012: Short-lived climate forcers from current shipping and petroleum activities in the Arctic. *Atmos. Chem. Phys.*, **12**, 1979–1993.

Olivié, D. J. L., G. Peters, and D. Saint-Martin, 2012: Atmosphere response time scales estimated from AOGCM Experiments. *J. Clim.*, **25**, 7956–7972.

Pinnock, S., M. D. Hurley, K. P. Shine, T. J. Wallington, and T. J. Smyth, 1995: Radiative forcing of climate by hydrochlorofluorocarbons and hydrofluorocarbons. *J. Geophys. Res. Atmos.*, **100**, 23227–23238.

Plattner, G. K., et al., 2008: Long-term climate commitments projected with climate-carbon cycle models. *J. Clim.*, **21**, 2721–2751.

Pongratz, J., T. Raddatz, C. H. Reick, M. Esch, and M. Claussen, 2009: Radiative forcing from anthropogenic land cover change since AD 800. *Geophys. Res. Lett.*, **36**, L02709.

Prather, M., 1994: Lifetimes and eigenstates in atmospheric chemistry. *Geophys. Res. Lett.*, **21**, 801–804.

Prather, M., 2007: Lifetimes and time scales in atmospheric chemistry. *Philos. Trans. R. Soc. London A*, **365**, 1705–1726.

Prather, M. J., C. D. Holmes, and J. Hsu, 2012: Reactive greenhouse gas scenarios: Systematic exploration of uncertainties and the role of atmospheric chemistry. *Geophys. Res. Lett.*, **39**, L09803.

Reisinger, A., M. Meinshausen, and M. Manning, 2011: Future changes in global warming potentials under representative concentration pathways. *Environ. Res. Lett.*, **6**, 024020.

Rigby, M., et al., 2013: Re-evaluation of the lifetimes of the major CFCs and CH_3CCl_3 using atmospheric trends. *Atmos. Chem. Phys.*, **13**, 2691–2702.

Rothman, L., et al., 2009: The HITRAN 2008 molecular spectroscopic database. *J. Quant. Spectrosc. Radiat. Transfer*, **110**, 533–572.

Sato, M., J. E. Hansen, M. P. McCormick, and J. B. Pollack, 1993: Stratospheric aerosol optical depths, 1850–1990. *J. Geophys. Res. Atmos.*, **98**, 22987–22994.

Schmidt, G., et al., 2011: Climate forcing reconstructions for use in PMIP simulations of the last millennium (v1.0). *Geosci. Model Dev.*, **4**, 33–45.

Schmidt, G. A., et al., 2012: Climate forcing reconstructions for use in PMIP simulations of the Last Millennium (v1.1). *Geosci. Model Dev.*, **5**, 185–191.

Schrijver, C., W. Livingston, T. Woods, and R. Mewaldt, 2011: The minimal solar activity in 2008–2009 and its implications for long-term climate modeling. *Geophys. Res. Lett.*, **38**, L06701.

Sellevåg, S. R., C. J. Nielsen, O. A. Søvde, G. Myhre, J. K. Sundet, F. Stordal, and I. S. A. Isaksen, 2004: Atmospheric gas-phase degradation and global warming potentials of 2-fluoro ethanol, 2,2-difluoroethanol, and 2,2,2-trifluoroethanol. *Atmos. Environ.*, **38**, 6725–6735.

Shapiro, A., W. Schmutz, E. Rozanov, M. Schoell, M. Haberreiter, A. Shapiro, and S. Nyeki, 2011: A new approach to the long-term reconstruction of the solar irradiance leads to large historical solar forcing. *Astron. Astrophys.*, **529**, A67.

Shindell, D., and G. Faluvegi, 2010: The net climate impact of coal-fired power plant emissions. *Atmos. Chem. Phys.*, **10**, 3247–3260.

Shindell, D., G. Faluvegi, N. Bell, and G. Schmidt, 2005: An emissions-based view of climate forcing by methane and tropospheric ozone. *Geophys. Res. Lett.*, **32**, L04803.

Shindell, D., et al., 2008: Climate forcing and air quality change due to regional emissions reductions by economic sector. *Atmos. Chem. Phys.*, **8**, 7101–7113.

Shindell, D., et al., 2012: Simultaneously mitigating near-term climate change and improving human health and food security. *Science*, **335**, 183–189.

Shindell, D. T., G. Faluvegi, D. M. Koch, G. A. Schmidt, N. Unger, and S. E. Bauer, 2009: Improved attribution of climate forcing to emissions. *Science*, **326**, 716–718.

Shindell, D. T., et al., 2013: Radiative forcing in the ACCMIP historical and future climate simulations. *Atmos. Chem. Phys.*, **13**, 2939–2974.

Shine, K., J. Fuglestvedt, K. Hailemariam, and N. Stuber, 2005: Alternatives to the global warming potential for comparing climate impacts of emissions of greenhouse gases. *Clim. Change*, **68**, 281–302.

Sihra, K., M. Hurley, K. Shine, and T. Wallington, 2001: Updated radiative forcing estimates of 65 halocarbons and nonmethane hydrocarbons. *J. Geophys. Res. Atmos.*, **106**, 20493–20505.

Skeie, R., T. Berntsen, G. Myhre, K. Tanaka, M. Kvalevag, and C. Hoyle, 2011a: Anthropogenic radiative forcing time series from pre-industrial times until 2010. *Atmos. Chem. Phys.*, **11**, 11827–11857.

Skeie, R., T. Berntsen, G. Myhre, C. Pedersen, J. Strom, S. Gerland, and J. Ogren, 2011b: Black carbon in the atmosphere and snow, from pre-industrial times until present. *Atmos. Chem. Phys.*, **11**, 6809–6836.

Søvde, O. A., M. Gauss, S. P. Smyshlyaev, and I. S. A. Isaksen, 2008: Evaluation of the chemical transport model Oslo CTM2 with focus on arctic winter ozone depletion. *J. Geophys. Res. Atmos.*, **113**, D09304.

Steinhilber, F., J. Beer, and C. Frohlich, 2009: Total solar irradiance during the Holocene. *Geophys. Res. Lett.*, **36**, L19704.

Stevenson, D., R. Doherty, M. Sanderson, W. Collins, C. Johnson, and R. Derwent, 2004: Radiative forcing from aircraft NOx emissions: Mechanisms and seasonal dependence. *J. Geophys. Res. Atmos.*, **109**, D17307.

Stevenson, D. S., et al., 2013: Tropospheric ozone changes, radiative forcing and attribution to emissions in the Atmospheric Chemistry and Climate Model Intercomparison Project (ACCMIP). *Atmos. Chem. Phys.*, **13**, 3063–3085.

Svalgaard, L., and E. Cliver, 2010: Heliospheric magnetic field 1835–2009. *J. Geophys. Res. Space Phys.*, **115**, A09111.

Svalgaard, L., C. Mandrini, and D. Webb, 2012: How well do we know the sunspot number? *Comp. Magnet. Min. Character. Quiet Times Sun Stars*, **286**, 27–33.

Trenberth, K., and L. Smith, 2005: The mass of the atmosphere: A constraint on global analyses. *J. Clim.*, **18**, 864–875.

van Vuuren, D., J. Edmonds, M. Kainuma, K. Riahi, and J. Weyant, 2011: A special issue on the RCPs. *Clim. Change*, **109**, 1–4.

Wang, Y., J. Lean, and N. Sheeley, 2005: Modeling the sun's magnetic field and irradiance since 1713. *Astrophys. J.*, **625**, 522–538.

Wild, O., M. Prather, and H. Akimoto, 2001: Indirect long-term global radiative cooling from NOx emissions. *Geophys. Res. Lett.*, **28**, 1719–1722.

WMO, 1999: *Scientific Assessment of Ozone Depletion: 1998, Global Ozone Research and Monitoring Project*. World Meteorological Organisation, Report No. 44. World Meterological Organisation, Geneva, Switzerland.

WMO, 2011: *Scientific Assessment of Ozone Depletion: 2010*. Global Ozone Research and Monitoring Project Report. World Meteorological Organisation, Geneva, Switzerland, 516 pp.

Wright, J., 2004: Do we know of any Maunder minimum stars? *Astron. J.*, **128**, 1273–1278.

10SM

Detection and Attribution of Climate Change: from Global to Regional

Supplementary Material

Coordinating Lead Authors:
Nathaniel L. Bindoff (Australia), Peter A. Stott (UK)

Lead Authors:
Krishna Mirle AchutaRao (India), Myles R. Allen (UK), Nathan Gillett (Canada), David Gutzler (USA), Kabumbwe Hansingo (Zambia), Gabriele Hegerl (UK/Germany), Yongyun Hu (China), Suman Jain (Zambia), Igor I. Mokhov (Russian Federation), James Overland (USA), Judith Perlwitz (USA), Rachid Sebbari (Morocco), Xuebin Zhang (Canada)

Contributing Authors:
Magne Aldrin (Norway), Beena Balan Sarojini (UK/India), Jürg Beer (Switzerland), Olivier Boucher (France), Pascale Braconnot (France), Oliver Browne (UK), Ping Chang (USA), Nikolaos Christidis (UK), Tim DelSole (USA), Catia M. Domingues (Australia/Brazil), Paul J. Durack (USA/Australia), Alexey Eliseev (Russian Federation), Kerry Emanuel (USA), Graham Feingold (USA), Chris Forest (USA), Jesus Fidel González Rouco (Spain), Hugues Goosse (Belgium), Lesley Gray (UK), Jonathan Gregory (UK), Isaac Held (USA), Greg Holland (USA), Jara Imbers Quintana (UK), William Ingram (UK), Johann Jungclaus (Germany), Georg Kaser (Austria), Veli-Matti Kerminen (Finland), Thomas Knutson (USA), Reto Knutti (Switzerland), James Kossin (USA), Mike Lockwood (UK), Ulrike Lohmann (Switzerland), Fraser Lott (UK), Jian Lu (USA/Canada), Irina Mahlstein (Switzerland), Valérie Masson-Delmotte (France), Damon Matthews (Canada), Gerald Meehl (USA), Blanca Mendoza (Mexico), Viviane Vasconcellos de Menezes (Australia/Brazil), Seung-Ki Min (Republic of Korea), Daniel Mitchell (UK), Thomas Mölg (Germany/Austria), Simone Morak (UK), Timothy Osborn (UK), Alexander Otto (UK), Friederike Otto (UK), David Pierce (USA), Debbie Polson (UK), Aurélien Ribes (France), Joeri Rogelj (Switzerland/Belgium), Andrew Schurer (UK), Vladimir Semenov (Russian Federation), Drew Shindell (USA), Dmitry Smirnov (Russian Federation), Peter W. Thorne (USA/Norway/UK), Muyin Wang (USA), Martin Wild (Switzerland), Rong Zhang (USA)

Review Editors:
Judit Bartholy (Hungary), Robert Vautard (France), Tetsuzo Yasunari (Japan)

This chapter supplementary material should be cited as:
Bindoff, N.L., P.A. Stott, K.M. AchutaRao, M.R. Allen, N. Gillett, D. Gutzler, K. Hansingo, G. Hegerl, Y. Hu, S. Jain, I.I. Mokhov, J. Overland, J. Perlwitz, R. Sebbari and X. Zhang, 2013: Detection and Attribution of Climate Change: from Global to Regional Supplementary Material. In: Climate Change 2013: *The Physical Science Basis. Contribution of Working Group I to the Fifth Assessment Report of the Intergovernmental Panel on Climate Change* [Stocker, T.F., D. Qin, G.-K. Plattner, M. Tignor, S.K. Allen, J. Boschung, A. Nauels, Y. Xia, V. Bex and P.M. Midgley (eds.)]. Available from www.climatechange2013.org and www.ipcc.ch.

Table of Contents

10.SM.1 Notes and Technical Details on Figures Displayed in Chapter 10

Box 10.1, Figure 1

a). Observed global annual mean temperatures 1860–2012 relative to the 1880–1919 climatology from the Hadley Centre/Climatic Research Unit gridded surface temperature data set 4 (HadCRUT4) data set (coloured dots, with colours also indicating observed temperature) compared with Coupled Model Intercomparison Project Phase 3 (CMIP3)/CMIP5 ensemble mean response to anthropogenic forcing (orange), natural forcing (blue) and best-fit linear combination (black). CMIP series was obtained by a simple average over the models available for each year, with equal weight given to each model. Anthropogenic signal obtained by differencing historical from natural simulations. Anthropogenic and natural simulations are masked to correspond to observations following Jones et al. (2013) and Figure 10.1 and noise-reduced with 5-point running mean. To avoid smoothing out the volcanic signals, smoothing is not performed over years where the ensemble mean natural simulations decreases by more than 0.05°C.

b). Same as panel a), but plotting against CMIP ensemble mean anthropogenic warming instead of time. Note that the only change from Box 10.1 Figure 1 (a) is the location of points in the horizontal.

c). Same as panel b), but plotting observed annual mean temperatures against CMIP ensemble mean anthropogenic warming in one direction, and naturally forced temperature change in the other. Mesh shows best-fit plane through the observed points, obtained by an ordinary least-squares fit giving equal weight to all points. Black line shows the best-fit linear combination of model-simulated anthropogenic and naturally forced temperature change. Length of pins shows residual climate variability (difference between observations and best-fit). Gradients of best-fit surface in anthropogenic and natural directions show best-fit scaling factors on CMIP5 ensemble mean anthropogenic and natural temperature change. For an animated visualisation of how this figure is constructed, please see the animation file provided as part of the Chapter 10 Supplementary Material. Uncertainty analysis of best-fit gradients in (c) using CMIP5 control variability.

d). Best-fit scaling factors on anthropogenic and natural temperature change, or gradients of the best-fit plane through observations from (c), shown by red diamond. Grey diamonds show corresponding gradients obtained applying an identical analysis to 114 non-overlapping 153-year segments (i.e., 17,442 years in total) of global mean surface temperature (GMST) from unforced control variability from the CMIP5 ensemble. For this heuristic example, control segments have not been masked as in the observations, but residuals are consistent with observed residual variability in both variance and power spectra. Black ellipse shows two-dimensional 90% confidence interval obtained by fitting an $F_{2,114}$ distribution to the grey diamonds. Red ellipse shows corresponding confidence interval centered on the best-fit gradients through the observations. Corresponding one-dimensional confidence intervals on scaling on model anthropogenic and natural warming shown by the red cross. Upper axis shows corresponding attributable anthropogenic warming 1951–2010 obtained from a straight-line fit to the CMIP ensemble mean anthropogenic warming. Location of red diamond and error bar on this axis indicate best-estimate and uncertainty in attributable anthropogenic warming.

Figure 10.1, Figure 10.2, Figure 10.3

The right panels of Figure 10.1 (Figures 10.1d, e, f) are taken from Figure 3a of Forster et al. (2013), except that data from Fgoals-S2 have been excluded, and that 3-year smoothing to the data has not been applied here.

Process and data to create the leftmost panels of Figure 10.1; Figures 10.2 and 10.3 are described below. These figures are adapted from Jones et al. (2013).

Data
All of the data used were provided as monthly Netcdf files, from the CMIP3 and CMIP5 archives, and Daithi Stone (providing data used in the AR4 figures that were not in the CMIP3 archive). CMIP3 20C3M experiments were extended to 2012 by using A1B scenario simulations. CMIP5 historical experiments were extended to 2012 by using historicalExt and rcp4.5 experiments.

Regridding
All data are re-gridded onto the HadCRUT4 spatial grid (5° × 5°) since HadCRUT4 generally has the most restricted spatial coverage of the data sets considered here. There is no infilling into grid boxes with no observations. The re-gridding is done by area averaging any part of the old grid that lies within the new grid to produce a new gridpoint value.

Masking
The data coverage is limited to where data exists in the equivalent month/gridpoint of HadCRUT4.

Creation of Annual Means
Anomalies are calculated for each month/gridpoint relative to the 1961–1990 average, where at least 50% of the data in the reference period are needed to calculate the average. Annual means are calculated from monthly data for each calendar year, where at least 2 months are non-missing.

Global Means
GMST anomalies are calculated by area averaging all available gridpoint data for each year. For Figure 10.1 the average of the global mean for the reference period is calculated (1880–1919). The anomalies are then calculated with respect to the reference period.

Figure 10.1

All model simulations are displayed even if they do not cover the whole period.

Figure 10.2

For each gridpoint a linear regression is applied to the available data to calculate the trend, requiring no period longer than 5 consecutive years with missing data.

Figure 10.3

For each latitude (on the HadCRUT4 grid), the average of the trend across the longitudes is calculated. Any of the observational data sets having less than 50% coverage of HadCRUT4's coverage at a given latitude are not shown on the figure at that latitude.

Model Spread

For Figures 10.2 and 10.3 showing estimates of the spread of models, the 5 to 95% ranges are estimated by ordering the data (after weighting each simulation by the inverse of the number of simulations the model it belongs to has and multiplied by the number of models) and then choosing the central 90% range as limits (see Jones et al., 2013).

Data

Table 10.SM.1 | Observational data sets.

Observational Data Set	Period Covered
GISTEMP	1880–2012
HadCRUT4	1850–2012
MLOST	1880–2012

Table 10.SM.2 | Model Data. Summary of data used. Historical data were extended into the 21st century either by using any available A1B SRES simulations for CMIP3, and RCP4.5 for CMIP5, or RCP8.5 in cases where RCP4.5 was not available.

	Archive	Number of models used (that cover 1901–2012 period)	Total number of members (that cover 1901–2012 period)
Historical	CMIP3	13 (9)	63 (35)
	CMIP5	44 (40)	147 (127)
historicalNat	CMIP3	6 (Hegerl et al., 2010)	30 (Hegerl et al., 2010)
	CMIP5	17 (10)	52 (38)
historicalGHG	CMIP3	NA	NA
	CMIP5	16 (9)	48 (35)

Figure 10.4

Scaling factors in (b) shown with a square are reproduced from Ribes and Terray (2013) (Figure 3, top right panel) and those in (d) are reproduced from Ribes and Terray (2013) (Figure 3, top left panel). In cases where Ribes and Terray (2013) show confidence ranges which include both plus and minus infinity, uncertainty bars are shown here as continuous across the range plotted. Scaling factors shown with a triangle in (b) are reproduced from Gillett et al. (2013) (Figure 4a), and those in (d) are reproduced from Gillett et al. (2013) (Figure S1). Results labelled 'multi' correspond to those labelled 'ObsU' in Gillett et al. (2013), and account for observational uncertainty and model uncertainty. Scaling factors in (b) shown with a diamond are reproduced from Jones et al. (2013) (Figure 16a). Results labelled 'multi' correspond to those labelled 'Weighted avg' in Jones et al. (2013). Corresponding attributable trends over the 1951–2010 period are taken directly from Jones et al. (2003) (Figure 16b), and are derived from the Ribes and Terray (2013) and Gillett et al. (2013) regression coefficients by multiplying regression coefficients for each forcing by the corresponding least squares trend in GMST simulated in response to that forcing over the 1951–2010 period. FGOALS-g2 was excluded from this figure because it did not include the effects of volcanic aerosol in its historicalNat simulations.

Figure 10.5

This figure shows the assessed ranges derived as described in Section 10.3.1.1.3. We derive assessed ranges for the attributable contribution of greenhouse gases (denoted GHG, green), other anthropogenic forcings (OA, orange) and natural forcings (NAT, blue) by taking the smallest ranges with a precision of one decimal place that span the 5 to 95% ranges of attributable trends for the 1951–2010 period from the Jones et al. (2013) weighed multi-model analysis and the Gillett et al. (2013) multi-model analysis considering observational uncertainty (Figure 10.4a). The assessed range for the attributable contribution of combined anthropogenic forcings was derived in the same way from the Gillett et al. (2013) multi-model attributable trend shown in Figure 10.4c. The assessment of the internal variability is taken from the estimates of the 5th to 95th percentiles of 60-year trends of internal variability estimated by Knutson et al. (2013). We moderate our likelihood assessment and report likely ranges rather than very likely ranges directly implied by these studies in order to account for residual sources of uncertainty (see Section 10.3.1.1.3). Shown on the figure are the likely ranges shown as the whiskers with the end of the coloured bars being at the mid point of the attributable trend ranges. The midpoint of NAT is zero but the blue NAT bar is widened to make it visible.

Figure 10.6

This figure is updated from the figure in Imbers et al. (2013) which is described in detail there. Estimates of contributions to global temperature changes are described in individual contributing papers.

Figure 10.6 is an updated version of an equivalent figure published in Imbers et al. (2013). The four studies represented in Figure 10.6 are identical to Figure 1 in Imbers et al. (2013); only the data from the Folland et al. (2013) have been updated. The four studies' aims were slightly different, as well as the signals included into the global mean temperature decomposition and length and sampling intervals of their time series. In what follows we briefly describe each of the studies represented in Figure 10.6.

The first study shown in Figure 10.6 is from Folland et al. (2013). Part of their aim was to forecast annual global mean temperature anomalies using a statistical model that estimates the contributions of six physical factors to GMST change and variability. The factors are net forcing from anthropogenic GHGs and aerosols, forcings from volcanic aerosols and changes in solar output, and the influences two internal modes of variability: El Niño-Southern Oscillation (ENSO) (represented by the first high-frequency eigenvector of global sea surface temperatures) and the Atlantic Multi-decadal Oscillation (AMO) (derived from the third low-frequency eigenvector of global sea surface temperatures of Parker et al. (2007)).

In their predictability analysis, the influence of these factors on observed surface temperatures is estimated from cross validated multiple linear regression using annual surface temperature values from 1891 to 2011 from an average of HadCRUT3, National Climate Data Centre (NCDC) and Goddard Institute of Space Studies (GISS). Owing to the cross validation method, an ensemble of 121 reconstructions of the observed variable is obtained. In our analysis we show the ensemble mean time series and its 95% confidence range resulting from regression with the HadCRUT3 data set alone to 2012, giving 122 reconstructions. There are two differences between the way the ENSO and volcanic predictors are used here and in Folland et al. (2013). In Figure 10.6 appropriately smoothed volcanic and solar data simulated to the end of each year are used as well as ENSO data simulated from January to September of each year. In Folland et al. (2013) the ENSO data used for the prediction of a year were averaged over October and November of the previous year while the volcanic and solar data used were simulated up to the end of the previous year. Imbers et al. (2013) used an earlier version of the data of Folland et al. (2013) with the same differences in the way ENSO and volcanic predictors are used but using annual surface temperature values from 1891 to 2010 from an average of HadCRUT3 as training data for the statistical model, updated here using annual surface temperature values from 1891 to 2012.

Lean and Rind's (2009) results are also shown in Figure 10.6. Their goal was to forecast global and regional climate change in the near future by decomposing the observed record of monthly mean surface air temperature in terms of its combined linear response to ENSO, solar and volcanic activity and anthropogenic influences (Lean and Rind, 2008; see also Kopp and Lean, 2011). They used 1980–2008 monthly time series of mean surface temperature anomalies with respect to 1951–1980 and performed a multivariate linear regression against the instrumental surface temperature record HadCRUT3v (Brohan et al., 2006) to find the optimal combination of those four signals that better explain that record. Their solar, volcanic, anthropogenic and ENSO signals are lagged by 1, 7, 120 and 4 months respectively with respect to the temperature observations in order to maximize the proportion of global variability that the statistical model captures (76% of the variance observed since 1980).

The results of the third study considered in Figure 10.6 are from Kaufmann et al. (2011), who used a statistical model derived to estimate the relation between emissions of carbon dioxide (CO_2) and methane (CH_4), the concentrations of these gases, and global surface temperature (Kaufmann et al., 2006), to evaluate whether anthropogenic emissions of radiative active gases along with variability can account for the 1998–2008 hiatus in warming. The model is estimated with annual data from 1960 to 1998 and used to project 1998–2008 temperatures. The signals included in this model are: GHGs, anthropogenic sulphur emissions, solar insolation, ENSO (represented by the Southern Oscillation Index (SOI)) and radiative forcing of volcanic sulphates.

The last study shown in Figure 10.6 is from Lockwood (2008). Lockwood (2008) intended to analyse the contribution of changes in solar output to global mean surface temperature. The statistical model consists on a multivariate fit to the global monthly mean surface temperature anomaly for the period 1953–2007. The signals included in the fit are the solar, volcanic and anthropogenic components (the latest as a linear trend), and the ENSO3.4 index to represent the effect of El Niño.

Figure 10.7

Taken from Figure 7 of Jones et al. (2013).

Figure 10.8

The figure is adapted from Lott et al. (2013).

Observational Data Sets

A number of new radiosonde data sets have been developed since the studies of a decade ago. Following the review by Thorne et al. (2011) and having assessed which sets had coverage for the entire period, four data sets were chosen for analysis. The first of these is Hadley Centre Atmospheric Temperature data set 2 (HadAT2) (Thorne et al., 2005). Of the observational data sets, this has the least spatial coverage, and thus is used as a common mask for all other data, both observations and models, to allow a like-for-like comparison.

The other three observational data sets are from the Radiosonde Innovation Composite Homogenization RAdiosone OBservation COrrection using REanalyses (RICH/RAOBCORE) family (Haimberger et al., 2012). The first of these sets used is RAOBCORE 1.5, which uses the European Centre for Medium Range Weather Forecasts (ECMRWF) 40-year reanalysis (ERA-40) (Uppala et al., 2005) and ERA-Interim reanalyses (Dee et al., 2011) to detect and adjust breakpoints. The other two are the ensembles of realizations known as RICH-obs 1.5 and RICH-τ 1.5. Both of these generate the ensemble by varying processing decisions (such as minimum number of data points or treatment of transitions), with breakpoint detection derived from RAOBCORE. However, they differ in the way they handle the adjustments. RICH-obs makes adjustments by directly comparing station time series, while RICH- τ compares the differences between the time series and the ERA-Interim background.

Model Data Sets

For the selection of model data sets, the decision was limited by the need for that model to have runs with natural forcings (NAT), as well as runs with only GHG forcings and finally with all historical (i.e., anthropogenic and natural) forcings (ALL), between 1961 and 2010 available on the CMIP5 (Taylor et al., 2012) archive at the time the analysis was undertaken. This led to the models shown in Table 10.SM.3 being used.

Table 10.SM.3 | CMIP5 models used for this study, and the number runs with each forcing.

Modelling Centre (or Group)	Model(s)	Members Included		
		ALL	NAT	GHG
Commonwealth Scientific and Industrial Research Organization in collaboration with Queensland Climate Change Centre of Excellence	CSIRO-Mk3.6.0	10	5	5
NASA Goddard Institute for Space Studies	GISS-E2-R	5	5	5
	GISS-E2-H	5	5	5
Canadian Centre for Climate Modelling and Analysis	CanESM2	5	5	5
Met Office Hadley Centre	HadGEM2-ES	4	4	4
Beijing Climate Center, China Meteorological Administration	BCC-CSM1.1	3	1	1

All data sets were adjusted to a common temperature anomaly relative to the 1961–1990 climatology, re-gridded to the HadAT2 grid and masked before zonal averages were taken. The following set of pressure levels common to all data sets was used: 850, 700, 500, 300, 200, 150, 100, 50 and 30 hPa. The three latitude bands analyzed are a tropical zone (20°S to 20°N) and north and south extratropical zones (60°S to 20°S and 20°N to 60°N), along with the average over the whole studied area (i.e., 60°S to 60°N).

Different from Lott et al. (2013) Figures 10.8 and 10.SM.1 do not include the Centre National de Recherches Météorologiques (CNRM-CM5) and Norwegian Earth System Model 1-M (NorESM1-M) models. CNRM-CM5 was excluded because of unrealistic stratospheric ozone forcing (Eyring et al., 2013). The NorESMI-M was not included because the GHG single forcing runs for this model also include ozone forcing.

Trend Calculations

For both the models and observations, the trends at each pressure level were calculated using a median pairwise algorithm (as this copes better with outliers than a conventional linear fit) (Lanzante, 1996). These trends were plotted against pressure level, for all models and forcings within them. For each forcing ensemble of model runs, the shaded region shows the 5 to 95% range determined based on individual runs. Red represents all-forcings runs, blue shows natural forcings and green is GHG-forced only. The thick black line is HadAT2, thin black line is RAOBCORE 1.5, while the dark grey band is the RICH-obs 1.5 ensemble range and light grey is the RICH-τ 1.5 ensemble range. Each band is displayed 25% translucent to better distinguish where forcings and observations overlap.

Trend caluclation shown in Figure 10.8 are for the period 1961–2010. Figure 10.SM.1 shows trend calcuations for the satellite period from 1979 to 2010.

Figure 10.9

This figure shows time series of annual mean lower stratosphere temperatures from three satellite data sets and CMIP5 experiments. It utilizes the same CMIP5 model runs as Figure 10. 8 and individual model runs are shown. Synthetic lower stratosphere temperatures were calculated using global Microwave Sounding Unit (MSU) vertical weighting functions for the lower stratosphere. The three observational data sets are used to address observational consistent: Remote Sensing System (RSS) Version 3.3, University of Alabama in Huntsville (UAH) version 5.4 and Situation, Task, Action, Result (STAR) version 2.0 (Santer et al., 2013).

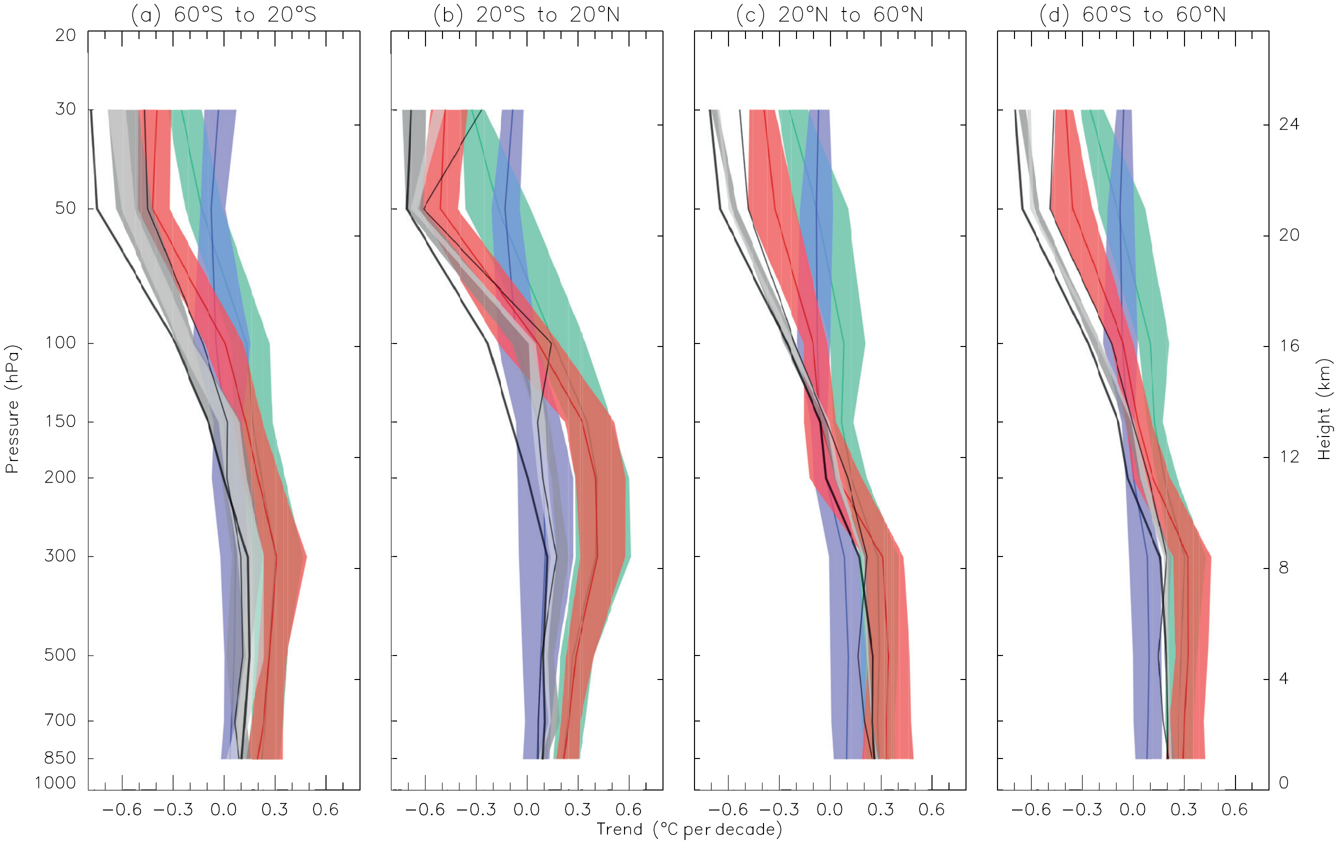

Figure 10.SM.1 | Observed and simulated zonal mean temperatures trends from 1979 to 2010 for CMIP5 simulations containing both anthropogenic and natural forcings (red), natural forcings only (blue) and greenhouse gas forcing only (green) where the 5th to 95th percentile ranges of the ensembles are shown. Three radiosonde observations are shown (thick black line: Hadley Centre Atmospheric Temperature data set 2 (HadAT2), thin black line: RAdiosone OBservation COrrection using REanalyses (RAOBCORE) 1.5, dark grey band: Radiosonde Innovation Composite Homogenization (RICH)-obs 1.5 ensemble and light grey: RICH- τ 1.5 ensemble. (Adapted from Lott et al. (2013) but for the more recent period from 1979 to 2010.)

Synthetic MSU temperature time series from model data were calculated as follows:

1. Select area from 82.5°S to 82.5°N of atmosphere temperature fields and time period and calculate area weighted averages.

2. Select time series from January 1979 to December 2010 and calculate annual averages and anomalies relative to the period 1996–2010.

3. Select pressure levels (hPa): 1000, 925, 850, 700, 600, 500, 400, 300, 250, 200, 150, 100, 70, 50, 30, 20, 10.

4. Apply vertical weighting function for MSU lower stratosphere temperature (channel 4) (Mears and Wentz, 2009).

Figure 10.10

Figure 10.10 is updated from Supplementary Information Figure S1 of Balan Sarojini et al. (2012). The updates include the use of a 11-year smoothing rather than a 5-year smoothing used in Balan Sarojini et al. (2012) and simulations from additional models for ALL that have become available since the publication of the paper and that are listed below.

Global and zonal average changes in annual mean precipitation (in mm day^{-1}) for the period 1951–2005, with regard to the baseline period of 1961–1990, are plotted based on Balan Sarojini et al. (2012).

CMIP5 Simulations used are:
Historical ('All'): HadGEM2-ES, CSIRO-Mk3-6-0, CNRM-CM5, NorESM1-M, CanESM2, BCC-CSM1-1, INMCM4_ESM, IPSL-CM5A-LR, GISS-E2-H, GISS-E2-R, MPI-ESM-LR, GFDL-ESM2G, GFDL-ESM2M, CCSM4, MIROC5, MIROC-ESM, MIROC-ESM-CHEM, MRI-CGCM3, IPSL-CM5A-MR, CESM1-BGC, CESM1-CAM5, CESM1-WACCM, CESM1-FASTCHEM, ACCESS1-0, GFDL-CM3, CMCC-CMS, CMCC-CESM, HadGEM2-CC, NorESM1-ME, MPI-ESM-MR.

HistoricalNat ('Nat'): HadGEM2-ES, CSIRO-Mk3-6-0, CNRM-CM5, NorESM1-M, CanESM2, BCC-CSM1-1, MIROC-ESM, MIROC-ESM-CHEM, MRI-CGCM3, GFDL-CM3.

There are 30 'All' runs (one each of 30 CMIP5 models forced with both anthropogenic and natural forcings) and 10 'Nat' runs (one each of 10 CMIP5 models forced with natural forcings only)

Observation used is a gridded observational data set based on station data extracted from the Global Historical Climatology Network (updated from Zhang et al. (2007)). Monthly data for the period 1951–2005, quality controlled and gridded at 5° × 5°, for all land grid squares on the globe for which station data are available, are used. In order to avoid artefacts arising from changes in data coverage, a sampling criterion of choosing data available for >90% of the analysis period is applied (i.e., each spatial grid point is chosen when data over 90% of the years (only those years that have data for all months) are present).

Masking of Simulated Data onto the Observational Grid

First, the land area of the simulated data available in different spatial resolutions is obtained by choosing a grid point as land when its land area fraction is greater than or equal to 70%. Second, the simulated land data are interpolated to the 5°× 5° observational grid using bilinear interpolation. Third, the 90% sampling criterion is applied to each regridded model data to obtain the consistent temporal and spatial data coverage for the simulated and observed data.

Calculation of Spatial and Annual Averages and Anomalies with regard to the Baseline Climatology

For each (regridded and sampled) monthly model data, spatial averages are first calculated for the global domain and zonal bands of 60°N to 90°N, 30°N to 60°N and 30°S to 30°N. Annual averages, baseline climatology (for 1961–1990) and anomalies from the baseline period are then calculated.

Calculation of Multi-model Means of 'All' and 'Nat' Runs

Multi-model averages of 30 All runs and 10 Nat runs are calculated.

Decadal Smoothing for both Observed and Simulated Data

A smoothing of boxcar average with 11-year width (with edges truncated) is applied to the resulting time series of annual precipitation anomalies.

Plotting

The yearly anomalies are plotted with a *y*-axis range of 1950–2010. Multi-model means are in thick solid lines (All in red and Nat in blue) and individual simulations are in thin solid lines.

Statistical Test of Significance for the Changes Between 'All' and 'Nat' Runs

Green stars are plotted when the changes are statistically significant at 5% level (p <0.05) between the ensemble of runs with both anthropogenic and natural forcings (red lines) and the ensemble of runs with just natural forcings (blue lines) using a two-sample two-tailed *t*-test for the last 30 years of the time series.

Supplementary Figure to Figure 10.10: Figure 10.SM.2

Global and zonal average changes in annual mean precipitation (in mm day^{-1}) for the period 1951–2005, with regard to the baseline period of 1961–1990, are plotted.

The details of the simulations and procedure for both simulations and observations are same as that for Figure 10.10 except for the observational data set used and an additional sampling criterion as described below (i.e., Steps 2 and 3).

Observation used is a gridded observational dataset based on station data extracted from the Climatic Research Unit (updated from CRU TS3.1 of Harris et al. (2013) and sampled as in Polson et al. (2013)). Monthly data for the period 1951–2005, quality controlled and gridded at 0.5° × 0.5°, are used.

This data is first interpolated to the common spatial resolution (as to Figure 10.10) of 5°× 5°. In order to avoid artefacts arising from changes in data coverage, two sampling criteria are applied: (1) station sampling criterion (Polson et al., 2013) of choosing only those 5° × 5° grid boxes that have at least one station (in any 0.5° × 0.5° grid box) for the coastal grid boxes and with at least two stations for the inland grid boxes. A 5° × 5° grid box is coastal when more than half of number of the 0.5° × 0.5° boxes is ocean points. (2) A criterion of choosing data available for >95% of the analysis period is applied, that is, each spatial grid point is chosen when data over 95% of the years (years that have data available for any number of months) are present.

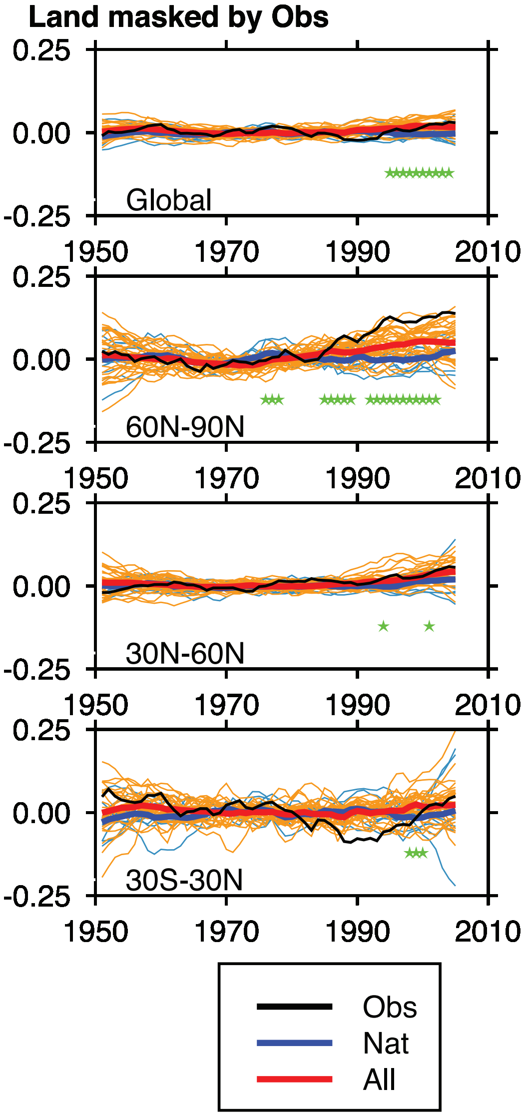

Figure 10.SM.2 | Global and zonal average changes in annual mean precipitation (mm day^{-1}) over areas of land where there are observations, expressed relative to the baseline period of 1961–1990, simulated by CMIP5 models forced with both anthropogenic and natural forcings (red lines) and natural forcings only (blue lines) for the global mean and for three latitude bands. Multi-model means are shown in thick solid lines. Observations (gridded values derived from Climatic Research Unit (CRU) station data, updated from CRU TS3.1 of Harris et al. (2013) and sampled as in Polson et al. (2013) are shown as a black solid line. An 11-year smoothing is applied to both simulations and observations. Green stars show statistically significant changes at 5% level (p <0.05) between the ensemble of runs with both anthropogenic and natural forcings (red lines) and the ensemble of runs with just natural forcings (blue lines) using a two-sample two-tailed *t*-test for the last 30 years of the time series.

Masking of Simulated Data onto the Observational Grid

First, the land area of the simulated data available in different spatial resolutions is obtained by choosing a grid point as land when its land area fraction is greater than or equal to 70%. Second, the simulated land data are interpolated to the 5° × 5° observational grid using bilinear interpolation. Third, the mask of station sampling and the 95% sampling (described in Step 2) is applied to each regridded model data to obtain the consistent temporal and spatial data coverage for the simulated and observed data.

Figure 10.11

Figure based on Zhang et al. (2007); Min et al. (2008); Min et al. (2011); Polson et al. (2013).

Left top panel: (a) Global land-annual results from Zhang et al. (2007) (first pair of bars) and Polson et al. (2013) (2nd to 5th pair of bars); (b) global land-seasonal results from Polson et al. (2013); (c) Arctic results from Min et al. (2008) and (d) extreme results from Min et al. (2011). Right top panel: After Zhang et al. (2007), but updated following Polson et al. (2013): changes expressed in percent climatology and CMIP5 models plotted. Bottom left and right panel: from Polson et al. (2013).

Figure 10.12

December to February mean change of southern border of the Hadley circulation. Unit is degree in latitude per decade. Reanalysis data sets are marked with different colours. Trends are all calculated over the period of 1979–2005. According to CMIP5, historicalNAT, historicalGHG and historical denote historical simulations with natural forcing, observed increasing GHG forcing and all forcings, respectively. For each reanalysis dataset, the error bars indicate the 95% confidence level of the standard *t*-test. For CMIP5 simulations, trends are first calculated for each model, and all ensemble members are used. Then, trends are averaged for multi-model ensembles. Trend uncertainty is estimated from multi-model ensembles, as twice the standard error. This figure is adapted from Hu et al. (2013) with additional trends derived from Climate Forecast System Reanalysis (CSFR) and Modern Era Retrospective-analysis for Research and Applications (MERRA) reanalyses.

Figure 10.13

Figure 10.13 is adapted from Gillett and Fyfe (2013) (Figure S4), with the following changes. Simulations from the following numbers of models which cover the 1951–2011 period were used: 106 historical simulations from 34 models, 26 historicalGHG simulations from 7 models, 11 aerosols-only simulations from 3 models, 15 ozone-only simulations from 3 models, and 48 historicalNat simulations from 10 models, and control simulations from 43 models. As well as the 5 to 95% range of trends simulated in the historical simulations (red boxes), the 5 to 95% ranges of trends simulated in the control simulations (grey bars) are also shown. These ranges were derived by weighting each simulation by the inverse of the product of the number of models and the number of simulations from the model concerned, ranking the trends, deriving a cumulative distribution function by summing the weights, and then interpolating to find the 5th and 95th percentiles, following Jones et al. (2013). Mean responses to each forcing were derived by first averaging ensemble members for each model, and then averaging across models. Uncertainty bars shown for individual forcings are uncertainties in the mean response to each forcing, calculated by dividing the standard deviation across models by the square root of the number of models, and multiplying by the Student-*t* statistic for a cutoff value of 0.05 and with the number of degrees of freedom equal to one less than the number of models. A minor error effecting Gillett and Fyfe (2013) Figure S4 only in which the northern reference latitude for the Southern Annular Mode (SAM) index was 45°S instead of 40°S following Gong and Wang (1999) was corrected.

Figure 10.14

Panel (a)
This figure is an update of Figure 2 of Domingues et al. (2008). In this figure:

CMIP5 simulations are:
HistoricalNat (can_esm2, ccsm4, cnrm_cm5, csiro_mk3.6, giss_e2_h, giss_e2_r, hadgem2-es, miroc_esm, mri_cgcm3, nor_esm1_m)

Historical (can_esm2, ccsm4, cnrm_cm5, csiro_mk3.6, giss_e2_h, giss_e2_r, hadgem2-es, miroc5, miroc4h, miroc_esm, mpi_esm_lr, mri_cgcm3, nor_esm1_m)

Annual mean ocean heat content (OHC) values are calculated from models by vertically integrating the annual mean temperature anomalies (with respect to a 1960–1980 reference period). Global mean time series are calculated by integrating over space.

Observed global OHC changes from Domingues et al. (2008); also with a reference period of 1960–1980) are smoothed (three-year running means) and plotted.

Stratospheric Aerosol loading (as global mean AOD) from Sato et al. (1993); data downloaded from the website http://data.giss.nasa.gov/modelforce/strataer/#References before their December 2012 update) is plotted. A three-year running mean is also calculated and plotted for comparison against smoothed data.

Panel (b)
This figure is based on Figure 5(c) of Gleckler et al. (2012).

Anomalies of volume average temperature ΔT rather than ocean heat content are used.

Observed ΔT estimates are based on globally gridded (1° × 1° latitude/longitude) products, not raw measurements. The observed datasets used are:

> Pre-XBT bias correction data: Levitus et al. (2005) and Ishii et al. (2006)
>
> XBT bias corrected data: Levitus et al. (2009), Ishii and Kimoto (2009) and Domingues et al. (2008)

Annual means of all model ocean temperature data 700 m of the ocean column have been interpolated to the spatial grid and standard vertical depth levels of the observational data (Ishii and Kimoto, 2009).

From the CMIP3, control and 20th century (20CEN) runs are considered. The models are further classified as:

> VOL models (those that included volcanic and other natural forcings) are CCSM3.0, GFDL-CM2.0, GISS-EH, GISS-ER, MIROC-CG-CM2.3.2, MRI-CGCM2.3.2
>
> NoV models are those that did not include natural forcings. These are CCCma-CGCM3.1, CNRM-CM3, CSIRO-Mk3.0, GISS-AOM, FGOALS-g1.0 and UKMO-HadCM3.

The observed and model simulated historical anomalies are calculated with respect to a 1957–1990 climatology and all control-run anomalies are with respect to the overall time mean of each model's control run.

Each 20CEN simulation is subsampled in the same manner using the 1960–1999 (Ishii, 2009).

Basin-scale ΔT changes in the North Atlantic, South Atlantic, North Pacific, South Pacific, North Indian, and South Indian oceans are computed.

Residual drift associated with the incomplete spin-up of model control runs is removed from all ΔT basin-average time series using a quadratic fit. Quadratic fits are computed for the entire control, yielding a drift estimate. This drift is then removed from the original control, yielding an estimate of the true model noise. For each 20CEN simulation, there is a contemporaneous section of the corresponding control and a contemporaneous section of the control-drift estimate. This section of the control drift is removed from the 20CEN simulation.

The ΔT anomalies of each ocean basin are then weighted by its volume.

CMIP3 20CEN runs (1870–1999) are averaged together to produce a Multi-Model Response (MMR). If more than one realization of the 20CEN experiment is available for an individual model, these realizations are averaged together before averaging across models.

The fingerprint is the first Empirical Orthogonal Function (EOF) of the MMR of ΔT in the six ocean basins, calculated over 1960–1999. Fingerprints are computed separately for the simulations that include volcanic (V) or exclude volcanic eruptions (NoV) MMRs.

The multimodel noise estimates are based on concatenating all available control data from VOL models.

The basin-average upper-ocean temperature changes from observations are projected onto the fingerprint yielding the signal projection time series $Z(t)$.

Trends of increasing length L (least squares fit starting from 1970 and with an initial L of 10 years) are fit to this time series to yield the "signal".

Similarly, the ΔT from the VOL concatenated control runs are projected onto the searched-for fingerprint. The resulting projection time series, $N(t)$, provides information about unforced changes in pattern similarity.

L-year, non-overlapping trends are fitted to $N(t)$, with L varying from 10, 11, 12,…39 years. For a given value of L, the noise is the standard deviation of the sampling distribution of the trends.

With these, the signal-to-noise (S/N) ratio is calculated as a function of L. The detection time is defined as the year at which S/N ratio exceeds and remains above a stipulated 5% significance threshold.

Figure 10.15

This figure is from three published studies. Panel A is adapted from Figure 3 of Helm et al. (2010). The top and bottom panels of Figure 3 are shown in Panel A of Figure 10.15. Panel B is redrafted and simplified from the original figure, Figure 2A of Durack et al. (2012). Panel C is taken from Figure 11a from Terray et al. (2012).

Figure 10.16

Figure 10.16: September sea ice extent for Arctic (top panel) and Antarctic (bottom panel) adapted from Wang and Overland (2012). Only CMIP5 models which simulated seasonal mean and magnitude of seasonal cycle in reasonable agreement with observations are included in the plot.

The grey lines are the runs from the pre-industrial control simulations, and the red lines are from Historical simulations patched with RCP8.5 runs for the period 2005–2012. The black line is based on the sea ice extent data are from National Snow and Ice Data Center (NSIDC).

There are 24 ensemble members from 11 models for the Arctic and 21 members from 6 models for the Antarctic plot.

The list of simulations that passed the acceptance criteria and plotted in the figure is:
Northern Hemisphere: ACCESS1.0, ACCESS1.3, CCSM4, CESM1-CAM5, EC-EARTH, HadGEM2AO, HadGEM2CC, HadGEM2ES, MIROC-ESM, MIROC-ESM-C, MPI-ESM-LR.

Southern Hemisphere: ACCESS1.3, CMCC-CM, CanESM2, EC-EARTH, MRI-CGCM3, NorESM1-M.

The underlined models are those identified and used by Wang and Overland (2012).

The criteria for choosing acceptable simulations models is as follows. The simulated mean and seasonal cycle of the sea ice extent is within 20% of the observations of the sea ice climatology for the 1981–2005 period. The 1981–2005 period was chosen because it overlaps with satellite observation period and 2005 is the last year of the historical simulations. The 20% bound chosen here is used in Wang and Overland (2012), and has also been used by Zhang (2010). A total of 36 models were evaluated against these selection criteria.

Figure 10.17

Figure 10.17: Zwiers et al. (2011).

Figure 10.17: Detection results for changes in intensity and frequency of extreme events. Right-hand sides of each panel show scaling factors and their 90% confidence intervals for changes in the frequency of temperature extremes for winter (October to March for Northern Hemisphere and April to September for Southern Hemisphere), and summer half years. TN10, TX10 are respectively the frequency for daily minimum and daily maximum temperatures falling below their 10th percentiles for the base period 1961–1990. TN90 and TX90 are the frequency of the occurrence of daily minimum and daily maximum temperatures above their respective 90th percentiles calculated for the 1961–1990 base period (Morak et al., 2013), fingerprints are based on simulations of Hadley Centre new Global Environmental Model 1 (HadGEM1) with both anthropogenic and natural forcings). Left side of each panel show scaling factors and their 90% confidence intervals for intensity of annual extreme temperatures in response to external forcings for the period 1951–2000. TNn and TXn represent annual minimum daily minimum and maximum temperatures, respectively, while TNx and TXx represent annual maximum daily minimum and maximum temperatures. This is updated from Zwiers et al. (2011) by conducting exactly the same type of analysis of Zwiers et al. (2011) using spatial domain defined in Morak et al. (2013), fingerprints are based on simulations of climate models with both anthropogenic and natural forcings). Detection is claimed at the 10% significance level if the 90% confidence interval of a scaling factor is above zero line.

Figure 10.18

Figure 10.18 combines three figures which are adapted from three different papers to provide an overview of different results for attribution studies using changes in return time as a measure for anthropogenic influence.

Figure 10.18a is directly taken from Pall et al. (2011). The figure is identical to Figure 3d in the paper.

Figure 10.18b is adapted from Kay et al. (2011). The first row of Figure 5 in the paper shows the return times of 1-day flood peaks in the catchment area 27007 (river Ure, UK) for the period October 2000 to March 2001 comparing simulations with actual year 2000 climate drivers to four (Figure 5 a–d) different sets of counterfactual year 2000 climate drivers. The counterfactual ensembles represent four possible sets of surface temperatures (SSTs) representative of a 'world that might have been' without anthropogenic climate forcing. Different SST patterns are obtained from four different models (columns a–d) with different scaling factors for the SSTs (colours). We adapted this figure as follows. Instead of calculating the 6-month period October 2000 to March 2001 we considered only the period January 2001 to March 2001 to assess changes in the return time of 1-day peak floods in spring. In addition, the catchment used for this study is not the river Ure but the river Don in South Yorkshire, UK. Furthermore we combined the different SST patterns from all models in one figure.

Figure 10.18c is directly taken from Otto et al. (2012). The figure is identical to Figure 4 in the paper but without displaying temperature equivalents for ERA-interim reanalysis data.

Figure 10.19

All reconstructions used are the same as in Schurer et al. (2013), with the exception of the Mann et al. (2009) reconstruction, which in the top panel is for 30°N to 90°N land and sea and in the bottom panel is for 0° to 60°E 25°N to 65°N land and sea and the Luterbacher et al. (2004) reconstruction which is for the region 25°W to 40°E 35°N to 70°N land only (bottom panel).

All models used to construct the multi-model ensemble and the control simulations used for samples of internal variability are the same as in Schurer et al. (2013) (see Table 10.SM.4). To calculate the multi-model mean each model set-up contributes equally, that is, the mean of the five Max Planck Institute Community Earth Systems Models (MPI-COSMOS) simulations counts as one model whereas the GISS-E2-R simulations are treated separately because they contain different forcings. The GISS-E2-R simulations included a significant initial model drift which was removed from the control simulation by fitting a second order polynomial to the control simulation. The bold orange line in the figure shows the noise reduced multi-model mean multiplied by the best-fit scaling factor. The uncertainty range is calculated by adding in quadrature the uncertainty in the scaling range to the uncertainty due to internal variability.

The Goosse simulations are taken directly from the simulation described in Goosse et al. (2012a, 2012b), constrained by the Mann et al. (2009) reconstruction from 30°N to 90°N.

In the top panel the annual mean of the region 30°N to 90°N land and sea is shown and in the bottom panel the annual mean of the region 0° to 60°E, 25°N to 65°N. The uncertainty range was estimated from the uncertainty given in Goosse et al. (2012a) and Goosse et al. (2012b) for the annual data-assimilated results. To account for the smoothing used in the figure these calculated annual standard deviations were scaled by the ratio between the standard deviation of the smoothed and un-smoothed control runs used in Schurer et al. (2013).

The instrumental data is taken from Morice et al. (2012).

All analysis is done on decadally smoothed time-series, using first a 10-year Butterworth filter and then an 11-year box car filter. The analysis shown in the bottom panel uses the same method and model data as used for the top panel, but is performed on the European domain, following Hegerl et al. (2011).

Figure 10.20a

The plot contains three different types of reporting on transient climate response (TCR) estimation studies: (A) bars indicating estimates of the range of possible TCR values (most, but not all, are 5 to 95% confidence interval estimates), (B) these studies are included with both, a confidence range represented by a bar and a corresponding probability density function (PDF), and (C) some studies from AR4 are included just with their PDFs to show the contrast between AR4 and AR5.

Bar-Plot (without Probability Density Functions)
Schwartz (2012) uses a two-time scale formulation of the climate system response (e.g., see Gregory, 2000; Held et al., 2010) to obtain TCR estimates (more specifically using the notion of transient climate sensitivity, more generally defined without reference to a specific rate of increase in concentration) ranging from 0.9°C to 1.9°C, the lower values corresponding to higher values of net forcing over the 20th century. The range in the figure is generated by multiplying the headline values from the paper (0.23 ± 0.01 to 0.51 ± 0.04) K $(\mathrm{W\ m^{-2}})^{-1}$, with an assumed forcing for a doubling of CO_2 of 3.7 W $\mathrm{m^{-2}}$ (leading to (0.85 to 1.89 K)). The given range originates from an ensemble of different published forcing estimates, and hence it cannot directly be interpreted as a 5 to 95% confidence interval.

Libardoni and Forest (2011) show that the TCR along with other climate system parameters (see below) can be estimated by comparing EMIC simulations with a range of 20th century surface temperature atmospheric and ocean temperature data sets. Under a variety of assumptions, they obtain 5 to 95% ranges for TCR spanning 0.9 to 2.4 K. These values are directly taken from the 2011 paper (0.87 to 2.41 K). Updating this study to include data to 2004 gives results that are essentially unchanged.

Table 10.SM.4 | Details of the models used.

Model	Ensemble Members	Resolution		Forcings			
		Atmosphere	Ocean	Volcanic	Solar	Greenhouse Gas	Land Use
CCSM4*	1	288 × 192 × L26	320 × 384 × L60	GRA	VK/WLS	SJA	PEA/Hur
MPI-COSMOS	5	96 × 48 × L19	GR3.0 × L40	CEA	JLT	Interactive	PEA
MPI-ESM-P*	1	196 × 98 × L47	256 × 220 × L40	CEA	VK/WLS	SJA	PEA
HadCM3	1	96 × 73 × L19	288 × 144 × L20	CEA	SBF/WLS	SJA	PEA
GISS-E2-R*	1	144 × 90 × L40	288 × 180 × L32	CEA	VK/WLS	SJA	PEA/Hur
GISS-E2-R*	1	144 × 90 × L40	288 × 180 × L32	GRA	VK/WLS	SJA	KK11/Hur
Bcc-csm1-1*	1	128 × 64 × L40	360 × 232 × L40	GRA	VK/WLS	SJA	X

Notes:

Further details can be found in the references for the model and the forcings used; the references for the models are: CCSM4 – Landrum et al. (2013); MPI-COSMOS – Jungclaus et al. (2010); HadCM3 – Schurer et al. (2013); Bcc-csm1-1 – Wu (2012). The references for the forcings are: CEA –Crowley et al. (2008), GRA –Gao et al. (2008), VSK –Vieira et al. (2011), SBF –Steinhilber et al. (2009) , WLS –Wang et al. (2005), SJA –Schmidt et al. (2012), PEA –Pongratz et al. (2008), Hur- Hurtt et al. (2009), KK11 –Kaplan et al. (2009), JLT –Jungclaus et al. (2010), MM - MacFarling Meure et al. (2006). An X indicates that the forcing is not included. The models indicated by asterisks have been made available as part of the CMIP5 project.

Padilla et al. (2011) use a simple two-time scale model (see the entry on Schwartz above) to derive an observationally constrained estimate of the TCR of 1.3°C to 2.6°C. The range is directly taken from the headline results of the cited paper, with a best estimate of 1.6 K, and including an estimate how the 90% confidence range will change in the future (reduction of 45% by 2030).

Gregory and Forster (2008) estimate real world TCR as 1.3 to 2.3 K (5 to 95% uncertainty range) from the data of 1970–2006, assuming a linear relationship between radiative forcing and GMST change and disregarding any trend caused by natural forcing. The numbers are directly taken from the cited paper (abstract).

Stott and Forest (2007) used the observed 20th century temperature change to constrain three models (HadCM3, GFDL-R30 and PCM) and then applied these models to the calculation of TCR for the future. The calculated TCR is around 2.1 K and the 5 to 95% probability range is 1.5 to 2.8 K. The numbers are directly taken from the description of Figure 8 of the cited paper.

Gillett et al. (2013) base their methodology on Gillett et al. (2012) and Stott and Jones (2012), but including a broader range of model and observational uncertainties, in particular addressing the efficacy of non-CO_2 gases, and find a TCR range of 0.9°C to 2.3°C. This confidence range is directly taken from Figure 7a of the cited paper.

Tung et al. (2008) examined the response to the 11-year solar cycle using discriminant analysis, and found a high range for TCR: >2.5°C to 3.6°C. These numbers are directly taken from Equation 7 of the cited paper. However, this estimate may be affected by different mechanisms by which solar forcing affects climate and possible aliasing with the response to other forcing in the 20th century and with internal climate variability, despite attempts to minimize these effects—see discussion in North and Stevens (1998).

Bars and Probability Density Functions

Otto et al. (2013) update the analysis of Gregory et al. (2002) and Gregory and Forster (2008) using forcing estimates from Forster et al. (2013) to obtain a 5 to 95% range for TCR of 0.9 to 2.0°C comparing the decade 2000–2009 with the period 1860–1879. They note, however, the danger of overinterpreting a single, possibly anomalous, decade, and report a larger TCR range of 0.7°C to 2.5°C replacing the 2000s with the 40 years 1970–2009. These PDFs are directly taken from Otto et al. (2013), renormalized to a (0.1 to 10) °C support.

Rogelj et al. (2012): This PDF is a TCR distribution implied by a 600-member parameter set ensemble drawn from an 82-dimensional parameter space in a way such that the posterior climate sensitivity distribution matches closely the distribution presented by Rogelj et al. (2012). The methodology for drawing the 600-member parameter sets is described in Meinshausen et al. (2009).

The PDF for the TCR predicted by the Bayesian methodology of Harris et al. (2013). The distribution is based upon a large sample of emulated General Circulation Model (GCM) equilibrium responses, constrained by multiannual mean observations of recent climate and adjusted to account for additional uncertainty associated with model structural deficiencies Sexton et al. (2012). The equilibrium responses are scaled by global temperature changes associated with the sampled model variants, reweighting the projections based on the likelihood that they correctly replicate observed historical changes in surface temperature, to predict the TCR distribution.

Meinshausen et al. (2009) compiled a large set of published marginal PDFs for equilibrium climate sensitivity (ECS) and TCR. In the absence of a formal method for combining all of them they chose an illustrative default, choosing a uniform TCR prior PDF from Frame et al. (2006) and constrained the their model parameter with observations. The TCR PDF is reproduced as shown in Figure 1b of the cited paper from supplementary data.

Knutti and Tomassini (2008) compare Earth System Model of Intermediate Complexity (EMIC) simulations with 20th century surface and ocean temperatures to derive a probability density function for TCR skewed slightly towards lower values with a 5 to 95% percent range of 1.1°C to 2.3°C. The PDFs for the expert ECS prior and the uniform ECS prior are reproduced as shown in Figure 1b of Meinshausen et al. (2009) from its supplementary data. The 5 to 95% confidence intervals are calculated from these numeric PDFs.

Dashed Probability Density Functions without Legend Entries (AR4 Studies)

The TCR PDFs for the GFDL, the HadCM3, and the PCM model as produced by Stott et al. (2006) and the TCR PDF from Frame et al. (2006) are reproduced in Figure 10.19 as shown in Figure 1b of Meinshausen et al. (2009) from its supplementary data.

Figure 10.20b

References for labelled plots: **20th Century:** violet: Aldrin et al. (2012), solid: uniform prior in ECS, dashed: uniform prior in 1/ECS, and dash-dotted is an update using data to 2010 (see below); gold: Bender et al. (2010); light red: Lewis (2013), dashed: using Forest et al. diagnostic and an objective Bayesian prior, solid using revised diagnostic; cyan: Lin et al. (2010); brown: Lindzen and Choi (2011); olive: Murphy et al., (2009); dark red: Olson et al. (2012); indigo: Otto et al. (2013), solid is an estimate using change to 1979–2009, dashed on the change to 2000–2009; lime: Schwartz (2012); blue: Tomassini et al. (2007) using a prior uniform in ECS (solid) and a density ratio prior based on expert elicitations (dashed). Repeated from AR4: green: Frame et al. (2005); result using uniform prior in ECS); orange: Gregory et al. (2002); purple: Knutti et al. (2002); Fuchsia: Forster and Gregory (2006) (solid: uniform prior in feedbacks; dashed transformed to uniform prior in ECS as used in AR4). **Palaeoclimate:** brown: (Chylek and Lohmann, 2008); orange: Hargreaves et al. (2012), solid, dashed showing an update based on PMIP3 simulations; turquoise: Holden et al. (2010); light red: Koehler et al. (2010); green: Paleosens Members (2012); purple: Schmittner et al. (2011), solid is land-and-ocean, dashed land-only, and dash-dotted is ocean-only diagnostic. Repeated from AR4: blue: Schneider von Deimling et al. (2006). lime: Annan et al. (2005); **Combination of evidence:** violet: Aldrin et al. (2012); turquoise: Libardoni and Forest (2013) with dashed being the average value, and solid an update using data to 2004; dark red: Olson et al. (2012) and repeated from AR4: lime: Annan and Hargreaves (2006); blue: Hegerl et al. (2006).

Processing details: All PDFs were scaled to integrate to 1.0 between 0 and 10.0; information only where further processing is used.

Instrumental

Aldrin et al. (2012) Solid: Main result from the paper, that is, with data up to 2007 and with radiative forcing (RF)-prior consistent with the IPCC AR4; result from their Figure 6a; dashed Figure 6f; and in bottom panel Figure 6k. The dash-dotted is as the first, but updated including 2010 and with updated RF prior based on Skeie et al. (2011).

Lewis (2013) – two sets of data are used, based on their Figure 3, a and b.

Murphy (2009) – the 5th, 50th and 95th percentile are shown, based on published range for feedbacks in paper.

Olson et al. (2012) use a uniform and an informed prior. Here we plot the result of using a uniform prior, the informed prior is shown in the 'combination' panel.

Otto et al. (2013) – Two sets of data are used: in solid is the 1979–2009 average, and in dashed is the 2000–2009 average. Distributions are shown with percentiles coinciding with corresponding confidence intervals from the likelihood profile reported in the paper.

Schwartz (2012) – sampling range from their paper.

Frame et al. (2005) as in AR4.

Forster and Gregory (2006) – two sets of data are shown: in solid is data produced using a prior that is uniform in feedback parameter space, whilst in dashed is a prior that is uniform in ECS space. Data for the dashed curve was based on AR4; for the solid curve based on the feedback range given in the paper.

Knutti et al. (2002) – data was provided as cumulative distribution frequency, so binned to get probability distribution, applied a two-stage boxcar average (three-box window followed by two-box window), and rescaled to ensure integral of PDF equaled 1.0

Palaeoclimate

Chylek and Lohmann (2008) (note range given is a 95% range).

Hargreaves et al. (2012) (solid: published estimate, dashed: updated).

Holden et al. (2010) – sampling range from their paper.

Schneider von Deimling et al. (2006) – sampling range from their paper.

Combination

Aldrin et al. (2012) – result from their panel Figure 6k.

Libardoni and Forest (2013) (solid: published; dashed update using data to 2004).

Olson et al. (2012) – this is the main result of their paper, using an informed prior in ECS.

The average distribution given for Libardoni and Forest (2013) are calculated from an average of the PDFs based on different observational data sets; namely HadCRUT3, NCDC and GISTEMP250. The average distributions were derived by drawing Latin Hypercube samples from the posteriors derived using the different data sets. Three 1000-member samples were drawn from each, merged together, and the resulting histogram used to obtain an estimate of the average posterior; which was then smoothed and plotted.

Additional Information to Version of Figure in Chapter 12

Climatological Constraints

Red: Sexton et al. (2012) – purple: Knutti et al. (2006) – no processing was required. Gold: Piani et al. (2005).

Raw Model Range: The bars show the results from five perturbed physics ensembles. Each ensemble provided its histogram, computed using 0.5° bins. For ease of viewing, the individual bar widths have been shrunk by 7 (i.e., each bar appears as 0.071° of ECS in width, with a 0.14° gap between bins). The bar height has not been rescaled. The individual dots below the curve represent data from models in the CMIP3 and CMIP5 database. Not all models had completed the necessary simulations, so this is a subset of the full models available based on Table 9.5.

The CMIP5 models shown are:
ACCESS1-0, BCC-CSM1-1, BCC-CSM1-1-M, BNU-ESM, CanESM2, CCSM4,CNRM-CM5, CSIRO-Mk3-6-0, GFDL-CM3, GFDL-ESM2G, GFDL-ESM2M,GISS-E2-H, GISS-E2-R, HadGEM2-ES, INM-CM4, IPSL-CM5A-LR, IPSL-CM5B-LR,MIROC5, MIROC-ESM, MPI-ESM-LR, MPI-ESM-P, MRI-CGCM3, NorESM1-M.

Data for the AR4 AOGCMs was provided by Chapter 9, Table 9.5.

Figure 10.21

This material documents the provenance of the data and plotting procedures that were used to create Figure 10.21 in the IPCC WG1 Fifth Assessment Report.

Continental Temperatures

Models and ensemble members used are listed in Table 10.SM.5.

Data

All of the data used were provided as monthly Netcdf files, from the CMIP3 and CMIP5 archives, and Daithi Stone (providing data used in the AR4 figures that were not in the CMIP3 archive). CMIP3 20C3M experiments were extended to 2012 by using A1B scenario simulations. CMIP5 historical experiments were extended to 2012 by using historicalExt and rcp45 experiments.

Observational Data

The observed surface temperature data is from HadCRUT4 (Morice et al., 2012).

Regridding

All data are re-gridded onto the HadCRUT4 spatial grid (5° × 5°) since HadCRUT4 generally has the most restricted spatial coverage of the datasets considered here. There is no infilling into grid boxes with no observations. The re-gridding is done by area averaging any part of the old grid that lies within the new grid to produce a new gridpoint value.

Table 10.SM.5 | Models and ensemble members used for continental temperatures. '20C2M' and 'A1B' are the names from CMIP3 for the quasi-equivalent experiments 'historical' and 'rcp45' in CMIP5.

	historical (20C3M)	historicalExt	rcp45 (A1B)	Overall period			historicalNat	Overall period		
Model	Realisation	Realisation	Realisation	Start Year	End Year	CMIP3/5	Realisation	Start Year	End Year	CMIP3/5
GFDL-CM2.0	r1		r1	1861	2012	3				
GFDL-CM2.0	r2			1861	2000	3				
GFDL-CM2.0	r3			1861	2000	3				
GFDL-CM2.1	r1		r3[a]	1861	2012	3				
GFDL-CM2.1	r2		r1	1861	2012	3				
GFDL-CM2.1	r3		r2[a]	1861	2012	3				
GFDL-CM2.1	r4			1861	2000	3				
GFDL-CM2.1	r5			1861	2000	3				
GISS-E-H	r1		r1	1880	2012	3				
GISS-E-H	r2		r2	1880	2012	3				
GISS-E-H	r3		r3	1880	2012	3				
GISS-E-H	r4			1880	1999	3				
GISS-E-H	r5			1880	1999	3				
GISS-E-R	r1			1880	2003	3				
GISS-E-R	r2			1880	2003	3				
GISS-E-R	r3		r1	1880	2012	3				
GISS-E-R	r4			1880	2003	3				
GISS-E-R	r5			1880	2003	3				
GISS-E-R	r6		r2	1880	2012	3				
GISS-E-R	r7		r3	1880	2012	3				
GISS-E-R	r8		r4	1880	2012	3				
GISS-E-R	r9		r5	1880	2012	3				
INM-CM3.0	r1		r1	1871	2012	3				
MIROC3.2(hires)	r1		r1	1900	2012	3				
MIROC3.2(medres)	r1		r1	1850	2012	3	r1	1850	2000	3
MIROC3.2(medres)	r2		r2	1850	2012	3	r2	1850	2000	3
MIROC3.2(medres)	r3		r3	1850	2012	3	r3	1850	2000	3
MIROC3.2(medres)	r4[a]			1850	2010	3	r4	1850	2000	3
MIROC3.2(medres)	r5[a]			1850	2010	3	r5	1850	2000	3
MIROC3.2(medres)	r6[a]			1850	2010	3	r6	1850	2000	3
MIROC3.2(medres)	r7 [a]			1850	2010	3	r7	1850	2000	3
MIROC3.2(medres)	r8[a]			1850	2010	3	r8	1850	2000	3
MIROC3.2(medres)	r9[a]			1850	2010	3	r9	1850	2000	3
MIROC3.2(medres)	r10[a]			1850	2010	3	r10	1850	2000	3
MIUB-ECHO-G	r1		r1	1860	2012	3	r1	1860	2000	3
MIUB-ECHO-G	r2		r2	1860	2012	3	r2	1860	2000	3
MIUB-ECHO-G	r3		r3	1860	2012	3	r3	1860	2000	3
MIUB-ECHO-G	r4			1860	2000	3				
MRI-CGCM2.3.2	r1			1851	2000	3	r1	1850	1999	3
MRI-CGCM2.3.2	r2			1851	2000	3	r2	1850	1999	3
MRI-CGCM2.3.2	r3			1851	2000	3	r3	1850	1999	3
MRI-CGCM2.3.2	r4			1851	2000	3	r4	1850	2000	3
MRI-CGCM2.3.2	r5			1851	2000	3				
CCSM3	r1		r1	1870	2012	3	r1	1870	1999	3
CCSM3	r2		r2	1870	2012	3	r2	1870	1999	3

(continued on next page)

Table 10.SM.5 (continued)

	historical (20C3M)	historicalExt	rcp45 (A1B)	Overall period			historicalNat	Overall period		
Model	**Realisation**	**Realisation**	**Realisation**	**Start Year**	**End Year**	**CMIP3/5**	**Realisation**	**Start Year**	**End Year**	**CMIP3/5**
CCSM3	r3		r3	1870	2012	3	r3	1870	1999	3
CCSM3	r4			1870	1999	3	r4	1870	1999	3
CCSM3	r5		r5	1870	2012	3	r5	1870	1999	3
CCSM3	r6		r6	1870	2012	3				
CCSM3	r7		r7	1870	2012	3				
CCSM3	r8		r8	1870	2011	3				
CCSM3	r9		r9	1870	2012	3				
PCM	r1			1890	1999	3	r1	1890	1999	3
PCM	r2			1890	1999	3	r2	1890	1999	3
PCM	r3			1890	1999	3	r3	1890	1999	3
PCM	r4			1890	1999	3	r4	1890	1999	3
UKMO_HadCM3	r1[a]			1860	2006	3	r1	1860	1998	3
UKMO_HadCM3							r2	1860	1998	3
UKMO_HadCM3	r3[a]			1860	2002	3	r3	1860	1998	3
UKMO_HadCM3	r4[a]			1860	2002	3	r4	1860	1998	3
UKMO_HadGEM1	r1[a]			1860	2009	3				
UKMO_HadGEM1	r2[a]			1860	2009	3				
UKMO_HadGEM1	r3[a]			1860	2009	3				
UKMO_HadGEM1	r4[a]			1860	2009	3				
ACCESS1.0	r1i1p1		r1i1p1	1850	2012	5				
ACCESS1.3	r1i1p1		r1i1p1	1850	2012	5				
ACCESS1.3	r2i1p1			1850	2005	5				
ACCESS1.3	r3i1p1			1850	2005	5				
BNU-ESM	r1i1p1		r1i1p1	1850	2012	5	r1i1p1	1850	2005	5
CCSM4	r1i1p1		r1i1p1	1850	2012	5	r1i1p1	1850	2005	5
CCSM4	r2i1p1		r2i1p1	1850	2012	5	r2i1p1	1850	2005	5
CCSM4	r3i1p1		r3i1p1	1850	2012	5				
CCSM4	r4i1p1		r4i1p1	1850	2012	5	r4i1p1	1850	2005	5
CCSM4	r5i1p1		r5i1p1	1850	2012	5				
CCSM4	r6i1p1		r6i1p1	1850	2012	5	r6i1p1	1850	2005	5
CESM1(BGC)	r1i1p1		r1i1p1	1850	2012	5				
CESM1(CAM5)	r1i1p1		r1i1p1	1850	2012	5				
CESM1(CAM5)	r2i1p1		r2i1p1	1850	2012	5				
CESM1(CAM5)	r3i1p1		r3i1p1	1850	2012	5				
CESM1(FASTCHEM)	r1i1p1			1850	2005	5				
CESM1(FASTCHEM)	r2i1p1			1850	2005	5				
CESM1(FASTCHEM)	r3i1p1			1850	2005	5				
CESM1(WACCM)	r1i1p1			1850	2005	5				
CMCC-CESM	r1i1p1			1850	2005	5				
CMCC-CMS	r1i1p1		r1i1p1	1850	2012	5				
CMCC-CM	r1i1p1		r1i1p1	1850	2012	5				
CNRM-CM5	r1i1p1	r1i1p1		1850	2012	5	r1i1p1	1850	2012	5
CNRM-CM5	r2i1p1	r2i1p1		1850	2012	5	r2i1p1	1850	2012	5
CNRM-CM5	r3i1p1	r3i1p1		1850	2012	5	r3i1p1	1850	2012	5
CNRM-CM5	r4i1p1	r4i1p1		1850	2012	5	r4i1p1	1850	2012	5
CNRM-CM5	r5i1p1	r5i1p1		1850	2012	5	r5i1p1	1850	2012	5

(continued on next page)

Table 10.SM.5 (continued)

	historical (20C3M)	historicalExt	rcp45 (A1B)	Overall period			historicalNat	Overall period		
Model	**Realisation**	**Realisation**	**Realisation**	**Start Year**	**End Year**	**CMIP3/5**	**Realisation**	**Start Year**	**End Year**	**CMIP3/5**
CNRM-CM5	r6i1p1	r6i1p1		1850	2012	5				
CNRM-CM5	r7i1p1	r7i1p1		1850	2012	5				
CNRM-CM5	r8i1p1	r8i1p1		1850	2012	5	r8i1p1	1850	2012	5
CNRM-CM5	r9i1p1	r9i1p1		1850	2012	5				
CNRM-CM5	r10i1p1	r10i1p1		1850	2012	5				
CSIRO-Mk3.6.0	r1i1p1		r1i1p1	1850	2012	2012	r1i1p1	1850	2012	**5**
CSIRO-Mk3.6.0	r2i1p1		r2i1p1	1850	2012	5	r2i1p1	1850	2012	5
CSIRO-Mk3.6.0	r3i1p1		r3i1p1	1850	2012	5	r3i1p1	1850	2012	5
CSIRO-Mk3.6.0	r4i1p1		r4i1p1	1850	2012	5	r4i1p1	1850	2012	5
CSIRO-Mk3.6.0	r5i1p1		r5i1p1	1850	2012	5	r5i1p1	1850	2012	5
CSIRO-Mk3.6.0	r6i1p1		r6i1p1	1850	2012	5				
CSIRO-Mk3.6.0	r7i1p1		r7i1p1	1850	2012	5				
CSIRO-Mk3.6.0	r8i1p1		r8i1p1	1850	2012	5				
CSIRO-Mk3.6.0	r9i1p1		r9i1p1	1850	2012	5				
CSIRO-Mk3.6.0	r10i1p1		r10i1p1	1850	2012	5				
CanESM2	r1i1p1	r1i1p1		1850	2012	5	r1i1p1	1850	2012	5
CanESM2	r2i1p1	r2i1p1		1850	2012	5	r2i1p1	1850	2012	5
CanESM2	r3i1p1	r3i1p1		1850	2012	5	r3i1p1	1850	2012	5
CanESM2	r4i1p1	r4i1p1		1850	2012	5	r4i1p1	1850	2012	5
CanESM2	r5i1p1	r5i1p1		1850	2012	5	r5i1p1	1850	2012	5
EC-EARTH	r1i1p1		r1i1p1	1850	2012	5				
EC-EARTH	r2i1p1		r2i1p1	1850	2012	5				
EC-EARTH	r6i1p1		r6i1p1	1850	2012	5				
EC-EARTH	r8i1p1		r8i1p1	1850	2012	5				
EC-EARTH	r9i1p1		r9i1p1	1850	2012	5				
EC-EARTH	r11i1p1			1850	2012	5				
EC-EARTH	r12i1p1		r12i1p1	1850	2012	5				
FIO-ESM	r1i1p1		r1i1p1	1850	2012	5				
FIO-ESM	r2i1p1		r2i1p1	1850	2012	5				
FIO-ESM	r3i1p1		r3i1p1	1850	2012	5				
GFDL-CM2p1	r1i1p1			1861	2012	5				
GFDL-CM2p1	r2i1p1			1861	2012	5				
GFDL-CM2p1	r3i1p1			1861	2012	5				
GFDL-CM2p1	r4i1p1			1861	2012	5				
GFDL-CM2p1	r5i1p1			1861	2012	5				
GFDL-CM2p1	r6i1p1			1861	2012	5				
GFDL-CM2p1	r7i1p1			1861	2012	5				
GFDL-CM2p1	r8i1p1			1861	2012	5				
GFDL-CM2p1	r9i1p1			1861	2012	5				
GFDL-CM2p1	r10i1p1			1861	2012	5				
GFDL-CM3	r1i1p1		r1i1p1	1860	2012	5	r1i1p1	1860	2005	5
GFDL-CM3	r2i1p1			1860	2005	5				
GFDL-CM3	r3i1p1			1860	2005	5	r3i1p1	1860	2005	5
GFDL-CM3	r4i1p1			1860	2005	5				
GFDL-CM3	r5i1p1			1860	2005	5	r5i1p1	1860	2005	5
GFDL-ESM2G	r1i1p1		r1i1p1	1861	2012	5				
GFDL-ESM2M	r1i1p1		r1i1p1	1861	2012	5	r1i1p1	1861	2005	5

(continued on next page)

Table 10.SM.5 (continued)

	historical (20C3M)	historicalExt	rcp45 (A1B)	Overall period			historicalNat	Overall period		
Model	**Realisation**	**Realisation**	**Realisation**	**Start Year**	**End Year**	**CMIP3/5**	**Realisation**	**Start Year**	**End Year**	**CMIP3/5**
GISS-E2-H-CC	r1i1p1		r1i1p1	1850	2012	5				
GISS-E2-H	r1i1p1	r1i1p1		1850	2012	5	r1i1p1	1850	2012	5
GISS-E2-H	r2i1p1	r2i1p1		1850	2012	5	r2i1p1	1850	2012	5
GISS-E2-H	r3i1p1	r3i1p1		1850	2012	5	r3i1p1	1850	2012	5
GISS-E2-H	r4i1p1	r4i1p1		1850	2012	5	r4i1p1	1850	2012	5
GISS-E2-H	r5i1p1	r5i1p1		1850	2012	5	r5i1p1	1850	2012	5
GISS-E2-H	r6i1p1			1850	2012	5				
GISS-E2-R-CC	r1i1p1		r1i1p1	1850	2012	5				
GISS-E2-R	r1i1p1	r1i1p1		1850	2012	5	r1i1p1	1850	2012	5
GISS-E2-R	r2i1p1	r2i1p1		1850	2012	5	r2i1p1	1850	2012	5
GISS-E2-R	r3i1p1	r3i1p1		1850	2012	5	r3i1p1	1850	2012	5
GISS-E2-R	r4i1p1	r4i1p1		1850	2012	5	r4i1p1	1850	2012	5
GISS-E2-R	r5i1p1	r5i1p1		1850	2012	5	r5i1p1	1850	2012	5
GISS-E2-R	r6i1p1		r6i1p1	1850	2012	5				
HadCM3	r1i1p1		r1i1p1	1860	2012	5				
HadCM3	r2i1p1		r2i1p1	1860	2012	5				
HadCM3	r3i1p1		r3i1p1	1860	2012	5				
HadCM3	r4i1p1		r4i1p1	1860	2012	5				
HadCM3	r5i1p1		r5i1p1	1860	2012	5				
HadCM3	r6i1p1		r6i1p1	1860	2012	5				
HadCM3	r7i1p1		r7i1p1	1860	2012	5				
HadCM3	r8i1p1		r8i1p1	1860	2012	5				
HadCM3	r9i1p1		r9i1p1	1860	2012	5				
HadCM3	r10i1p1		r10i1p1	1860	2012	5				
HadGEM2-AO	r1i1p1		r1i1p1	1860	2012	5				
HadGEM2-CC	r1i1p1		r1i1p1	1860	2012	5				
HadGEM2-ES	r1i1p1		r1i1p1	1860	2012	5	r1i1p1	1860	2012	5
HadGEM2-ES	r2i1p1	r2i1p1		1860	2012	5	r2i1p1	1860	2012	5
HadGEM2-ES	r3i1p1	r3i1p1		1860	2012	5	r3i1p1	1860	2012	5
HadGEM2-ES	r4i1p1	r4i1p1		1860	2012	5	r4i1p1	1860	2012	5
HadGEM2-ES	r5i1p1			1860	2005	5				
IPSL-CM5A-LR	r1i1p1		r1i1p1	1850	2012	5	r1i1p1	1850	2012	5
IPSL-CM5A-LR	r2i1p1		r2i1p1	1850	2012	5	r2i1p1	1850	2012	5
IPSL-CM5A-LR	r3i1p1		r3i1p1	1850	2012	5	r3i1p1	1850	2012	5
IPSL-CM5A-LR	r4i1p1		r4i1p1	1850	2012	5				
IPSL-CM5A-LR	r5i1p1			1850	2005	5				
IPSL-CM5A-LR	r6i1p1			1850	2005	5				
IPSL-CM5A-MR	r1i1p1		r1i1p1	1850	2012	5	r1i1p1	1850	2012	5
IPSL-CM5A-MR	r2i1p1			1850	2005	5	r2i1p1	1850	2012	5
IPSL-CM5A-MR	r3i1p1			1850	2005	5	r3i1p1	1850	2012	5
IPSL-CM5B-LR	r1i1p1		r1i1p1	1850	2012	5				
MIROC-ESM-CHEM	r1i1p1		r1i1p1	1850	2012	5	r1i1p1	1850	2005	5
MIROC-ESM	r1i1p1		r1i1p1	1850	2012	5	r1i1p1	1850	2005	5
MIROC-ESM	r2i1p1			1850	2005	5	r2i1p1	1850	2005	5
MIROC-ESM	r3i1p1			1850	2005	5	r3i1p1	1850	2005	5
MIROC5	r1i1p1		r1i1p1	1850	2012	5				
MIROC5	r2i1p1		r2i1p1	1850	2012	5				

(continued on next page)

Table 10.SM.5 (continued)

	historical (20C3M)	historicalExt	rcp45 (A1B)	Overall period			historicalNat	Overall period		
Model	**Realisation**	**Realisation**	**Realisation**	**Start Year**	**End Year**	**CMIP3/5**	**Realisation**	**Start Year**	**End Year**	**CMIP3/5**
MIROC5	r3i1p1		r3i1p1	1850	2012	5				
MIROC5	r4i1p1			1850	2012	5				
MIROC5	r5i1p1			1850	2012	5				
MPI-ESM-LR	r1i1p1		r1i1p1	1850	2012	5				
MPI-ESM-LR	r2i1p1		r2i1p1	1850	2012	5				
MPI-ESM-LR	r3i1p1		r3i1p1	1850	2012	5				
MPI-ESM-MR	r1i1p1		r1i1p1	1850	2012	5				
MPI-ESM-MR	r2i1p1		r2i1p1	1850	2012	5				
MPI-ESM-MR	r3i1p1		r3i1p1	1850	2012	5				
MPI-ESM-P	r1i1p1			1850	2005	5				
MPI-ESM-P	r2i1p1			1850	2005	5				
MRI-CGCM3	r1i1p1	r1i1p1		1850	2012	5	r1i1p1	1850	2005	5
MRI-CGCM3	r2i1p1	r2i1p1		1850	2012	5				
MRI-CGCM3	r3i1p1	r3i1p1		1850	2012	5				
MRI-ESM1	r1i1p1			1851	2005	5				
NorESM1-ME	r1i1p1		r1i1p1	1850	2012	5	r1i1p1	1850	2012	5
NorESM1-M	r1i1p1	r1i1p1		1850	2012	5				
NorESM1-M	r2i1p1	r2i1p1		1850	2012	5				
NorESM1-M	r3i1p1	r3i1p1		1850	2012	5				
BCC-CSM1.1(m)	r1i1p1		r1i1p1	1850	2012	5				
BCC-CSM1.1(m)	r2i1p1			1850	2012	5				
BCC-CSM1.1(m)	r3i1p1			1850	2012	5				
BCC-CSM1.1	r1i1p1		r1i1p1	1850	2012	5	r1i1p1	1850	2012	5
BCC-CSM1.1	r2i1p1			1850	2012	5				
BCC-CSM1.1	r3i1p1			1850	2012	5				
INM-CM4	r1i1p1		r1i1p1	1850	2012	5				

Notes:

[a] Simulation not in CMIP3 archive. Obtained from model institution or Daithi Stone (as used in figures in IPCC WG1 2007)

Masking

The data coverage is limited to where data exists in the equivalent month/gridpoint of HadCRUT4. Note that this shortens some model time series (e.g., Antarctica).

Multi-Model Mean

All ensemble members of a specific simulation of a specific model are averaged into an ensemble mean for a specific simulation and model before the models are averaged into a multi-model mean (details in supplementary material to Jones et al., 2013). Therewith, models with more ensemble members are not weighted disproportional to models with less ensemble members.

Creation of Annual Means

Anomalies are calculated for each month/gridpoint relative to the 1880–1919 average (except Antarctica where anomalies are relative to 1950–2010), where at least 50% of the data in the reference period are needed to calculate the average. Annual means are calculated from monthly data for each calendar year, where at least 2 months are non-missing. Shadings are the 5 and 95 percentile among the models.

Global Means

Global and regional mean anomalies are calculated by area averaging all available gridpoint data for each year.

Regions

Continental land areas are based on the SREX defined regions (IPCC, 2012) shown pictorially in the bottom right most panel of Figure 10.7.

Precipitation

Models and ensemble members used are listed in Table 10.SM.6.

Data and Region

50°N–90°N average changes in annual mean precipitation (in mm day^{-1}) for the period 1951–2005, with regard to the baseline period of 1961–1990, are plotted based on Balan Sarojini et al. (2012).

Observational Data

The first observational dataset used (black solid line) is a gridded observational dataset based on station data extracted from the Global

Table 10.SM.6 | Models and ensemble members used for precipitation.

	historicalNat	Overall period		historical	Overall period		
Model	**Realisation**	**Start Year**	**End Year**	**Realisation**	**Start Year**	**End Year**	**CMIP3/5**
ACCESS1.0				r1i1p1	1951	2005	5
BCC-CSM1.1	r1i1p1	1951	2005	r1i1p1	1951	2005	5
CanESM2	r1i1p1	1951	2005	r1i1p1	1951	2005	5
CCSM4				r1i1p1	1951	2005	5
CESM1(BGC)				r1i1p1	1951	2005	5
CESM1(CAM5)				r1i1p1	1951	2005	5
CESM1 (FASTCHEM)				r1i1p1	1951	2005	5
CESM1(WACCM)				r1i1p1	1951	2005	5
CMCC-CESM				r1i1p1	1951	2005	5
CMCC-CMS				r1i1p1	1951	2005	5
CNRM-CM5	r1i1p1	1951	2005	r1i1p1	1951	2005	5
CSIRO-Mk3.6.0	r1i1p1	1951	2005	r1i1p1	1951	2005	5
GFDL-CM3	r1i1p1	1951	2005	r1i1p1	1951	2005	5
GFDL-ESM2G				r1i1p1	1951	2005	5
GFDL-ESM2M				r1i1p1	1951	2005	5
GISS-E2-H				r1i1p1	1951	2005	5
GISS-E2-R				r1i1p1	1951	2005	5
HadGEM2-CC				r1i1p1	1951	2005	5
HadGEM2-ES	r1i1p1	1850	2005	r1i1p1	1850	2005	5
INMCM4_ESM				r1i1p1	1850	2005	5
IPSL-CM5A-LR				r1i1p1	1850	2005	5
IPSL-CM5A-MR				r1i1p1	1951	2005	5
MIROC5				r1i1p1	1951	2005	5
MIROC-ESM	r1i1p1	1951	2005	r1i1p1	1951	2005	5
MIROC-ESM-CHEM	r1i1p1	1951	2005	r1i1p1	1951	2005	5
MPI-ESM-LR				r1i1p1	1951	2005	5
MPI-ESM-MR				r1i1p1	1951	2005	5
MRI-CGCM3	r1i1p1	1951	2005	r1i1p1	1951	2005	5
NorESM1-M	r1i1p1	1951	2005	r1i1p1	1951	2005	5
NorESM1-ME				r1i1p1	1951	2005	5

Historical Climatology Network (updated from Zhang et al., 2007). Monthly data for the period 1951–2005, quality controlled and gridded at 5° × 5°, for all land grid squares on the globe for which station data are available, are used. In order to avoid artefacts arising from changes in data coverage, a sampling criterion of choosing data available for >90% of the analysis period is applied (i.e., each spatial grid point is chosen when data over 90% of the years (only those years which have data for all months) are present).

The second observational dataset (grey solid line) used is a gridded observational dataset based on station data extracted from the Climatic Research Unit, (updated from CRU TS3.1 of Harris et al., 2013) and sampled as in Polson et al. (2013). Monthly data for the period 1951–2005, quality controlled and gridded at 0.5° × 0.5°, are used. This data is first interpolated to the common spatial resolution of 5° × 5°. In order to avoid artefacts arising from changes in data coverage, two sampling criteria are applied: 1) station sampling criterion (Polson et al., 2013) of choosing only those 5° × 5° grid boxes that have at least 1 station (in any 0.5° × 0.5° grid box) for the coastal grid boxes and with at least 2 stations for the inland grid boxes. A 5° × 5° grid box is coastal when over half of number of the 0.5° × 0.5° boxes is ocean points. 2) a criterion of choosing data available for >95% of the analysis period is applied. i.e., each spatial grid point is chosen when data over 95% of the years (years which have data available for any no of months) are present.

Masking of Simulated Data onto the Observational Grid

First, the land area of the simulated data available in different spatial resolutions is obtained by choosing a grid point as land when its land-area fraction is greater than or equal to 70%. Second, the simulated land data are interpolated to the 5° × 5° observational grid using bi-linear interpolation. Third, the 90% sampling criterion derived from the observations is applied to each regridded model data to obtain the consistent temporal and spatial data coverage for the simulated and observed data.

Calculation of Spatial and Annual Averages and Anomalies with regard to the Baseline Climatology

For each (regridded and sampled) monthly model data, spatial averages are first calculated for the zonal band of 50°N–90°N. Annual averages, baseline climatology (for 1961–1990) and anomalies from the baseline period are then calculated.

Plotting

The yearly anomalies are plotted with a y-axis range of 1950–2010. Multi-model means are in thick solid lines (historical in red and historicalNat in blue).

The 5-95% confidence interval of the models is in pink shading for historical runs and in blue shading for historicalNat runs.

Ocean Heat Content

Models and ensemble members used are listed in Table 10.SM.7.

Observational Data

Three observational data sets are updated from Domingues et al. (2008), Levitus et al. (2012) and sourced from http://www.nodc.noaa.gov/OC5/3M_HEAT_CONTENT/index.html and Ishii and Kimoto (2009) and sourced from http://www.data.kishou.go.jp/kaiyou/english/ohc/ohc_data_en.html (version August 2012).

Data Treatment

Before computing the ocean heat content the model output has been treated as in Pierce et al. (2012), i.e., horizontal regridding to a 10° x 10° latitude/longitude grid between 60°S and 60°N over the top 700 m; masking the grid boxes that lack observations; fields are de-drifted using second order polynomials fit to the pre-industrial control runs ('piControl').

Annual mean OHC values are calculated from models by vertically integrating the annual mean temperature anomalies (with respect to a 1960–1980 reference period). Global mean time series are calculated by integrating over space.

All OHC time series are relative to the reference period of 1960–1980. Only Domingues et al. (2008) OHC data are smoothed with a three-year running means.

Regions

Ocean basin definition (Latitudes) are:

- Southern Ocean: south of 50°S
- South Pacific: 50°S to Equator
- South Atlantic : 50°S to Equator; up to 20°E;
- Indian Ocean: 50°S to 30°N; 20°E to Australia (Tasmania)
- North Pacific, North Atlantic: Equator to 70°N

Sea Ice

September sea ice extent (concentration >15%) anomalies for the Northern Hemisphere (Arctic) and Southern Hemisphere (Antarctic), relative to 1979–1999. Models and ensemble members used for the final figure are listed in Table 10.SM.8. Observational data is from NSIDC bootstrap algorithm (SBA; Cavalieri and Parkinson, 2012; Parkinson and Cavalieri, 2012).

The historical simulations are extended with rcp85 to the year 2012. For both the historicalNat and historical extended with rcp85 the multi-model mean and 5–95% confidence interval for each year are calculated from all models available for that year.

Table 10.SM.7 | Models and ensemble members used for ocean heat content.

	historicalNat	Overall period		historical	Overall period		
Model	**Realisation**	**Start Year**	**End Year**	**Realisation**	**Start Year**	**End Year**	**CMIP3/5**
CanESM2	r1i1p1	1950	2012	r1i1p1	1950	2005	5
CCSM4	r1i1p1	1950	2005	r1i1p1	1950	2005	5
CNRM-CM5	r1i1p1	1950	2012	r1i1p1	1950	2005	5
CSIRO-MK3.6.0	r1i1p1	1950	2012	r1i1p1	1950	2005	5
GISS-E2-H	r1i1p1	1950	2012	r1i1p1	1950	2005	5
GISS-E2-R	r1i1p1	1950	2012	r1i1p1	1950	2005	5
HADGEM2-ES	r1i1p1	1950	2012	r1i1p1	1950	2003	5
MIROC5				r1i1p1	1950	2005	5
MIROC-ESM	r1i1p1	1950	2005	r1i1p1	1950	2005	5
MPI-ESM-LR				r1i1p1	1950	2005	5
MRI-CGCM3	r1i1p1	1950	2005	r1i1p1	1950	2005	5
NorESM1-M	r1i1p1	1950	2005	r1i1p1	1950	2005	5

The simulations have been plotted as anomalies from the mean for the reference period (1979–1999) with 5-95% confidence interval of the models as shading. The observations are the September sea ice extent anomalies relative to 1979–1999 period mean from the NSIDC sea-ice data set.

Data Quality

For land and ocean surface temperatures and precipitation panels, solid green lines at bottom of panels indicate where data spatial coverage, of areas being examined, is above 50% coverage and dashed green lines where coverage is below 50%. For example, data coverage of Antarctica never goes above 50% of the land area of the continent. For ocean heat content and sea-ice panels the solid line is where the coverage of data is good and higher in quality, and the dashed line is where the data coverage is only adequate, based on a qualitative expert assessment. See the Table 10.SM.9 for the years of change from adequate to higher quality data.

Table 10.SM.8 | Models and ensemble members used for sea ice.

	historicalNat	Overall period		historical	rcp85	Overall period		
Model	**Realisation**	**Start Year**	**End Year**	**Realisation**	**Realisation**	**Start Year**	**End Year**	**CMIP3/5**
BCC-CSM1.1	r1i1p1	1950	2012	r1i1p1	r1i1p1	1950	2012	5
BNU-ESM	r1i1p1	1950	2005	r1i1p1	r1i1p1	1950	2012	5
CanESM2	r1i1p1	1950	2012	r1i1p1	r1i1p1	1950	2012	5
CCSM4	r1i1p1	1950	2005	r1i1p1	r1i1p1	1950	2012	5
CNRM-CM5	r1i1p1	1950	2012	r1i1p1	r1i1p1	1950	2012	5
CSIRO-MK3.6.0	r1i1p1	1950	2012	r1i1p1	r1i1p1	1950	2012	5
FGOALS-g2	r1i1p1	1950	2009	r1i1p1	r1i1p1	1950	2012	5
GFDL-ESM2M	r1i1p1	1950	2005	r1i1p1	r1i1p1	1950	2012	5
GISS-E2-H	r1i1p1	1950	2012	r1i1p1	r1i1p1	1950	2012	5
GISS-E2-R	r1i1p1	1950	2012	r1i1p1	r1i1p1	1950	2012	5
HADGEM2-ES	r1i1p1	1950	2012	r1i1p1	r1i1p1	1950	2012	5
IPSL-CM5A-LR	r1i1p1	1950	2012	r1i1p1	r1i1p1	1950	2012	5
IPSL-CM5A-MR	r1i1p1	1950	2012	r1i1p1	r1i1p1	1950	2012	5
MIROC-ESM	r1i1p1	1950	2005	r1i1p1	r1i1p1	1950	2012	5
MIROC-ESM-CHEM	r1i1p1	1950	2005	r1i1p1	r1i1p1	1950	2012	5
MRI-CGCM3	r1i1p1	1950	2005	r1i1p1	r1i1p1	1950	2012	5
NorESM1-M	r1i1p1	1950	2012	r1i1p1	r1i1p1	1950	2012	5

Table 10.SM.9 | Years of change from adequate to higher quality data, i.e., when dashed lines change to solid lines.

Element of climate system	Region	Year of change from dashed to solid line
Continental temperatures	Global Land+Ocean	1880
	Global Land	1930
	Global Ocean	1880
	North America	1910
	South America	1930
	Europe	1860
	Africa	1950
	Asia	1925
	Australia	1910
	Antarctica	1944
Ocean Heat Content	All basins	1970
Sea Ice	Arctic and Antarctica	1979
Precipitation	Precipitation	1985

FAQ 10.1, Figure 1

This figure is a condensed version of Figures 10.1 and 10.2, so the supplemental information for those figures applies to this set of panels too.

FAQ 10.2, Figure 1

Data

One run each of the historical and RCP8.5 simulations is used from 24 CMIP5 models. The models are ACCESS1.0, CCSM4, CNRM CM5, CSIRO Mk3.6.0, CanESM2, EC EARTH, FGOALS g2, FGOALS s2, GFDL CM3, GFDL ESM2G, GFDL ESM2M, GISS E2 R, HadGEM2 CC, HadGEM2 ES, IPSL CM5A LR, IPSL CM5A MR, MIROC ESM CHEM, MIROC ESM, MIROC5, MPI ESM LR, MRI CGCM3, NorESM1 M, bcc csm1.1, inmcm4.

Method

The primary test on summer surface temperature is applied using 30-year moving windows at 10-year steps, starting with 1900–1929 as a baseline and ending in 2070–2099 for the RCP8.5 model runs. This procedure is applied to each model and grid cell. The local warming is considered statistically significant when a Kolmogorov–Smirnov test rejects with 95% significance that the samples of the two 30-year windows are drawn from the same distribution. The last year of the moving window is taken as the year of emergence in one model. Changes are considered significant in the year when the signal is detected in 80% of the models. This procedure is done for each grid point. The year is then used to estimate the corresponding global temperature change based on the historical and RCP8.5 simulation in each model.

References

Aldrin, M., M. Holden, P. Guttorp, R. B. Skeie, G. Myhre, and T. K. Berntsen, 2012: Bayesian estimation of climate sensitivity based on a simple climate model fitted to observations of hemispheric temperatures and global ocean heat content. *Environmetrics*, **23**, 253–271.

Annan, J. D., and J. C. Hargreaves, 2006: Using multiple observationally-based constraints to estimate climate sensitivity. *Geophys. Res. Lett.*, **33**, L06704.

Annan, J. D., J. C. Hargreaves, R. Ohgaito, A. Abe-Ouchi, and S. Emori, 2005: Efficiently constraining climate sensitivity with ensembles of paleoclimate simulations. *Sci. Online Lett. Atmos. (SOLA)*, **1**, 181–184.

Balan Sarojini, B., P. Stott, E. Black, and D. Polson, 2012 Fingerprints of changes in annual and seasonal precipitation from CMIP5 models over land and ocean. *Geophys. Res. Lett.*, **39**, L23706.

Bender, F. A. M., A. M. L. Ekman, and H. Rodhe, 2010: Response to the eruption of Mount Pinatubo in relation to climate sensitivity in the CMIP3 models. *Clim. Dyn.*, **35**, 875–886.

Brohan, P., J. J. Kennedy, I. Harris, S. F. B. Tett, and P. D. Jones, 2006: Uncertainty estimates in regional and global observed temperature changes: A new data set from 1850. *J. Geophys. Res. Atmos.*, **111**, D12106.

Cavalieri, D. J., and C. L. Parkinson, 2012: Arctic sea ice variability and trends, 1979–2010, *Cryosphere*, **6**, 881–889.

Chylek, P., and U. Lohmann, 2008: Aerosol radiative forcing and climate sensitivity deduced from the last glacial maximum to Holocene transition. *Geophys. Res. Lett.*, **35**, L04804.

Crowley, T. J., G. Zielinski, B. Vinther, R. Udisti, K. Kreutzs, J. Cole-Dai, and E. Castellano, 2008: Volcanism and the Little Ice age. *PAGES News*, **16**, 22–23.

Dee, D. P., et al., 2011: The ERA-Interim reanalysis: configuration and performance of the data assimilation system. *Q. J. R. Meteor. Soc.*, **137**, 553–597.

Domingues, C., J. Church, N. White, P. Gleckler, S. Wijffels, P. Barker, and J. Dunn, 2008: Improved estimates of upper-ocean warming and multi-decadal sea-level rise. *Nature*, **453**, 1090–1093.

Durack, P., S. Wijffels, and R. Matear, 2012: Ocean salinities reveal strong global water cycle intensification during 1950 to 2000. *Science*, **336**, 455–458.

Eyring, V., et al., 2013: Long-term changes in tropospheric and stratospheric ozone and associated climate impacts in CMIP5 simulations. *J. Geophys. Res. Atmos.*, doi:10.1002/jgrd.50316.

Folland, C. K., et al., 2013 High predictive skill of global surface temperature a year ahead. *Geophys. Res. Lett.*, **40**, 761–767.

Forster, P. M., T. Andrews, P. Good, J. M. Gregory, L. S. Jackson, and M. Zelinka, 2013 Evaluating adjusted forcing and model spread for historical and future scenarios in the CMIP5 generation of climate models. *J. Geophys. Res. Atmos.*, **118**, 1139–1150.

Forster, P. M. D., and J. M. Gregory, 2006: The climate sensitivity and its components diagnosed from Earth Radiation Budget data. *J. Clim.*, **19**, 39–52.

Frame, D. J., D. A. Stone, P. A. Stott, and M. R. Allen, 2006: Alternatives to stabilization scenarios. *Geophys. Res. Lett.*, **33**, L14707.

Frame, D. J., B. B. B. Booth, J. A. Kettleborough, D. A. Stainforth, J. M. Gregory, M. Collins, and M. R. Allen, 2005: Constraining climate forecasts: The role of prior assumptions. *Geophys. Res. Lett.*, **32**, L09702.

Gao, C., A. Robock, and C. Ammann, 2008: Volcanic forcing of climate over the past 1500 years: An improved ice core-based index for climate models. *J. Geophys. Res. Atmos.*, **113**, D23111.

Gillett, N. A., and J. C. Fyfe, 2013: Annular Mode change in the CMIP5 simulations. *Geophys. Res. Lett.*, **40**, 1189–1193.

Gillett, N. P., V. K. Arora, G. M. Flato, J. F. Scinocca, and K. von Salzen, 2012: Improved constraints on 21st-century warming derived using 160 years of temperature observations. *Geophys. Res. Lett.*, **39**, L01704.

Gillett, N. P., V. K. Arora, D. Matthews, P. A. Stott, and M. R. Allen, 2013 Constraining the ratio of global warming to cumulative CO2 emissions using CMIP5 simulations. *J. Clim.*, doi:10.1175/JCLI-D-12-00476.1.

Gleckler, P. J., et al., 2012: Human-induced global ocean warming on multidecadal timescales. *Nature Clim. Change*, **2**, 524–529.

Gong, D., and S. Wang, 1999: Definition of Antarctic oscillation index. *Geophys. Res. Lett.*, **26**, 459–462.

Goosse, H., J. Guiot, M. E. Mann, S. Dubinkina, and Y. Sallaz-Damaz, 2012a: The medieval climate anomaly in Europe: Comparison of the summer and annual mean signals in two reconstructions and in simulations with data assimilation. *Global Planet. Change*, **84–85**, 35–47.

Goosse, H., et al., 2012b: The role of forcing and internal dynamics in explaining the "Medieval Climate Anomaly'. *Clim. Dyn.*, **39**, 2847–2866.

Gregory, J. M., 2000: Vertical heat transports in the ocean and their effect an time-dependent climate change. *Clim. Dyn.*, **16**, 501–515.

Gregory, J. M., and P. M. Forster, 2008: Transient climate response estimated from radiative forcing and observed temperature change. *J. Geophys. Res. Atmos.*, **113**, D23105.

Gregory, J. M., R. J. Stouffer, S. C. B. Raper, P. A. Stott, and N. A. Rayner, 2002: An observationally based estimate of the climate sensitivity. *J. Clim.*, **15**, 3117–3121.

Haimberger, L., C. Tavolato, and S. Sperka, 2012: Homogenization of the global radiosonde temperature dataset through combined comparison with reanalysis background series and neighboring stations. *J. Clim.*, **25**, 8108–8131.

Hargreaves, J. C., J. D. Annan, M. Yoshimori, and A. Abe-Ouchi, 2012: Can the Last Glacial Maximum constrain climate sensitivity? *Geophys. Res. Lett.*, **39**, L24702.

Harris, G. R., D. M. H. Sexton, B. B. B. Booth, M. Collins, and J. M. Murphy, 2013: Probabilistic projections of transient climate change. *Clim. Dyn.*, doi:10.1007/s00382-012-1647-y.

Hegerl, G., J. Luterbacher, F. Gonzalez-Rouco, S. F. B. Tett, T. Crowley, and E. Xoplaki, 2011: Influence of human and natural forcing on European seasonal temperatures. *Nature Geosci.*, **4**, 99–103.

Hegerl, G. C., T. J. Crowley, W. T. Hyde, and D. J. Frame, 2006: Climate sensitivity constrained by temperature reconstructions over the past seven centuries. *Nature*, **440**, 1029–1032.

Hegerl, G. C., et al., 2010: Good practice guidance paper on detection and attribution related to anthropogenic climate change. In: *Meeting Report of the Intergovernmental Panel on Climate Change Expert Meeting on Detection and Attribution of Anthropogenic Climate Change* [T. F. Stocker, et al. (eds.)]. IPCC Working Group I Technical Support Unit, University of Bern, Bern, Switzerland, 8 pp.

Held, I. M., M. Winton, K. Takahashi, T. Delworth, F. R. Zeng, and G. K. Vallis, 2010: Probing the fast and slow components of global warming by returning abruptly to preindustrial forcing. *J. Clim.*, **23**, 2418–2427.

Helm, K. P., N. L. Bindoff, and J. A. Church, 2010: Changes in the global hydrological-cycle inferred from ocean salinity. *Geophys. Res. Lett.*, **37**, L18701.

Holden, P. B., N. R. Edwards, K. I. C. Oliver, T. M. Lenton, and R. D. Wilkinson, 2010: A probabilistic calibration of climate sensitivity and terrestrial carbon change in GENIE-1. *Clim. Dyn.*, **35**, 785–806.

Hu, Y. Y., L. J. Tao, and J. P. Liu, 2013: Poleward expansion of the Hadley circulation in CMIP5 simulations. *Adv. Atmos. Sci.*, **30**, 790–795.

Hurtt, G. C., et al., 2009: Harmonization of global land-use scenarios for the period 1500–2100 for IPCC-AR5. *Integrat. Land Ecosyst. Atmos. Process. Study (iLEAPS) Newslett.*, **7**, 6–8.

Imbers, J., A. Lopez, C. Huntingford, and M. R. Allen, 2013: Testing the robustness of the anthropogenic climate change detection statements using different empirical models. *J. Geophys. Res. Atmos.*, doi:10.1002/jgrd.50296.

IPCC, 2012: *Managing the Risks of Extreme Events and Disasters to Advance Climate Change Adaptation. A Special Report of Working Groups I and II of the Intergovernmental Panel on Climate Change* [Field, C.B., et al. (eds.)]. Cambridge University Press, Cambridge, UK, and New York, NY, USA, 582 pp.

Ishii, M., and M. Kimoto, 2009: Reevaluation of historical ocean heat content variations with time-varying XBT and MBT depth bias corrections. *J. Oceanogr.*, **65**, 287–299.

Ishii, M., M. Kimoto, K. Sakamoto, and S.-I. Iwasaki, 2006: Steric sea level changes estimated from historical subsurface temperature and salinity analyses. *J. Oceanogr.*, **62**, 155–170.

Jones, G. S., S. F. B. Tett, and P. A. Stott, 2003: Causes of atmospheric temperature change 1960–2000: A combined attribution analysis. *Geophys. Res. Lett.*, **30**, 1228.

Jones, G. S., P. A. Stott, and N. Christidis, 2013 Attribution of observed historical near surface temperature variations to anthropogenic and natural causes using CMIP5 simulations. *J. Geophys. Res. Atmos.*, doi:10.1002/jgrd.50239.

Jungclaus, J. H., et al., 2010: Climate and carbon-cycle variability over the last millennium. *Clim. Past*, **6**, 723–737.

Kaplan, J. O., K. M. Krumhardt, and N. Zimmermann, 2009: The prehistoric and preindustrial deforestation of Europe. *Quat. Sci. Rev.*, **28**, 3016–3034.

Kaufmann, R. K., H. Kauppi, and J. H. Stock, 2006: Emission, concentrations, & temperature: A time series analysis. *Clim. Change*, **77**, 249–278.

Kaufmann, R. K., H. Kauppi, M. L. Mann, and J. H. Stock, 2011: Reconciling anthropogenic climate change with observed temperature 1998–2008. *Proc. Natl. Acad. Sci. U.S.A.*, **108**, 11790–11793.

Kay, A. L., S. M. Crooks, P. Pall, and D. A. Stone, 2011: Attribution of Autumn/Winter 2000 flood risk in England to anthropogenic climate change: A catchment-based study. *J. Hydrol.*, **406**, 97–112.

Knutson, T. R., F. Zeng, and A. T. Wittenberg, 2013: Multi-model assessment of regional surface temperature trends. *J. Clim.*, doi:10.1175/JCLI-D-12-00567.1.

Knutti, R., and L. Tomassini, 2008: Constraints on the transient climate response from observed global temperature and ocean heat uptake. *Geophys. Res. Lett.*, **35**, L09701.

Knutti, R., T. F. Stocker, F. Joos, and G.-K. Plattner, 2002: Constraints on radiative forcing and future climate change from observations and climate model ensembles. *Nature*, **416**, 719–723.

Knutti, R., G. A. Meehl, M. R. Allen, and D. A. Stainforth, 2006: Constraining climate sensitivity from the seasonal cycle in surface temperature. *J. Clim.*, **19**, 4224–4233.

Koehler, P., R. Bintanja, H. Fischer, F. Joos, R. Knutti, G. Lohmann, and V. Masson-Delmotte, 2010: What caused Earth's temperature variations during the last 800,000 years? Data-based evidence on radiative forcing and constraints on climate sensitivity. *Quat. Sci. Rev.*, **29**, 129–145.

Kopp, G., and J. L. Lean, 2011: A new, lower value of total solar irradiance: Evidence and climate significance. *Geophys. Res. Lett.*, **38**, L01706.

Lanzante, J. R., 1996: Resistant, robust and non-parametric techniques for the analysis of climate data: Theory and examples, including applications to historical radiosonde station data. *Int. J. Climatol.*, **16**, 1197–1226.

Lean, J. L., and D. H. Rind, 2008: How natural and anthropogenic influences alter global and regional surface temperatures: 1889 to 2006. *Geophys. Res. Lett.*, **35**, L18701.

Lean, J. L., and D. H. Rind, 2009: How will Earth's surface temperature change in future decades? *Geophys. Res. Lett.*, **36**, L15708.

Levitus, S., J. Antonov, and T. Boyer, 2005: Warming of the world ocean, 1955–2003. *Geophys. Res. Lett.*, **32**, L02604.

Levitus, S., J. I. Antonov, T. P. Boyer, R. A. Locarnini, H. E. Garcia, and A. V. Mishonov, 2009: Global ocean heat content 1955–2008 in light of recently revealed instrumentation problems. *Geophys. Res. Lett.*, **36**, L07608.

Levitus, S., et al., 2012: World ocean heat content and thermosteric sea level change (0–2000 m), 1955–2010. *Geophys. Res. Lett.*, **39**, L10603.

Lewis, N., 2013: An objective Bayesian, improved approach for applying optimal fingerprint techniques to estimate climate sensitivity. *J. Clim.*, doi:10.1175/JCLI-D-12-00473.1.

Libardoni, A. G., and C. E. Forest, 2011: Sensitivity of distributions of climate system properties to the surface temperature dataset. *Geophys. Res. Lett.*, **38**, L22705.

Libardoni, A. G., and C. E. Forest, 2013: Correction to "Sensitivity of distributions of climate system properties to the surface temperature dataset". *Geophys. Res. Lett.*, doi:10.1002/grl.50480.

Lin, B., et al., 2010: Estimations of climate sensitivity based on top-of-atmosphere radiation imbalance. *Atmos. Chem. Phys.*, **10**, 1923–1930.

Lindzen, R. S., and Y. S. Choi, 2011: On the observational determination of climate sensitivity and its implications. *Asia-Pacif. J. Atmos. Sci.*, **47**, 377–390.

Lockwood, M., 2008: Recent changes in solar outputs and the global mean surface temperature. III. Analysis of contributions to global mean air surface temperature rise. *Proc. R. Soc. A*, **464**, 1387–1404.

Lott, F. C., et al., 2013: Models versus radiosondes in the free atmosphere: A new detection and attribution analysis of temperature. *J. Geophys. Res. Atmos.*, **118**, 2609–2619.

Luterbacher, J., D. Dietrich, E. Xoplaki, M. Grosjean, and H. Wanner, 2004: European seasonal and annual temperature variability, trend, and extremes since 1500. *Science*, **303**, 1499–1503.

MacFarling Meure, C., et al., 2006: Law Dome CO(2), CH(4) and N(2)O ice core records extended to 2000 years BP. *Geophys. Res. Lett.*, **33**, L14810.

Mann, M. E., et al., 2009: Global signatures and dynamical origins of the Little Ice age and medieval climate anomaly. *Science*, **326**, 1256–1260.

Mears, C. A., and F. J. Wentz, 2009: Construction of the remote sensing systems V3.2 atmospheric temperature records from the MSU and AMSU microwave sounders. *J. Atmos. Ocean. Technol.*, **26**, 1040–1056.

Meinshausen, M., et al., 2009: Greenhouse-gas emission targets for limiting global warming to 2 degrees C. *Nature*, **458**, 1158–U96.

Min, S.-K., X. B. Zhang, and F. Zwiers, 2008: Human-induced arctic moistening. *Science*, **320**, 518–520.

Min, S.-K., X. Zhang, F. W. Zwiers, and G. C. Hegerl, 2011: Human contribution to more intense precipitation extremes. *Nature*, **470**, 378–381.

Morak, S., G. C. Hegerl, and N. Christidis, 2013: Detectable changes in the frequency of temperature extremes. *J. Clim.*, **26**, 1561–1574.

Morice, C. P., J. J. Kennedy, N. A. Rayner, and P. D. Jones, 2012: Quantifying uncertainties in global and regional temperature change using an ensemble of observational estimates: The HadCRUT4 data set. *J. Geophys. Res. Atmos.*, **117**, D08101.

Murphy, D. M., S. Solomon, R. W. Portmann, K. H. Rosenlof, P. M. Forster, and T. Wong, 2009: An observationally based energy balance for the Earth since 1950. *J. Geophys. Res. Atmos.*, **114**, D17107.

North, G. R., and M. J. Stevens, 1998: Detecting climate signals in the surface temperature record. *J. Clim.*, **11**, 563–577.

Olson, R., R. Sriver, M. Goes, N. M. Urban, H. D. Matthews, M. Haran, and K. Keller, 2012: A climate sensitivity estimate using Bayesian fusion of instrumental observations and an Earth System model. *J. Geophys. Res. Atmos.*, **117**, D04103.

Otto, A., et al., 2013: Energy budget constraints on climate response. *Nature Geosci.*, **6**, 415–416.

Otto, F. E. L., N. Massey, G. J. van Oldenborgh, R. G. Jones, and M. R. Allen, 2012: Reconciling two approaches to attribution of the 2010 Russian heat wave. *Geophys. Res. Lett.*, **39**, L04702.

Padilla, L. E., G. K. Vallis, and C. W. Rowley, 2011: Probabilistic estimates of transient climate sensitivity subject to uncertainty in forcing and natural variability. *J. Clim.*, **24**, 5521–5537.

Paleosens Members, 2012: Making sense of palaeoclimate sensitivity. *Nature*, **491**, 683–691.

Pall, P., et al., 2011: Anthropogenic greenhouse gas contribution to UK autumn flood risk. *Nature*, **470**, 382–385.

Parker, D., C. Folland, A. Scaife, J. Knight, A. Colman, P. Baines, and B. Dong, 2007: Decadal to multidecadal variability and the climate change background. *J. Geophys. Res. Atmos.*, **112**, D18115.

Parkinson, C. L., and D. J. Cavalieri, 2012: Antarctic sea ice variability and trends, 1979–2010, *Cryosphere*, **6**, 871–880.

Pierce, D.W., P. J.Gleckler, T. P. Barnett, B. D. Santer, and P. J. Durack, 2012: The fingerprint of humaninduced changes in the ocean's salinity and temperature fields. *Geophys. Res. Lett*., **39**, L21704.

Piani, C., D. J. Frame, D. A. Stainforth, and M. R. Allen, 2005: Constraints on climate change from a multi-thousand member ensemble of simulations. *Geophys. Res. Lett.*, **32**, L23825.

Polson, D., G. C. Hegerl, X. Zhang, and T. J. Osborn, 2013: Causes of robust seasonal land precipitation changes. *J. Clim.*, doi:10.1175/JCLI-D-12-00474.1.

Pongratz, J., C. Reick, T. Raddatz, and M. Claussen, 2008: A reconstruction of global agricultural areas and land cover for the last millennium. *Global Biogeochem. Cycles*, **22**, GB3018.

Ribes, A., and L. Terray, 2013: Application of regularised optimal fingerprint analysis for attribution. Part II: Application to global near-surface temperature *Clim. Dyn.*, doi:10.1007/s00382-013-1736-6.

Rogelj, J., M. Meinshausen, and R. Knutti, 2012: Global warming under old and new scenarios using IPCC climate sensitivity range estimates. *Nature Clim. Change*, **2**, 248–253.

Santer, B. D., et al., 2013: Identifying human influences on atmospheric temperature. *Proc. Natl. Acad. Sci. U.S.A.*, **110**, 26–33.

Sato, M., J. E. Hansen, M. P. McCormick, and J. B. Pollack, 1993: Stratospheric aerosol optical depth, 1850–1990. *J. Geophys. Res. Atmos.*, **98**, 22987–22994.

Schmidt, G., et al., 2012: Climate forcing reconstructions for use in PMIP simulations of the last millennium (v1.1). *Geoscientif. Model Dev.*, **5**, 185–191.

Schmittner, A., et al., 2011: Climate sensitivity estimated from temperature reconstructions of the last glacial maximum. *Science*, **334**, 1385–1388.

Schneider von Deimling, T., H. Held, A. Ganopolski, and S. Rahmstorf, 2006: Climate sensitivity estimated from ensemble simulations of glacial climate. *Clim. Dyn.*, **27**, 149–163.

Schurer, A., G. Hegerl, M. E. Mann, S. F. B. Tett, and S. J. Phipps, 2013: Separating forced from chaotic climate variability over the past millennium. *J. Clim.*, doi:10.1175/JCLI-D-12-00826.1.

Schwartz, S. E., 2012: Determination of Earth's transient and equilibrium climate sensitivities from observations over the twentieth century: Strong dependence on assumed forcing. *Surv. Geophys.*, **33** 745–777.

Sexton, D. M. H., J. M. Murphy, M. Collins, and M. J. Webb, 2012: Multivariate probabilistic projections using imperfect climate models part I: outline of methodology. *Clim. Dyn.*, **38**, 2513–2542.

Skeie, R. B., T. K. Berntsen, G. Myhre, K. Tanaka, M. M. Kvalevåg, and C. R. Hoyle, 2011: Anthropogenic radiative forcing time series from pre-industrial times until 2010. *Atmos. Chem. Phys.*, **11**, 11827–11857.

Steinhilber, F., J. Beer, and C. Froehlich, 2009: Total solar irradiance during the Holocene. *Geophys. Res. Lett.*, **36**, L19704.

Stott, P. A., and C. E. Forest, 2007: Ensemble climate predictions using climate models and observational constraints. *Philos. Trans. R. Soc. A*, **365**, 2029–2052.

Stott, P. A., and G. S. Jones, 2012: Observed 21st century temperatures further constrain decadal predictions of future warming. *Atmos. Sci. Lett.*, **13**, 151–156.

Stott, P. A., J. F. B. Mitchell, M. R. Allen, T. L. Delworth, J. M. Gregory, G. A. Meehl, and B. D. Santer, 2006: Observational constraints on past attributable warming and predictions of future global warming. *J. Clim.*, **19**, 3055–3069.

Taylor, K. E., R. J. Stouffer, and G. A. Meehl, 2012: An overview of CMIP5 and the experiment design. *Bull. Am. Meteorol. Soc.*, **93**, 485–498.

Terray, L., L. Corre, S. Cravatte, T. Delcroix, G. Reverdin, and A. Ribes, 2012: Near-surface salinity as nature's rain gauge to detect human influence on the tropical water cycle. *J. Clim.*, **25**, 958–977.

Thorne, P. W., J. R. Lanzante, T. C. Peterson, D. J. Seidel, and K. P. Shine, 2011: Tropospheric temperature trends: history of an ongoing controversy. *WIREs Clim. Change*, **2**, 66–88.

Thorne, P. W., D. E. Parker, S. F. B. Tett, P. D. Jones, M. McCarthy, H. Coleman, and P. Brohan, 2005: Revisiting radiosonde upper air temperatures from 1958 to 2002. *J. Geophys. Res. Atmos.*, **110**, D18105

Tomassini, L., P. Reichert, R. Knutti, T. F. Stocker, and M. E. Borsuk, 2007: Robust bayesian uncertainty analysis of climate system properties using Markov chain Monte Carlo methods. *J. Clim.*, **20**, 1239–1254.

Tung, K. K., J. S. Zhou, and C. D. Camp, 2008: Constraining model transient climate response using independent observations of solar-cycle forcing and response. *Geophys. Res. Lett.*, **35** L17707.

Uppala, S. M., et al., 2005: The ERA-40 re-analysis. *Q. J. R. Meteor. Soc.*, **131**, 2961–3012.

Vieira, L. E. A., S. K. Solanki, N. A. Krivova, and I. Usoskin, 2011: Evolution of the solar irradiance during the Holocene. *Astron. Astrophys.*, **531**, A6.

Wang, M., and J. E. Overland, 2012: A sea ice free summer Arctic within 30 years: An update from CMIP5 models. *Geophys. Res. Lett.*, **39**, L18501.

Wang, Y. M., J. L. Lean, and N. R. Sheeley, 2005: Modeling the sun's magnetic field and irradiance since 1713. *Astrophys. J.*, **625**, 522–538.

Zhang, X. B., et al., 2007: Detection of human influence on twentieth-century precipitation trends. *Nature*, **448**, 461–465.

Zhang, X. D., 2010: Sensitivity of arctic summer sea ice coverage to global warming forcing: towards reducing uncertainty in arctic climate change projections. *Tellus A*, **62**, 220–227.

Zwiers, F. W., X. Zhang, and Y. Feng, 2011: Anthropogenic influence on long return period daily temperature extremes at regional scales. *J. Clim.*, **24**, 881–892.

13SM

Sea Level Change

Supplementary Material

Coordinating Lead Authors:

John A. Church (Australia), Peter U. Clark (USA)

Lead Authors:

Anny Cazenave (France), Jonathan M. Gregory (UK), Svetlana Jevrejeva (UK), Anders Levermann (Germany), Mark A. Merrifield (USA), Glenn A. Milne (Canada), R. Steven Nerem (USA), Patrick D. Nunn (Australia), Antony J. Payne (UK), W. Tad Pfeffer (USA), Detlef Stammer (Germany), Alakkat S. Unnikrishnan (India)

Contributing Authors:

David Bahr (USA), Jason E. Box (Denmark/USA), David H. Bromwich (USA), Mark Carson (Germany), William Collins (UK), Xavier Fettweis (Belgium), Piers Forster (UK), Alex Gardner (USA), W. Roland Gehrels (UK), Rianne Giesen (Netherlands), Peter J. Gleckler (USA), Peter Good (UK), Rune Grand Graversen (Sweden), Ralf Greve (Japan), Stephen Griffies (USA), Edward Hanna (UK), Mark Hemer (Australia), Regine Hock (USA), Simon J. Holgate (UK), John Hunter (Australia), Philippe Huybrechts (Belgium), Gregory Johnson (USA), Ian Joughin (USA), Georg Kaser (Austria), Caroline Katsman (Netherlands), Leonard Konikow (USA), Gerhard Krinner (France), Anne Le Brocq (UK), Jan Lenaerts (Netherlands), Stefan Ligtenberg (Netherlands), Christopher M. Little (USA), Ben Marzeion (Austria), Kathleen L. McInnes (Australia), Sebastian H. Mernild (USA), Didier Monselesan (Australia), Ruth Mottram (Denmark), Tavi Murray (UK), Gunnar Myhre (Norway), J.P. Nicholas (USA), Faezeh Nick (Norway), Mahé Perrette (Germany), David Pollard (USA), Valentina Radić (Canada), Jamie Rae (UK), Markku Rummukainen (Sweden), Christian Schoof (Canada), Aimée Slangen (Australia/Netherlands), Jan H. van Angelen (Netherlands), Willem Jan van de Berg (Netherlands), Michiel van den Broeke (Netherlands), Miren Vizcaíno (Netherlands), Yoshihide Wada (Netherlands), Neil J. White (Australia), Ricarda Winkelmann (Germany), Jianjun Yin (USA), Masakazu Yoshimori (Japan), Kirsten Zickfeld (Canada)

Review Editors:

Jean Jouzel (France), Roderik van de Wal (Netherlands), Philip L. Woodworth (UK), Cunde Xiao (China)

This chapter supplementary material should be cited as:

Church, J.A., P.U. Clark, A. Cazenave, J.M. Gregory, S. Jevrejeva, A. Levermann, M.A. Merrifield, G.A. Milne, R.S. Nerem, P.D. Nunn, A.J. Payne, W.T. Pfeffer, D. Stammer and A.S. Unnikrishnan, 2013: Sea Level Change Supplementary Material. In: *Climate Change 2013: The Physical Science Basis. Contribution of Working Group I to the Fifth Assessment Report of the Intergovernmental Panel on Climate Change* [Stocker, T.F., D. Qin, G.-K. Plattner, M. Tignor, S.K. Allen, J. Boschung, A. Nauels, Y. Xia, V. Bex and P.M. Midgley (eds.)]. Available from www.climatechange2013.org and www.ipcc.ch.

Table of Contents

13.SM.1 Methods of Global Mean Sea Level Projections for the 21st Century

This section summarizes the methods used to produce the projections shown in Section 13.5.1 for the Representative Concentration Pathway (RCP) scenarios and the Special Report on Emission Scenarios (SRES) A1B scenario. The Supplementary Material includes files of the annual time series of median, 5th percentile and 95th percentile for each of the contributions to global mean sea level rise and the sum, corresponding to the results shown in Table 13.5. The data files are named as follows:

scenario _ quantity statistic . suffix

for instance *rcp45_summid.nc*. In each name,

scenario is **rcp26**, **rcp45**, **rcp60** or **rcp85**, corresponding to the four representative concentration pathways used in CMIP5, or **sresa1b** for SRES A1B used in CMIP3.

quantity is **temperature** for global mean surface temperature change, **expansion** for thermal expansion (sections 13.4.1 and 13.SM.1.2), **glacier** for glaciers (13.4.2 and 13.SM.1.3), **greensmb** for Greenland ice-sheet SMB (13.4.3.1 and 13.SM.1.4), **antsmb** for Antarctic ice-sheet SMB (13.4.4.1 and 13.SM.1.5), **greendyn** for Greenland ice-sheet rapid dynamical change (13.4.3.2 and 13.SM.1.6), **antdyn** for Antarctic ice-sheet rapid dynamical change (13.4.4.2 and 13.SM.1.6), **landwater** for anthropogenic intervention in water storage on land (13.4.5 and 13.SM.1.6), **greennet** for the sum of SMB and rapid dynamical contributions from the Greenland ice-sheet, **antnet** for the sum of SMB and rapid dynamical contributions from the Antarctic ice-sheet, **sheetdyn** for the sum of the rapid dynamical contributions from the Greenland and Antarctic ice-sheets, or **sum** for the sea level projection including all contributions. Except for temperature, these are the quantities shown in Table 13.5.

statistic is **mid** for the median, or **lower** or **upper** for the limits of the range.

suffix is **txt** for plain ASCII text, or **nc** for netCDF.

The text files have two columns, year and sea level change in metres. The netCDF files describe their contents using the CF convention.

13.SM.1.1 Derivation of Global Surface Temperature and Thermal Expansion Time Series from Coupled Model Intercomparison Project Phase 5

Annual time series for change in global mean surface air temperature (SAT) ('tas' in the CMIP5 archive) and global-mean sea level (GMSL) rise due to thermal expansion ('zostoga') in the historical period and during the 21st century under RCP scenarios (Section 13.4.1) were obtained from a set of 21 CMIP5 AOGCMs (ACCESS1-0, ACCESS1-3, CCSM4, CNRM-CM5, CSIRO-Mk3-6-0, CanESM2, GFDL-CM3, GFDL-ES-M2G, GFDL-ESM2M, HadGEM2-ES, IPSL-CM5A-LR, IPSL-CM5A-MR, MIROC-ESM, MIROC-ESM-CHEM, MIROC5, MPI-ESM-LR, MPI-ESM-MR, MRI-CGCM3, NorESM1-M, NorESM1-ME, inmcm4). These were all those for which thermal expansion was available, including from a parallel pre-industrial control experiment, which is required to remove the thermal expansion due to climate drift in deep-ocean temperatures (Gleckler et al., 2012). The drift was removed by subtracting a polynomial fit as a function of time to the control thermal expansion time series. Where CMIP5 results were not available for a particular Atmosphere–Ocean General Circulation Model (AOGCM) and scenario, they were estimated by the method of Good et al. (2011) and Good et al. (2013) using the response of that AOGCM to an instantaneous quadrupling of carbon dioxide (CO_2) concentration. The same method was used to estimate the CMIP5 projections for scenario SRES A1B. The method gives estimates of change in global mean surface air temperature and net radiative flux at the top of the atmosphere. The

Table 13.SM.1 | Median values and *likely* ranges for projections of global-mean sea level rise and its contributions in metres in 2100 relative to 1986–2005 for the four RCP scenarios and SRES A1B. See Section 13.5.1 concerning how the *likely* range is defined. Because some of the uncertainties in modelling the contributions are treated as uncorrelated, the sum of the lower bound of contributions does not equal the lower bound of the sum, and similarly for the upper bound. Because of imprecision from rounding, the sum of the medians of contributions may not exactly equal the median of the sum.

	SRES A1B	RCP2.6	RCP4.5	RCP6.0	RCP8.5
Thermal expansion	0.24 [0.18 to 0.30]	0.15 [0.11 to 0.20]	0.20 [0.15 to 0.25]	0.22 [0.17 to 0.27]	0.32 [0.25 to 0.39]
Glaciers	0.16 [0.09 to 0.23]	0.11 [0.05 to 0.17]	0.13 [0.07 to 0.20]	0.14 [0.07 to 0.20]	0.18 [0.10 to 0.26]
Greenland Ice Sheet SMB[a]	0.07 [0.03 to 0.15]	0.03 [0.01 to 0.08]	0.05 [0.02 to 0.11]	0.05 [0.02 to 0.12]	0.10 [0.04 to 0.22]
Antarctic Ice Sheet SMB[b]	–0.04 [–0.07 to –0.01]	–0.02 [–0.05 to –0.00]	–0.03 [–0.06 to –0.01]	–0.03 [–0.06 to –0.01]	–0.05 [–0.09 to –0.02]
Greenland Ice Sheet Rapid Dynamics	0.04 [0.01 to 0.06]	0.04 [0.01 to 0.06]	0.04 [0.01 to 0.06]	0.04 [0.01 to 0.06]	0.05 [0.02 to 0.09]
Antarctic Ice Sheet Rapid Dynamics	0.08 [–0.02 to 0.19]	0.08 [–0.02 to 0.19]	0.08 [–0.02 to 0.19]	0.08 [–0.02 to 0.19]	0.08 [–0.02 to 0.19]
Land Water Storage	0.05 [–0.01 to 0.11]	0.05 [–0.01 to 0.11]	0.05 [–0.01 to 0.11]	0.05 [–0.01 to 0.11]	0.05 [–0.01 to 0.11]
Sea Level Rise	0.60 [0.42 to 0.80]	0.44 [0.28 to 0.61]	0.53 [0.36 to 0.71]	0.55 [0.38 to 0.73]	0.74 [0.52 to 0.98]
Greenland Ice Sheet	0.11 [0.07 to 0.19]	0.08 [0.04 to 0.12]	0.09 [0.05 to 0.16]	0.09 [0.06 to 0.16]	0.15 [0.09 to 0.28]
Antarctic Ice Sheet	0.05 [–0.06 to 0.15]	0.06 [–0.04 to 0.16]	0.05 [–0.05 to 0.15]	0.05 [–0.05 to 0.15]	0.04 [–0.08 to 0.14]
Ice-Sheet Rapid Dynamics	0.12 [0.03 to 0.22]	0.12 [0.03 to 0.22]	0.12 [0.03 to 0.22]	0.12 [0.03 to 0.22]	0.14 [0.04 to 0.24]

Only the collapse of the marine-based sectors of the Antarctic Ice Sheet could cause GMSL to rise substantially above the *likely* range during the 21st century. This potential additional contribution cannot be precisely quantified but there is *medium confidence* that it would not exceed several tenths of a meter of sea level rise.

Notes:

[a] Including the height-SMB feedback.

[b] Including the interaction between SMB change and outflow.

latter was integrated in time to obtain the estimated change in heat content of the climate system, and converted to thermal expansion using the expansion efficiency of heat appropriate to each AOGCM, as diagnosed from all the available RCPs for that AOGCM. The correlation between heat content change and thermal expansion is very high and the relationship can be accurately treated as linear (Kuhlbrodt and Gregory, 2012).

13.SM.1.2 Interpretation and Combination of Uncertainties

Uncertainties were derived from the CMIP5 ensemble by treating the model spread as a normal distribution, and following Section 12.4.1.2 it was assumed that the 5 to 95% interval of CMIP5 projections for the 21st century for each RCP scenario can be interpreted as a *likely* range (Section 13.5.1). The CMIP5 timeseries of thermal expansion X and global mean surface air temperature T were expressed as anomalies as a function of time t with respect to their time-means for 1986-2005, and the timeseries of ensemble means $X_M(t)$ and $T_M(t)$ and ensemble standard deviations $X_S(t)$ and $T_S(t)$ were calculated. As in the AR4, a Monte Carlo was used to generate distributions of timeseries of X and T in a perfectly correlated way; for each member of the ensemble, a random number r was chosen from a normal distribution, giving $X(t) = X_M(t) + r\, X_S(t)$ and $T(t) = T_M(t) + r\, T_S(t)$, and $T(t)$ was used to estimate land ice contributions to GMSLR, as described in the following sections. As in the AR4, all the uncertainties described by the land ice methods were assumed to be independent of the climate change uncertainty represented by the variation of r and of one another, except where stated, and were combined by Monte Carlo. Because of the use of Monte Carlo, the results for GMSLR have a random uncertainty. For different random samples of the sizes used to compute the results in Table 13.5, the results vary by up to 0.01 m in GMSLR and its contributions, and 0.1 mm yr^{-1} in the rate of GMSLR. The projections are shown for 2081-2100 in Table 13.5, and for 2100 in Table 13.SM.1.

13.SM.1.3 Glaciers

Changes in glacier mass in all regions excluding Antarctica from 2006 onwards were projected using a parameterized scheme which was fitted separately to results from each of the global glacier models of Giesen and Oerlemans (2013), Marzeion et al. (2012), Radić et al. (2014) and Slangen and van de Wal (2011). For the model of Giesen and Oerlemans (2013), only the dependence on temperature was considered; the dependences on precipitation and atmospheric transmissivity were not included. All of these global glacier models have been used to make projections using output from several AOGCMs. Giesen and Oerlemans used results from CMIP3 AOGCMs for scenario SRES A1B, and the other authors used results from different sets of CMIP5 AOGCMs for RCPs. The RCP results of Slangen and van de Wal (2011) are not included in their published paper, but use the same glacier model as in the paper. The parameterized scheme enables estimates to be made for the glacier contribution to GMSL rise g_I as a function of time t for the consistent set of CMIP3 and CMIP5 AOGCMs across all RCPs and SRES A1B. The scheme gives $g_I(t)$ in millimetres with respect to 2006 as $fI(t)^p$, where $I(t)$ is the time integral of T from 2006 to time t in degrees Celsius year, and the constants f and p used for each glacier model are shown in Table 13.SM.2. The constants were fitted by linear regression of $\log(g)$ against $\log(I)$. The global glacier models on which this formula is based calculate their results from geographically dependent climate change with detailed treatments of glacier surface mass balance (SMB) and the evolution of hypsometry; their complexity cannot be accurately reproduced by a simple formula, and the spread of their results around the prediction of this formula has a coefficient of variation (standard deviation divided by mean) of 20% or less for decadal means for all glacier models and RCPs, except for the early decades of the 21st century under RCP2.6 for the model of Slangen and van de Wal (2011) for which there are fractional errors of up to 40%, but the absolute error is small. Therefore we take 20% of the projection of the formula made using the CMIP5 ensemble mean $I(t)$ as the standard deviation of a normally distributed methodological uncertainty in the glacier projection for each global glacier model. In order to incorporate this uncertainty into the projections, for each member of the Monte Carlo ensemble of glacier time-series, a normally distributed random number was chosen, independent of time, as a factor by which the time-dependent standard deviation should be multiplied, giving the uncertainty to be added to the glacier time-series. We give the four global glacier models equal weight in the projections. Because the time integration began in 2006, a constant 9.5 mm was added to the projections to account for the glacier contribution from 1996 (the centre of the reference period for projections) to 2005; this is the mean result from the model of Marzeion et al. (2012) using input from CMIP5 AOGCM historical experiments. The formula is not applicable beyond 2100 because it does not represent the tendency of global glacier mass to reach a new steady value when global climate stabilizes, although the global glacier models on which it is based can predict this as a consequence of the evolution of hypsometry. Glaciers on Antarctica were not included in the global glacier projections because they are included in the projections for the Antarctic ice sheet.

Table 13.SM.2 | Parameters for the fits to the global glacier models.

Global Glacier Model	f (mm °C^{-1} yr^{-1})	p (no unit)
Giesen and Oerlemans (2013)	3.02	0.733
Marzeion et al. (2012)	4.96	0.685
Radić et al. (2013)	5.45	0.676
Slangen and van de Wal (2011)	3.44	0.742

13.SM.1.4 Greenland Ice Sheet Surface Mass Balance

The change in Greenland ice sheet SMB $G_e(t)$, excluding changes in ice sheet topography, was computed from $T(t)$ using the cubic polynomial formula, Equation (2) of Fettweis et al., which predicts the Greenland SMB anomaly as a function of T, and was obtained by fitting results from an RCM using input from several CMIP5 AOGCMs for RCP4.5 and RCP8.5. Their Equation (2) $G_e = -71.5T - 20.4T^2 - 2.8T^3$ gives G_e in Gt yr^{-1}, which we convert to mm yr^{-1} SLE. In this formula, T is relative to the time mean of 1980–1999, rather than 1986–2005; in the CMIP5 AOGCM results, the former period is cooler by 0.15°C. The results of this formula were compared with those for the same AOGCMs and RCP from Equation (1) of Fettweis et al. (2013), which predicts $G(t)$ from summer (June to August) air temperature at 600 hPa over Greenland. Equation (1) reproduces the RCM results more accurately but cannot be used for the consistent set of CMIP5 AOGCMs and all RCPs because their required input data are not available. The results of Equation (2) were also compared with those for the same AOGCMs and RCPs with results obtained from the models of Gregory and Huybrechts (2006) and Yoshimori and Abe-Ouchi (2012), the former being the one used in the AR4. As a result of this comparison of projections (Section 13.4.3.1, Table 13.4), $G_e(t)$ was estimated as $FG_2(t)$, where $G_2(t)$ is calculated from T using Fettweis et al. Equation (2), and F is a factor representing methodological uncertainty. This factor is taken to have a log-normal distribution i.e. one of the form $F = e^N$, where N is a normal distribution having a mean of zero. A log-normal distribution is used because the distributions of $G_e(t)$ from the various Greenland ice sheet SMB models are positively skewed. None of these models simulates the change in SMB caused by the evolution of the ice sheet surface topography, which gives a positive feedback on mass loss (Section 13.4.3.2). To allow for this effect, the Greenland ice sheet SMB change $G(t)$ with respect to 1986–2005 was estimated as $EG_e(t)$, where E is a randomly varying factor with a uniform probability distribution in the range 1.00 to 1.15. The uncertainties of E and F were assumed not be correlated, and independent of time. The ice sheet SMB change $G(t)$ was integrated in time to obtain the change in ice sheet mass, starting in 2006. A constant 1.5 mm was added to the projections to account for the Greenland SMB contribution from 1996 (the centre of the reference period for projections) to 2005; this is half of the central observational estimate of the rate of Greenland ice sheet mass loss during this period (Section 13.3.3.2, using data presented in Figure 4.15).

13.SM.1.5 Antarctic Ice Sheet Surface Mass Balance

The change in Antarctic ice sheet SMB $A(t)$ with respect to 1986–2005 was assumed to be due solely to an increase in accumulation (thus, $A < 0$ in units of sea level equivalent, because accumulation on the ice sheet removes mass from the ocean), which was estimated using the results of Gregory and Huybrechts (2006) from CMIP3 AOGCMs. Accumulation was taken to increase at 5.1 ± 1.5% $°C^{-1}$ of warming in Antarctica relative to 1985–2005, the ratio of warming in Antarctic to T was taken to be 1.1 ± 0.2, and the accumulation for the reference period was taken to be 1923 Gt yr^{-1} (Section 13.3.3.2). Both of these uncertainties (standard deviations) were treated as normally distributed methodological uncertainties in the projections. The resulting spread of projections is very close to the spread of the results from the high-resolution Antarctic SMB models of Krinner et al. (2007), Bengtsson et al. (2011) and Ligtenberg et al. (2013) assessed in Section 13.4.4.1. The effect of increased accumulation on the dynamics of the Antarctic ice sheet (Section 13.4.4.2) was taken into account by adding a rate $-SA(t)$ (a positive number in units of sea level equivalent, because the increase in outflow opposes the increase in accumulation and adds mass to the ocean) to the GMSL projections, where S is a randomly varying factor with a uniform probability distribution in the range 0.00 to 0.35. The uncertainties in accumulation sensitivity, Antarctic warming ratio, and the factor S were assumed not to be correlated, but S was perfectly correlated with the distribution of Antarctic rapid ice sheet dynamics (next paragraph), in the sense that when the rapid dynamical increase in outflow is large, the increase in outflow due to the dynamical reaction to increased accumulation is also large. The mass balance changes A and $-SA$ were integrated in time to obtain the change in the ice sheet mass, starting from 2006. Unlike for Greenland ice sheet SMB, no addition to the projections was made to account for the period 1996–2005 for the contribution from Antarctic ice-sheet SMB, because changes during this period are judged to be due solely to dynamical change (Section 13.3.3.2).

13.SM.1.6 Rapid Ice Sheet Dynamics and Anthropogenic Change in Land Water Storage

Following Section 13.3.3.2, the contributions from rapid ice-sheet dynamics at the start of the projections were taken to be half of the observed rate of loss for 2005-2010 from Greenland (half of 0.46-0.80 mm yr^{-1} from Table 4.6) and all of that from Antarctica (0.21-0.61 mm yr^{-1} from Table 4.6). The contributions reach 0.020 to 0.085 m at 2100 from Greenland for RCP8.5, 0.014 to 0.063 m for the other RCPs and –0.020 to 0.185 m from Antarctica for all RCPs; these are the likely ranges from our assessment of existing studies (Sections 13.4.3.2 and 13.4.4.2). For each ice sheet, a quadratic function of time was fitted which begins at the minimal initial rate and reaches the minimum final amount, and another for the maxima. Time series for the rapid dynamic contribution lying between these extremes were constructed as combinations of the extreme time series assuming a uniform probability density between the extremes. Finally, a constant 1.5 mm was added to the contribution from the Greenland ice sheet, and 2.5 mm to the contribution from the Antarctic ice sheet, these being the estimates of those contributions from 1996 to 2005 (using the data presented in Figures 4.15 and 4.16).

The same method was followed for the anthropogenic land water storage contribution (initial rates as for 1993–2010 from Table 13.1 and amounts for the time-mean of 2081-2100 from Section 13.4.5, with no additional amount for land water storage from 1996 to 2005). These contributions are treated as uncorrelated with the magnitude of global climate change and as independent of scenario (except for the higher rate of change for Greenland ice sheet outflow under RCP8.5). This treatment does not imply that the contributions concerned will not depend on the scenario followed, only that the current state of knowledge does not permit a quantitative assessment of the dependence.

13.SM.2 Computation of Regional Maps of Sea Level Change from Coupled Model Intercomparison Project Phase 5 Model Output

Several results and figures in Section 13.6 are based on published methods as referred to in the main text but have not been published independently. This document details all information that led to numbers and figures shown in Section 13.6 on regional sea level projections. Data files for each figure are available.

For each figure or each step involved, the underlying technical details that were used are described. The Supplementary Material includes files containing the data in each case.

Figures 13.15, 13.16 and 13.24 show maps of regional sea level changes computed from CMIP5 coupled climate models. The following steps were pursued in the preparation of those figures.

13.SM.2.1 Sea Surface Height from Coupled Climate Models

Sea surface height (SSH) data, labeled the 'zos' variable, from the CMIP5 AOGCM database, are used to show regional changes in SSH over time, and include the regional variability of dynamic topography changes due to water mass advection, thermohaline circulation and to the wind-driven circulation (see Table 13.SM.3). These regional changes are corrected for regional control drift by removing the linearly fitted control run drift from each latitude–longitude grid box individually, on a per-model basis. After this correction, the global average of this regional SSH field (a function of x, y, t) is forced to be the global thermal expansion ('zostoga' variable) at each time step by first subtracting the globally averaged regional SSH field at each time step from each grid box, and then adding the global thermal expansion time series to each grid box (the same number at every grid box, for a given time). The global thermal expansion time series was also corrected for control drift by removing a quadratic fit to the control run's thermal expansion time series before being added to the regional SSH data. As not all models had multiple ensemble forced runs for the various RCP scenarios, only one run from each model (in each RCP scenario) was used to compute the multi-model ensemble means (i.e., the results for each individual model are only a single realization per scenario, as shown in Figure 13.24).

13.SM.2.2 Interpolation

All of the steps outlined above were performed on each model's own grid, with interpolation to a common 1° × 1° grid only being applied after statistical analyses, to each model's relative sea level changes, means and variances. The interpolation procedure involves applying a nearest-neighbour interpolation and a bilinear interpolation, with the nearest-neighbour interpolation chosen close to the coasts where the bilinear interpolation loses grid boxes.

13.SM.2.3 Masking

Some of the models, on their original grids, had detached marginal seas (e.g., the Mediterranean, Hudson Bay, Baltic Sea, etc.), and in most cases, the SSH in the marginal seas behaved differently than in the nearby ocean, with some models having significant numerical instability, and others undergoing a different SSH evolution in these seas. To remove large and obvious errors from the ensemble mean (and other ensemble statistics) and to treat all the models consistently, marginal seas were masked out from individual models, if they were detached from the adjacent ocean basin, on the common 1° × 1° grid. This results in a final ensemble mean product that consists of, for example, for the RCP4.5 run, a 21-model mean over most of the ocean, but has only as few as 12 ensemble members contributing to the mean for some marginal seas (9 is the lowest number of RCP4.5/8.5 members for which regional data are shown for ensemble statistics).

13.SM.2.4 Combining All Sea Level Rise Components

Figures 13.18, 13.19, 13.22 and 13.23 show projected sea level changes as they result after combining various different contributions to sea level change in addition to those available from CMIP5 models. The following steps were necessary to obtain those maps and figures.

Contributions to regional sea level change due to changes in other components of the climate system were added to the thermosteric/dynamic SSH from the AOGCMs. These components include surface mass balance and dynamic ice sheet contributions from Greenland and Antarctica, a glacier contribution, a land water storage contribution, glacial isostatic adjustment (GIA), and the inverse barometer effect (IBE). The projections of the various land ice contributions and the land water storage contribution are described elsewhere (Sections 13.4, 13.5.1 and 13.SM.1 in the Supplementary Material). These global estimates were turned into regional maps of sea level response, due to the addition of mass increasing the global ocean volume (the barystatic contribution) plus the resultant gravitational and rotational changes, through application of an iterative sea level equation solver (Slangen et al., 2012). The groundwater storage change contribution to regional sea level rise was also found similarly by taking estimates of its geographical distribution from Wada et al. (2012) and applying the same sea level equation solver. The GIA contribution was calculated from the mean of the ICE-5G model (Peltier 2004) and the ANU ice sheet model (Lambeck et al. 1998 and subsequent improvements) with the SELEN code for the sea level equation (Farrell and Clark 1976; Spada and Stocchi 2006, 2007), including updates to allow for coastline variation through time, near-field meltwater damping and Earth rotation in a self-consistent manner (Milne and Mitrovica, 1998; Kendall et al., 2006). The IBE contribution was found by using an ensemble of atmospheric results from the atmospheric component of the same CMIP5 models used for the SSH data. All of these components were calculated 'offline' (i.e., were not part of diagnostic 'zos' and 'zostoga' variables in the models) and then added to the regional sea level rise results previously derived from CMIP5 'zos' and 'zostoga' variables.

13.SM.2.5 Uncertainties

Figures 13.19, 13.21 and 13.23 show uncertainty measures for sea level projections. Those uncertainties were computed as follows.

The uncertainties in the results directly from the CMIP5 model data are estimated with the ensemble spread: one standard deviation of the members' means is treated as the standard error for the ensemble mean. This applies to the dynamic/thermosteric SSH ocean data, and the IBE atmospheric data. The ice sheet, glacier and land water storage uncertainties are found regionally from the global uncertainties of the sources using the same iterative sea level equation solver used to obtain the regional distribution from their means. The one standard error of the GIA uncertainty is evaluated as the departures of the two different GIA estimates (from ICE-5G and ANU/SELEN models) from their mean value. To combine these uncertainties, for both maps of uncertainty as well as time series of uncertainty at individual stations, it is assumed that contributions that correlate with global air temperature have correlated uncertainties, which are therefore added linearly. This combined uncertainty is then added to the other components' uncertainties in quadrature. The uncertainties in the projected ice sheet SMB changes were assumed to be dominated by the magnitude of climate change, rather than their methodological uncertainty, while the uncertainty in the projected glacier change was assumed to be dominated by its methodological uncertainty. The formula shown below for the regional error, when applied to the global contributions, estimates a global uncertainty close to that given in Table 13.5. The estimated squared uncertainty (standard error) at each grid box is found as follows:

$$\sigma^2_{tot} = (\sigma_{steric/dyn} + \sigma_{smb\_a} + \sigma_{smb\_g})^2 + \sigma^2_{glac} + \sigma^2_{IBE} + \sigma^2_{GIA} + \sigma^2_{LW} + \sigma^2_{dyn\_a} + \sigma^2_{dyn\_g} \tag{13.SM.1}$$

where:

steric/dyn = global thermal expansion uncertainty + dynamic SSH (ensemble spread)

smb_a = Antarctic ice sheet SMB uncertainty (including interaction of SMB and dynamics)

smb_g = Greenland ice sheet SMB uncertainty (including interaction of SMB and dynamics)

glac = Glacier uncertainty

IBE = inverse barometer effect uncertainty (ensemble spread)

GIA = glacial isostatic adjustment uncertainty

LW = land water storage uncertainty

dyn_a = Antarctica ice sheet rapid dynamics uncertainty

dyn_g = Greenland ice sheet rapid dynamics uncertainty

The 90% confidence limits for the ice components are asymmetric and were combined with the 90% confidence limit uncertainties of the CMIP5 ocean components to find the lower and upper uncertainty limits separately (Figures 13.19 and 13.23), using the given equation. In Figure 13.21, in which a single standard error at each location is used, the σ used in the equation were standard deviations for all components except *LW*, *dyn_a* and *dyn_g*; these latter had uniform PDFs in the global projections, and the half-range of the distribution was used for σ. To find the 90% confidence limits of the ocean components, regional uncertainties were multiplied by 1.645, thus treating them as methodological, normally distributed uncertainties.

Table 13.SM.3 | Availability of 'zos' variable from CMIP5.

Model	RCP2.6	RCP6.0	RCP4.5 / RCP8.5
ACCESS-1.0			X
BCC-CSM1.1	X	X	X
CanESM2			X
CNRM-CM5			X
CSIRO-MK3.6.0	X	X	X
GFDL-ESM2G	X	X	X
GFDL-ESM2M	X	X	X
GISS-E2-R	X	X	X
HadGEM2-CC			X
HadGEM2-ES	X		X
INM-CM4			X
IPSL-CM5A-LR	X	X	X
IPSL-CM5A-MR	X		X
MIROC5	X	X	X
MIROC-ESM	X	X	X
MIROC-ESM-CHEM	X	X	X
MPI-ESM-LR	X		X
MPI-ESM-MR	X		X
MRI-CGCM3	X	X	X
NorESM1-M	X	X	X
NorESM1-ME	X	X	X

References

Bengtsson, L., S. Koumoutsaris, and K. Hodges, 2011: Large-scale surface mass balance of ice sheets from a comprehensive atmosphere model. *Surv. Geophys.*, **32**, 459–474.

Farrell, W.E., and Clark, J.A., 1976. On postglacial sea-level, *Geophys. J. R. Astr. Soc.*, **46**, 647–667.

Fettweis, X., B. Franco, M. Tedesco, J. H. van Angelen, J. T. M. Lenaerts, M. R. van den Broeke, and H. Gallee, 2013: Estimating Greenland ice sheet surface mass balance contribution to future sea level rise using the regional atmospheric model MAR. *Cryosphere*, **7**, 469–489.

Giesen, R. H., and J. Oerlemans, 2013: Climate-model induced differences in the 21st century global and regional glacier contributions to sea-level rise. *Clim. Dyn*., **41**, 3283–3300.

Gleckler, P. J., et al., 2012: Human-induced global ocean warming on multidecadal timescales. *Nature Clim. Change*, **2**, 524–529.

Good, P., J. M. Gregory, and J. A. Lowe, 2011: A step-response simple climate model to reconstruct and interpret AOGCM projections. *Geophys. Res. Lett.*, **38**, L01703.

Good, P., J. M. Gregory, J. A. Lowe, and T. Andrews, 2013: Abrupt CO_2 experiments as tools for predicting and understanding CMIP5 representative concentration pathway projections. *Clim. Dyn.*, **40**, 1041–1053.

Gregory, J. M., and P. Huybrechts, 2006: Ice-sheet contributions to future sea-level change. *Philos. Trans. R. Soc. London A*, **364**, 1709–1731.

Kendall, R., Latychev, K., Mitrovica, J.X., Davis, J.E., and Tamisiea, M., 2006. Decontaminating tide gauge records for the influence of Glacial Isostatic Adjustment: the potential impact of 3-D Earth structure, *Geophys. Res. Lett.*, **33**, L24318, doi:10.1029/2006GL028448.

Krinner, G., O. Magand, I. Simmonds, C. Genthon, and J. L. Dufresne, 2007: Simulated Antarctic precipitation and surface mass balance at the end of the twentieth and twenty-first centuries. *Clim. Dyn.*, **28**, 215–230.

Kuhlbrodt, T., and J. M. Gregory, 2012: Ocean heat uptake and its consequences for the magnitude of sea level rise and climate change. *Geophys. Res. Lett.*, **39**, L18608.

Lambeck, K., C. Smither, and P. Johnston, 1998: Sea-level change, glacial rebound and mantle viscosity for northern Europe. *Geophys. J. Int.*, **134**, 102–144.

Ligtenberg, S. R. M., W. J. van de Berg, M. R. van den Broeke, J. G. L. Rae, and E. van Meijgaard, 2013: Future surface mass balance of the Antarctic ice sheet and its influence on sea level change, simulated by a regional atmospheric climate model. *Clim. Dyn.*, **41**, 867–884.

Marzeion, B., A. H. Jarosch, and M. Hofer, 2012: Past and future sea-level changes from the surface mass balance of glaciers. *Cryosphere*, **6**, 1295–1322.

Milne, G.A., and Mitrovica, J.X., 1998. Postglacial sea-level change on a rotating Earth, *Geophys. J. Int.*, **133**, 1–19.

Peltier, W. R., 2004: Global glacial isostasy and the surface of the ice-age earth: The ICE-5G (VM2) model and GRACE. *Annu. Rev. Earth Planet. Sci.*, **32**, 111–149.

Radić, V., A. Bliss, A. D. Beedlow, R. Hock, E. Miles, and J. G. Cogley, 2014: Regional and global projections of twenty-first century glacier mass changes in response to climate scenarios from global climate models. *Clim. Dyn.*, **42**, 37–58.

Slangen, A. B. A., and R. S. W. van de Wal, 2011: An assessment of uncertainties in using volume-area modelling for computing the twenty-first century glacier contribution to sea-level change. *Cryosphere*, **5**, 673–686.

Slangen, A. B. A., C. A. Katsman, R. S. W. van de Wal, L. L. A. Vermeersen, and R. E. M. Riva, 2012: Towards regional projections of twenty-first century sea-level change based on IPCC SRES scenarios. *Clim. Dyn.*, **38**, 1191–1209.

Spada, G., and Stocchi, P., 2006. The Sea Level Equation, Theory and Numerical Examples, Aracne, Roma, p. 96, ISBN: 88–548–0384–7.

Spada, G., and Stocchi, P., 2007. SELEN: a Fortran 90 program for solving the 'Sea Level Equation', *Comput. Geosci.*, **33**(4), 538–562, doi:10.1016/j.cageo.2006.08.006.

Wada, Y., L. P. H. van Beek, F. C. S. Weiland, B. F. Chao, Y. H. Wu, and M. F. P. Bierkens, 2012: Past and future contribution of global groundwater depletion to sea-level rise. *Geophys. Res. Lett.*, **39**, L09402.

Yoshimori, M., and A. Abe-Ouchi, 2012: Sources of spread in multi-model projections of the Greenland ice-sheet surface mass balance. *J. Clim.*, **25**, 1157–1175.

14SM

Climate Phenomena and their Relevance for Future Regional Climate Change

Supplementary Material

Coordinating Lead Authors:
Jens Hesselbjerg Christensen (Denmark), Krishna Kumar Kanikicharla (India)

Lead Authors:
Edvin Aldrian (Indonesia), Soon-Il An (Republic of Korea), Iracema Fonseca Albuquerque Cavalcanti (Brazil), Manuel de Castro (Spain), Wenjie Dong (China), Prashant Goswami (India), Alex Hall (USA), Joseph Katongo Kanyanga (Zambia), Akio Kitoh (Japan), James Kossin (USA), Ngar-Cheung Lau (USA), James Renwick (New Zealand), David B. Stephenson (UK), Shang-Ping Xie (USA), Tianjun Zhou (China)

Contributing Authors:
Libu Abraham (Qatar), Tércio Ambrizzi (Brazil), Bruce Anderson (USA), Osamu Arakawa (Japan), Raymond Arritt (USA), Mark Baldwin (UK), Mathew Barlow (USA), David Barriopedro (Spain), Michela Biasutti (USA), Sébastien Biner (Canada), David Bromwich (USA), Josephine Brown (Australia), Wenju Cai (Australia), Leila V. Carvalho (USA/Brazil), Ping Chang (USA), Xiaolong Chen (China), Jung Choi (Republic of Korea), Ole Bøssing Christensen (Denmark), Clara Deser (USA), Kerry Emanuel (USA), Hirokazu Endo (Japan), David B. Enfield (USA), Amato Evan (USA), Alessandra Giannini (USA), Nathan Gillett (Canada), Annamalai Hariharasubramanian (USA), Ping Huang (China), Julie Jones (UK), Ashok Karumuri (India), Jack Katzfey (Australia), Erik Kjellström (Sweden), Jeff Knight (UK), Thomas Knutson (USA), Ashwini Kulkarni (India), Koteswara Rao Kundeti (India), William K. Lau (USA), Geert Lenderink (Netherlands), Chris Lennard (South Africa), Lai-yung Ruby Leung (USA), Renping Lin (China), Teresa Losada (Spain), Neil C. Mackellar (South Africa), Victor Magaña (Mexico), Gareth Marshall (UK), Linda Mearns (USA), Gerald Meehl (USA), Claudio Menéndez (Argentina), Hiroyuki Murakami (USA/Japan), Mary Jo Nath (USA), J. David Neelin (USA), Geert Jan van Oldenborgh (Netherlands), Martin Olesen (Denmark), Jan Polcher (France), Yun Qian (USA), Suchanda Ray (India), Katharine Davis Reich (USA), Belén Rodriguez de Fonseca (Spain), Paolo Ruti (Italy), James Screen (UK), Jan Sedláček (Switzerland) Silvina Solman (Argentina), Martin Stendel (Denmark), Samantha Stevenson (USA), Izuru Takayabu (Japan), John Turner (UK), Caroline Ummenhofer (USA), Kevin Walsh (Australia), Bin Wang (USA), Chunzai Wang (USA), Ian Watterson (Australia), Matthew Widlansky (USA), Andrew Wittenberg (USA), Tim Woollings (UK), Sang-Wook Yeh (Republic of Korea), Chidong Zhang (USA), Lixia Zhang (China), Xiaotong Zheng (China), Liwei Zou (China)

Review Editors:
John Fyfe (Canada), Won-Tae Kwon (Republic of Korea), Kevin Trenberth (USA), David Wratt (New Zealand)

This chapter supplementary material should be cited as:
Christensen, J.H., K. Krishna Kumar, E. Aldrian, S.-I. An, I.F.A. Cavalcanti, M. de Castro, W. Dong, P. Goswami, A. Hall, J.K. Kanyanga, A. Kitoh, J. Kossin, N.-C. Lau, J. Renwick, D.B. Stephenson, S.-P. Xie and T. Zhou, 2013: Climate Phenomena and their Relevance for Future Regional Climate Change Supplementary Material. In: *Climate Change 2013: The Physical Science Basis. Contribution of Working Group I to the Fifth Assessment Report of the Intergovernmental Panel on Climate Change* [Stocker, T.F., D. Qin, G.-K. Plattner, M. Tignor, S.K. Allen, J. Boschung, A. Nauels, Y. Xia, V. Bex and P.M. Midgley (eds.)]. Available from www.climatechange2013.org and www.ipcc.ch.

Table of Contents

14.SM.1 Monsoon Systems

14.SM.1.1 Global Overview

Monsoons are seasonal phenomena and are responsible for the majority of summer rainfall within the tropics. In the classical view, the monsoon is driven by the seasonal cycle of solar heating and difference in thermal inertia of land and ocean that establish a land–sea temperature difference. This contrast, with the land being warmer than the surrounding ocean in late spring and summer, gives favourable conditions for the occurrence of convection in the summer hemisphere, allowing the monsoon to be viewed as a seasonal migration of the Inter-Tropical Convergence Zone (ITCZ). As the monsoon season matures, latent heat released by convection high above the land surface helps to pull in additional moisture from nearby oceans over the land, maintaining the wet season. This thermal forcing depends on large-scale orography and controls the regional monsoon domain and intensity. The land–sea temperature difference is projected to become larger in the summer season as seen from larger warming over land than ocean (Section 12.4.3.1 and Annex I Figures AI.4 to AI.5). However, this does not lead to a generally stronger monsoon circulations in the future, as changes in regional monsoon characteristics are rather complex. In broad terms, the precipitation characteristics over Asia-Australia, Americas and Africa can be viewed as an integrated global monsoon system, associated with a global-scale persistent atmospheric overturning circulation (Trenberth et al., 2000). Wang and Ding (2008) demonstrated that the global monsoon is the dominant mode of annual variation of the tropical circulation, characterizing the seasonality of the Earth's climate in tropical latitudes. The monsoon-affected region is, however, not uniform in the historical record (Conroy and Overpeck, 2011), and it could vary in the future.

14.SM.1.2 Definition of Global Monsoon Area, Global Monsoon Total Precipitation and Global Monsoon Precipitation Intensity

The global monsoon area (GMA) is defined as where the annual range of precipitation exceeds 2.5 mm day^{-1}. Here, the annual range is defined as the difference between the May to September (MJJAS) mean and the November to March (NDJFM) mean. The global monsoon total precipitation (GMP) is defined as the mean of summer rainfall in the monsoon area. The global monsoon precipitation intensity (GMI) is defined as GMP divided by GMA.

14.SM.1.3 Definition of Monsoon Onset, Retreat and Duration

Monsoon onset date, retreat date and its duration are determined using the criteria proposed by Wang and LinHo (2002) utilizing only precipitation data. Based on the regionally averaged relative climatological mean daily precipitation, which is the difference between the climatological daily precipitation and dry month (January in the Northern Hemisphere and July in the Southern Hemisphere) mean precipitation, the onset (retreat) date is defined as the date when the relative precipitation first exceeds (last drops below) 5 mm day^{-1}, and the duration is defined as their difference. The daily climatology of precipitation was defined as the sum of the first 12 harmonics of daily average precipitation.

14.SM.1.3.1 South America Monsoon System

Although the changes in wind direction from winter to summer occur only in a small area within South America, there are large differences in the atmospheric circulation and in sources of humidity from winter to summer. These differences are related to the rainy season in central and southeastern Brazil, which begins at the middle/end of spring and finishes at the middle/end of autumn (Silva and Carvalho, 2007; Raia and Cavalcanti, 2008).

The lifecycle of the South America Monsoon System (SAMS) is discussed in Raia and Cavalcanti (2008), where the main atmospheric characteristics in the onset and demise are related to the rainy season. The changes in humidity flux linked to the low-level flow changes over the northernmost part of South America and the Amazonia region, eastward shifting of subtropical high, strong northwesterly moisture flux east of tropical Andes, are the main features in the onset. At high levels, the Bolivian High and the Northeast High Level Cyclonic Vortex are established during this period. The moisture flux from the Atlantic Ocean over northern South America, crossing the Amazonia region and directed to the southeast, increases the humidity over southeastern Brazil, favouring the intensification of convection there. The resulting coupling between Amazonia convection and frontal systems, and the favourable high-level anomalous circulation over the continent, often associated with the Pacific–South American (PSA) wave train, originate the South Atlantic Convergence Zone (SACZ). The whole cycle of SAMS comprises three stages, the rainfall beginning over northwestern South America, SACZ establishment and precipitation increase over the mouth of Amazon River (Nieto-Ferreira and Rickenbach, 2010).

In a recent review of SAMS, the main structure and lifecycle; the onset features; and the diurnal, mesoscale, synoptic, intraseasonal, interannual and inter-decadal variability are discussed, as well as the long-term variability and climate change (Marengo et al., 2010).

Jones and Carvalho (2013) used the Large–scale Index for South America Monsoon LISAM index (Silva and Carvalho, 2007), which is obtained from the combined Empirical Orthogonal Function (EOF) analysis of low-level (850 hPa) zonal and meridional winds, temperature and specific humidity.

Seasonal precipitation variability over South America is well represented by Atmospheric General Circulation Models (AGCMs) and Coupled General Circulation Models (CGCMs), mainly the large differences between summer and winter. However, the intensity or configuration of rainfall patterns in the summer season is not well represented by some models. Vera et al. (2006), and Vera and Silvestri (2009) analysed seven models of World Climate Research Programme–Coupled Model Intercomparison Project Phase 3 (WCRP–CMIP3) for the 20th century and showed that seasonal precipitation differences are well represented. Some models capture the precipitation variability, indicated by the standard deviation, and maximum rainfall associated with the SACZ, in the first three months (January, February and March (JFM)) and the last three months (October, November and December (OND)), but with different intensities compared to the observations. The ensemble mean precipitation analysis of nine models WRCP-CMIP3, also for the 20th century, by Seth et al. (2010), indicated reasonable comparisons of

SON and DJF with observations, although specific features as the ITCZ intensity and position, and extension of SACZ to the ocean, were not properly represented.

Other comparisons of IPCC CMIP3 models with observed precipitation, in Bombardi and Carvalho (2009), show that some models capture the main features of SAMS, as the NW–SE band from Amazonia to the southeast, representing SACZ occurrences, and the Atlantic ITCZ. However, intensities and positions of maximum precipitation are not well represented. The annual cycle in small areas of South America is not well represented by the majority of models, but has good representation in southern Amazon and central Brazil. The duration of the rainy season is overestimated over west South America and underestimated over central Brazil, in CMIP3 models (Bombardi and Carvalho, 2009). Some aspects of the humidity flux over South America are well represented by a set of CMIP3 models (Gulizia et al., 2013).

The South Indian, Pacific and Atlantic Oceans have a role on SAMS variability (Drumond and Ambrizzi, 2005; Grimm et al., 2007); therefore it is expected that projected changes in sea surface temperature (SST) patterns may affect this variability.

Changes in the annual cycle of the SAMS, from the 20th to the end of 21st century, projected by nine models, considering the A2 scenario were presented by Seth et al. (2010). The ensemble shows increased precipitation over SESA region (southern sector of southeastern South America).

Some CMIP3 models project precipitation increase in austral summer and a decrease in austral spring in the SAMS region (Seth et al., 2011). Precipitation increase at the end of the monsoon cycle and reduced precipitation in the onset in central monsoon region could indicate a shifting in the lifecycle monsoon period. These changes were related to less moisture convergence in the austral spring and more convergence during summer. During the dry season, the changes are very small. The warmer troposphere and increased stability due to global warming (Chou and Chen, 2010) act as a remote mechanism to reduced precipitation of SAMS in the winter. During summer, the local mechanisms, such as increased evaporation and decreased stability, contribute to the increased precipitation. Both mechanisms seem to reduce precipitation during spring, when there is not enough soil moisture and still atmospheric stability.

Idealized experiments with a coupled atmospheric–ocean model subjected to increasing carbon dioxide (CO_2) show intensification of the precipitation difference between summer and winter in the global monsoon regions, including the SAMS region (Cherchi et al., 2011).

14.SM.1.4 What Is a Stronger East Asian Summer Monsoon?

Unlike the Indian summer monsoon, which can be defined in terms of simple scalar indices partly due to its homogeneity in rainfall distribution, it is more complicated to define an index for the East Asian Summer Monsoon (EASM; Zhou et al., 2009b). Wang et al. (2008) discussed the meanings of 25 existing EASM indices and classify these indices into five categories: the east–west thermal contrast, north–south thermal contrast, the shear vorticity of zonal winds, the southwesterly monsoon and the South China Sea monsoon. Although the existing indices highlight different aspects of the EASM, they agree well in the traditional Chinese meaning of a strong EASM, viz. an abnormal northward extension of the southerlies into North China. The associated precipitation anomaly appears as excessive rainfall in North China along with a deficient Meiyu in the Yangtze River Valley (see Figure 3 of Zhou et al., 2009b for patterns of precipitation over eastern China associated with stronger and weaker monsoon circulations).

14.SM.1.5 Present Understanding of the Weakening Tendency of East Asian Summer Monsoon Circulation Since the End of the 1970s

From 1950 to present, the EASM circulation has experienced an inter-decadal scale weakening after the 1970s (Figure 14.SM.1), resulting in deficient rainfall in North China but excessive rainfall in central East China along 30°N (Hu, 1997; Wang, 2001; Gong and Ho, 2002; Yu et al., 2004). The weakening of EASM is associated with weakening of 850 hPa southwesterly wind (Xu et al., 2006), a tropospheric cooling over East Asia (Yu and Zhou, 2007; Zhou and Zhang, 2009), a westward extension of the western Pacific Subtropical High (Zhou et al., 2009a), a zonal expansion of South Asian High (Gong and Ho, 2002; Zhou et al., 2009a) and an enhanced subtropical westerly jet (Zhang et al., 2006; Yu and Zhou, 2007). The circulation changes have led to significant changes in mean and extreme precipitation (Zhai et al., 2005), frequency and intensity of rainfall events (Qian et al., 2009; Yu et al., 2010c; Bennartz et al., 2011; Li et al., 2011a; Liu et al., 2011; Guo et al., 2013).

The weakening of the EASM circulation since the 1970s is dominated by natural decadal variability (Lei et al., 2011; Zhu et al., 2012). The combination of tropical ocean warming associated with the phase transition of Pacific Decadal Oscillation (PDO; see Figure 14.SM.1 for the EASM circulation response to PDO-related SST forcing in AGCM experiments, Zhou et al., 2008; Li et al., 2010c; Zhou and Zou, 2010) and weakening of atmospheric heating over the Tibetan Plateau leads to a reduction of land–sea thermal contrast, and thereby a weakened monsoon circulation (Ding et al., 2008, 2009; Duan and Wu, 2008). The weakening of the Tibetan Plateau heating is caused by increased snow cover and depth in winter associated with North Atlantic Oscillation (NAO) phase change and North Indian Ocean warming (Zhang et al., 2004; Ding and Wang, 2009). The specified aerosol forcing cannot reproduce the observed EASM circulation changes (Figure 14.SM.1).

14.SM.1.6 Details of Precipitation Changes over East China Associated with the Weakening Tendency of East Asian Summer monsoon Circulation Since the End of the 1970s

Precipitation changes due to the weakening tendency of the EASM circulation are evident in both mean and extreme precipitation (Zhai et al., 2005). Analysis based on daily data shows that both the frequency and amount of light rain have decreased in eastern China during 1956–2005, with high spatial coherency, attributable in part to the warm rain suppression by aerosols (Qian et al., 2009; Liu et al., 2011; McKee et al., 2011). The results of early studies based on daily precipitation data have been argued by recent studies based on hourly data. Recent

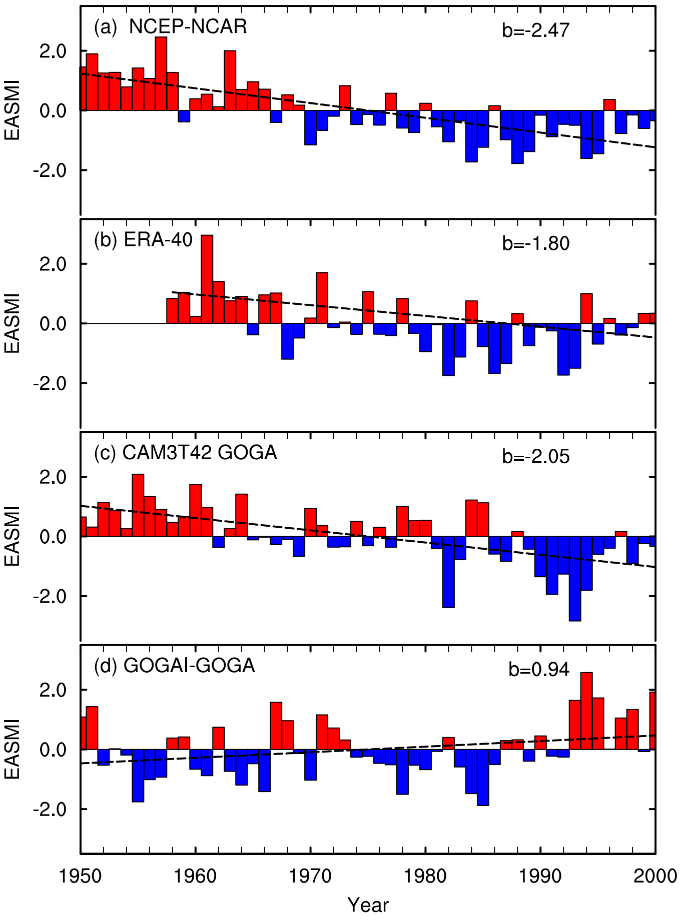

Figure 14.SM.1 | Time series of East Asian Summer Monsoon (EASM) indices (bars) and their trend lines (dashed line) from National Centers for Environmental Prediction/National Center for Atmospheric Research (NCEP/NCAR) reanalysis, (b) European Centre for Medium range Weather Forecast (ECMWF) 40-year reanalysis of the global atmosphere and surface conditions (ERA-40 reanalysis, (c) Global Ocean Global Atmosphere (GOGA) run of Community Atmosphere Model version 3 (CAM3), (d) difference between GOGAI and GOGA run of CAM3. Also shown is the slope of the trend (b, change per 50 years). The EASM index is defined as the normalized zonal wind shear between 850 and 200 hPa averaged over 20°N to 40°N and 110°E to 140°E. GOGA run is forced by observed monthly SSTs over the global oceans from 1950 to 2000, while GOGAI is driven by global sea surface temperature (SST) plus IPCC 20th century atmospheric (primarily greenhouse gases and direct aerosol) forcings (Li et al., 2010b). This figure demonstrated that the weakening tendency of EASM circulation was driven by Pacific Decadal Oscillation (PDO).

analysis of hourly data finds that the rainfall amount and frequency have significantly increased (decreased) but the rainfall intensity has decreased (increased) in the middle to lower reaches of the Yangtze River valley (North China).The "wetter South-drier North" pattern of mean precipitation is mostly attributed to moderate and low intensity rainfall (≤10 mm hr^{-1}) rather than the extreme rainfall (≥20 mm/hour, Yu et al., 2010c), although the frequency of extreme rain events has substantially increased along the Yangtze River (Qian et al., 2007a, 2007b). The drier North China is dominated by decreased long duration (persist longer than 6 hours) rainfall events, especially those occurring between midnight and morning, while the wetter South China is associated with both the substantially increased frequency and amount of long duration precipitation (Li et al., 2011a).

14.SM.1.7 Uncertainties in the Aerosol Effects on the Observed East Asian Summer Monsoon Changes

The aerosol effect on EASM circulation and precipitation changes during the past 60 years has large uncertainties. The combined effect of BC and sulphate aerosols is hypothesized to produce a weakened EASM but enhanced precipitation over South China (Liu et al., 2009a). Sulphate aerosol may reduce the surface heating over land and diminish land–sea thermal contrast). The increases of both sulphate and black carbon aerosol since 1950 may have weakened the land-sea temperature contrast and curtailed the monsoon in East Asia by acting to reduce September's rainfall (Guo et al., 2013). However, some aerosols (e.g., sulphate) could cool the atmosphere and surface but some (e.g., EC and dust) could cool the surface and warm the atmosphere. So the aerosol forcing impacts on land-ocean temperature contrast and hence EASM circulation is not well known yet. GCM experiments have shown that increased aerosol optical depth in China causes a noticeable increase in precipitation in the southern part of China in July, through induced surface cooling in mid-latitude leading to strengthening of the Hadley circulation (Gu et al., 2006). However, the inclusion of black carbon in the simulations does not necessarily produce the observed "north drought/south flood" precipitation pattern in China during the past 50 years (Wang and Zhou, 2005).Sulphate aerosols have been shown to affect rainfall redistribution over East Asia in late spring and early summer, and weaken monsoon rainfall through direct (Kim et al., 2007; Liu et al., 2009b) or semi-direct (Zhang et al., 2009) effects. However, these results do not explain the observations of the north/dry and south/wet pattern in East Asia in recent decades. Some GCM experiments showed that the aerosol forcing may not be a forcing mechanism for the weakening tendency of EASM circulation and precipitation (Li et al., 2007, 2010c).

14.SM.1.8 The Dynamics of the North American Monsoon System

Seasonal mean precipitation in the North American monsoon region (mainly Mexico and the extreme Southwestern USA) is generally controlled by the establishment of a continental-scale upper-level anticyclone and a lower-level thermal low (Higgins et al., 1997; Vera et al., 2006), it is also under the influence of factors operating at multiple spatial and temporal scales, including propagating waves and troughs in the tropics, synoptic disturbances and fronts entering the domain from the mid-latitudes and land-falling tropical cyclones (Douglas and Englehart, 2007). It is fed by two distinct, relatively narrow low-level moisture sources—the Great Plains Low-level Jet (LLJ) to the east of the Sierra Madres, which is approximately 200 to 400 km in width, and the narrower Gulf of California LLJ to the west of the Sierra Madres, which is approximately 100 km in width. Further, the large-scale circulation features—including the upper-tropospheric monsoon ridge, the North Atlantic subtropical (or Bermuda) high, the ITCZ, and the subtropical jet stream—in which these phenomena develop are modified by slowly evolving coupled climate features associated with the PDO, the Atlantic Multi-decadal Oscillation (AMO) and solar activity (van Loon et al., 2004; Feng and Hu, 2008; Seager et al., 2009; Metcalfe et al., 2010; Arias et al., 2012). Dust aerosol may also have an impact on the North American monsoonal precipitation (Zhao et al., 2012).

14.SM.2 El Niño-Southern Oscillation and Its Flavours

The El Niño-Southern Oscillation (ENSO) is a coupled ocean–atmosphere phenomenon naturally occurring at the interannual time scale. El Niño involves anomalous warming of tropical eastern-to-central Pacific SST usually peaking at the end of the calendar year, which leads to a weakening of zonal SST contrast between the tropical western Pacific 'warm pool' and the tropical eastern Pacific 'cold tongue' (Figure 14.12). It is closely linked to its atmospheric counterpart, the Southern Oscillation, which is a surface pressure seesaw between Darwin and Tahiti or more comprehensively the equatorial zonal-overturning called the 'Walker Circulation'. El Niño and Southern Oscillation are two different aspects of ENSO and are caused by a positive feedback between the atmosphere and the tropical Pacific Ocean referred to as Bjerknes feedback (Bjerknes, 1966, 1969). The opposite phase to El Niño, when the eastern equatorial Pacific cools, has been named La Niña.

Beyond the classical view of the El Niño pattern, another structure of anomalous warm SST, that is, the warming in the equatorial central Pacific (CP) sandwiched by anomalous cooling to the east and west (hereafter referred to as CP El Niño; other names are listed in Table 14.SM.3; Trenberth and Tepaniak, 2001; Larkin and Harrison, 2005), has been frequently observed in the tropical Pacific since the 1990s (Ashok et al., 2007; Kao and Yu, 2009; Kug et al., 2009; see also Section 2.7.8; Table 14.SM.3; Yeh et al., 2009). CP El Niño shows no basin-wide features or distinct propagation of SST anomalies and it occurs rather episodically in comparison with the conventional El Niño (Yu et al., 2010b). Many indices of CP El Niño have been proposed, but no clear and agreed definition has yet emerged to identify both CP El Niño and conventional El Niño (see Table 14.SM.3). Furthermore, several studies using other classification methods do not find such a distinction between CP and 'conventional' El Niño events (Newman et al., 2011; Lian and Chen, 2012), seeing changes in the location of El Niño from the western to the eastern Pacific as part of a continuous random distribution (Giese and Ray, 2011). Hence, CP El Niño and conventional El Niño may not be different phenomena but rather a nonlinear evolution of the ENSO phenomenon (Takahashi et al., 2011). A debate remains as to whether the CP El Niño is intrinsically different from the conventional El Niño or if every event is a varying mix of these two patterns.

The global impacts of CP El Niño are different from those of the conventional El Niño (Ashok et al., 2007; Kao and Yu, 2009; Hu et al., 2012), including monsoonal rainfall over India (Kumar et al., 2006), China, Korea (Feng et al., 2010; Feng and Li, 2011; Kim et al., 2012) and over Australia (Ashok et al., 2007; Wang and Hendon, 2007; Taschetto and England, 2009; Taschetto et al., 2009), USA air temperature and rainfall (Mo, 2010), winter temperature over the North Atlantic and Eurasian regions (Graf and Zanchettin, 2012), typhoon activity in the western North Pacific (Guanghua and Chi-Yung, 2010; Hong et al., 2011; Kim et al., 2011) and the warming in West Antarctica (Lee et al., 2010b; Ding et al., 2011). The influence of CP El Niño on Atlantic hurricanes may also be different from the conventional El Niño (Kim et al., 2009), but it has been shown that the anomalous atmospheric circulation in the hurricane main development region during CP El Niño is similar to that during conventional El Niño (Lee et al., 2010a).

Changes in the impacts from conventional El Niño to CP El Niño are possibly due to the change in the location of tropical atmospheric heating source (Hoerling et al., 1997; Kug et al., 2010a). For example, conventional El Niño leads to the Pacific North American (PNA)-like atmospheric pattern along with changes in the Aleutian low strength (Müller and Roeckner, 2008), while CP El Niño is more linked to the atmospheric variability over the North Pacific such as the North Pacific Oscillation (NPO), which represents a meridional shift of the Aleutian low pressure centre (Di Lorenzo et al., 2010).

Some studies argue that more frequent occurrence of CP El Niño events during recent decades is related to the changes in the tropical Pacific mean state in response to increased greenhouse gas (GHG) forcing (Yeh et al., 2009). In particular, a flattening of thermocline depth in the equatorial Pacific and a weakened Walker Circulation under global warming modulate the relative importance of feedback processes associated with El Niño dynamics (Yeh et al., 2009). A heat budget analysis in the ocean mixed layer reveals that zonal advection is a major dynamical feedback process in developing of CP El Niño and the anomalous surface heat flux in the decaying of CP El Niño (Kug et al., 2010b; Yu et al., 2010b). On the other hand, other studies (Lee and McPhaden, 2010; McPhaden et al., 2011) further showed that the future climate condition change associated with the increased occurrence of CP El Niño is not consistent with the observed climate condition that leads to more frequent occurrence of CP El Niño. Thus, whether the mean climate state change leads to more frequent emergence of CP El Niño or the other way around is not yet known. The increase in the frequency of CP El Niño during recent decades may be a manifestation of natural climate variability (Na et al., 2011; Yeh et al., 2011).

14.SM.3 Annular and Dipolar Modes

14.SM.3.1 Southern Annular Mode

The Southern Annular Mode (SAM, also known as Antarctic Oscillation (AAO)), is the leading mode of climate variability in the Southern Hemisphere extratropics, comprising co-varying sea level pressure or geopotential height anomalies of opposite sign in middle and high latitudes, extending through the depth of the troposphere, which are related to fluctuations in the latitudinal position and strength of the mid-latitude jet. When pressures/heights are below (or above) average over Antarctica the SAM is defined as being in its positive (or negative) phase and the circumpolar westerly winds are stronger (or weaker) than average. Associated with this, the storm tracks move poleward during the positive SAM and equatorward during the negative SAM. Although broadly annular in nature, hence its name, the spatial pattern of the SAM includes a substantial non-annular component in the Pacific sector (Figure 14.27, Kidston et al., 2009; Fogt et al., 2012). SAM variability has a major influence on the climate of Antarctica, Australasia, southern South America and South Africa (Watterson, 2009; Thompson et al., 2011 and references therein).

The SAM exhibits marked seasonal variability in both its structure and in its effects on regional climate. For example, correlations between the SAM and temperature at some Antarctic Peninsula stations change sign between seasons (Marshall, 2007) while the effect of the SAM on temperature and rainfall over New Zealand (Kidston et al., 2009) and on regional Australian rainfall (Hendon et al., 2007) changes markedly through the year. Moreover, nonlinearities in the structure of the positive and negative polarities of the SAM result in polarity-specific changes in surface climate impacts (Fogt et al., 2012).

Silvestri and Vera (2009) discussed decadal variability in the effects of the SAM on regional climate, emphasising broad-scale changes in the sign of precipitation relationships over southern South America and temperature relationships over Australia during 1958–1979 and 1983–2004. Marshall et al. (2011) examined a regional change in the sign of a SAM–temperature relationship in part of East Antarctica and demonstrated that changes in the phase and magnitude of the zonal wave-number 3 pattern, superimposed upon the annular structure of the SAM, were responsible for the reversal. Using ice core data they also showed that such changes occurred throughout the 20th century and hence were likely to reflect internal natural variability rather than an anthropogenic forcing. Such changes in coastal Antarctica will impact the role of the SAM in driving the formation of Antarctic Bottom Water, a central component of the global thermohaline circulation (McKee et al., 2011). Others have shown that the impact of the SAM on Antarctic climate also depends on how it interacts with other modes of circulation variability, such as those related to ENSO (e.g., Fogt and Bromwich, 2006).

The physical mechanisms of the SAM are generally well understood, and the SAM is well represented in many climate models, although the detailed spatial and temporal characteristics vary between models (Raphael and Holland, 2006). In the past few decades the SAM index has exhibited a positive trend in austral summer and autumn (Marshall, 2007; Figure 14.6.1; e.g., Jones et al., 2009), a change attributed primarily to the effects of ozone depletion and, to a lesser extent, the increase in GHGs (Thompson et al., 2011, see also Section 10.3.3.5), thus demonstrating that ozone depletion has had a direct effect on surface climate in the Southern Hemisphere, through its influence on the SAM trend. It is likely that these two factors will continue to be the principal drivers into the future, but as the ozone hole recovers they will be competing to push the SAM in opposite directions (Arblaster et al., 2011; Thompson et al., 2011; Bracegirdle et al., 2013), at least during late austral spring and summer, when ozone depletion has had its greatest impact on the SAM. The SAM is also influenced by teleconnections to the tropics, primarily associated with ENSO (Carvalho et al., 2005; L'Heureux and Thompson, 2006). Changes to the tropical circulation, and to such teleconnections, as the climate warms could further affect SAM variability (Karpechko et al., 2010).

14.SM.4 Large-scale Storm Systems

14.SM.4.1 Tropical Cyclones

14.SM.4.1.1 Regional Detection of Past Changes

Annual mean global tropical cyclone frequency since 1980 (within the modern geostationary satellite era) has remained roughly steady at about 90 per year, with a standard deviation of about 10% (9 storms), consistent with the expectations of a Poisson process. Standard deviations of annual frequency in individual ocean basins, however, can be greater than 40% of the means in those basins, which reduces the signal-to-noise ratio and introduces substantial uncertainty into regional tropical cyclone frequency trend detection.

Detection of past trends in various measures of tropical cyclone activity is constrained by the quality of the historical data records and uncertain quantification of natural variability in these measures (Knutson et al., 2010; Lee et al., 2012; Seneviratne et al., 2012; see also Chapters 2 and 10). Consideration of global trends as well as trends in specific regions is further complicated by substantial regional differences in data quality, collection protocols and record length (Knapp and Kruk, 2010; Song et al., 2010). Attempts to detect trends in even smaller intra-basin regions such as those defined by islands or archipelagos are further constrained by the reduced data sample size associated with finely subdividing the global data. Intra-basin regional trend detection is also substantially challenged by variability in tropical cyclone tracks (Kossin and Camargo, 2009).

This variability is driven largely by random fluctuations in atmospheric steering currents, but also is observed across a broad range of time scales in response to more systematic modes of climate variability such as the ENSO, PDO, NAO, Atlantic Meridional Mode (AMM), NPO, and Madden–Julian Oscillation (MJO; Ho et al., 2004; Wu et al., 2005; Camargo et al., 2007, 2008; Kossin and Vimont, 2007; Wang et al., 2007; Chand and Walsh, 2009; Tu et al., 2009; Kossin et al., 2010; Wang et al., 2010; Chu et al., 2012), and potentially in response to global warming (Wang et al., 2011). Even modest tropical cyclone track variability can lead to large differences in associated impacts at a specific location. For example, a particular group of islands can be affected by multiple tropical cyclones in one season (e.g., the Philippines in 2009) and then remain largely unaffected for multiple subsequent years even while the total number of storms in the larger, but immediate surrounding region exhibits normal variability. This type of "temporal clustering" can occur randomly or via systematic modulation by climate variability, and can also strongly affect the impact of tropical cyclones on ecosystems such as coral reefs (Mumby et al., 2011). The combination of data issues (quality and sample size), signal-to-noise issues and the natural variability of tropical cyclone tracks introduce substantial uncertainties into detection-attribution studies as well as disaster and mitigation planning aimed at specific intra-basin regions. Furthermore, while theoretical arguments have been put forward linking tropical cyclone intensity and genesis with anthropogenic climate change (Emanuel, 1987; Rappin et al., 2010), there is little theoretical guidance available to help elucidate the relationships between climate and tropical cyclone track variability.

Regional analyses of century-scale variability and trends of various measures of tropical cyclone activity provide mixed results from which robust conclusions are difficult to establish (also see Chapter 2). Regional trends in tropical cyclone frequency have been identified in the North Atlantic, with storm frequency increasing sharply over the past 20 to 30 years. Over longer time periods, especially since the late 19th Century, the fidelity of the reported trends is debated (Holland and Webster, 2007; Landsea, 2007; Mann et al., 2007b). Different methods for estimating undercounts in the earlier part of the North Atlantic tropical cyclone record provide mixed conclusions (Chang and

Guo, 2007; Mann et al., 2007a; Kunkel and coauthors, 2008; Vecchi and Knutson, 2008, 2011). Trends in cyclone frequency have also been identified over the past 50 to 60 years in the North Indian Ocean and may be due to changes in the strength of the tropical easterly jet (Rao et al., 2008; Krishna, 2009) but again uncertainties in the regional tropical cyclone data quality substantially limit reliability, particularly when attempting to detect Century-scale trends (Mohapatra et al., 2011). Furthermore, metrics based solely on storm frequency can be strongly influenced by weak and/or short-lived storms (Landsea et al., 2010), which are arguably of much lesser physical relevance than stronger and/or longer-lived storms. This limits the usefulness of such metrics that do not take storm intensity or duration into account.

Regional trends in the frequency of very intense tropical cyclones can be identified in the historical data over the past 30 to 40 years (Webster et al., 2005), although confidence in the amplitude of these trends is compromised by data homogeneity uncertainties (Landsea et al., 2006; Kossin et al., 2007). There has been a sharp increase in annual tropical cyclone power dissipation (which represents an amalgamation of frequency, intensity and storm duration) in the Atlantic since 1970 (Emanuel, 2005; Kossin et al., 2007), but longer-term trends are more uncertain because of data heterogeneities, particularly in the records of storm intensity (Hagen and Landsea, 2012; Hagen et al., 2012; Landsea et al., 2012). Upward regional and global trends in the intensity of the strongest storms have been identified in a more homogeneous data record by Elsner et al. (2008), but their analysis was necessarily limited to the modern geostationary satellite period and spans only about 30 years. Consistently positive trends in the duration of the active part of the Atlantic hurricane season over the period 1851–2007 have been identified, but confidence in these trends remains low due to a combination of marginal statistical significance (*p*-values near or below 0.9), and the potential for data heterogeneity to artificially amplify the trends (Kossin, 2008).

Increasing trends in the frequency of land-falling tropical cyclones have not been identified in any region (Wang and Lee, 2008; Chan and Xu, 2009; Kubota and Chan, 2009; Lee et al., 2012; Weinkle et al., 2012) although Callaghan and Power (2010) identified a statistically significant downward trend in the number of severe tropical cyclones making landfall over northeastern Australia since the late 19th century. Measurements of tropical cyclone landfall frequency are generally considered to be more reliable than those of storms that remain at sea throughout their lifetimes, particularly in the earlier parts of the historical records. But as described above, confining storm counts to any pre-defined region cannot discriminate between basin-wide frequency variability and track variability, and it remains uncertain whether the trend reported by Callaghan and Power (2010) is driven by natural processes or whether some part is anthropogenically forced. A significant positive trend has been identified in the frequency of large sea level anomaly events along the USA East and Gulf Coast in a tide-gauge record spanning 1923–2008 and this trend has been argued to represent a trend in storm surge associated with landfalling hurricanes (Grinsted et al., 2012). The long-term (86-year) and roughly linear nature of the trend identified by Grinsted et al. (2012) is compelling and the relevance is high because the trend is argued to relate to high-impact surge events, but there is still the question of what portion of the trend is due to systematic track shifts, as previously identified in trends in wave power in Atlantic buoy data (Bromirski and Kossin, 2008), and what part is due to trends in basin-wide frequency or intensity. The difference between Callaghan and Power (2010), who show a long-term decreasing trend in Australian landfall events and Grinsted et al. (2012), suggesting a long-term increasing trend in storm surge associated with USA landfall events, underscores the challenge of understanding and projecting region-specific changes in tropical cyclones.

When data uncertainties due to past changes in observing capabilities are taken into account, confidence in the fidelity of any reported *basin-wide* trends in tropical cyclone activity on time scales longer than about 50 years is compromised. Shorter term increases, such as observed in the Atlantic since 1970, appear to be robust (Kossin et al., 2007), and have been hypothesized to be related, in part, to regional external forcing by greenhouse gasses and aerosols (discussed below), but the more steady century-scale trends that may be expected from CO_2 forcing alone are much more difficult to assess given the data uncertainty in the available tropical cyclone records. This presents a confounding factor to formal detection of trends that may be attributed to anthropogenic effects because the expected natural variability on multi-decadal time scales is not yet well quantified in the various regions.

14.SM.4.1.2 Understanding the Causes of Past and Projected Regional Changes

Although there is evidence that SST in the tropics has increased due to increasing GHGs (Karoly and Wu, 2005; Knutson et al., 2006; Santer et al., 2006; see also Chapter 10 and Section 3.1.1.4; Gillett et al., 2008) and there is a theoretical expectation that increases in potential intensity (PI) will lead to stronger tropical cyclones (Emanuel, 2000; Wing et al., 2007; Elsner et al., 2008), the relationship between SST and PI under CO_2 warming has not yet been fully elucidated (see also Chapter 10). PI describes the theoretical limit to how strong a tropical cyclone can become based on the three-dimensional thermodynamic environment that the storm moves through (Emanuel, 1987). Observations demonstrate a strong positive correlation between SST and PI, but it is known that this relationship is not unique. For example, raising SST by reducing surface wind speed produces a much more rapid increase in PI with SST than does raising it by increasing CO_2 because other factors that control PI will vary differently according to each process (Emanuel et al., 2012). Similarly, vertical wind shear, which affects tropical cyclone genesis and intensification, is apparently modulated differently by internal variability versus external radiative forcing of regional SST (e.g., Zhang and Delworth, 2009).

Because of the known non-uniqueness of the relationship between SST and PI, it is generally agreed that regional projections of SST by themselves are not a useful proxy for future PI. For example, the relationship between SST and PI in CMIP3 projections in the western North Pacific has been shown to be non-stationary because the projected tropical warming anomalies in the SRES A1B scenario are amplified in the upper troposphere, which convectively stabilizes the atmosphere and suppresses the increase in PI for a given increase in SST (Tsutsui, 2010, 2012). However, there is a growing body of research since the IPCC Fourth Assessment Report suggesting that the difference between regional SST and spatially averaged SST in the tropics (typically referred to as "relative SST") *can* serve as a useful proxy for regional PI (Vecchi and Soden, 2007b; Xie et al., 2010; Ramsay and Sobel, 2011; Camargo et al., 2012). The hypothesis is largely phenomenological and based on observed correlation, but has some physical basis in the theory that upper tropospheric temperatures are sensitive to mean tropical SST (Sobel et al., 2002), while regional lower tropospheric temperatures are more sensitive to local SST. This combination of factors affects regional lapse rates, which in turn affects PI. In this case, localized SST changes are hypothesized to be more effective at altering PI than a more globally uniform tropical SST change (e.g., as would be expected from forcing by well-mixed greenhouse gases (WMGHGs)) of the same magnitude.

However, it has been argued that the physical link between relative SST and PI is only valid on time scales shorter than the ocean mixed-layer equilibration time scale (Emanuel, 2010; Emanuel et al., 2012). On longer time scales of a few years or more, which allow the ocean mixed layer to equilibrate to surface forcing, Emanuel et al. (2012) argue that PI is mostly controlled by local surface radiative balance and ocean heat flux convergence and in general, SST cannot be considered an external control on PI, but merely a co-factor. By this argument (and the assumptions that it is based on), projections of SST by themselves, whether absolute SST or relative SST, cannot uniquely determine future PI changes, and hence they cannot uniquely determine future tropical cyclone changes. Still, the studies of Camargo et al. (2012), Ramsay and Sobel (2011), Vecchi and Soden (2007b), Xie et al. (2010), and others have demonstrated that the correlation between relative SST and PI is in fact consistently evident on multi-decadal and longer time scales. Thus, while the presumptive theoretical arguments of Emanuel (2010) and Emanuel et al. (2012) suggest that there is no reason to expect such a relationship (and therefore there is no physical justification for using 21st century relative SST projections to statistically infer future PI), both data and model projections support the existence of a useful relationship between relative SST and PI on decadal and longer time scales. Although the balance of relevant literature supports the hypothesis that long-term relative SST projections can serve as a useful proxy for future tropical cyclone PI, this remains an active area of research (and debate) without a clear consensus yet.

The distinction between the competing hypotheses described above is a critical one because while tropical SST is expected to continue to increase under global warming, there is much more uncertainty in how regional SST is expected to change relative to the tropical mean (Vecchi et al., 2008; Villarini et al., 2011). In general, future relative SST changes forced by increasing WMGHG in the tropics are not expected to be large in regions where storms form and track (Vecchi and Soden, 2007b) and thus if relative SST is a useful proxy for PI, there would not be an expectation for large increases in future tropical cyclone intensity (Vecchi et al., 2008). The results of Emanuel (2010) and Emanuel et al. (2012) do not provide alternative projections of PI, but only state that they are not constrained by any measure of future SST alone. As an example of the ramifications of the differences, the present approximately 40-year period of heightened tropical cyclone activity in the North Atlantic, concurrent with comparative recent quiescence in most other ocean basins (Maue, 2011), is apparently related to differences in the rate of SST increases, as global SST has been rising steadily but at a slower rate than the Atlantic (Trenberth and Shea, 2006). The present period of relatively enhanced warming in the tropical North Atlantic has been proposed to be due primarily to internal variability (Ting et al., 2009; Zhang and Delworth, 2009; Camargo et al., 2012), and both direct (dimming) and indirect (cloud–albedo) effects of radiative forcing by anthropogenic tropospheric aerosols (Mann and Emanuel, 2006; Booth et al., 2012) and mineral (dust) and volcanic aerosols (Evan et al., 2009, 2011, 2012). None of these proposed mechanisms provide a clear expectation that North Atlantic SST will continue to increase at a greater rate than the tropical mean SST and thus if future PI can be described by relative SST, the present steep upward trend in tropical cyclone intensity in the North Atlantic would be expected to abate.

Projected changes in potential intensity calculated from CMIP5 multi-model ensembles are shown in Figure 14.SM.2.

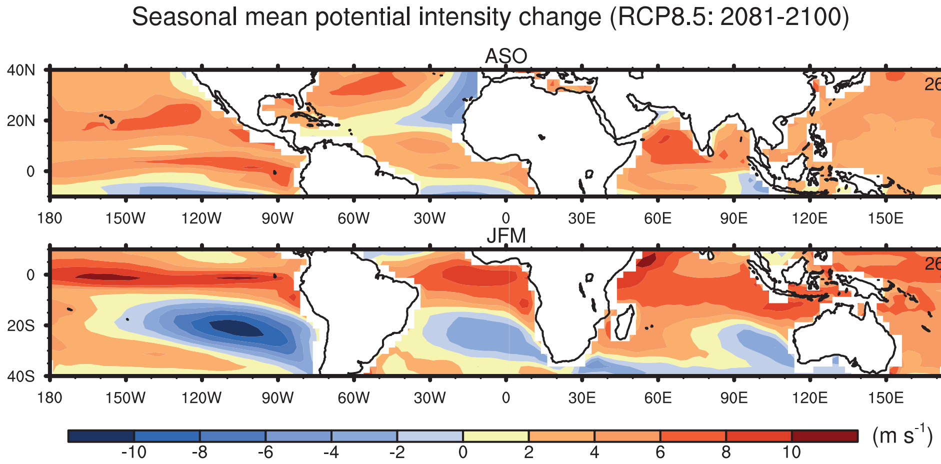

Figure 14.SM.2 | Change in seasonal mean tropical cyclone potential intensity for end of the century RCP8.5 (2081–2100) minus Historical Control (1986–2005) in CMIP5 multi-model ensembles. (Top) August to October, 10°S to 40°N and (bottom) January to March, 40°S to 10°N. Potential intensity computation uses the method of Bister and Emanuel (1998) applied to monthly means fields to compute the potential maximum surface wind speed (m s^{-1}) of tropical cyclones. The seasons for each panel are the historical high frequency periods for tropical cyclones in each hemisphere. The number of models in the ensemble appears in the upper right of each panel.

14.SM.5 Additional Phenomena of Relevance

14.SM.5.1 The Role of the Pacific–North American Pattern in Linking El Niño-Southern Oscillation and the North Atlantic Oscillation

Recent diagnoses (see review by Bronnimann, 2007) show that ENSO may impact European climate through modulation of the NAO, especially during late winter and early spring. The observational and model results reported by Li and Lau (2012b) and Li and Lau (2012a) illustrate that one possible mechanism for this connection is related to the PNA-like teleconnection pattern forced by ENSO events. Specifically, this response pattern is accompanied by systematic changes in the position and intensity of the storm tracks over the North Pacific and North America. The transient disturbances along the storm tracks propagate farther eastward and reach the North Atlantic. The ensuing dynamical interactions between these stormtrack eddies and the local quasi-stationary circulation lead to changes in the NAO. In addition to tropospheric processes, Ineson and Scaife (2009), Bell et al. (2009) and Cagnazzo and Manzini (2009) have demonstrated a stratospheric link between ENSO and NAO in late winter.

14.SM.5.2 Tropospheric Biennial Oscillation

It has long been noted that there is a biennial tendency of many phenomena in the Indo-Pacific region that affects droughts and floods over large areas of south Asia and Australia (e.g., Troup, 1965; Trenberth, 1975; Nicholls, 1978; Mooley and Parthasarathy, 1983). Brier (1978) suggested a possible central role of air–sea coupling, and Meehl (1987) proposed a mechanism involving large-scale dynamically coupled interactions across the Indo-Pacific to account for the biennial tendency, termed the Tropospheric Biennial Oscillation (TBO, Meehl, 1997). There was also a role for atmospheric circulation anomalies over south Asia and consequent land surface temperature anomalies that contributed to anomalous meridional temperature gradients and biennial monsoon variability (Meehl, 1994a, 1994b), thus giving rise to explanations of the TBO that involved processes in the Indian sector (Chang and Li, 2000; Li et al., 2001). SST anomalies in the equatorial eastern Pacific Ocean in the TBO tend to transition from positive to negative (or vice versa) in northern spring, so the seasons leading up to those transitions are crucial to the TBO (e.g., Meehl and Arblaster, 2002a, 2002b). The fundamental nature of the dynamically coupled processes involved with the TBO have been additionally documented in a number of global coupled climate model simulations (e.g., Meehl, 1997; Ogasawara et al., 1999; Loschnigg et al., 2003; Nanjundiah et al., 2005; Meehl and Arblaster, 2011).

Regional patterns of SST anomalies in the TBO in the Indian Ocean during the northern fall season following the south Asian monsoon subsequently became known as the Indian Ocean Dipole (IOD, e.g., Saji et al., 1999; Webster et al., 1999; Section 14.3.3). Thus, a "negative IOD" in northern fall (negative SST anomalies in the western tropical Indian Ocean, and positive SST anomalies in the eastern tropical Indian Ocean), with negative SST anomalies in the equatorial eastern Pacific, transition to basin-wide negative SST anomalies across the Indian Ocean in northern winter, with positive SST anomalies in the eastern equatorial Pacific in the following northern spring and summer in the TBO (Meehl et al., 2003). Izumo et al. (2010) made use of these transition processes in the TBO to document El Nino forecast skill by monitoring the state of the IOD in northern fall. In addition, convective heating anomalies in the Pacific (Wu and Kirtman, 2004), or in the Indian Ocean associated with the IOD (e.g., Annamalai et al., 2005), or a combination from the southeastern Indian Ocean and western Pacific (Clarke et al., 1998; Li et al., 2001, 2006) affect the southeastern Indian Ocean and western north Pacific anticyclones. The resulting wind stress anomalies in the equatorial western Pacific contribute to TBO SST transitions in the eastern equatorial Pacific (Lau and Wu, 2001; Turner et al., 2007). Such consecutive annual SST anomaly and anomalous monsoon transitions from one sign to another characterize the TBO. Thus, the TBO provides the fundamental framework for understanding coupled processes across the Indo-Pacific region involving the Asian-Australian monsoon, the IOD, and ENSO.

The processes that produce the TBO are affected by internally generated decadal-time scale variability. Just as the Inter-decadal Pacific Oscillation (IPO) influences the nature of interannual variability in the Australia-Pacific region (Power et al., 1999), so does the IPO affect the decade-to-decade strength of the TBO (Meehl and Arblaster, 2011). During periods of positive IPO (warmer SSTs in the tropical Pacific on the decadal timescale, e.g., from the 1970s to 1990s), the TBO was weak, and vice versa for negative IPO with a stronger TBO (post-1990s; Meehl and Arblaster, 2012). Thus, prediction of decadal time scale variability assessed in Chapter 11 that can be associated, for example, with the IPO (e.g., Meehl et al., 2010) can influence the accuracy of shorter term predictions of interannual variability associated with the TBO across the entire Indo-Pacific region (Turner et al., 2011). This set of regional processes from interannual to decadal is of great relevance for decadal climate prediction and the short-term climate change problem (Chapter 11).

14.SM.6 Future Regional Climate Change

14.SM.6.1 Future Regional Climate Change, Overview

14.SM.6.1.1 How the Confidence Table Was Constructed

The confidence levels in Columns 2, 3, 6 and 7 of the confidence table (Table.14.2) are based on subjectively determined criteria, but the criteria are applied objectively.

Each regional entry in Column 2 of the table, evaluating confidence in models' ability to simulate present-day temperature, is based on values shown in Figures 9.39 and 9.40.

The following criteria have been applied to determine confidence level (see table, next page):

For precipitation (Column 3), replace 2°C in the above table with 20%. For both temperature and precipitation, these values are chosen to represent the accuracy with which the models simulate gross features of present-day mean climate.

For future projections (Columns 6 and 7), confidence levels are based on analyses of how much the model signals rise above natural variability.

		Model Spread (difference between 25th and 75th percentiles)		
		>2°C in both seasons	<2°C in only one season	<2°C in both seasons
Bias of Ensemble Mean	<2°C in both seasons	Medium (M)	High (H)	High (H)
	<2°C in only one season	Low (L)	Medium (M)	High (H)
	>2°C in both seasons	Low (L)	Low (L)	Medium (M)

Both the signals and the natural variability are based on averages over the SREX regions. Natural variability is quantified in a similar way as in Annex I—standard deviations of model-estimated present-day natural variability of 20-year mean differences. The framework for comparing the signal to natural variability is similar to that adopted in Annex I (see Annex I definition of *hatching*), except that here we require the signal to be larger than two standard deviations of natural variability rather than one, because averaging over a region gives a much more robust signal than for individual grid points used in Annex I.

Then the following principles were applied:

- High confidence is assigned when all 3 percentiles of the model signal distribution (25%, 50% and 75%) rise above the natural variability. In other words, the great majority of models give signals that rise above the noise.
- Medium confidence is assigned when 2 out of 3 percentiles rise above the natural variability. This means that a majority of the models give a signal that rises above the noise.
- Low confidence is assigned when one or none of the 3 percentiles rises above the natural variability. There is no significant fraction of the models giving a signal that rises above the noise.
- In the case of precipitation, if any of the 3 percentiles disagree with the others on the sign of the change, the projected change is deemed to be not significantly different from zero. The assigned confidence is medium, marked by an asterisk (*), no matter what confidence level arises from the 3 principles above. In these regions, no change is projected.

14.SM.6.1.2 How the Relevance Table Was Constructed

Table 14.3 is a summary of the relevance of anthropogenically forced changes in major climate phenomena for future regional climate. For the sake of brevity, we present only the most relevant highlights for the major phenomena discussed in Sections 14.2 to 14.7.

14.SM.6.1.3 Assignment of Relevance Levels

Relevance is based on the confidence that there will be a change in the phenomenon, and the confidence that the phenomenon has an impact on the regional climate.

Four levels of relevance are assigned (*high, medium, low, not yet evident*) and colour coded as follows:

		Confidence in Future Projections of the Phenomenon		
		Low **(LP)**	*Medium* **(MP)**	*High* **(HP)**
Confidence in the Regional **Impact** of the Phenomenon	*High* (HI)	Medium relevance	High relevance	High relevance
	Medium (MI)	Low relevance	Medium relevance	High relevance
	Low (LI)	Not yet evident	Low relevance	Medium relevance

Each assessment of relevance is traceable back to confidence statements. So for example, if there is *high confidence* in the projected change in a phenomenon (HP) and also *high confidence* that the phenomenon has an impact on temperature or precipitation of a certain region (HI) it is then assigned high relevance (red). Or, if there is only *low confidence* in the projected change in a phenomenon (LP) but there is *high confidence* that it has a strong impact on a region (HI) then the phenomenon is assigned medium relevance (yellow) for the region.

The confidence statements in projections of the phenomena concern whether or not there will be an effect rather than the magnitude of the effect. Thus, when a phenomenon has high relevance for a region it is meant that there will be a change in the regional climate due to the future change in the phenomenon, but it does not imply that the regional change is necessarily dominated by changes in the phenomenon.

14.SM.6.1.4 Assignment of Confidence in Projections of Major Climate Phenomena

The level of confidence in the major phenomena changing due to anthropogenic forcing is assigned as follows based on the model projections assessed in Sections 14.2 to 14.7.

14.SM.6.1.5 Assignment of Confidence in Regional Impact of Major Climate Phenomena

The confidence in the impact of major phenomena on each region is assessed to be as follows (see table next page):

Arctic
There is *high confidence* that both the NAO and extratropical cyclones (ETCs) impact the Arctic climate; *high confidence* in NAO projections and *medium confidence* in ETC projected change, resulting in high relevance for both.

North America
This climatically diverse continent is influenced to varying degrees by many of the major phenomena: Monsoons, ITCZ, ENSO, NAO/NAM, and tropical and ETCs. The high relevance N. American monsoon results from the *high confidence* that this phenomenon has an impact on the annual cycle of rainfall in the western sector and the *medium confidence* in future changes in the phenomenon, especially the shift in

Major Climate Phenomenon	*Confidence*	Relevant Section
Monsoons	*Medium*	14.2
Tropical Phenomena, Convergence Zones	*High*	14.3.1
Tropical Phenomena, MJO	*Low*	14.3.2
Tropical Phenomena, IOD	*Medium*	14.3.3
Tropical Phenomena, AOM	*Low*	14.3.4
El Niño-Southern Oscillation	*Low*	14.4
Annular and Dipolar Modes	*High*	14.5
Tropical Cyclones	*Medium*	14.6.1
Extratropical cyclones	*Medium* NH/*High* SH	14.6.2

timing to later in the season. The *high confidence* in projected ITCZ shifts combined with the *low confidence* in impact on regional climate in North America results in medium relevance. The *low confidence* in future projections of ENSO and *high confidence* in impacts lead to an assignment of medium relevance. The *high confidence* in NAO projections and the medium impact of this phenomenon in the eastern sector of the region lead to high relevance. The *high confidence* that tropical and ETCs have impact in this region and the *medium confidence* in their projected change, gives high relevance.

Central America and Caribbean

Climate in this region is influenced by Monsoons, ITCZ, ENSO and tropical cyclones. The *high confidence* that monsoon has an impact on precipitation in the region and the medium confidence in a projected change in the phenomenon results in the high relevance. The *high confidence* in projected ITCZ shifts combined with the *high confidence* in the regional climate change result in a medium relevance. The *low confidence* in ENSO future projections and its high impact on the regional climate lead to an assignment of medium relevance (yellow shading) of this phenomenon for future regional change. The *high confidence* that tropical cyclones have a climate impact and the *medium confidence* in the projected change in tropical cyclones result in a high level of relevance (red shading) for those systems in future climate change in the region.

South America

Climate over this large latitudinal region has impacts from all of the major phenomena apart from tropical cyclones. The high relevance assigned to the South American Monsoon results from the *high confidence* that this phenomenon influences precipitation extremes within the monsoon-affected area and the *medium confidence* in the phenomenon future change. The *high confidence* in projected SACZ displacement combined with the *high confidence* in the southeast sector climate impact gives a high relevance for this phenomenon. The *low confidence* in ENSO future projections and its high impact lead to an assignment of medium relevance. The *high confidence* in SAM projections and the high impact of this phenomenon in the southern sector of the region give it a high relevance. As ETCs have *high confidence* in a projected poleward movement and *medium confidence* in their impact on the regional climate, they are assigned a high relevance.

Europe and Mediterranean

There is *high confidence* in projections of increasing NAO and also a *high confidence* that this phenomenon has an impact on regional climate which leads to high relevance, especially over NW Europe. The high impact of ETCs on the regional climate and the *medium confidence* in projections of this phenomenon give a high level of relevance.

Africa

There is *medium confidence* in changes in projections of the West African monsoon but *high confidence* in impact leading to high relevance. The *high confidence* that tropical cyclones have a climate impact and the *medium confidence* in the projected change in tropical cyclones results in a high level of relevance. The high impact of ETCs on the regional climate and the *medium confidence* in projections of this phenomenon give a high level of relevance. The *low confidence* in ENSO future projections and its high impact lead to an assignment of medium relevance. The *high confidence* in projected ITCZ shifts combined with *low confidence* in the regional climate signal determines a medium relevance. There is *low confidence* in projections of Atlantic Ocean SSTs, but *medium confidence* in Indian Ocean projections both with a high impact on West, resp. East Africa, all together resulting in medium relevance.

Central and North Asia

Medium confidence in projections of monsoon change and also *medium confidence* in impact lead to medium relevance. The *low confidence* that NAO/NAM has an impact on the regional climate and the *high confidence* in projections of this phenomenon determines its medium level of relevance.

East Asia

There is *medium confidence* in the impact of Monsoon over East Asia and there is also a *medium confidence* in the projected changes in the East Asia Monsoon resulting in the medium level of relevance for Monsoon for East Asia. Although there is a high impact of ENSO on the region, there is *low confidence* in the future projections of ENSO leading to a medium level of relevance of ENSO for the East Asia region. There is a *high confidence* in the impact of TC on East Asia and also given that there is a *medium confidence* in the future projections of the characteristics of TC, a high level of relevance is assigned for TC for East Asia. There is a *medium confidence* in the projections of ETCs and also a *medium confidence* in their impact on the winter precipitation over East Asia resulting in a medium level of relevance of this phenomenon to East Asia.

West Asia

The *low confidence* in the impact of ITCZ over the southern sector of the region and the *high confidence* in projected changes of this phenomenon result in the assigned medium level of relevance. There is *medium confidence* in projections of tropical cyclones change but a *high confidence* in its impact on precipitation over the southern sector, hence it is assessed a high relevance to this phenomena for regional climate change. Finally, *medium confidence* in projected poleward shift of ETCs but a *low confidence* in their impact on the northern sector gives a low level of relevance.

South Asia

There is a *medium confidence* that Indian Monsoon will impact South Asia but with a *medium confidence* in the projections of Indian Monsoon, a medium level of relevance is assigned to this phenomenon for South Asia. Although tropical phenomena such as ITCZ, MJO and IOD can potential impact South Asia, there is *low confidence* in the projection of some of these phenomena and also a *medium confidence* in their impact resulting in a low level of relevance of these phenomena for South Asia. There is *medium confidence* that ENSO will impact both the precipitation and temperature over South Asia but with *low confidence* in the projections of ENSO, a medium level of relevance is assigned to ENSO for South Asia. There is *high confidence* that rainfall extremes will impact South Asia but with a *medium confidence* in the projections of TC, a high level of relevance is assigned to TC for South Asia.

Southeast Asia

There is a *medium confidence* that Mari-time continent Monsoon will impact the precipitation in South East Asia but there is *low confidence* in the projections of Maritime Continent Monsoon resulting in a low level of relevance of this phenomenon for South East Asia. There is a *medium confidence* that warming associated with IOD will reduce the rainfall over Indonesia during July to October period and with *high confidence* in the projection of IOD, a high level of relevance is given to this phenomenon for Southeast Asia. While the impact of ENSO has a *high confidence*, the *low confidence* in the projection of ENSO results in a medium level of relevance of ENSO to Southeast Asia. There is a *high confidence* that the extreme precipitation associated with TCs will increase while there is a *medium confidence* in the projection of TC characteristics leading to a high level of relevance of TC to Southeast Asia.

Australia and New Zealand

Climates in this large region are influenced to varying degrees by all of the major phenomena. The low relevance assigned to monsoon results from the *low confidence* in how this phenomenon influences the climate in northern Australia and the *medium confidence* in the phenomenon's projected future change. The *high confidence* in projected SPCZ changes combined with the *low confidence* in the associated NE Australia climate impact lead to a medium relevance level. The *low confidence* in ENSO future projections and its strong impact on the regional climate lead to medium relevance. The *high confidence* in SAM projections and the medium impact of this phenomenon in the southern sector of the region lead to high relevance. As TCs have high impact and there is *medium confidence* in the projections, the assigned level of relevance is high. Finally, extra-tropical cyclones have both *high confidence* in projected change and in their impact on the regional climate and thus have a high relevance for future climate change.

Pacific Islands Region

The *high confidence* in projected changes in the SPCZ, combined with *high confidence* in impact results in high relevance. The *high confidence* in the impact of ENSO combined with *low confidence* in projected future changes in ENSO gives medium relevance. As tropical cyclones have high impact and there is *medium confidence* in projected changes in tropical cyclone behaviour, the assigned level of relevance is high.

Antarctica

The *low confidence* in ENSO projections and the *medium confidence* in its impact on Antarctica climate lead to assess a low relevance. As there is a *high confidence* in SAM projected changes and also *high confidence* in its influence the assigned level of relevance is high. Finally, given the *medium confidence* that ETCs have impact on the regional climate and the *high confidence* in projections, these systems have a high level of relevance.

14.SM.6.2 South America

ENSO is the main source of interannual variability over South America. There are several regions that are influenced by Pacific SST, such as Peru, Ecuador (Lagos et al., 2008), Chile (Garreaud and Falvey, 2009), Bolivia (Ronchail and Gallaire, 2006), Brazil (Grimm and Tedeschi, 2009; Tedeschi et al., 2013), Paraguay (Fraisse et al., 2008), Uruguay and Argentina (Barros et al., 2008). The mechanisms of these influences are changes in the Walker Circulation that affect tropical South America, and influences of wave trains from tropical Pacific to South America that affect the southern and southeastern continent. A reconstruction of ENSO events since 16th century indicated the increase of frequency of such events in the 20th century, likely related to anthropogenic forcing (Gergis and Fowler, 2009). Atmospheric Global Circulation Models represent well this influence, in simulations with prescribed SST (Pezzi and Cavalcanti, 2001). A study with the European Centre for Medium Range Weather Forecasts (ECMWF) and Hamburg (ECHAM5-OM) model indicated that the ENSO connection with southeastern South America could weaken in the projected future climate (Grimm and Natori, 2006; Grimm, 2011).

Aside from Pacific Ocean influences on South America, tropical Atlantic SST anomalies also affect precipitation over northern and northeastern South America. Northeastern Brazil, a region with high temporal and spatial variability, is frequently affected by droughts associated with the ITCZ anomalies. Tropical North Atlantic SST anomalies can be related to displacements of NAO centres which changes the atmospheric circulation and affect ITCZ position (Souza and Cavalcanti, 2009). A positive trend of tropical Atlantic interhemispheric gradient of SST, observed from the beginning of 20th century up to 1980, indicated strong warming in the south sector compared to the north (Chang et al., 2011). This trend was associated with the aerosol increase over the North Atlantic, implying a southward shift of the ITCZ (Chang et al., 2011). However, the reduction of aerosol in the first decade of the 21st century and continuous increase of the GHGs in the atmosphere promoted a reversal in the SST gradient, with observed increases of North Atlantic SST and effects on South America (Cox et al., 2008).

Analysis of north–south Atlantic SST gradient in Good et al. (2008) during June, July and August (JJA) showed high negative correlation with precipitation over Amazonia, and also over northeast Brazil. Relations between this gradient and precipitation in southern Amazonia were also obtained in a CGCM under 1% CO_2 increase by Good et al. (2008), who suggested that uncertainties in projected changes of the meridional Atlantic SST gradient would be linked to uncertainties in southern Amazonia precipitation during the dry season. This SST gradient also occurs during the rainy season, similar to what occurred in 2005 and 2010 associated with the extreme droughts. AGCM experiments in Harris et al. (2008) also indicate the influence of Atlantic SST north–south gradient and Pacific SST on Amazonia precipitation.

Amazonia has a large influence on the global climate, as it has large contribution to the hydrological cycle. It is one of the three regions with maximum tropical precipitation, together with Indonesia and Tropical Africa. The source of humidity to the atmosphere due to evapotranspiration is also large, being responsible for precipitation in other areas of South America. Extreme droughts in the first decade of 21st century in Amazonia (2005 and 2010) were considered the worst droughts since 1950 (Marengo et al., 2008). These extreme precipitation conditions over Amazonia affected the Amazonas and Solimões River discharges in 2005 and 2010 (Espinoza et al., 2011; Marengo et al., 2011; Tomasella et al., 2011). Studies on the causes of these droughts indicated the role of North Atlantic warmer than normal SST (Marengo et al., 2008, 2011; Yoon and Zeng, 2010; Espinoza et al., 2011; Lewis et al., 2011). The related atmospheric circulation anomalies were also discussed in Trenberth and Fasullo (2012). This condition enhanced ascent motion over North Atlantic and forced subsidence over Amazonia. The north–south SST gradient was favourable for the ITCZ displacement northward, and it was consistent with convection shift to the north and changes in the low-level trade winds, which normally brings humidity to the continent in the beginning of the South America Monsoon.

The deforestation in the region has been reduced in recent years, but large areas in the southern sector were already changed to agriculture or pastures areas. Changes in the vegetation due to projected warming in future climate can contribute to precipitation reduction in Amazonia, as shown in experiments of Salazar et al. (2007) and Sampaio et al. (2007). Replacement of forest by pasture or soybean cropland reduced precipitation in the region in model experiments (Costa et al., 2007). The risk of fires in projected deforested areas of Amazonia (eastern and southern areas) increases under projected changes in CMIP3 models (Golding and Betts, 2008). However, only some local stations show a significant precipitation decrease in the last 80 years (Satyamurty et al., 2010).

In Central Chile the negative trends in precipitation during the 20th century were related to a weakening of the Pacific subtropical High in the northern sector and to the positive trends of the Southern Annular Mode (SAM) in the southern sector (Quintana and Aceituno, 2012).

In the Andes, warmer and drier conditions in future projections resulted in snow and streamflow reduction (Vicuña et al., 2011). Projections using a tropical glacier–climate model indicate Andean glaciers will continue to retreat (Vuille et al., 2008).

Other region that is influenced by modes of variability is the La Plata Basin (LPB) region in southeastern South America. This is the second largest basin in South America and has the main hydroelectric power plant of this continent. The region has been recognized as sensitive to climate variability and change because of potential consequences for water resources and agriculture activity over the region (Boulanger et al., 2011). LPB receives large portion of humidity from the Amazon region through the Low-Level Jet (LLJ), which feeds mesoscale convective systems frequent in the region and several times responsible for flooding.

Atmospheric circulation and precipitation changes over southern South America, in future projections of a regional model, were related to the shifting of Atlantic and Pacific subtropical highs southward and increase of the Chaco low, through a decreased sea level pressure (SLP) over northern Argentina, an increase in northerly winds over northeastern Argentina, which causes moisture convergence and precipitation in that region (Nuñez et al., 2009). The geopotential height increase over southern South America, in projections of JJA, indicates a strengthening of the meridional gradient and stronger westerlies. The changes are consistent with a poleward shifting in the subtropical storm tracks. The changes in circulation induce the projected precipitation changes: increased precipitation in central Argentina associated with the enhanced cyclonic circulation of the Chaco low, southward shifting of the Atlantic subtropical high, with humidity advection displaced to that area, in the summer. In the winter, there is reduced precipitation projection over southeastern South America, due to a poleward shift of the stormtracks that reduces the cyclonic activity over the region. The shifting of the subtropical high polewards agrees with results of Lu et al. (2007) on the Hadley Cell expansion under global warming. This expansion changes the region of subsidence and the subtropical high pressures moves southwards.

Occurrences of extreme droughts and floods in South America have contributions from large-scale atmospheric and oceanic features, synoptic conditions (Cavalcanti, 2012) and also from local conditions. Local responses resulting from changes in the main regional systems and in the large-scale modes of variability can be reinforced through land feedback to precipitation or temperature (e.g., reduced soil moisture during spring over Amazonia contributes to a delayed onset of the monsoon season (Collini et al., 2008). Southeastern South America is a hotspot of strong coupling between land and both evapotranspiration and precipitation during summer (Sörensson and Menendez, 2011).

Precipitation over southeastern South America and southeastern Brazil is influenced by the Southern Annular Mode (SAM; Reboita et al., 2009; Vasconcellos and Cavalcanti, 2010). The mechanisms of these influences are related to changes in storm tracks, jet streams position and intensification of PSA anomalous centres by the SAM. The wave train over South America intensified by the influence of SAM on PSA, results in a cyclonic/anticyclonic pair over the continent and a related precipitation dipole anomaly, responsible for extreme precipitation in the South Atlantic Convergence Zone (SACZ), as discussed in Vasconcellos and Cavalcanti (2010). The future projections indicate increase of SLP at middle latitudes of South Atlantic Ocean (Seth et al., 2010), as the Atlantic Subtropical High is displaced polewards, behaviour that can be related to the positive trend of the AAO index and poleward shifting of the stormtracks. The southward shift of the South Atlantic High and moisture transport from the Atlantic Ocean towards western and then eastern Argentina resulted in a significant increase of annual precipitation during the 20th century over the southern sector of southeastern South America and a negative trend in the SACZ continental area (Barros et al., 2008).

Correlations of SAM index with precipitation over South America show a strong influence in OND, with negative correlations over part of La Plata basin and positive in central-north continent (Vera and Silvestri, 2009). In AMJ there is also this kind of dipole correlation over South America, but covering a smaller area in southern SA and positive over northwestern Amazonia. The correlations in JAS are opposite to OND, when positive correlations occur over part of La Plata basin, and negative over extreme northern South America. Seven models analysed by Vera and Silvestri (2009) did not reproduce such correlations.

Significant correlations were found between number of cold nights in Uruguay and SAM negative phase in the summer period of 1949–1975, which were not seen in the period of 1976–2005 (Renom et al., 2011). The number of warm nights in the winter had high correlations with Tropical Pacific SST in the first period, which weakened in the second period. Correlations of warm nights with Atlantic SST anomalies were high during the second period.

The influence of IOD on South America is view through a wave train pattern that extends from the Indian Ocean to South Pacific and South Atlantic and over South America (Saji and Yamagata, 2003). Similar to PSA influence, the centres over the continent can affect precipitation and temperature. IOD influence on South America temperature was discussed by Saji et al. (2005). Influences on South America precipitation is presented in Chan et al. (2008).

14.SM.6.3 Europe and Mediterranean

14.SM.6.3.1 Phenomena Affecting Regional Climate

The most relevant phenomena affecting climate variability in diverse periods and time scales are those related to the extratropical large-scale atmospheric circulation: ETCs (see Section 14.6.2), NAO (see Section 14.5.1) and blocking (see Section 14.6.3). Other patterns such as the East-Atlantic pattern (EAP) are also required to describe the strength and position of the North Atlantic jet and storm track (Seierstad et al., 2007; Woollings et al., 2010a). The EAP resembles NAO although displaced and enhanced over MED (Krichak and Alpert, 2005).These variability modes in turn seem to be modulated by interactions with the North Atlantic AMO pattern (Section 14,7,6) and with lesser intensity diverse tropical phenomena, in particular ENSO, MJO and Indian summer Monsoon (see Sections 14.5 and 14.6).

The NAO influence on winter temperature anomalies is very relevant in Northern Europe (NEU) and Central Europe (CEU) due to the relative mild (cold) air westerly (easterly) advections prevailing over these sectors during its positive (negative) phase. The cold season precipitation (October to March) interannual variability is controlled mainly by NAO. In the positive (negative) phase higher (lower) than normal precipitation prevails in the NEU and CEU sub-regions while in Southern Europe/Mediterranean (MED) an opposite behaviour is observed, possibly with the exception of the eastern and southeastern rims of the basin (Feliks et al., 2010). There is evidence that the NAO precipitation teleconnection patterns have changed in the past (Hirschi and Seneviratne, 2010) and that the relationships are scenario dependent in climate simulations (Vicente-Serrano and López-Moreno, 2008). The summertime NAO has a more northerly position and a smaller extent and thus a weaker but still perceptible influence on the region. In its positive (negative) phase higher (lower) than normal summer temperatures are experienced all over Europe, except in the eastern MED, and less (more) than normal precipitation in NEU and CEU and the opposite in eastern MED (Folland et al., 2009; Bladé et al., 2012; Mariotti and Dell'Aquila, 2012).

Europe is among the regions with most frequent blocking events in the world (Woollings et al., 2010b). The persistence of this phenomenon leads to strong climate anomalies of different sign depending on the location of the high-pressure centre that diverts the westerly storms around. When it is located over Scandinavia–West Russia higher than normal precipitation (dry, cold) prevails over MED (NEU and CEU) in the winter half, while the opposite occurs when the blocking forms over west-central Europe (Barriopedro et al., 2006). In the summer season heat waves mostly occur during blocking situations (Dole et al., 2011).

Several studies have shown that the NAO and blocking phenomena non-locally interact with other phenomena (Küttel and Lutterbacher, 2011; Pinto and Raible, 2012). Diverse authors showed that winter NAO anti-correlates with AMO (e.g., Marullo et al., 2011; Sutton and Dong, 2012) and a significant relationship between AMO and summer NAO variations (Folland et al., 2009) or western European and MED summer heat waves (Della-Marte et al., 2007; Mariotti and Dell'Aquila, 2012). Through a complex chain of air–sea interactions, Bulic et al. (2012) explain the often observed time-lagged anomalies that ENSO events induce in large-scale circulation over the North Atlantic European region: a positive (negative) ENSO event in winter leads to positive (negative) spring precipitation anomalies in Europe (Bronnimann, 2007; Shaman and Tziperman, 2011). Also Cassou (2008) showed that the diverse phases of MJO affects the wintertime daily NAO regimes with a time lag of few days by an interaction mechanism between tropical forced Rossby waves and mid-latitude transient eddies. A similar mechanism is proposed between a strong Indian summer monsoon and above normal rainfall and below normal temperature over CEU and the western NEU along with positive temperature anomalies in the eastern MED, being the opposite situation during a weak monsoon (Lin and Wu, 2012).

Table 14.SM.1a | Temperature and precipitation projections by the CMIP5 global models. The figures shown are averages over SREX regions (Seneviratne et al., 2012) of the projections by a set of 32 global models for the RCP2.6 scenario. Added to the SREX regions are an additional six regions containing the two polar regions, the Caribbean, Indian Ocean and Pacific Island States (see Annex I for further details). The 26 SREX regions are: Alaska/NW Canada (ALA), Eastern Canada/Greenland/Iceland (CGI), Western North America (WNA), Central North America (CNA), Eastern North America (ENA), Central America/Mexico (CAM), Amazon (AMZ), NE Brazil (NEB), West Coast South America (WSA), South-Eastern South America (SSA), Northern Europe (NEU), Central Europe (CEU), Southern Europe/the Mediterranean (MED), Sahara (SAH), Western Africa (WAF), Eastern Africa (EAF), Southern Africa (SAF), Northern Asia (NAS), Western Asia (WAS), Central Asia (CAS), Tibetan Plateau (TIB), Eastern Asia (EAS), Southern Asia (SAS), Southeast Asia (SEA), Northern Australia (NAS) and Southern Australia/New Zealand (SAU). The area mean temperature and precipitation responses are first averaged for each model over the 1986–2005 period from the historical simulations and the 2016–2035, 2046–2065 and 2081–2100 periods of the RCP2.6 experiments. Based on the difference between these two periods, the table shows the 25th, 50th and 75th percentiles, and the lowest and highest response among the 32 models, for temperature in degrees Celsius and precipitation as a per cent change. Regions in which the middle half (25 to 75%) of this distribution is all of the same sign in the precipitation response are coloured light brown for decreasing and light green for increasing precipitation. Information is provided for land areas contained in the boxes unless otherwise indicated. The temperature responses are averaged over the boreal winter and summer seasons; December, January and February (DJF) and June, July and August (JJA) respectively. The precipitation responses are averaged over half year periods, boreal winter; October, November, December, January, February and March (ONDJFM) and summer; April, May, June, July, August and September (AMJJAS).

RCP2.6			Temperature (°C)					Precipitation (%)				
REGION	**MONTH**[a]	**Year**	**min**	**25%**	**50%**	**75%**	**max**	**min**	**25%**	**50%**	**75%**	**max**
Arctic												
(land)	**DJF**	**2035**	0.5	1.2	1.8	2.1	3.8	1	5	8	12	18
		2065	–1.2	2.0	2.6	3.2	6.5	–4	10	12	18	32
		2100	–3.9	1.9	2.5	3.3	6.7	–11	9	12	18	36
	JJA	**2035**	0.3	0.7	1.0	1.5	2.6	0	3	5	7	21
		2065	–0.2	0.9	1.2	2.1	4.1	–1	5	7	10	31
		2100	–1.1	0.7	1.0	2.2	4.4	–4	4	6	10	33
	Annual	**2035**	0.3	1.1	1.4	1.8	3.4	1	4	6	8	20
		2065	–1.1	1.7	2.1	2.7	5.5	–3	7	9	11	31
		2100	–2.9	1.4	1.9	2.8	5.6	–8	6	9	11	34
(sea)	**DJF**	**2035**	0.3	1.9	2.5	3.2	5.2	–2	6	10	13	25
		2065	–2.2	3.0	3.9	5.0	9.3	–9	11	15	22	31
		2100	–7.3	2.8	3.6	5.2	10.5	–23	9	15	20	37
	JJA	**2035**	0.0	0.4	0.6	0.8	1.5	–1	5	6	7	16
		2065	–0.6	0.7	0.9	1.2	2.4	–4	6	9	12	19
		2100	–1.5	0.5	0.8	1.3	2.7	–3	4	8	12	20
	Annual	**2035**	0.3	1.4	1.8	2.5	3.8	–1	6	8	9	18
		2065	–1.5	2.2	2.7	3.6	6.3	–7	9	11	15	25
		2100	–4.6	1.9	2.6	3.6	6.8	–15	7	11	16	28
High latitudes												
Canada/ Greenland/ Iceland	**DJF**	**2035**	0.2	1.2	1.5	1.8	3.3	–1	3	5	7	13
		2065	–1.1	1.9	2.3	3.0	5.3	–3	5	7	12	18
		2100	–3.5	1.6	2.4	3.2	5.0	–9	4	9	13	20
	JJA	**2035**	0.3	0.7	1.0	1.3	2.5	–1	2	4	5	10
		2065	–0.4	0.8	1.4	1.7	3.9	0	4	5	8	13
		2100	–1.2	0.7	1.2	1.9	4.1	–1	3	5	7	14
	Annual	**2035**	0.4	1.0	1.2	1.4	2.7	–1	2	4	6	10
		2065	–1.1	1.3	1.8	2.4	4.4	–2	5	6	9	14
		2100	–2.5	1.3	1.7	2.5	4.4	–4	4	7	9	16
North Asia	**DJF**	**2035**	–0.1	0.9	1.6	2.1	3.4	2	5	7	10	18
		2065	–0.4	1.6	2.1	2.4	5.7	0	7	9	13	32
		2100	–1.9	1.4	2.0	2.7	5.4	1	7	10	13	29
	JJA	**2035**	0.3	0.7	1.1	1.5	2.7	1	2	4	6	12
		2065	0.3	0.9	1.4	2.0	3.8	–2	4	5	8	22
		2100	–0.7	0.8	1.3	2.1	3.8	–5	4	6	8	21
	Annual	**2035**	0.3	0.9	1.3	1.7	2.9	2	3	5	8	14
		2065	–0.2	1.4	1.7	2.3	4.4	1	5	7	8	25
		2100	–1.7	1.2	1.6	2.4	4.3	–2	5	7	9	24

(continued on next page)

Table 14.SM.1a (continued)

RCP2.6			Temperature (°C)					Precipitation (%)				
REGION	**MONTH**[a]	**Year**	**min**	**25%**	**50%**	**75%**	**max**	**min**	**25%**	**50%**	**75%**	**max**
North America												
Alaska/ NW Canada	**DJF**	**2035**	0.3	1.1	2.0	2.6	3.5	–2	2	7	9	17
		2065	0.3	1.8	2.7	3.4	5.6	–2	5	10	14	25
		2100	0.2	1.6	2.3	3.6	5.8	–2	5	8	14	25
	JJA	**2035**	0.3	0.7	0.9	1.5	3.1	–1	4	6	7	15
		2065	0.4	0.8	1.5	2.1	3.5	–1	4	8	10	24
		2100	–0.3	0.7	1.2	2.2	3.6	–7	5	7	11	27
	Annual	**2035**	0.5	1.1	1.4	1.8	2.7	0	4	6	7	14
		2065	0.6	1.4	1.9	2.5	4.1	0	6	8	11	23
		2100	–0.5	1.2	1.9	2.6	4.0	–2	5	8	10	25
West North America	**DJF**	**2035**	–0.2	0.6	1.0	1.4	2.6	–3	–1	2	5	9
		2065	0.3	1.0	1.6	2.1	4.0	–3	1	4	6	11
		2100	0.3	1.1	1.7	2.1	4.2	–1	3	4	6	12
	JJA	**2035**	0.4	0.8	1.1	1.3	2.0	–6	–2	1	5	11
		2065	0.2	1.0	1.4	1.8	3.0	–4	0	2	4	13
		2100	–0.4	0.8	1.3	1.9	3.1	–3	1	4	7	13
	Annual	**2035**	0.5	0.8	1.0	1.3	2.0	–3	–1	2	3	8
		2065	0.6	1.1	1.5	1.7	3.0	–1	1	3	5	13
		2100	–0.3	1.0	1.4	1.9	3.2	0	2	3	7	12
Central North America	**DJF**	**2035**	–0.2	0.6	1.1	1.4	2.5	–7	–2	2	4	10
		2065	0.2	0.9	1.5	1.9	3.3	–4	–1	2	6	18
		2100	–0.2	0.8	1.5	2.1	3.4	–10	0	2	6	15
	JJA	**2035**	0.4	0.7	1.2	1.4	2.2	–8	–1	1	4	8
		2065	0.5	1.0	1.4	2.0	2.9	–8	0	2	4	9
		2100	–0.1	0.8	1.2	1.7	3.4	–6	0	2	6	12
	Annual	**2035**	0.4	0.8	1.0	1.2	2.0	–5	–1	2	3	7
		2065	0.4	0.9	1.4	1.9	2.6	–6	0	2	5	11
		2100	–0.1	0.8	1.4	1.8	2.8	–6	1	2	5	10
Eastern North America	**DJF**	**2035**	–0.5	0.5	1.0	1.5	2.4	–5	0	4	6	9
		2065	–0.1	0.8	1.4	2.1	3.5	–4	2	5	6	16
		2100	–0.3	0.9	1.6	2.3	3.6	–4	0	3	7	16
	JJA	**2035**	0.5	0.7	1.0	1.3	2.2	–3	0	3	5	6
		2065	0.4	1.0	1.3	1.8	3.2	–5	2	3	7	12
		2100	–0.1	0.9	1.2	1.7	3.6	–2	1	3	7	15
	Annual	**2035**	0.3	0.8	1.0	1.2	1.9	–2	1	3	5	6
		2065	0.4	0.9	1.4	1.8	2.9	–1	2	4	6	11
		2100	0.0	0.9	1.2	1.8	3.2	–1	1	3	6	15
Central America												
Central America	**DJF**	**2035**	0.3	0.6	0.7	0.9	1.2	–6	–2	0	3	8
		2065	0.5	0.8	1.0	1.2	1.7	–8	–2	1	5	12
		2100	0.4	0.7	0.9	1.3	2.0	–21	–2	1	5	14
	JJA	**2035**	0.5	0.7	0.8	0.9	1.4	–6	–2	–1	2	7
		2065	0.7	0.9	1.0	1.4	2.0	–10	–4	0	2	7
		2100	0.3	0.7	1.0	1.4	2.2	–11	–2	–1	2	10
	Annual	**2035**	0.5	0.7	0.7	0.8	1.3	–6	–2	0	2	6
		2065	0.6	0.9	1.0	1.3	1.9	–9	–3	0	3	6
		2100	0.4	0.7	1.0	1.3	2.1	–15	–1	0	2	9

(continued on next page)

Table 14.SM.1a (continued)

RCP2.6			Temperature (°C)					Precipitation (%)				
REGION	**MONTH[a]**	**Year**	**min**	**25%**	**50%**	**75%**	**max**	**min**	**25%**	**50%**	**75%**	**max**
Caribbean (land and sea)	**DJF**	**2035**	0.3	0.5	0.6	0.7	1.0	–12	–3	3	5	10
		2065	0.4	0.7	0.8	1.1	1.6	–6	–1	2	7	13
		2100	0.0	0.6	0.8	1.1	1.6	–16	–3	1	6	15
	JJA	**2035**	0.3	0.5	0.5	0.7	1.2	–12	–7	–4	0	11
		2065	0.4	0.7	0.8	1.0	1.6	–15	–6	–3	2	19
		2100	–0.1	0.6	0.8	1.1	1.7	–34	–6	0	3	9
	Annual	**2035**	0.4	0.5	0.6	0.7	1.1	–11	–3	–1	0	7
		2065	0.4	0.7	0.8	1.0	1.6	–9	–5	0	1	0
		2100	–0.1	0.6	0.8	1.1	1.7	–25	–4	0	0	4
South America												
Amazon	**DJF**	**2035**	0.4	0.7	0.8	0.9	1.6	–12	–3	0	1	5
		2065	0.6	0.8	1.0	1.3	2.2	–10	–3	–1	2	6
		2100	0.0	0.8	1.0	1.3	2.5	–20	–4	–1	1	6
	JJA	**2035**	0.6	0.7	0.9	1.1	1.9	–11	–3	0	1	5
		2065	0.8	1.0	1.1	1.6	2.9	–19	–4	0	2	7
		2100	0.5	0.9	1.1	1.5	2.8	–17	–5	–2	1	10
	Annual	**2035**	0.5	0.7	0.8	1.0	1.8	–12	–3	0	1	5
		2065	0.7	0.9	1.1	1.4	2.5	–14	–3	0	1	5
		2100	0.3	0.9	1.1	1.4	2.8	–19	–3	–1	0	5
Northeast Brazil	**DJF**	**2035**	0.2	0.6	0.8	0.9	1.4	–12	–7	–1	5	13
		2065	0.6	0.8	1.0	1.2	1.8	–11	–6	–1	4	16
		2100	0.1	0.7	1.0	1.2	2.2	–14	–4	–2	4	18
	JJA	**2035**	0.1	0.7	0.8	0.9	1.5	–22	–9	–3	1	15
		2065	0.6	0.9	1.1	1.3	2.4	–24	–12	–6	1	16
		2100	0.1	0.8	1.1	1.4	2.0	–31	–11	–4	2	21
	Annual	**2035**	0.4	0.6	0.8	0.9	1.3	–12	–6	–1	4	11
		2065	0.6	0.8	1.1	1.3	2.1	–15	–7	–2	1	15
		2100	0.3	0.8	1.0	1.3	2.0	–19	–5	–2	3	20
West Coast South America	**DJF**	**2035**	0.4	0.6	0.7	0.9	1.1	–6	–1	1	2	5
		2065	0.5	0.8	1.0	1.2	1.6	–8	–1	1	3	5
		2100	0.3	0.7	0.9	1.2	1.9	–7	0	2	5	7
	JJA	**2035**	0.3	0.6	0.8	0.8	1.4	–10	–2	0	2	7
		2065	0.6	0.9	1.0	1.3	1.8	–8	–1	1	2	8
		2100	0.4	0.8	0.9	1.3	2.1	–11	–1	1	4	7
	Annual	**2035**	0.4	0.6	0.7	0.8	1.2	–7	–1	1	2	5
		2065	0.6	0.8	1.0	1.2	1.7	–8	0	1	2	5
		2100	0.3	0.8	0.9	1.2	2.0	–8	0	2	3	6
Southeastern South America	**DJF**	**2035**	0.2	0.5	0.7	0.8	1.4	–6	–1	0	2	8
		2065	0.3	0.6	0.9	1.2	1.8	–6	–1	0	3	11
		2100	0.3	0.7	0.8	1.2	2.0	–7	–2	1	3	9
	JJA	**2035**	0.1	0.3	0.7	0.8	1.1	–13	–3	2	4	14
		2065	0.2	0.5	0.7	1.1	1.6	–15	–1	1	3	14
		2100	0.3	0.5	0.8	1.1	1.7	–17	–4	0	7	17
	Annual	**2035**	0.3	0.5	0.6	0.7	1.3	–7	–1	0	2	10
		2065	0.4	0.7	0.9	1.0	1.7	–7	–1	1	2	13
		2100	0.4	0.7	0.8	1.1	1.8	–9	–1	1	3	9

(continued on next page)

Table 14.SM.1a (continued)

RCP2.6			Temperature (°C)					Precipitation (%)				
REGION	**MONTH**[a]	**Year**	**min**	**25%**	**50%**	**75%**	**max**	**min**	**25%**	**50%**	**75%**	**max**
Europe												
Northern Europe	**DJF**	**2035**	–0.6	0.7	1.4	2.0	3.4	–5	1	4	7	15
		2065	–2.7	1.3	2.1	2.5	4.1	–3	2	6	9	17
		2100	–8.0	1.5	1.8	2.5	3.8	–3	3	5	11	16
	JJA	**2035**	0.0	0.6	1.0	1.3	2.7	–8	0	3	5	10
		2065	–1.1	0.9	1.3	2.0	3.6	–5	0	4	7	20
		2100	–2.5	0.7	1.2	1.8	3.6	–12	2	4	7	14
	Annual	**2035**	0.1	0.6	1.2	1.5	2.4	–6	2	4	5	9
		2065	–1.9	1.3	1.6	2.0	3.2	–3	3	5	7	18
		2100	–5.2	1.1	1.5	2.1	3.3	–4	2	5	8	15
Central Europe	**DJF**	**2035**	–0.2	0.6	1.0	1.5	2.3	–4	–1	2	5	11
		2065	–0.9	0.6	1.3	1.9	3.4	–4	1	3	7	11
		2100	–1.9	1.0	1.3	2.4	2.9	–1	2	4	6	16
	JJA	**2035**	0.4	0.7	1.1	1.4	2.5	–6	–1	2	3	6
		2065	–0.4	0.9	1.4	2.0	3.3	–9	0	2	6	8
		2100	–0.7	0.8	1.3	2.0	3.4	–12	1	4	8	14
	Annual	**2035**	0.1	0.7	1.0	1.3	1.9	–2	0	1	4	9
		2065	–0.5	1.0	1.3	1.8	2.9	–4	0	3	5	9
		2100	–1.4	0.9	1.3	1.9	2.8	–5	2	3	7	12
Southern Europe/ Mediterranean	**DJF**	**2035**	0.2	0.7	0.7	1.0	1.4	–10	–5	–1	2	10
		2065	–0.1	0.8	1.1	1.5	1.9	–12	–7	–1	4	12
		2100	–0.9	0.8	1.1	1.3	1.8	–23	–4	0	4	9
	JJA	**2035**	0.4	1.0	1.1	1.5	2.6	–15	–7	–2	1	9
		2065	0.4	1.0	1.6	1.9	3.6	–17	–7	–2	0	12
		2100	–0.2	1.0	1.4	1.8	3.9	–18	–4	–2	0	18
	Annual	**2035**	0.4	0.8	0.9	1.1	1.7	–9	–4	–2	0	7
		2065	0.2	1.0	1.3	1.5	2.6	–13	–6	–2	1	6
		2100	–0.4	0.9	1.2	1.5	2.7	–21	–5	–1	2	10
Africa												
Sahara	**DJF**	**2035**	0.1	0.7	0.9	1.0	1.3	–37	–6	2	8	77
		2065	0.4	1.0	1.3	1.5	1.8	–27	–11	–3	12	74
		2100	–0.3	0.9	1.2	1.4	1.7	–33	–8	–2	6	90
	JJA	**2035**	0.5	0.9	0.9	1.1	2.0	–18	–5	3	11	44
		2065	0.7	1.0	1.2	1.7	2.9	–26	–5	6	14	56
		2100	0.2	1.0	1.2	1.8	3.0	–41	–4	4	13	60
	Annual	**2035**	0.6	0.8	0.9	1.1	1.6	–17	–5	2	9	36
		2065	0.5	1.1	1.2	1.5	2.3	–26	–6	6	13	44
		2100	–0.1	0.9	1.1	1.5	2.4	–36	–4	1	11	61
West Africa	**DJF**	**2035**	0.4	0.6	0.7	0.9	1.4	–5	–1	1	2	6
		2065	0.6	0.9	1.1	1.3	2.0	–4	–1	1	5	8
		2100	0.4	0.9	1.0	1.3	2.2	–7	0	1	3	7
	JJA	**2035**	0.4	0.6	0.7	0.9	1.4	–4	–1	0	2	6
		2065	0.5	0.9	1.0	1.3	2.0	–7	–1	0	1	4
		2100	0.2	0.8	1.0	1.2	2.3	–8	–2	0	1	4
	Annual	**2035**	0.4	0.6	0.7	0.9	1.3	–4	–1	1	2	5
		2065	0.6	0.9	1.0	1.3	1.9	–6	–1	1	2	4
		2100	0.2	0.8	1.0	1.2	2.2	–7	–1	0	2	4

(continued on next page)

Table 14.SM.1a (continued)

RCP2.6			Temperature (°C)					Precipitation (%)				
REGION	MONTH[a]	Year	min	25%	50%	75%	max	min	25%	50%	75%	max
East Africa	DJF	2035	0.4	0.6	0.7	0.8	1.4	–4	–1	2	5	8
		2065	0.6	0.9	1.0	1.3	1.9	–6	–1	1	6	13
		2100	0.3	0.7	0.9	1.3	2.0	–4	–2	2	5	16
	JJA	2035	0.3	0.6	0.8	0.9	1.3	–7	–3	0	2	10
		2065	0.5	0.9	1.0	1.3	1.8	–11	–5	–2	2	14
		2100	0.0	0.8	1.0	1.2	2.1	–10	–4	–1	2	15
	Annual	2035	0.4	0.6	0.7	0.9	1.3	–5	–1	1	3	9
		2065	0.6	0.8	1.0	1.2	1.8	–8	–2	0	4	13
		2100	0.2	0.7	0.9	1.3	2.0	–7	–2	0	2	14
Southern Africa	DJF	2035	0.4	0.7	0.8	1.0	1.2	–11	–4	–2	0	9
		2065	0.6	1.0	1.1	1.4	2.0	–13	–7	–3	0	4
		2100	0.2	0.8	1.1	1.5	2.1	–13	–7	–3	0	4
	JJA	2035	0.5	0.7	0.8	0.9	1.3	–24	–8	–3	0	10
		2065	0.7	0.9	1.1	1.3	1.9	–30	–9	–5	–2	8
		2100	0.4	0.8	1.0	1.3	2.1	–32	–11	–8	–1	12
	Annual	2035	0.5	0.7	0.8	0.9	1.4	–12	–4	–2	–1	9
		2065	0.7	1.0	1.1	1.3	2.0	–13	–6	–4	0	4
		2100	0.4	0.9	1.1	1.5	2.1	–13	–8	–4	–1	3
West Indian Ocean	DJF	2035	0.3	0.5	0.5	0.7	1.0	–4	0	1	3	10
		2065	0.5	0.6	0.7	1.0	1.4	–6	1	2	4	12
		2100	0.2	0.6	0.7	1.0	1.6	–2	1	3	6	14
	JJA	2035	0.3	0.5	0.5	0.7	1.0	–6	0	1	4	9
		2065	0.4	0.6	0.7	1.0	1.4	–3	0	2	6	12
		2100	0.1	0.6	0.7	1.0	1.6	–3	1	4	7	11
	Annual	2035	0.3	0.5	0.5	0.7	1.0	–4	0	2	2	9
		2065	0.5	0.6	0.7	1.0	1.3	–2	1	2	3	12
		2100	0.2	0.6	0.7	1.0	1.6	–1	2	3	6	11
Asia												
West Asia	DJF	2035	0.3	0.7	0.9	1.2	1.8	–6	1	3	5	12
		2065	0.1	0.9	1.3	1.9	2.6	–13	0	5	9	25
		2100	–0.9	0.8	1.3	1.7	2.7	–13	0	3	8	16
	JJA	2035	0.7	0.8	1.1	1.4	2.2	–14	–3	3	6	42
		2065	0.3	1.1	1.4	1.9	3.1	–17	–4	5	9	38
		2100	0.0	0.9	1.3	1.9	3.4	–31	–1	3	11	67
	Annual	2035	0.6	0.8	1.0	1.2	1.8	–7	–1	2	6	21
		2065	0.2	1.0	1.3	1.8	2.7	–15	1	6	8	20
		2100	–0.4	0.9	1.2	1.7	2.7	–23	1	3	9	31
Central Asia	DJF	2035	0.4	0.8	1.0	1.5	2.2	–9	0	4	7	14
		2065	–0.2	1.0	1.5	2.1	3.6	–10	0	4	12	19
		2100	–1.3	0.7	1.6	2.2	3.3	–13	0	5	10	18
	JJA	2035	0.3	0.8	1.1	1.4	2.0	–14	–1	3	7	16
		2065	0.1	0.9	1.4	2.0	3.5	–9	0	3	8	21
		2100	–0.5	0.6	1.2	1.7	3.8	–19	1	5	10	17
	Annual	2035	0.4	0.9	1.1	1.3	1.8	–9	0	3	6	14
		2065	0.0	1.1	1.4	1.9	3.2	–9	1	4	8	18
		2100	–0.8	1.0	1.4	1.8	3.1	–16	0	5	7	17

(continued on next page)

Table 14.SM.1a (continued)

RCP2.6			Temperature (°C)					Precipitation (%)				
REGION	**MONTH**[a]	**Year**	**min**	**25%**	**50%**	**75%**	**max**	**min**	**25%**	**50%**	**75%**	**max**
Eastern Asia	**DJF**	**2035**	0.3	0.6	1.1	1.4	2.0	–6	–1	2	4	8
		2065	–0.2	1.2	1.5	1.9	3.4	–6	1	4	10	15
		2100	–0.5	1.0	1.4	2.0	3.3	–5	2	6	11	22
	JJA	**2035**	0.2	0.8	0.9	1.1	1.7	–3	0	2	3	7
		2065	0.2	0.9	1.3	1.7	2.7	–1	3	5	6	17
		2100	–0.3	0.8	1.2	1.7	2.8	–4	2	5	7	20
	Annual	**2035**	0.4	0.8	1.0	1.1	1.7	–2	0	2	3	7
		2065	0.2	1.0	1.4	1.7	2.7	–3	3	5	6	16
		2100	–0.4	0.9	1.3	1.7	2.7	–4	2	5	7	21
Tibetan Plateau	**DJF**	**2035**	0.3	0.8	1.0	1.5	2.1	–2	2	4	6	12
		2065	0.1	1.2	1.6	2.1	3.6	–3	4	6	10	17
		2100	–0.9	0.9	1.5	2.0	3.4	–4	4	7	10	22
	JJA	**2035**	0.2	0.8	1.1	1.3	2.4	–3	1	4	6	19
		2065	0.3	1.1	1.4	1.8	3.8	–3	3	5	8	24
		2100	–0.4	0.9	1.3	1.8	3.9	–4	4	6	9	24
	Annual	**2035**	0.4	0.8	1.1	1.4	2.0	–2	2	4	5	16
		2065	0.2	1.1	1.5	1.9	3.3	–2	3	5	9	20
		2100	–0.6	0.9	1.4	1.9	3.2	–4	4	6	9	22
South Asia	**DJF**	**2035**	0.2	0.7	0.8	1.1	1.7	–11	–2	0	5	10
		2065	0.5	0.9	1.2	1.6	2.3	–13	0	3	7	19
		2100	0.1	0.8	1.1	1.5	2.4	–20	2	5	9	27
	JJA	**2035**	0.2	0.5	0.7	0.9	1.2	–3	1	3	5	9
		2065	0.5	0.8	0.9	1.3	1.9	–7	3	5	7	15
		2100	–0.1	0.7	0.9	1.1	2.2	–10	1	5	7	17
	Annual	**2035**	0.2	0.6	0.8	0.9	1.3	–2	0	3	4	8
		2065	0.7	0.9	1.0	1.4	2.0	–5	2	5	7	14
		2100	0.2	0.9	1.0	1.4	2.3	–5	1	5	8	15
North Indian Ocean	**DJF**	**2035**	0.3	0.5	0.5	0.7	1.0	–9	0	4	10	19
		2065	0.3	0.7	0.8	1.1	1.4	–15	–2	5	13	27
		2100	0.3	0.5	0.8	1.1	1.7	–17	1	8	14	28
	JJA	**2035**	0.3	0.5	0.5	0.7	1.0	–6	–1	2	6	18
		2065	0.5	0.7	0.7	1.0	1.5	–8	1	3	8	27
		2100	0.2	0.6	0.7	1.0	1.7	–16	1	4	7	17
	Annual	**2035**	0.3	0.5	0.5	0.6	1.0	–3	–1	3	5	18
		2065	0.5	0.6	0.8	1.1	1.4	–4	–2	5	9	23
		2100	0.3	0.6	0.7	1.1	1.7	–11	1	6	9	23
Southeast Asia (land)	**DJF**	**2035**	0.3	0.5	0.6	0.7	1.2	–5	–1	0	2	10
		2065	0.4	0.7	0.9	1.1	1.6	–5	–1	2	4	9
		2100	0.2	0.7	0.8	1.2	2.0	–5	0	2	4	9
	JJA	**2035**	0.3	0.5	0.6	0.7	1.2	–5	–1	1	3	6
		2065	0.5	0.7	0.8	1.1	1.7	–5	–1	1	5	7
		2100	0.2	0.6	0.8	1.0	1.8	–6	0	1	3	11
	Annual	**2035**	0.3	0.5	0.6	0.7	1.2	–5	–1	0	2	8
		2065	0.5	0.7	0.8	1.1	1.6	–4	0	1	4	7
		2100	0.2	0.7	0.8	1.2	1.9	–5	0	1	4	10

(continued on next page)

Table 14.SM.1a (continued)

RCP2.6			Temperature (°C)					Precipitation (%)				
REGION	**MONTH[a]**	**Year**	**min**	**25%**	**50%**	**75%**	**max**	**min**	**25%**	**50%**	**75%**	**max**
Southeast Asia (sea)	**DJF**	**2035**	0.3	0.5	0.5	0.6	1.1	–5	–1	0	3	6
		2065	0.5	0.6	0.7	1.0	1.5	–2	0	2	4	6
		2100	0.3	0.6	0.7	1.0	1.7	–3	0	2	4	7
	JJA	**2035**	0.2	0.5	0.5	0.6	1.0	–5	0	1	3	6
		2065	0.5	0.6	0.7	0.9	1.5	–3	1	2	3	7
		2100	0.3	0.5	0.7	1.0	1.7	–5	1	2	4	9
	Annual	**2035**	0.3	0.5	0.5	0.6	1.0	–4	0	1	2	4
		2065	0.5	0.6	0.7	1.0	1.5	–2	1	2	4	6
		2100	0.3	0.5	0.7	1.0	1.6	–2	1	2	4	7
Australia												
North Australia	**DJF**	**2035**	0.5	0.6	0.8	1.0	1.7	–17	–6	0	3	8
		2065	0.6	0.9	1.1	1.5	2.4	–23	–9	–2	0	13
		2100	0.4	0.9	1.1	1.5	3.2	–26	–12	–7	0	3
	JJA	**2035**	0.5	0.6	0.7	1.1	1.6	–41	–11	–7	1	4
		2065	0.6	0.9	1.1	1.3	1.8	–47	–15	–6	1	15
		2100	0.5	0.8	1.0	1.2	1.8	–38	–14	–6	1	8
	Annual	**2035**	0.5	0.7	0.8	1.0	1.3	–17	–6	0	2	8
		2065	0.5	0.9	1.1	1.4	1.8	–21	–10	–4	0	10
		2100	0.4	0.8	1.1	1.4	2.4	–24	–11	–6	0	4
South Australia/ New Zealand		**2065**	0.5	0.8	1.0	1.3	1.8	–18	–6	–3	2	6
		2100	0.3	0.8	1.0	1.3	1.9	–23	–10	–3	0	7
	JJA	**2035**	0.3	0.5	0.6	0.7	0.9	–18	–3	0	1	5
		2065	0.4	0.7	0.8	1.0	1.4	–22	–6	–2	3	9
		2100	0.3	0.6	0.7	1.0	1.5	–16	–6	–1	1	9
	Annual	**2035**	0.4	0.5	0.7	0.8	0.9	–16	–4	0	1	4
		2065	0.6	0.7	0.9	1.1	1.4	–18	–5	–1	0	4
		2100	0.3	0.7	0.9	1.0	1.5	–19	–6	–3	0	8
The Pacific												
Northern Tropical Pacific	**DJF**	**2035**	0.3	0.5	0.6	0.6	1.0	–5	0	2	3	7
		2065	0.4	0.6	0.8	1.0	1.4	–5	0	3	4	13
		2100	0.3	0.6	0.8	1.1	1.5	–6	–1	2	4	14
	JJA	**2035**	0.3	0.4	0.5	0.7	1.1	–7	–1	1	2	8
		2065	0.4	0.6	0.7	1.0	1.5	–5	–2	0	3	8
		2100	0.2	0.6	0.7	1.1	1.7	–5	–1	1	3	6
	Annual	**2035**	0.3	0.5	0.6	0.6	1.1	–3	–1	1	2	6
		2065	0.5	0.6	0.8	1.0	1.5	–5	–1	1	3	10
		2100	0.3	0.6	0.7	1.1	1.6	–4	–1	2	3	7
Equatorial Pacific	**DJF**	**2035**	0.2	0.5	0.6	0.8	1.1	–25	3	7	10	78
		2065	0.4	0.7	0.8	1.1	1.6	–25	3	9	19	112
		2100	–0.1	0.6	0.9	1.1	2.2	–25	5	12	27	230
	JJA	**2035**	0.3	0.5	0.6	0.8	1.2	–31	4	10	15	68
		2065	0.4	0.7	0.8	1.0	1.8	–12	7	12	23	81
		2100	0.0	0.6	0.8	1.1	2.0	–16	7	15	25	199
	Annual	**2035**	0.3	0.5	0.6	0.8	1.1	–14	4	8	11	72
		2065	0.4	0.7	0.8	1.0	1.6	–18	7	11	20	98
		2100	0.0	0.6	0.8	1.1	2.1	–21	5	14	25	218

(continued on next page)

Table 14.SM.1a (continued)

RCP2.6			Temperature (°C)					Precipitation (%)				
REGION	**MONTH[a]**	**Year**	**min**	**25%**	**50%**	**75%**	**max**	**min**	**25%**	**50%**	**75%**	**max**
Southern Pacific	**DJF**	**2035**	0.3	0.4	0.5	0.6	0.9	–10	0	1	2	4
		2065	0.4	0.5	0.7	0.9	1.1	–20	–1	2	3	5
		2100	0.3	0.5	0.6	0.9	1.3	–19	–1	2	3	6
	JJA	**2035**	0.1	0.4	0.4	0.6	0.9	–11	–1	0	3	6
		2065	0.3	0.5	0.6	0.8	1.2	–15	–1	1	3	8
		2100	0.3	0.5	0.6	0.8	1.4	–19	–1	1	2	6
	Annual	**2035**	0.3	0.4	0.5	0.6	0.9	–12	0	1	1	4
		2065	0.4	0.5	0.6	0.8	1.2	–18	–1	1	3	7
		2100	0.3	0.5	0.6	0.9	1.4	–19	0	1	2	6
Antarctica												
(land)	**DJF**	**2035**	0.1	0.4	0.6	0.8	1.2	–3	1	2	5	7
		2065	–0.3	0.6	0.9	1.2	1.8	–9	1	3	6	11
		2100	0.0	0.6	0.8	1.3	2.1	–6	1	3	5	12
	JJA	**2035**	–0.3	0.4	0.7	0.9	1.9	0	2	3	6	13
		2065	–0.5	0.6	0.9	1.4	1.9	–2	3	5	10	12
		2100	–0.8	0.7	1.0	1.2	2.3	–4	3	6	9	16
	Annual	**2035**	0.0	0.5	0.6	0.9	1.4	–1	2	3	6	10
		2065	–0.3	0.6	0.8	1.3	1.8	–5	2	4	8	11
		2100	–0.3	0.7	0.9	1.3	2.2	–5	3	5	6	14
(sea)	DJF	**2035**	–0.2	0.1	0.2	0.5	0.7	–1	1	2	3	5
		2065	–0.5	0.3	0.5	0.7	1.0	–1	1	3	4	7
		2100	–0.3	0.3	0.5	0.8	1.2	–2	1	2	3	7
	JJA	**2035**	–0.6	0.3	0.4	0.9	2.0	0	1	2	3	5
		2065	–1.1	0.4	0.7	1.3	2.2	–1	2	3	5	9
		2100	–1.2	0.3	0.7	1.6	2.3	–1	2	3	5	8
	Annual	**2035**	–0.4	0.2	0.3	0.7	1.3	0	1	2	3	5
		2065	–0.7	0.3	0.5	1.0	1.5	–1	2	3	4	8
		2100	–0.7	0.4	0.6	1.2	1.8	–1	1	3	4	7

Notes:

[a] *Precipitation changes cover 6 months; ONDJFM and AMJJAS for winter and summer (northern hemisphere)

Table 14.SM.1b | Temperature and precipitation projections by the CMIP5 global models. The figures shown are averages over SREX regions (Seneviratne et al., 2012) of the projections by a set of 25 global models for the RCP6.0 scenario. Added to the SREX regions are an additional six regions containing the two polar regions, the Caribbean, Indian Ocean and Pacific Island States (see Annex I for further details). The 26 SREX regions are: Alaska/NW Canada (ALA), Eastern Canada/Greenland/Iceland (CGI), Western North America (WNA), Central North America (CNA), Eastern North America (ENA), Central America/Mexico (CAM), Amazon (AMZ), NE Brazil (NEB), West Coast South America (WSA), South-Eastern South America (SSA), Northern Europe (NEU), Central Europe (CEU), Southern Europe/the Mediterranean (MED), Sahara (SAH), Western Africa (WAF), Eastern Africa (EAF), Southern Africa (SAF), Northern Asia (NAS), Western Asia (WAS), Central Asia (CAS), Tibetan Plateau (TIB), Eastern Asia (EAS), Southern Asia (SAS), Southeast Asia (SEA), Northern Australia (NAS) and Southern Australia/New Zealand (SAU). The area-mean temperature and precipitation responses are first averaged for each model over the 1986–2005 period from the historical simulations and the 2016–2035, 2046–2065 and 2081–2100 periods of the RCP6.0 experiments. Based on the difference between these two periods, the table shows the 25th, 50th and 75th percentiles, and the lowest and highest response among the 25 models, for temperature in degrees Celsius and precipitation as a per cent change. Regions in which the middle half (25 to 75%) of this distribution is all of the same sign in the precipitation response are coloured light brown for decreasing and light green for increasing precipitation. Information is provided for land areas contained in the boxes unless otherwise indicated. The temperature responses are averaged over the boreal winter and summer seasons; December, January and February (DJF) and June, July and August (JJA) respectively. The precipitation responses are averaged over half year periods, boreal winter; October, November, December, January, February and March (ONDJFM) and summer; April, May, June, July, August and September (AMJJAS).

RCP6.0			Temperature (°C)					Precipitation (%)				
REGION	**MONTH**[a]	**Year**	**min**	**25%**	**50%**	**75%**	**max**	**min**	**25%**	**50%**	**75%**	**max**
Arctic												
(land)	**DJF**	**2035**	0.1	1.3	1.5	1.9	4.0	–4	6	8	11	21
		2065	1.0	2.5	3.0	4.0	6.4	3	12	16	19	30
		2100	1.1	5.0	5.8	6.8	12.3	8	24	29	35	62
	JJA	**2035**	0.2	0.7	0.8	1.3	2.8	2	3	5	6	20
		2065	0.8	1.3	1.7	2.3	4.1	–1	6	9	11	29
		2100	1.1	2.1	2.8	4.0	6.8	4	11	14	19	42
	Annual	**2035**	0.1	1.2	1.3	1.6	3.6	0	4	6	7	21
		2065	0.8	1.9	2.6	3.1	5.5	2	9	11	14	30
		2100	1.0	3.7	4.5	5.4	9.1	5	16	20	23	50
(sea)	**DJF**	**2035**	0.0	1.9	2.4	2.9	5.9	–8	6	10	14	22
		2065	0.5	3.2	4.3	6.2	9.5	0	11	18	26	37
		2100	0.3	7.1	8.0	10.2	17.1	–2	26	32	41	54
	JJA	**2035**	–0.1	0.4	0.5	0.7	1.6	1	4	6	7	13
		2065	0.3	0.7	1.0	1.4	2.4	–2	8	10	12	19
		2100	0.0	1.4	1.9	2.3	4.8	1	14	17	21	32
	Annual	**2035**	–0.1	1.3	1.7	2.2	4.1	–3	6	7	10	17
		2065	0.5	2.3	3.1	4.1	6.3	–1	10	13	19	24
		2100	0.5	4.5	5.5	7.0	10.6	–1	20	24	27	43
High latitudes												
Canada/ Greenland/ Iceland	**DJF**	**2035**	–0.2	1.1	1.4	1.8	3.4	–2	3	5	7	12
		2065	1.1	2.4	3.1	3.8	4.9	1	9	10	14	21
		2100	1.7	4.4	5.1	6.5	9.9	2	14	19	24	36
	JJA	**2035**	0.3	0.6	0.9	1.2	2.5	–2	2	3	4	7
		2065	0.8	1.2	1.7	2.2	3.9	1	4	6	9	14
		2100	1.0	2.3	3.1	3.6	6.4	4	8	10	14	23
	Annual	**2035**	0.0	1.0	1.1	1.4	2.9	–2	3	4	6	8
		2065	0.8	1.9	2.3	2.8	4.3	2	6	8	11	15
		2100	1.2	3.3	3.9	4.8	7.6	3	11	14	18	25
North Asia	**DJF**	**2035**	0.5	1.0	1.4	2.1	3.2	1	4	7	9	17
		2065	1.3	1.8	3.0	3.3	5.8	1	9	13	15	29
		2100	1.8	4.2	4.8	5.6	8.5	6	17	21	28	47
	JJA	**2035**	0.4	0.8	1.0	1.2	2.4	0	2	3	6	14
		2065	0.5	1.3	1.9	2.3	3.7	0	3	6	10	19
		2100	1.5	2.3	3.1	4.1	6.0	–2	7	10	13	28
	Annual	**2035**	0.5	0.9	1.2	1.7	2.7	1	3	5	7	15
		2065	1.1	1.7	2.3	2.7	4.3	2	5	7	11	23
		2100	1.3	3.1	3.7	4.7	6.6	2	12	14	18	34

(continued on next page)

Table 14.SM.1b (continued)

RCP6.0			Temperature (°C)					Precipitation (%)				
REGION	**MONTH^a**	**Year**	**min**	**25%**	**50%**	**75%**	**max**	**min**	**25%**	**50%**	**75%**	**max**
North America												
Alaska/ NW Canada	**DJF**	**2035**	–0.3	1.1	1.6	2.4	3.5	–7	3	6	10	19
		2065	1.0	2.5	3.0	4.4	5.9	0	6	10	15	27
		2100	3.5	4.6	5.4	6.4	10.4	5	14	18	23	43
	JJA	**2035**	0.3	0.7	1.0	1.3	2.1	–1	2	4	5	16
		2065	0.6	1.3	1.6	2.3	3.3	0	5	7	9	26
		2100	1.4	2.0	3.0	4.1	5.9	1	10	13	18	38
	Annual	**2035**	0.3	0.9	1.2	1.6	2.6	–1	3	5	7	14
		2065	1.3	1.8	2.2	2.9	4.3	3	6	8	11	24
		2100	2.5	3.3	4.0	4.9	7.2	4	13	15	18	37
West North America	**DJF**	**2035**	0.0	0.6	1.0	1.2	2.0	–4	0	2	3	7
		2065	0.7	1.4	2.0	2.4	3.9	–1	2	3	6	10
		2100	1.5	2.4	3.2	3.9	6.1	1	6	7	10	16
	JJA	**2035**	0.3	0.8	1.0	1.1	1.9	–4	0	2	4	8
		2065	0.9	1.5	1.8	2.2	3.1	–5	–2	1	3	9
		2100	1.6	2.5	3.2	4.0	5.0	–6	0	3	5	10
	Annual	**2035**	0.5	0.7	0.9	1.1	1.5	–2	0	1	2	6
		2065	1.0	1.4	1.8	2.2	3.2	–2	1	2	4	7
		2100	1.8	2.4	3.1	3.8	5.0	–1	2	6	8	12
Central North America	**DJF**	**2035**	–0.4	0.6	0.9	1.1	2.1	–4	–1	2	5	11
		2065	0.2	1.3	1.8	2.2	3.4	–13	–3	4	7	13
		2100	1.3	2.3	3.0	4.4	5.7	–9	–1	5	12	19
	JJA	**2035**	0.4	0.6	0.9	1.2	1.8	–6	0	2	3	9
		2065	1.0	1.4	1.9	2.2	2.9	–7	–2	0	5	10
		2100	1.7	2.5	3.1	4.1	5.1	–13	–2	3	7	17
	Annual	**2035**	0.4	0.6	0.9	1.2	1.6	–5	1	1	3	9
		2065	1.0	1.4	1.7	2.1	3.0	–10	–2	2	6	11
		2100	1.8	2.5	3.0	3.7	5.0	–6	–1	3	9	15
Eastern North America	**DJF**	**2035**	–0.3	0.8	1.0	1.2	2.1	–2	0	3	6	13
		2065	0.7	1.4	1.9	2.3	3.8	0	4	7	11	15
		2100	1.5	2.5	3.2	4.4	6.1	0	7	12	14	20
	JJA	**2035**	0.6	0.7	0.9	1.0	1.9	–7	0	3	4	9
		2065	1.1	1.4	1.7	2.1	3.3	–4	1	4	6	10
		2100	1.8	2.4	3.1	3.8	5.7	–4	2	4	7	15
	Annual	**2035**	0.3	0.6	0.9	1.1	2.0	–4	1	3	5	7
		2065	1.0	1.5	1.7	1.9	3.2	–1	2	5	8	11
		2100	1.8	2.5	3.2	3.8	5.2	–1	5	8	10	13
Central America												
Central America	**DJF**	**2035**	0.4	0.5	0.6	0.8	1.1	–8	–2	–1	4	9
		2065	0.9	1.2	1.3	1.6	2.1	–17	–3	–1	4	11
		2100	1.5	2.0	2.2	2.8	3.4	–21	–6	–3	3	11
	JJA	**2035**	0.4	0.6	0.7	0.8	1.3	–5	–2	0	3	6
		2065	1.1	1.2	1.4	1.7	2.2	–12	–5	–2	2	7
		2100	1.9	2.2	2.3	3.1	3.8	–14	–6	–3	3	5
	Annual	**2035**	0.4	0.6	0.7	0.8	1.2	–4	–2	0	2	7
		2065	1.1	1.2	1.4	1.7	2.1	–15	–3	–1	2	5
		2100	1.8	2.1	2.3	2.9	3.5	–17	–5	–3	1	5

(continued on next page)

Table 14.SM.1b (continued)

RCP6.0			Temperature (°C)					Precipitation (%)				
REGION	**MONTH**[a]	**Year**	**min**	**25%**	**50%**	**75%**	**max**	**min**	**25%**	**50%**	**75%**	**max**
Caribbean (land and sea)	**DJF**	**2035**	0.3	0.5	0.5	0.7	1.0	–7	–4	–1	3	6
		2065	0.8	0.9	1.0	1.2	1.7	–9	–5	–3	3	11
		2100	1.0	1.5	1.6	2.2	2.7	–23	–8	–1	5	10
	JJA	**2035**	0.3	0.4	0.5	0.7	1.0	–14	–7	–4	1	9
		2065	0.7	0.9	0.9	1.2	1.8	–19	–9	–6	–3	6
		2100	1.0	1.4	1.7	2.1	2.9	–43	–21	–9	–5	10
	Annual	**2035**	0.3	0.5	0.5	0.7	1.0	–11	–5	–2	1	7
		2065	0.8	0.9	1.0	1.2	1.7	–15	–7	–2	–1	10
		2100	1.0	1.5	1.7	2.2	2.9	–33	–13	–7	–2	8
South America												
Amazon	**DJF**	**2035**	0.5	0.6	0.7	0.9	1.4	–7	–2	0	2	7
		2065	0.9	1.3	1.5	1.7	2.2	–9	–3	–1	2	5
		2100	1.9	2.1	2.4	3.0	3.9	–14	–5	–1	2	5
	JJA	**2035**	0.5	0.7	0.8	1.0	1.6	–6	–1	0	3	7
		2065	1.0	1.3	1.6	1.9	2.9	–9	–5	0	2	11
		2100	1.8	2.2	2.8	3.3	4.2	–12	–5	–2	3	12
	Annual	**2035**	0.5	0.7	0.8	0.9	1.7	–6	–1	1	2	7
		2065	1.1	1.3	1.5	1.8	2.8	–8	–3	0	2	8
		2100	1.9	2.2	2.5	3.3	4.4	–9	–5	0	1	7
Northeast Brazil	**DJF**	**2035**	0.4	0.5	0.7	0.9	1.3	–7	–2	2	5	14
		2065	0.8	1.1	1.5	1.7	2.1	–13	–4	–2	4	23
		2100	1.5	2.0	2.4	2.9	3.7	–13	–6	–4	7	38
	JJA	**2035**	0.3	0.6	0.8	0.9	1.2	–18	–8	–3	1	15
		2065	0.7	1.2	1.5	1.7	2.4	–16	–10	–5	0	21
		2100	1.5	2.1	2.5	2.9	3.5	–39	–14	–9	–6	21
	Annual	**2035**	0.4	0.6	0.8	0.9	1.2	–10	–3	0	3	15
		2065	1.0	1.2	1.5	1.7	2.2	–13	–5	–2	2	23
		2100	1.6	2.1	2.5	3.0	3.6	–13	–9	–5	2	34
West Coast South America	**DJF**	**2035**	0.3	0.6	0.7	0.8	1.0	–5	–1	1	2	3
		2065	0.9	1.1	1.3	1.6	1.9	–6	–1	2	4	6
		2100	1.7	2.0	2.2	2.7	3.2	–8	–1	3	6	12
	JJA	**2035**	0.5	0.6	0.7	0.9	1.2	–8	–2	–1	0	7
		2065	1.0	1.2	1.3	1.6	2.2	–10	–3	0	3	8
		2100	1.8	2.0	2.1	2.8	3.5	–15	–4	1	5	12
	Annual	**2035**	0.4	0.6	0.7	0.8	1.1	–4	–1	0	1	3
		2065	1.0	1.2	1.4	1.6	2.1	–8	–1	2	3	4
		2100	1.8	2.0	2.2	2.7	3.4	–11	–1	3	5	10
Southeastern South America	**DJF**	**2035**	0.1	0.5	0.6	0.8	1.2	–6	–1	1	3	6
		2065	0.9	1.0	1.3	1.4	2.0	–4	1	3	6	9
		2100	1.4	1.9	2.1	2.7	3.5	–9	0	4	6	15
	JJA	**2035**	0.1	0.4	0.6	0.8	1.0	–12	–3	0	5	14
		2065	0.6	0.9	1.1	1.3	1.9	–16	–1	3	6	16
		2100	1.3	1.4	1.7	2.6	3.0	–24	–4	4	14	30
	Annual	**2035**	0.3	0.5	0.6	0.7	1.0	–5	–1	1	3	8
		2065	0.7	1.0	1.1	1.4	1.9	–7	0	3	6	11
		2100	1.4	1.6	2.0	2.7	3.3	–12	–1	3	8	16

(continued on next page)

Table 14.SM.1b (continued)

RCP6.0			Temperature (°C)					Precipitation (%)				
REGION	MONTH[a]	Year	min	25%	50%	75%	max	min	25%	50%	75%	max
Europe												
Northern Europe	DJF	2035	–0.4	0.6	1.4	2.2	2.8	–5	1	5	5	11
		2065	–0.6	1.7	2.5	3.5	5.4	–2	4	8	10	18
		2100	–1.4	3.3	4.0	5.2	6.6	5	9	14	17	29
	JJA	2035	–0.2	0.5	0.8	1.3	2.4	–7	0	3	6	8
		2065	0.2	1.1	1.7	2.3	3.9	–6	1	3	7	16
		2100	–0.8	2.0	2.8	3.8	5.4	–13	2	5	9	21
	Annual	2035	0.1	0.7	1.2	1.5	2.3	–2	0	4	6	9
		2065	–0.1	1.5	1.9	2.6	3.9	–4	4	6	8	17
		2100	–1.3	2.7	3.1	4.2	5.3	–4	8	8	11	25
Central Europe	DJF	2035	–0.4	0.6	0.8	1.3	3.2	–2	1	2	3	10
		2065	0.7	1.5	1.7	2.6	3.7	–1	2	5	7	14
		2100	0.6	2.5	3.1	3.8	5.1	0	5	7	11	18
	JJA	2035	0.3	0.7	0.9	1.2	2.0	–9	–3	0	5	10
		2065	0.6	1.5	1.9	2.6	3.4	–11	–3	0	5	9
		2100	1.3	2.4	3.2	4.2	5.6	–20	–7	–1	3	10
	Annual	2035	0.3	0.7	1.0	1.2	2.0	–4	–1	1	3	9
		2065	0.8	1.4	1.9	2.2	3.1	–4	0	1	5	10
		2100	0.8	2.4	3.1	3.6	4.7	–5	–1	2	6	11
Southern Europe/ Mediterranean	DJF	2035	–0.3	0.5	0.7	0.8	1.3	–11	–4	–3	2	4
		2065	0.4	1.2	1.5	1.7	2.1	–15	–8	–2	0	8
		2100	0.5	1.9	2.3	2.9	3.3	–23	–14	–5	–2	11
	JJA	2035	0.4	0.8	1.1	1.3	2.3	–12	–6	–4	2	7
		2065	1.0	1.6	2.0	2.2	3.6	–14	–10	–6	–3	9
		2100	2.0	2.8	3.5	4.0	6.2	–30	–19	–15	–7	11
	Annual	2035	0.3	0.7	0.9	1.0	1.6	–8	–5	–2	0	5
		2065	0.8	1.5	1.6	1.9	2.6	–13	–9	–4	0	4
		2100	1.3	2.4	2.8	3.2	4.6	–21	–14	–9	–6	5
Africa												
Sahara	DJF	2035	0.2	0.6	0.8	1.0	1.6	–36	–6	0	18	38
		2065	1.0	1.3	1.6	1.9	2.3	–39	–11	0	12	26
		2100	1.4	2.3	2.9	3.2	3.7	–22	–11	1	15	45
	JJA	2035	0.3	0.9	1.0	1.1	1.9	–13	–8	2	11	31
		2065	1.3	1.7	1.9	2.0	3.1	–15	–9	1	14	64
		2100	2.1	2.8	3.1	3.7	5.1	–23	–11	–2	16	101
	Annual	2035	0.6	0.7	0.9	1.1	1.5	–13	–5	0	9	24
		2065	1.3	1.5	1.7	2.0	2.5	–20	–7	0	12	54
		2100	1.8	2.6	3.0	3.5	4.4	–19	–9	–2	17	86
West Africa	DJF	2035	0.4	0.6	0.8	0.9	1.2	–5	0	2	3	6
		2065	1.1	1.3	1.5	1.7	2.3	–7	–1	3	4	12
		2100	1.7	2.2	2.5	3.0	4.1	–8	3	6	7	19
	JJA	2035	0.5	0.6	0.7	0.9	1.3	–6	0	2	3	5
		2065	1.0	1.2	1.4	1.6	2.4	–5	0	2	4	6
		2100	1.9	2.1	2.3	3.0	3.9	–7	1	2	5	13
	Annual	2035	0.5	0.7	0.7	0.9	1.2	–6	0	2	3	4
		2065	1.1	1.3	1.4	1.6	2.4	–5	0	2	4	7
		2100	1.8	2.2	2.3	2.9	4.0	–5	2	4	5	12

(continued on next page)

Table 14.SM.1b (continued)

RCP6.0			Temperature (°C)					Precipitation (%)				
REGION	**MONTH**[a]	**Year**	**min**	**25%**	**50%**	**75%**	**max**	**min**	**25%**	**50%**	**75%**	**max**
East Africa	**DJF**	**2035**	0.4	0.6	0.7	0.8	1.2	–3	0	2	5	10
		2065	0.9	1.2	1.4	1.7	2.2	–4	0	3	7	12
		2100	1.6	2.0	2.3	2.8	3.9	–5	2	9	14	23
	JJA	**2035**	0.5	0.7	0.8	0.9	1.1	–8	–3	0	2	5
		2065	1.0	1.3	1.5	1.8	2.4	–8	–5	–2	3	14
		2100	1.8	2.2	2.6	2.9	3.8	–9	–6	–1	7	24
	Annual	**2035**	0.5	0.6	0.8	0.9	1.1	–4	–1	0	3	8
		2065	1.0	1.2	1.5	1.8	2.3	–5	–2	1	4	13
		2100	1.7	2.1	2.4	2.9	3.9	–6	–1	4	10	21
Southern Africa	**DJF**	**2035**	0.5	0.7	0.8	1.0	1.5	–12	–4	–1	2	8
		2065	1.0	1.3	1.6	2.0	2.2	–13	–7	–2	1	5
		2100	1.9	2.2	2.8	3.3	4.0	–20	–9	–2	0	5
	JJA	**2035**	0.4	0.7	0.8	0.9	1.3	–17	–4	–1	2	11
		2065	1.1	1.4	1.6	1.8	2.3	–15	–10	–6	–1	2
		2100	2.0	2.3	2.7	3.2	3.9	–33	–15	–8	–3	5
	Annual	**2035**	0.5	0.7	0.8	0.9	1.3	–10	–3	–1	1	8
		2065	1.2	1.4	1.7	1.9	2.3	–10	–7	–2	1	4
		2100	2.0	2.4	2.8	3.3	4.0	–18	–10	–3	–1	5
West Indian Ocean	**DJF**	**2035**	0.3	0.5	0.5	0.7	0.9	–2	0	2	4	7
		2065	0.8	0.9	1.0	1.3	1.6	–5	1	3	6	14
		2100	1.4	1.5	1.6	2.3	2.7	–11	0	3	8	18
	JJA	**2035**	0.3	0.5	0.5	0.7	1.0	–4	0	4	5	9
		2065	0.7	0.9	1.0	1.2	1.7	–5	0	3	7	14
		2100	1.4	1.5	1.7	2.2	2.8	–7	0	4	9	17
	Annual	**2035**	0.3	0.5	0.5	0.7	1.0	–2	0	2	3	7
		2065	0.8	0.9	1.0	1.2	1.6	–2	1	3	5	14
		2100	1.4	1.5	1.6	2.2	2.7	–4	0	3	8	18
Asia												
West Asia	DJF	**2035**	0.5	0.7	1.0	1.2	1.6	–7	–2	3	6	13
		2065	0.9	1.4	1.7	2.0	2.9	–9	–1	4	7	10
		2100	1.2	2.5	2.9	3.4	4.9	–17	–3	4	9	19
	JJA	**2035**	0.6	0.8	1.0	1.2	2.2	–16	–4	2	5	22
		2065	1.3	1.5	2.0	2.2	3.4	–16	–4	2	9	11
		2100	2.1	2.6	3.2	3.9	5.6	–22	–11	0	10	22
	Annual	**2035**	0.7	0.7	0.9	1.2	1.6	–7	–2	2	5	12
		2065	1.1	1.5	1.8	2.1	2.7	–10	–2	3	7	9
		2100	1.5	2.5	3.0	3.7	4.7	–18	–5	4	6	15
Central Asia	**DJF**	**2035**	0.3	0.9	1.1	1.5	2.1	–9	2	4	11	14
		2065	0.9	1.6	2.0	2.5	4.0	–14	0	4	9	18
		2100	1.1	2.8	3.3	4.0	5.8	–15	–5	6	12	24
	JJA	**2035**	0.3	0.7	1.0	1.2	2.2	–12	–2	3	7	14
		2065	0.8	1.4	1.8	2.3	3.7	–16	0	4	9	18
		2100	1.6	2.5	3.3	4.2	6.1	–29	–2	2	11	16
	Annual	**2035**	0.6	0.9	1.0	1.2	1.9	–7	0	5	7	13
		2065	0.9	1.6	1.9	2.2	3.0	–10	1	5	8	18
		2100	1.2	2.7	3.3	3.9	5.3	–19	–2	3	8	22

(continued on next page)

Table 14.SM.1b (continued)

RCP6.0			Temperature (°C)					Precipitation (%)				
REGION	MONTH[a]	Year	min	25%	50%	75%	max	min	25%	50%	75%	max
Eastern Asia	DJF	2035	0.0	0.8	1.0	1.3	2.0	–4	0	2	4	11
		2065	0.5	1.5	1.9	2.3	3.1	–12	–1	3	5	13
		2100	1.2	2.7	3.1	3.8	5.0	–7	4	8	12	19
	JJA	2035	0.4	0.6	0.7	0.9	1.5	–3	1	2	4	6
		2065	0.9	1.3	1.6	1.8	2.7	–3	1	2	5	7
		2100	1.4	2.2	2.8	3.6	4.5	2	5	7	10	21
	Annual	2035	0.4	0.7	0.9	1.1	1.4	–2	1	2	3	6
		2065	0.9	1.5	1.6	1.9	2.7	–3	1	3	4	6
		2100	1.2	2.3	2.9	3.5	4.5	0	5	8	10	18
Tibetan Plateau	DJF	2035	0.3	0.8	1.1	1.5	2.1	0	3	6	8	13
		2065	0.9	1.7	2.0	2.6	3.5	–1	6	8	12	17
		2100	1.7	2.9	3.4	4.3	5.8	1	7	12	18	30
	JJA	2035	0.4	0.8	0.9	1.1	2.3	–3	1	3	6	15
		2065	1.1	1.6	1.8	2.1	4.0	–4	3	6	9	23
		2100	1.7	2.7	3.2	3.9	6.2	–4	5	9	14	40
	Annual	2035	0.6	0.7	1.1	1.2	1.8	–1	2	4	6	13
		2065	1.2	1.7	2.0	2.2	3.2	–2	5	6	10	20
		2100	1.5	2.7	3.3	3.9	5.4	1	7	12	14	35
South Asia	DJF	2035	0.3	0.6	0.9	1.1	1.3	–7	–1	5	8	14
		2065	0.8	1.3	1.5	1.8	2.4	–9	–1	7	10	22
		2100	1.9	2.3	2.7	3.3	3.9	–12	5	10	13	51
	JJA	2035	0.2	0.5	0.7	0.8	1.1	–3	1	3	4	7
		2065	0.7	1.0	1.3	1.5	2.2	–5	3	5	6	15
		2100	1.6	1.9	2.2	2.8	3.8	–8	8	11	14	25
	Annual	2035	0.3	0.6	0.8	0.9	1.2	–2	1	4	5	7
		2065	1.1	1.2	1.3	1.7	2.0	–5	2	5	6	16
		2100	1.9	2.2	2.4	3.3	3.8	–5	9	11	14	24
North Indian Ocean	DJF	2035	0.3	0.5	0.6	0.7	1.0	–7	–1	6	10	16
		2065	0.7	0.9	1.0	1.3	1.6	–8	3	8	19	25
		2100	1.3	1.6	1.7	2.3	2.8	–7	8	14	27	57
	JJA	2035	0.3	0.5	0.6	0.7	1.0	–6	–2	1	5	10
		2065	0.8	0.9	1.1	1.3	1.7	–6	0	4	8	21
		2100	1.5	1.6	1.8	2.3	2.9	–13	3	6	13	36
	Annual	2035	0.3	0.5	0.6	0.7	1.0	–3	–1	3	6	12
		2065	0.8	0.9	1.0	1.3	1.6	–4	2	6	9	23
		2100	1.5	1.6	1.7	2.4	2.8	–7	3	12	15	47
Southeast Asia (land)	DJF	2035	0.3	0.5	0.6	0.7	1.0	–8	–1	0	1	4
		2065	0.7	0.9	1.1	1.4	1.8	–6	–2	1	4	8
		2100	1.3	1.7	1.8	2.4	3.2	–9	0	4	8	14
	JJA	2035	0.4	0.5	0.6	0.7	1.1	–5	–2	0	2	5
		2065	0.7	1.0	1.2	1.4	2.0	–5	–2	0	4	6
		2100	1.5	1.8	1.9	2.4	3.4	–6	–1	4	8	13
	Annual	2035	0.4	0.5	0.6	0.7	1.0	–6	–1	0	2	4
		2065	0.8	1.0	1.1	1.4	1.8	–5	–1	1	4	7
		2100	1.5	1.7	1.9	2.5	3.2	–4	0	3	8	14

(continued on next page)

Table 14.SM.1b (continued)

RCP6.0			Temperature (°C)					Precipitation (%)				
REGION	**MONTH[a]**	**Year**	**min**	**25%**	**50%**	**75%**	**max**	**min**	**25%**	**50%**	**75%**	**max**
Southeast Asia (sea)	**DJF**	**2035**	0.3	0.5	0.5	0.6	1.1	–3	–1	0	1	5
		2065	0.7	0.8	1.0	1.2	1.7	–5	–1	2	4	7
		2100	1.4	1.5	1.5	2.1	2.9	–5	0	3	6	14
	JJA	**2035**	0.2	0.5	0.5	0.6	1.0	–4	0	1	2	5
		2065	0.8	0.8	1.0	1.2	1.7	–4	0	2	4	9
		2100	1.4	1.5	1.6	2.1	2.9	–4	2	3	5	13
	Annual	**2035**	0.2	0.5	0.5	0.6	1.0	–3	0	1	2	3
		2065	0.7	0.9	0.9	1.2	1.7	–2	–1	2	4	7
		2100	1.4	1.5	1.6	2.1	2.8	–2	1	3	5	13
Australia												
North Australia	**DJF**	**2035**	0.3	0.6	0.7	1.0	1.9	–17	–5	–3	1	9
		2065	0.9	1.4	1.5	1.9	2.7	–16	–4	–1	3	10
		2100	1.3	2.2	2.6	3.0	4.0	–30	–8	–1	6	18
	JJA	**2035**	0.1	0.6	0.8	1.1	1.3	–36	–12	–5	2	17
		2065	0.9	1.4	1.5	1.9	2.1	–46	–12	–3	2	14
		2100	1.8	2.1	2.8	3.1	3.5	–57	–18	–4	5	15
	Annual	**2035**	0.4	0.6	0.8	1.0	1.4	–14	–8	–3	1	9
		2065	1.0	1.3	1.6	1.8	2.2	–18	–5	–1	3	9
		2100	1.5	2.3	2.7	3.1	3.6	–29	–9	0	3	15
South Australia/ New Zealand	**DJF**	**2035**	0.5	0.6	0.7	0.9	1.4	–22	–5	–1	1	6
		2065	0.8	1.3	1.4	1.6	2.1	–24	–6	–1	3	10
		2100	1.6	1.9	2.3	2.9	3.7	–19	–5	–1	2	11
	JJA	**2035**	0.4	0.5	0.7	0.7	0.9	–16	–4	–1	1	4
		2065	0.6	1.0	1.2	1.4	1.6	–27	–6	–1	2	5
		2100	1.3	1.7	2.1	2.3	2.8	–28	–9	–2	3	10
	Annual	**2035**	0.5	0.6	0.7	0.8	1.0	–17	–3	–1	0	5
		2065	0.9	1.1	1.4	1.5	1.7	–24	–4	–1	3	4
		2100	1.5	1.9	2.3	2.5	2.9	–23	–5	–1	2	9
The Pacific												
Northern Tropical Pacific	**DJF**	**2035**	0.3	0.4	0.5	0.6	0.9	–4	–1	0	2	7
		2065	0.7	0.8	1.0	1.2	1.6	–5	–1	2	4	7
		2100	1.2	1.5	1.7	2.2	2.8	–9	–1	2	6	13
	JJA	**2035**	0.3	0.4	0.5	0.6	1.0	–7	–2	1	3	6
		2065	0.7	0.9	0.9	1.2	1.8	–5	–1	1	4	6
		2100	1.3	1.4	1.6	2.3	3.0	–10	–2	2	6	12
	Annual	**2035**	0.3	0.5	0.5	0.6	0.9	–4	–2	0	2	6
		2065	0.7	0.9	1.0	1.2	1.7	–4	–1	1	3	6
		2100	1.3	1.4	1.7	2.3	2.9	–9	0	2	5	9
Equatorial Pacific	**DJF**	**2035**	0.4	0.5	0.6	0.8	1.0	–2	1	6	14	41
		2065	0.5	1.0	1.1	1.4	1.9	–6	9	14	20	133
		2100	1.0	1.6	1.8	2.4	3.3	–11	7	18	32	250
	JJA	**2035**	0.4	0.5	0.6	0.7	1.1	–1	5	9	13	21
		2065	0.7	0.9	1.1	1.3	2.1	–15	11	16	25	87
		2100	1.2	1.5	1.8	2.3	3.4	–3	21	29	42	164
	Annual	**2035**	0.4	0.5	0.6	0.7	0.9	–1	5	7	12	33
		2065	0.6	1.0	1.1	1.3	1.9	–1	9	14	21	113
		2100	1.2	1.6	1.8	2.3	3.1	–5	16	22	31	215

(continued on next page)

Table 14.SM.1b (continued)

RCP6.0			Temperature (°C)					Precipitation (%)				
REGION	MONTH[a]	Year	min	25%	50%	75%	max	min	25%	50%	75%	max
Southern Pacific	DJF	2035	0.2	0.4	0.5	0.6	0.8	–7	–1	1	2	4
		2065	0.6	0.8	0.9	1.1	1.5	–18	–2	2	3	5
		2100	1.0	1.3	1.5	1.8	2.4	–32	–4	3	5	8
	JJA	2035	0.2	0.4	0.5	0.6	0.9	–7	–1	1	3	7
		2065	0.6	0.8	0.9	1.0	1.5	–15	–2	1	4	6
		2100	1.1	1.3	1.5	1.8	2.5	–24	–2	0	4	9
	Annual	2035	0.2	0.4	0.5	0.5	0.8	–8	0	1	2	4
		2065	0.7	0.8	0.8	1.1	1.5	–18	–1	2	3	5
		2100	1.1	1.3	1.5	1.8	2.4	–29	–2	2	4	9
Antarctica												
(land)	DJF	2035	–0.1	0.3	0.5	0.7	1.2	–6	1	2	4	7
		2065	0.1	1.0	1.3	1.5	2.1	–6	2	5	7	13
		2100	0.7	1.7	2.2	2.8	3.7	–6	5	6	13	22
	JJA	2035	–0.4	0.2	0.6	0.8	1.7	–2	1	3	5	10
		2065	–0.1	1.1	1.4	1.7	2.2	0	5	8	11	15
		2100	0.0	1.9	2.1	3.0	3.9	2	10	12	20	29
	Annual	2035	–0.3	0.4	0.5	0.8	1.2	–3	1	3	5	9
		2065	0.0	1.1	1.2	1.6	2.2	–3	3	7	9	14
		2100	0.5	1.7	2.0	2.9	3.8	–2	7	10	17	25
(sea)	DJF	2035	–0.5	0.1	0.3	0.4	0.8	0	1	3	3	4
		2065	–0.4	0.4	0.6	0.8	1.2	–1	2	4	5	7
		2100	–0.3	0.7	1.0	1.4	2.2	2	4	7	10	12
	JJA	2035	–1.0	0.2	0.5	0.8	1.8	0	2	2	4	6
		2065	–0.8	0.5	1.0	1.6	2.2	1	3	5	7	9
		2100	–0.4	1.1	1.6	2.8	3.8	4	6	7	12	16
	Annual	2035	–0.7	0.1	0.4	0.6	1.2	0	1	2	3	5
		2065	–0.6	0.5	0.7	1.2	1.8	1	2	4	6	8
		2100	–0.3	1.0	1.3	2.1	3.0	4	5	7	11	13

Notes:

[a] *Precipitation changes cover 6 months; ONDJFM and AMJJAS for winter and summer (northern hemisphere)

Table 14.SM.1c | Temperature and precipitation projections by the CMIP5 global models. The figures shown are averages over SREX regions (Seneviratne et al., 2012) of the projections by a set of 39 global models for the RCP8.5 scenario. Added to the SREX regions are an additional six regions containing the two polar regions, the Caribbean, Indian Ocean and Pacific Island States (see Annex I for further details). The 26 SREX regions are: Alaska/NW Canada (ALA), Eastern Canada/Greenland/Iceland (CGI), Western North America (WNA), Central North America (CNA), Eastern North America (ENA), Central America/Mexico (CAM), Amazon (AMZ), NE Brazil (NEB), West Coast South America (WSA), South-Eastern South America (SSA), Northern Europe (NEU), Central Europe (CEU), Southern Europe/the Mediterranean (MED), Sahara (SAH), Western Africa (WAF), Eastern Africa (EAF), Southern Africa (SAF), Northern Asia (NAS), Western Asia (WAS), Central Asia (CAS), Tibetan Plateau (TIB), Eastern Asia (EAS), Southern Asia (SAS), Southeast Asia (SEA), Northern Australia (NAS) and Southern Australia/New Zealand (SAU). The area mean temperature and precipitation responses are first averaged for each model over the 1986–2005 period from the historical simulations and the 2016–2035, 2046–2065 and 2081–2100 periods of the RCP8.5 experiments. Based on the difference between these two periods, the table shows the 25th, 50th and 75th percentiles, and the lowest and highest response among the 39 models, for temperature in degrees Celsius and precipitation as a per cent change. Regions in which the middle half (25 to 75%) of this distribution is all of the same sign in the precipitation response are colored light brown for decreasing and light green for increasing precipitation. Information is provided for land areas contained in the boxes unless otherwise indicated. The temperature responses are averaged over the boreal winter and summer seasons; December, January and February (DJF) and June, July and August (JJA) respectively. The precipitation responses are averaged over half year periods, boreal winter; October, November, December, January, February and March (ONDJFM) and summer; April, May, June, July, August and September (AMJJAS).

RCP8.5			**Temperature (°C)**					**Precipitation (%)**				
REGION	**MONTH**[a]	**Year**	**min**	**25%**	**50%**	**75%**	**max**	**min**	**25%**	**50%**	**75%**	**max**
Arctic												
(land)	**DJF**	**2035**	0.7	1.7	2.1	2.5	4.3	0	8	10	14	19
		2065	2.4	4.5	5.3	6.2	10.1	11	21	23	29	51
		2100	5.3	8.6	9.6	12.4	16.8	27	40	47	64	93
	JJA	**2035**	0.4	0.8	1.1	1.4	2.8	0	4	6	8	23
		2065	1.1	2.0	2.6	3.3	5.9	3	11	13	18	41
		2100	2.6	4.0	4.7	6.1	9.2	9	20	25	32	61
	Annual	**2035**	0.5	1.4	1.7	2.0	3.7	2	6	7	10	22
		2065	1.7	3.7	4.1	4.6	7.8	6	15	17	21	45
		2100	4.4	6.3	7.5	8.6	12.4	17	30	34	40	74
(sea)	**DJF**	**2035**	0.7	2.4	3.1	3.5	6.3	–2	7	11	15	23
		2065	2.0	6.3	7.4	8.7	14.2	2	21	27	32	47
		2100	7.8	12.2	13.5	17.4	23.3	19	44	53	61	83
	JJA	**2035**	0.2	0.5	0.7	0.9	1.7	–2	5	6	8	15
		2065	0.4	1.4	1.6	2.1	3.8	–2	12	16	18	30
		2100	1.3	2.6	3.3	4.8	8.1	0	23	27	34	45
	Annual	**2035**	0.6	1.9	2.3	2.5	4.4	1	6	9	11	19
		2065	1.4	4.5	5.1	6.3	9.0	0	16	20	24	39
		2100	5.2	7.7	9.2	11.5	14.8	11	32	38	46	63
High latitudes												
Canada/ Greenland/ Iceland	**DJF**	**2035**	0.6	1.5	2.0	2.2	3.4	1	4	6	8	13
		2065	2.6	4.2	4.8	5.9	7.9	3	12	15	21	29
		2100	4.6	7.2	8.7	10.8	13.3	13	25	29	41	55
	JJA	**2035**	0.5	0.9	1.1	1.3	2.7	0	3	4	6	11
		2065	1.2	2.3	2.6	3.1	5.6	5	7	9	12	21
		2100	2.2	4.1	4.6	5.9	9.0	7	14	16	21	35
	Annual	**2035**	0.6	1.3	1.5	1.7	2.9	1	4	5	6	10
		2065	1.8	3.2	3.6	4.2	6.3	4	10	12	16	22
		2100	4.2	5.6	6.4	7.9	10.5	11	19	22	28	40
North Asia	**DJF**	**2035**	0.6	1.3	1.9	2.2	4.0	1	6	8	11	23
		2065	2.4	3.5	4.1	5.2	7.9	8	14	19	24	45
		2100	4.7	6.9	7.9	9.6	12.4	18	28	33	46	74
	JJA	**2035**	0.4	0.9	1.2	1.5	2.9	–1	3	5	6	14
		2065	1.3	2.0	2.9	3.8	5.3	1	6	9	12	26
		2100	2.6	4.1	5.1	7.0	8.3	0	9	14	19	37
	Annual	**2035**	0.6	1.2	1.5	2.0	3.3	1	5	5	8	17
		2065	1.9	2.8	3.6	4.2	6.1	6	9	12	15	32
		2100	3.9	5.2	6.5	7.6	9.8	11	19	22	26	50

(continued on next page)

Table 14.SM.1c (continued)

RCP8.5			Temperature (°C)					Precipitation (%)				
REGION	**MONTH**[a]	**Year**	**min**	**25%**	**50%**	**75%**	**max**	**min**	**25%**	**50%**	**75%**	**max**
North America												
Alaska/ NW Canada	**DJF**	**2035**	–0.8	1.6	2.1	3.2	4.8	–5	4	6	11	17
		2065	2.9	4.5	5.1	6.3	8.8	2	10	17	21	37
		2100	5.3	7.7	9.3	11.8	14.8	12	22	33	43	73
	JJA	**2035**	0.2	0.8	1.2	1.5	2.6	–1	3	6	7	16
		2065	0.9	2.0	2.7	3.4	5.4	4	10	13	14	32
		2100	2.3	3.8	4.9	6.0	8.3	10	17	23	27	47
	Annual	**2035**	0.4	1.3	1.7	2.3	3.0	–2	4	5	8	16
		2065	2.3	3.3	3.7	4.6	6.1	7	10	14	18	32
		2100	4.1	5.6	6.9	8.5	10.5	11	23	26	32	51
West North America	**DJF**	**2035**	0.2	1.0	1.3	1.7	2.5	–4	1	3	4	8
		2065	1.0	2.5	3.0	3.4	5.0	–2	3	6	8	20
		2100	2.7	4.1	5.0	6.1	8.7	–3	8	12	13	27
	JJA	**2035**	0.6	1.0	1.3	1.5	2.2	–4	0	2	3	8
		2065	1.6	2.3	2.9	3.7	4.4	–7	–1	2	4	15
		2100	3.5	4.7	5.2	6.5	7.8	–16	–4	0	5	20
	Annual	**2035**	0.5	1.0	1.2	1.5	2.0	–2	1	2	4	7
		2065	1.7	2.4	2.8	3.4	4.2	–2	1	4	6	18
		2100	3.1	4.2	5.0	6.1	7.7	–2	3	6	8	25
Central North America	**DJF**	**2035**	0.0	1.0	1.2	1.7	2.3	–6	–2	2	6	11
		2065	1.1	2.2	2.7	3.6	4.8	–12	1	7	10	17
		2100	2.9	4.1	5.0	5.9	7.7	–18	4	11	17	28
	JJA	**2035**	0.5	1.1	1.2	1.4	2.3	–9	–2	1	3	9
		2065	1.7	2.3	2.9	3.4	4.6	–19	–1	3	6	13
		2100	3.6	4.6	5.4	6.2	8.0	–19	–4	3	7	16
	Annual	**2035**	0.6	1.0	1.2	1.5	2.0	–5	–1	2	4	10
		2065	1.7	2.4	2.8	3.3	4.2	–10	1	4	7	15
		2100	3.4	4.4	5.1	5.7	7.4	–14	0	7	9	16
Eastern North America	**DJF**	**2035**	0.0	0.9	1.4	1.6	2.7	–3	1	4	6	11
		2065	1.8	2.4	3.0	3.7	5.1	–1	6	9	15	20
		2100	3.2	4.6	5.5	6.4	8.6	–2	12	17	24	32
	JJA	**2035**	0.4	0.9	1.1	1.4	2.3	–7	1	3	5	10
		2065	1.4	2.4	2.8	3.3	4.8	–8	2	5	7	12
		2100	2.8	4.2	5.1	5.9	8.3	–11	1	7	9	25
	Annual	**2035**	0.4	0.9	1.2	1.4	2.1	–3	1	4	5	7
		2065	1.7	2.5	2.8	3.3	4.5	1	4	7	10	14
		2100	3.5	4.3	5.1	6.0	7.6	0	6	11	15	22
Central America												
Central America	**DJF**	**2035**	0.5	0.7	0.9	1.0	1.3	–12	–4	0	3	13
		2065	1.4	1.9	2.1	2.4	2.9	–17	–6	–2	1	12
		2100	2.3	3.3	3.9	4.6	5.3	–27	–11	–5	4	13
	JJA	**2035**	0.6	0.8	0.9	1.1	1.5	–14	–4	–1	3	9
		2065	1.6	2.0	2.3	2.6	3.2	–14	–7	–5	0	11
		2100	2.9	3.6	4.2	5.1	6.0	–27	–14	–11	–1	16
	Annual	**2035**	0.5	0.8	0.9	1.1	1.4	–11	–3	–1	3	6
		2065	1.5	1.9	2.1	2.6	3.0	–14	–7	–5	1	7
		2100	2.9	3.5	3.9	4.9	5.5	–26	–12	–8	0	11

(continued on next page)

Table 14.SM.1c (continued)

RCP8.5			Temperature (°C)					Precipitation (%)				
REGION	**MONTH[a]**	**Year**	**min**	**25%**	**50%**	**75%**	**max**	**min**	**25%**	**50%**	**75%**	**max**
Caribbean (land and sea)	**DJF**	**2035**	0.3	0.6	0.7	0.9	1.1	−11	−3	0	5	7
		2065	1.0	1.4	1.6	1.9	2.4	−13	−5	−1	3	10
		2100	2.0	2.5	3.0	3.6	4.0	−39	−13	−5	3	19
	JJA	**2035**	0.3	0.6	0.7	0.8	1.2	−17	−9	−6	−2	16
		2065	1.2	1.4	1.6	1.9	2.5	−34	−24	−12	−5	13
		2100	2.2	2.4	2.9	3.4	4.2	−60	−39	−24	−17	2
	Annual	**2035**	0.4	0.6	0.7	0.9	1.1	−14	−5	−2	−1	11
		2065	1.1	1.4	1.6	1.9	2.5	−19	−14	−8	−2	10
		2100	2.1	2.5	3.0	3.6	4.1	−50	−23	−16	−7	9
South America												
Amazon	**DJF**	**2035**	0.5	0.8	0.9	1.1	1.8	−12	−4	−1	1	5
		2065	1.3	1.9	2.3	2.8	3.9	−20	−6	−1	2	7
		2100	1.9	3.5	4.3	5.3	6.3	−26	−11	−3	3	16
	JJA	**2035**	0.5	0.8	1.0	1.2	2.1	−17	−3	−1	1	6
		2065	1.5	2.1	2.6	2.9	4.2	−28	−6	−2	2	13
		2100	3.0	3.8	4.7	5.7	7.6	−44	−11	−5	1	12
	Annual	**2035**	0.5	0.8	1.1	1.2	1.9	−12	−3	−1	1	4
		2065	1.4	2.0	2.5	2.8	4.1	−23	−5	−1	2	8
		2100	2.4	3.7	4.3	5.7	7.0	−33	−11	−2	1	14
Northeast Brazil	**DJF**	**2035**	0.5	0.7	0.9	1.1	1.5	−13	−6	−1	3	9
		2065	1.2	1.8	2.1	2.4	3.2	−16	−9	0	4	39
		2100	2.1	3.4	3.8	4.6	5.6	−29	−11	−4	5	48
	JJA	**2035**	0.4	0.7	0.9	1.1	1.3	−22	−10	−4	1	17
		2065	1.2	1.8	2.2	2.5	3.1	−24	−13	−8	−3	32
		2100	2.6	3.6	4.1	4.8	5.7	−41	−25	−18	−5	37
	Annual	**2035**	0.5	0.8	1.0	1.1	1.5	−14	−6	0	2	7
		2065	1.3	1.9	2.2	2.6	3.1	−16	−10	−2	1	38
		2100	2.5	3.5	4.1	4.8	5.6	−31	−14	−6	6	45
West Coast South America	**DJF**	**2035**	0.4	0.7	0.8	1.0	1.3	−5	0	1	3	6
		2065	1.6	1.8	2.1	2.4	2.9	−8	−1	2	4	10
		2100	2.6	3.2	3.8	4.7	5.2	−11	1	3	7	14
	JJA	**2035**	0.5	0.8	0.9	1.0	1.4	−9	−2	0	2	6
		2065	1.5	1.9	2.2	2.5	3.0	−13	−3	−1	3	8
		2100	2.9	3.3	3.8	4.8	5.3	−20	−6	−1	3	12
	Annual	**2035**	0.5	0.7	0.9	1.0	1.4	−6	−1	1	2	5
		2065	1.5	1.8	2.1	2.4	2.9	−9	−1	1	3	8
		2100	2.8	3.3	3.8	4.8	5.1	−14	−1	1	6	11
Southeastern South America	**DJF**	**2035**	0.1	0.6	0.8	1.0	1.5	−4	−1	2	4	13
		2065	1.0	1.7	1.9	2.2	3.5	−7	−1	3	7	14
		2100	1.9	3.0	3.8	4.4	6.2	−10	1	6	11	24
	JJA	**2035**	0.2	0.5	0.7	0.9	1.2	−12	−1	1	4	22
		2065	0.9	1.5	1.8	2.1	2.7	−21	−2	4	8	27
		2100	1.9	2.8	3.4	3.9	4.6	−24	−3	7	21	41
	Annual	**2035**	0.2	0.6	0.8	0.9	1.4	−6	0	1	3	14
		2065	1.1	1.7	1.9	2.2	3.1	−11	−1	3	8	18
		2100	1.9	3.0	3.6	4.2	5.3	−11	1	7	14	27

(continued on next page)

Table 14.SM.1c (continued)

RCP8.5			Temperature (°C)					Precipitation (%)				
REGION	MONTH[a]	Year	min	25%	50%	75%	max	min	25%	50%	75%	max
Europe												
Northern Europe	DJF	2035	–0.1	1.1	1.5	2.4	3.5	–3	3	5	7	16
		2065	–0.6	2.9	3.4	4.7	6.8	2	8	11	15	26
		2100	2.6	5.3	6.1	7.5	10.4	8	15	20	29	42
	JJA	2035	0.3	0.8	1.1	1.5	2.8	–4	1	4	7	9
		2065	0.1	1.9	2.5	3.2	4.9	–8	1	4	10	19
		2100	2.1	3.5	4.5	5.8	7.6	–17	2	8	12	26
	Annual	2035	0.3	0.9	1.2	1.8	2.7	–3	3	4	6	12
		2065	–0.4	2.4	2.9	3.5	4.7	–2	6	8	11	23
		2100	1.9	4.3	5.0	6.3	7.7	–2	12	14	18	34
Central Europe	DJF	2035	–0.3	0.6	1.0	1.8	3.3	–7	1	4	6	15
		2065	1.2	2.1	2.6	3.8	5.8	1	4	7	11	19
		2100	3.4	4.2	4.9	5.9	8.2	–4	7	11	18	29
	JJA	2035	0.4	1.0	1.3	1.6	2.8	–8	–2	1	5	8
		2065	1.3	2.3	2.7	3.6	5.5	–18	–6	–2	4	10
		2100	2.8	4.3	5.3	6.6	8.5	–28	–16	–8	–2	11
	Annual	2035	0.5	0.9	1.1	1.6	2.5	–4	0	3	5	11
		2065	1.0	2.2	2.7	3.3	4.6	–5	0	3	6	10
		2100	3.1	4.0	4.8	5.8	7.1	–8	–3	0	7	14
Southern Europe/ Mediterranean	DJF	2035	0.0	0.6	0.9	1.1	1.7	–10	–4	–1	1	8
		2065	0.7	1.8	2.2	2.7	3.1	–24	–9	–4	–2	6
		2100	2.4	3.3	3.8	4.6	5.7	–35	–18	–12	–7	0
	JJA	2035	0.6	1.1	1.4	1.6	2.7	–15	–7	–3	1	8
		2065	2.1	2.6	3.3	3.7	5.6	–31	–18	–12	–7	9
		2100	3.9	4.9	6.0	6.8	9.3	–58	–35	–24	–17	–4
	Annual	2035	0.4	1.0	1.1	1.3	2.0	–8	–4	–2	0	5
		2065	1.6	2.3	2.5	3.0	4.1	–23	–11	–7	–5	1
		2100	3.3	4.1	4.5	5.6	6.9	–35	–23	–19	–13	–2
Africa												
Sahara	DJF	2035	0.2	0.9	1.1	1.2	1.6	–35	–13	–1	8	67
		2065	1.3	2.2	2.5	2.9	3.2	–35	–15	–2	15	128
		2100	3.2	3.8	4.4	5.3	6.4	–49	–26	–10	19	319
	JJA	2035	0.4	1.0	1.2	1.4	2.0	–24	–3	6	19	34
		2065	1.9	2.5	2.9	3.3	4.5	–23	–7	5	16	98
		2100	3.4	4.6	5.0	6.5	7.8	–41	–14	9	25	147
	Annual	2035	0.5	1.0	1.1	1.3	1.7	–25	–3	5	13	28
		2065	1.8	2.4	2.7	3.2	3.7	–18	–8	4	13	84
		2100	3.8	4.3	4.6	6.1	6.5	–42	–15	–2	18	155
West Africa	DJF	2035	0.5	0.8	1.0	1.1	1.6	–6	0	2	4	8
		2065	1.5	2.0	2.3	2.7	3.4	–2	2	4	9	13
		2100	3.1	3.7	4.0	4.9	6.1	–8	3	7	13	23
	JJA	2035	0.6	0.8	0.8	1.0	1.5	–6	–1	1	2	8
		2065	1.6	1.9	2.0	2.8	3.3	–10	–1	1	4	9
		2100	2.2	3.5	3.9	5.3	5.9	–13	–2	2	6	13
	Annual	2035	0.7	0.8	0.9	1.1	1.5	–4	0	1	3	8
		2065	1.6	1.9	2.1	2.7	3.3	–8	1	2	6	8
		2100	2.6	3.6	4.0	5.1	5.9	–10	0	5	8	16

(continued on next page)

Table 14.SM.1c (continued)

RCP8.5			Temperature (°C)					Precipitation (%)				
REGION	**MONTH**[a]	**Year**	**min**	**25%**	**50%**	**75%**	**max**	**min**	**25%**	**50%**	**75%**	**max**
East Africa	**DJF**	**2035**	0.6	0.8	0.9	1.1	1.6	–5	–1	2	6	10
		2065	1.3	1.8	2.2	2.5	3.2	–8	1	6	12	23
		2100	2.8	3.4	3.9	4.6	5.6	–11	6	15	22	35
	JJA	**2035**	0.6	0.8	0.9	1.2	1.5	–8	–4	–1	3	11
		2065	1.3	2.0	2.1	2.8	3.2	–12	–6	0	5	21
		2100	1.8	3.5	4.1	5.2	5.6	–15	–5	4	13	33
	Annual	**2035**	0.6	0.7	0.9	1.1	1.5	–6	–2	0	3	9
		2065	1.6	1.9	2.2	2.7	3.2	–9	–1	4	7	20
		2100	2.4	3.5	4.0	5.0	5.6	–11	0	11	16	34
Southern Africa	**DJF**	**2035**	0.5	0.8	1.0	1.2	1.5	–10	–4	–2	0	5
		2065	1.5	2.0	2.5	2.8	3.3	–19	–8	–4	–1	5
		2100	3.1	3.8	4.4	5.2	6.2	–26	–12	–5	–3	2
	JJA	**2035**	0.5	0.8	1.0	1.1	1.6	–19	–9	–4	–1	5
		2065	1.9	2.1	2.4	2.7	3.3	–31	–18	–11	–6	6
		2100	3.3	4.0	4.5	5.2	6.1	–48	–27	–18	–13	1
	Annual	**2035**	0.6	0.9	1.1	1.2	1.6	–11	–4	–2	0	2
		2065	1.7	2.2	2.5	2.9	3.4	–19	–9	–5	–2	5
		2100	3.3	4.1	4.5	5.5	6.3	–24	–14	–9	–5	3
West Indian Ocean	**DJF**	**2035**	0.3	0.6	0.7	0.8	1.1	–4	–1	0	3	10
		2065	1.1	1.4	1.6	1.9	2.2	–6	–2	2	5	17
		2100	2.1	2.6	2.9	3.5	4.1	–10	–1	4	11	25
	JJA	**2035**	0.3	0.6	0.7	0.8	1.2	–8	–2	2	5	9
		2065	1.0	1.4	1.6	1.8	2.2	–13	–1	2	5	17
		2100	1.7	2.5	2.9	3.5	4.3	–10	–1	4	7	24
	Annual	**2035**	0.3	0.6	0.7	0.7	1.1	–3	0	1	3	9
		2065	1.1	1.4	1.5	1.8	2.2	–7	–1	1	5	16
		2100	2.0	2.6	2.9	3.5	4.2	–6	–2	4	9	24
Asia												
West Asia	**DJF**	**2035**	0.5	0.8	1.2	1.4	1.9	–10	–2	4	6	19
		2065	1.1	2.2	2.6	3.2	4.1	–14	0	3	6	36
		2100	3.1	4.0	4.6	5.6	6.8	–17	–2	4	9	45
	JJA	**2035**	0.5	1.0	1.2	1.4	2.4	–10	–4	1	7	24
		2065	1.8	2.6	3.1	3.6	4.8	–23	–7	–4	5	52
		2100	3.8	4.6	5.3	6.6	8.2	–38	–15	–8	11	84
	Annual	**2035**	0.5	1.0	1.1	1.4	2.0	–8	–2	3	7	22
		2065	1.6	2.5	2.8	3.4	4.1	–14	–5	0	6	24
		2100	3.7	4.5	5.0	6.2	6.9	–21	–7	–1	8	40
Central Asia	**DJF**	**2035**	0.4	0.9	1.3	1.6	2.6	–11	0	3	7	17
		2065	0.8	2.4	3.0	3.6	5.6	–13	–3	3	13	31
		2100	3.5	4.3	5.3	6.3	8.0	–20	–5	7	14	41
	JJA	**2035**	0.5	1.0	1.3	1.6	2.4	–15	–1	4	9	24
		2065	1.9	2.4	3.0	3.7	5.1	–27	–5	1	8	18
		2100	3.2	4.5	5.7	6.5	8.6	–30	–7	1	6	26
	Annual	**2035**	0.4	1.0	1.3	1.5	2.1	–9	–2	3	9	16
		2065	1.7	2.5	3.1	3.4	4.4	–14	–3	4	8	21
		2100	3.7	4.6	5.3	6.3	7.6	–20	–6	2	11	35

(continued on next page)

Table 14.SM.1c (continued)

RCP8.5			Temperature (°C)					Precipitation (%)				
REGION	**MONTH**[a]	**Year**	**min**	**25%**	**50%**	**75%**	**max**	**min**	**25%**	**50%**	**75%**	**max**
Eastern Asia	**DJF**	**2035**	0.1	0.9	1.2	1.5	2.4	–7	–1	1	3	14
		2065	1.3	2.3	2.9	3.3	4.7	–10	3	6	9	23
		2100	3.5	4.2	5.4	6.1	7.5	–15	9	13	19	32
	JJA	**2035**	0.5	0.9	1.0	1.2	1.9	–4	0	1	3	5
		2065	1.4	2.1	2.6	3.1	3.9	–3	3	6	9	15
		2100	2.8	3.8	4.8	5.7	6.8	1	7	9	15	28
	Annual	**2035**	0.5	0.9	1.1	1.3	1.9	–2	0	1	3	5
		2065	1.6	2.2	2.7	3.1	4.2	–1	4	6	9	14
		2100	3.3	4.0	4.9	5.6	7.2	–3	7	10	16	22
Tibetan Plateau	**DJF**	**2035**	0.2	1.1	1.3	1.7	2.4	–2	2	5	7	12
		2065	1.6	2.6	3.2	3.8	5.3	–1	8	13	16	26
		2100	3.9	4.8	5.8	7.0	9.1	0	15	20	28	46
	JJA	**2035**	0.6	1.0	1.2	1.4	2.5	–3	2	4	6	14
		2065	1.8	2.4	2.9	3.3	5.3	–2	5	8	11	32
		2100	3.6	4.6	5.3	6.0	8.8	–3	8	13	18	55
	Annual	**2035**	0.6	1.0	1.3	1.5	2.0	–2	3	4	5	13
		2065	1.9	2.5	3.0	3.5	4.8	–2	6	9	12	28
		2100	3.9	4.7	5.5	6.3	8.4	–2	10	16	21	47
South Asia	**DJF**	**2035**	0.3	0.8	1.0	1.2	1.6	–13	–2	1	6	20
		2065	1.5	2.2	2.6	3.0	3.7	–16	–4	4	10	23
		2100	3.5	4.1	4.6	5.7	7.1	–17	–1	12	21	42
	JJA	**2035**	0.3	0.6	0.8	1.0	1.3	–3	1	3	5	16
		2065	1.2	1.7	2.0	2.3	3.3	–1	7	10	13	27
		2100	1.3	3.0	3.7	4.6	5.6	–9	13	17	23	57
	Annual	**2035**	0.4	0.8	0.9	1.0	1.4	–2	1	3	5	11
		2065	1.5	2.0	2.2	2.6	3.1	0	6	8	11	17
		2100	3.1	3.7	4.1	5.2	6.0	–7	11	18	21	45
North Indian Ocean	**DJF**	**2035**	0.3	0.6	0.7	0.8	1.0	–10	0	5	8	22
		2065	0.9	1.5	1.6	2.0	2.5	–18	3	13	21	44
		2100	2.1	2.7	3.0	3.9	4.5	–7	9	19	34	65
	JJA	**2035**	0.3	0.6	0.7	0.8	1.1	–10	0	3	5	10
		2065	1.0	1.5	1.6	2.0	2.4	–7	3	6	11	29
		2100	1.9	2.7	3.0	3.6	4.3	–14	7	14	20	52
	Annual	**2035**	0.3	0.6	0.7	0.8	1.0	–4	2	3	5	16
		2065	1.0	1.5	1.6	2.0	2.4	–5	3	7	14	29
		2100	2.1	2.7	3.0	3.8	4.3	–9	8	18	23	56
Southeast Asia (land)	**DJF**	**2035**	0.3	0.6	0.7	0.9	1.2	–6	0	2	4	10
		2065	1.1	1.5	1.8	2.2	2.7	–3	1	5	10	19
		2100	2.1	2.9	3.2	4.2	4.9	–8	2	8	19	31
	JJA	**2035**	0.4	0.6	0.7	0.9	1.3	–4	–1	0	2	7
		2065	1.1	1.6	1.8	2.1	2.8	–5	0	5	9	17
		2100	2.1	2.9	3.3	4.2	5.1	–8	–1	7	16	30
	Annual	**2035**	0.3	0.6	0.8	0.9	1.2	–4	0	1	3	8
		2065	1.1	1.6	1.7	2.2	2.7	–3	0	5	10	17
		2100	2.1	3.0	3.2	4.4	4.9	–7	0	8	19	29

(continued on next page)

Table 14.SM.1c (continued)

RCP8.5			Temperature (°C)					Precipitation (%)				
REGION	**MONTH**[a]	**Year**	**min**	**25%**	**50%**	**75%**	**max**	**min**	**25%**	**50%**	**75%**	**max**
Southeast Asia (sea)	**DJF**	**2035**	0.2	0.6	0.6	0.7	1.1	–5	–1	1	3	7
		2065	1.0	1.4	1.6	1.9	2.5	–4	0	3	5	12
		2100	2.1	2.5	2.7	3.4	4.3	–12	–1	6	11	21
	JJA	**2035**	0.3	0.6	0.6	0.7	1.1	–4	0	1	3	5
		2065	1.1	1.4	1.5	1.8	2.4	–3	2	4	7	12
		2100	2.1	2.6	2.8	3.4	4.2	–6	2	6	10	22
	Annual	**2035**	0.3	0.6	0.7	0.7	1.1	–1	0	1	3	5
		2065	1.0	1.4	1.5	1.9	2.4	–1	1	4	6	10
		2100	2.1	2.6	2.8	3.5	4.2	–3	2	6	9	20
Australia												
North Australia	**DJF**	**2035**	0.3	0.7	0.9	1.2	1.8	–20	–7	–1	3	14
		2065	1.4	1.8	2.2	2.8	3.6	–27	–8	–2	7	15
		2100	1.9	3.3	3.9	4.9	5.9	–50	–13	–2	8	33
	JJA	**2035**	0.5	0.8	1.0	1.1	1.5	–43	–13	–4	–1	23
		2065	1.6	1.9	2.2	2.5	3.0	–46	–19	–6	2	16
		2100	2.5	3.6	4.4	4.8	5.5	–66	–27	–15	–1	48
	Annual	**2035**	0.5	0.8	1.0	1.1	1.6	–17	–6	–1	2	8
		2065	1.6	1.8	2.2	2.7	3.4	–26	–11	–3	4	12
		2100	2.4	3.6	4.3	5.1	5.8	–51	–14	–4	5	33
South Australia/ New Zealand	**DJF**	**2035**	0.2	0.7	0.9	1.1	1.5	–17	–5	–1	3	7
		2065	1.3	1.7	2.1	2.3	3.0	–24	–5	0	4	8
		2100	2.6	3.0	3.8	4.3	5.9	–30	–8	–1	3	21
	JJA	**2035**	0.3	0.6	0.7	0.9	1.1	–19	–4	–2	1	4
		2065	1.2	1.5	1.7	1.9	2.1	–25	–9	–2	2	8
		2100	2.2	2.8	3.4	3.8	4.3	–39	–18	–7	4	10
	Annual	**2035**	0.4	0.7	0.8	0.9	1.1	–17	–5	–1	1	6
		2065	1.4	1.6	1.9	2.2	2.5	–22	–6	–1	2	6
		2100	2.6	3.0	3.9	4.1	5.0	–33	–11	–3	2	15
The Pacific												
Northern Tropical Pacific	**DJF**	**2035**	0.4	0.5	0.6	0.8	1.0	–6	–1	1	3	18
		2065	1.1	1.4	1.6	1.9	2.3	–6	–1	2	7	21
		2100	2.1	2.5	2.9	3.6	4.2	–8	–1	3	11	31
	JJA	**2035**	0.4	0.5	0.6	0.8	1.1	–6	–1	1	4	12
		2065	1.0	1.4	1.6	2.0	2.5	–9	–1	3	5	17
		2100	2.0	2.5	2.8	3.8	4.3	–16	0	6	11	26
	Annual	**2035**	0.3	0.6	0.7	0.8	1.1	–4	0	1	3	14
		2065	1.0	1.4	1.6	2.0	2.4	–6	0	2	6	19
		2100	2.1	2.5	2.8	3.6	4.2	–11	–1	5	10	29
Equatorial Pacific	**DJF**	**2035**	0.4	0.6	0.7	0.9	1.1	–12	–1	9	16	77
		2065	1.0	1.4	1.7	2.0	2.9	–11	4	15	21	257
		2100	1.0	2.6	3.1	3.7	5.6	–43	10	28	38	635
	JJA	**2035**	0.4	0.6	0.7	0.9	1.3	–2	7	12	21	45
		2065	0.9	1.5	1.6	2.0	2.9	–5	17	23	39	102
		2100	1.1	2.5	3.1	3.7	5.0	–39	28	48	63	407
	Annual	**2035**	0.4	0.5	0.7	0.8	1.1	–5	5	9	15	62
		2065	1.0	1.4	1.6	2.0	2.6	–8	14	19	30	184
		2100	1.0	2.6	3.1	3.7	5.1	–42	24	33	54	537

(continued on next page)

Table 14.SM.1c (continued)

RCP8.5			Temperature (°C)					Precipitation (%)				
REGION	**MONTH[a]**	**Year**	**min**	**25%**	**50%**	**75%**	**max**	**min**	**25%**	**50%**	**75%**	**max**
Southern Pacific	**DJF**	**2035**	0.3	0.5	0.6	0.7	0.9	–10	–1	1	3	8
		2065	1.0	1.2	1.4	1.6	2.1	–27	–1	3	5	11
		2100	1.8	2.2	2.6	3.2	3.9	–30	0	5	8	17
	JJA	**2035**	0.3	0.5	0.6	0.6	0.9	–10	–1	1	2	5
		2065	1.1	1.2	1.4	1.6	2.1	–19	–2	0	5	8
		2100	2.0	2.2	2.6	3.0	4.0	–21	–3	2	5	16
	Annual	**2035**	0.3	0.5	0.6	0.7	0.9	–10	0	1	2	5
		2065	1.0	1.2	1.4	1.6	2.1	–24	0	1	4	9
		2100	2.0	2.3	2.6	3.1	4.0	–24	0	3	6	15
Antarctica												
(land)	**DJF**	**2035**	0.1	0.6	0.8	0.9	1.4	–5	0	3	5	10
		2065	0.4	1.7	1.9	2.3	3.1	–6	4	8	12	17
		2100	1.8	3.2	3.5	4.4	5.3	–2	10	18	24	41
	JJA	**2035**	–0.1	0.5	0.8	1.1	1.8	–1	2	5	7	11
		2065	0.2	1.7	2.2	2.6	3.3	1	8	12	17	24
		2100	1.4	3.4	4.0	4.9	6.0	7	17	27	36	44
	Annual	**2035**	0.0	0.6	0.7	1.0	1.4	–3	1	5	7	9
		2065	0.3	1.7	2.0	2.5	3.1	–2	7	10	15	18
		2100	1.6	3.2	3.8	4.9	5.5	2	14	23	31	40
(sea)	**DJF**	**2035**	–0.3	0.2	0.3	0.6	0.8	1	2	3	3	5
		2065	–0.4	0.6	0.9	1.2	1.8	1	4	6	8	11
		2100	0.2	1.2	1.7	2.2	3.4	5	8	12	16	21
	JJA	**2035**	–0.6	0.4	0.6	1.1	2.2	1	2	3	4	6
		2065	–0.5	1.1	1.6	2.4	4.3	4	5	7	10	13
		2100	0.6	2.3	3.6	4.4	7.2	6	10	15	19	27
	Annual	**2035**	–0.4	0.3	0.5	0.8	1.5	1	2	3	4	6
		2065	–0.4	0.9	1.2	1.8	3.0	3	4	7	9	12
		2100	0.4	1.8	2.7	3.3	5.1	6	10	14	18	23

Notes:

[a] *Precipitation changes cover 6 months; ONDJFM and AMJJAS for winter and summer (northern hemisphere)

Table 14.SM.2a | Projected changes for the future (2080–2099) relative to the present-day (1986–2005) at the 10th, 25th, 50th, 75th and 90th percentile values of global monsoon area (GMA), global monsoon precipitation intensity (GMI), global monsoon total precipitation (GMP), standard deviation of interannual variability in seasonal average precipitation (Psd), simple daily precipitation intensity index (SDII), seasonal maximum 5-day precipitation total (R5d), seasonal maximum consecutive dry days (CDD) and monsoon season duration (DUR) in global monsoon domain for RCP2.6, RCP4.5, RCP6.0, and RCP8.5 scenario. Percentage of number of models with positive changes is also shown.

Index	Scenario	10	25	50	75	90	Ratio
GLB							
GMA	RCP2.6	1.5	1.9	3.6	5.5	7.1	100.0
	RCP4.5	1.6	3.2	4.3	7.3	8.7	95.8
	RCP6.0	2.2	4.3	6.4	8.5	9.8	92.9
	RCP8.5	5.2	7.6	9.4	12.0	14.5	96.2
GMI	RCP2.6	–0.4	1.2	1.7	2.3	3.2	88.9
	RCP4.5	–0.4	1.4	3.6	4.7	5.0	87.5
	RCP6.0	–0.7	1.7	3.3	4.5	5.1	78.6
	RCP8.5	–0.4	3.5	5.2	7.6	8.3	88.5
GMP	RCP2.6	3.0	3.5	5.0	7.6	9.3	100.0
	RCP4.5	2.5	4.1	8.6	11.8	13.2	95.8
	RCP6.0	1.8	6.9	10.0	12.1	14.7	92.9
	RCP8.5	4.9	9.5	16.6	19.8	22.5	100.0
Psd	RCP2.6	–4.0	0.0	3.5	5.8	11.2	77.8
	RCP4.5	–1.5	3.0	8.7	11.0	16.6	87.5
	RCP6.0	–4.8	2.9	7.8	12.3	14.1	85.7
	RCP8.5	–3.0	5.1	10.9	20.0	25.4	84.6
SDII	RCP2.6	1.0	2.1	2.4	3.0	3.8	100.0
	RCP4.5	1.7	2.2	4.0	5.8	7.1	100.0
	RCP6.0	1.9	3.2	4.7	6.0	6.7	100.0
	RCP8.5	2.5	4.7	7.0	10.3	16.2	100.0
R5d	RCP2.6	0.7	3.6	4.1	5.7	7.1	100.0
	RCP4.5	2.1	4.3	7.4	9.0	12.1	95.8
	RCP6.0	2.0	7.4	8.8	12.1	16.1	100.0
	RCP8.5	1.5	8.9	16.0	20.7	26.2	96.2
CDD	RCP2.6	–1.6	0.7	3.9	7.5	8.5	77.8
	RCP4.5	–0.5	1.9	5.1	8.3	12.0	87.5
	RCP6.0	–0.8	3.0	6.6	8.2	13.2	85.7
	RCP8.5	1.6	7.9	12.9	18.4	28.2	96.2
DUR	RCP2.6	–2.2	0.2	2.4	4.0	9.3	77.8
	RCP4.5	–0.5	3.3	5.4	7.8	9.0	87.5
	RCP6.0	0.7	4.0	4.9	8.5	12.6	92.9
	RCP8.5	–3.4	4.2	8.5	13.9	16.1	88.5

Table 14.SM.2b | Projected changes for the future (2080–2099) relative to the present–day (1986–2005) at the 10th, 25th, 50th, 75th and 90th percentile values of global monsoon area (GMA), global monsoon precipitation intensity (GMI), global monsoon total precipitation (GMP), standard deviation of interannual variability in seasonal average precipitation (Psd), simple daily precipitation intensity index (SDII), seasonal maximum 5-day precipitation total (R5d), seasonal maximum consecutive dry days (CDD) and monsoon season duration (DUR) in each regional land monsoon domain for RCP2.6, RCP4.5, RCP6.0, and RCP8.5 scenario. Percentage of number of models with positive changes is also shown.

Index	Scenario	10	25	50	75	90	Ratio
EAS							
Pav	RCP2.6	–0.5	0.8	1.6	5.0	8.4	88.9
	RCP4.5	1.3	2.7	5.7	9.0	9.8	91.7
	RCP6.0	1.3	2.5	5.3	8.6	12.1	100.0
	RCP8.5	2.6	4.1	7.8	12.5	17.0	92.3
Psd	RCP2.6	–10.6	–2.3	6.5	10.3	18.2	72.2
	RCP4.5	3.2	6.2	12.1	14.2	25.4	91.7
	RCP6.0	2.4	8.7	9.9	23.2	29.0	100.0
	RCP8.5	10.9	17.7	25.4	30.2	32.8	96.2
SDII	RCP2.6	1.9	3.0	4.0	4.8	6.4	94.4
	RCP4.5	2.9	6.0	7.8	9.1	12.3	95.8
	RCP6.0	5.0	6.7	8.4	10.6	11.0	100.0
	RCP8.5	8.3	12.6	14.2	17.1	20.8	96.2
R5d	RCP2.6	–1.0	2.3	4.0	8.3	10.5	88.9
	RCP4.5	4.1	5.6	11.0	13.4	18.8	95.8
	RCP6.0	7.5	9.6	10.4	16.9	20.9	100.0
	RCP8.5	9.0	15.4	19.5	26.0	32.7	96.2
CDD	RCP2.6	–5.2	–3.3	1.1	6.8	14.5	61.1
	RCP4.5	–6.8	–3.0	2.8	9.3	13.5	58.3
	RCP6.0	–3.4	–1.9	–0.1	13.0	15.9	42.9
	RCP8.5	–4.8	0.0	6.0	18.6	23.0	73.1
ONS	RCP2.6	–18	–10	–5	2	3	33.3
	RCP4.5	–22	–15	–8	–2	0	8.3
	RCP6.0	–17	–12	–6	3	8	28.6
	RCP8.5	–30	–21	–11	–5	4	15.4
RET	RCP2.6	–22	0	3	13	20	66.7
	RCP4.5	–3	2	8	12	38	79.2
	RCP6.0	0	3	5	11	41	78.6
	RCP8.5	–1	4	10	15	41	84.6
DUR	RCP2.6	–14	0	7	18	37	72.2
	RCP4.5	–3	8	15	31	47	83.3
	RCP6.0	–12	1	6	39	53	78.6
	RCP8.5	4	7	20	42	54	92.3
SAS							
Pav	RCP2.6	–0.4	1.9	4.5	6.7	7.8	88.9
	RCP4.5	4.8	6.5	7.5	10.6	12.4	100.0
	RCP6.0	4.3	6.2	8.2	10.1	10.8	100.0
	RCP8.5	6.6	10.2	13.0	16.3	17.7	100.0
Psd	RCP2.6	–5.2	4.4	6.2	11.8	16.3	88.9
	RCP4.5	1.5	6.9	13.9	20.3	25.4	95.8
	RCP6.0	6.4	16.9	17.9	20.4	22.6	100.0
	RCP8.5	7.8	10.9	25.5	32.0	49.1	100.0
SDII	RCP2.6	2.1	2.8	3.8	5.2	9.1	100.0
	RCP4.5	5.2	6.2	7.2	10.1	13.5	100.0
	RCP6.0	6.1	7.2	7.8	9.7	11.9	100.0
	RCP8.5	8.8	10.8	15.1	17.5	23.1	100.0

(continued on next page)

Table 14.SM.2b (continued)

Index	Scenario	10	25	50	75	90	Ratio
R5d	RCP2.6	2.2	5.3	5.8	9.3	15.3	100.0
	RCP4.5	5.1	9.8	12.4	16.2	21.2	100.0
	RCP6.0	10.1	11.1	15.4	20.2	24.2	100.0
	RCP8.5	11.7	18.3	22.4	38.0	47.5	96.2
CDD	RCP2.6	–7.2	–1.2	1.9	3.2	6.8	72.2
	RCP4.5	–7.9	–5.0	–0.4	5.5	8.9	50.0
	RCP6.0	–7.9	–5.4	–1.3	9.4	16.7	50.0
	RCP8.5	–11.6	–4.9	6.7	11.7	17.1	69.2
ONS	RCP2.6	–7	–2	–1	2	3	33.3
	RCP4.5	–6	–5	–3	0	1	16.7
	RCP6.0	–7	–5	–2	2	5	42.9
	RCP8.5	–11	–9	–5	–1	1	11.5
RET	RCP2.6	–2	1	2	6	10	77.8
	RCP4.5	1	3	5	8	9	91.7
	RCP6.0	2	3	4	10	13	92.9
	RCP8.5	2	6	8	12	17	96.2
DUR	RCP2.6	–6	–2	4	7	15	72.2
	RCP4.5	2	4	7	13	15	91.7
	RCP6.0	–2	4	7	11	19	78.6
	RCP8.5	4	8	13	19	24	96.2
AUSMC							
Pav	RCP2.6	–8.1	–3.6	–1.5	2.1	4.0	44.4
	RCP4.5	–8.7	0.3	3.2	7.1	8.7	83.3
	RCP6.0	–4.2	–0.3	3.6	10.2	10.5	64.3
	RCP8.5	–14.4	0.1	7.3	14.9	19.1	76.9
Psd	RCP2.6	–10.1	–0.1	3.2	11.1	20.9	72.2
	RCP4.5	–1.2	1.0	6.8	12.6	28.2	83.3
	RCP6.0	–2.6	–1.7	7.4	17.3	26.6	71.4
	RCP8.5	–12.5	5.0	11.0	20.9	40.7	80.8
SDII	RCP2.6	–2.6	0.1	1.4	3.9	5.6	77.8
	RCP4.5	–1.5	1.1	4.3	8.3	11.5	83.3
	RCP6.0	–0.7	2.2	4.7	6.8	12.5	85.7
	RCP8.5	–4.1	2.5	7.2	13.9	24.6	84.6
R5d	RCP2.6	–2.8	1.5	4.6	7.2	9.2	77.8
	RCP4.5	–0.9	2.1	8.0	12.5	17.2	87.5
	RCP6.0	1.2	1.9	9.8	15.7	27.7	92.9
	RCP8.5	–3.8	3.5	15.0	26.7	36.5	88.5
CDD	RCP2.6	–1.7	–0.2	6.3	12.4	13.6	72.2
	RCP4.5	–4.1	–0.6	4.1	12.5	21.5	75.0
	RCP6.0	–8.0	–4.4	3.2	14.6	17.7	71.4
	RCP8.5	–10.7	–2.4	6.8	25.8	36.8	69.2
ONS	RCP2.6	–19	–6	–2	6	21	38.9
	RCP4.5	–12	–6	–5	4	11	37.5
	RCP6.0	–13	–7	–4	5	9	28.6
	RCP8.5	–18	–12	–6	8	13	36.0
RET	RCP2.6	–12	–2	5	10	15	55.6
	RCP4.5	–5	–2	4	15	20	70.8
	RCP6.0	2	3	6	11	17	92.9
	RCP8.5	–8	1	8	13	27	76.0

(continued on next page)

Table 14.SM.2b (continued)

Index	Scenario	10	25	50	75	90	Ratio
DUR	RCP2.6	–16	–13	4	15	25	66.7
	RCP4.5	–6	–2	7	14	21	75.0
	RCP6.0	–4	1	5	18	26	78.6
	RCP8.5	–21	–3	16	24	38	72.0
NAMS							
Pav	RCP2.6	–5.3	–3.2	–1.9	2.6	5.5	44.4
	RCP4.5	–12.9	–5.8	–2.9	0.8	5.0	33.3
	RCP6.0	–6.0	–3.4	–2.0	6.7	7.0	42.9
	RCP8.5	–25.4	–11.8	–6.5	3.5	6.9	26.9
Psd	RCP2.6	–7.8	–0.1	2.9	9.9	13.3	72.2
	RCP4.5	–15.5	–5.5	2.5	13.5	18.4	62.5
	RCP6.0	–7.3	–3.4	0.4	15.2	21.6	57.1
	RCP8.5	–14.8	–9.1	1.5	17.1	37.2	61.5
SDII	RCP2.6	–2.6	–0.5	1.4	3.2	4.7	72.2
	RCP4.5	–8.2	–3.0	0.1	3.9	10.9	54.2
	RCP6.0	–2.7	0.3	1.3	7.6	10.8	85.7
	RCP8.5	–16.5	–7.2	–0.1	13.1	19.1	50.0
R5d	RCP2.6	–1.6	0.2	3.6	4.6	11.8	77.8
	RCP4.5	–6.5	–1.5	2.5	9.9	15.1	70.8
	RCP6.0	–2.0	1.9	6.2	15.8	21.1	78.6
	RCP8.5	–14.6	–3.0	6.7	21.0	38.5	69.2
CDD	RCP2.6	–3.2	0.9	3.9	10.2	16.6	77.8
	RCP4.5	5.6	7.6	10.9	18.3	26.5	95.8
	RCP6.0	3.0	4.8	9.4	14.0	15.9	92.9
	RCP8.5	12.0	17.4	23.1	37.1	70.9	100.0
ONS	RCP2.6	–6	–3	1	3	7	58.8
	RCP4.5	–7	–4	1	5	8	54.5
	RCP6.0	–11	–4	–3	0	2	23.1
	RCP8.5	–9	–4	1	8	13	52.2
RET	RCP2.6	–27	–8	2	8	12	52.9
	RCP4.5	–7	–3	5	10	11	63.6
	RCP6.0	–14	–8	1	10	18	53.8
	RCP8.5	–47	–20	–1	20	23	47.8
DUR	RCP2.6	–29	–2	0	12	17	47.1
	RCP4.5	–13	–3	2	10	16	54.5
	RCP6.0	–10	–3	5	13	18	69.2
	RCP8.5	–54	–29	8	18	22	52.2
SAMS							
Pav	RCP2.6	–4.1	–3.2	–0.3	2.2	4.2	44.4
	RCP4.5	–3.3	–1.1	1.2	4.2	6.5	66.7
	RCP6.0	–2.4	–1.4	1.7	4.2	7.4	64.3
	RCP8.5	–7.7	–2.6	2.4	6.2	11.2	69.2
Psd	RCP2.6	–4.1	–2.4	3.6	12.5	27.7	61.1
	RCP4.5	–5.6	0.6	9.5	19.5	23.9	79.2
	RCP6.0	–8.8	–4.1	3.9	10.7	25.7	71.4
	RCP8.5	–9.2	2.5	16.8	27.1	46.0	84.6

(continued on next page)

Table 14.SM.2b (continued)

Index	Scenario	10	25	50	75	90	Ratio
SDII	RCP2.6	–1.9	0.7	1.6	2.6	4.8	83.3
	RCP4.5	–0.6	1.1	3.1	6.0	11.1	83.3
	RCP6.0	0.0	1.8	4.1	5.7	7.8	85.7
	RCP8.5	–0.9	4.4	7.2	10.9	18.9	84.6
R5d	RCP2.6	–2.5	2.3	3.6	4.9	6.6	83.3
	RCP4.5	–0.7	3.7	7.9	10.4	13.6	83.3
	RCP6.0	–0.2	5.4	7.2	11.5	18.9	85.7
	RCP8.5	–2.8	7.6	17.5	20.4	30.7	84.6
CDD	RCP2.6	–3.5	3.0	5.9	13.7	29.2	88.9
	RCP4.5	1.9	3.0	9.0	14.1	19.3	95.8
	RCP6.0	1.2	4.3	6.2	13.0	18.3	92.9
	RCP8.5	7.7	15.5	19.3	38.8	48.4	96.2
ONS	RCP2.6	–6	–4	1	5	8	55.6
	RCP4.5	–7	–4	1	5	7	54.2
	RCP6.0	–6	–2	3	5	12	64.3
	RCP8.5	–7	–5	0	9	14	50.0
RET	RCP2.6	–4	–2	0	0	2	22.2
	RCP4.5	–4	–2	0	2	5	50.0
	RCP6.0	–4	–2	0	2	3	42.9
	RCP8.5	–8	–2	1	5	6	57.7
DUR	RCP2.6	–8	–5	–2	2	5	38.9
	RCP4.5	–9	–7	–1	5	8	41.7
	RCP6.0	–12	–8	–3	4	7	35.7
	RCP8.5	–17	–10	0	8	11	50.0
NAF							
Pav	RCP2.6	–3.7	–2.1	–0.4	2.3	3.5	50.0
	RCP4.5	–4.4	–1.4	2.2	3.3	7.9	66.7
	RCP6.0	–3.4	–1.6	1.0	6.4	13.7	64.3
	RCP8.5	–6.7	–4.3	3.0	7.9	11.0	61.5
Psd	RCP2.6	–2.6	–1.4	2.2	6.5	16.7	72.2
	RCP4.5	–4.6	–2.8	3.2	8.4	20.4	66.7
	RCP6.0	–5.1	–2.3	5.1	15.6	28.0	71.4
	RCP8.5	0.8	4.2	9.9	20.7	44.0	92.3
SDII	RCP2.6	–1.6	0.0	1.5	2.9	6.3	72.2
	RCP4.5	–1.6	–0.5	2.9	6.4	9.3	75.0
	RCP6.0	–1.7	0.9	1.8	7.3	8.4	85.7
	RCP8.5	–0.6	1.4	6.8	9.9	23.1	84.6
R5d	RCP2.6	–0.6	0.6	1.8	5.3	15.8	88.9
	RCP4.5	–2.9	1.1	6.6	9.5	16.9	79.2
	RCP6.0	1.8	4.9	7.3	9.0	11.8	92.9
	RCP8.5	1.9	8.8	13.2	22.4	40.3	96.2
CDD	RCP2.6	–5.7	2.1	3.4	9.3	13.1	88.9
	RCP4.5	–4.9	–2.7	1.9	13.7	24.4	58.3
	RCP6.0	–7.9	–4.1	4.2	7.9	11.1	57.1
	RCP8.5	–0.2	5.2	10.9	39.9	49.2	88.5
ONS	RCP2.6	–8	–1	4	8	19	58.8
	RCP4.5	–16	–1	2	9	14	73.9
	RCP6.0	–11	–3	3	6	14	69.2
	RCP8.5	–10	–8	–1	6	16	48.0

(continued on next page)

Table 14.SM.2b (continued)

Index	Scenario	10	25	50	75	90	Ratio
RET	RCP2.6	–4	–1	2	4	8	64.7
	RCP4.5	–4	1	4	6	8	78.3
	RCP6.0	4	4	6	13	14	92.3
	RCP8.5	–4	5	9	15	20	88.0
DUR	RCP2.6	–23	–7	–4	4	14	35.3
	RCP4.5	–15	–8	–1	8	20	43.5
	RCP6.0	–4	–2	4	11	24	61.5
	RCP8.5	–8	0	6	19	25	72.0
SAF							
Pav	RCP2.6	–6.0	–3.4	–0.9	1.7	2.9	38.9
	RCP4.5	–4.3	–1.6	2.1	3.4	4.1	62.5
	RCP6.0	–4.2	–2.2	1.9	3.5	5.2	64.3
	RCP8.5	–5.0	–1.2	2.6	5.4	7.0	69.2
Psd	RCP2.6	–6.9	–4.6	1.7	5.7	10.8	66.7
	RCP4.5	–6.8	1.2	6.6	12.3	21.7	79.2
	RCP6.0	–9.7	–0.7	0.6	16.0	24.7	57.1
	RCP8.5	–1.9	6.0	14.3	24.7	33.0	84.6
SDII	RCP2.6	–1.9	0.9	1.7	2.5	3.6	83.3
	RCP4.5	0.7	2.4	3.5	6.8	9.2	91.7
	RCP6.0	–3.4	3.3	4.1	6.0	8.1	85.7
	RCP8.5	4.1	5.5	7.5	12.2	21.3	92.3
R5d	RCP2.6	–3.8	0.6	2.4	4.6	6.8	83.3
	RCP4.5	2.3	3.3	6.6	9.8	12.2	91.7
	RCP6.0	–6.7	8.1	9.2	10.6	16.9	85.7
	RCP8.5	5.7	10.2	16.7	19.8	24.0	92.3
CDD	RCP2.6	–3.6	0.5	6.6	13.7	16.0	77.8
	RCP4.5	–1.5	2.5	9.2	15.8	18.4	87.5
	RCP6.0	0.1	1.3	9.2	19.3	22.1	92.9
	RCP8.5	7.0	12.8	20.3	32.0	38.7	96.2
ONS	RCP2.6	–11	–1	2	5	8	66.7
	RCP4.5	–3	–1	2	4	5	70.8
	RCP6.0	–2	1	2	7	10	78.6
	RCP8.5	–2	1	5	10	14	80.8
RET	RCP2.6	–6	–3	–1	3	5	33.3
	RCP4.5	–4	–2	0	4	9	50.0
	RCP6.0	–5	1	1	9	12	78.6
	RCP8.5	–2	3	6	9	14	80.8
DUR	RCP2.6	–14	–6	–3	2	8	33.3
	RCP4.5	–7	–6	–1	6	9	45.8
	RCP6.0	–14	–5	0	6	8	50.0
	RCP8.5	–12	–5	–1	8	18	50.0

Table 14.SM.3 | Lists of years for Eastern Pacific and Central Pacific El Niño events. A: Types based on Empirical Orthogonal Function (EOF) by (Ashok et al., 2007), B: Types based on the relative amplitude between NINO3 and NINO4 sea surface temperature (SST) index by (Yeh et al., 2009), C: similar to Yeh et al. (2009) but 1982–2010 climatology by Lee and McPhaden (2010), D: As in C but 1948-2006 climatology by Li et al. (2011b), E: similar to B but including 'Mixed type, M' by Kug et al. (2009), F: Types based on subsurface temperature by Yu et al. (2011), G: Types based on sea surface salinity for 1977–2008 by Singh et al. (2011), H: Modified Ashok et al. (2007) by Li et al. (2010a), I: Similar to Yeh et al. (2009) but 1950–2008 climatology by Hu et al. (2012). CP indicates 'Central Pacific El Niño', 'date line El Niño', or 'El Niño-Modoki' events; EP indicates 'Eastern Pacific El Niño' or 'conventional El Niño'; M indicates the mixed type that belongs to neither EP nor CP type. Each paper uses different terminology but here EP, CP and M instead of various names.

El Niño	A	B	C	D	E	F	G	H	I
1950–1951		EP							
1957–1958		EP		EP					EP
1963–1964	CP	EP		EP		CP			
1965–1966		EP		EP		M			EP
1968–1969	CP	CP		CP		CP			CP
1969–1970		EP		EP		CP			EP
1972–1973		EP		EP	EP	M			EP
1976–1977		EP		EP	EP	M			
1977–1978	CP	CP		CP	CP	CP	CP		
1979–1980	CP	EP		EP					
1982–1983		EP	EP	EP	EP	M	EP	EP	EP
1986–1987		EP		EP	M	M	CP	EP	EP
1987–1988	CP	EP	EP	EP	M	M			CP
1990–1991	CP	CP		CP	CP		CP	CP	
1991–1992	CP	EP	CP	EP	M	M	EP	EP	EP
1992–1993	CP	CP					CP		
1994–1995	CP	CP	CP	CP	CP	M	CP	CP	CP
1997–1998		EP	EP	EP	EP	EP	EP	EP	EP
2001–2002		CP							
2002–2003	CP	EP	CP	CP	CP		CP	CP	CP
2003–2004		EP							
2004–2005	CP	CP	CP	CP	CP		CP	CP	
2006–2007		EP	EP	EP			CP		CP
2009–2010		CP	CP		CP				

Table 14.SM.4a | Projected change in frequency of tropical storms in warm climate runs relative to control run in percent. Red and blue numbers/text denote projected increases and decreases, respectively. Bold text denotes where a statistical significance test was reported that showed significance. The frequency projections from Emanuel et al. (2008) have been computed slightly differently from those shown in Figure 8 of the original paper in order to facilitate intercomparison with projection results from other studies.

Tropical Storm Frequency Projections (%)												
Reference	**Model/type**	**Resolution: high to low**	**Experiment**	**Basin**								
				Global	**NH**	**SH**	**N Atl.**	**NW Pac.**	**NE Pac.**	**N Ind.**	**S. Ind.**	**SW Pac.**
(Sugi et al., 2002)	JMA time slice	T106 L21 (~120 km)	10 yr 1 × CO_2, 2 × CO_2	**−34**	**−28**	**−39**	**+61**	**−66**	−67	+9	**−57**	**−31**
(McDonald et al., 2005)	HadAM3 time slice	N144 L30 (~100 km)	15 yr IS95a 1979–1994 2082–2097	**−6**	−3	**−10**	**−30**	**−30**	**+80**	**+42**	+10	**−18**
(Hasegawa and Emori, 2005)	CCSR/NIES/ FRCGC time slice	T106 L56 (~120 km)	5 × 20 yr at 1 × CO_2 7 × 20 yr at 2 × CO_2					−4				
(Yoshimura et al., 2006)	JMA time slice	T106 L21 (~120 km)	10 yr 1 × CO_2, 2 × CO_2	**−15**								
(Oouchi et al., 2006)	MRI/JMA time slice	TL959 L60 (~20 km)	10 yr A1B 1982–1993 2080–2099	**−30**	**−28**	**−32**	**+34**	**−38**	**−34**	**−52**	**−28**	**−43**
(Chauvin et al., 2006)	ARPEGE Climat time slice	~50 km	Downscale CNRM B2 Downscale Hadley A2				+18 −25					
(Stowasser et al., 2007)	IPRC Regional		Downscale NCAR CCSM2, 6 × CO_2					+19				
(Bengtsson et al., 2007)	ECHAM5 time slice	T213 (~60 km)	2071–2100, A1B		−13		−8	−20	+4	−26		
(Bengtsson et al., 2007)	ECHAM5 time slice	T319 (~40 km)	2071–2100, A1B		−19		−13	−28	+7	−51		
(Emanuel et al., 2008)	Statistical- deterministic	---	Downscale 7 CMIP3 mods.: A1B, 2180–2200 Average over seven models	−7	+2	−13	+4	+6	−5	−7	−12	−15
(Knutson et al., 2008)	GFDL Zetac regional	18 km	Downscale CMIP3 ens. A1B, 2080–2100				−27					
(Knutson et al., 2013)	GFDL Zetac regional	18 km	Downscale (yr 2081–2100) CMIP3 ens. A1B CMIP5 ens Rcp45 Gfdl CM2.1 A1B MPI A1B HadCM3 A1B MRI A1B Gfdl CM2.0 A1B HadGEM1 A1B MIROC hi A1B CCMS3 A1B INGV A1B MIROC med A1B				 **−27** **−23** −9 **−38** **−52** −25 +8 **−62** **−33** −28 −22 **−43**					
(Leslie et al., 2007)	OU-CGCM with high-res. window	Up to 50 km	2000 to 2050 control and IS92a (6 members)									~0

(continued on next page)

Table 14.SM.4a (continued)

Tropical Storm Frequency Projections (%)												
Reference	Model/type	Resolution: high to low	Experiment	Basin								
				Global	NH	SH	N Atl.	NW Pac.	NE Pac.	N Ind.	S. Ind.	SW Pac.
(Gualdi et al., 2008)	SINTEX-G coupled model	T106 (~120 km)	30 yr 1 × CO_2, 2 × CO_2, 4 × CO_2	−16 (2×) −44 (4×)			−14	−20	−3	−13	−14	−22
(Semmler et al., 2008)	Rossby Centre regional model	28 km	16 yr control and A2, 2085–2100				−13					
(Zhao et al., 2009)	GFDL HIRAM time slice	50 km	Downscale A1B:									
			CMIP3 n =18 ens.	−20	−14	−32	−39	−29	+15	−2	−30	−32
			GFDL CM2.1	−20	−14	−33	−5	−5	−23	−43	−33	−31
			HadCM3	−11	+5	−42	−62	−12	+61	−2	−41	−42
			ECHAM5	−20	−17	−27	−1	−52	+35	−25	−13	−48
(Sugi et al., 2009)	JMA/MRI global AGCM time slice		Downscale A1B:									
		20 km	MRI CGCM2.3	−29	−31	−27	+22	−36	−39	−39	−28	−22
		20 km	MRI CGCM2.3	−25	−25	−25	+23	−29	−30	−29	−25	−27
		20 km	MIROC-H	−27	−15	−42	−18	+28	−50	+32	−24	−90
		20 km	CMIP3 n = 18 ens.	−20	−21	−19	+5	−26	−25	−15	−5	−42
		60 km	MRI CGCM2.3	−20	−21	−17	+58	−36	−31	−12	−22	−8
		60 km	MIROC-H	−6	0	−16	+6	+64	−42	+79	+10	−69
		60 km	CMIP3 n = 18 ens.	−21	−19	−25	+4	−14	−33	+33	−18	−36
		60 km	CSIRO	−22	−29	−11	−37	+13	−49	−7	−22	+10
(Murakami et al., 2012)	JMA/MRI global AGCM time slice	V3.1 20 km	Downscale CMIP3 multi-model ens. A1B change (2075–2099 minus control)	−23	−20	−25	+8	−27	−24	−14	−10	−45
		V3.2 20 km		−15	−14	−18	−29	−23	+1	−2	−23	−15
		V3.1 60 km		−23	−23	−24	−2	−20	−32	+21	−15	−39
		V3.2 60 km		−24	−23	−25	−39	−28	−10	−14	−24	−27
(Murakami et al., 2011)	JMA/MRI global AGCM time slice	V3.2 60 km	Downscale A1B:									
			YS, CMIP3 ens.	−27	−27	−27	−44	−33	−11	−16	−29	−31
			YS, Cluster 1	−25	−25	−27	−24	−32	−30	+19	−24	−37
			YS, Cluster 2	−28	−30	−26	−23	−42	−9	−21	−20	−42
			YS, Cluster 3	−14	−3	−35	−31	−2	+6	+1	−46	−25
			KF, CMIP3 ens.	−20	−24	−16	−39	−28	−3	−42	−24	−11
			KF, Cluster 1	−20	−27	−10	−40	−33	−15	−28	−20	−6
			KF, Cluster 2	−21	−28	−12	−21	−44	+5	−50	−10	−24
			KF, Cluster 3	−14	−12	−15	−53	−8	+17	−48	−26	−6
			AS, CMIP3 ens.	−20	−11	−33	+1	−19	−22	+1	−31	−43
			AS, Cluster 1	−22	−22	−24	−27	−19	−42	−20	−25	−27
			AS, Cluster 2	−13	−11	−17	+28	−32	+24	−5	−2	−44
			AS, Cluster 3	−14	0	−32	−24	+8	+15	−15	−48	−11
(Villarini et al., 2011)	Statistical downscale of CMIP3 models	---	24 CMIP3 model mean and ±1 σ range; A1B scenario, 21st century trend				Basin: −10 ± 29% US land: −3 ± 26					
(Emanuel et al., 2010)	Statistical-deterministic	--	Time slice using CMIP3 model mean SST change, 1990–2090, NICAM model 14 km		+45 (global but June to October only)							
(Yamada et al., 2010)	NICAM	14 km	Time slice using CMIP3 model mean SST change, 1990–2090		−35 (global but June to October only)		−80	0	0	−77		

(continued on next page)

Table 14.SM.4a (continued)

Tropical Storm Frequency Projections (%)												
Reference	Model/type	Resolution: high to low	Experiment	Basin								
				Global	NH	SH	N Atl.	NW Pac.	NE Pac.	N Ind.	S. Ind.	SW Pac.
(Lavender and Walsh, 2011)	CSIRO CCAM regional model nested in a suite of GCMs	15 km	A2 1990, 2090 GFDL CM2.1 MPI ECHAM5 CSIRO Mk3.5									 –38 –33 –27
(Li et al., 2010d)	ECHAM5 time slice	40 km	A1B change (2080–2009)					–31	+65			
(Yokoi and Takayabu, 2009)	CMIP3 ensemble	Various	A1B (2081–2100)					–1				
(Murakami et al., 2013)	JMA/MRI global AGCM time slice	V3.2 60 km	As in Murakami et al. (2011), but using different criteria for TC detection							–2		
(Villarini and Vecchi, 2012)	Statistical downscale of CMIP5 models	--	17 CMIP5 models Mean and (min/max range) RCP2.6 RCP4.5 RCP8.5 (late 21st century)				4 (–17,32) 4 (–30,57) 2 (–49,45)					

Table 14.SM.4b | Projected change in frequency of intense tropical cyclones (i.e., more intense than tropical storms) in warm climate runs relative to control run in percent. The rows of reported results are ordered from top to bottom generally in order of decreasing model horizontal resolution. Red and blue numbers/text denote projected increases and decreases, respectively. Bold text denotes where a statistical significance test was reported that showed significance.

Intense Tropical Cyclone Frequency Projections (%)												
Reference	**Model/type**	**Resolution: high to low**	**Experiment**	**Basin**								
				Global	**NH**	**SH**	**N Atl.**	**NW Pac.**	**NE Pac.**	**N Ind.**	**S. Ind.**	**SW Pac.**
(Bender et al., 2010)	GFDL Hurricane model, with ocean coupling	9 km	Downscale TCs from ref 22 18-mod ensemble: (range over 4 indiv. models)				cat 4–5 freq: **+100%** (–66 to +138%)					
(Knutson et al., 2013)	GFDL Hurricane model, with ocean coupling	9 km	Downscale TCs (2081–2100) CMIP3 ens. A1B CMIP5 ens RCP45 Gfdl CM2.1 A1B MPI A1B HadCM3 A1B MRI A1B Gfdl CM2.0 A1B HadGEM1 A1B MIROC hi A1B CCMS3 A1B INGV A1B MIROC med A1B				cat 4–5 freq: **+87%** +39% **+116%** +21% –53% **+110%** **+211%** –100% –42% +26% +47% –32%					
(Knutson et al., 2008)	GFDL Zetac regional	18 km	Downscale CMIP3 ens. A1B, 2080–2100				+140% (12 vs 5) # w/$V_{sfc} > 45$ m s^{-1}					
(Murakami et al., 2013)	JMA/MRI global AGCM time slice	V3.2 20 km	Downscale CMIP3 multi-model ens. A1B change (2075–2099 minus control)	**# Cat 4–5:** +4% **# Cat. 5:** **+56%**	+9% **+60%**	–7% +43%	+15% **+287%**	–4% **+45%**	**+179%** Increase from 0	+35% +100%	**+45%** **+261%**	**–54%** **–61%**
(Oouchi et al., 2006)	MRI/JMA time slice	TL959 L60 (~20 km)	10 yr A1B 1982–1993 2080–2099	**Signif. Increase, # V_{850} of 55–60 m s^{-1}**								
(Walsh et al., 2004)	CSIRO DARLAM regional model	30 km	3 × CO_2; 2061–2090 minus 1961–1990									+26% P < 970 mb
(Bengtsson et al., 2007)	ECHAM5 time slice	T319 (~40 km)	2071–2100, A1B		+42%, # > 50 m s^{-1}							
(Zhao and Held, 2010)	GFDL HIRAM time slice with statistical refinement of intensity	50 km	Downscale A1B: CMIP3 *n* = 7 ens. GFDL CM2.0 GFDL CM2.1 HadCM3 HadGem1 ECHAM5 MRI_CGCM2.3 MIROC High				cat 3–5 hurr % –13 +9 +5 –28 –53 +24 0 –27					

(continued on next page)

Table 14.SM.4b (continued)

Intense Tropical Cyclone Frequency Projections (%)													
Reference	**Model/type**	**Resolution: high to low**	**Experiment**	**Basin**									
				Global	**NH**	**SH**	**N Atl.**	**NW Pac.**	**NE Pac.**	**N Ind.**	**S. Ind.**	**SW Pac.**
(Zhao and Held, 2012)	GFDL HIRAM time slice	50 km	Downscale A1B: CMIP3 $n = 8$ ens. GFDL CM2.0 GFDL CM2.1 HadCM3 HadGem1 ECHAM5 CCCMA MRI_CGCM2.3 MIROC High	# > 33 m s^{-1}, % **–15** –6 **–11** +6 **–11** **–14** **–22** **–16** –5	# > 33 **–16** –1 –5 **+17** –3 **–13** **–24** **–18** –6	# > 33 **–13** **–21** **–26** **–26** **–31** **–16** –16 –10 –4	# > 33 m s^{-1} **–20** +16 –4 **–51** **–84** **+25** **–42** +20 **–31**	# > 33 m s^{-1} **–30** **–19** +9 –11 **–29** **–49** **–37** **–33** **–17**	# > 33 +14 **+30** **–34** **+121** **+115** **+58** +17 –3 **+44**	# > 33 +6 +20 –31 +39 –35 –21 –21 –12 –40	# > 33 –11 –14 **–30** **–20** **–46** +9 –2 –12 +16	# > 33 –14 **–30** –19 **–35** –9 **–56** **–37** –7 **–34**
(Leslie et al., 2007)	OU-CGCM with high-res. window	Up to 50 km	2000 to 2050 control and IS92a (6 members)									+100% # > 30 m s^{-1} by 2050
(Bengtsson et al., 2007)	ECHAM5 time slice	T213 (~60 km)	2071–2100, A1B		+32%, # > 50 m s^{-1}							
(McDonald et al., 2005)	HadAM3 time slice	N144 L30 (~100 km)	15 yr IS95a 1979–1994 2082–2097	Increase In # strong TCs (vort > 24–30 × 10^{-5} s^{-1})								
(Sugi et al., 2002)	JMA time slice	T106 L21 (~120km)	10 yr 1 × CO_2, 2 × CO_2	~0 # >40 m s^{-1}								
(Gualdi et al., 2008)	SINTEX-G coupled model	T106 (~120 km)	30 yr 1 × CO_2, 2 × CO_2, 4 × CO_2	~0								
(Hasegawa and Emori, 2007)	CCSR/NIES/ Coupled model	T106 L56 (~120 km)	20 yr control Vs +1% yr^{-1} CO_2 (yr 61–80)	Rel. freq. of Pc <985 mb +21 couple +59 uncoup								
(Yoshimura et al., 2006)	JMA time slice	T106 L21 (~120 km)	10 yr 1 × CO_2, 2 × CO_2	Mixed changes: # >25 m s^{-1}								

Table 14.SM.4c | Tropical cyclone intensity change projections (percent change in maximum wind speed or central pressure fall, except as noted in the table). The dynamical model projections are ordered from top to bottom in order of decreasing model horizontal resolution. Red and blue colours denote increases and decreases, respectively. Pairs of numbers in parentheses denote ranges obtained using different models as input to a downscaling model or theory. The potential intensity change projections from Emanuel et al. (2008), Knutson and Tuleya (2004) and Vecchi and Soden (2007a) in the table include some unpublished supplemental results (personal communication from the authors) such as results for individual basins, ranges of results across models and results for additional or modified calculations that are adapted from the original papers but have been modified in order to facilitate intercomparison of methods and projection results from different studies. In some cases, Accumulated Cyclone Energy (ACE) or Power Dissipation Index (PDI) changes are reported, which depend on intensity, frequency and lifetime.

Tropical Cyclone Intensity Projections (%)													
Metric/ Reference	**Technique/ Model**	**Resolution/ Metric Type**	**Climate Change Scenario**	**Global**	**NH**	**SH**	**N Atl, NW Pac, NE Pac**	**N Atl.**	**NW Pac.**	**NE Pac.**	**N Ind.**	**S. Ind.**	**SW Pac.**
Dynamical or Stat/Dyn. Model Projections (Max wind speed % change)								Avg (low, high)					
(Emanuel et al., 2008)	Stat./Dyn. Model	Max Wind speed (%)	CMIP3 7-model A1B (2181–2200 minus 1981–2000)	1.7	3.1	0.2	3.3	2.0	4.1	–0.1	0.2	0.5	–0.8
(Bender et al., 2010)	GFDL Hurricane model	9 km; Max Wind speed (%)	Downscale TCs from ref 22 18-mod ensemble: CMIP3 A1B; yrs 2081–2100 minus 2001–2020					+0.7 (trop. storms) +6 (hurricanes)					
(Knutson et al., 2013)	GFDL Hurricane model	9 km; With ocean coupling; Max Wind speed change (%) of hurricanes	Downscale TCs (2081–2100) CMIP3 ens. A1B CMIP5 ens RCP45 Gfdl CM2.1 A1B MPI A1B HadCM3 A1B MRI A1B Gfdl CM2.0 A1B HadGEM1 A1B MIROC hi A1B CCMS3 A1B INGV A1B MIROC med A1B					**+6.1** **+4.0** **+8.6** **+4.2** +2.0 **+9.2** **+11** –2.7 +2.9 **+5.3** +5.9 +2.9					
(Knutson and Tuleya, 2004)	GFDL Hurricane Model	9 km grid inner nest; Max Wind speed (%)	CMIP2+ +1% yr^{-1} CO$_2$ 80-year trend				5.9	5.5 (1.5, 8.1)	5.4 (3.3, 6.7)	6.6 (1.1, 10.1)			
(Knutson and Tuleya, 2004)	GFDL Hurricane Model	9 km grid inner nest; Pressure fall (%)	CMIP2+ +1%/yr CO$_2$ 80-year trend				13.8	13.0 (3.2, 21.6)	13.6 (8.0, 16.5)	14.8 (3.6, 25.0)			
(Lavender and Walsh, 2011)	CCAM regional model nested in a suite of GCMs	15 km Max winds	A2 1990, 2090										+5 to +10%
(Knutson et al., 2001)	GFDL Hurricane Model	18 km grid w./ ocean coupling; Max Wind speed (%)	GFDL R30 downscale, +1% yr^{-1} CO$_2$ yr 71–120 avg	6									
(Knutson et al., 2008)	GFDL Zetac regional	18 km; Max Wind speed (%)	Downscale CMIP3 ens. A1B, 2080–2100					+2.9					

(continued on next page)

Table 14.SM.4c (continued)

Tropical Cyclone Intensity Projections (%)														
Metric/ Reference	**Technique/ Model**	**Resolution/ Metric Type**	**Climate Change Scenario**	**Global**	**NH**	**SH**	**N Atl, NW Pac, NE Pac**	**N Atl.**	**NW Pac.**	**NE Pac.**	**N Ind.**	**S. Ind.**	**SW Pac.**
(Knutson et al., 2013)	GFDL Zetac regional	18 km; Max Wind speed (%) of hurricanes	Downscale TCs (2081–2100)										
			CMIP3 ens. A1B					**+2.0**					
			CMIP5 ens RCP45					**+2.2**					
			Gfdl CM2.1 A1B					**+2.8**					
			MPI A1B					+3.6					
			HadCM3 A1B					+0.9					
			MRI A1B					+4.0					
			Gfdl CM2.0 A1B					**+3.6**					
			HadGEM1 A1B					+1.5					
			MIROC hi A1B					+2.3					
			CCMS3 A1B					+3.8					
			INGV A1B					+2.0					
			MIROC med A1B					+2.1					
(Murakami et al., 2013)	JMA/MRI global AGCM time slice	V3.1 20 km V3.2 20 km; Avg. max winds over lifetime of all TCs	Downscale CMIP3 multi-model ens. A1B change (2075–2099 minus control)	**11** **4**	**12** **6**	**10** 0		**5** **10**	**18** **7**	**12** **6**	**5** **7**	**10** **7**	**8** **–10**
(Oouchi et al., 2006)	MRI/JMA Time slice	TL959 L60 (~20 km) Avg. lifetime max windspeed	10 yr A1B 1982–1993 2080–2099	10.7	8.5	14.1		11.2	4.2	0.6	–12.8	17.3	–2.0
(Oouchi et al., 2006)	MRI/JMA time slice	TL959 L60 (~20 km) Avg. annual max winds	10 yr A1B 1982–1993 2080–2099	13.7	15.5	6.9		20.1	–2.0	–5.0	–16.7	8.2	–22.5
(Semmler et al., 2008)	Rossby Centre regional model	28 km; Max winds	16-year control and A2, 2085–2100					+4					
(Chauvin et al., 2006)	ARPEGE Climat time slice	~50 km Max winds	Downscale - CNRM B2 - Hadley A2					 ~0 ~0					
(Sugi et al., 2002)	JMA time slice	T106 L21 (~120 km) Max winds	10 yr 1 × CO_2, 2 × CO_2	~0									
(Gualdi et al., 2008)	SINTEX-G coupled model	T106 (~120 km); Max winds	30 yr 1 × CO_2, 2 × CO_2, 4 × CO_2	~0									
(Hasegawa and Emori, 2005)	CCSR/NIES/FRCGC time slice	T106 L56 (~120 km) Max winds	5 × 20 yr at 1 × CO_2 7 × 20 yr at 2 × CO_2						Decrease				
(Yoshimura et al., 2006)	JMA time slice	T106 L21 (~120 km) Max winds	10 yr 1 × CO_2, 2 × CO_2	~0									
(Hasegawa and Emori, 2007)	CCSR/NICS/FRC Coupled GCM	T106 L56 (~120 km) Max winds	20-year control Vs +1% yr^{-1} CO_2 (yr 61–80)	~0 for Pc < 985 mb									

(continued on next page)

Table 14.SM.4c (continued)

Tropical Cyclone Intensity Projections (%)													
Metric/ Reference	**Technique/ Model**	**Resolution/ Metric Type**	**Climate Change Scenario**	**Global**	**NH**	**SH**	**N Atl, NW Pac, NE Pac**	**N Atl.**	**NW Pac.**	**NE Pac.**	**N Ind.**	**S. Ind.**	**SW Pac.**
Potential Intensity Theory Projections of Intensity (% Change)								Avg (low, high)					
(Vecchi and Soden, 2007b)	Emanuel PI, reversible w/ diss. heating	Max Wind speed (%)	CMIP3 18-model A1B (100-year trend)	2.6	2.7	2.4	2.1	0.05 (−8.0, 4.6)	2.9 (−3.1, 12.6)	3.5 (−6.4 16.1)	4.4 (−3.3, 16.0)	3.7 (−7.6, 17.1)	0.99 (−8.6, 8.6)
(Knutson and Tuleya, 2004)	Potential Intensity Emanuel, reversible	Pressure fall (%)	CMIP2+ +1% yr^{-1} CO$_2$ 80-year trend				5.0	2.6 (−5.6, 12.6)	7.0 (−1.0, 19.6)	5.4 (−5.0, 21.9)			
(Knutson and Tuleya, 2004)	Potential Intensity, Emanuel, pseudoadiabatic	Pressure fall (%)	CMIP2+ +1% yr^{-1} CO$_2$ 80-year trend				7.6	6.0 (1.6, 13.2)	8.5 (2.8, 25.2)	8.2 (−3.3, 28.0)			
(Knutson and Tuleya, 2004)	Potential Intensity, Holland	Pressure fall (%)	CMIP2+ +1% yr^{-1} CO$_2$ 80-year trend				15.2	12.4 (−4.0, 28.9)	17.3 (9.4, 30.6)	15.8 (3.4, 42.5)			
(Yu et al., 2010a)	Emanuel PI modified by vertical wind shear	Max Wind speed (%)	CMIP3 18 model ensemble 1% yr^{-1} CO$_2$, 70-year trend					−0.1 to 2.3	2.3	2.4	3.3	3.4	1.0
ACE or PDI (% change) using Dynamical or Stat/Dyn. Models													
(Emanuel et al., 2010)	Stat./Dyn. Model	Power Dissipation Index (%)	Time slice using CMIP3 ens. mean SST change, 1990–2090, and NICAM model 14 km fields		+65% in PDI,; (global but June to October only)								
(Yamada et al., 2010)	NICAM GCM	14 km Metric: ACE (Accum. Cyclone Energy)	Time slice using CMIP3 model mean SST change, 1990–2090		−14% (ACE) (global but June to October only)			−88% (ACE)	+17% (ACE)	+65% (ACE)	−86% ACE	−14% ACE	
(Stowasser et al., 2007)	IPRC Regional model	~50 km PDI	Downscale NCAR CCSM2, 6 × CO$_2$						+50% in PDI,; incr. intensity				
(Villarini and Vecchi, 2012)	Statistical downscale of CMIP5 models	—	17 CMIP5 models Mean and (min/max range) RCP2.6 RCP4.5 RCP8.5 (late 21st century)					PDI: **34** (−1,126) **57** (−21,270) **110** (−23,320)					

Table 14.SM.4d | Tropical cyclone-related precipitation projected changes (%) for the late 21st century (relative to present day). Results from Gualdi et al. (2008) are from original paper and personal communication with the authors (2009, 2010).

Tropical Cyclone Precipitation Projections						
Reference	**Model/Type**	**Resolution/**	**Experiment**	**Basins**	**Radius Around Storm Center**	**Percent Change**
(Hasegawa and Emori, 2005)	CCSR/NIES/FRCGC time slice	T106 L56 (~120 km)	5 × 20 yr at 1 × CO_2 7 × 20 yr at 2 × CO_2	NW Pacific	1000 km	+8.4 (all TC periods)
(Yoshimura et al., 2006)	JMA GSM8911 time slice	T106 L21 (~120 km)	10 yr 1 × CO_2, 2 × CO_2	Global	300 km	+10 (all TC periods) Arakawa-Schubert +15 (all TC periods) Kuo
(Chauvin et al., 2006)	ARPEGE Climat time slice	~50 km	Downscale CNRM B2 Downscale Hadley A2	Atlantic	n/a	Substantial increase
(Bengtsson et al., 2007)	ECHAM5 time slice	T213 (~60 km)	2071–2100, A1B	Northern Hemisphere	550 km Accum. along path	+21 (all TCs) +30 (TC > 33 m s^{-1} intensity)
(Knutson et al., 2008)	GFDL Zetac regional	18 km	Downscale CMIP3 ens. A1B, 2080–2100	Atlantic	50 km 100 km 400 km	+37 (all hurricane periods) +23 " +10 "
(Knutson et al., 2013)	GFDL Zetac regional/ GFDL hurricane model	18 km/9 km	Downscale TCs (2081–2100)	Atlantic		Zetac/Hurr. Model
			CMIP3 ens. A1B		100 km	+19/+22 (all TC periods)
			CMIP5 ens: RCP 4.5		100 km	+13/+19 " " "
			GFDL CM2.1 A1B		100 km	+22/+28 " " "
			MPI A1B		100 km	+24/+33 " " "
			HadCM3 A1B		100 km	+12/+8.2 " " "
			MRI A1B		100 km	+28/+24 " " "
			GFDL CM2.0 A1B		100 km	+26/+34 " " "
			HadGEM1 A1B		100 km	+11/-4.3 " " "
			MIROC hi A1B		100 km	+22/+14 " " "
			NCAR CCMS3 A1B		100 km	+23/+29 " " "
			INGV A1B		100 km	+19/+26 " " "
			MIROC med A1B		100 km	+22/+12 " " "
(Knutson and Tuleya, 2004)	GFDL Hurricane Model (idealized)	9 km inner nest	CMIP2+ +1% yr^{-1} CO_2 80-year trend	Atlantic, NE Pacific, NW Pacific	~100 km	+22 (at time of max hurricane intensity)
(Gualdi et al., 2008)	SINTEX-G coupled model	T106 (~120 km)	30 yr 1 × CO_2, 2 × CO_2	Global	100 km 400 km 100 km 400 km	+6.1 (all TC periods) +2.8 (all TC periods) +11 (at time of max winds) +4.9 (at time of max winds)

References

Annamalai, H., S. Xie, J. McCreary, and R. Murtugudde, 2005: Impact of Indian Ocean sea surface temperature on developing El Nino. *J. Clim.*, **18**, 302–319.

Arblaster, J. M., G. A. Meehl, and D. J. Karoly, 2011: Future climate change in the Southern Hemisphere: Competing effects of ozone and greenhouse gases. *Geophys. Res. Lett.*, **38**, L02701.

Arias, P. A., R. Fu, and C. M. Kingtse, 2012: Decadal variation of rainfall seasonality in the North American monsoon region and its potential causes. *J. Clim.*, **25**, 4258–4274.

Ashok, K., S. K. Behera, S. A. Rao, H. Y. Weng, and T. Yamagata, 2007: El Nino Modoki and its possible teleconnection. *J. Geophys. Res. Oceans*, **112**, C11007.

Barriopedro, D., R. Garcia-Herrera, A. R. Lupo, and E. Hernandez, 2006: A climatology of Northern Hemisphere blocking. *J. Clim.*, **19**, 1042–1063.

Barros, V. R., M. Doyle, and I. Camilloni, 2008: Precipitation trends in southeastern South America: Relationship with ENSO phases and the low-level circulation. *Theor. Appl. Climatol.*, **93**, 19–33.

Bell, C. J., L. J. Gray, A. J. Charlton-Perez, M. M. Joshi, and A. A. Scaife, 2009: Stratospheric communication of El Nino teleconnections to European winter. *J. Clim.*, **22**, 4083–4096.

Bender, M. A., T. R. Knutson, R. E. Tuleya, J. J. Sirutis, G. A. Vecchi, S. T. Garner, and I. M. Held, 2010: Modeled impact of anthropogenic warming on the frequency of intense Atlantic hurricanes. *Science*, **327**, 454–458.

Bengtsson, L., K. I. Hodges, M. Esch, N. Keenlyside, L. Kornblueh, J.-J. Luo, and T. Yamagata, 2007: How may tropical cyclones change in a warmer climate? *Tellus A*, **59**, 539–561.

Bennartz, R., J. Fan, J. Rausch, L. Y. R. Leung, and A. K. Heidinger, 2011: Pollution from China increases cloud droplet number, suppresses rain over the East China Sea. *Geophys. Res. Lett.*, **38**, doi: 10.1029/2011GL047235.

Bister, M., and K. A. Emanuel, 1998: Dissipative heating and hurricane intensity. *Meteorol. Atmos. Phys.*, **65**, 233–240.

Bjerknes, J., 1966: A possible response of atmospheric Hadley circulation to equatorial anomalies of ocean temperature. *Tellus*, **18**, 820–829.

Bjerknes, J, 1969: Atmospheric teleconnections from the Equatorial Pacific. *Mon. Weather Rev.*, **97**, 163–172.

Bladé, I., B. Liebmann, D. Fortuny, and G. Oldenborgh, 2012: Observed and simulated impacts of the summer NAO in Europe: Implications for projected drying in the Mediterranean region. *Clim. Dyn.*, **39**, 709–727.

Bombardi, R. J., and L. M. V. Carvalho, 2009: IPCC global coupled model simulations of the South America monsoon system. *Clim. Dyn.*, **33**, 893–916.

Booth, B. B. B., N. J. Dunstone, P. R. Halloran, T. Andrews, and N. Bellouin, 2012: Aerosols implicated as a prime driver of twentieth-century North Atlantic climate variability. *Nature*, **484**, 228–232.

Boulanger, J., S. Schlindwein, and E. Gentile, 2011: CLARIS LPB WP1: Metamorphosis of the CLARIS LPB European project: From a mechanistic to a systemic approach. *CLIVAR Exchanges no. 57 (World Climate Research Programme)*, **16**, 7–10.

Bracegirdle, T. J., et al., 2013: Assessment of surface winds over the Atlantic, Indian, and Pacific Ocean sectors of the Southern Ocean in CMIP5 models: Historical bias, forcing response, and state dependence. *J. Geophys. Res. Atmos.*, **118**, 547–562.

Brier, G. W., 1978: The Quasi-Biennial Oscillation and feedback processes in the atmosphere-ocean-earth system. *Mon. Weather Rev.*, **106**, 938–946.

Bromirski, P. D., and J. P. Kossin, 2008: Increasing hurricane wave power along the U.S. Atlantic and Gulf coasts. *J. Geophys. Res. Oceans*, **113**, C07012.

Bronnimann, S., 2007: Impact of El Nino Southern Oscillation on European climate. *Rev. Geophys.*, **45**, doi: 10.1029/2006RG000199.

Bulic, I., C. Brankovic, and F. Kucharski, 2012: Winter ENSO teleconnections in a warmer climate. *Clim. Dyn.*, **38**, 1593–1613.

Cagnazzo, C., and E. Manzini, 2009: Impact of the stratosphere on the winter tropospheric teleconnections between ENSO and the North Atlantic and European region. *J. Clim.*, **22**, 1223–1238.

Callaghan, J., and S. Power, 2010: A reduction in the frequency of severe land-falling tropical cyclones over eastern Australia in recent decades. *Clim. Dyn.*, doi:10.1007/s00382-010-0883-2.

Camargo, S., M. Ting, and Y. Kushnir, 2012: Influence of local and remote SST on North Atlantic tropical cyclone potential intensity *Clim. Dyn.*, **40**, 1515–1529.

Camargo, S. J., A. W. Robertson, A. G. Barnston, and M. Ghil, 2008: Clustering of eastern North Pacific tropical cyclone tracks: ENSO and MJO effects. *Geochem. Geophys. Geosyst.*, **9**, doi: 10.1029/2007GC001861.

Camargo, S. J., A. W. Robertson, S. J. Gaffney, P. Smyth, and M. Ghil, 2007: Cluster analysis of typhoon tracks. Part I: General properties. *J. Clim.*, **20**, 3635–3653.

Carvalho, L. M. V., C. Jones, and T. Ambrizzi, 2005: Opposite phases of the antarctic oscillation and relationships with intraseasonal to interannual activity in the tropics during the austral summer. *J. Clim.*, **18**, 702–718.

Cassou, C., 2008: Intraseasonal interaction between the Madden-Julian Oscillation and the North Atlantic Oscillation. *Nature*, **455**, 523–527.

Cavalcanti, I. F. A., 2012: Large scale and synoptic features associated with extreme precipitation over South America: A review and case studies for the first decade of the 21st century. *Atmos. Res.*, **118**, 27–40.

Chan, J. C. L., and M. Xu, 2009: Inter-annual and inter-decadal variations of landfalling tropical cyclones in East Asia. Part I: Time series analysis. *Int. J. Climatol.*, **29**, 1285–1293.

Chan, S. C., S. K. Behera, and T. Yamagata, 2008: Indian Ocean Dipole influence on South American rainfall. *Geophys. Res. Lett.*, **35**, L14S12.

Chand, S. S., and K. J. E. Walsh, 2009: Tropical cyclone activity in the Fiji region: Spatial patterns and relationship to large-scale circulation. *J. Clim.*, **22**, 3877–3893.

Chang, C., and T. Li, 2000: A theory for the tropical tropospheric biennial oscillation. *J. Atmos. Sci.*, **57**, 2209–2224.

Chang, C., J. Chiang, M. Wehner, A. Friedman, and R. Ruedy, 2011: Sulfate aerosol control of tropical Atlantic climate over the twentieth century. *J. Clim.*, **24**, 2540–2555.

Chang, E. K. M., and Y. Guo, 2007: Is the number of North Atlantic tropical cyclones significantly underestimated prior to the availability of satellite observations? *Geophys. Res. Lett.*, **34**, L14801.

Chauvin, F., J.-F. Royer, and M. Déqué, 2006: Response of hurricane-type vortices to global warming as simulated by ARPEGE-Climat at high resolution. *Clim. Dyn.*, **27**, 377–399.

Chen, G., and C.-Y. Tam, 2010: Different impacts of two kinds of Pacific Ocean warming on tropical cyclone frequency over the western North Pacific. *Geophysical Research Letters*, **37**, doi: 10.1029/2009gl041708.

Cherchi, A., A. Alessandri, S. Masina, and A. Navarra, 2011: Effects of increased CO_2 levels on monsoons. *Clim. Dyn.*, **37**, 83–101.

Chou, C., and C.-A. Chen, 2010: Depth of convection and the weakening of tropical circulation in global warming. *J. Clim.*, **23**, 3019–3030.

Chu, P., J. Kim, and Y. Chen, 2012: Have steering flows in the western North Pacific and the South China Sea changed over the last 50 years? *Geophys. Res. Lett.*, **39**.

Clarke, A., X. Liu, and S. Van Gorder, 1998: Dynamics of the biennial oscillation in the equatorial Indian and far western Pacific Oceans. *J. Clim.*, **11**, 987–1001.

Collini, E. A., E. H. Berbery, V. R. Barros, and M. E. Pyle, 2008: How does soil moisture influence the early stages of the South American monsoon? *J. Clim.*, **21**, 195–213.

Conroy, J., and J. Overpeck, 2011: Regionalization of present-day precipitation in the greater monsoon region of Asia. *J. Clim.*, **24**, 4073–4095.

Costa, M. H., S. N. M. Yanagi, P. J. O. P. Souza, A. Ribeiro, and E. J. P. Rocha, 2007: Climate change in Amazonia caused by soybean cropland expansion, as compared to caused by pastureland expansion. *Geophys. Res. Lett.*, **34**, L07706.

Cox, P. M., et al., 2008: Increasing risk of Amazonian drought due to decreasing aerosol pollution. *Nature*, **453**, 212–215.

Della-Marte, F., J. Lutterbacher, H. von Weissenfluh, E. Xoplaki, M. Brunet, and H. Wanner, 2007: Summer heat waves over western Europe 1880–2003, their relationship to large-scale forcings and predictability, *Clim. Dyn.* **29**, 251-275.

Di Lorenzo, E., et al., 2010: Central Pacific El Nino and decadal climate change in the North Pacific Ocean. *Nature Geosci.*, **3**, 762–765.

Ding, Q., E. Steig, D. Battisti, and M. Kuttel, 2011: Winter warming in West Antarctica caused by central tropical Pacific warming. *Nature Geosci.*, **4**, 398–403.

Ding, Q. H., and B. Wang, 2009: Predicting extreme phases of the Indian summer monsoon. *J. Clim.*, **22**, 346–363.

Ding, Y., Z. Wang, and Y. Sun, 2008: Inter-decadal variation of the summer precipitation in East China and its association with decreasing Asian summer monsoon. Part I: Observed evidences. *Int. J. Climatol.*, **28**, 1139–1161.

Ding, Y., Y. Sun, Z. Wang, Y. Zhu, and Y. Song, 2009: Inter-decadal variation of the summer precipitation in China and its association with decreasing Asian summer monsoon Part II: Possible causes. *Int. J. Climatol.*, **29**, 1926–1944.

Dole, R., M. Hoerling, J. Perlwitz, J. Eischeid, and P. Pegion, 2011: Was there a basis for anticipating the 2010 Russian heat wave? doi 10.1029/2010GL046582.

Douglas, A. V., and P. J. Englehart, 2007: A climatological perspective of transient synoptic features during NAME 2004. *J. Clim.*, **20**, 1947–1954.

Drumond, A. R. M., and T. Ambrizzi, 2005: The role of SST on the South American atmospheric circulation during January, February and March 2001. *Clim. Dyn.*, **24**, 781–791.

Duan, A., and G. Wu, 2008: Weakening trend in the atmospheric heat source over the Tibetan Plateau during recent decades. Part I: Observations. *J. Clim.*, **21**, 3149–3164.

Elsner, J. B., J. P. Kossin, and T. H. Jagger, 2008: The increasing intensity of the strongest tropical cyclones. *Nature*, **455**, 92–95.

Emanuel, K., 2005: Increasing destructiveness of tropical cyclones over the past 30 years. *Nature*, **436**, 686–688.

Emanuel, K., 2010: Tropical cyclone activity downscaled from NOAA-CIRES reanalysis, 1908–1958. *J. Adv. Model. Earth Syst.*, **2**, 12.

Emanuel, K., R. Sundararajan, and J. Williams, 2008: Hurricanes and global warming: Results from downscaling IPCC AR4 simulations. *Bull. Am. Meteorol. Soc.*, **89**, 347–367.

Emanuel, K., K. Oouchi, M. Satoh, H. Tomita, and Y. Yamada, 2010: Comparison of explicitly simulated and downscaled tropical cyclone activity in a high-resolution global climate model. *J. Adv. Model. Earth Syst.*, **2**, doi: 10.3894/JAMES.2010.2.9.

Emanuel, K., S. Solomon, D. Folini, S. Davis, and C. Cagnazzo, 2012: Influence of tropical tropopause layer cooling on Atlantic hurricane activity. *J. Clim.*, **26**, 2288–2301.

Emanuel, K. A., 1987: Dependence of hurricane intensity on climate. *Nature*, **326**, 483–485.

Emanuel, K. A., 2000: A statistical analysis of tropical cyclone intensity. *Mon. Weather Rev.*, **128**, 1139–1152.

Espinoza, J. C., et al., 2011: Climate variability and extreme drought in the upper SolimÕes River (western Amazon Basin): Understanding the exceptional 2010 drought. *Geophys. Res. Lett.*, **38**, L13406.

Evan, A., G. Foltz, and D. Zhang, 2012: Physical response of the tropical-subtropical North Atlantic Ocean to decadal-multidecadal forcing by African dust. *J. Clim.*, **25**, 5817–5829.

Evan, A., G. Foltz, D. Zhang, and D. Vimont, 2011: Influence of African dust on ocean-atmosphere variability in the tropical Atlantic. *Nature Geosci.*, **4**, 762–765.

Evan, A. T., D. J. Vimont, A. K. Heidinger, J. P. Kossin, and R. Bennartz, 2009: The Role of Aerosols in the Evolution of Tropical North Atlantic Ocean Temperature Anomalies. *Science*, **324**, 778–781.

Feliks, Y., M. Ghil, and A. W. Robertson, 2010: Oscillatory climate modes in the eastern Mediterranean and their synchronization with the North Atlantic Oscillation. *J. Clim.*, **23**, 4060–4079.

Feng, J., and J. P. Li, 2011: Influence of El Nino Modoki on spring rainfall over south China. *J. Geophys. Res. Atmos.*, **116**, doi: 10.1029/2010jd015160.

Feng, J., L. Wang, W. Chen, S. Fong, and K. Leong, 2010: Different impacts of two types of Pacific Ocean warming on Southeast Asian rainfall during boreal winter. *J. Geophys. Res. Atmos.*, **115**, doi: 10.1029/2010JD014761.

Feng, S., and Q. Hu, 2008: How the North Atlantic Multidecadal Oscillation may have influenced the Indian summer monsoon during the past two millennia? *Geophys. Res. Lett.*, **35**, doi:10.1029/2007GL032484.

Fogt, R. L., and D. H. Bromwich, 2006: Decadal variability of the ENSO teleconnection to the high-latitude South Pacific governed by coupling with the Southern Annular Mode. *J. Clim.*, **19**, 979–997.

Fogt, R. L., J. M. Jones, and J. A. Renwick, 2012: Seasonal zonal asymmetries in the Southern Annular Mode and their impact on regional temperature anomalies. *J. Clim.*, **25**, 6253-6270.

Folland, C. K., J. Knight, H. W. Linderholm, D. Fereday, S. Ineson, and J. W. Hurrell, 2009: The summer North Atlantic Oscillation: Past, present, and future. *J. Clim.*, **22**, 1082–1103.

Fraisse, C. W., V. E. Cabrera, N. E. Breuer, J. Baez, J. Quispe, and E. Matos, 2008: El Niño—Southern Oscillation influences on soybean yields in eastern Paraguay. *Int. J. Climatol.*, **28**, 1399–1407.

Garreaud, R. D., and M. Falvey, 2009: The coastal winds off western subtropical South America in future climate scenarios. *Int. J. Climatol.*, **29**, 543–554.

Gergis, J., and A. Fowler, 2009: A history of ENSO events since A.D. 1525: Implications for future climate change. *Clim. Change*, **92**, 343–387.

Giese, B., and S. Ray, 2011: El Niño variability in simple ocean data assimilation (SODA), 1871–2008. *J. Geophys. Res. Oceans*, **116**.

Gillett, N. P., P. A. Stott, and B. D. Santer, 2008: Attribution of cyclogenesis region sea surface temperature change to anthropogenic influence. *Geophys. Res. Lett.*, **35**, L09707.

Golding, N., and R. Betts, 2008: Fire risk in Amazonia due to climate change in the HadCM3 climate model: Potential interactions with deforestation. *Global Biogeochem. Cycles*, **22**, GB4007.

Gong, D. Y., and C. H. Ho, 2002: The Siberian High and climate change over middle to high latitude Asia. *Theor. Appl. Climatol.*, **72**, 1–9.

Good, P., J. A. Lowe, M. Collins, and W. Moufouma-Okia, 2008: An objective tropical Atlantic sea surface temperature gradient index for studies of south Amazon dry-season climate variability and change. *Philos. Trans. R. Soc. B*, **363**, 1761–1766.

Graf, H., and D. Zanchettin, 2012: Central Pacific El Nino, the "subtropical bridge," and Eurasian climate. *J. Geophys. Res. Atmos.*, **117**, doi: 10.1029/2011JD016493.

Grimm, A. M., 2011: Interannual climate variability in South America: Impacts on seasonal precipitation, extreme events and possible effects of climate change. *Stochast. Environ. Res. Risk Assess.*, **25**, 537–554.

Grimm, A. M., and A. A. Natori, 2006: Climate change and interannual variability of precipitation in South America. *Geophys. Res. Lett.*, **33**, L19706.

Grimm, A. M., and R. G. Tedeschi, 2009: ENSO and extreme rainfall events in South America. *J. Clim.*, **22**, 1589–1609.

Grimm, A. M., J. S. Pal, and F. Giorgi, 2007: Connection between spring conditions and peak summer monsoon rainfall in South America: Role of soil moisture, surface temperature, and topography in eastern Brazil. *J. Clim.*, **20**, 5929–5945.

Grinsted, A., J. C. Moore, and S. Jevrejeva, 2012: Homogeneous record of Atlantic hurricane surge threat since 1923. *Proc. Natl. Acad. Sci. U.S.A.*, **109**, 19601–19605.

Gu, Y., K. Liou, Y. Xue, C. Mechoso, W. Li, and Y. Luo, 2006: Climatic effects of different aerosol types in China simulated by the UCLA general circulation model. *J. Geophys. Res.*, **111**, D15201.

Gualdi, S., E. Scoccimarro, and A. Navarra, 2008: Changes in tropical cyclone activity due to global warming: Results from a high-resolution coupled general circulation model. *J. Clim.*, **21**, 5204–5228.

Guanghua, C., and T. Chi-Yung, 2010: Different impacts of two kinds of Pacific Ocean warming on tropical cyclone frequency over the western North Pacific. *Geophys. Res. Lett.*, **37**, doi: 10.1029/2009gl041708.

Gulizia, C., I. Camilloni, and M. Doyle, 2013: Identification of the principal patterns of summer moisture transport in South America and their representation by WCRP/CMIP3 global climate models. *Theor. Appl. Climatol.*, **112**, 227–241.

Guo, L., E. J. Highwood, L. C. Shaffrey, and A. G. Turner, 2013: The effect of regional changes in anthropogenic aerosols on rainfall of the East Asian Summer Monsoon. *Atmos. Chem. Phys.*, **13**, 1521–1534.

Hagen, A. B., and C. W. Landsea, 2012: On the classification of extreme Atlantic hurricanes utilizing mid-twentieth-century monitoring capabilities. *J. Clim.*, **25**, 4461–4475.

Hagen, A. B., D. Strahan-Sakoskie, and C. Luckett, 2012: A reanalysis of the 1944–53 Atlantic hurricane seasons — The first decade of aircraft reconnaissance. *J. Clim.*, **25**, 4441–4460.

Harris, P. P., C. Huntingford, and P. M. Cox, 2008: Amazon Basin climate under global warming: The role of the sea surface temperature. *Philos. Trans. R. Soc. B*, **363**, 1753–1759.

Hasegawa, A., and S. Emori, 2005: Tropical cyclones and associated precipitation over the western north Pacific: T106 atmospheric GCM simulation for present-day and doubled CO_2 climates. *Sola*, **1**, 145–148.

Hasegawa, A., and S. Emori, 2007: Effect of air-sea coupling in the assessment of CO_2-induced intensification of tropical cyclone activity. *Geophys. Res. Lett.*, **34**, doi: 10.1029/2006GL028275.

Hendon, H. H., D. W. J. Thompson, and M. C. Wheeler, 2007: Australian rainfall and surface temperature variations associated with the Southern Hemisphere annular mode. *J. Clim.*, **20**, 2452–2467.

Higgins, R. W., Y. Yao, and X. L. Wang, 1997: Influence of the North American monsoon system on the U.S. summer Precipitation. *J. Clim.*, **10**, 2600-2622.

Hirschi, M., and S. I. Seneviratne, 2010: Intra-annual link of spring and autumn precipitation over France. *Clim. Dyn.*, **35**, 1207–1218.

Ho, C., J. Baik, J. Kim, D. Gong, and C. Sui, 2004: Interdecadal changes in summertime typhoon tracks. *J. Clim.*, **17**, 1767–1776.

Hoerling, M. P., A. Kumar, and M. Zhong, 1997: El Nino, La Nina, and the nonlinearity of their teleconnections. *J. Clim.*, **10**, 1769–1786.

Holland, G. J., and P. J. Webster, 2007: Heightened tropical cyclone activity in the North Atlantic: Natural variability or climate trend? *Philos. Trans. R. Soc. A*, **365**, 2695–2716.

Hong, C.-C., Y.-H. Li, T. Li, and M.-Y. Lee, 2011: Impacts of central Pacific and eastern Pacific El Ninos on tropical cyclone tracks over the western North Pacific. *Geophys. Res. Lett.*, **38**, doi: 10.1029/2011gl048821.

Hu, Z., A. Kumar, B. Jha, W. Wang, B. Huang, and B. Huang, 2012: An analysis of warm pool and cold tongue El Niños: Air-sea coupling processes, global influences, and recent trends. *Clim. Dyn.*, **38**, 2017–2035.

Hu, Z. Z., 1997: Interdecadal variability of summer climate over East Asia and its association with 500 hPa height and global sea surface temperature. *J. Geophys. Res. Atmos.*, **102**, 19403–19412.

Ineson, S., and A. Scaife, 2009: The role of the stratosphere in the European climate response to El Nino. *Nature Geosci.*, doi:DOI 10.1038/NGEO381, 32–36.

Izumo, T., et al., 2010: Influence of the state of the Indian Ocean Dipole on the following year's El Nino. *Nature Geosci.*, **3**, 168–172.

Jones, C., and L. M. V. Carvalho, 2013: Climate change in the South American Monsoon System:present climate and CMIP5 projections. *J. Clim.*, doi:10.1175/JCLI-D-12–00412.1.

Jones, J. M., R. L. Fogt, M. Widmann, G. J. Marshall, P. D. Jones, and M. Visbeck, 2009: Historical SAM variability. Part I: Century-length seasonal reconstructions. *J. Clim.*, **22**, 5319–5345.

Kao, H. Y., and J. Y. Yu, 2009: Contrasting Eastern-Pacific and Central-Pacific types of ENSO. *J. Clim.*, **22**, 615–632.

Karoly, D. J., and Q. G. Wu, 2005: Detection of regional surface temperature trends. *J. Clim.*, **18**, 4337–4343.

Karpechko, A. Y., N. P. Gillett, L. J. Gray, and M. Dall'Amico, 2010: Influence of ozone recovery and greenhouse gas increases on Southern Hemisphere circulation. *J. Geophys. Res.*, **115**, D22117.

Kidston, J., J. A. Renwick, and J. McGregor, 2009: Hemispheric-scale seasonality of the Southern Annular Mode and impacts on the climate of New Zealand. *J. Clim.*, **22**, 4759–4770.

Kim, D., K. Choi, and H. Byun, 2012: Effects of El Nino Modoki on winter precipitation in Korea. *Clim. Dyn.*, **38**, 1313–1324.

Kim, H. M., P. J. Webster, and J. A. Curry, 2009: Impact of shifting patterns of Pacific Ocean warming on north Atlantic tropical cyclones. *Science*, **325**, 77–80.

Kim, H. M., P. J. Webster, and J. A. Curry, 2011: Modulation of North Pacific tropical cyclone activity by three phases of ENSO. *J. Clim.*, **24**, 1839–1849.

Kim, M. K., W. K. M. Lau, K. M. Kim, and W. S. Lee, 2007: A GCM study of effects of radiative forcing of sulfate aerosol on large scale circulation and rainfall in East Asia during boreal spring. *Geophys. Res. Lett.*, **34**, L24701.

Knapp, K. R., and M. C. Kruk, 2010: Quantifying inter-agency differences in tropical cyclone best track wind speed estimates. *Mon. Weather Rev.*, **138**, 1459–1473.

Knutson, T., R. Tuleya, W. Shen, and I. Ginis, 2001: Impact of CO2–induced warming on hurricane intensities as simulated in a hurricane model with ocean coupling. *J. Clim.*, **14**, 2458–2468.

Knutson, T. R., and R. E. Tuleya, 2004: Impact of CO_2-induced warming on simulated hurricane intensity and precipitation: Sensitivity to the choice of climate model and convective parameterization. *J. Clim.*, **17**, 3477–3495.

Knutson, T. R., J. J. Sirutis, S. T. Garner, G. A. Vecchi, and I. M. Held, 2008: Simulated reduction in Atlantic hurricane frequency under twenty-first-century warming conditions. *Nature Geosci.*, **1**, 479.

Knutson, T. R., et al., 2006: Assessment of twentieth-century regional surface temperature trends using the GFDL CM2 coupled models. *J. Clim.*, **19**, 1624–1651.

Knutson, T. R., et al., 2010: Tropical cyclones and climate change. *Nature Geosci.*, **3**, 157–163.

Knutson, T. R., et al., 2013: Dynamical downscaling projections of 21st century Atlantic hurricane activity: CMIP3 and CMIP5 model-based scenarios. *J. Clim.*,**26**, 6591–6617.

Kossin, J., K. Knapp, D. Vimont, R. Murnane, and B. Harper, 2007: A globally consistent reanalysis of hurricane variability and trends. *Geophys. Res. Lett.*, **34**, doi: 10.1029/2006GL028836.

Kossin, J. P., 2008: Is the North Atlantic hurricane season getting longer? *Geophys. Res. Lett.*, **35**, L23705.

Kossin, J. P., and D. J. Vimont, 2007: A more general framework for understanding Atlantic hurricane variability and trends. *Bull. Am. Meteorol. Soc.*, **88**, 1767–1781.

Kossin, J. P., and S. J. Camargo, 2009: Hurricane track variability and secular potential intensity trends. *Clim. Change*, **97**, 329–337.

Kossin, J. P., S. J. Camargo, and M. Sitkowski, 2010: Climate modulation of North Atlantic hurricane tracks. *J. Clim.*, **23**, 3057–3076.

Krichak, S. O., and P. Alpert, 2005: Signatures of the NAO in the atmospheric circulation during wet winter months over the Mediterranean region. *Theor. Appl. Climatol.*, **82**, 27–39.

Krishna, K. M., 2009: Intensifying tropical cyclones over the North Indian Ocean during summer monsoon – Global warming. *Global Planet. Change*, **65**, 12–16.

Kubota, H., and J. C. L. Chan, 2009: Interdecadal variability of tropical cyclone landfall in the Philippines from 1902 to 2005. *Geophys. Res. Lett.*, **36**, doi: 10.1029/2009GL038108.

Kug, J.-S., F.-F. Jin, and S.-I. An, 2009: Two types of El Nino events: Cold tongue El Niño and warm pool El Niño. *J. Clim.*, **22**, 1499–1515.

Kug, J. S., S. I. An, Y. G. Ham, and I. S. Kang, 2010a: Changes in El Niño and La Niña teleconnections over North Pacific-America in the global warming simulations. *Theor. Appl. Climatol.*, **100**, 275–282.

Kug, J. S., J. Choi, S. I. An, F. F. Jin, and A. T. Wittenberg, 2010b: Warm pool and cold tongue El Nino events as simulated by the GFDL 2.1 coupled GCM. *J. Clim.*, **23**, 1226–1239.

Kumar, V., R. Deo, and V. Ramachandran, 2006: Total rain accumulation and rain-rate analysis for small tropical Pacific islands: A case study of Suva, Fiji. *Atmos. Sci. Lett.*, **7**, 53–58.

Kunkel, K. E., et al., 2008: Observed changes in weather and climate extremes. In: *Weather and Climate Extremes in a Changing Climate. Regions of Focus: North America, Hawaii, Caribbean, and U.S. Pacific Islands* [T. R. Karl et al. (eds.)]. U.S. Climate Change Science Program and the Subcommittee on Global Change Research, Washington DC, USA, pp. 35–80.

Küttel, M., J. Luterbacher, and H. Wanner, 2011: Multidecadal changes in winter circulation-climate relationship in Europe: frequency variations, within-type modifications, and long-term trends. *Climate Dynamics*, **36**, 957-972.

L'Heureux, M. L., and D. W. J. Thompson, 2006: Observed relationships between the El Niño–Southern Oscillation and the extratropical zonal-mean circulation. *J. Clim.*, **19**, 276–287.

Lagos, P., Y. Silva, E. Nickl, and K. Mosquera, 2008: El Niño-related precipitation variability in Perú. *Adv. Geosci.*, **14**, 231–237.

Landsea, C., G. Vecchi, L. Bengtsson, and T. Knutson, 2010: Impact of duration thresholds on Atlantic tropical cyclone counts. *J. Clim.*, **23**, 2508–2519.

Landsea, C., et al., 2012: A reanalysis of the 1921–30 Atlantic Hurricane Database. *J. Clim.*, **25**, 865–885.

Landsea, C. W., 2007: Counting Atlantic tropical cyclones back to 1900. *Eos Trans. (AGU)*, **88**, 197–202.

Landsea, C. W., B. A. Harper, K. Hoarau, and J. A. Knaff, 2006: Can we detect trends in extreme tropical cyclones? *Science*, **313**, 452–454.

Larkin, N. K., and D. E. Harrison, 2005: On the definition of El Nino and associated seasonal average US weather anomalies. *Geophys. Res. Lett.*, **32**, doi: 10.1029/2005gl022738.

Lau, K., and H. Wu, 2001: Principal modes of rainfall-SST variability of the Asian summer monsoon: A reassessment of the monsoon-ENSO relationship. *J. Clim.*, **14**, 2880–2895.

Lavender, S., and K. Walsh, 2011: Dynamically downscaled simulations of Australian region tropical cyclones in current and future climates. *Geophys. Res. Lett.*, **38**, doi: 10.1029/2011GL047499.

Lee, S.-K., C. Wang, and D. B. Enfield, 2010a: On the impact of central Pacific warming events on Atlantic tropical storm activity. *Geophys. Res. Lett.*, **37**, doi: 10.1029/2010gl044459.

Lee, T.-C., T. R. Knutson, H. Kamahori, and M. Ying, 2012: Impacts of climate change on tropical cyclones in the western North Pacific basin. Part I: Past observations. *Trop. Cyclone Res. Rev.*, **1**, 213–230.

Lee, T., and M. J. McPhaden, 2010: Increasing intensity of El Nino in the central-equatorial Pacific. *Geophys. Res. Lett.*, **37**, doi: 10.1029/2010gl044007.

Lee, T., W. Hobbs, J. Willis, D. Halkides, I. Fukumori, E. Armstrong, A. Hayashi, W. Liu, W. Patzert, and O. Wang, 2010: Record warming in the South Pacific and western Antarctica associated with the strong central-Pacific El Nino in 2009-10. *Geophys. Res. Lett.*, **37**, doi: 10.1029/2010GL044865.

Lei, Y., B. Hoskins, and J. Slingo, 2011: Exploring the interplay between natural decadal variability and anthropogenic climate change in summer rainfall over China. Part I: Observational evidence. *J. Clim.*, **24**, 4584–4599.

Leslie, L., D. Karoly, M. Leplastrier, and B. Buckley, 2007: Variability of tropical cyclones over the southwest Pacific Ocean using a high-resolution climate model. *Meteorol. Atmos. Phys.*, **97**, 171–180.

Lewis, S. L., P. M. Brando, O. L. Phillips, G. M. F. van der Heijden, and D. Nepstad, 2011: The 2010 Amazon drought. *Science*, **331**, 554–554.

Li, G., B. H. Ren, C. Y. Yang, and J. Q. Zheng, 2010a: Indices of El Niño and El Niño Modoki: An improved El Niño Modoki index. *Adv. Atmos. Sci.*, **27**, 1210–1220.

Li, H., T. Zhou, and C. Li, 2010b: Decreasing trend in global land monsoon precipitation over the past 50 years simulated by a coupled climate model. *Adv. Atmos. Sci.*, **27**, 285–292.

Li, H., A. Dai, T. Zhou, and J. Lu, 2010c: Responses of East Asian summer monsoon to historical SST and atmospheric forcing during 1950–2000. *Clim. Dyn.*, **34**, 501–514.

Li, J., R. Yu, W. Yuan, and H. Chen, 2011a: Changes in duration-related characteristics of late-summer precipitation over eastern China in the past 40 years. *J. Clim.* **24,** 5683–5690.

Li, L., B. Wang, and T. Zhou, 2007: Contributions of natural and anthropogenic forcings to the summer cooling over eastern China: An AGCM study. *Geophys. Res. Lett.*, **34**, doi: 10.1029/2007gl030541.

Li, T., C. Tham, and C. Chang, 2001: A coupled air-sea-monsoon oscillator for the tropospheric biennial oscillation. *J. Clim.*, **14**, 752–764.

Li, T., P. Liu, X. Fu, B. Wang, and G. Meehl, 2006: Spatiotemporal structures and mechanisms of the tropospheric biennial oscillation in the Indo-Pacific warm ocean regions. *J. Clim.*, **19**, 3070–3087.

Li, T., M. Kwon, M. Zhao, J. Kug, J. Luo, and W. Yu, 2010d: Global warming shifts Pacific tropical cyclone location. *Geophys. Res. Lett.*, **37**, doi: 10.1029/2010GL045124.

Li, W., P. Zhang, J. Ye, L. Li, and P. Baker, 2011b: Impact of two different types of El Nino events on the Amazon climate and ecosystem productivity. *J. Plant Ecol.*, **4**, 91–99.

Li, Y., and N.-C. Lau, 2012a: Contributions of downstream eddy development to the teleconnection between ENSO and atmospheric circulation over the North Atlantic. *J. Clim.*, **25**, 4993–5010.

Li, Y., and N. Lau, 2012b: Impact of ENSO on the atmospheric variability over the north Atlantic in late winter-Role of transient eddies. *J. Clim.*, **25**, 320–342.

Lian, T., and D. Chen, 2012: An evaluation of rotated EOF analysis and its application to tropical Pacific SST variability. *J. Clim.*, **25**, 5361–5373.

Lin, H., and Z. Wu, 2012: Indian summer monsoon influence on the climate in the North Atlantic–European region. *Clim. Dyn.*, **39**, 303–311.

Liu, B., M. Xu, and M. Henderson, 2011: Where have all the showers gone? Regional declines in light precipitation events in China, 1960–2000. *Int. J. Climatol.*, **31**, 1177–1191.

Liu, J., B. Wang, Q. H. Ding, X. Y. Kuang, W. L. Soon, and E. Zorita, 2009a: Centennial variations of the global monsoon precipitation in the last millennium: Results from ECHO-G model. *J. Clim.*, **22**, 2356–2371.

Liu, Y., J. Sun, and B. Yang, 2009b: The effects of black carbon and sulfate aerosols in China regions on East Asian monsoon. *Tellus B*, **61**, 642–656.

Loschnigg, J., G. Meehl, P. Webster, J. Arblaster, and G. Compo, 2003: The Asian monsoon, the tropospheric biennial oscillation, and the Indian Ocean zonal mode in the NCAR CSM. *J. Clim.*, **16**, 1617–1642.

Lu, J., G. A. Vecchi, and T. Reichler, 2007: Expansion of the Hadley cell under global warming. *Geophys. Res. Lett.*, **34**, doi: 10.1029/2006gl028443.

Mann, M. E., and K. A. Emanuel, 2006: Atlantic hurricane trends linked to climate change. *Eos Trans. (AGU)*, **87**, 233–241.

Mann, M. E., T. A. Sabbatelli, and U. Neu, 2007a: Evidence for a modest undercount bias in early historical Atlantic tropical cyclone counts. *Geophys. Res. Lett.*, **34**, L22707.

Mann, M. E., K. A. Emanuel, G. J. Holland, and P. J. Webster, 2007b: Atlantic tropical cyclones revisited. *Eos Trans. (AGU)*, **88**, 349–350.

Marengo, J., et al., 2010: Recent developments on the South American Monsoon system. *Int. J. Climatol.*, **32**, 1–21.

Marengo, J. A., J. Tomasella, L. M. Alves, W. R. Soares, and D. A. Rodriguez, 2011: The drought of 2010 in the context of historical droughts in the Amazon region. *Geophys. Res. Lett.*, **38**, L12703.

Marengo, J. A., et al., 2008: The drought of Amazonia in 2005. *J. Clim.*, **21**, 495–516.

Mariotti, A., and A. Dell'Aquila, 2012: Decadal climate variability in the Mediterranean region: Roles of large-scale forcings and regional processes. *Clim. Dyn.*, **38**, 1129–1145.

Marshall, G. J., 2007: Half-century seasonal relationships between the Southern Annular Mode and Antarctic temperatures. *Int. J. Climatol.*, **27**, 373–383.

Marshall, G. J., S. di Battista, S. S. Naik, and M. Thamban, 2011: Analysis of a regional change in the sign of the SAM-temperature relationship in Antarctica. *Clim. Dyn.*, **36**, 277–287.

Marullo, S., V. Artale, and R. Santoleri, 2011: The SST multidecadal variability in the Atlantic–Mediterranean region and its relation to AMO. *J. Clim.*, **24**, 4385–4401.

Maue, R., 2011: Recent historically low global tropical cyclone activity. *Geophys. Res. Lett.*, **38**, doi: 10.1029/2011GL047711.

McDonald, R., D. Bleaken, D. Cresswell, V. Pope, and C. Senior, 2005: Tropical storms: Representation and diagnosis in climate models and the impacts of climate change. *Clim. Dyn.*, **25**, 19–36.

McKee, D. C., X. Yuan, A. L. Gordon, B. A. Huber, and Z. Dong, 2011: Climate impact on interannual variability of Weddell Sea Bottom Water. *J. Geophys. Res.*, **116**, doi: 10.1029/2010jc006484.

McPhaden, M. J., T. Lee, and D. McClurg, 2011: El Nino and its relationship to changing background conditions in the tropical Pacific Ocean. *Geophys. Res. Lett.*, **38**, doi: 10.1029/2011gl048275.

Meehl, G., and J. Arblaster, 2002a: The tropospheric biennial oscillation and Asian-Australian monsoon rainfall. *J. Clim.*, **15**, 722–744.

Meehl, G., and J. Arblaster, 2002b: Indian monsoon GCM sensitivity experiments testing tropospheric biennial oscillation transition conditions. *J. Clim.*, **15**, 923–944.

Meehl, G., and J. Arblaster, 2011: Decadal Variability of Asian-Australian Monsoon-ENSO-TBO Relationships. *J. Clim.*, **24**, 4925–4940.

Meehl, G., J. Arblaster, and J. Loschnigg, 2003: Coupled ocean-atmosphere dynamical processes in the tropical Indian and Pacific Oceans and the TBO. *J. Clim.*, **16**, 2138–2158.

Meehl, G., A. Hu, and C. Tebaldi, 2010: Decadal prediction in the Pacific Region. *J. Clim.*, **23**, 2959–2973.

Meehl, G. A., 1987: The annual cycle and interannual variability in the tropical Pacific and Indian-Ocean regions. *Mon. Weather Rev.*, **115**, 27–50.

Meehl, G. A., 1994a: Coupled land-ocean-atmosphere processes and south Asian monsoon variability. *Science*, **266**, 263–267.

Meehl, G. A., 1994b: Influence of the land-surface in the Asian summer monsoon - external conditions versus internal feedbacks. *J. Clim.*, **7**, 1033–1049.

Meehl, G. A., 1997: The south Asian monsoon and the tropospheric biennial oscillation. *J. Clim.*, **10**, 1921–1943.

Meehl, G. A., and J. M. Arblaster, 2012: Relating the strength of the tropospheric biennial oscillation (TBO) to the phase of the Interdecadal Pacific Oscillation (IPO). *Geophys. Res. Lett.*, **39**, L20716.

Metcalfe, S. E., M. D. Jones, S. J. Davies, A. Noren, and A. MacKenzie, 2010: Climate variability over the last two millennia in the North American Monsoon, recorded in laminated lake sediments from Laguna de Juanacatlan, Mexico. *Holocene*, **20**, 1195–1206.

Mo, K. C., 2010: Interdecadal Modulation of the Impact of ENSO on Precipitation and Temperature over the United States. *J. Clim.*, **23**, 3639–3656.

Mohapatra, M., B. K. Bandyopadhyay, and A. Tyagi, 2011: Best track parameters of tropical cyclones over the North Indian Ocean: A review. *Nat. Hazards*, doi:10.1007/s11069–011–9935–0.

Mooley, D. A., and B. Parthasarathy, 1983: Variability of the Indian-summer monsoon and tropical circulation features. *Mon. Weather Rev.*, **111**, 967–978.

MÜller, W. A., and E. Roeckner, 2008: ENSO teleconnections in projections of future climate in ECHAM5/MPI-OM. *Clim. Dyn.*, **31**, 533–549.

Mumby, P., R. Vitolo, and D. Stephenson, 2011: Temporal clustering of tropical cyclones and its ecosystem impacts. *Proc. Natl. Acad. Sci. U.S.A.*, **108**, 17626–17630.

Murakami, H., R. Mizuta, and E. Shindo, 2011: Future changes in tropical cyclone activity projected by multi-physics and multi-SST ensemble experiments using the 60-km-mesh MRI-AGCM. *Clim. Dyn.*, doi:10.1007/s00382–011–1223–x.

Murakami, H., M. Sugi, and A. Kitoh, 2013: Future changes in tropical cyclone activity in the North Indian Ocean projected by high-resolution MRI-AGCMs. *Clim. Dyn.*, **40**, 1949–1968.

Murakami, H., et al., 2012: Future changes in tropical cyclone activity projected by the new high-resolution MRI-AGCM. *J. Clim.*, **25**, 3237–3260.

Na, H., B.-G. Jang, W.-M. Choi, and K.-Y. Kim, 2011: Statistical simulations of the future 50–year statistics of cold-tongue El Niño and warm-pool El Niño. *Asia-Pacif. J. Atmos. Sci.*, **47**, 223–233.

Nanjundiah, R., V. Vidyunmala, and J. Srinivasan, 2005: The impact of increase in CO_2 on the simulation of tropical biennial oscillations (TBO) in 12 coupled general circulation models. *Atmos. Sci. Lett.*, **6**, 183–191.

Newman, M., S. Shin, and M. Alexander, 2011: Natural variation in ENSO flavors. *Geophys. Res. Lett.*, **38**.

Nicholls, N., 1978: Air-sea interaction and Quasi-Biennial Oscillation. *Mon. Weather Rev.*, **106**, 1505–1508.

Nieto-Ferreira, R., and T. Rickenbach, 2010: Regionality of monsoon onset in South America: A three-stage conceptual model. *Int. J. Climatol.*, **31**, 1309–1321.

Nuñez, M. N., S. A. Solman, and M. F. Cabre, 2009: Regional climate change experiments over southern South America. II: Climate change scenarios in the late twenty-first century. *Clim. Dyn.*, **32**, 1081–1095.

Ogasawara, N., A. Kitoh, T. Yasunari, and A. Noda, 1999: Tropospheric biennial oscillation of ENSO-monsoon system in the MRI coupled GCM. *J. Meteorol. Soc. Jpn.*, **77**, 1247–1270.

Oouchi, K., J. Yoshimura, H. Yoshimura, R. Mizuta, S. Kusunoki, and A. Noda, 2006: Tropical cyclone climatology in a global-warming climate as simulated in a 20 km-mesh global atmospheric model: Frequency and wind intensity analyses. *J. Meteorol. Soc. Jpn.*, **84**, 259–276.

Pezzi, L. P., and I. F. A. Cavalcanti, 2001: The relative importance of ENSO and tropical Atlantic sea surface temperature anomalies for seasonal precipitation over South America: A numerical study. *Clim. Dyn.*, **17**, 205–212.

Pinto, J., and C. Raible, 2012: Past and recent changes in the North Atlantic oscillation. *Clim. Change*, **3**, 79–90.

Power, S., T. Casey, C. Folland, A. Colman, and V. Mehta, 1999: Inter-decadal modulation of the impact of ENSO on Australia. *Clim. Dyn.*, **15**, 319–324.

Qian, W., J. Fu, and Z. Yan, 2007a: Decrease of light rain events in summer associated with a warming environment in China during 1961–2005. *Geophys. Res. Lett.*, **34**, L11705.

Qian, Y., D. P. Kaiser, L. R. Leung, and M. Xu, 2006: More frequent cloud-free sky and less surface solar radiation in China from 1955 to 2000. *Geophys. Res. Lett.*, **33**, doi: 10.1029/2005GL024586.

Qian, Y., W. G. Wang, L. R. Leung, and D. P. Kaiser, 2007b: Variability of solar radiation under cloud-free skies in China: The role of aerosols. *Geophys. Res. Lett.*, **34**, doi: 10.1029/2006GL028800.

Qian, Y., D. Gong, J. Fan, L. R. Leung, R. Bennartz, D. Chen, and W. Wang, 2009: Heavy pollution suppresses light rain in China: Observations and modeling. *J. Geophys. Res*, **114**, D00K02.

Quintana, J. M., and P. Aceituno, 2012: Changes in the rainfall regime along the extratropical west coast of South America (Chile): 30–43°S. *Atmosfera*, **25**, 1–22.

Raia, A., and I. F. A. Cavalcanti, 2008: The life cycle of the South American Monsoon System. *J. Clim.*, **21**, 6227–6246.

Ramsay, H. A., and A. H. Sobel, 2011: The effects of relative and absolute sea surface temperature on tropical cyclone potential intensity using a single column model. *J. Clim.*, **24**, 183–193.

Rao, V. B., C. C. Ferreira, S. H. Franchito, and S. S. V. S. Ramakrishna, 2008: In a changing climate weakening tropical easterly jet induces more violent tropical storms over the north Indian Ocean. *Geophys. Res. Lett.*, **35**, L15710.

Raphael, M. N., and M. M. Holland, 2006: Twentieth century simulation of the southern hemisphere climate in coupled models. Part 1: Large scale circulation variability. *Clim. Dyn.*, **26**, 217–228.

Rappin, E. D., D. S. Nolan, and K. A. Emanuel, 2010: Thermodynamic control of tropical cyclogenesis in environments of radiative-convective equilibrium with shear. *Q. J. R. Meteorol. Soc.*, **136**, 1954–1971.

Reboita, M. S., T. Ambrizzi, and R. P. da Rocha, 2009: Relationship between the southern annular mode and southern hemisphere atmospheric systems. *Rev. Brasil. Meteorol*., **24,** doi: 10.1590/S0102-77862009000100005.

Renom, M., M. Rusticucci, and M. Barreiro, 2011: Multidecadal changes in the relationship between extreme temperature events in Uruguay and the general atmospheric circulation. *Clim. Dyn.*, doi:10.1007/s00382-010-0986-9.

Ronchail, J., and R. Gallaire, 2006: ENSO and rainfall along the Zongo valley (Bolivia) from the Altiplano to the Amazon basin. *Int. J. Climatol.*, **26**, 1223–1236.

Saji, N. H., and T. Yamagata, 2003: Possible impacts of Indian Ocean Dipole mode events on global climate. *Clim. Res.*, **25**, 151–169.

Saji, N. H., T. Ambrizzi, and S. E. T. Ferraz, 2005: Indian Ocean Dipole mode events and austral surface air temperature anomalies. *Dyn. Atmos. Oceans*, **39**, 87–101.

Saji, N. H., B. N. Goswami, P. N. Vinayachandran, and T. Yamagata, 1999: A dipole mode in the tropical Indian Ocean. *Nature*, **401**, 360–363.

Salazar, L. F., C. A. Nobre, and M. D. Oyama, 2007: Climate change consequences on the biome distribution in tropical South America. *Geophys. Res. Lett.*, **34**, doi: 10.1029/2007gl029695.

Sampaio, G., C. Nobre, M. H. Costa, P. Satyamurty, B. S. Soares, and M. Cardoso, 2007: Regional climate change over eastern Amazonia caused by pasture and soybean cropland expansion. *Geophys. Res. Lett.*, **34**, doi: 10.1029/2007gl030612.

Santer, B., et al., 2006: Forced and unforced ocean temperature changes in Atlantic and Pacific tropical cyclogenesis regions. *Proc. Natl. Acad. Sci. U.S.A.*, **103**, 13905–13910.

Satyamurty, P., A. A. de Castro, J. Tota, L. E. D. Gularte, and A. O. Manzi, 2010: Rainfall trends in the Brazilian Amazon Basin in the past eight decades. *Theor. Appl. Climatol.*, **99**, 139–148.

Seager, R., et al., 2009: Mexican drought: An observational modeling and tree ring study of variability and climate change. *Atmosfera*, **22**, 1–31.

Seierstad, I., D. Stephenson, and N. Kvamsto, 2007: How useful are teleconnection patterns for explaining variability in extratropical storminess ? *Tellus A*, **59**, 170–181.

Semmler, T., S. Varghese, R. McGrath, P. Nolan, S. Wang, P. Lynch, and C. O'Dowd, 2008: Regional climate model simulations of North Atlantic cyclones: Frequency and intensity changes. *Clim. Res.*, **36**, 1–16.

Seneviratne, S. I., et al., 2012: Changes in climate extremes and their impacts on the natural physical environment. In: *Managing the Risks of Extreme Events and Disasters to Advance Climate Change Adaptation*. *A Special Report of Working Groups I and II of the Intergovernmental Panel on Climate Change (IPCC)* [C. B. Field, V. Barros, T. F. Stocker, D. Qin, D. J. Dokken, K. L. Ebi, M. D. Mastrandrea, K. J. Mach, G. -K. Plattner, S. K. Allen, M. Tignor, and P. M. Midgley (eds.)]. Cambridge University Press, Cambridge, United Kingdom and New York, NY, USA, pp. 109–230.

Seth, A., M. Rojas, and S. A. Rauscher, 2010: CMIP3 projected changes in the annual cycle of the South American Monsoon. *Clim. Change*, **98**, 331–357.

Seth, A., S. A. Rauscher, M. Rojas, A. Giannini, and S. J. Camargo, 2011: Enhanced spring convective barrier for monsoons in a warmer world? *Clim. Change*, **104**, 403–414.

Shaman, J., and E. Tziperman, 2011: An atmospheric teleconnection linking ENSO and Southwestern European precipitation. *J. Clim.*, **24**, 124–139.

Silva, A. E., and L. M. V. Carvalho, 2007: Large-scale index for South America Monsoon (LISAM). *Atmos. Sci. Lett.*, **8**, 51–57.

Silvestri, G., and C. Vera, 2009: Nonstationary Impacts of the Southern Annular Mode on Southern Hemisphere Climate. *J. Clim.*, **22**, 6142–6148.

Singh, A., T. Delcroix, and S. Cravatte, 2011: Contrasting the flavors of El Nino-Southern Oscillation using sea surface salinity observations. *J. Geophys. Res. Oceans*, **116**, doi: 10.1029/2010JC006862.

Sobel, A. H., I. M. Held, and C. S. Bretherton, 2002: The ENSO Signal in Tropical Tropospheric Temperature. *J. Clim.*, **15**, 2702–2706.

Song, J., Y. Wang, and L. Wu, 2010: Trend discrepancies among three best track data sets of western North Pacific tropical cyclones. *J. Geophys. Res. Atmos.*, **115**, doi: 10.1029/2009JD013058.

SÖrensson, A. A., and C. G. Menendez, 2011: Summer soil–precipitation coupling in South America. *Tellus A*, **63**, 56–68.

Souza, P., and I. F. A. Cavalcanti, 2009: Atmospheric centres of action associated with the Atlantic ITCZ position. *Int. J. Climatol.*, **29**, 2091–2105.

Stowasser, M., Y. Wang, and K. Hamilton, 2007: Tropical cyclone changes in the western North Pacific in a global warming scenario. *J. Clim.*, **20**, 2378–2396.

Sugi, M., A. Noda, and N. Sato, 2002: Influence of the global warming on tropical cyclone climatology: An experiment with the JMA global model. *J. Meteorol. Soc. Jpn.*, **80**, 249–272.

Sugi, M., H. Murakami, and J. Yoshimura, 2009: A reduction in global tropical cyclone frequency due to global warming. *Sola*, **5**, 164–167.

Sutton, R. T., and B. Dong, 2012: Atlantic Ocean influence on a shift in European climate in the 1990s. *Nature Geosci.*, **5**, 788–792.

Takahashi, K., A. Montecinos, K. Goubanova, and B. Dewitte, 2011: ENSO regimes: Reinterpreting the canonical and Modoki El Nino. *Geophys. Res. Lett.*, **38**, doi: 10.1029/2011gl047364.

Taschetto, A. S., and M. H. England, 2009: El Nino Modoki Impacts on Australian Rainfall. *J. Clim.*, **22**, 3167–3174.

Taschetto, A. S., C. C. Ummenhofer, A. Sen Gupta, and M. H. England, 2009: Effect of anomalous warming in the central Pacific on the Australian monsoon. *Geophys. Res. Lett.*, **36**, doi: 10.1029/2009gl038416.

Tedeschi, R. G., I. F. A. Cavalcanti, and A. M. Grimm, 2013: Influences of two types of ENSO on South American precipitation. *Int. J. Climatol.*, **33**, 1382–1400.

Thompson, D. W. J., S. Solomon, P. J. Kushner, M. H. England, K. M. Grise, and D. J. Karoly, 2011: Signatures of the Antarctic ozone hole in Southern Hemisphere surface climate change. *Nature Geosci.*, **4**, 741–749.

Ting, M., Y. Kushnir, R. Seager, and C. Li, 2009: Forced and internal twentieth-century SST trends in the north Atlantic. *J. Clim.*, **22**, 1469–1481.

Tomasella, J., L. S. Borma, J. A. Marengo, D. A. Rodriguez, L. A. Cuartas, C. A. Nobre, and M. C. R. Prado, 2011: The droughts of 1996–1997 and 2004–2005 in Amazonia: Hydrological response in the river main-stem. *Hydrological Processes*, **25**, 1228–1242.

Trenberth, K. E., 1975: A quasi-biennial standing wave in the Southern Hemisphere and interrelations with sea surface temperature. *Q. J. R. Meteorol. Soc.*, **101**, 55–74.

Trenberth, K. E., and D. P. Tepaniak, 2001: Indices of El Nino evolution. *J. Clim.*, **14**, 1697–1701.

Trenberth, K. E., and D. J. Shea, 2006: Atlantic hurricanes and natural variability in 2005. *Geophys. Res. Lett.*, **33**, L12704.

Trenberth, K. E., and J. T. Fasullo, 2012: Climate extremes and climate change: The Russian heat wave and other climate extremes of 2010. *J. Geophys. Res. Atmos.*, **117**, doi: 10.1029/2012jd018020.

Trenberth, K. E., D. P. Stepaniak, and J. M. Caron, 2000: The global monsoon as seen through the divergent atmospheric circulation. *J. Clim.*, **13**, 3969–3993.

Troup, A., 1965: Southern Oscillation. *Q. J. R. Meteorol. Soc.*, **91**, 490–&.

Tsutsui, J., 2010: Changes in potential intensity of tropical cyclones approaching Japan due to anthropogenic warming in sea surface and upper-air temperatures. *J. Meteorol. Soc. Jpn. II*, **88**, 263–284.

Tsutsui, J., 2012: Estimation of changes in tropical cyclone intensities and associated precipitation extremes due to anthropogenic climate change. In: *Cyclones: Formation, Triggers and Control* [K. Oouchi and H. Fudeyasu (eds.)]. Nova Science Publishers, Hauppauge, NY, USA, pp. 125–143.

Tu, J., C. Chou, and P. Chu, 2009: The Abrupt Shift of Typhoon Activity in the Vicinity of Taiwan and Its Association with Western North Pacific-East Asian Climate Change. *J. Clim.*, **22**, 3617–3628.

Turner, A., K. Sperber, J. Slingo, G. A. Meehl, C. R. Mechoso, M. Kimoto, and A. Giannini, 2011: Modelling monsoons: Understanding and predicting current and future behaviour. World Scientific Series on Asia-Pacific Weather and Climate, Vol. 5. *The Global Monsoon System: Research and Forecast* ,2nd ed. [C. P. Chang, Y. Ding, N.-C. Lau, R. H. Johnson, B. Wang and T. Yasunari (eds.)]. World Scientific, Singapore, p 421-454.

Turner, A. G., P. M. Inness, and J. M. Slingo, 2007: The effect of doubled CO_2 and model basic state biases on the monsoon-ENSO system. I: Mean response and interannual variability. *Q. J. R. Meteorol. Soc.*, **133**, 1143–1157.

van Loon, H., G. A. Meehl, and J. M. Arblaster, 2004: A decadal solar effect in the tropics in July-August. *J. Atmos. Solar-Terres. Phys.*, **66**, 1767–1178.

Vasconcellos, F. C., and I. F. A. Cavalcanti, 2010: Extreme precipitation over Southeastern Brazil in the austral summer and relations with the Southern Hemisphere annular mode. *Atmos. Sci. Lett.*, **11**, 21–26.

Vecchi, G., and T. Knutson, 2011: Estimating annual numbers of Atlantic hurricanes missing from the HURDAT database (1878–1965) using ship track density. *J. Clim.*, **24**, 1736–1746.

Vecchi, G. A., and B. J. Soden, 2007a: Increased tropical Atlantic wind shear in model projections of global warming. *Geophys. Res. Lett.*, **34**, L08702.

Vecchi, G. A., and B. J. Soden, 2007b: Effect of remote sea surface temperature change on tropical cyclone potential intensity. *Nature*, **450**, 1066–1069.

Vecchi, G. A., and T. R. Knutson, 2008: On estimates of historical North Atlantic tropical cyclone activity. *J. Clim.*, **21**, 3580–3600.

Vecchi, G. A., K. L. Swanson, and B. J. Soden, 2008: Whither hurricane activity. *Science*, **322**, 687-689.

Vera, C., and G. Silvestri, 2009: Precipitation interannual variability in South America from the WCRP-CMIP3 multi-model dataset. *Clim. Dyn.*, **32**, 1003–1014.

Vera, C., et al., 2006: Toward a unified view of the American Monsoon Systems. *J. Clim.*, **19**, 4977–5000.

Vicente-Serrano, S., and J. LÓpez-Moreno, 2008: Nonstationary influence of the North Atlantic Oscillation on European precipitation. *J. Geophys. Res.*, **113**, doi: 10.1029/2008JD010382.

Vicuña, S., R. Garreaud, and J. McPhee, 2011: Climate change impacts on the hydrology of a snowmelt driven basin in semiarid Chile. *Clim. Change*, **105**, 469–488.

Villarini, G., and G. A. Vecchi, 2012: Twenty-first-century projections of North Atlantic tropical storms from CMIP5 models. *Nature Clim. Change*, **2**, 604–607.

Villarini, G., G. Vecchi, T. Knutson, M. Zhao, and J. Smith, 2011: North Atlantic tropical storm frequency response to anthropogenic forcing: Projections and sources of uncertainty. *J. Clim.*, **24**, 3224–3238.

Vuille, M., B. Francou, P. Wagnon, I. Juen, G. Kaser, B. G. Mark, and R. S. Bradley, 2008: Climate change and tropical Andean glaciers: Past, present and future. *Earth Sci. Rev.*, **89**, 79–96.

Walsh, K., K. Nguyen, and J. McGregor, 2004: Fine-resolution regional climate model simulations of the impact of climate change on tropical cyclones near Australia. *Clim. Dyn.*, **22**, 47–56.

Wang, B., and LinHo, 2002: Rainy season of the Asian-Pacific summer monsoon. *J. Clim.*, **15**, 386–398.

Wang, B., and Q. Ding, 2008: Global monsoon: Dominant mode of annual variation in the tropics. *Dyn. Atmos. Oceans*, **44**, 165–183.

Wang, B., Y. Yang, Q. Ding, H. Murakami, and F. Huang, 2010: Climate control of the global tropical storm days (1965–2008). *Geophys. Res. Lett.*, **37**, doi: 10.1029/2010GL042487.

Wang, B., Z. Wu, J. Li, J. Liu, C.-P. Chang, Y. Ding, and G. Wu, 2008: How to measure the strength of the East Asian summer monsoon. *J. Clim.*, **21**, 4449–4463.

Wang, C., and S. Lee, 2008: Global warming and United States landfalling hurricanes. *Geophys. Res. Lett.*, **35**, doi: 10.1029/2007GL032396.

Wang, G., and H. H. Hendon, 2007: Sensitivity of Australian rainfall to inter-El Nino variations. *J. Clim.*, **20**, 4211–4226.

Wang, H., 2001: The weakening of the Asian monsoon circulation after the end of 1970's. *Adv. Atmos. Sci.*, **18**, 376–386.

Wang, H., J. Sun, and K. Fan, 2007: Relationships between the North Pacific Oscillation and the typhoon/hurricane frequencies. *Sci. China D Earth Sci.*, **50**, 1409–1416.

Wang, R., L. Wu, and C. Wang, 2011: Typhoon track changes associated with global warming. *J. Clim.*, **24**, 3748–3752.

Wang, Y., and L. Zhou, 2005: Observed trends in extreme precipitation events in China during 1961–2001 and the associated changes in large-scale circulation. *Geophys. Res. Lett.*, **32**, L09707.

Watterson, I. G., 2009: Components of precipitation and temperature anomalies and change associated with modes of the Southern Hemisphere. *Int. J. Climatol.*, **29**, 809–826.

Webster, P., G. Holland, J. Curry, and H. Chang, 2005: Changes in tropical cyclone number, duration, and intensity in a warming environment. *Science*, **309**, 1844–1846.

Webster, P. J., A. M. Moore, J. P. Loschnigg, and R. R. Leben, 1999: Coupled ocean-atmosphere dynamics in the Indian Ocean during 1997–98. *Nature*, **401**, 356–360.

Weinkle, J., R. Maue, and R. Pielke, 2012: Historical global tropical cyclone landfalls. *J. Clim.*, **25**, 4729–4735.

Wing, A. A., A. H. Sobel, and S. J. Camargo, 2007: Relationship between the potential and actual intensities of tropical cyclones on interannual time scales. *Geophys. Res. Lett.*, **34**, L08810.

Woollings, T., A. Hannachi, B. Hoskins, and A. Turner, 2010a: A regime view of the North Atlantic Oscillation and Its response to anthropogenic forcing. *J. Clim.*, **23**, 1291–1307.

Woollings, T., A. Charlton-Perez, S. Ineson, A. G. Marshall, and G. Masato, 2010b: Associations between stratospheric variability and tropospheric blocking. *J. Geophys. Res. Atmos.*, **115**, D06108.

Wu, L., B. Wang, and S. Geng, 2005: Growing typhoon influence on east Asia. *Geophys. Res. Lett.*, **32**, doi: 10.1029/2005GL022937.

Wu, R., and B. Kirtman, 2004: Impacts of the Indian Ocean on the Indian summer monsoon-ENSO relationship. *J. Clim.*, **17**, 3037–3054.

Xie, S. P. D., C. Deser, G. A. Vecchi, J. Ma, H. Teng, and A. T. Wittenberg, 2010: Global warming pattern formation: Sea surface temperature and rainfall. *J. Clim.*, **23**, 966–986.

Xu, M., C. Chang, C. Fu, Y. Qi, A. Robock, D. Robinson, and H. Zhang, 2006: Steady decline of east Asian monsoon winds, 1969–2000: Evidence from direct ground measurements of wind speed. *J. Geophys. Res. Atmos.*, doi:10.1029/2006JD007337.

Yamada, Y., K. Oouchi, M. Satoh, H. Tomita, and W. Yanase, 2010: Projection of changes in tropical cyclone activity and cloud height due to greenhouse warming: Global cloud-system-resolving approach. *Geophys. Res. Lett.*, **37**, L07709.

Yeh, S.-W., B. P. Kirtman, J.-S. Kug, W. Park, and M. Latif, 2011: Natural variability of the central Pacific El Nino event on multi-centennial timescales. *Geophys. Res. Lett.*, **38**, L02704.

Yeh, S. W., J. S. Kug, B. Dewitte, M. H. Kwon, B. P. Kirtman, and F. F. Jin, 2009: El Nino in a changing climate. *Nature*, **461**, 511–515.

Yokoi, S., and Y. Takayabu, 2009: Multi-model projection of global warming impact on tropical cyclone genesis frequency over the western north Pacific. *J. Meteorol. Soc. Jpn.*, **87**, 525–538.

Yoon, J. H., and N. Zeng, 2010: An Atlantic influence on Amazon rainfall. *Clim. Dyn.*, **34**, 249–264.

Yoshimura, J., M. Sugi, and A. Noda, 2006: Influence of greenhouse warming on tropical cyclone frequency. *J. Meteorol. Soc. Jpn.*, **84**, 405–428.

Yu, J., Y. Wang, and K. Hamilton, 2010a: Response of tropical cyclone potential intensity to a global warming scenario in the IPCC AR4 CGCMs. *J. Clim.*, **23**, 1354–1373.

Yu, J. Y., H. Y. Kao, and T. Lee, 2010b: Subtropics-related interannual sea surface temperature variability in the central equatorial Pacific. *J. Clim.*, **23**, 2869–2884.

Yu, J. Y., H. Y. Kao, T. Lee, and S. T. Kim, 2011: Subsurface ocean temperature indices for Central-Pacific and Eastern-Pacific types of El Nio and La Nia events. *Theor. Appl. Climatol.*, **103**, 337–344.

Yu, R., J. Li, W. Yuan, and H. Chen, 2010c: Changes in characteristics of late-summer precipitation over eastern China in the past 40 years revealed by hourly precipitation data. *J. Clim.*, **23**, 3390–3396.

Yu, R. C., and T. J. Zhou, 2007: Seasonality and three-dimensional structure of interdecadal change in the East Asian monsoon. *J. Clim.*, **20**, 5344–5355.

Yu, R. C., B. Wang, and T. J. Zhou, 2004: Tropospheric cooling and summer monsoon weakening trend over East Asia. *Geophys. Res. Lett.*, **31**, L22212.

Zhai, P., X. Zhang, H. Wan, and X. Pan, 2005: Trends in total precipitation and frequency of daily precipitation extremes over China. *J. Clim.*, **18**, 1096–1108.

Zhang, H., Z. Wang, and P. Guo, 2009: A modeling study of the effects of direct radiative forcing due to carbonaceous aerosol on the climate in East Asia. *Adv. Atmos. Sci.*, **26**, 57–66.

Zhang, R., and T. L. Delworth, 2009: A new method for attributing climate variations over the Atlantic Hurricane Basin's main development region. *Geophys. Res. Lett.*, **36**, L06701.

Zhang, Y., T. Li, and B. Wang, 2004: Decadal change of the spring snow depth over the Tibetan Plateau: The associated circulation and influence on the East Asian summer monsoon. *J. Clim.*, **17**, 2780–2793.

Zhang, Y. C., X. Y. Kuang, W. D. Guo, and T. J. Zhou, 2006: Seasonal evolution of the upper-tropospheric westerly jet core over East Asia. *Geophys. Res. Lett.*, **33**, L11708.

Zhao, C., X. Liu, and L. R. Leung, 2012: Impact of desert dust on the summer monsoon system over Southwestern North America. *Atmos. Chem. Phys.*, **12**, 3717–3731.

Zhao, M., and I. M. Held, 2010: An analysis of the effect of global warming on the intensity of Atlantic hurricanes using a GCM with statistical refinement. *J. Clim.*, **23**, 6382–6393.

Zhao, M., and I. Held, 2012: TC-permitting GCM simulations of hurricane frequency response to sea surface temperature anomalies projected for the late twenty-first century. *J. Clim.*, **25**, 2995–3009.

Zhao, M., I. M. Held, S. J. Lin, and G. A. Vecchi, 2009: Simulations of global hurricane climatology, interannual variability, and response to global warming using a 50-km resolution GCM. *J. Clim.*, **22**, 6653–6678.

Zhou, T., and J. Zhang, 2009: Harmonious inter-decadal changes of July-August upper tropospheric temperature across the north Atlantic, Eurasian continent, and north Pacific. *Adv. Atmos. Sci.*, **26**, 656–665.

Zhou, T., R. Yu, H. Li, and B. Wang, 2008: Ocean forcing to changes in global monsoon precipitation over the recent half-century. *J. Clim.*, **21**, 3833–3852.

Zhou, T., et al., 2009a: Why the western Pacific subtropical high has extended westward since the late 1970s. *J. Clim.*, **22**, 2199–2215.

Zhou, T. J., and L. W. Zou, 2010: Understanding the predictability of East Asian summer monsoon from the reproduction of land-sea thermal contrast change in AMIP-type simulation. *J. Clim.*, **23**, 6009–6026.

Zhou, T. J., D. Y. Gong, J. Li, and B. Li, 2009b: Detecting and understanding the multi-decadal variability of the East Asian Summer Monsoon - Recent progress and state of affairs. *Meteorol. Z.*, **18**, 455–467.

Zhu, C., B. Wang, W. Qian, and B. Zhang, 2012: Recent weakening of northern East Asian summer monsoon: A possible response to global warming. *Geophys. Res. Lett.*, **39**, doi: 10.1029/2012GL051155.